

THEORETICAL NEUROSCIENCE

Peter Dayan and L.F. Abbott

Preface

PART I - ANALYZING AND MODELING NEURAL RESPONSES

Chapter 1 - Neural Encoding I: Firing Rates and Spike Statistics

Introduction

- Properties of Neurons
- Recording Neuronal Responses
- From Stimulus to Response

Spike Trains and Firing Rates

- Measuring Firing Rates
- Tuning Curves
- Spike-Count Variability

What Makes a Neuron Fire?

- Describing the Stimulus
- The Spike-Triggered Average
- White-Noise Stimuli
- Multiple-Spike-Triggered Averages and Spike-Triggered Correlations

Spike Train Statistics

- The Homogeneous Poisson Process
- The Spike-Train Autocorrelation Function
- The Inhomogeneous Poisson Process
- The Poisson Spike Generator
- Comparison with Data

The Neural Code

- Independent-Spike, Independent Neuron and Correlation Codes
- Temporal Codes

Chapter Summary

Appendices

- A) The Power Spectrum of White Noise
- B) Moments of the Poisson Distribution
- D) Inhomogeneous Poisson Statistics

Annotated Bibliography

Chapter 2 - Neural Encoding II: Reverse Correlation and Receptive Fields

Introduction

Estimating Firing Rates

- The Most Effective Stimulus
- Static Nonlinearities

Introduction to the Early Visual System

The Retinotopic Map

Visual Stimuli

The Nyquist Frequency

Reverse Correlation Methods - Simple Cells

Spatial Receptive Fields

Temporal Receptive Fields

Response of a Simple Cell to a Counterphase Grating

Space-Time Receptive Fields

Nonseparable Receptive Fields

Static Nonlinearities - Simple Cells

Static Nonlinearities - Complex Cells

Receptive Fields in the Retina and LGN

Constructing V1 Receptive Fields

Chapter Summary

Appendices

A) The Optimal Kernel

B) The Most Effective Stimulus

C) Bussgang's Theorem

Annotated Bibliography

Chapter 3 - Neural Decoding

Encoding and Decoding

Discrimination

ROC Curves

ROC Analysis of Motion Discrimination

The Likelihood Ratio Test

Population Decoding

Encoding and Decoding Direction

Optimal Decoding Methods

Fisher Information

Optimal Discrimination

Spike Train Decoding

Chapter Summary

Appendices

A) The Neymann-Pearson Lemma

B) The Cramér-Rao Bound

C) The Optimal Spike-Decoding Filter

Annotated Bibliography

Chapter 4 - Information Theory

Entropy and Mutual Information

Entropy

Mutual Information

Entropy and Mutual Information for Continuous Variables

Information and Entropy Maximization

- Entropy Maximization for a Single Neuron
- Populations of Neurons
- Application to Retinal Ganglion Cell Receptive Fields

- The Whitening Filter
- Filtering Input Noise

- Temporal Processing in the LGN
- Cortical Coding

- Entropy and Information for Spike Trains

- Chapter Summary

- Appendix

- Positivity of the Kulback-Leibler Divergence

- Annotated Bibliography

PART II - MODELING NEURONS AND NETWORKS

Chapter 5 - Model Neurons I: Neuroelectronics

- Levels of Neuron Modeling
- Electrical Properties of Neurons
 - Intracellular Resistance
 - Membrane Capacitance and Resistance
 - Equilibrium and Reversal Potentials
 - The Membrane Current
- Single-Compartment Models
 - Integrate-and-Fire Models
 - Spike-Rate Adaptation and Refractoriness

- Voltage-Dependent Conductances
 - Persistent Conductances
 - Transient Conductances
 - Hyperpolarization-Activated Conductances

- The Hodgkin-Huxley Model

- Modeling Channels

- Synaptic Conductances

- The Postsynaptic Conductance
- Release Probability and Short-Term Plasticity

- Synapses on Integrate-and-Fire Neurons
 - Regular and Irregular Firing Modes

- Chapter Summary

- Appendices

- A) Integrating the Membrane Potential
- B) Integrating the Gating Variables

- Annotated Bibliography

Chapter 6 - Model Neurons II: Conductances and Morphology

Levels of Neuron Modeling

Conductance-Based Models

- The Connor-Stevens Model**
- Postinhibitory Rebound and Bursting**

The Cable Equation

- Linear Cable Theory**
- An Infinite Cable**
- An Isolated Branching Node**
- The Rall Model**
- The Morphoelectrotomographic Transform**

Multi-Compartment Models

- Action Potential Propagation Along an Unmyelinated Axon**
- Propagation Along a Myelinated Axon**

Chapter Summary

Appendices

- A) Gating Functions for Conductance-Based Models**
 - Connor-Stevens Model**
 - Transient Ca^{2+} Conductances**
 - Ca^{2+} -dependent K^+ Conductances**
- B) Integrating Multi-Compartment Models**

Annotated Bibliography

Chapter 7 - Network Models

Introduction

Firing-Rate Models

- Feedforward and Recurrent Networks**
- Continuously Labelled Networks**

Feedforward Networks

Neural Coordinate Transformations

Recurrent Networks

- Linear Recurrent Networks**
 - Selective Amplification**
 - Input Integration**
 - Continuous Linear Recurrent Networks**

Nonlinear Recurrent Networks

Nonlinear Amplification

- A Recurrent Model of Simple Cells in Primary Visual Cortex**
- A Recurrent Model of Complex Cells in Primary Visual Cortex**
- Winner-Take-All Input Selection**
- Gain Modulation**
- Sustained Activity**
- Maximum Likelihood and Network Recoding**
- Network Stability**

Associative Memory

Excitatory-Inhibitory Networks

Homogeneous Excitatory and Inhibitory Populations

Phase-Plane Methods and Stability Analysis

The Olfactory Bulb

Oscillatory Amplification

Stochastic Networks

Chapter Summary

Appendix

Lyapunov Function for the Boltzman Machine

Annotated Bibliography

PART III - PLASTICITY AND LEARNING

Chapter 8 - Plasticity and Learning

Introduction

 Stability and Competition

Synaptic Plasticity Rules

 The Basic Hebb Rule

 The Covariance Rule

 The BCM Rule

 Synaptic Normalization

 Subtractive Normalization

 Multiplicative Normalization and the Oja Rule

 Timing-Based Rules

Unsupervised Learning

 Single Postsynaptic Neuron

 Principal Component Projection

 Hebbian Development and Ocular Dominance

 Hebbian Development of Orientation Selectivity

 Temporoal Hebbian Rules and Trace Learning

 Multiple Postsynaptic Neurons

 Fixed Linear Recurrent Connections

 Competitive Hebbian Learning

 Feature-Based Models

 Anti-Hebbian Modification

 Timing-Based Plasticity and Prediction

Supervised Learning

 Supervised Hebbian Learning

 Classification and the Perceptron

 Function Approximation

 Supervised Error-Correcting Rules

 The Perceptron Learning Rule

 The Delta Rule

 Contrastive Hebbian Learning

Chapter Summary

Appendix

Convergence of the Perceptron Learning Rule

Annotated Bibliography

Chapter 9 - Classical Conditioning and Reinforcement Learning

Introduction

Classical Conditioning

Predicting Reward - The Rescola-Wagner Rule

Predicting Reward Timing - Temporal-Difference Learning

Dopamine and Prediction of Reward

Static Action Choice

The Indirect Actor

The Direct Actor

Sequential Action Choice

The Maze Task

Policy Evaluation

Policy Improvement

Generalizations of Actor-Critic Learning

Learning the Water Maze

Chapter Summary

Appendix - Markov Decision Problems

The Bellman Equation

Policy Iteration

Annotated Bibliography

Chapter 10 - Representational Learning

Introduction

Density Estimation

Factor Analysis

Principal Components Analysis

Clustering

Sparse Coding

Independent Components Analysis

Multi-Resolution and Wavelet Models

The Helmholtz Machine

Chapter Summary

Annotated Bibliography

Appendix - Mathematical Methods

Introduction

Linear Algebra

Differential Equations

Probability Theory

Fourier Transforms

[**Electrical Circuits**](#)
[**The \$\delta\$ Function**](#)
[**Lagrange Multipliers**](#)
[**Annotated Bibliography**](#)

Preface

Theoretical analysis and computational modeling are important tools for characterizing what nervous systems do, determining how they function, and understanding why they operate in particular ways. Neuroscience encompasses approaches ranging from molecular and cellular studies to human psychophysics and psychology. Theoretical neuroscience encourages cross-talk among these sub-disciplines by constructing compact representations of what has been learned, building bridges between different levels of description, and identifying unifying concepts and principles. In this book, we present the basic methods used for these purposes and discuss examples in which theoretical approaches have yielded insight into nervous system function.

The questions what, how, and why are addressed by descriptive, mechanistic, and interpretive models, each of which we discuss in the following chapters. Descriptive models summarize large amounts of experimental data compactly yet accurately, thereby characterizing what neurons and neural circuits do. These models may be based loosely on biophysical, anatomical, and physiological findings, but their primary purpose is to describe phenomena not to explain them. Mechanistic models, on the other hand, address the question of how nervous systems operate on the basis of known anatomy, physiology, and circuitry. Such models often form a bridge between descriptive models couched at different levels. Interpretive models use computational and information-theoretic principles to explore the behavioral and cognitive significance of various aspects of nervous system function, addressing the question of why nervous system operate as they do.

descriptive models

mechanistic models

interpretive models

It is often difficult to identify the appropriate level of modeling for a particular problem. A frequent mistake is to assume that a more detailed model is necessarily superior. Because models act as bridges between levels of understanding, they must be detailed enough to make contact with the lower level yet simple enough to yield clear results at the higher level.

Organization and Approach

This book is organized into three parts on the basis of general themes. Part I (chapters 1-4) is devoted to the coding of information by action potentials and the representation of information by populations of neurons with selective responses. Modeling of neurons and neural circuits on the basis of cellular and synaptic biophysics is presented in part II (chapters 5-7). The role of plasticity in development and learning is discussed in Part III (chapters 8-10). With the exception of chapters 5 and 6, which jointly cover neuronal modeling, the chapters are largely independent and can be selected and ordered in a variety of ways for a one- or two-semester course at either the undergraduate or graduate level.

Although we provide some background material, readers without previous exposure to neuroscience should refer to a neuroscience textbook such as Kandel, Schwartz & Jessell (2000); Nicholls, Martin & Wallace (1992); Bear, Connors & Paradiso (1996); Shepherd (1997); Zigmund, Bloom, Lansdell & Squire (1998); Purves et al (2000).

Theoretical neuroscience is based on the belief that methods of mathematics, physics, and computer science can elucidate nervous system function. Unfortunately, mathematics can sometimes seem more of an obstacle than an aid to understanding. We have not hesitated to employ the level of analysis needed to be precise and rigorous. At times, this may stretch the tolerance of some of our readers. We encourage such readers to consult the mathematical appendix, which provides a brief review of most of the mathematical methods used in the text, but also to persevere and attempt to understand the implications and consequences of a difficult derivation even if its steps are unclear.

Theoretical neuroscience, like any skill, can only be mastered with practice. We have provided exercises for this purpose on the web site for this book and urge the reader to do them. In addition, it will be highly instructive for the reader to construct the models discussed in the text and explore their properties beyond what we have been able to do in the available space.

Referencing

In order to maintain the flow of the text, we have kept citations within the chapters to a minimum. Each chapter ends with an annotated bibliography containing suggestions for further reading (which are denoted by a bold font), information about work cited within the chapter, and references to related studies. We concentrate on introducing the basic tools of computational neuroscience and discussing applications that we think best help the reader to understand and appreciate them. This means that a number of systems where computational approaches have been applied

with significant success are not discussed. References given in the annotated bibliographies lead the reader toward such applications. In most of the areas we cover, many people have provided critical insights. The books and review articles in the further reading category provide more comprehensive references to work that we apologetically have failed to cite.

Acknowledgments

We are extremely grateful to a large number of students at Brandeis, the Gatsby Computational Neuroscience Unit and MIT, and colleagues at many institutions, who have painstakingly read, commented on, and criticized, numerous versions of all the chapters. We particularly thank Bard Ermentrout, Mark Kvale, Mark Goldman, John Hertz, Zhaoping Li, Eve Marder, and Read Montague for providing extensive discussion and advice on the whole book. A number of people read significant portions of the text and provided valuable comments, criticism, and insight: Bill Bialek, Pat Churchland, Nathaniel Daw, Dawei Dong, Peter Földiák, Fabrizio Gabbiani, Zoubin Ghahramani, Geoff Goodhill, David Heeger, Geoff Hinton, Ken Miller, Tony Movshon, Phil Nelson, Sacha Nelson, Bruno Olshausen, Mark Plumbley, Alex Pouget, Fred Rieke, John Rinzel, Emilio Salinas, Sebastian Seung, Mike Shadlen, Satinder Singh, Rich Sutton, Nick Swindale, Carl Van Vreeswijk, Chris Williams, David Willshaw, Charlie Wilson, Angela Yu, and Rich Zemel. We have received significant additional assistance and advice from: Greg DeAngelis, Matt Beal, Sue Becker, Tony Bell, Paul Bressloff, Emery Brown, Matteo Carandini, Frances Chance, Yang Dan, Kenji Doya, Ed Erwin, John Fitzpatrick, David Foster, Marcus Frean, Ralph Freeman, Enrique Garibay, Frederico Girosi, Charlie Gross, Mike Jordan, Sham Kakade, Szabolcs Káli, Christof Koch, Simon Laughlin, John Lisman, Shawn Lockery, Guy Mayraz, Quaid Morris, Randy O'Reilly, Max Riesenhuber, Sam Roweis, Simon Osindero, Tomaso Poggio, Clay Reid, Dario Ringach, Horacio Rotstein, Lana Rutherford, Ken Sagino, Maneesh Sahani, Alexei Samsonovich, Idan Segev, Terry Sejnowski, Haim Sompolinsky, Fiona Stevens, David Tank, Alessandro Treves, Gina Turrigiano, David Van Essen, Martin Wainwright, Xiao-Jing Wang, Max Welling, Matt Wilson, Danny Young, and Ketchen Zhang. We apologise to anyone we may have inadvertently omitted from these lists. Karen Abbott provided valuable help with the figures. From MIT Press, we thank Michael Rutter for his patience and consistent commitment, and Sara Meiowitz and Larry Cohen for picking up where Michael left off.

Chapter 1

Neural Encoding I: Firing Rates and Spike Statistics

1.1 Introduction

Neurons are remarkable among the cells of the body in their ability to propagate signals rapidly over large distances. They do this by generating characteristic electrical pulses called action potentials, or more simply spikes, that can travel down nerve fibers. Neurons represent and transmit information by firing sequences of spikes in various temporal patterns. The study of neural coding, which is the subject of the first four chapters of this book, involves measuring and characterizing how stimulus attributes, such as light or sound intensity, or motor actions, such as the direction of an arm movement, are represented by action potentials.

The link between stimulus and response can be studied from two opposite points of view. Neural encoding, the subject of chapters 1 and 2, refers to the map from stimulus to response. For example, we can catalogue how neurons respond to a wide variety of stimuli, and then construct models that attempt to predict responses to other stimuli. Neural decoding refers to the reverse map, from response to stimulus, and the challenge is to reconstruct a stimulus, or certain aspects of that stimulus, from the spike sequences it evokes. Neural decoding is discussed in chapter 3. In chapter 4, we consider how the amount of information encoded by sequences of action potentials can be quantified and maximized. Before embarking on this tour of neural coding, we briefly review how neurons generate their responses and discuss how neural activity is recorded. The biophysical mechanisms underlying neural responses and action potential generation are treated in greater detail in chapters 5 and 6.

Properties of Neurons

Neurons are highly specialized for generating electrical signals in response to chemical and other inputs, and transmitting them to other cells. Some important morphological specializations, seen in the drawings of figure 1.1, are the dendrites that receive inputs from other neurons and the axon that carries the neuronal output to other cells. The elaborate branching structure of the dendritic tree allows a neuron to receive inputs from many other neurons through synaptic connections. The cortical pyramidal neuron of figure 1.1A and the cortical interneuron of figure 1.1C each receives thousands of synaptic inputs, and for the cerebellar Purkinje cell of figure 1.1B the number is over 100,000. Figure 1.1 does not show the full extent of the axons of these neurons. Axons from single neurons can traverse large fractions of the brain or, in some cases, of the entire body. In the mouse brain, it has been estimated that cortical neurons typically send out a total of about 40 mm of axon and have approximately 4 mm of total dendritic cable in their branched dendritic trees. The axon makes an average of 180 synaptic connections with other neurons per mm of length while the dendritic tree receives, on average, 2 synaptic inputs per μm . The cell body or soma of a typical cortical neurons ranges in diameter from about 10 to 50 μm .

Along with these morphological features, neurons have physiological specializations. Most prominent among these are a wide variety of membrane-spanning ion channels that allow ions, predominantly sodium (Na^+), potassium (K^+), calcium (Ca^{2+}), and chloride (Cl^-), to move into and out of the cell. Ion channels control the flow of ions across the cell membrane by opening and closing in response to voltage changes and both internal and external signals.

The electrical signal of relevance to the nervous system is the difference in electrical potential between the interior of a neuron and the surrounding extracellular medium. Under resting conditions, the potential inside the cell membrane of a neuron is about -70 mV relative to that of the surrounding bath (which is conventionally defined to be 0 mV), and the cell is said to be polarized. Ion pumps located in the cell membrane maintain concentration gradients that support this membrane potential difference. For example, Na^+ is much more concentrated outside a neuron than inside it, and the concentration of K^+ is significantly higher inside the neuron than in the extracellular medium. Ions thus flow into and out of a cell due to both voltage and concentration gradients. Current, in the form of positively charged ions flowing out of the cell (or negatively charged ions flowing into the cell) through open channels makes the membrane potential more negative, a process called hyperpolarization. Current flowing into the cell changes the membrane potential to less negative or even positive values. This is called depolarization.

If a neuron is depolarized sufficiently to raise the membrane potential above a threshold level, a positive feedback process is initiated, and the

*axons and
dendrites*

ion channels

*membrane
potential*

*hyperpolarization
and depolarization*

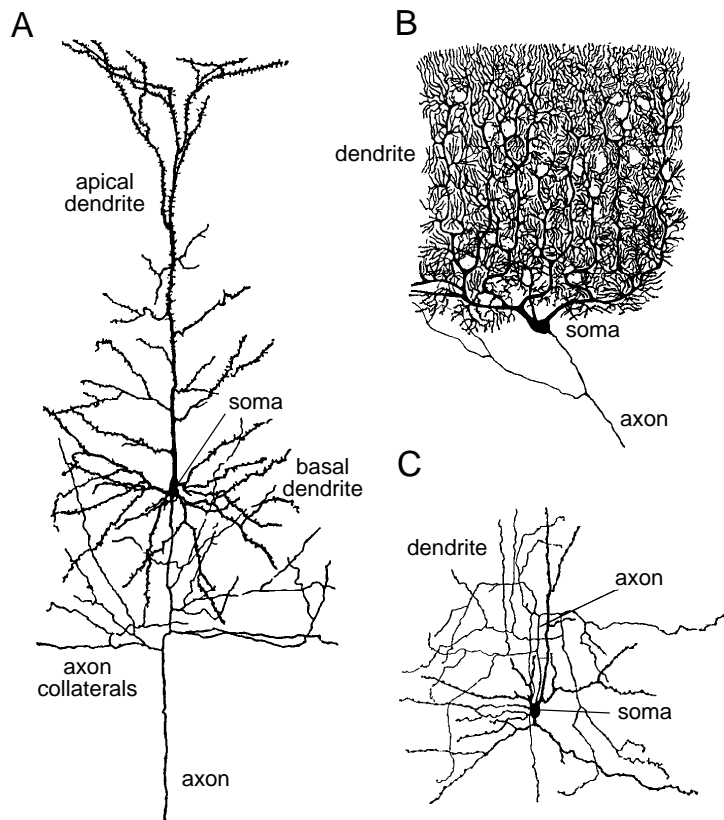


Figure 1.1: Diagrams of three neurons. A) A cortical pyramidal cell. These are the primary excitatory neurons of the cerebral cortex. Pyramidal cell axons branch locally, sending axon collaterals to synapse with nearby neurons, and also project more distally to conduct signals to other parts of the brain and nervous system. B) A Purkinje cell of the cerebellum. Purkinje cell axons transmit the output of the cerebellar cortex. C) A stellate cell of the cerebral cortex. Stellate cells are one of a large class of cells that provide inhibitory input to the neurons of the cerebral cortex. To give an idea of scale, these figures are magnified about 150 fold. (Drawings from Cajal, 1911; figure from Dowling, 1992.)

neuron generates an action potential. An action potential is a roughly 100 mV fluctuation in the electrical potential across the cell membrane that lasts for about 1 ms (figure 1.2A). Action potential generation also depends on the recent history of cell firing. For a few milliseconds just after an action potential has been fired, it may be virtually impossible to initiate another spike. This is called the absolute refractory period. For a longer interval known as the relative refractory period, lasting up to tens of milliseconds after a spike, it is more difficult to evoke an action potential.

action potential

refractory period

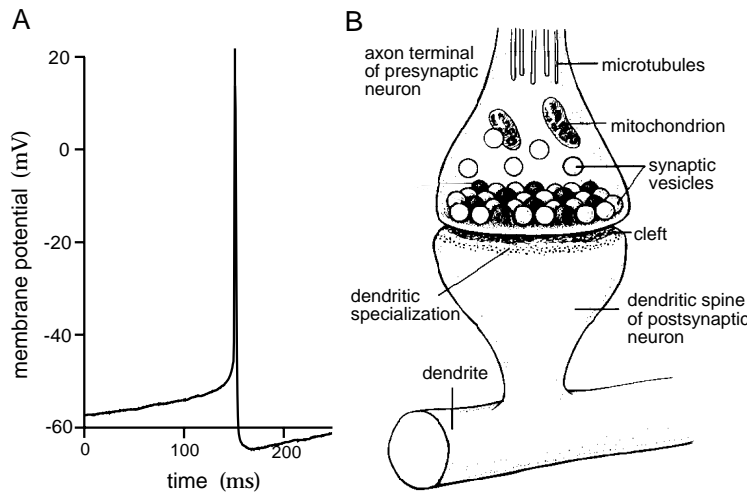


Figure 1.2: A) An action potential recorded intracellularly from a cultured rat neocortical pyramidal cell. B) Diagram of a synapse. The axon terminal or bouton is at the end of the axonal branch seen entering from the top of the figure. It is filled with synaptic vesicles containing the neurotransmitter that is released when an action potential arrives from the presynaptic neuron. Transmitter crosses the synaptic cleft and binds to receptors on the dendritic spine, a roughly $1\text{ }\mu\text{m}$ long process extending from the dendrite of the postsynaptic neuron. Excitatory synapses onto cortical pyramidal cells form on dendritic spines as shown here. Other synapses form directly on the dendrites, axon, or soma of the postsynaptic neuron. (A recorded by L. Rutherford in the laboratory of G. Turrigiano. B adapted from Kandel et al., 1991.)

Action potentials are of great importance because they are the only form of membrane potential fluctuation that can propagate over large distances. Subthreshold potential fluctuations are severely attenuated over distances of 1 mm or less. Action potentials, on the other hand, are regenerated actively along axon processes and can travel rapidly over large distances without attenuation.

synapse

Axons terminate at synapses where the voltage transient of the action potential opens ion channels producing an influx of Ca^{2+} that leads to the release of a neurotransmitter (figure 1.2B). The neurotransmitter binds to receptors at the signal receiving or postsynaptic side of the synapse causing ion-conducting channels to open. Depending on the nature of the ion flow, the synapses can have either an excitatory, depolarizing, or an inhibitory, typically hyperpolarizing, effect on the postsynaptic neuron.

Recording Neuronal Responses

Figure 1.3 illustrates intracellular and extracellular methods for recording neuronal responses electrically (they can also be recorded optically). Mem-

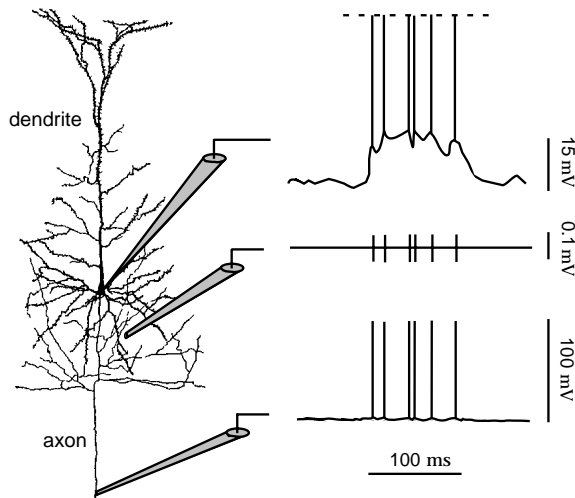


Figure 1.3: Three simulated recordings from a neuron. The top trace represents a recording from an intracellular electrode connected to the soma of the neuron. The height of the action potentials has been clipped to show the subthreshold membrane potential more clearly. The time scale is such that the action potential trajectory cannot be resolved. The bottom trace represents a recording from an intracellular electrode connected to the axon some distance away from the soma. The full height of the action potentials is indicated in this trace. The middle trace is a simulated extracellular recording. Action potentials appear as roughly equal positive and negative potential fluctuations with an amplitude of around 0.1 mV. This is roughly 1000 times smaller than the approximately 0.1 V amplitude of an intracellularly recorded action potential. (Neuron drawing is the same as figure 1.1A.)

brane potentials are measured intracellularly by connecting to a neuron a hollow glass electrode filled with a conducting electrolyte, and comparing the potential it records to that of a reference electrode placed in the extracellular medium. Intracellular recordings are made either with sharp electrodes inserted through the membrane into the cell, or patch electrodes that have broader tips and are sealed tightly to the surface of the membrane. After the patch electrode seals, the membrane beneath its tip is either broken or perforated providing electrical contact with the interior of the cell. The top trace in figure 1.3 is a schematic of an intracellular recording from the soma of a neuron firing a sequence of action potentials. The recording shows rapid spikes riding on top of a more slowly varying subthreshold potential. The bottom trace in figure 1.3 is a schematic of an intracellular recording made some distance out on the axon of the neuron. These traces are drawings, not real recordings, and such intracellular axon recordings, although possible in some types of cells, are difficult and rare. Intracellular recordings from the soma are the norm, but intracellular dendritic recordings are increasingly being made as well. The subthreshold membrane potential waveform, apparent in the soma record-

*sharp and patch
electrodes*

ing, is completely absent on the axon due to attenuation, but the action potential sequence in the two recordings is the same. This illustrates the important point that spikes, but not subthreshold potentials, propagate regeneratively down axons.

The middle trace in figure 1.3 illustrates an idealized, noise-free extracellular recording. Here an electrode is placed near a neuron but it does not penetrate the cell membrane. Such recordings can reveal the action potentials fired by a neuron, but not its subthreshold membrane potentials. Extracellular recordings are typically used for *in vivo* experiments, especially those involving behaving animals. Intracellular recordings are sometimes made *in vivo*, but are more commonly used for *in vitro* preparations such as experiments on slices of neural tissue. The responses studied in this chapter are action potential sequences that can be recorded either intra- or extra-cellularly.

From Stimulus to Response

Characterizing the relationship between stimulus and response is difficult because neuronal responses are complex and variable. Neurons typically respond by producing complex spike sequences that reflect both the intrinsic dynamics of the neuron and the temporal characteristics of the stimulus. Isolating features of the response that encode changes in the stimulus can be difficult, especially if the time scale for these changes is of the same order as the average interval between spikes. Neural responses can vary from trial to trial even when the same stimulus is presented repeatedly. There are many potential sources of this variability including variable levels of arousal and attention, randomness associated with various biophysical processes that affect neuronal firing, and the effects of other cognitive processes taking place during a trial. The complexity and trial-to-trial variability of action potential sequences make it unlikely that we can describe and predict the timing of each spike deterministically. Instead, we seek a model that can account for the probabilities that different spike sequences are evoked by a specific stimulus.

Typically, many neurons respond to a given stimulus, and stimulus features are therefore encoded by the activities of large neural populations. In studying population coding, we must examine not only the firing patterns of individual neurons, but also the relationships of these firing patterns to each other across the population of responding cells.

In this chapter, we introduce the firing rate and spike-train correlation functions, which are basic measures of spiking probability and statistics. We also discuss spike-triggered averaging, a method for relating action potentials to the stimulus that evoked them. Finally, we present basic stochastic descriptions of spike generation, the homogeneous and inhomogeneous Poisson models, and discuss a simple model of neural responses to which they lead. In chapter 2, we continue our discussion of

neural encoding by showing how reverse-correlation methods are used to construct estimates of firing rates in response to time-varying stimuli. These methods have been applied extensively to neural responses in the retina, lateral geniculate nucleus (LGN) of the thalamus, and primary visual cortex, and we review the resulting models.

1.2 Spike Trains and Firing Rates

Action potentials convey information through their timing. Although action potentials can vary somewhat in duration, amplitude, and shape, they are typically treated in neural encoding studies as identical stereotyped events. If we ignore the brief duration of an action potential (about 1 ms), an action potential sequence can be characterized simply by a list of the times when spikes occurred. For n spikes, we denote these times by t_i with $i = 1, 2, \dots, n$. The trial during which the spikes are recorded is taken to start at time zero and end at time T , so $0 \leq t_i \leq T$ for all i . The spike sequence can also be represented as a sum of infinitesimally narrow, idealized spikes in the form of Dirac δ functions (see the Mathematical Appendix),

$$\rho(t) = \sum_{i=1}^n \delta(t - t_i). \quad (1.1)$$

We call $\rho(t)$ the neural response function and use it to re-express sums over spikes as integrals over time. For example, for any well-behaved function $h(t)$, we can write

$$\sum_{i=1}^n h(t - t_i) = \int_0^T d\tau h(\tau) \rho(t - \tau) \quad (1.2)$$

where the integral is over the duration of the trial. The equality follows from the basic defining equation for a δ function,

$$\int d\tau \delta(t - \tau) h(\tau) = h(t), \quad (1.3)$$

provided that the limits of the integral surround the point t (if they do not, the integral is zero).

Because the sequence of action potentials generated by a given stimulus typically varies from trial to trial, neuronal responses are typically treated probabilistically, and characterized, for example, by the probability that a spike occurs at a particular time during a trial. Spike times are continuous variables, and, as a result, the probability for a spike to occur at any precisely specified time is actually zero. To get a nonzero value, we must ask for the probability that a spike occurs within a specified interval, for example the interval between times t and $t + \Delta t$. For small Δt , the probability

*neural response
function $\rho(t)$*

δ function

of a spike falling in this interval is proportional to the size of the interval, Δt . A similar relation holds for any continuous stochastic variable z . The probability that z takes a value between z and $z + \Delta z$, for small Δz (strictly speaking, as $\Delta z \rightarrow 0$) is equal to $p[z]\Delta z$, where $p[z]$ is called a probability density. Throughout this book, we use the notation $P[]$ to denote probabilities and $p[]$ to denote probability densities. We use the bracket notation, $P[]$, generically for the probability of something occurring and also to denote a specific probability function. In the latter case, the notation $P()$ would be more appropriate, but switching between square brackets and parentheses is confusing, so the reader will have to use the context to distinguish between these cases.

For the particular case of spike occurrences, we can write the probability that a spike occurs between times t and $t + \Delta t$, for small Δt as $p[t]\Delta t$, where $p[t]$ is the single spike probability density. The probability density for the occurrence of a spike is, by definition, the firing rate of the cell, and we use the notation $p[t] = r(t)$ for this important quantity.

The firing rate at time t , $r(t)$, can be estimated by determining the fraction of trials with a given stimulus on which a spike occurred between the times t and $t + \Delta t$. For sufficiently small Δt and sufficiently large numbers of trials, this fraction provides a good estimate of $r(t)$, as guaranteed by the law of large numbers. The fraction of trials on which a spike occurs can be computed from the neural response function averaged over trials. We use angle brackets, $\langle \rangle$, to denote averages over trials that use the same stimulus, so that $\langle z \rangle$ for any quantity z is the sum of the values of z obtained from many trials involving the same stimulus, divided by the number of trials. The trial-averaged neural response function is thus denoted by $\langle \rho(t) \rangle$. In any integral expression such as equation 1.2, the neural response function generates a contribution whenever a spike occurs. If instead, we use the trial-average response function in equation 1.2, this generates contributions proportional to the fraction of trials on which a spike occurred. Because of the relationship between this fraction and the firing rate, we find that

$$r(t)\Delta t = \int_t^{t+\Delta t} d\tau \langle \rho(\tau) \rangle. \quad (1.4)$$

Furthermore, within any well-behaved integral, we can replace the trial-averaged neural response function by the single-spike probability density or firing rate and write

$$\int d\tau h(\tau) \langle \rho(t - \tau) \rangle = \int d\tau h(\tau) r(t - \tau) \quad (1.5)$$

for any function h . This establishes an important relationship between the average neural response function and the firing rate; the two are equivalent when used inside integrals.

We call the single-spike probability density, $r(t)$, the firing rate. However, this term is conventionally applied to more than one quantity. A differ-

ent firing rate, which we call the spike-count rate, is obtained simply by counting the number of action potentials that appear during a trial and dividing by the duration of the trial. Unlike $r(t)$, the spike-count rate can be determined for a single trial. We denote the spike-count rate by r (as opposed to $r(t)$ for the single-spike probability density) where

$$r = \frac{n}{T} = \frac{1}{T} \int_0^T d\tau \rho(\tau). \quad (1.6)$$

The second equality follows from the fact that $\int d\tau \rho(\tau) = n$ and indicates that the spike-count rate is the time average of the neural response function over the duration of the trial.

In the same way that the response function $\rho(t)$ can be averaged across trials to give the firing rate $r(t)$, the spike-count firing rate can be averaged over trials yielding a quantity that we refer to as the average firing rate. This is denoted by $\langle r \rangle$ and given by

$$\langle r \rangle = \frac{\langle n \rangle}{T} = \frac{1}{T} \int_0^T d\tau \langle \rho(\tau) \rangle = \frac{1}{T} \int_0^T dt r(t). \quad (1.7)$$

The third equality follows from the equivalence of the firing rate and the trial averaged neural response function within integrals, equation 1.5. The average firing rate is equal to both the time average of $r(t)$ and the trial average of the spike-count rate r . Of course, a spike-count rate and average firing rate can be defined by counting spikes over any time period, not necessarily the entire duration of a trial.

The term firing rate is commonly used for all three quantities, $r(t)$, r , and $\langle r \rangle$. We use the terms firing rate, spike-count rate, and average firing rate for $r(t)$, r , and $\langle r \rangle$ respectively whenever possible but, when this becomes too cumbersome, the different mathematical notations serve to distinguish them. In particular, we distinguish the spike-count rate r from the single-spike probability density $r(t)$ by using a different font and by including the time argument in the latter expression (unless $r(t)$ is independent of time). The difference between the fonts is rather subtle, but the context should make it clear which rate is being used.

Measuring Firing Rates

The firing rate $r(t)$, being a probability density, cannot be determined exactly from the limited amounts of data available from a finite number of trials. In addition, there is no unique way to approximate $r(t)$. A discussion of the different methods allows us to introduce the concept of a linear filter and kernel that will be used extensively in the following chapters. We illustrate these methods by extracting firing rates from a single trial, but more accurate results could be obtained by averaging over multiple trials.

spike-count rate r

*trial average
rate $\langle r \rangle$*

Figure 1.4 compares a number of ways of approximating $r(t)$ from a spike sequence. Figure 1.4A shows three seconds of the response of a neuron in the inferior temporal cortex recorded while a monkey watched a video. Neurons in the region of cortex where this recording was made are selective for complex visual images including faces. A simple way of extracting an estimate of the firing rate from a spike train like this is to divide time into discrete bins of duration Δt , count the number of spikes within each bin, and divide by Δt . Figure 1.4B shows the approximate firing rate computed using this procedure with a bin size of 100 ms. Note that, with this procedure, the quantity being computed is really the spike-count firing rate over the duration of the bin, and that the firing rate $r(t)$ within a given bin is approximated by this spike-count rate.

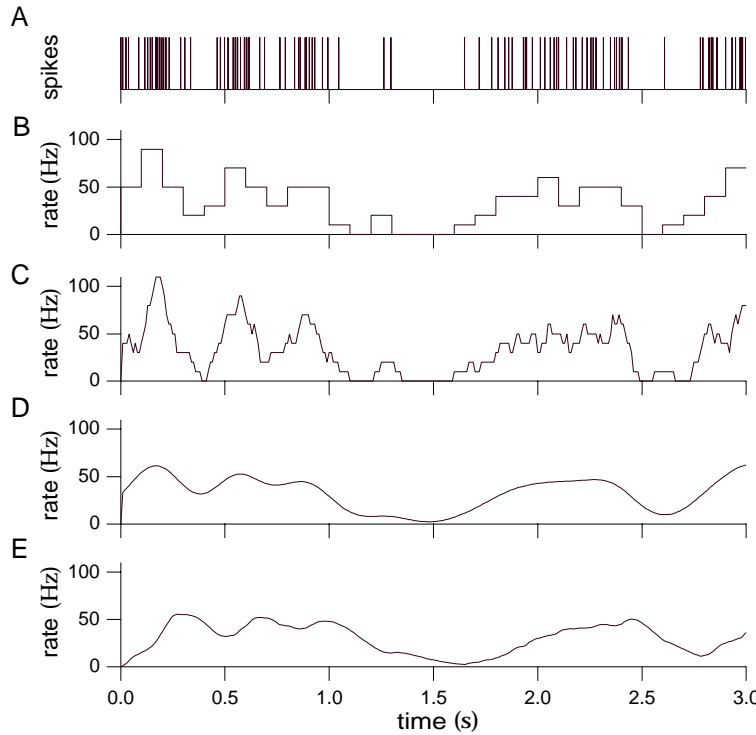


Figure 1.4: Firing rates approximated by different procedures. A) A spike train from a neuron in the inferior temporal cortex of a monkey recorded while that animal watched a video on a monitor under free viewing conditions. B) Discrete-time firing rate obtained by binning time and counting spikes with $\Delta t = 100$ ms. C) Approximate firing rate determined by sliding a rectangular window function along the spike train with $\Delta t = 100$ ms. D) Approximate firing rate computed using a Gaussian window function with $\sigma_t = 100$ ms. E) Approximate firing rate for an α function window with $1/\alpha = 100$ ms. (Data from Baddeley et al., 1997.)

The binning and counting procedure illustrated in figure 1.4B generates an estimate of the firing rate that is a piecewise constant function of time,

resembling a histogram. Because spike counts can only take integer values, the rates computed by this method will always be integer multiples of $1/\Delta t$, and thus they take discrete values. Decreasing the value of Δt increases temporal resolution by providing an estimate of the firing rate at more finely spaced intervals of time, but at the expense of decreasing the resolution for distinguishing different rates. One way to avoid quantized firing rates is to vary the bin size so that a fixed number of spikes appears in each bin. The firing rate is then approximated as that fixed number of spikes divided by the variable bin width.

Counting spikes in preassigned bins produces a firing-rate estimate that depends not only on the size of the time bins, but also on their placement. To avoid the arbitrariness in the placement of bins, we can instead take a single bin or window of duration Δt and slide it along the spike train, counting the number of spikes within the window at each location. The jagged curve in figure 1.4C shows the result of sliding a 100 ms wide window along the spike train. The firing rate approximated in this way can be expressed as the sum of a window function over the times t_i for $i = 1, 2, \dots, n$ when the n spikes in a particular sequence occurred,

$$r_{\text{approx}}(t) = \sum_{i=1}^n w(t - t_i) \quad (1.8)$$

the window function

$$w(t) = \begin{cases} 1/\Delta t & \text{if } -\Delta t/2 \leq t < \Delta t/2 \\ 0 & \text{otherwise.} \end{cases} \quad (1.9)$$

Use of a sliding window avoids the arbitrariness of bin placement and produces a rate that might appear to have a better temporal resolution. However, it must be remembered that the rates obtained at times separated by less than one bin width are correlated because they involve some of the same spikes.

The sum in equation 1.8 can also be written as the integral of the window function times the neural response function (see equation 1.2),

$$r_{\text{approx}}(t) = \int_{-\infty}^{\infty} d\tau w(\tau) \rho(t - \tau). \quad (1.10)$$

The integral in equation 1.10 is called a linear filter, and the window function w , also called the filter kernel, specifies how the neural response function evaluated at time $t - \tau$ contributes to the firing rate approximated at time t .

*linear filter
and kernel*

The jagged appearance of the curve in figure 1.4C is caused by the discontinuous shape of the window function used. An approximate firing rate can be computed using virtually any window function $w(\tau)$ that goes to zero outside a region near $\tau = 0$ provided that its time integral is equal to one. For example, instead of the rectangular window function used in

figure 1.4C, $w(\tau)$ can be a Gaussian

$$w(\tau) = \frac{1}{\sqrt{2\pi}\sigma_w} \exp\left(-\frac{\tau^2}{2\sigma_w^2}\right). \quad (1.11)$$

In this case, σ_w controls the temporal resolution of the resulting rate, playing a role analogous to Δt . A continuous window function like the Gaussian used in equation 1.8 generates a firing-rate estimate that is a smooth function of time (figure 1.4D).

Both the rectangular and Gaussian window functions approximate the firing rate at any time using spikes fired both before and after that time. A postsynaptic neuron monitoring the spike train of a presynaptic cell only has access to spikes that have previously occurred. An approximation of the firing rate at time t that only depends on spikes fired before t can be calculated using a window function that vanishes when its argument is negative. Such a window function or kernel is called causal. One commonly used form is the α function

$$w(\tau) = [\alpha^2 \tau \exp(-\alpha\tau)]_+ \quad (1.12)$$

where $1/\alpha$ determines the temporal resolution of the resulting firing-rate estimate. The notation $[z]_+$ for any quantity z stands for the half-wave rectification operation,

$$[z]_+ = \begin{cases} z & \text{if } z \geq 0 \\ 0 & \text{otherwise.} \end{cases} \quad (1.13)$$

Figure 1.4E shows the firing rate approximated by such a causal scheme. Note that this rate tends to peak later than the rate computed in figure 1.4D using a temporally symmetric window function.

Tuning Curves

Neuronal responses typically depend on many different properties of a stimulus. In this chapter, we characterize responses of neurons as functions of just one of the stimulus attributes to which they may be sensitive. The value of this single attribute is denoted by s . In chapter 2, we consider more complete stimulus characterizations.

A simple way of characterizing the response of a neuron is to count the number of action potentials fired during the presentation of a stimulus. This approach is most appropriate if the parameter s characterizing the stimulus is held constant over the trial. If we average the number of action potentials fired over (in theory, an infinite number of) trials and divide by the trial duration, we obtain the average firing rate, $\langle r \rangle$ defined in equation 1.7. The average firing rate written as a function of s , $\langle r \rangle = f(s)$, is called the neural response tuning curve. The functional form of a tuning curve depends on the parameter s used to describe the stimulus. The precise

half-wave
rectification $[]_+$

stimulus s

response tuning
curve $f(s)$

choice of parameters used as arguments of tuning curve functions is partially a matter of convention. Because tuning curves correspond to firing rates, they are measured in units of spikes per second or Hz.

Figure 1.5A shows extracellular recordings of a neuron in the primary visual cortex (V1) of a monkey. While these recordings were being made, a bar of light was moved at different angles across the region of the visual field where the cell responded to light. This region is called the receptive field of the neuron. Note that the number of action potentials fired depends on the angle of orientation of the bar. The same effect is shown in figure 1.5B in the form of a response tuning curve, which indicates how the average firing rate depends on the orientation of the light bar stimulus. The data have been fit by a response tuning curve of the form

primary visual cortex V1

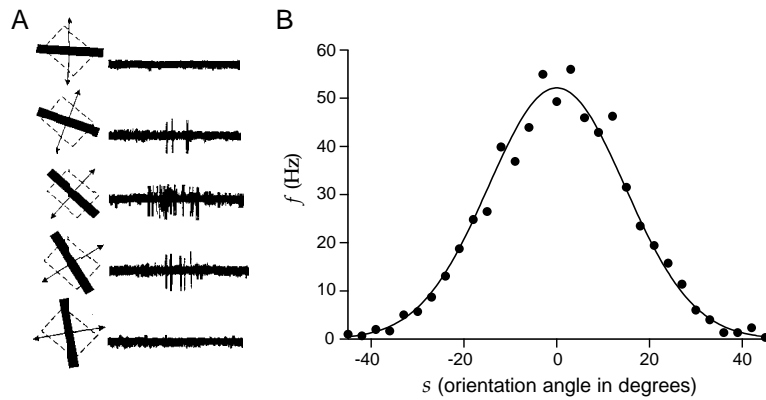


Figure 1.5: A) Recordings from a neuron in the primary visual cortex of a monkey. A bar of light was moved across the receptive field of the cell at different angles. The diagrams to the left of each trace show the receptive field as a dashed square and the light source as a black bar. The bidirectional motion of the light bar is indicated by the arrows. The angle of the bar indicates the orientation of the light bar for the corresponding trace. B) Average firing rate of a cat V1 neuron plotted as a function of the orientation angle of the light bar stimulus. The curve is a fit using the function 1.14 with parameters $r_{\max} = 52.14$ Hz, $s_{\max} = 0^\circ$, and $\sigma_f = 14.73^\circ$. (A from Hubel and Wiesel, 1968; adapted from Wandell, 1995. B data points from Henry et al., 1974.)

Gaussian tuning curve

$$f(s) = r_{\max} \exp \left(-\frac{1}{2} \left(\frac{s - s_{\max}}{\sigma_f} \right)^2 \right) \quad (1.14)$$

where s is the orientation angle of the light bar, s_{\max} is the orientation angle evoking the maximum average response rate r_{\max} (with $s - s_{\max}$ taken to lie in the range between -90° and $+90^\circ$), and σ_f determines the width of the tuning curve. The neuron responds most vigorously when a stimulus having $s = s_{\max}$ is presented, so we call s_{\max} the preferred orientation angle of the neuron.

primary motor cortex M1

Response tuning curves can be used to characterize the selectivities of neurons in visual and other sensory areas to a variety of stimulus parameters. Tuning curves can also be measured for neurons in motor areas, in which case the average firing rate is expressed as a function of one or more parameters describing a motor action. Figure 1.6A shows an example of extracellular recordings from a neuron in primary motor cortex in a monkey that has been trained to reach in different directions. The stacked traces for each direction are rasters showing the results of five different trials. The horizontal axis in these traces represents time, and each mark indicates an action potential. The firing pattern of the cell, in particular the rate at which spikes are generated, is correlated with the direction of arm movement and thus encodes information about this aspect of the motor action.

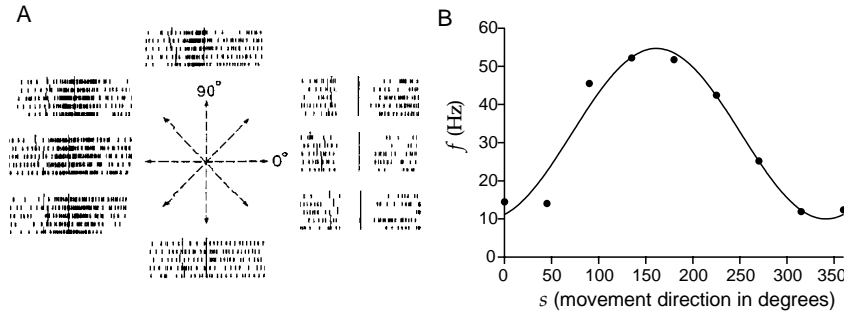


Figure 1.6: A) Recordings from the primary motor cortex of a monkey performing an arm reaching task. The hand of the monkey started from a central resting location and reaching movements were made in the directions indicated by the arrows. The rasters for each direction show action potentials fired on five trials. B) Average firing rate plotted as a function of the direction in which the monkey moved its arm. The curve is a fit using the function 1.15 with parameters $r_{\max} = 54.69$ Hz, $r_0 = 32.34$ Hz, and $s_{\max} = 161.25^\circ$. (A adapted from Georgopoulos et al., 1982 which is also the source of the data points in B.)

cosine tuning curve

Figure 1.6B shows the response tuning curve of an M1 neuron plotted as a function of the direction of arm movement. Here the data points have been fit by a tuning curve of the form

$$f(s) = r_0 + (r_{\max} - r_0) \cos(s - s_{\max}) \quad (1.15)$$

where s is the reaching angle of the arm, s_{\max} is the reaching angle associated with the maximum response r_{\max} , and r_0 is an offset or background firing rate that shifts the tuning curve up from the zero axis. The minimum firing rate predicted by equation 1.15 is $2r_0 - r_{\max}$. For the neuron of figure 1.6B, this is a positive quantity, but for some M1 neurons $2r_0 - r_{\max} < 0$, and the function 1.15 is negative over some range of angles. Because firing rates cannot be negative, the cosine tuning curve must be half-wave rectified in these cases (see equation 1.13),

$$f(s) = [r_0 + (r_{\max} - r_0) \cos(s - s_{\max})]_+ . \quad (1.16)$$

Figure 1.7B shows how the average firing rate of a V1 neuron depends on retinal disparity and illustrates another important type of tuning curve.

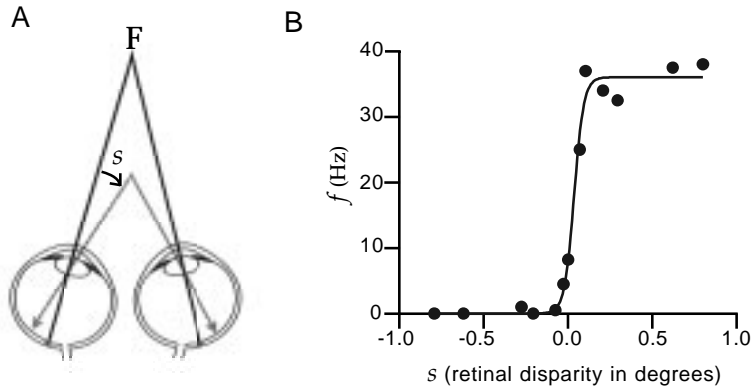


Figure 1.7: A) Definition of retinal disparity. The grey lines show the location on each retina of an object located nearer than the fixation point F. The image from the fixation point falls at the fovea in each eye, the small pit where the black lines meet the retina. The image from a nearer object falls to the left of the fovea in the left eye and to the right of the fovea in the right eye. For objects further away than the fixation point, this would be reversed. The disparity angle s is indicated in the figure. B) Average firing rate of a cat V1 neuron responding to separate bars of light illuminating each eye plotted as a function of the disparity. Because this neuron fires for positive s values it is called a far-tuned cell. The curve is a fit using the function 1.17 with parameters $r_{\max} = 36.03$ Hz, $s_{1/2} = 0.036^\circ$, and $\Delta_s = 0.029^\circ$. (A adapted from Wandell, 1995; B data points from Poggio and Talbot, 1981.)

Retinal disparity is a difference in the retinal location of an image between the two eyes (figure 1.7A). Some neurons in area V1 are sensitive to disparity, representing an early stage in the representation of viewing distance. In figure 1.7B, the data points have been fit with a tuning curve called a logistic or sigmoidal function,

$$f(s) = \frac{r_{\max}}{1 + \exp((s_{1/2} - s)/\Delta_s)}. \quad (1.17)$$

In this case, s is the retinal disparity, the parameter $s_{1/2}$ is the disparity that produces a firing rate half as big as the maximum value r_{\max} , and Δ_s controls how quickly the firing rate increases as a function of s . If Δ_s is negative, the firing rate is a monotonically decreasing function of s rather than a monotonically increasing function as in figure 1.7B.

sigmoidal
tuning curve

Spike-Count Variability

Tuning curves allow us to predict the average firing rate, but they do not describe how the spike-count firing rate r varies about its mean value $\langle r \rangle = f(s)$ from trial to trial. While the map from stimulus to average

response may be described deterministically, it is likely that single-trial responses such as spike-count rates can only be modeled in a probabilistic manner. For example, r values can be generated from a probability distribution with mean $f(s)$. The trial-to-trial deviation of r from $f(s)$ is considered to be noise, and such models are often called noise models. The standard deviation for the noise distribution can either be independent of $f(s)$, in which case the variability is called additive noise, or it can depend on $f(s)$. Multiplicative noise corresponds to having the standard deviation proportional to $f(s)$.

Response variability extends beyond the level of spike counts to the entire temporal pattern of action potentials. Later in this chapter, we discuss a model of the neuronal response that uses a stochastic spike generator to produce response variability. This approach takes a deterministic estimate of the firing rate, $r_{\text{est}}(t)$, and produces a stochastic spiking pattern from it. The spike generator produces variable numbers and patterns of action potentials, even if the same estimated firing rate is used on each trial.

1.3 What Makes a Neuron Fire?

Response tuning curves characterize the average response of a neuron to a given stimulus. We now consider the complementary procedure of averaging the stimuli that produce a given response. To average stimuli in this way, we need to specify what fixed response we will use to ‘trigger’ the average. The most obvious choice is the firing of an action potential. Thus, we ask, “what on average did the stimulus do before an action potential was fired?” The resulting quantity, called the spike-triggered average stimulus, provides a useful way of characterizing neuronal selectivity. Spike-triggered averages are computed using stimuli characterized by a parameter $s(t)$ that varies over time. Before beginning our discussion of spike triggering, we describe some features of such stimuli.

Describing the Stimulus

Neurons responding to sensory stimuli face the difficult task of encoding parameters that can vary over an enormous dynamic range. For example, photoreceptors in the retina can respond to single photons or can operate in bright light with an influx of millions of photons per second. To deal with such wide-ranging stimuli, sensory neurons often respond most strongly to rapid changes in stimulus properties and are relatively insensitive to steady-state levels. Steady-state responses are highly compressed functions of stimulus intensity, typically with logarithmic or weak power-law dependences. This compression has an interesting psychophysical correlate. Weber measured how different the intensity of two stimuli had to be for them to be reliably discriminated, the ‘just noticeable’ difference

Δs . He found that, for a given stimulus, Δs was proportional to the magnitude of the stimulus s , so that $\Delta s/s$ was constant. This relationship is called Weber's law. Fechner suggested that noticeable differences set the scale for perceived stimulus intensities. Integrating Weber's law, this means that the perceived intensity of a stimulus of absolute intensity s varies as $\log s$, and this is known as Fechner's law.

Weber's law

Sensory systems make numerous adaptations, using a variety of mechanisms, to adjust to the average level of stimulus intensity. When a stimulus generates such adaptation, the relationship between stimulus and response is often studied in a potentially simpler regime by describing responses to fluctuations about a mean stimulus level. In this case, $s(t)$ is defined so that its time average over the duration of a trial is zero. We frequently assume that this condition, $\int_0^T dt s(t)/T = 0$.

$$\int_0^T dt s(t)/T = 0$$

Our analysis of neural encoding involves two different types of averages: averages over repeated trials that employ the same stimulus, which we denote by angle brackets, and averages over different stimuli. We could introduce a second notation for averages over stimuli, but this can be avoided when using time-dependent stimuli. Instead of presenting a number of different stimuli and averaging over them, we can string together all of the stimuli we wish to consider into a single time-dependent stimulus sequence and average over time. Thus, stimulus averages are replaced by time averages.

stimulus and time averages

Although a response recorded over a trial only depends on the values taken by $s(t)$ during that trial, some of the mathematical analyses presented in this chapter and in chapter 2 are simplified if we define the stimulus at other times as well. It is convenient if integrals involving the stimulus are time-translationally invariant so that for any function h and time interval τ

$$\int_0^T dt h(s(t + \tau)) = \int_{\tau}^{T+\tau} dt h(s(t)) = \int_0^T dt h(s(t)). \quad (1.18)$$

To assure the last equality, we define the stimulus outside the time limits of the trial by the relation $s(T + \tau) = s(\tau)$ for any τ , thereby making the stimulus periodic.

periodic stimulus

The Spike-Triggered Average

The spike-triggered average stimulus, $C(\tau)$, is the average value of the stimulus a time interval τ before a spike is fired. In other words, for a spike occurring at time t_i , we determine $s(t_i - \tau)$, and then we sum over all n spikes in a trial, $i = 1, 2, \dots, n$ and divide the total by n . In addition, we average over trials. Thus,

$$C(\tau) = \left\langle \frac{1}{n} \sum_{i=1}^n s(t_i - \tau) \right\rangle \approx \frac{1}{\langle n \rangle} \left\langle \sum_{i=1}^n s(t_i - \tau) \right\rangle. \quad (1.19)$$

spike-triggered average $C(\tau)$

The approximate equality of the last expression follows from the fact that, if n is large, the total number of spikes on each trial is well approximated by the average number of spikes per trial, $n \approx \langle n \rangle$. We make use of this approximation because it allows us to relate the spike-triggered average to other quantities commonly used to characterize the relationship between stimulus and response (see below). Figure 1.8 provides a schematic description of the computation of the spike-triggered average. Each time a spike appears, the stimulus in a time window preceding the spike is recorded. Although the range of τ values in equation 1.19 is unlimited, the response is typically affected only by the stimulus in a window a few hundred milliseconds wide immediately preceding a spike. More precisely, we expect $C(\tau)$ to approach zero for positive τ values larger than the correlation time between the stimulus and the response. If the stimulus has no temporal correlations with itself, we also expect for $C(\tau)$ to be zero for $\tau < 0$, because the response of a neuron cannot depend on future stimuli. In practice, the stimulus is only recorded over a finite time period as indicated by the shaded areas in figure 1.8. The recorded stimuli for all spikes are then summed and the procedure is repeated over multiple trials.

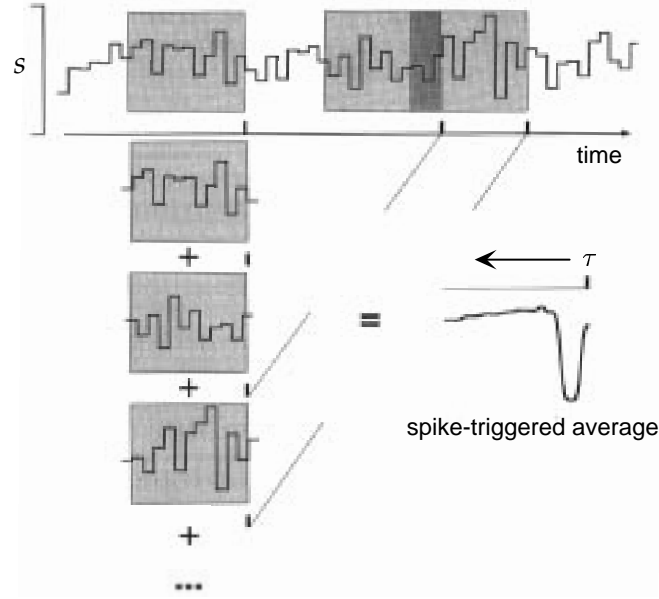


Figure 1.8: Schematic of the procedure for computing the spike-triggered average stimulus. Each grey rectangle contains the stimulus prior to one of the spikes shown along the time axis. These are averaged to produce the waveform shown at the lower right, which is the average stimulus before a spike. The stimulus in this example is a piecewise constant function of time. (Adapted from Rieke et al. 1997.)

The spike-triggered average stimulus can be expressed as an integral of the stimulus times the neural response function of equation 1.1. If we replace the sum over spikes by an integral, as in equation 1.2, and use the

approximate expression for $C(\tau)$ in equation 1.19, we find

$$C(\tau) = \frac{1}{\langle n \rangle} \int_0^T dt \langle \rho(t) \rangle s(t - \tau) = \frac{1}{\langle n \rangle} \int_0^T dt r(t) s(t - \tau). \quad (1.20)$$

The second equality is due to the equivalence of $\langle \rho(t) \rangle$ and $r(t)$ within integrals. Equation 1.20 allows us to relate the spike-triggered average to the correlation function of the firing rate and the stimulus.

Correlation functions are a useful way of determining how two quantities that vary over time are related to each other. The two quantities being related are evaluated at different times, one at time t and the other at time $t + \tau$. The correlation function is then obtained by averaging their product over all t values, and it is a function of τ . The correlation function of the firing rate and the stimulus is

$$Q_{rs}(\tau) = \frac{1}{T} \int_0^T dt r(t) s(t + \tau). \quad (1.21)$$

By comparing equations 1.20 and 1.21, we find that

$$C(\tau) = \frac{1}{\langle r \rangle} Q_{rs}(-\tau) \quad (1.22)$$

where $\langle r \rangle = \langle n \rangle / T$ is the average firing rate over the set of trials. Because the argument of the correlation function in equation 1.22 is $-\tau$, the spike-triggered average stimulus is often called the reverse correlation function. It is proportional to the correlation of the firing rate with the stimulus at preceding times.

*firing-rate stimulus
correlation function*

Q_{rs}

*reverse correlation
function*

The spike-triggered average stimulus is widely used to study and characterize neural responses. Because $C(\tau)$ is the average value of the stimulus a time τ before a spike, larger values of τ represent times further in the past relative to the time of the triggering spike. For this reason, we plot spike-triggered averages with the time axis going backward compared to the normal convention. This allows the average spike-triggering stimulus to be read off from the plots in the usual left to right order.

Figure 1.9 shows the spike-triggered average stimulus for a neuron in the electrosensory lateral-line lobe of the weakly electric fish *Eigenmannia*. Weakly electric fish generate oscillating electric fields from an internal electric organ. Distortions in the electric field produced by nearby objects are detected by sensors spread over the skin of the fish. The lateral-line lobe acts as a relay station along the processing pathway for electrosensory signals. Fluctuating electrical potentials, such as that shown in the upper left trace of figure 1.9 elicit responses from electrosensory lateral-line lobe neurons, as seen in the lower left trace. The spike-triggered average stimulus, plotted at the right, indicates that, on average, the electric potential made a positive upswing followed by a large negative deviation prior to a spike being fired by this neuron.

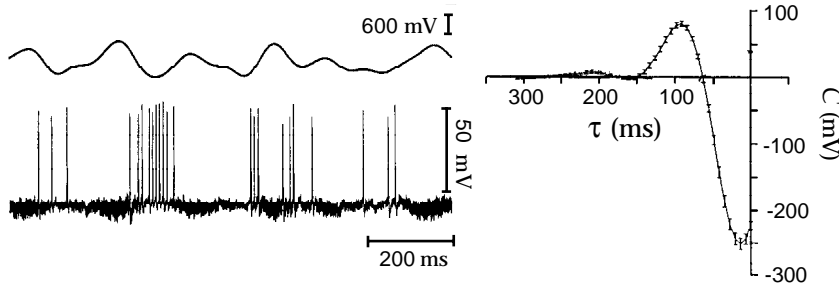


Figure 1.9: The spike-triggered average stimulus for a neuron of the electrosensory lateral-line lobe of the weakly electric fish *Eigenmannia*. The upper left trace is the potential used to generate the electric field to which this neuron is sensitive. The evoked spike train is plotted below the stimulus potential. The plot on the right is the spike-triggered average stimulus. (Adapted from Gabbiani et al., 1996.)

The results obtained by spike-triggered averaging depend on the particular set of stimuli used during an experiment. How should this set be chosen? In chapter 2, we show that there are certain advantages to using a stimulus that is uncorrelated from one time to the next, a white-noise stimulus. A heuristic argument supporting the use of such stimuli is that, in asking what makes a neuron fire, we may want to sample its responses to stimulus fluctuations at all frequencies with equal weight (i.e. equal power), and this is one of the properties of white noise stimuli. In practice, white-noise stimuli can only be generated with equal power up to a finite frequency cutoff, but neurons only respond to stimulus fluctuations within a limited frequency range anyway. Figure 1.9 is based on a such an approximate white-noise stimulus. The power in a signal as a function of its frequency is called the power spectrum or power spectral density, and white noise has a flat power spectrum.

White-Noise Stimuli

The defining characteristic of a white-noise stimulus is that its value at any one time is uncorrelated with its value at any other time. This condition can be expressed using the stimulus-stimulus correlation function, also called the stimulus autocorrelation, which is defined by analogy with equation 1.21 as

$$Q_{ss}(\tau) = \frac{1}{T} \int_0^T dt s(t)s(t + \tau). \quad (1.23)$$

*stimulus
autocorrelation
function Q_{ss}*

Just as a correlation function provides information about the temporal relationship between two quantities, an autocorrelation function tells us about how a quantity at one time is related to itself, evaluated at another

time. For white-noise, the stimulus autocorrelation function is zero in the range $-T/2 < \tau < T/2$ except when $\tau = 0$, and over this range

$$Q_{ss}(\tau) = \sigma_s^2 \delta(\tau). \quad (1.24)$$

The constant σ_s , which has the units of the stimulus times the square root of the unit of time, determines the magnitude of the variability of the white-noise. In appendix A, we show that equation 1.24 is equivalent to the statement that white-noise has equal power at all frequencies.

No physical system can generate noise that is white to arbitrarily high frequencies. Approximations of white-noise that are missing high-frequency components can be used provided that the missing frequencies are well above the sensitivity of the neuron under investigation. To approximate white-noise, we consider times that are integer multiples of a basic unit of duration Δt , that is, times $t = m\Delta t$ for $m = 1, 2, \dots, M$ where $M\Delta t = T$. The function $s(t)$ is then constructed as a discrete sequence of stimulus values. This produces a step-like stimulus waveform, like the one that appears in figure 1.8, with a constant stimulus value s_m presented during time bin m . In terms of the discrete-time values s_m , the condition that the stimulus is uncorrelated is

$$\frac{1}{M} \sum_{m=1}^M s_m s_{m+p} = \begin{cases} \sigma_s^2 / \Delta t & \text{if } p = 0 \\ 0 & \text{otherwise.} \end{cases} \quad (1.25)$$

The factor of $1/\Delta t$ on the right side of this equation reproduces the δ function of equation 1.24 in the limit $\Delta t \rightarrow 0$. For approximate white-noise, the autocorrelation function is zero except for a region around $\tau = 0$ with width of order Δt . Similarly, the binning of time into discrete intervals of size Δt means that the noise generated only has a flat power spectrum up to frequencies of order $1/(2\Delta t)$.

An approximation to white-noise can be generated by choosing each s_m independently from a probability density with mean zero and variance $\sigma_s^2 / \Delta t$. Any reasonable probability density function satisfying these two conditions can be used to generate the stimulus values within each time bin. A special class of white-noise stimuli, Gaussian white-noise, results when the probability density used to generate the s_m values is a Gaussian function. The factor of $1/\Delta t$ in the variance indicates that the variability must be increased as the time bins gets smaller. A number of other schemes for efficiently generating approximately white-noise stimuli are discussed in the references at the end of this chapter.

Multiple-Spike-Triggered Averages and Spike-Triggered Correlations

In addition to triggering on single spikes, stimulus averages can be computed by triggering on various combinations of spikes. Figure 1.10 shows

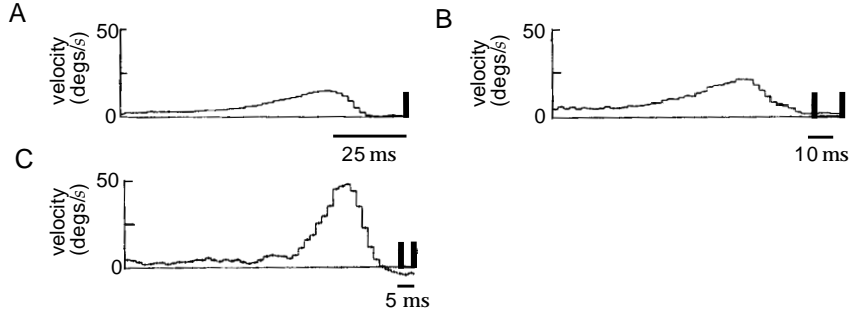


Figure 1.10: Single- and multiple-spike-triggered average stimuli for a blowfly H1 neuron responding to a moving visual image. A) The average stimulus velocity triggered on a single spike. B) The average stimulus velocity before two spikes with a separation of 10 ± 1 ms. C) The average stimulus before two spikes with a separation of 5 ± 1 ms. (Data from de Ruyter van Steveninck and Bialek, 1988; figure adapted from Rieke et al., 1997.)

some examples of two-spike triggers. These results come from a study of the H1 movement-sensitive visual neuron of the blowfly. The H1 neuron detects the motion of visual images during flight to generate and guide stabilizing motor corrections. It responds to motion of the visual scene. In the experiments, the fly is held fixed while a visual image with a time-varying velocity $s(t)$ is presented. Figure 1.10A, showing the spike-triggered average stimulus, indicates that this neuron responds to positive angular velocities after a latency of about 15 ms. Figure 1.10B is the average stimulus prior to the appearance of two spikes separated by 10 ± 1 ms. This two-spike average is approximately equal to the sum of two single-spike-triggered average stimuli displaced from each other by 10 ms. Thus, for 10 ms separations, two spikes occurring together tell us no more as a two-spike unit than they would individually. This result changes when shorter separations are considered. Figure 1.10C shows the average stimulus triggered on two spikes separated by 5 ± 1 ms. The average stimulus triggered on a pair of spikes separated by 5 ms is not the same as the sum of the average stimuli for each spike separately.

Spike-triggered averages of other stimulus-dependent quantities can provide additional insight into neural encoding, for example spike-triggered average autocorrelation functions. Obviously spike-triggered averages of higher-order stimulus combinations can be considered as well.

1.4 Spike Train Statistics

A complete description of the stochastic relationship between a stimulus and response would require us to know the probabilities corresponding to every sequence of spikes that can be evoked by the stimulus. The prob-

ability of a spike sequence appearing is proportional to the probability density of spike times, $p[t_1, t_2, \dots, t_n]$. In other words, the probability $P[t_1, t_2, \dots, t_n]$ that a sequence of n spikes occurs with spike i falling between times t_i and $t_i + \Delta t$ for $i = 1, 2, \dots, n$ is given in terms of this density by the relation $P[t_1, t_2, \dots, t_n] = p[t_1, t_2, \dots, t_n](\Delta t)^n$.

Unfortunately, the number of possible spike sequences is typically so large that determining or even roughly estimating all of their probabilities of occurrence is impossible. Instead, we must rely on some statistical model that allows us to estimate the probability of an arbitrary spike sequence occurring, given our knowledge of the responses actually recorded. The firing rate $r(t)$ determines the probability of firing a single spike in a small interval around the time t , but $r(t)$ is not, in general, sufficient information to predict the probabilities of spike sequences. For example, the probability of two spike occurring together in a sequence is not necessarily equal to the product of the probabilities that they occur individually, because the presence of one spike may effect the occurrence of the other. If, however, the probability of generating an action potential is independent of the presence or timing of other spikes, i.e. if the spikes are statistically independent, the firing rate is all that is needed to compute the probabilities for all possible action potential sequences.

A stochastic process that generates a sequence of events, such as action potentials, is called a point process. In general, the probability of an event occurring at any given time could depend on the entire history of preceding events. If this dependence extends only to the immediately preceding event, so that the intervals between successive events are independent, the point process is called a renewal process. If there is no dependence at all on preceding events, so that the events themselves are statistically independent, we have a Poisson process. The Poisson process provides an extremely useful approximation of stochastic neuronal firing. To make the presentation easier to follow we separate two cases, the homogeneous Poisson process, for which the firing rate is constant over time, and the inhomogeneous Poisson process, which involves a time-dependent firing rate.

point process

renewal process

Poisson process

The Homogeneous Poisson Process

We denote the firing rate for a homogeneous Poisson process by $r(t) = r$ because it is independent of time. When the firing rate is constant, the Poisson process generates every sequence of n spikes with equal probability. As a result, the probability $P[t_1, t_2, \dots, t_n]$ can be expressed in terms of another probability function $P_T[n]$ which is the probability that any sequence of n spikes occurs within a trial of duration T . Assuming that the spike times are ordered, so that $0 \leq t_1 \leq t_2 \leq \dots \leq t_n \leq T$, the relationship

is

$$P[t_1, t_2, \dots, t_n] = n! P_T[n] \left(\frac{\Delta t}{T} \right)^n. \quad (1.26)$$

This relationship is a special case of equation 1.37 derived below.

To compute $P_T[n]$, we divide the time T into M bins of size $\Delta t = T/M$. We can assume that Δt is small enough so that we never get two spikes within any one bin because, at the end of the calculation, we take the limit $\Delta t \rightarrow 0$. $P_T[n]$ is the product of three factors: the probability of generating n spikes within a specified set of the M bins, the probability of not generating spikes in the remaining $M - n$ bins, and a combinatorial factor equal to the number of ways of putting n spikes into M bins. The probability of a spike occurring in one specific bin is $r\Delta t$, and the probability of n spikes appearing in n specific bins is $(r\Delta t)^n$. Similarly the probability of not having a spike in a given bin is $(1 - r\Delta t)$, so the probability of having the remaining $M - n$ bins without any spikes in them is $(1 - r\Delta t)^{M-n}$. Finally, the number of ways of putting n spikes into M bins is given by the binomial coefficient $M!/(M - n)!n!$. Putting all these factors together we find,

$$P_T[n] = \lim_{\Delta t \rightarrow 0} \frac{M!}{(M - n)!n!} (r\Delta t)^n (1 - r\Delta t)^{M-n}. \quad (1.27)$$

To take the limit we note that as $\Delta t \rightarrow 0$, M grows without bound because $M\Delta t = T$. Because n is fixed, we can write $M - n \approx M = T/\Delta t$. Using this approximation and defining $\epsilon = -r\Delta t$, we find that

$$\lim_{\Delta t \rightarrow 0} (1 - r\Delta t)^{M-n} = \lim_{\epsilon \rightarrow 0} ((1 + \epsilon)^{1/\epsilon})^{-rT} = e^{-rT} = \exp(-rT) \quad (1.28)$$

because $\lim_{\epsilon \rightarrow 0} (1 + \epsilon)^{1/\epsilon}$ is, by definition, $e = \exp(1)$. For large M , $M!/(M - n)! \approx M^n = (T/\Delta t)^n$ so

$$P_T[n] = \frac{(rT)^n}{n!} \exp(-rT). \quad (1.29)$$

Poisson distribution

This is called the Poisson distribution. The probabilities $P_T[n]$, for a few n values, are plotted as a function of rT in figure 1.11A. Note that, as n increases, the probability reaches its maximum at larger T values and that large n values are more likely than small ones for large T . Figure 1.11B shows the probabilities of various numbers of spikes occurring when the average number of spikes is 10. For large rT , which corresponds to a large expected number of spikes, the Poisson distribution approaches a Gaussian distribution with mean and variance equal to rT . Figure 1.11B shows that this approximation is already quite good for $rT = 10$.

We can compute the variance of spike counts produced by a Poisson process from the probabilities 1.29. For spikes counted over an interval of duration T , the variance of the spike count (derived in appendix B) is

$$\sigma_n^2 = \langle n^2 \rangle - \langle n \rangle^2 = rT. \quad (1.30)$$

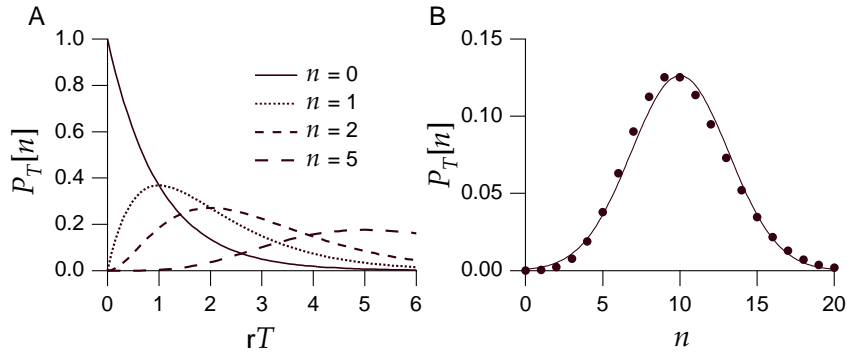


Figure 1.11: A) The probability that a homogeneous Poisson process generates n spikes in a time period of duration T plotted for $n = 0, 1, 2$, and 5. The probability is plotted as function of the rate times the duration of the interval, rT , to make the plot applicable for any rate. B) The probability of finding n spikes during a time period for which $rT = 10$ (dots) compared with a Gaussian distribution with mean and variance equal to 10 (line).

Fano factor

Thus the variance and mean of the spike count are equal. The ratio of these two quantities, $\sigma_n^2/\langle n \rangle$, is called the Fano factor and takes the value one for a homogeneous Poisson process, independent of the time interval T .

The probability density of time intervals between adjacent spikes is called the interspike interval distribution, and it is a useful statistic for characterizing spiking patterns. Suppose that a spike occurs at a time t_i for some value of i . The probability of a homogeneous Poisson process generating the next spike somewhere in the interval $t_i + \tau \leq t_{i+1} < t_i + \tau + \Delta t$, for small Δt , is the probability that no spike is fired for a time τ , times the probability, $r\Delta t$, of generating a spike within the following small interval Δt . From equation 1.29, with $n = 0$, the probability of not firing a spike for period τ is $\exp(-r\tau)$, so the probability of an interspike interval falling between τ and $\tau + \Delta t$ is

$$P[\tau \leq t_{i+1} - t_i < \tau + \Delta t] = r\Delta t \exp(-r\tau). \quad (1.31)$$

The probability density of interspike intervals is, by definition, this probability with the factor Δt removed. Thus, the interspike interval distribution for a homogeneous Poisson spike train is an exponential. The most likely interspike intervals are short ones, and long intervals have a probability that falls exponentially as a function of their duration.

From the interspike interval distribution of a homogeneous Poisson spike train, we can compute the mean interspike interval,

$$\langle \tau \rangle = \int_0^\infty d\tau \tau r \exp(-r\tau) = \frac{1}{r}, \quad (1.32)$$

interspike interval distribution

and the variance of the interspike intervals,

$$\sigma_\tau^2 = \int_0^\infty d\tau \tau^2 r \exp(-r\tau) - \langle \tau \rangle^2 = \frac{1}{r^2}. \quad (1.33)$$

coefficient of variation C_V

The ratio of the standard deviation to the mean is called the coefficient of variation

$$C_V = \frac{\sigma_\tau}{\langle \tau \rangle}, \quad (1.34)$$

and it takes the value one for a homogeneous Poisson process. This is a necessary, though not sufficient, condition to identify a Poisson spike train. Recall that the Fano factor for a Poisson process is also one. For any renewal process, the Fano factor evaluated over long time intervals approaches the value C_V^2 .

The Spike-Train Autocorrelation Function

The spike interval distribution measures the distribution of times between successive action potentials in a train. It is useful to generalize this concept and determine the distribution of times between any two spikes in a train. This is called the spike-train autocorrelation function, and it is particularly useful for detecting patterns in spike trains, most notably oscillations. The spike-train autocorrelation function is the autocorrelation of the neural response function of equation 1.1 with its average over time and trials subtracted out. The time average of the neural response function, from equation 1.6, is the spike-count rate r , and the trial average of this quantity is $\langle r \rangle = \langle n \rangle / T$. Thus, the spike-train autocorrelation function is

$$Q_{\rho\rho}(\tau) = \frac{1}{T} \int_0^T dt \langle (\rho(t) - \langle r \rangle)(\rho(t + \tau) - \langle r \rangle) \rangle. \quad (1.35)$$

Because the average is subtracted from the neural response function in this expression, $Q_{\rho\rho}$ should really be called an autocovariance, not an autocorrelation, but in practice it isn't.

The spike-train autocorrelation function is constructed from data in the form of a histogram by dividing time into bins. The value of the histogram for a bin labeled by a positive or negative integer m is computed by determining the number of the times that any two spikes in the train are separated by a time interval lying between $(m - 1/2)\Delta t$ and $(m + 1/2)\Delta t$ with Δt the bin size. This includes all pairings, even between a spike and itself. We call this number N_m . If the intervals between the n^2 spike pairs in the train were uniformly distributed over the range from zero to T , there would be $n^2\Delta t/T$ intervals in each bin. This uniform term is removed from the autocorrelation histogram by subtracting $n^2\Delta t/T$ from N_m for

all m . The spike-train autocorrelation histogram is then defined by dividing the resulting numbers by T , so the value of the histogram in bin m is $H_m = N_m/T - n^2 \Delta t/T^2$. For small bin sizes, the $m = 0$ term in the histogram counts the average number of spikes, that is $N_m = \langle n \rangle$ and, in the limit $\Delta t \rightarrow 0$, $H_0 = \langle n \rangle/T$ is the average firing rate $\langle r \rangle$. Because other bins have H_m of order Δt , the large $m = 0$ term is often removed from histogram plots. The spike-train autocorrelation function is defined as $H_m/\Delta t$ in the limit $\Delta t \rightarrow 0$, and it has the units of a firing rate squared. In this limit, the $m = 0$ bin becomes a δ function, $H_0/\Delta t \rightarrow \langle r \rangle \delta(\tau)$.

As we have seen, the distribution of interspike intervals for adjacent spikes in a homogeneous Poisson spike train is exponential (equation 1.31). By contrast, the intervals between any two spikes (not necessarily adjacent) in such a train are uniformly distributed. As a result, the subtraction procedure outlined above gives $H_m=0$ for all bins except for the $m=0$ bin that contains the contribution of the zero intervals between spikes and themselves. The autocorrelation function for a Poisson spike train generated at a constant rate $\langle r \rangle = r$ is thus

$$Q_{\rho\rho}(\tau) = r\delta(\tau). \quad (1.36)$$

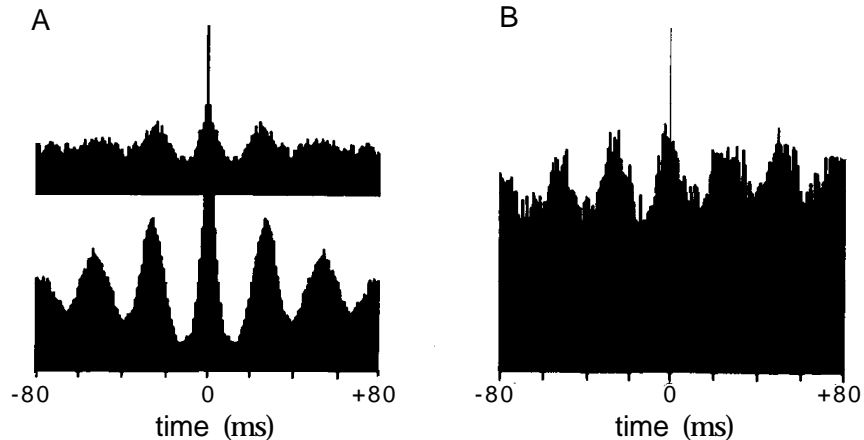


Figure 1.12: Autocorrelation and cross-correlation histograms for neurons in the primary visual cortex of a cat. A) Autocorrelation histograms for neurons recorded in the right (upper) and left (lower) hemispheres show a periodic pattern indicating oscillations at about 40 Hz. The lower diagram indicates stronger oscillations in the left hemisphere. B) The cross-correlation histogram for these two neurons shows that their oscillations are synchronized with little time delay. (Adapted from Engel et al., 1991.)

A cross-correlation function between spike trains from two different neurons can be defined by analogy with the autocorrelation function by determining the distribution of intervals between pairs of spikes, one taken from each train. The spike-train autocorrelation function is an even function of τ , $Q_{\rho\rho}(\tau) = Q_{\rho\rho}(-\tau)$, but the cross-correlation function is not necessarily even. A peak at zero interval in a cross-correlation function signifies

*cross-correlation
function*

that the two neurons are firing synchronously. Asymmetric shifts in this peak away from zero result from fixed delays between the firing of the two neurons, and they indicate non-synchronous but phase-locked firing. Periodic structure in either an autocorrelation or cross-correlation function or histogram indicates that the firing probability oscillates. Such periodic structure is seen in the histograms of figure 1.12 showing 40 Hz oscillations in neurons of cat primary visual cortex that are roughly synchronized between the two cerebral hemispheres.

The Inhomogeneous Poisson Process

When the firing rate depends on time, different sequences of n spikes occur with different probabilities, and $p[t_1, t_2, \dots, t_n]$ depends on the spike times. Because spikes are still generated independently by an inhomogeneous Poisson process, their times only enter into $p[t_1, t_2, \dots, t_n]$ through the time-dependent firing rate $r(t)$. Assuming, as before, that the spike times are ordered, $0 \leq t_1 \leq t_2 \leq \dots \leq t_n \leq T$, the probability density for n spike times (derived in appendix C) is

$$p[t_1, t_2, \dots, t_n] = \exp\left(-\int_0^T dt r(t)\right) \prod_{i=1}^n r(t_i). \quad (1.37)$$

This result applies if the spike times have been written in temporal order. If the spike times are not ordered, so that, for example, we are interested in the probability density for any spike occurring at the time t_1 , not necessarily the first spike, these expression should be divided by a factor of $n!$ to account for the number of different possible orderings of spike times.

The Poisson Spike Generator

Spike sequences can be simulated by using some estimate of the firing rate, $r_{\text{est}}(t)$, predicted from knowledge of the stimulus, to drive a Poisson process. A simple procedure for generating spikes in a computer program is based on the fact that the estimated probability of firing a spike during a short interval of duration Δt is $r_{\text{est}}(t)\Delta t$. The program progresses through time in small steps of size Δt and generates, at each time step, a random number x_{rand} chosen uniformly in the range between zero and one. If $r_{\text{est}}(t)\Delta t > x_{\text{rand}}$ at that time step, a spike is fired, otherwise it is not.

For a constant firing rate, it is faster to compute spike times t_i for $i = 1, 2, \dots$ iteratively by generating interspike intervals from an exponential probability density (equation 1.31). If x_{rand} is uniformly distributed over the range between zero and one, the negative of its logarithm is exponentially distributed. Thus, we can generate spike times iteratively from the formula $t_{i+1} = t_i - \ln(x_{\text{rand}})/r$. Unlike, the algorithm discussed in the previous paragraph, this method only works for constant firing rates. However, it can be extended to time-dependent rates by using a procedure

called the rejection sampling or spike thinning. The thinning technique requires a bound r_{\max} on the estimated firing rate such that $r_{\text{est}}(t) \leq r_{\max}$ at all times. We first generate a spike sequence corresponding to the constant rate r_{\max} by iterating the rule $t_{i+1} = t_i - \ln(x_{\text{rand}})/r_{\max}$. The spikes are then thinned by generating another x_{rand} for each i and removing the spike at time t_i from the train if $r_{\text{est}}(t_i)/r_{\max} < x_{\text{rand}}$. If $r_{\text{est}}(t_i)/r_{\max} \geq x_{\text{rand}}$, spike i is retained. Thinning corrects for the difference between the estimated time-dependent rate and the maximum rate.

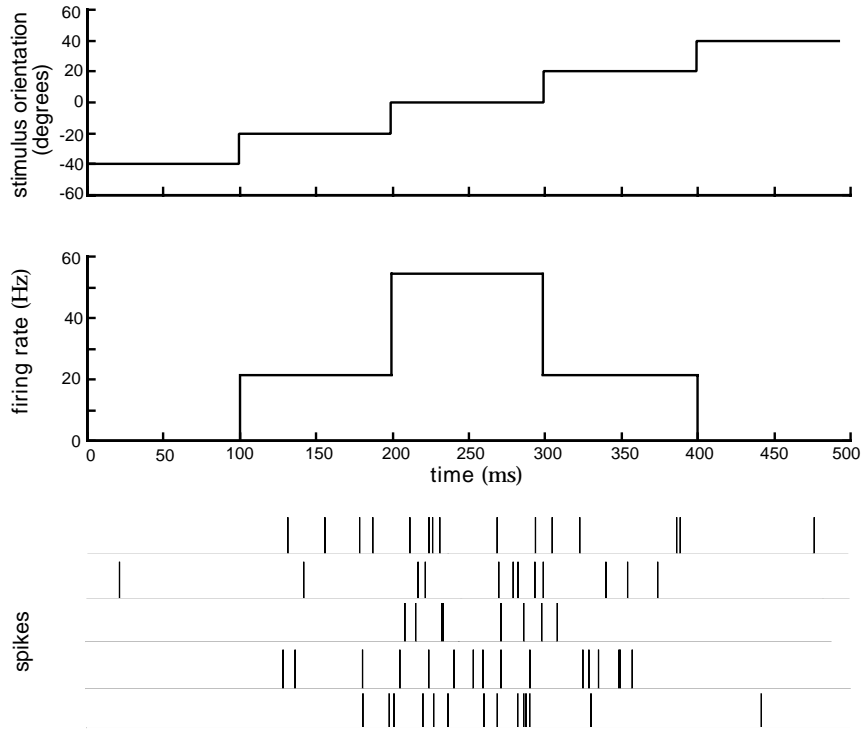


Figure 1.13: Model of an orientation selective neuron. The orientation angle (top panel) was increased from an initial value of -40° by 10° every 100 ms. The firing rate (middle panel) was used to generate spikes (bottom panel) using a Poisson spike generator. The bottom panel shows spike sequences generated on five different trials.

Figure 1.13 shows an example of a model of an orientation selective V1 neuron constructed in this way. In this model, the estimated firing rate is determined from the response tuning curve of figure 1.5B,

$$r_{\text{est}}(t) = f(s(t)) = r_{\max} \exp\left(-\frac{1}{2} \left(\frac{s(t) - s_{\max}}{\sigma_f}\right)^2\right). \quad (1.38)$$

This is an extremely simplified model of response dynamics, because the firing rate at any given time depends only on the value of the stimulus at

that instant of time and not on its recent history. Models that allow for a dependence of firing rate on stimulus history are discussed in chapter 2. In figure 1.13, the orientation angle increases in a sequence of steps. The firing rate follows these changes, and the Poisson process generates an irregular firing pattern that reflects the underlying rate but varies from trial to trial.

Certain features of neuronal firing violate the independence assumption that forms the basis of the Poisson model, at least if a constant firing rate is used. We have already noted that there are periods of time, the absolute and relative refractory periods, following the generation of an action potential when the probability of a spike occurring is greatly or somewhat reduced. Refractory effects can be incorporated into a Poisson model of spike generation by setting the firing rate to zero immediately after a spike is fired, and then letting it return to its predicted value according to some dynamic rule such as an exponential recovery.

Comparison with Data

The Poisson process is simple and useful, but does it match data on neural response variability? To address this question we examine Fano factors, interspike interval distributions, and coefficients of variation.

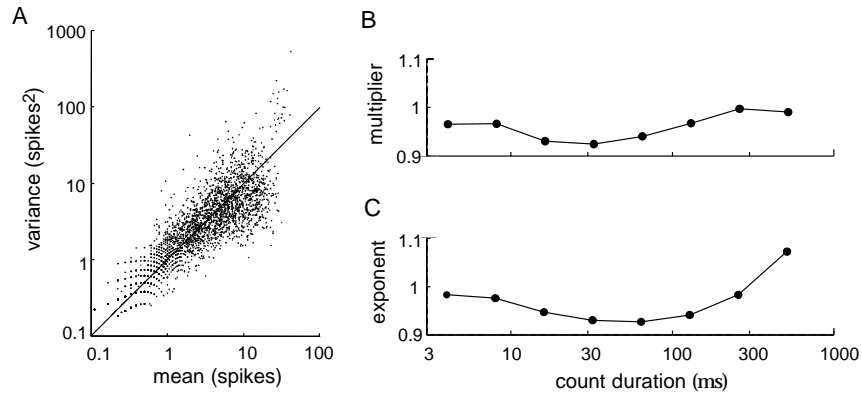


Figure 1.14: Variability of MT neurons in alert macaque monkeys responding to moving visual images. A) Variance of the spike counts for a 256 ms counting period plotted against the mean spike count. The straight line is the prediction of the Poisson model. Data are from 94 cells recorded under a variety of stimulus conditions. B) The multiplier A in the relationship between spike-count variance and mean as a function of the duration of the counting interval. C) The exponent B in this relation as a function of the duration of the counting interval. (Adapted from O'Keefe et al., 1997.)

The Fano factor describes the relationship between the mean spike count over a given interval and the spike-count variance. Mean spike counts $\langle n \rangle$ and variances σ_n^2 from a wide variety of neuronal recordings have been

fit to the equation $\sigma_n^2 = A\langle n \rangle^B$, and the multiplier A and exponent B have been determined. The values of both A and B typically lie between 1.0 and 1.5. Because the Poisson model predicts $A = B = 1$, this indicates that the data show a higher degree of variability than the Poisson model would predict. However, many of these experiments involve anesthetized animals, and it is known that response variability is higher in anesthetized than in alert animals. Figure 1.14 shows their data for spike-count means and variances extracted from recordings of MT neurons in alert macaque monkeys using a number of different stimuli. The MT (medial temporal) area is a visual region of the primate cortex where many neurons are sensitive to image motion. The individual means and variances are scattered in figure 1.14A, but they cluster around the diagonal which is the Poisson prediction. Similarly, the results show A and B values close to one, the Poisson values (figure 1.14B). Of course, many neural responses cannot be described by Poisson statistics, but it is reassuring to see a case where the Poisson model seems a reasonable approximation.

area MT

Interspike interval distributions are extracted from data as interspike interval histograms by counting the number of intervals falling in discrete time bins. Figure 1.15A presents an example, from the responses of a non-bursting cell in area MT of a monkey in response to images consisting of randomly moving dots with a variable amount of coherence imposed on their motion (see chapter 3 for a more detailed description). For interspike intervals longer than about 10 ms, the shape of this histogram is exponential, in agreement with equation 1.31. However, for shorter intervals there is a discrepancy. While the homogeneous Poisson distribution 1.31 rises for short interspike intervals, the experimental results show a rapid decrease. This is the result of refractoriness making short interspike intervals less likely than the Poisson model would predict. Data on interspike intervals can be fit more accurately by a gamma distribution,

gamma distribution

$$p[\tau] = \frac{r(\tau)^k \exp(-r\tau)}{k!} \quad (1.39)$$

with $k > 0$ than by the exponential distribution of the Poisson model, which has $k = 0$.

Figure 1.15B shows a theoretical histogram obtained by adding a refractory period of a variable duration to the Poisson model. Spiking was prohibited during the refractory period, and then was described once again by a homogeneous Poisson process. The refractory period was randomly chosen from a Gaussian distribution with a mean of 5 ms and a standard deviation of 2 ms (only random draws that generated positive refractory periods were included). The resulting interspike interval distribution of figure 1.15B agrees quite well with the data.

C_V values extracted from the spike trains of neurons recorded in monkeys from area MT and primary visual cortex (V1) are shown in figure 1.16. The data have been divided into groups based on the mean interspike interval, and the coefficient of variation is plotted as a function of this mean inter-

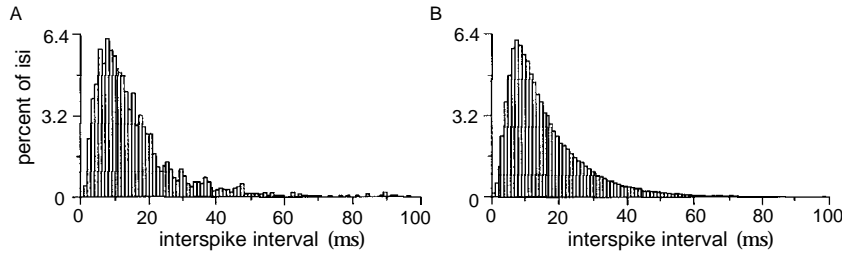


Figure 1.15: (A) Interspike interval distribution from an MT neuron responding to a moving random dot image. The probability of interspike intervals falling into the different bins, expressed as a percentage, is plotted against interspike interval. B) Interspike interval histogram generated from a Poisson model with a stochastic refractory period. (Adapted from Bair et al., 1994.)

val, equivalent to $1/\langle r \rangle$. Except for short mean interspike intervals, the values are near one, although they tend to cluster slightly lower than one, the Poisson value. The small C_V values for short interspike intervals are due to the refractory period. The solid curve is the prediction of a Poisson model with refractoriness.

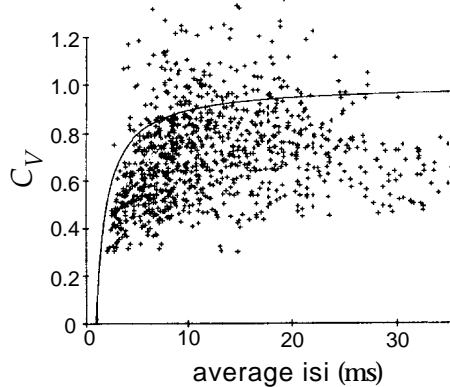


Figure 1.16: Coefficients of variation for a large number of V1 and MT neurons plotted as a function of mean interspike interval. The solid curve is the result of a Poisson model with a refractory period. (Adapted from Softky and Koch, 1992.)

The Poisson model with refractoriness provides a reasonably good description of a significant amount of data, especially considering its simplicity. However, there are cases when the accuracy in the timing and numbers of spikes fired by a neuron is considerably higher than would be implied by Poisson statistics. Furthermore, even when it successfully describes data, the Poisson model does not provide a mechanistic explanation of neuronal response variability. Spike generation, by itself, is highly reliable in real neurons. Figure 1.17 compares the response of V1 cells to constant current injection *in vivo* and *in vitro*. The *in vitro* response is a reg-

ular and reproducible spike train (left panel). The same current injection

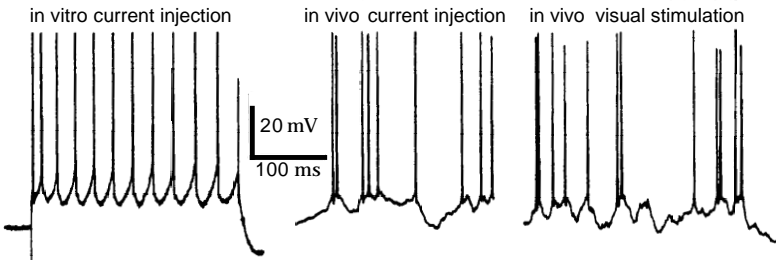


Figure 1.17: Intracellular recordings from cat V1 neurons. The left panel is the response of a neuron in an *in vitro* slice preparation to constant current injection. The center and right panels show recordings from neurons *in vivo* responding to either injected current (center), or a moving visual image (right). (Adapted from Holt et al., 1996.)

paradigm applied *in vivo* produces a highly irregular pattern of firing (center panel) similar to the response to a moving bar stimulus (right panel). Although some of the basic statistical properties of firing variability may be captured by the Poisson model of spike generation, the spike generating mechanism itself in real neurons is clearly not responsible for the variability. We explore ideas about possible sources of spike-train variability in chapter 5.

Some neurons fire action potentials in clusters or bursts of spikes that cannot be described by a Poisson process with a fixed rate. Bursting can be included in a Poisson model by allowing the firing rate to fluctuate to describe the high rate of firing during a burst. Sometimes the distribution of bursts themselves can be described by a Poisson process (such a doubly stochastic process is called a Cox process).

1.5 The Neural Code

The nature of the neural code is a topic of intense debate within the neuroscience community. Much of the discussion has focused on whether neurons use rate coding or temporal coding, often without a clear definition of what these terms mean. We feel that the central issue in neural coding is whether individual action potentials and individual neurons encode independently of each other, or whether correlations between different spikes and different neurons carry significant amounts of information. We therefore contrast independent-spike and independent-neuron codes with correlation codes before addressing the issue of temporal coding.

Independent-Spike, Independent-Neuron, and Correlation Codes

The neural response, and its relation to the stimulus, is completely characterized by the probability distribution of spike times as a function of the stimulus. If spike generation can be described as an inhomogeneous Poisson process, this probability distribution can be computed from the time-dependent firing rate $r(t)$ using equation 1.37. In this case, $r(t)$ contains all the information about the stimulus that can be extracted from the spike train, and the neural code could reasonably be called a rate code. Unfortunately, this definition does not agree with common usage. Instead, we will call a code based solely on the time-dependent firing rate an independent-spike code. This refers to the fact that the generation of each spike is independent of all the other spikes in the train. If individual spikes do not encode independently of each other, we call the code a correlation code, because correlations between spike times may carry additional information. In reality, information is likely to be carried both by individual spikes and through correlations, and some arbitrary dividing line must be established to characterize the code. Identifying a correlation code should require that a significant amount of information be carried by correlations, say as much as is carried by the individual spikes.

A simple example of a correlation code would be if significant amounts of information about a stimulus were carried by interspike intervals. In this case, if we considered spike times individually, independently of each other, we would miss the information carried by the intervals between them. This is just one example of a correlation code. Information could be carried by more complex relationships between spikes.

Independent-spike codes are much simpler to analyze than correlation codes, and most work on neural coding assumes spike independence. When careful studies have been done, it has been found that some information is carried by correlations between two or more spikes, but this information is rarely larger than 10% of the information carried by spikes considered independently. Of course, it is possible that, due to our ignorance of the ‘real’ neural code, we have not yet uncovered or examined the types of correlations that are most significant for neural coding. Although this is not impossible, we view it as unlikely and feel that the evidence for independent-spike coding, at least as a fairly accurate approximation, is quite convincing.

The discussion to this point has focused on information carried by single neurons, but information is typically encoded by neuronal populations. When we study population coding, we must consider whether individual neurons act independently, or whether correlations between different neurons carry additional information. The analysis of population coding is easiest if the response of each neuron is considered statistically independent, and such independent-neuron coding is typically assumed in the analysis of population codes (chapter 3). The independent-neuron

*independent-spike
code*

correlation code

*independent-
neuron
code*

hypothesis does not mean that the spike trains of different neurons are not combined into an ensemble code. Rather it means that they can be combined without taking correlations into account. To test the validity of this assumption, we must ask whether correlations between the spiking of different neurons provide additional information about a stimulus that cannot be obtained by considering all of their firing patterns individually.

Synchronous firing of two or more neurons is one mechanism for conveying information in a population correlation code. Rhythmic oscillations of population activity provides another possible mechanism, as discussed below. Both synchronous firing and oscillations are common features of the activity of neuronal populations. However, the existence of these features is not sufficient for establishing a correlation code, because it is essential to show that a significant amount of information is carried by the resulting correlations. The assumption of independent-neuron coding is a useful simplification that is not in gross contradiction with experimental data, but it is less well established and more likely to be challenged in the future than the independent-spike hypothesis.

synchrony and oscillations

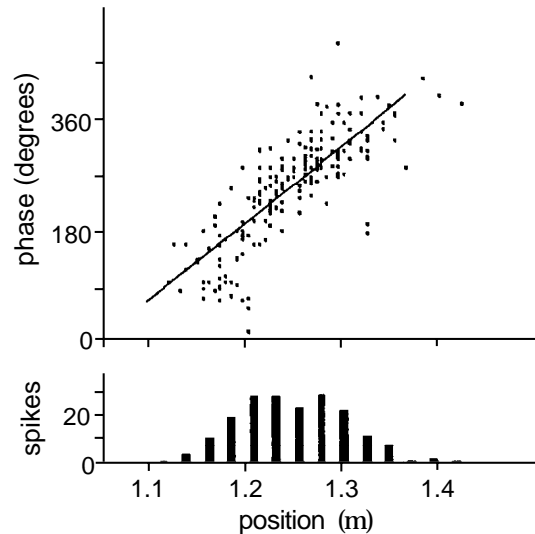


Figure 1.18: Position versus phase for a hippocampal place cell. Each dot in the upper figure shows the phase of the theta rhythm plotted against the position of the animal at the time when a spike was fired. The linear relation shows that information about position is contained in the relative phase of firing. The lower plot is a conventional place field tuning curve of spike count versus position. (Adapted from O'Keefe and Recce, 1993.)

Place cell coding of spatial location in the rat hippocampus is an example where at least some additional information appears to be carried by correlations between the firing patterns of neurons in a population. The hippocampus is a structure located deep inside the temporal lobe that plays

hippocampal place cells

an important role in memory formation and is involved in a variety of spatial tasks. The firing rates of many hippocampal neurons, recorded when a rat is moving around a familiar environment, depend on the location of the animal, and are restricted to spatially localized areas called the place fields of the cells. In addition, when a rat explores an environment, hippocampal neurons fire collectively in a rhythmic pattern with a frequency in the theta range, 7-12 Hz. The spiking time of an individual place cell relative to the phase of the population theta rhythm actually gives additional information about the location of the rat not provided by place cells considered individually. The relationship between location and phase of place cell firing shown in figure 1.18 means, for example, that we can distinguish two locations on opposite sides of the peak of a single neuron's tuning curve that correspond to the same firing rate, by knowing when the spikes occurred relative to the theta rhythm. However, the amount of additional information carried by correlations between place field firing and the theta rhythm has not been fully quantified.

Temporal Codes

The concept of temporal coding arises when we consider how precisely we must measure spike times to extract most of the information from a neuronal response. This precision determines the temporal resolution of the neural code. A number of studies have found that this temporal resolution is on a millisecond time scale, indicating that precise spike timing is a significant element in neural encoding. Similarly, we can ask whether high-frequency firing-rate fluctuations carry significant information about a stimulus. When precise spike timing or high-frequency firing-rate fluctuations are found to carry information, the neural code is often identified as a temporal code.

The temporal structure of a spike train or firing rate evoked by a stimulus is determined both by the dynamics of the stimulus and by the nature of the neural encoding process. Stimuli that change rapidly tend to generate precisely timed spikes and rapidly changing firing rates no matter what neural coding strategy is being used. Temporal coding refers to (or should refer to) temporal precision in the response that does not arise solely from the dynamics of the stimulus, but that nevertheless relates to properties of the stimulus. The interplay between stimulus and encoding dynamics makes the identification of a temporal code difficult.

The issue of temporal coding is distinct and independent from the issue of independent-spike coding discussed above. If the independent-spike hypothesis is valid, the temporal character of the neural code is determined by the behavior of $r(t)$. If $r(t)$ varies slowly with time, the code is typically called a rate code, and if it varies rapidly, the code is called temporal. Figure 1.19 provides an example of different firing-rate behaviors for a neuron in area MT of a monkey recorded over multiple trials with three different

stimuli (consisting of moving random dots). The activity in the top panel would typically be regarded as reflecting rate coding, and the activity in the bottom panel as reflecting temporal coding. However, the identification of rate and temporal coding in this way is ambiguous because it is not obvious what criterion should be used to characterize the changes in $r(t)$ as slow or rapid.

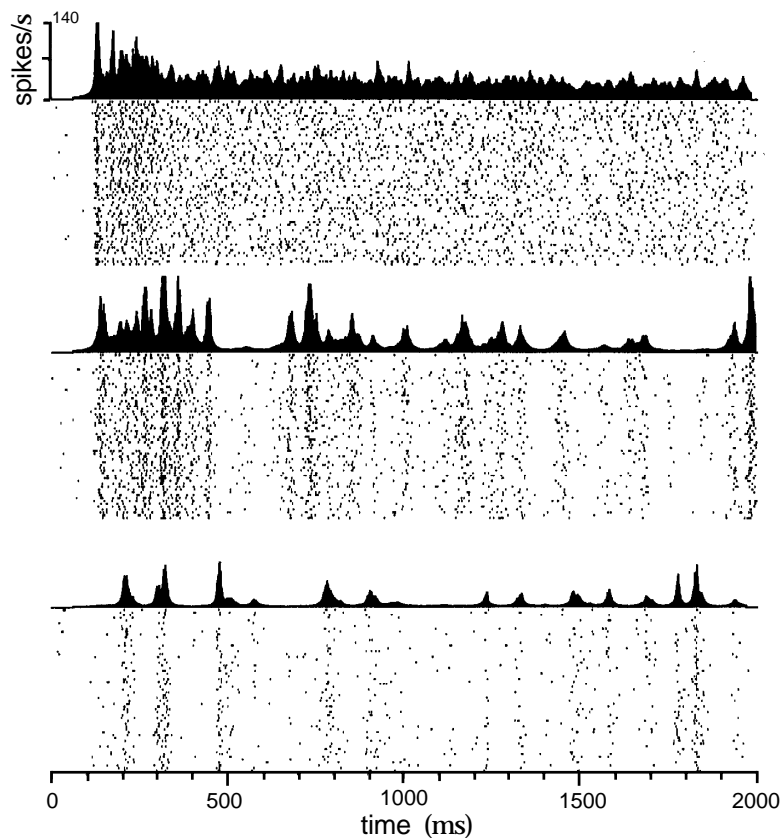


Figure 1.19: Time-dependent firing rates for different stimulus parameters. The rasters show multiple trials during which an MT neuron responded to the same moving random dot stimulus. Firing rates, shown above the raster plots, were constructed from the multiple trials by counting spikes within discrete time bins and averaging over trials. The three different results are from the same neuron but using different stimuli. The stimuli were always patterns of moving random dots but the coherence of the motion was varied (see chapter 3 for more information about this stimulus). (Adapted from Bair and Koch, 1996.)

One possibility is to use the spikes to distinguish slow from rapid, so that a temporal code is identified when peaks in the firing rate occur with roughly the same frequency as the spikes themselves. In this case, each peak corresponds to the firing of only one, or at most a few action po-

tentials. While this definition makes intuitive sense, it is problematic to extend it to the case of population coding. When many neurons are involved, any single neuron may fire only a few spikes before its firing rate changes, but collectively the population may produce a large number of spikes over the same time period. Thus, a neuron that appears to employ a temporal code, by this definition, may be part of a population that does not.

Another proposal is to use the stimulus, rather than the response, to establish what makes a temporal code. In this case, a temporal code is defined as one in which information is carried by details of spike timing on a scale shorter than the fastest time characterizing variations of the stimulus. This requires that information about the stimulus be carried by Fourier components of $r(t)$ at frequencies higher than those present in the stimulus. Many of the cases where a temporal code has been reported using spikes to define the nature of the code would be called rate codes if the stimulus were used instead.

The debate between rate and temporal coding dominates discussions about the nature of the neural code. Determining the temporal resolution of the neural code is clearly important, but much of this debate seems uninformative. We feel that the central challenge is to identify relationships between the firing patterns of different neurons in a responding population and to understand their significance for neural coding.

1.6 Chapter Summary

With this chapter, we have begun our study of the way that neurons encode information using spikes. We used a sequence of δ functions, the neural response function, to represent a spike train and defined three types of firing rates: the single-spike probability density $r(t)$, the spike-count rate r and the average firing rate $\langle r \rangle$. In the discussion of how the firing rate $r(t)$ could be extracted from data, we introduced the important concepts of a linear filter and a kernel acting as a sliding window function. The average firing rate expressed as a function of a static stimulus parameter is called the response tuning curve, and we presented examples of Gaussian, cosine and sigmoidal tuning curves. Spike-triggered averages of stimuli, or reverse correlation functions, were introduced to characterize the selectivity of neurons to dynamic stimuli. The homogeneous and inhomogeneous Poisson processes were presented as models of stochastic spike sequences. We defined correlation functions, auto- and cross-correlations, and power spectra, and used the Fano factor, interspike-interval histogram, and coefficient of variation to characterize the stochastic properties of spiking. We concluded with a discussion of independent-spike and independent-neuron codes versus correlation codes, and of the temporal precision of spike timing as addressed in discussion of temporal coding.

1.7 Appendices

A) The Power Spectrum of White-Noise

The Fourier transform of the stimulus autocorrelation function (see the Mathematical Appendix),

$$\tilde{Q}_{ss}(\omega) = \frac{1}{T} \int_{-T/2}^{T/2} d\tau Q_{ss}(\tau) \exp(i\omega\tau), \quad (1.40)$$

is called the power spectrum. Because we have defined the stimulus as periodic outside the range of the trial T , we have used a finite-time Fourier transform and ω should be restricted to values that are integer multiples of $2\pi/T$. We can compute the power spectrum for a white-noise stimulus using the fact the $Q_{ss}(\tau) = \sigma_s^2 \delta(\tau)$ for white-noise,

$$\tilde{Q}_{ss}(\omega) = \frac{\sigma_s^2}{T} \int_{-T/2}^{T/2} d\tau \delta(\tau) \exp(i\omega\tau) = \frac{\sigma_s^2}{T}. \quad (1.41)$$

This is the defining characteristic of white-noise; its power spectrum is independent of frequency.

Using the definition of the stimulus autocorrelation function, we can also write

$$\begin{aligned} \tilde{Q}_{ss}(\omega) &= \frac{1}{T} \int_0^T dt s(t) \frac{1}{T} \int_{-T/2}^{T/2} d\tau s(t + \tau) \exp(i\omega\tau) \\ &= \frac{1}{T} \int_0^T dt s(t) \exp(-i\omega t) \frac{1}{T} \int_{-T/2}^{T/2} d\tau s(t + \tau) \exp(i\omega(t + \tau)). \end{aligned} \quad (1.42)$$

The first integral on the right side of the second equality is the complex conjugate of the Fourier transform of the stimulus,

$$\tilde{s}(\omega) = \frac{1}{T} \int_0^T dt s(t) \exp(i\omega t). \quad (1.43)$$

The second integral, because of the periodicity of the integrand (when ω is an integer multiple of $2\pi/T$) is equal to $\tilde{s}(\omega)$. Therefore,

$$\tilde{Q}_{ss}(\omega) = |\tilde{s}(\omega)|^2, \quad (1.44)$$

which provides another definition of the stimulus power spectrum. It is the absolute square of the Fourier transform of the stimulus.

Although equations 1.40 and 1.44 are both sound, they do not provide a statistically efficient method of estimating the power spectrum of discrete approximations to white-noise sequences generated by the methods described in this chapter. That is, the apparently natural procedure of taking

a white noise sequence $s(m\Delta t)$ for $m = 1, 2, \dots, T/\Delta t$, and computing the square amplitude of its Fourier transform at frequency ω

$$\frac{\Delta T}{T} \left| \sum_{m=1}^{T/\Delta t} s(t) \exp(-i\omega m \Delta t) \right|^2$$

periodogram
is a biased and extremely noisy way of estimating $\tilde{Q}_{ss}(\omega)$. This estimator is called the periodogram. The statistical problems with the periodogram, and some of the many suggested solutions, are discussed in almost any textbook on spectral analysis (see, for example, Percival and Waldron, 1993).

B) Moments of the Poisson Distribution

The average number of spikes generated by a Poisson process with constant rate r over a time T is

$$\langle n \rangle = \sum_{n=0}^{\infty} n P_T[n] = \sum_{n=0}^{\infty} \frac{n(rT)^n}{n!} \exp(-rT), \quad (1.45)$$

and the variance in the spike count is

$$\sigma_n^2(T) = \sum_{n=1}^{\infty} n^2 P_T[n] - \langle n \rangle^2 = \sum_{n=1}^{\infty} \frac{n^2(rT)^n}{n!} \exp(-rT) - \langle n \rangle^2. \quad (1.46)$$

To compute these quantities we need to calculate the two sums appearing in these equations. A good way to do this is to compute the moment generating function

$$g(\alpha) = \sum_{n=0}^{\infty} \frac{(rT)^n \exp(\alpha n)}{n!} \exp(-rT). \quad (1.47)$$

The k^{th} derivative of g with respect to α , evaluated at the point $\alpha = 0$, is

$$\frac{d^k g}{d\alpha^k} \Big|_{\alpha=0} = \sum_{n=0}^{\infty} \frac{n^k (rT)^n}{n!} \exp(-rT), \quad (1.48)$$

so once we have computed g we only need to calculate its first and second derivatives to determine the sums we need. Rearranging the terms a bit, and recalling that $\exp(z) = \sum z^n / n!$, we find

$$g(\alpha) = \exp(-rT) \sum_{n=0}^{\infty} \frac{(rT \exp(\alpha))^n}{n!} = \exp(-rT) \exp(rT e^\alpha). \quad (1.49)$$

The derivatives are then

$$\frac{dg}{d\alpha} = rT e^\alpha \exp(-rT) \exp(rT e^\alpha) \quad (1.50)$$

and

$$\frac{d^2g}{d\alpha^2} = (rTe^\alpha)^2 \exp(-rT) \exp(rTe^\alpha) + rTe^\alpha \exp(-rT) \exp(rTe^\alpha). \quad (1.51)$$

Evaluating these at $\alpha = 0$ and putting the results into equation 1.45 and 1.46 gives the results $\langle n \rangle = rT$ and $\sigma_n^2(T) = (rT)^2 + rT - (rT)^2 = rT$.

C) Inhomogeneous Poisson Statistics

The probability density for a particular spike sequence t_i with $i = 1, 2, \dots, n$ is obtained from the corresponding probability distribution by multiplying the probability that the spikes occur when they do by the probability that no other spikes occur. We begin by computing the probability that no spikes are generated during the time interval from t_i to t_{i+1} between two adjacent spikes. We determine this by dividing the interval into M bins of size Δt assuming that $M\Delta t = t_{i+1} - t_i$. We will ultimately take the limit $\Delta t \rightarrow 0$. The firing rate during bin m within this interval is $r(t_i + m\Delta t)$. Because the probability of firing a spike in this bin is $r(t_i + m\Delta t)\Delta t$, the probability of not firing a spike is $1 - r(t_i + m\Delta t)\Delta t$. To have no spikes during the entire interval, we must string together M such bins, and the probability of this occurring is the product of the individual probabilities,

$$P[\text{no spikes}] = \prod_{m=1}^M (1 - r(t_i + m\Delta t)\Delta t). \quad (1.52)$$

We evaluate this expression by taking its logarithm,

$$\ln P[\text{no spikes}] = \sum_{m=1}^M \ln (1 - r(t_i + m\Delta t)\Delta t), \quad (1.53)$$

using the fact that the logarithm of a product is the sum of the logarithms of the multiplied terms. Using the approximation $\ln(1 - r(t_i + m\Delta t)\Delta t) \approx -r(t_i + m\Delta t)\Delta t$, valid for small Δt , we can simplify this to

$$\ln P[\text{no spikes}] = - \sum_{m=1}^M r(t_i + m\Delta t)\Delta t. \quad (1.54)$$

In the limit $\Delta t \rightarrow 0$, the approximation becomes exact and this sum becomes the integral of $r(t)$ from t_i to t_{i+1} ,

$$\ln P[\text{no spikes}] = - \int_{t_i}^{t_{i+1}} dt r(t). \quad (1.55)$$

Exponentiating this equation gives the result we need

$$P[\text{no spikes}] = \exp \left(- \int_{t_i}^{t_{i+1}} dt r(t) \right). \quad (1.56)$$

The probability density $p[t_1, t_2, \dots, t_n]$ is the product of the densities for the individual spikes and the probabilities of not generating spikes during the interspike intervals, between time 0 and the first spike, and between the time of the last spike and the end of the trial period,

$$\begin{aligned} p[t_1, t_2, \dots, t_n] &= \exp\left(-\int_0^{t_1} dt r(t)\right) \exp\left(-\int_{t_n}^T dt r(t)\right) \times \\ &\quad r(t_n) \prod_{i=1}^{n-1} r(t_i) \exp\left(-\int_{t_i}^{t_{i+1}} dt r(t)\right). \end{aligned} \quad (1.57)$$

The exponentials in this expression all combine because the product of exponentials is the exponential of the sum, so the different integrals in this sum add up to form a single integral,

$$\begin{aligned} &\exp\left(-\int_0^{t_1} dt r(t)\right) \exp\left(-\int_{t_n}^T dt r(t)\right) \prod_{i=1}^{n-1} \exp\left(-\int_{t_i}^{t_{i+1}} dt r(t)\right) \\ &= \exp\left(-\left(\int_0^{t_1} dt r(t) + \sum_{i=1}^{n-1} \int_{t_i}^{t_{i+1}} dt r(t) + \int_{t_n}^T dt r(t)\right)\right) \\ &= \exp\left(-\int_0^T dt r(t)\right). \end{aligned} \quad (1.58)$$

Substituting this into 1.57 gives the result 1.37.

1.8 Annotated Bibliography

Braitenberg & Schuz (1991) provide some of the quantitative measures of neuroanatomical properties of cortex that we quote. Rieke et al. (1997) describe the analysis of spikes and the relationships between neural responses and stimuli and is a general reference for material we present in chapters 1-4. Gabbiani & Koch (1998) provide another account of some of this material. The mathematics underlying point processes, the natural statistical model for spike sequences, can be found in Cox (1962) and Cox & Isham (1980), including the relationship between the Fano factor and the coefficient of variation. A general analysis of histogram representations can be found in Scott (1992), and white-noise and filtering techniques (our analysis of which continues in chapter 2) are described in de Boer & Kuyper (1968), Marmarelis & Marmarelis (1978), and Wiener (1958).

In chapters 1 and 3, we discuss two systems associated with studies of spike encoding; the H1 neuron in the visual system of flies, reviewed by Rieke et al. (1997), and area MT of monkeys, discussed by Parker & Newsome (1998). Wandell (1995) introduces orientation and disparity tuning, relevant to examples presented in this chapter.

Chapter 2

Neural Encoding II: Reverse Correlation and Visual Receptive Fields

2.1 Introduction

The spike-triggered average stimulus introduced in chapter 1 is a standard way of characterizing the selectivity of a neuron. In this chapter, we show how spike-triggered averages and reverse-correlation techniques can be used to construct estimates of firing rates evoked by arbitrary time-dependent stimuli. Firing rates calculated directly from reverse-correlation functions provide only a linear estimate of the response of a neuron, but we also present in this chapter various methods for including nonlinear effects such as firing thresholds.

Spike-triggered averages and reverse-correlation techniques have been used extensively to study properties of visually responsive neurons in the retina (retinal ganglion cells), lateral geniculate nucleus (LGN), and primary visual cortex (V1, or area 17 in the cat). At these early stages of visual processing, the responses of some neurons (simple cells in primary visual cortex, for example) can be described quite accurately using this approach. Other neurons (complex cells in primary visual cortex, for example) can be described by extending the formalism. Reverse-correlation techniques have also been applied to responses of neurons in visual areas V2, area 18, and MT, but they generally fail to capture the more complex and nonlinear features typical of responses at later stages of the visual system. Descriptions of visual responses based on reverse correlation are approximate, and they do not explain how visual responses arise from the synaptic, cellular, and network properties of retinal, LGN, and cortical circuits. Nevertheless, they provide an important framework for character-

retina
LGN
V1, area 17

2 Neural Encoding II: Reverse Correlation and Visual Receptive Fields

izing response selectivities, a reference point for identifying and characterizing novel effects, and a basis for building mechanistic models, some of which are discussed at the end of this chapter and in chapter 7.

2.2 Estimating Firing Rates

In chapter 1, we discussed a simple model in which firing rates were estimated as instantaneous functions of the stimulus, using response tuning curves. The activity of a neuron at time t typically depends on the behavior of the stimulus over a period of time starting a few hundred milliseconds prior to t and ending perhaps tens of milliseconds before t . Reverse correlation methods can be used to construct a more accurate model that includes the effects of the stimulus over such an extended period of time. The basic problem is to construct an estimate $r_{\text{est}}(t)$ of the firing rate $r(t)$ evoked by a stimulus $s(t)$. The simplest way to construct an estimate is to assume that the firing rate at any given time can be expressed as a weighted sum of the values taken by the stimulus at earlier times. Since time is a continuous variable this ‘sum’ actually takes the form of an integral, and we write

$$r_{\text{est}}(t) = r_0 + \int_0^\infty d\tau D(\tau)s(t - \tau). \quad (2.1)$$

The term r_0 accounts for any background firing that may occur when $s = 0$. $D(\tau)$ is a weighting factor that determines how strongly, and with what sign, the value of the stimulus at time $t - \tau$ affects the firing rate at time t . Note that the integral in equation 2.1 is a linear filter of the same form as the expressions used to compute $r_{\text{approx}}(t)$ in chapter 1.

As discussed in chapter 1, sensory systems tend to adapt to the absolute intensity of a stimulus. It is easier to account for the responses to fluctuations of a stimulus around some mean background level than it is to account for adaptation processes. We therefore assume throughout this chapter that the stimulus parameter $s(t)$ has been defined with its mean value subtracted out. This means that the time integral of $s(t)$ over the duration of a trial is zero.

We have provided a heuristic justification for the terms in equation 2.1 but, more formally, they correspond to the first two terms in a systematic expansion of the response in powers of the stimulus. Such an expansion is the functional equivalent of the Taylor series expansion used to generate power series approximations of functions, and it is called the Volterra expansion. For the case we are considering, it takes the form

$$\begin{aligned} r_{\text{est}}(t) = & r_0 + \int d\tau D(\tau)s(t - \tau) + \int d\tau_1 d\tau_2 D_2(\tau_1, \tau_2)s(t - \tau_1)s(t - \tau_2) + \\ & \int d\tau_1 d\tau_2 d\tau_3 D_3(\tau_1, \tau_2, \tau_3)s(t - \tau_1)s(t - \tau_2)s(t - \tau_3) + \dots \end{aligned} \quad (2.2)$$

*firing rate
estimate $r_{\text{est}}(t)$*

Volterra expansion

This series was rearranged by Wiener to make the terms easier to compute. The first two terms of the Volterra and Wiener expansions are identical and are given by the two expressions on the right side of equation 2.1. For this reason, D is called the first Wiener kernel, the linear kernel, or, when higher-order terms (terms involving more than one factor of the stimulus) are not being considered, simply the kernel.

To construct an estimate of the firing rate based on an expression of the form 2.1, we choose the kernel D to minimize the squared difference between the estimated response to a stimulus and the actual measured response averaged over time,

$$E = \frac{1}{T} \int_0^T dt (r_{\text{est}}(t) - r(t))^2. \quad (2.3)$$

This expression can be minimized by setting its derivative with respect to the function D to zero (see appendix A). The result is that D satisfies an equation involving two quantities introduced in chapter 1, the firing rate-stimulus correlation function, $Q_{rs}(\tau) = \int dt r(t) s(t + \tau)/T$, and the stimulus autocorrelation function, $Q_{ss}(\tau) = \int dt s(t) s(t + \tau)/T$,

$$\int_0^\infty d\tau' Q_{ss}(\tau - \tau') D(\tau') = Q_{rs}(-\tau). \quad (2.4)$$

The method we are describing is called reverse correlation because the firing rate-stimulus correlation function is evaluated at $-\tau$ in this equation.

Equation 2.4 can be solved most easily if the stimulus is white noise, although it can be solved in the general case as well (see appendix A). For a white-noise stimulus $Q_{ss}(\tau) = \sigma_s^2 \delta(\tau)$ (see chapter 1), so the left side of equation 2.4 is

$$\sigma_s^2 \int_0^\infty d\tau' \delta(\tau - \tau') D(\tau') = \sigma_s^2 D(\tau). \quad (2.5)$$

As a result, the kernel that provides the best linear estimate of the firing rate is

$$D(\tau) = \frac{Q_{rs}(-\tau)}{\sigma_s^2} = \frac{\langle r \rangle C(\tau)}{\sigma_s^2} \quad (2.6)$$

where $C(\tau)$ is the spike-triggered average stimulus, and $\langle r \rangle$ is the average firing rate of the neuron. For the second equality, we have used the relation $Q_{rs}(-\tau) = \langle r \rangle C(\tau)$ from chapter 1. Based on this result, the standard method used to determine the optimal kernel is to measure the spike-triggered average stimulus in response to a white-noise stimulus.

In chapter 1, we introduce the H1 neuron of the fly visual system, which responds to moving images. Figure 2.1 shows a prediction of the firing rate of this neuron obtained from a linear filter. The velocity of the moving image is plotted in 2.1A, and two typical responses are shown in 2.1B.

Wiener expansion

Wiener kernel

optimal kernel

white-noise kernel

4 Neural Encoding II: Reverse Correlation and Visual Receptive Fields

The firing rate predicted from a linear estimator, as discussed above, and the firing rate computed from the data by binning and counting spikes are compared in Figure 2.1C. The agreement is good in regions where the measured rate varies slowly but the estimate fails to capture high-frequency fluctuations of the firing rate, presumably because of nonlinear effects not captured by the linear kernel. Some such effects can be described by a static nonlinear function, as discussed below. Others may require including higher-order terms in a Volterra or Wiener expansion.

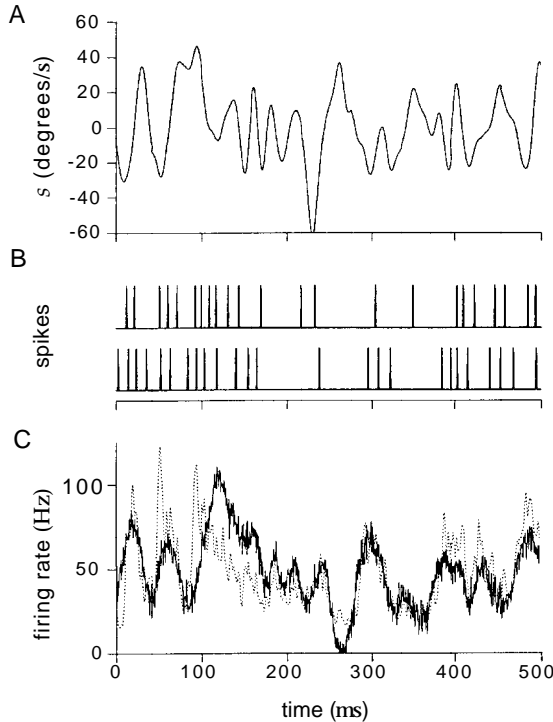


Figure 2.1: Prediction of the firing rate for an H1 neuron responding to a moving visual image. A) The velocity of the image used to stimulate the neuron. B) Two of the 100 spike sequences used in this experiment. C) Comparison of the measured and computed firing rates. The dashed line is the firing rate extracted directly from the spike trains. The solid line is an estimate of the firing rate constructed by linearly filtering the stimulus with an optimal kernel. (Adapted from Rieke et al., 1997.)

The Most Effective Stimulus

Neuronal selectivity is often characterized by describing stimuli that evoke maximal responses. The reverse-correlation approach provides a justification for this procedure by relating the optimal kernel for firing rate estimation to the stimulus predicted to evoke the maximum firing rate, subject

to a constraint. A constraint is essential because the linear estimate 2.1 is unbounded. The constraint we use is that the time integral of the square of the stimulus over the duration of the trial is held fixed. We call this integral the stimulus energy. The stimulus for which equation 2.1 predicts the maximum response at some fixed time subject to this constraint, is computed in appendix B. The result is that the stimulus producing the maximum response is proportional to the optimal linear kernel, or equivalently to the white-noise spike-triggered average stimulus. This is an important result because in cases where a white-noise analysis has not been done, we may still have some idea what stimulus produces the maximum response.

The maximum stimulus analysis provides an intuitive interpretation of the linear estimate of equation 2.1. At fixed stimulus energy, the integral in 2.1 measures the overlap between the actual stimulus and the most effective stimulus. In other words, it indicates how well the actual stimulus matches the most effective stimulus. Mismatches between these two reduce the value of the integral and result in lower predictions for the firing rate.

Static Nonlinearities

The optimal kernel produces an estimate of the firing rate that is a linear function of the stimulus. Neurons and nervous systems are nonlinear, so a linear estimate is only an approximation, albeit a useful one. The linear prediction has two obvious problems: there is nothing to prevent the predicted firing rate from becoming negative, and the predicted rate does not saturate, but instead increases without bound as the magnitude of the stimulus increases. One way to deal with these and some of the other deficiencies of a linear prediction is to write the firing rate as a background rate plus a nonlinear function of the linearly filtered stimulus. We use L to represent the linear term we have been discussing thus far,

$$L(t) = \int_0^\infty d\tau D(\tau)s(t - \tau). \quad (2.7)$$

The modification is to replace the linear prediction $r_{\text{est}}(t) = r_0 + L(t)$ by the generalization

$$r_{\text{est}}(t) = r_0 + F(L(t)) \quad (2.8)$$

$r_{\text{est}}(t)$ with static nonlinearity

where F is an arbitrary function. F is called a static nonlinearity to stress that it is a function of the linear filter value evaluated instantaneously at the time of the rate estimation. If F is appropriately bounded from above and below, the estimated firing rate will never be negative or unrealistically large.

F can be extracted from data by means of the graphical procedure illustrated in figure 2.2A. First, a linear estimate of the firing rate is computed

6 Neural Encoding II: Reverse Correlation and Visual Receptive Fields

using the optimal kernel defined by equation 2.4. Next a plot is made of the pairs of points $(L(t), r(t))$ at various times and for various stimuli, where $r(t)$ is the actual rate extracted from the data. There will be a certain amount of scatter in this plot due to the inaccuracy of the estimation. If the scatter is not too large, however, the points should fall along a curve, and this curve is a plot of the function $F(L)$. It can be extracted by fitting a function to the points on the scatter plot. The function F typically con-

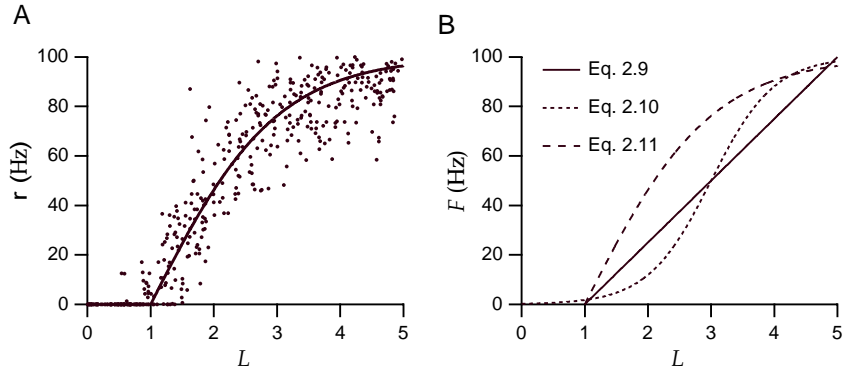


Figure 2.2: A) A graphical procedure for determining static nonlinearities. The linear estimate L and the actual firing rate r are plotted (solid points) and fit by the function $F(L)$ (solid line). B) Different static nonlinearities used in estimating neural responses. L is dimensionless, and equations 2.9, 2.10, and 2.11 have been used with $G = 25 \text{ Hz}$, $L_0 = 1$, $L_{1/2} = 3$, $r_{\max} = 100 \text{ Hz}$, $g_1 = 2$, and $g_2 = 1/2$.

tains constants used to set the firing rate to realistic values. These give us the freedom to normalize $D(\tau)$ in some convenient way, correcting for the arbitrary normalization by adjusting the parameters within F .

Static nonlinearities are used to introduce both firing thresholds and saturation into estimates of neural responses. Thresholds can be described by writing

$$F(L) = G[L - L_0]_+ \quad (2.9)$$

where L_0 is the threshold value that L must attain before firing begins. Above the threshold, the firing rate is a linear function of L , with G acting as the constant of proportionality. Half-wave rectification is a special case of this with $L_0=0$. That this function does not saturate is not a problem if large stimulus values are avoided. If needed, a saturating nonlinearity can be included in F , and a sigmoidal function is often used for this purpose,

$$F(L) = \frac{r_{\max}}{1 + \exp(g_1(L_{1/2} - L))}. \quad (2.10)$$

Here r_{\max} is the maximum possible firing rate, $L_{1/2}$ is the value of L for which F achieves half of this maximal value, and g_1 determines how rapidly the firing rate increases as a function of L . Another choice that

threshold function

rectification

sigmoid function

combines a hard threshold with saturation uses a rectified hyperbolic tangent function,

$$F(L) = r_{\max}[\tanh(g_2(L - L_0))]_+ \quad (2.11)$$

where r_{\max} and g_2 play similar roles as in equation 2.10, and L_0 is the threshold. Figure 2.2B shows the different nonlinear functions that we have discussed.

Although the static nonlinearity can be any function, the estimate of equation 2.8 is still restrictive because it allows for no dependence on weighted autocorrelations of the stimulus or other higher-order terms in the Volterra series. Furthermore, once the static nonlinearity is introduced, the linear kernel derived from equation 2.4 is no longer optimal because it was chosen to minimize the squared error of the linear estimate $r_{\text{est}}(t) = L(t)$, not the estimate with the static nonlinearity $r_{\text{est}}(t) = F(L(t))$. A theorem due to Bussgang (see appendix C) suggests that equation 2.6 will provide a reasonable kernel, even in the presence of a static nonlinearity, if the white noise stimulus used is Gaussian.

In some cases, the linear term of the Volterra series fails to predict the response even when static nonlinearities are included. Systematic improvements can be attempted by including more terms in the Volterra or Wiener series, but in practice it is quite difficult to go beyond the first few terms. The accuracy with which the first term, or first few terms, in a Volterra series can predict the responses of a neuron can sometimes be improved by replacing the parameter s in equation 2.7 by an appropriately chosen function of s , so that

$$L(t) = \int_0^\infty d\tau D(\tau) f(s(t - \tau)). \quad (2.12)$$

A reasonable choice for this function is the response tuning curve. With this choice, the linear prediction is equal to the response tuning curve, $L = f(s)$, for static stimuli provided that the integral of the kernel D is equal to one. For time-dependent stimuli, we can think of equation 2.12 as a dynamic extension of the response tuning curve.

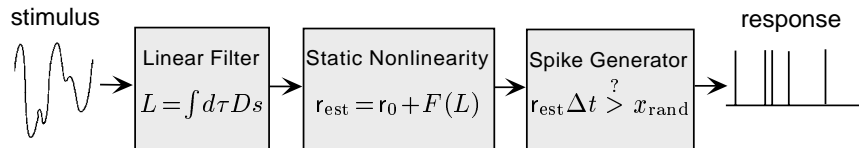


Figure 2.3: Simulating spiking responses to stimuli. The integral of the stimulus s times the optimal kernel D is first computed. The estimated firing rate is the background rate r_0 plus a nonlinear function of the output of the linear filter calculation. Finally, the estimated firing rate is used to drive a Poisson process that generates spikes.

A model of the spike trains evoked by a stimulus can be constructed by using the firing rate estimate of equation 2.8 to drive a Poisson spike generator (see chapter 1). Figure 2.3 shows the structure of such a model with a linear filter, a static nonlinearity, and a stochastic spike-generator. In the figure, spikes are shown being generated by comparing the spiking probability $r(t)\Delta t$ to a random number, although the other methods discussed in chapter 1 could be used instead. Also, the linear filter acts directly on the stimulus s in figure 2.3, but it could act instead on some function $f(s)$ such as the response tuning curve.

2.3 Introduction to the Early Visual System

Before discussing how reverse correlation methods are applied to visually responsive neurons, we review the basic anatomy and physiology of the early stages of the visual system. The conversion of a light stimulus into an electrical signal and ultimately an action potential sequence occurs in the retina. Figure 2.4A is an anatomical diagram showing the five principal cell types of the retina, and figure 2.4B is a rough circuit diagram. In the retina, light is first converted into an electrical signal by a photo-transduction cascade within rod and cone photoreceptor cells. Figure 2.4B shows intracellular recordings made in neurons of the retina of a mud-puppy (an amphibian). The stimulus used for these recordings was a flash of light falling primarily in the region of the photoreceptor at the left of figure 2.4B. The rod cells, especially the one on the left side of figure 2.4B, are hyperpolarized by the light flash. This electrical signal is passed along to bipolar and horizontal cells through synaptic connections. Note that in one of the bipolar cells, the signal has been inverted leading to depolarization. These smoothly changing membrane potentials provide a graded representation of the light intensity during the flash. This form of coding is adequate for signaling within the retina, where distances are small. However, it is inadequate for the task of conveying information from the retina to the brain.

retinal ganglion cells

The output neurons of the retina are the retinal ganglion cells whose axons form the optic nerve. As seen in figure 2.4B, the subthreshold potentials of the two retinal ganglion cells shown are similar to those of the bipolar cells immediately above them in the figure, but now with superimposed action potentials. The two retinal ganglion cells shown in the figure have different responses and transmit different sequences of action potentials. G_2 fires while the light is on, and G_1 fires when it turns off. These are called ON and OFF responses, respectively. The optic nerve conducts the output spike trains of retinal ganglion cells to the lateral geniculate nucleus of the thalamus, which acts as a relay station between the retina and primary visual cortex (figure 2.5). Prior to arriving at the LGN, some retinal ganglion cell axons cross the midline at the optic chiasm. This allows the left and right sides of the visual fields from both eyes to be represented on the

ON and OFF responses

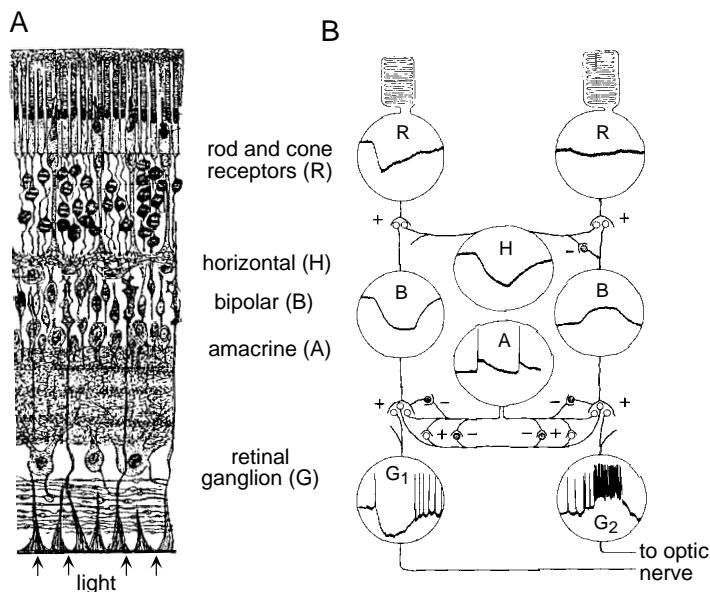


Figure 2.4: A) An anatomical diagram of the circuitry of the retina of a dog. Cell types are identified at right. In the intact eye, illumination is, counter-intuitively, from the bottom of this figure. B) Intracellular recordings from retinal neurons of the mudpuppy responding to flash of light lasting for one second. In the column of cells on the left side of the diagram, the resulting hyperpolarizations are about 4 mV in the rod and retinal ganglion cells, and 8 mV in the bipolar cell. Pluses and minuses represent excitatory and inhibitory synapses respectively. (A adapted from Nicholls et al., 1992; drawing from Cajal, 1911. B data from Werblin and Dowling 1969; figure adapted from Dowling, 1992.)

right and left sides of the brain respectively (figure 2.5).

Neurons in the retina, LGN, and primary visual cortex respond to light stimuli in restricted regions of the visual field called their receptive fields. Patterns of illumination outside the receptive field of a given neuron cannot generate a response directly, although they can significantly affect responses to stimuli within the receptive field. We do not consider such effects, although they are a current focus of experimental and theoretical interest. In the monkey, cortical receptive fields range in size from around a tenth of a degree near the fovea to several degrees in the periphery. Within the receptive fields, there are regions where illumination higher than the background light intensity enhances firing, and other regions where lower illumination enhances firing. The spatial arrangement of these regions determines the selectivity of the neuron to different inputs. The term receptive field is often generalized to refer not only to the overall region where light affects neuronal firing, but also to the spatial and temporal structure within this region.

Visually responsive neurons in the retina, LGN, and primary visual cortex

10 Neural Encoding II: Reverse Correlation and Visual Receptive Fields

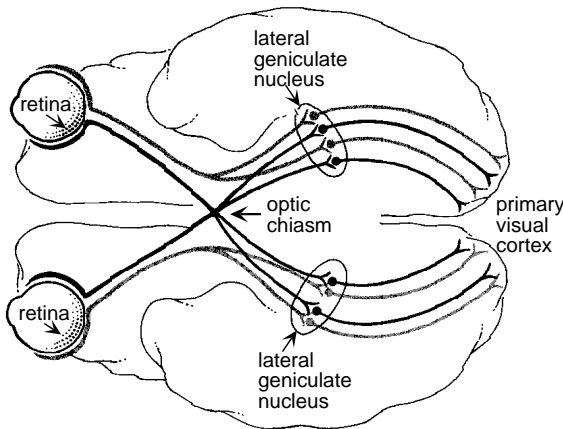


Figure 2.5: Pathway from the retina through the lateral geniculate nucleus (LGN) of the thalamus to the primary visual cortex in the human brain. (Adapted from Nicholls et al., 1992.)

are divided into two classes depending on whether or not the contributions from different locations within the visual field sum linearly, as assumed in equation 2.24. X-cells in the cat retina and LGN, P-cells in the monkey retina and LGN, and simple cells in primary visual cortex appear to satisfy this assumption. Other neurons, such as Y cells in the cat retina and LGN, M cells in the monkey retina and LGN, and complex cells in primary visual cortex, do not show linear summation across the spatial receptive field and nonlinearities must be included in descriptions of their responses. We do this for complex cells later in this chapter.

A first step in studying the selectivity of any neuron is to identify the types of stimuli that evoke strong responses. Retinal ganglion cells and LGN neurons have similar selectivities and respond best to circular spots of light surrounded by darkness or dark spots surrounded by light. In primary visual cortex, many neurons respond best to elongated light or dark bars or to boundaries between light and dark regions. Gratings with alternating light and dark bands are effective and frequently used stimuli for these neurons.

Many visually responsive neurons react strongly to sudden transitions in the level of image illumination, a temporal analog of their responsiveness to light-dark spatial boundaries. Static images are not very effective at evoking visual responses. In awake animals, images are constantly kept in motion across the retina by eye movements. In experiments in which the eyes are fixed, moving light bars and gratings, or gratings undergoing periodic light-dark reversals (called counterphase gratings) are used as more effective stimuli than static images. Some neurons in primary visual cortex are directionally selective; they respond more strongly to stimuli moving in one direction than in the other.

simple and complex cells

To streamline the discussion in this chapter, we consider only greyscale images, although the methods presented can be extended to include color. We also restrict the discussion to two-dimensional visual images, ignoring how visual responses depend on viewing distance and encode depth. In discussing the response properties of retinal, LGN, and V1 neurons, we do not follow the path of the visual signal, nor the historical order of experimentation, but, instead, begin with primary visual cortex and then move back to the LGN and retina. The emphasis is on properties of individual neurons, so we do not discuss encoding by populations of visually responsive neurons. For V1, this has been analyzed in terms of wavelets, a scheme for decomposing images into component pieces, as discussed in chapter 10.

The Retinotopic Map

A striking feature of most visual areas in the brain, including primary visual cortex, is that the visual world is mapped onto the cortical surface in a topographic manner. This means that neighboring points in a visual image evoke activity in neighboring regions of visual cortex. The retinotopic map refers to the transformation from the coordinates of the visual world to the corresponding locations on the cortical surface.

Objects located a fixed distance from one eye lie on a sphere. Locations on this sphere can be represented using the same longitude and latitude angles used for the surface of the earth. Typically, the ‘north pole’ for this spherical coordinate system is located at the fixation point, the image point that focuses onto the fovea or center of the retina. In this system of coordinates (figure 2.6), the latitude coordinate is called the eccentricity, ϵ , and the longitude coordinate, measured from the horizontal meridian, is called the azimuth a . In primary visual cortex, the visual world is split in half, with the region $-90^\circ \leq a \leq +90^\circ$ for ϵ from 0° to about 70° (for both eyes) represented on the left side of the brain, and the reflection of this region about the vertical meridian represented on the right side of the brain.

*eccentricity ϵ
azimuth a*

In most experiments, images are displayed on a flat screen (called a tangent screen) that does not coincide exactly with the sphere discussed in the previous paragraph. However, if the screen is not too large the difference is negligible, and the eccentricity and azimuth angles approximately coincide with polar coordinates on the screen (figure 2.6A). Ordinary Cartesian coordinates can also be used to identify points on the screen (figure 2.6). The eccentricity ϵ and the x and y coordinates of the Cartesian system are based on measuring distances on the screen. However, it is customary to divide these measured distances by the distance from the eye to the screen and to multiply the result by $180^\circ/\pi$ so that these coordinates are ultimately expressed in units of degrees. This makes sense because it is the angular not the absolute size and location of an image that is typically relevant for studies of the visual system.

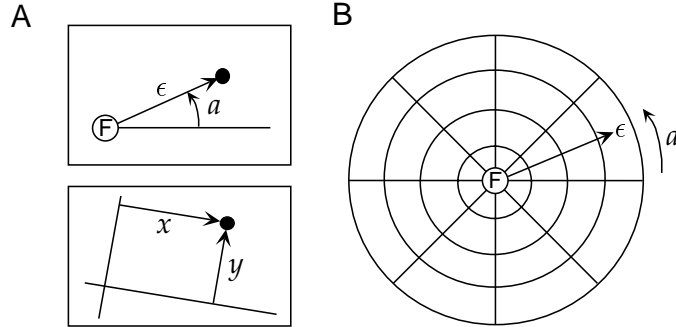


Figure 2.6: A) Two coordinate systems used to parameterize image location. Each rectangle represents a tangent screen, and the filled circle is the location of a particular image point on the screen. The upper panel shows polar coordinates. The origin of the coordinate system is the fixation point F, the eccentricity ϵ is proportional to the radial distance from the fixation point to the image point, and a is the angle between the radial line from F to the image point and the horizontal axis. The lower panel shows Cartesian coordinates. The location of the origin for these coordinates and the orientation of the axes are arbitrary. They are usually chosen to center and align the coordinate system with respect to a particular receptive field being studied. B) A bullseye pattern of radial lines of constant azimuth, and circles of constant eccentricity. The center of this pattern at zero eccentricity is the fixation point F. Such a pattern was used to generate the image in figure 2.7A.

Figure 2.7A shows a dramatic illustration of the retinotopic map in the primary visual cortex of a monkey. The pattern on the cortex seen in figure 2.7A was produced by imaging a radioactive analog of glucose that was taken up by active neurons while a monkey viewed a visual image consisting of concentric circles and radial lines, similar to the pattern in figure 2.6B. The vertical lines correspond to the circles in the image, and the roughly horizontal lines are due to the activity evoked by the radial lines. The fovea is represented at the left-most pole of this piece of cortex and eccentricity increases toward the right. Azimuthal angles are positive in the lower half of the piece of cortex shown, and negative in the upper half.

Figure 2.7B is an approximate mathematical description of the map illustrated in figure 2.7A. To construct this map we assume that eccentricity is mapped onto the horizontal coordinate X of the cortical sheet, and a is mapped onto its Y coordinate. The equations for X and Y as functions of ϵ and a can be obtained through knowledge of a quantity called the cortical magnification factor, $M(\epsilon)$. This determines the distance across a flattened sheet of cortex separating the activity evoked by two nearby image points. Suppose that the two image points in question have eccentricities ϵ and $\epsilon + \Delta\epsilon$ but the same value of the azimuthal coordinate a . The angular distance between these two points is $\Delta\epsilon$. The distance separating the activity evoked by these two image points on the cortex is ΔX . By the definition of the cortical magnification factor, these two quantities satisfy

cortical
magnification
factor

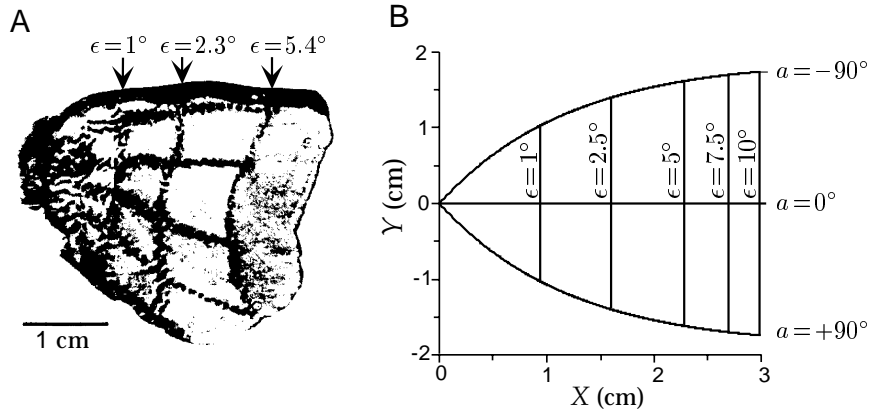


Figure 2.7: A) An autoradiograph of the posterior region of the primary visual cortex from the left side of a macaque monkey brain. The pattern is a radioactive trace of the activity evoked by an image like that in figure 2.6B. The vertical lines correspond to circles at eccentricities of 1° , 2.3° , and 5.4° , and the horizontal lines (from top to bottom) represent radial lines in the visual image at a values of -90° , -45° , 0° , 45° , and 90° . Only the part of cortex corresponding to the central region of the visual field on one side is shown. B) The mathematical map from the visual coordinates ϵ and a to the cortical coordinates X and Y described by equations 2.15 and 2.17. (A adapted from Tootell et al., 1982.)

$\Delta X = M(\epsilon)\Delta\epsilon$ or, taking the limit as ΔX and $\Delta\epsilon$ go to zero,

$$\frac{dX}{d\epsilon} = M(\epsilon). \quad (2.13)$$

The cortical magnification factor for the macaque monkey, obtained from results such as figure 2.7A is approximately

$$M(\epsilon) = \frac{\lambda}{\epsilon_0 + \epsilon}. \quad (2.14)$$

with $\lambda \approx 12$ mm and $\epsilon_0 \approx 1^\circ$. Integrating equation 2.13 and defining $X = 0$ to be the point representing $\epsilon = 0$, we find

$$X = \lambda \ln(1 + \epsilon/\epsilon_0). \quad (2.15)$$

We can apply the same cortical amplification factor to points with the same eccentricity but different a values. The angular distance between two points at eccentricity ϵ with an azimuthal angle difference of Δa is $\Delta a \epsilon \pi / 180^\circ$. In this expression, the factor of ϵ corrects for the increase of arc length as a function of eccentricity, and the factor of $\pi/180^\circ$ converts ϵ from degrees to radians. The separation on the cortex, ΔY , corresponding to these points has a magnitude given by the cortical amplification times this distance. Taking the limit $\Delta a \rightarrow 0$, we find that we find that

$$\frac{dY}{da} = -\frac{\epsilon \pi}{180^\circ} M(\epsilon). \quad (2.16)$$

14 Neural Encoding II: Reverse Correlation and Visual Receptive Fields

The minus sign in this relationship appears because the visual field is inverted on the cortex. Solving equation 2.16 gives

$$Y = -\frac{\lambda \epsilon a \pi}{(\epsilon_0 + \epsilon) 180^\circ}. \quad (2.17)$$

Figure 2.7B shows that these coordinates agree fairly well with the map in figure 2.7A.

For eccentricities appreciably greater than 1° , equations 2.15 and 2.17 reduce to $X \approx \lambda \ln(\epsilon/\epsilon_0)$ and $Y \approx -\lambda \pi a / 180^\circ$. These two formulae can be combined by defining the complex numbers $Z = X + iY$ and $z = (\epsilon/\epsilon_0) \exp(-i\pi a / 180^\circ)$ (with i equal to the square root of -1) and writing $Z = \lambda \ln(z)$. For this reason, the cortical map is sometimes called a complex logarithmic map (see Schwartz, 1977). For an image scaled radially by a factor γ , eccentricities change according to $\epsilon \rightarrow \gamma \epsilon$ while a is unaffected. Scaling of the eccentricity produces a shift $X \rightarrow X + \lambda \ln(\gamma)$ over the range of values where the simple logarithmic form of the map is valid. The logarithmic transformation thus causes images that are scaled radially outward on the retina to be represented at locations on the cortex translated in the X direction. For smaller eccentricities, the map we have derived is only approximate even in the complete form given by equations 2.15 and 2.17. This is because the cortical magnification factor is not really isotropic as we have assumed in this derivation, and a complete description requires accounting for the curvature of the cortical surface.

Visual Stimuli

Earlier in this chapter, we used the function $s(t)$ to characterize a time-dependent stimulus. The description of visual stimuli is more complex. Greyscale images appearing on a two-dimensional surface, such as a video monitor, can be described by giving the luminance, or light intensity, at each point on the screen. These pixel locations are parameterized by Cartesian coordinates x and y , as in the lower panel of figure 2.6A. However, pixel-by-pixel light intensities are not a useful way of parameterizing a visual image for the purposes of characterizing neuronal responses. This is because visually responsive neurons, like many sensory neurons, adapt to the overall level of screen illumination. To avoid dealing with adaptation effects, we describe the stimulus by a function $s(x, y, t)$ that is proportional to the difference between the luminance at the point (x, y) at time t and the average or background level of luminance. Often $s(x, y, t)$ is also divided by the background luminance level, making it dimensionless. The resulting quantity is called the contrast.

During recordings, visual neurons are usually stimulated by images that vary over both space and time. A commonly used stimulus, the counterphase sinusoidal grating, is described by

$$s(x, y, t) = A \cos(Kx \cos \Theta + Ky \sin \Theta - \Phi) \cos(\omega t). \quad (2.18)$$

complex
logarithmic map

counterphase
sinusoidal grating

Figure 2.8 shows a cartoon of a similar grating (a spatial square-wave is drawn rather than a sinusoid) and illustrates the significance of the parameters K , Θ , Φ , and ω . K and ω are the spatial and temporal frequencies of the grating (these are angular frequencies), Θ is its orientation, Φ its spatial phase, and A its contrast amplitude. This stimulus oscillates in both space and time. At any fixed time, it oscillates in the direction perpendicular to the orientation angle Θ as a function of position, with wavelength $2\pi/K$ (figure 2.8A). At any fixed position, it oscillates in time with period $2\pi/\omega$ (figure 2.8B). For convenience, Θ is measured relative to the y axis rather than the x axis so that a stimulus with $\Theta = 0$, varies in the x , but not in the y , direction. Φ determines the spatial location of the light and dark stripes of the grating. Changing Φ by an amount $\Delta\Phi$ shifts the grating in the direction perpendicular to its orientation by a fraction $\Delta\Phi/2\pi$ of its wavelength. The contrast amplitude A controls the maximum degree of difference between light and dark areas. Because x and y are measured in degrees, K has the rather unusual units of radians per degree and $K/2\pi$ is typically reported in units of cycles per degree. Φ has units of radians, ω is in radians per s, and $\omega/2\pi$ is in Hz.

spatial frequency K
 frequency ω
 orientation Θ
 spatial phase Φ
 amplitude A

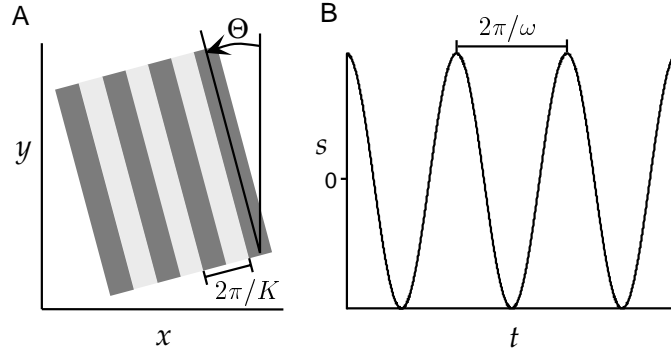


Figure 2.8: A counterphase grating. A) A portion of a square-wave grating analogous to the sinusoidal grating of equation 2.18. The lighter stripes are regions where $s > 0$, and $s < 0$ within the darker stripes. K determines the wavelength of the grating and Θ its orientation. Changing its spatial phase Φ shifts the entire light-dark pattern in the direction perpendicular to the stripes. B) The light-dark intensity at any point of the spatial grating oscillates sinusoidally in time with period $2\pi/\omega$.

Experiments that consider reverse correlation and spike-triggered averages use various types of random and white-noise stimuli in addition to bars and gratings. A white-noise stimulus, in this case, is one that is uncorrelated in both space and time so that

$$\frac{1}{T} \int_0^T dt s(x, y, t)s(x', y', t + \tau) = \sigma_s^2 \delta(\tau)\delta(x - x')\delta(y - y'). \quad (2.19)$$

Of course, in practice a discrete approximation of such a stimulus must be used by dividing the image space into pixels and time into small bins. In

white-noise image

addition, more structured random sets of images (randomly oriented bars, for example) are sometime used to enhance the responses obtained during stimulation.

The Nyquist Frequency

Many factors limit the maximal spatial frequency that can be resolved by the visual system, but one interesting effect arises from the size and spacing of individual photoreceptors on the retina. The region of the retina with the highest resolution is the fovea at the center of the visual field. Within the macaque or human fovea, cone photoreceptors are densely packed in a regular array. Along any direction in the visual field, a regular array of tightly packed photoreceptors of size Δx samples points at locations $m\Delta x$ for $m = 1, 2, \dots$. The (angular) frequency that defines the resolution of such an array is called the Nyquist frequency and is given by

$$K_{\text{nyq}} = \frac{\pi}{\Delta x}. \quad (2.20)$$

To understand the significance of the Nyquist frequency, consider sampling two cosine gratings with spatial frequencies of K and $2K_{\text{nyq}} - K$, with $K < K_{\text{nyq}}$. These are described by $s = \cos(Kx)$ and $s = \cos((2K_{\text{nyq}} - K)x)$. At the sampled points, these functions are identical because $\cos((2K_{\text{nyq}} - K)m\Delta x) = \cos(2\pi m - Km\Delta x) = \cos(-Km\Delta x) = \cos(Km\Delta x)$ by the periodicity and evenness of the cosine function (see figure 2.9). As a result, these two gratings cannot be distinguished by examining them only at the sampled points. Any two spatial frequencies $K < K_{\text{nyq}}$ and $2K_{\text{nyq}} - K$ can be confused with each other in this way, a phenomenon known as aliasing. Conversely, if an image is constructed solely of frequencies less than K_{nyq} , it can be reconstructed perfectly from the finite set of samples provided by the array. There are 120 cones per degree at the fovea of the macaque retina which makes $K_{\text{nyq}}/(2\pi) = 1/(2\Delta x) = 60$ cycles per degree. In this result, we have divided the right side of equation 2.20, which gives K_{nyq} in units of radians per degree, by 2π to convert the answer to cycles per degree.

2.4 Reverse Correlation Methods - Simple Cells

The spike-triggered average for visual stimuli is defined, as in chapter 1, as the average over trials of stimuli evaluated at times $t_i - \tau$, where t_i for $i = 1, 2, \dots, n$ are the spike times. Because the light intensity of a visual image depends on location as well as time, the spike-triggered average stimulus is a function of three variables,

$$C(x, y, \tau) = \frac{1}{\langle n \rangle} \left\langle \sum_{i=1}^n s(x, y, t_i - \tau) \right\rangle. \quad (2.21)$$

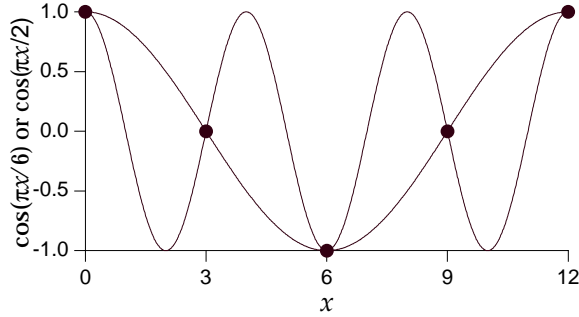


Figure 2.9: Aliasing and the Nyquist frequency. The two curves are the functions $\cos(\pi x/6)$ and $\cos(\pi x/2)$ plotted against x , and the dots show points sampled with a spacing of $\Delta x = 3$. The Nyquist frequency in this case is $\pi/3$, and the two cosine curves match at the sampled points because their spatial frequencies satisfy $2\pi/3 - \pi/6 = \pi/2$.

Here, as in chapter 1, the brackets denote trial averaging, and we have used the approximation $1/n \approx 1/\langle n \rangle$. $C(x, y, \tau)$ is the average value of the visual stimulus at the point (x, y) a time τ before a spike was fired. Similarly, we can define the correlation function between the firing rate at time t and the stimulus at time $t + \tau$, for trials of duration T , as

$$Q_{rs}(x, y, \tau) = \frac{1}{T} \int_0^T dt r(t)s(x, y, t + \tau). \quad (2.22)$$

The spike-triggered average is related to the reverse correlation function, as discussed in chapter 1, by

$$C(x, y, \tau) = \frac{Q_{rs}(x, y, -\tau)}{\langle r \rangle}, \quad (2.23)$$

where $\langle r \rangle$ is, as usual, the average firing rate over the entire trial, $\langle r \rangle = \langle n \rangle / T$.

To estimate the firing rate of a neuron in response to a particular image, we add a function of the output of a linear filter of the stimulus to the background firing rate r_0 , as in equation 2.8, $r_{\text{est}}(t) = r_0 + F(L(t))$. As in equation 2.7, the linear estimate $L(t)$ is obtained by integrating over the past history of the stimulus with a kernel acting as the weighting function. Because visual stimuli depend on spatial location, we must decide how contributions from different image locations are to be combined to determine $L(t)$. The simplest assumption is that the contributions from different spatial points add linearly so that $L(t)$ is obtained by integrating over all x and y values,

$$L(t) = \int_0^\infty d\tau \int dx dy D(x, y, \tau) s(x, y, t - \tau). \quad (2.24)$$

The kernel $D(x, y, \tau)$ determines how strongly, and with what sign, the visual stimulus at the point (x, y) and at time $t - \tau$ affects the firing

*linear response
estimate*

18 Neural Encoding II: Reverse Correlation and Visual Receptive Fields

rate of the neuron at time t . As in equation 2.6, the optimal kernel is given in terms of the firing rate-stimulus correlation function, or the spike-triggered average, for a white-noise stimulus with variance parameter σ_s^2 by

$$D(x, y, \tau) = \frac{Q_{rs}(x, y, -\tau)}{\sigma_s^2} = \frac{\langle r \rangle C(x, y, \tau)}{\sigma_s^2}. \quad (2.25)$$

*space-time
receptive field*

The kernel $D(x, y, \tau)$ defines the space-time receptive field of a neuron. Because $D(x, y, \tau)$ is a function of three variables, it can be difficult to measure and visualize. For some neurons, the kernel can be written as a product of two functions, one that describes the spatial receptive field and the other the temporal receptive field,

$$D(x, y, \tau) = D_s(x, y)D_t(\tau). \quad (2.26)$$

*separable
receptive field*

Such neurons are said to have separable space-time receptive fields. Separability requires that the spatial structure of the receptive field does not change over time except by an overall multiplicative factor. When $D(x, y, \tau)$ cannot be written as the product of two terms, the neuron is said to have a nonseparable space-time receptive field. Given the freedom in equation 2.8 to set the scale of D (by suitably adjusting the function F), we typically normalize D_s so that its integral is one, and use a similar rule for the components from which D_t is constructed. We begin our analysis by studying first the spatial and then the temporal components of a separable space-time receptive field and then proceed to the nonseparable case. For simplicity, we ignore the possibility that cells can have slightly different receptive fields for the two eyes, which underlies the disparity tuning considered in chapter 1.

Spatial Receptive Fields

Figures 2.10A and C show the spatial structure of spike-triggered average stimuli for two simple cells in the primary visual cortex of a cat (area 17) with approximately separable space-time receptive fields. These receptive fields are elongated in one direction, and there are some regions within the receptive field where D_s is positive, called ON regions, and others where it is negative, called OFF regions. The integral of the linear kernel times the stimulus can be visualized by noting how the OFF (black) and ON (white) regions overlap the image (see figure 2.11). The response of a neuron is enhanced if ON regions are illuminated ($s > 0$) or if OFF regions are darkened ($s < 0$) relative to the background level of illumination. Conversely, they are suppressed by darkening ON regions or illuminating OFF regions. As a result, the neurons of figures 2.10A and C respond most vigorously to light-dark edges positioned along the border between the ON and OFF regions and oriented parallel to this border and to the elongated direction of the receptive fields (figure 2.11). Figures 2.10 and 2.11 show

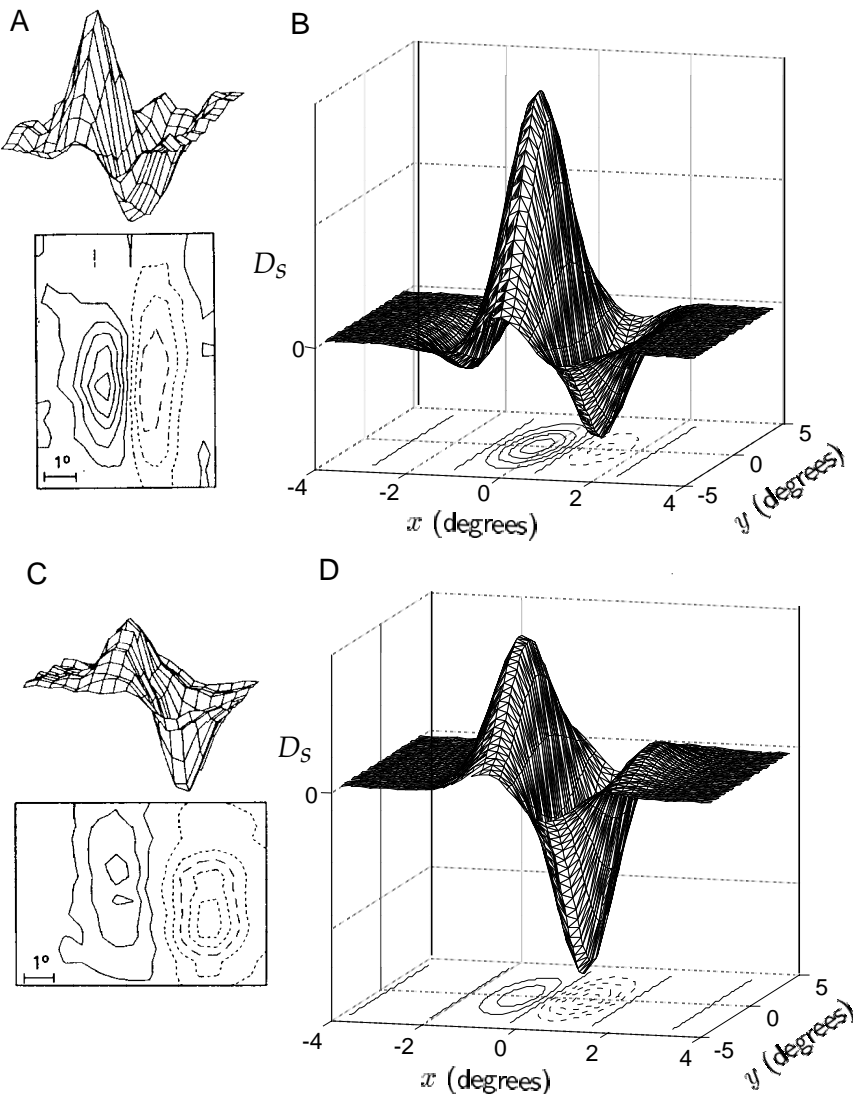


Figure 2.10: Spatial receptive field structure of simple cells. A) and C) Spatial structure of the receptive fields of two neurons in cat primary visual cortex determined by averaging stimuli between 50 ms and 100 ms prior to an action potential. The upper plots are three-dimensional representations, with the horizontal dimensions acting as the x - y plane and the vertical dimension indicating the magnitude and sign of $D_s(x, y)$. The lower contour plots represent the x - y plane. Regions with solid contour curves are ON areas where $D_s(x, y) > 0$ and regions with dashed contours show OFF areas where $D_s(x, y) < 0$. B) and D) Gabor functions of the form 2.27 with $\sigma_x = 1^\circ$, $\sigma_y = 2^\circ$, $1/k = 0.56^\circ$, and $\phi = 1 - \pi/2$ (B) or $\phi = 1 - \pi$ (D) chosen to match the receptive fields in A and C. (A and C adapted from Jones and Palmer, 1987a.)

receptive fields with two major subregions. Simple cells are found with from one to five subregions. Along with the ON-OFF patterns we have seen, another typical arrangement is a three-lobed receptive field with an OFF-ON-OFF or ON-OFF-ON subregions, as seen in figure 2.17B.

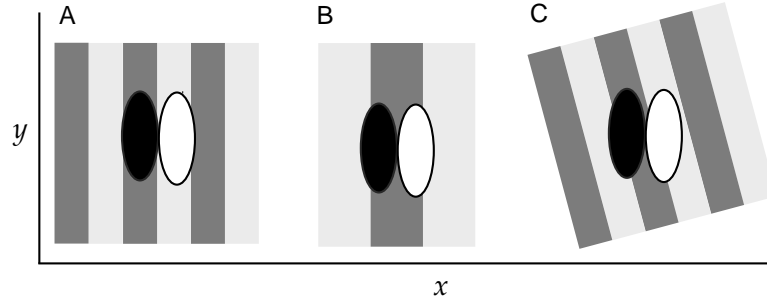


Figure 2.11: Grating stimuli superimposed on spatial receptive fields similar to those shown in figure 2.10. The receptive field is shown as two oval regions, one dark to represent an OFF area where $D_s < 0$ and one white to denote an ON region where $D_s > 0$. A) A grating with the spatial wavelength, orientation, and spatial phase shown produces a high firing rate because a dark band completely overlaps the OFF area of the receptive field and a light band overlaps the ON area. B) The grating shown is non-optimal due to a mismatch in both the spatial phase and frequency, so that the ON and OFF regions each overlap both light and dark stripes. C) The grating shown is at a non-optimal orientation because each region of the receptive field overlaps both light and dark stripes.

Gabor function

A mathematical approximation of the spatial receptive field of a simple cell is provided by a Gabor function, which is a product of a Gaussian function and a sinusoidal function. Gabor functions are by no means the only functions used to fit spatial receptive fields of simple cells. For example, gradients of Gaussians are sometimes used. However, we will stick to Gabor functions, and to simplify the notation, we choose the coordinates x and y so that the borders between the ON and OFF regions are parallel to the y axis. We also place the origin of the coordinates at the center of the receptive field. With these choices, we can approximate the observed receptive field structures using the Gabor function

$$D_s(x, y) = \frac{1}{2\pi\sigma_x\sigma_y} \exp\left(-\frac{x^2}{2\sigma_x^2} - \frac{y^2}{2\sigma_y^2}\right) \cos(kx - \phi). \quad (2.27)$$

rf size σ_x, σ_y
preferred spatial frequency k
preferred spatial phase ϕ

The parameters in this function determine the properties of the spatial receptive field: σ_x and σ_y determine its extent in the x and y directions respectively; k , the preferred spatial frequency, determines the spacing of light and dark bars that produce the maximum response (the preferred spatial wavelength is $2\pi/k$); and ϕ is the preferred spatial phase which determines where the ON-OFF boundaries fall within the receptive field. For this spatial receptive field, the sinusoidal grating of the form 2.18 that produces the maximum response for a fixed value of A has $K = k$, $\Phi = \phi$, and $\Theta = 0$.

Figures 2.10B and D, show Gabor functions chosen specifically to match the data in figures 2.10A and C. Figure 2.12 shows x and y plots of a variety of Gabor functions with different parameter values. As seen in figure 2.12, Gabor functions can have various types of symmetry, and variable numbers of significant oscillations (or subregions) within the Gaussian envelope. The number of subregions within the receptive field is determined by the product $k\sigma_x$ and is typically expressed in terms of a quantity known as the bandwidth b . The bandwidth is defined as $b = \log_2(K_+/K_-)$ where $K_+ > k$ and $K_- < k$ are the spatial frequencies of gratings that produce one half the response amplitude of a grating with $K = k$. High bandwidths correspond to low values of $k\sigma_x$, meaning that the receptive field has few subregions and poor spatial frequency selectivity. Neurons with more subfields are more selective to spatial frequency, and they have smaller bandwidths and larger values of $k\sigma_x$.

bandwidth

The bandwidth is the width of the spatial frequency tuning curve measured in octaves. The spatial frequency tuning curve as a function of K for a Gabor receptive field with preferred spatial frequency k and receptive field width σ_x is proportional to $\exp(-\sigma_x^2(k - K)^2/2)$ (see equation 2.34 below). The values of K_+ and K_- needed to compute the bandwidth are thus determined by the condition $\exp(-\sigma_x^2(k - K_\pm)^2/2) = 1/2$. Solving this equation gives $K_\pm = k \pm (2 \ln(2))^{1/2}/\sigma_x$ from which we obtain

$$b = \log_2 \left(\frac{k\sigma_x + \sqrt{2 \ln(2)}}{k\sigma_x - \sqrt{2 \ln(2)}} \right) \quad \text{or} \quad k\sigma_x = \sqrt{2 \ln(2)} \frac{2^b + 1}{2^b - 1}. \quad (2.28)$$

Bandwidth is only defined if $k\sigma_x > \sqrt{2 \ln(2)}$, but this is usually the case for V1 neurons. For V1 neurons, bandwidths range from about 0.5 to 2.5 corresponding to $k\sigma_x$ between 1.7 and 6.9.

The response characterized by equation 2.27 is maximal if light-dark edges are parallel to the y axis, so the preferred orientation angle is zero. An arbitrary preferred orientation θ can be generated by rotating the coordinates, making the substitutions $x \rightarrow x \cos(\theta) + y \sin(\theta)$ and $y \rightarrow y \cos(\theta) - x \sin(\theta)$ in equation 2.27. This produces a spatial receptive field that is maximally responsive to a grating with $\Theta = \theta$. Similarly, a receptive field centered at the point (x_0, y_0) rather than at the origin can be constructed by making the substitutions $x \rightarrow x - x_0$ and $y \rightarrow y - y_0$.

preferred orientation θ

rf center x_0, y_0

Temporal Receptive Fields

Figure 2.13 reveals the temporal development of the space-time receptive field of a neuron in the cat primary visual cortex through a series of snapshots of its spatial receptive field. More than 300 ms prior to a spike, there is little correlation between the visual stimulus and the upcoming spike. Around 210 ms before the spike ($\tau = 210$ ms), a two-lobed OFF-ON receptive field, similar to the ones in figures 2.10, is evident. As τ decreases (recall that τ measures time in a reversed sense), this structure first fades

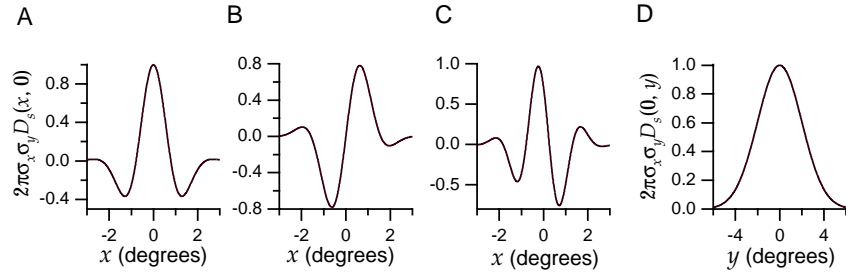


Figure 2.12: Gabor functions of the form given by equation 2.27. For convenience we plot the dimensionless function $2\pi\sigma_x\sigma_yD_s$. A) A Gabor function with $\sigma_x = 1^\circ$, $1/k = 0.5^\circ$, and $\phi = 0$ plotted as a function of x for $y = 0$. This function is symmetric about $x = 0$. B) A Gabor function with $\sigma_x = 1^\circ$, $1/k = 0.5^\circ$, and $\phi = \pi/2$ plotted as a function of x for $y = 0$. This function is antisymmetric about $x = 0$ and corresponds to using a sine instead of a cosine function in equation 2.27. C) A Gabor function with $\sigma_x = 1^\circ$, $1/k = 0.33^\circ$, and $\phi = \pi/4$ plotted as a function of x for $y = 0$. This function has no particular symmetry properties with respect to $x = 0$. D) The Gabor function of equation 2.27 with $\sigma_y = 2^\circ$ plotted as a function of y for $x = 0$. This function is simply a Gaussian.

away and then reverses, so that the receptive field 75 ms before a spike has the opposite sign from what appeared at $\tau = 210$ ms. Due to latency effects, the spatial structure of the receptive field is less significant for $\tau < 75$ ms. The stimulus preferred by this cell is thus an appropriately aligned dark-light boundary that reverses to a light-dark boundary over time.

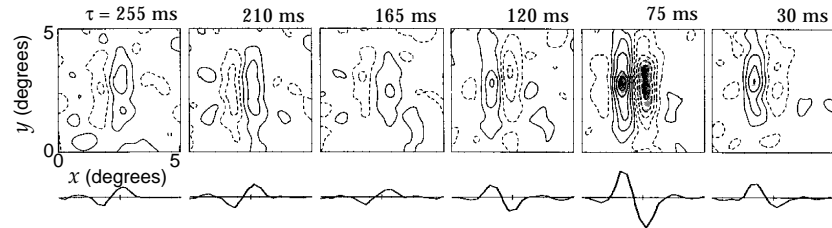


Figure 2.13: Temporal evolution of a spatial receptive field. Each panel is a plot of $D(x, y, \tau)$ for a different value of τ . As in figure 2.10, regions with solid contour curves are areas where $D(x, y, \tau) > 0$ and regions with dashed contours have $D(x, y, \tau) < 0$. The curves below the contour diagrams are one-dimension plots of the receptive field as a function of x alone. The receptive field is maximally different from zero for $\tau = 75$ ms with the spatial receptive field reversed from what it was at $\tau = 210$ ms. (Adapted from DeAngelis et al., 1995.)

Reversal effects like those seen in figure 2.13 are a common feature of space-time receptive fields. Although the magnitudes and signs of the different spatial regions in figure 2.13 vary over time, their locations and shapes remain fairly constant. This indicates that the neuron has, to a good approximation, a separable space-time receptive field. When a space-time

receptive field is separable, the reversal can be described by a function $D_t(\tau)$ that rises from zero, becomes positive, then negative, and ultimately goes to zero as τ increases. Adelson and Bergen (1985) proposed the function shown in Figure 2.14,

$$D_t(\tau) = \alpha \exp(-\alpha\tau) \left(\frac{(\alpha\tau)^5}{5!} - \frac{(\alpha\tau)^7}{7!} \right) \quad (2.29)$$

for $\tau \geq 0$, and $D_t(\tau) = 0$ for $\tau < 0$. Here, α is a constant that sets the scale for the temporal development of the function. Single phase responses are also seen for V1 neurons and these can be described by eliminating the second term in equation 2.29. Three-phase responses, which are sometimes seen, must be described by a more complicated function.

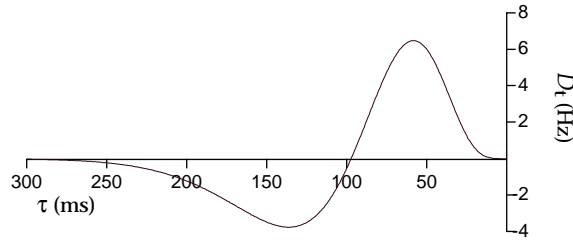


Figure 2.14: Temporal structure of a receptive field. The function $D_t(\tau)$ of equation 2.29 with $\alpha = 1/(15 \text{ ms})$.

Response of a Simple Cell to a Counterphase Grating

The response of a simple cell to a counterphase grating stimulus (equation 2.18) can be estimated by computing the function $L(t)$. For the separable receptive field given by the product of the spatial factor in equation 2.27 and the temporal factor in 2.29, the linear estimate of the response can be written a product of two terms,

$$L(t) = L_s L_t(t), \quad (2.30)$$

where

$$L_s = \int dx dy D_s(x, y) A \cos(Kx \cos(\Theta) + Ky \sin(\Theta) - \Phi). \quad (2.31)$$

and

$$L_t(t) = \int_0^\infty d\tau D_t(\tau) \cos(\omega(t - \tau)). \quad (2.32)$$

The reader is invited to compute these integrals for the case $\sigma_x = \sigma_y = \sigma$. To show the selectivity of the resulting spatial receptive fields, we plot (in

24 Neural Encoding II: Reverse Correlation and Visual Receptive Fields

figure 2.15) L_s as functions of the parameters Θ , K , and Φ that determine the orientation, spatial frequency, and spatial phase of the stimulus. It is also instructive to write out L_s for various special parameter values. First, if the spatial phase of the stimulus and the preferred spatial phase of the receptive field are zero ($\Phi = \phi = 0$), we find that

$$L_s = A \exp\left(-\frac{\sigma^2(k^2 + K^2)}{2}\right) \cosh(\sigma^2 k K \cos(\Theta)), \quad (2.33)$$

which determines the orientation and spatial frequency tuning for an optimal spatial phase. Second, for a grating with the preferred orientation $\Theta = 0$ and a spatial frequency that is not too small, the full expression for L_s can be simplified by noting that $\exp(-\sigma^2 k K) \approx 0$ for the values of $k\sigma$ normally encountered (for example, if $K = k$ and $k\sigma = 2$, $\exp(-\sigma^2 k K) = 0.02$). Using this approximation, we find

$$L_s = \frac{A}{2} \exp\left(-\frac{\sigma^2(k - K)^2}{2}\right) \cos(\phi - \Phi) \quad (2.34)$$

which reveals a Gaussian dependence on spatial frequency and a cosine dependence on spatial phase.

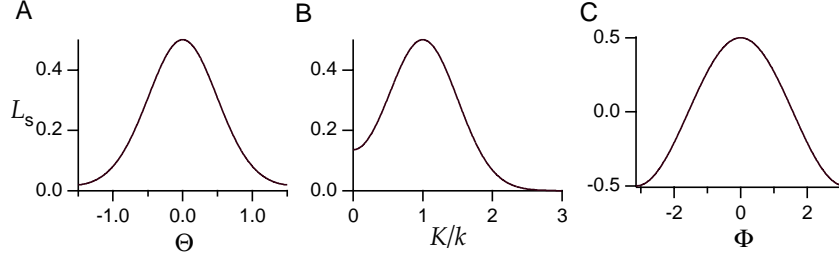


Figure 2.15: Selectivity of a Gabor filter with $\theta = \phi = 0$, $\sigma_x = \sigma_y = \sigma$ and $k\sigma = 2$ acting on a cosine grating with $A = 1$. A) L_s as a function of stimulus orientation Θ for a grating with the preferred spatial frequency and phase, $K = k$ and $\Phi = 0$. B) L_s as a function of the ratio of the stimulus spatial frequency to its preferred value, K/k , for a grating oriented in the preferred direction $\Theta = 0$ and with the preferred phase $\Phi = 0$. C) L_s as a function of stimulus spatial phase Φ for a grating with the preferred spatial frequency and orientation, $K = k$ and $\Theta = 0$.

The temporal frequency dependence of the amplitude of the linear response estimate is plotted as a function of the temporal frequency of the stimulus ($\omega/2\pi$ rather than the angular frequency ω) in figure 2.16. The peak value around 4 Hz and roll off above 10 Hz are typical for V1 neurons and for cortical neurons in other primary sensory areas as well.

Space-Time Receptive Fields

It is instructive to display the function $D(x, y, \tau)$ in a space-time plot rather than as a sequence of spatial plots (as in figure 2.13). To do this, we sup-

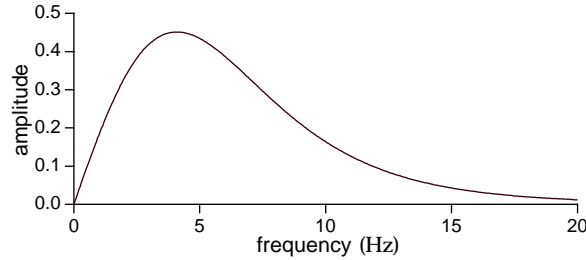


Figure 2.16: Frequency response of a model simple cell based on the temporal kernel of equation 2.29. The amplitude of the sinusoidal oscillations of $L_t(t)$ produced by a counterphase grating is plotted as a function of the temporal oscillation frequency, $\omega/2\pi$.

press the y dependence and plot x - τ projections of the space-time kernel. Space-time plots of receptive fields from two simple cells of the cat primary visual cortex are shown in figure 2.17. The receptive field in figure 2.17A is approximately separable, and it has OFF and ON subregions that

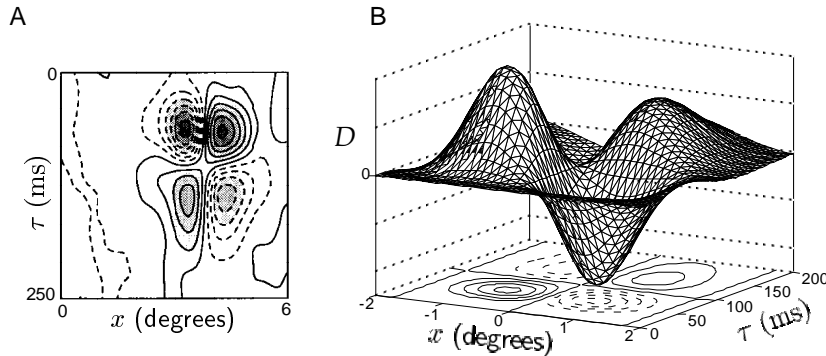


Figure 2.17: A separable space-time receptive field. A) An x - τ plot of an approximately separable space-time receptive field from cat primary visual cortex. OFF regions are shown with dashed contour lines and ON regions with solid contour lines. The receptive field has side-by-side OFF and ON regions that reverse as a function of τ . B) Mathematical descriptions of the space-time receptive field in A constructed by multiplying a Gabor function (evaluated at $y = 0$) with $\sigma_x = 1^\circ$, $1/k = 0.56^\circ$, and $\phi = \pi/2$ by the temporal kernel of equation 2.29 with $1/\alpha = 15$ ms. (A adapted from DeAngelis et al., 1995.)

reverse to ON and OFF subregions as a function of τ , similar to the reversal seen in figure 2.13. Figure 2.17B shows an x - τ contour plot of a separable space-time kernel, similar to the one in figure 2.17A, generated by multiplying a Gabor function by the temporal kernel of equation 2.29.

We can also plot the visual stimulus in a space-time diagram, suppressing the y coordinate by assuming that the image does not vary as a function of y . For example, figure 2.18A shows a grating of vertically oriented stripes

26 Neural Encoding II: Reverse Correlation and Visual Receptive Fields

moving to the left on an x - y plot. In the x - t plot of figure 2.18B, this image appears as a series of sloped dark and light bands. These represent the projection of the image in figure 2.18A onto the x axis evolving as a function of time. The leftward slope of the bands corresponds to the leftward movement of the image.

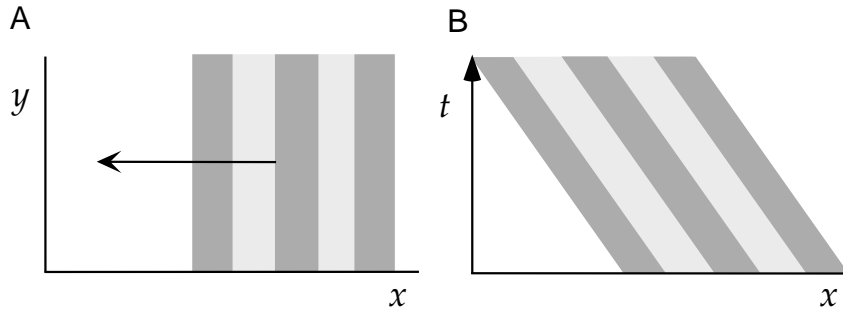


Figure 2.18: Space and space-time diagrams of a moving grating. A) A vertically oriented grating moves to the left on a two-dimensional screen. B) The space-time diagram of the image in A. The x location of the dark and light bands moves to the left as time progresses upward, representing the motion of the grating.

Most neurons in primary visual cortex do not respond strongly to static images, but respond vigorously to flashed and moving bars and gratings. The receptive field structure of figure 2.17 reveals why this is the case, as is shown in figures 2.19 and 2.20. The image in figures 2.19A-C is a dark bar that is flashed on for a brief period of time. To describe the linear response estimate at different times we show a cartoon of a space-time receptive field similar to the one in figure 2.17A. The receptive field is positioned at three different times in figures 2.19A, B, and C. The height of the horizontal axis of the receptive field diagram indicates the time when the estimation is being made. Figure 2.19A corresponds to an estimate of $L(t)$ at the moment when the image first appears. At this time, $L(t) = 0$. As time progresses, the receptive field diagram moves upward. Figure 2.19B generates an estimate at the moment of maximum response when the dark image overlaps the OFF area of the space-time receptive field, producing a positive contribution to $L(t)$. Figure 2.19C shows a later time when the dark image overlaps an ON region, generating a negative $L(t)$. The response for this flashed image is thus transient firing followed by suppression, as shown in Figure 2.19D.

Figures 2.19E and F show why a static dark bar is an ineffective stimulus. The static bar overlaps both the OFF region for small τ and the reversed ON region for large τ , generating opposing positive and negative contributions to $L(t)$. The flashed dark bar of figures 2.19A-C is a more effective stimulus because there is a time when it overlaps only the OFF region.

Figure 2.20 shows why a moving grating is a particularly effective stimulus. The grating moves to the left in 2.20A-C. At the time corresponding to

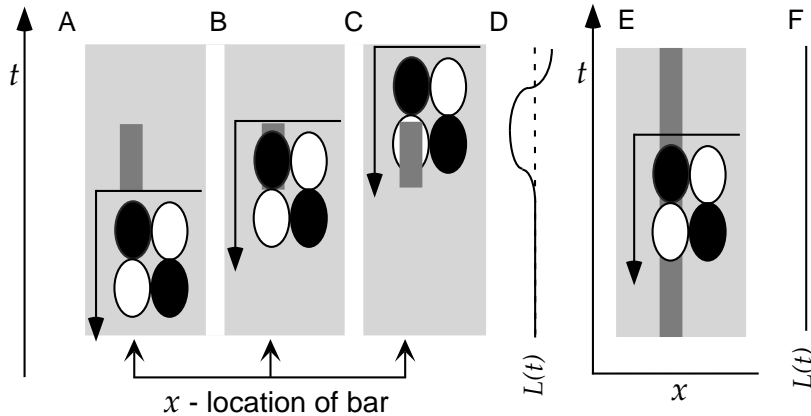


Figure 2.19: Responses to dark bars estimated from a separable space-time receptive field. Dark ovals in the receptive field diagrams are OFF regions and light circles are ON regions. The linear estimate of the response at any time is determined by positioning the receptive field diagram so that its horizontal axis matches the time of response estimation and noting how the OFF and ON regions overlap with the image. A-C) The image is a dark bar that is flashed on for a short interval of time. There is no response (A) until the dark image overlaps the OFF region (B) when $L(t) > 0$. The response is later suppressed when the dark bar overlaps the ON region (C) and $L(t) < 0$. D) A plot of $L(t)$ versus time corresponding to the responses generated in A-C. Time runs vertically in this plot, and $L(t)$ is plotted horizontally with the dashed line indicating the zero axis and positive values plotted to the left. E) The image is a static dark bar. The bar overlaps both an OFF and an ON region generating opposing positive and negative contributions to $L(t)$. F) The weak response corresponding to E, plotted as in D.

the positioning of the receptive field diagram in 2.20A, a dark band stimulus overlaps both OFF regions and light bands overlap both ON regions. Thus, all four regions contribute positive amounts to $L(t)$. As time progresses and the receptive field moves upward in the figure, the alignment will sometimes be optimal, as in 2.20A, and sometimes non-optimal, as in 2.20B. This produces an $L(t)$ that oscillates as a function of time between positive and negative values (2.20C). Figures 2.20D-F show that a neuron with this receptive field responds equally to a grating moving to the right. Like the left-moving grating in figures 2.20A-C, the right-moving grating can overlap the receptive field in an optimal manner (2.20D) producing a strong response, or in a maximally negative manner (2.20E) producing strong suppression of response, again resulting in an oscillating response (2.20F). Separable space-time receptive fields can produce responses that are maximal for certain speeds of grating motion, but they are not sensitive to the direction of motion.

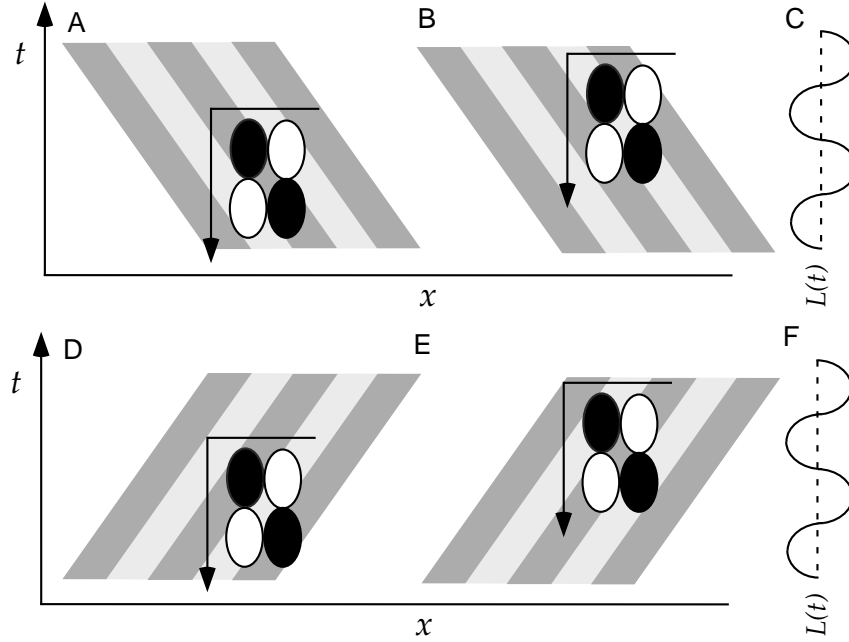


Figure 2.20: Responses to moving gratings estimated from a separable space-time receptive field. The receptive field is the same as in figure 2.19. A-C) The stimulus is a grating moving to the left. At the time corresponding to A, OFF regions overlap with dark bands and ON regions with light bands generating a strong response. At the time of the estimate in B, the alignment is reversed, and $L(t)$ is negative. C) A plot of $L(t)$ versus time corresponding to the responses generated in A-B. Time runs vertically in this plot and $L(t)$ is plotted horizontally with the dashed line indicating the zero axis and positive values plotted to the left. D-F) The stimulus is a grating moving to the right. The responses are identical to those in A-C.

Nonseparable Receptive Fields

Many neurons in primary visual cortex are selective for the direction of motion of an image. Accounting for direction selectivity requires nonseparable space-time receptive fields. An example of a nonseparable receptive field is shown in figure 2.21A. This neuron has a three-lobed OFF-ON-OFF spatial receptive field, and these subregions shift to the left as time moves forward (and τ decreases). This means that the optimal stimulus for this neuron has light and dark areas that move toward the left. One way to describe a nonseparable receptive field structure is to use a separable function constructed from a product of a Gabor function for D_s and equation 2.29 for D_t , but express these as functions of a mixture or rotation of the x and τ variables. The rotation of the space-time receptive field, as seen in figure 2.21B, is achieved by mixing the space and time coordinates using the transformation

$$D(x, y, \tau) = D_s(x', y)D_t(\tau') \quad (2.35)$$

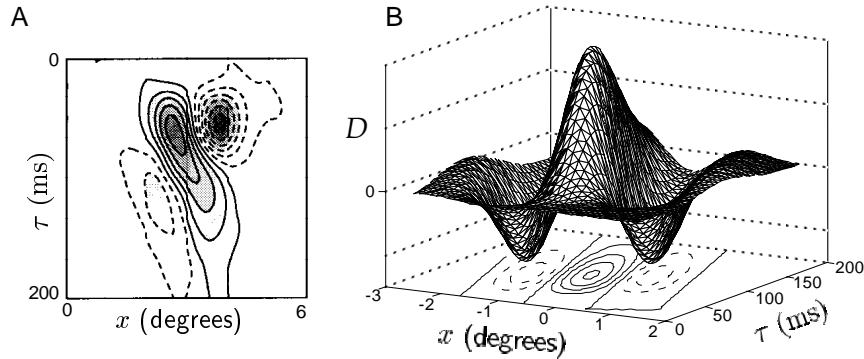


Figure 2.21: A nonseparable space-time receptive field. A) An x - τ plot of the space-time receptive field of a neuron from cat primary visual cortex. OFF regions are shown with dashed contour lines and ON regions with solid contour lines. The receptive field has a central ON region and two flanking OFF regions that shift to the left over time. B) Mathematical description of the space-time receptive field in A constructed from equations 2.35 - 2.37. The Gabor function used (evaluated at $y = 0$) had $\sigma_x = 1^\circ$, $1/k = 0.5^\circ$, and $\phi = 0$. D_t is given by the expression in equation 2.29 with $\alpha = 20$ ms except that the second term, with the seventh power function, was omitted because the receptive field does not reverse sign in this example. The x - τ rotation angle used was $\psi = \pi/9$ and the conversion factor was $c = 0.02^\circ/\text{ms}$. (A adapted from DeAngelis et al., 1995.)

with

$$x' = x \cos(\psi) - c\tau \sin(\psi) \quad (2.36)$$

and

$$\tau' = \tau \cos(\psi) + \frac{x}{c} \sin(\psi). \quad (2.37)$$

The factor c converts between the units of time (ms) and space (degrees) and ψ is the space-time rotation angle. The rotation operation is not the only way to generate nonseparable space-time receptive fields. They are often constructed by adding together two or more separable space-time receptive fields with different spatial and temporal characteristics.

Figure 2.22 shows how a nonseparable space-time receptive field can produce a response that is sensitive to the direction of motion of a grating. Figures 2.22A-C show a left-moving grating and, in 2.22A, the cartoon of the receptive field is positioned at a time when a light area of the image overlaps the central ON region and dark areas overlap the flanking OFF regions. This produces a large positive $L(t)$. At other times, the alignment is non-optimal (2.22B), and over time, $L(t)$ oscillates between fairly large positive and negative values (2.22C). The nonseparable space-time receptive field does not overlap optimally with the right-moving grating of figures 2.22D-F at any time and the response is correspondingly weaker (2.22F). Thus, a neuron with a nonseparable space-time receptive field can

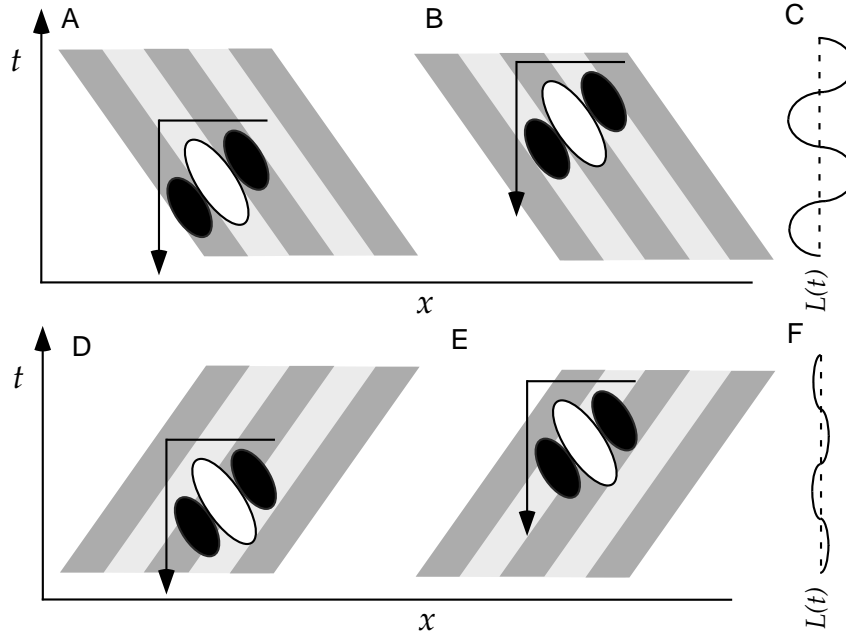


Figure 2.22: Responses to moving gratings estimated from a nonseparable space-time receptive field. Dark areas in the receptive field diagrams represent OFF regions and light areas ON regions. A-C) The stimulus is a grating moving to the left. At the time corresponding to A, OFF regions overlap with dark bands and the ON region overlaps a light band generating a strong response. At the time of the estimate in B, the alignment is reversed, and $L(t)$ is negative. C) A plot of $L(t)$ versus time corresponding to the responses generated in A-B. Time runs vertically in this plot and $L(t)$ is plotted horizontally with the dashed line indicating the zero axis. D-F) The stimulus is a grating moving to the right. Because of the tilt of the space-time receptive field, the alignment with the right-moving grating is never optimal and the response is weak (F).

be selective for the direction of motion of a grating and for its velocity, *direction selectivity*
responding most vigorously to an optimally spaced grating moving at a *preferred velocity*
velocity given, in terms of the parameters in equation 2.36, by $c \tan(\psi)$.

Static Nonlinearities - Simple Cells

Once the linear response estimate $L(t)$ has been computed, the firing rate of a visually responsive neuron can be approximated by using equation 2.8, $r_{\text{est}}(t) = r_0 + F(L(t))$ where F is an appropriately chosen static nonlinearity. The simplest choice for F consistent with the positive nature of firing rates, is rectification, $F = G[L]_+$, with G set to fit the magnitude of the measured firing rates. However, this choice makes the firing rate a linear function of the contrast amplitude, which does not match the data on the contrast dependence of visual responses. Neural responses saturate as

contrast saturation

the contrast of the image increases and are more accurately described by $r \propto A^n / (A_{1/2}^n + A^n)$ where n is near two, and $A_{1/2}$ is a parameter equal to the contrast amplitude that produces a half-maximal response. This led Heeger (1992) to propose that an appropriate static nonlinearity to use is

$$F(L) = \frac{G[L]_+^2}{A_{1/2}^2 + G[L]_+^2} \quad (2.38)$$

because this reproduces the observed contrast dependence. A number of variants and extensions of this idea have also been considered, including, for example, that the denominator of this expression should include L factors for additional neurons with nearby receptive fields. This can account for the effects of visual stimuli outside the ‘classical’ receptive field. Discussion of these effects is beyond the scope of this chapter.

2.5 Static Nonlinearities - Complex Cells

Recall that a large proportion of the neurons in primary visual cortex is separated into classes of simple and complex cells. While linear methods, such as spike-triggered averages, are useful for revealing the properties of simple cells, at least to a first approximation, complex cells display features that are fundamentally incompatible with a linear description. The spatial receptive fields of complex cells cannot be divided into separate ON and OFF regions that sum linearly to generate the response. Areas where light and dark images excite the neuron overlap making it difficult to measure and interpret spike-triggered average stimuli. Nevertheless, like simple cells, complex cells are selective to the spatial frequency and orientation of a grating. However, unlike simple cells, complex cells respond to bars of light or dark no matter where they are placed within the overall receptive field. Likewise, the responses of complex cells to grating stimuli show little dependence on spatial phase. Thus, a complex cell is selective for a particular type of image independent of its exact spatial position within the receptive field. This may represent an early stage in the visual processing that ultimately leads to position-invariant object recognition.

Complex cells also have temporal response characteristics that distinguish them from simple cells. Complex cell responses to moving gratings are approximately constant, not oscillatory as in figures 2.20 and 2.22. The firing rate of a complex cell responding to a counterphase grating oscillating with frequency ω has both a constant component and an oscillatory component with a frequency of 2ω , a phenomenon known as frequency doubling.

spatial phase invariance

frequency doubling

Even though spike-triggered average stimuli and reverse correlation functions fail to capture the response properties of complex cells, complex-cell responses can be described, to a first approximation, by a relatively

straightforward extension of the reverse correlation approach. The key observation comes from equation 2.34, which shows how the linear response estimate of a simple cell depends on spatial phase for an optimally oriented grating with K not too small. Consider two such responses, labeled L_1 and L_2 , with preferred spatial phases ϕ and $\phi - \pi/2$. Including both the spatial and temporal response factors, we find, for preferred spatial phase ϕ ,

$$L_1 = AB(\omega, K) \cos(\phi - \Phi) \cos(\omega t - \delta) \quad (2.39)$$

where $B(\omega, K)$ is a temporal and spatial frequency-dependent amplitude factor. We do not need the explicit form of $B(\omega, K)$ here, but the reader is urged to derive it. For preferred spatial phase $\phi - \pi/2$,

$$L_2 = AB(\omega, K) \sin(\phi - \Phi) \cos(\omega t - \delta) \quad (2.40)$$

because $\cos(\phi - \pi/2 - \Phi) = \sin(\phi - \Phi)$. If we square and add these two terms, we obtain a result that does not depend on Φ ,

$$L_1^2 + L_2^2 = A^2 B^2(\omega, K) \cos^2(\omega t - \delta), \quad (2.41)$$

because $\cos^2(\phi - \Phi) + \sin^2(\phi - \Phi) = 1$. Thus, we can describe the re-

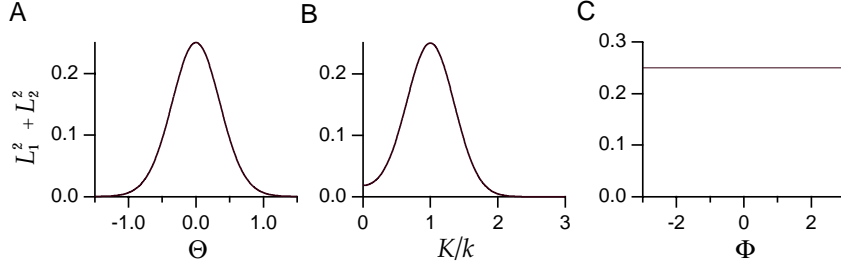


Figure 2.23: Selectivity of a complex cell model in response to a sinusoidal grating. The width and preferred spatial frequency of the Gabor functions underlying the estimated firing rate satisfy $k\sigma = 2$. A) The complex cell response estimate, $L_1^2 + L_2^2$, as a function of stimulus orientation Θ for a grating with the preferred spatial frequency $K = k$. B) $L_1^2 + L_2^2$ as a function of the ratio of the stimulus spatial frequency to its preferred value, K/k , for a grating oriented in the preferred direction $\Theta = 0$. C) $L_1^2 + L_2^2$ as a function of stimulus spatial phase Φ for a grating with the preferred spatial frequency and orientation $K = k$ and $\Theta = 0$.

sponse of a complex cell by writing

$$r(t) = r_0 + G(L_1^2 + L_2^2). \quad (2.42)$$

The selectivities of such a response estimate to grating orientation, spatial frequency, and spatial phase are shown in figure 2.23. The response of the model complex cell is tuned to orientation and spatial frequency, but the spatial phase dependence, illustrated for a simple cell in figure 2.15C, is

absent. In computing the curve for figure 2.23C, we used the exact expressions for L_1 and L_2 from the integrals in equations 2.31 and 2.32, not the approximation 2.34 used to simplify the discussion above. Although it is not visible in the figure, there is a weak dependence on Φ when the exact expressions are used.

The complex cell response given by equations 2.42 and 2.41 reproduces the frequency doubling effect seen in complex cell responses because the factor $\cos^2(\omega t - \delta)$ oscillates with frequency 2ω . This follows from the identity

$$\cos^2(\omega t - \delta) = \frac{1}{2} \cos(2(\omega t - \delta)) + \frac{1}{2}. \quad (2.43)$$

In addition, the last term on the right side of this equation generates the constant component of the complex cell response to a counterphase grating. Figure 2.24 shows a comparison of model simple and complex cell responses to a counterphase grating and illustrates this phenomenon.

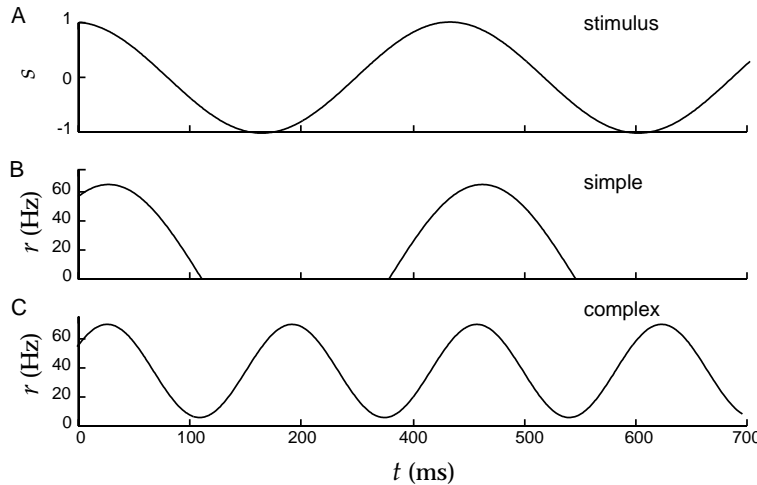


Figure 2.24: Temporal responses of model simple and complex cells to a counterphase grating. A) The stimulus $s(x, y, t)$ at a given point (x, y) plotted as a function of time. B) The rectified linear response estimate of a model simple cell to this grating with a temporal kernel given by equation 2.29 with $\alpha = 1/(15 \text{ ms})$. C) The frequency doubled response of a model complex cell with the same temporal kernel but with the estimated rate given by a squaring operation rather than rectification. The background firing rate is $r_0 = 5 \text{ Hz}$. Note the temporal phase shift of both B and C relative to A.

The description of a complex cell response that we have presented is called an ‘energy’ model because of its resemblance to the equation for the energy of a simple harmonic oscillator. The pair of linear filters used, with preferred spatial phases separated by $\pi/2$ is called a quadrature pair. Because of rectification, the terms L_1^2 and L_2^2 cannot be constructed by squaring the

energy model

outputs of single simple cells. However, they can each be constructed by summing the squares of rectified outputs from two simple cells with preferred spatial phases separated by π . Thus, we can write the complex cell response as the sum of the squares of four rectified simple cell responses,

$$r(t) = r_0 + G([L_1]_+^2 + [L_2]_+^2 + [L_3]_+^2 + [L_4]_+^2), \quad (2.44)$$

where the different $[L]_+$ terms represent the responses of simple cells with preferred spatial phases ϕ , $\phi + \pi/2$, $\phi + \pi$, and $\phi + 3\pi/2$. While such a construction is possible, it should not be interpreted too literally because complex cells receive input from many sources including the LGN and other complex cells. Rather, this model should be viewed as purely descriptive. Mechanistic models of complex cells are described at the end of this chapter and in chapter 7.

2.6 Receptive Fields in the Retina and LGN

We end this discussion of the visual system by returning to the initial stages of the visual pathway and briefly describing the receptive field properties of neurons in the retina and LGN. Retinal ganglion cells display a wide variety of response characteristics, including nonlinear and direction-selective responses. However, a class of retinal ganglion cells (X cells in the cat or P cells in the monkey retina and LGN) can be described by a linear model built using reverse correlation methods. The receptive fields of this class of retinal ganglion cells and an analogous type of LGN relay neurons are similar, so we do not treat them separately. The spatial structure of the receptive fields of these neurons has a center-surround structure consisting either of a circular central ON region surrounded by an annular OFF region, or the opposite arrangement of a central OFF region surrounded by an ON region. Such receptive fields are called ON-center or OFF-center respectively. Figure 2.25A shows the spatial receptive fields of an ON-center cat LGN neuron.

The spatial structure of retinal ganglion and LGN receptive fields is well-captured by a difference-of-Gaussians model in which the spatial receptive field is expressed as

$$D_s(x, y) = \pm \left(\frac{1}{2\pi\sigma_{\text{cen}}^2} \exp\left(-\frac{x^2 + y^2}{2\sigma_{\text{cen}}^2}\right) - \frac{B}{2\pi\sigma_{\text{sur}}^2} \exp\left(-\frac{x^2 + y^2}{2\sigma_{\text{sur}}^2}\right) \right). \quad (2.45)$$

Here the center of the receptive field has been placed at $x = y = 0$. The first Gaussian function in equation 2.45 describes the center and the second the surround. The size of the central region is determined by the parameter σ_{cen} , while σ_{sur} , which is greater than σ_{cen} , determines the size of the surround. B controls the balance between center and surround contributions.

*difference of
Gaussians*

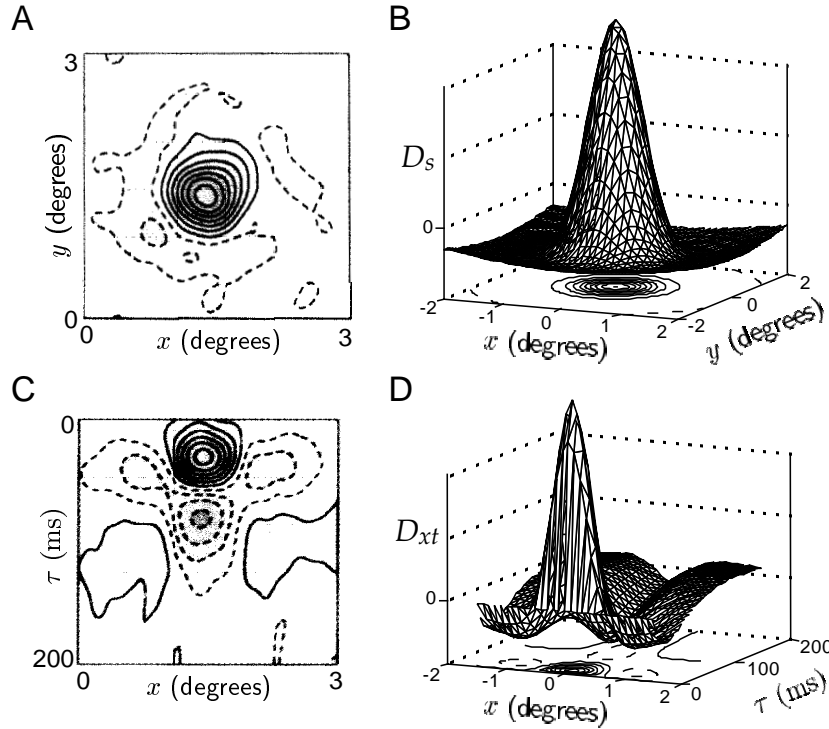


Figure 2.25: Receptive fields of LGN neurons. A) The center-surround spatial structure of the receptive field of a cat LGN X cell. This has a central ON region (solid contours) and a surrounding OFF region (dashed contours). B) A fit of the receptive field shown in A using a difference of Gaussian function (equation 2.45) with $\sigma_{cen} = 0.3^\circ$, $\sigma_{sur} = 1.5^\circ$, and $B = 5$. C) The space-time receptive field of a cat LGN X cell. Note that both the center and surround regions reverse sign as a function of τ and that the temporal evolution is slower for the surround than for the center. D) A fit of the space-time receptive field in C using 2.46 with the same parameters for the Gaussian functions as in B, and temporal factors given by equation 2.47 with $1/\alpha_{cen} = 16$ ms for the center, $1/\alpha_{sur} = 32$ ms for the surround, and $1/\beta_{cen} = 1/\beta_{sur} = 64$ ms. (A and C adapted from DeAngelis et al., 1995.)

The \pm sign allows both ON-center (+) and OFF-center (-) cases to be represented. Figure 2.25B shows a spatial receptive field formed from the difference of two Gaussians that approximates the receptive field structure in figure 2.25A.

Figure 2.25C shows that the spatial structure of the receptive field reverses over time with, in this case, a central ON region reversing to an OFF region as τ increases. Similarly, the OFF surround region changes to an ON region with increasing τ , although the reversal and the onset are slower for the surround than for the central region. Because of the difference between the time course of the center and surround regions, the space-time receptive field is not separable, although the center and surround components

36 Neural Encoding II: Reverse Correlation and Visual Receptive Fields

are individually separable. The basic features of LGN neuron space-time receptive fields are captured by the mathematical caricature

$$D(x, y, \tau) = \pm \left(\frac{D_t^{\text{cen}}(\tau)}{2\pi\sigma_{\text{cen}}^2} \exp\left(-\frac{x^2 + y^2}{2\sigma_{\text{cen}}^2}\right) - \frac{BD_t^{\text{sur}}(\tau)}{2\pi\sigma_{\text{sur}}^2} \exp\left(-\frac{x^2 + y^2}{2\sigma_{\text{sur}}^2}\right) \right). \quad (2.46)$$

Separate functions of time multiply the center and surround, but they can both be described by the same functions using two sets of parameters,

$$D_t^{\text{cen,sur}}(\tau) = \alpha_{\text{cen,sur}}^2 \tau \exp(-\alpha_{\text{cen,sur}} \tau) - \beta_{\text{cen,sur}}^2 \tau \exp(-\beta_{\text{cen,sur}} \tau). \quad (2.47)$$

The parameters α_{cen} and α_{sur} control the latency of the response in the center and surround regions respectively, and β_{cen} and β_{sur} affect the time of the reversal. This function has characteristics similar to the function 2.29, but the latency effect is less pronounced. Figure 2.25D shows the space-time receptive field of equation 2.46 with parameters chosen to match figure 2.25C.

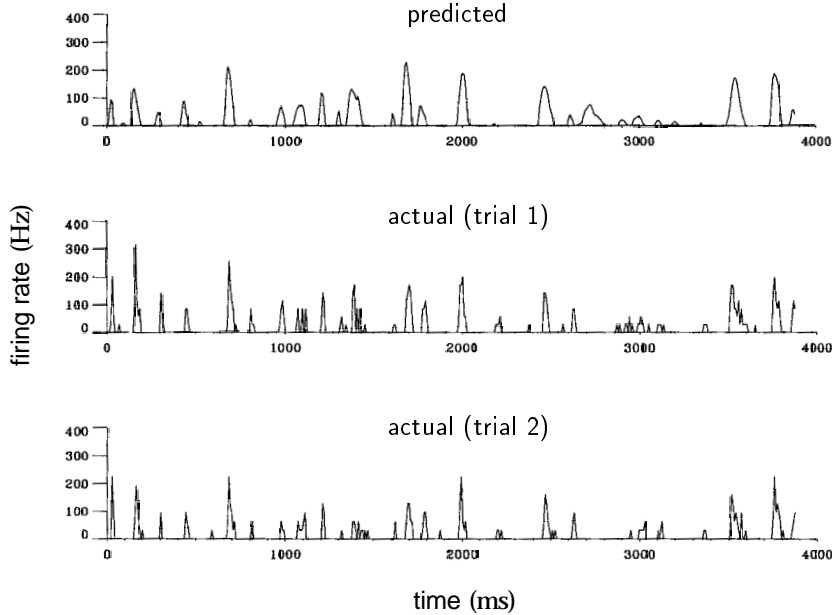


Figure 2.26: Comparison of predicted and measured firing rates for a cat LGN neuron responding to a video movie. The top panel is the rate predicted by integrating the product of the video image intensity and a linear filter obtained for this neuron from a spike-triggered average of a white-noise stimulus. The resulting linear prediction was rectified. The middle and lower panels are measured firing rates extracted from two different sets of trials. (From Dan et al., 1996.)

Figure 2.26 shows the results of a direct test of a reverse correlation model of an LGN neuron. The kernel needed to describe a particular LGN cell was first extracted using a white-noise stimulus. This, together with a rectifying static nonlinearity, was used to predict the firing rate of the neuron

in response to a video movie. The top panel in figure 2.26 shows the resulting prediction while the middle and lower panels show the actual firing rates extracted from two different groups of trials. The correlation coefficient between the predicted and actual firing rates was 0.5, which was very close to the correlation coefficient between firing rates extracted from different groups of trials. This means that the error of the prediction was no worse than the variability of the neural response itself.

2.7 Constructing V1 Receptive Fields

The models of visual receptive fields we have been discussing are purely descriptive, but they provide an important framework for studying how the circuits of the retina, LGN, and primary visual cortex generate neural responses. In an example of a more mechanistic model, Hubel and Wiesel (1962) showed how the oriented receptive fields of cortical neurons could be generated by summing the input from appropriately selected LGN neurons. Their construction, shown in figure 2.27A, consists of alternating rows of ON-center and OFF-center LGN cells providing convergent input to a cortical simple cell. The left side of figure 2.27A shows the spatial arrangement of LGN receptive fields that, when summed, form bands of ON and OFF regions resembling the receptive field of an oriented simple cell. This model accounts for the selectivity of a simple cell purely on the basis of feedforward input from the LGN. We leave the study of this model as an exercise for the reader. Other models, which we discuss in chapter 7, include the effects of recurrent intracortical connections as well.

*Hubel-Wiesel
simple cell model*

In a previous section, we showed how the properties of complex cell responses could be accounted for using a squaring static nonlinearity. While this provides a good description of complex cells, there is little indication that complex cells actually square their inputs. Models of complex cells can be constructed without introducing a squaring nonlinearity. One such example is another model proposed by Hubel and Wiesel (1962), which is depicted in figure 2.27B. Here the phase-invariant response of a complex cell is produced by summing together the responses of several simple cells with similar orientation and spatial frequency tuning, but different preferred spatial phases. In this model, the complex cell inherits its orientation and spatial frequency preference from the simple cells that drive it, but spatial phase selectivity is reduced because the outputs of simple cells with a variety of spatial phases selectivities are summed linearly. Analysis of this model is left as an exercise. While the model generates complex cell responses, there are indications that complex cells in primary visual cortex are not exclusively driven by simple cell input. An alternative model is considered in chapter 7.

*Hubel-Wiesel
complex cell model*

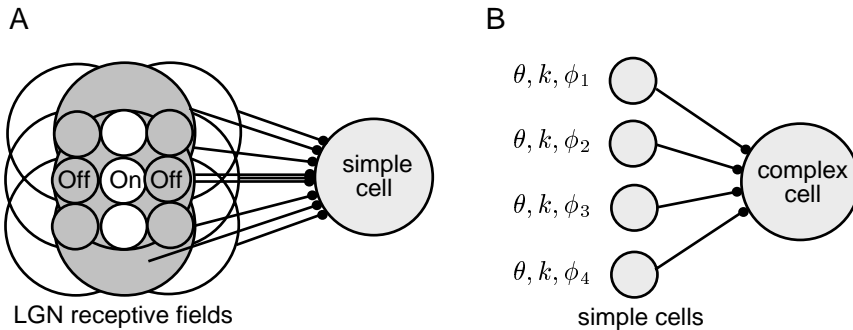


Figure 2.27: A) The Hubel-Wiesel model of orientation selectivity. The spatial arrangement of the receptive fields of nine LGN neurons are shown, with a row of three ON-center fields flanked on either side by rows of three OFF-center fields. White areas denote ON fields and grey areas OFF fields. In the model, the converging LGN inputs are summed linearly by the simple cell. This arrangement produces a receptive field oriented in the vertical direction. B) The Hubel-Wiesel model of a complex cell. Inputs from a number of simple cells with similar orientation and spatial frequency preferences (θ and k), but different spatial phase preferences (ϕ_1 , ϕ_2 , ϕ_3 , and ϕ_4), converge on a complex cell and are summed linearly. This produces a complex cell output that is selective for orientation and spatial frequency, but not for spatial phase. The figure shows four simple cells converging on a complex cell, but additional simple cells can be included to give a more complete coverage of spatial phase.

2.8 Chapter Summary

We continued from chapter 1 our study of the ways that neurons encode information, focusing on reverse-correlation analysis, particularly as applied to neurons in the retina, visual thalamus (LGN), and primary visual cortex. We used the tools of systems identification, especially the linear filter, Wiener kernel, and static nonlinearity to build descriptive linear and nonlinear models of the transformation from dynamic stimuli to time-dependent firing rates. We discussed the complex logarithmic map governing the way that neighborhood relationships in the retina are transformed into cortex, Nyquist sampling in the retina, and Gabor functions as descriptive models of separable and nonseparable receptive fields. Models based on Gabor filters and static nonlinearities were shown to account for the basic response properties of simple and complex cells in primary visual cortex, including selectivity for orientation, spatial frequency and phase, velocity, and direction. Retinal ganglion cell and LGN responses were modeled using a difference-of-Gaussians kernel. We briefly described simple circuit models of simple and complex cells.

2.9 Appendices

A) The Optimal Kernel

Using equation 2.1 for the estimated firing rate, the expression 2.3 to be minimized is

$$E = \frac{1}{T} \int_0^T dt \left(r_0 + \int_0^\infty d\tau D(\tau) s(t - \tau) - r(t) \right)^2. \quad (2.48)$$

The minimum is obtained by setting the derivative of E with respect to the function D to zero. A quantity, such as E , that depends on a function, D in this case, is called a functional, and the derivative we need is a functional derivative. Finding the extrema of functionals is the subject of a branch of mathematics called the calculus of variations. A simple way to define a functional derivative is to introduce a small time interval Δt and evaluate all functions at integer multiples of Δt . We define $r_i = r(i\Delta t)$, $D_k = D(k\Delta t)$, and $s_{i-k} = s((i-k)\Delta t)$. If Δt is small enough, the integrals in equation 2.48 can be approximated by sums, and we can write

$$E = \frac{\Delta t}{T} \sum_{i=0}^{T/\Delta t} \left(r_0 + \Delta t \sum_{k=0}^{\infty} D_k s_{i-k} - r_i \right)^2. \quad (2.49)$$

functional derivative
 E is minimized by setting its derivative with respect to D_j for all values of j to zero,

$$\frac{\partial E}{\partial D_j} = 0 = \frac{2\Delta t}{T} \sum_{i=0}^{T/\Delta t} \left(r_0 + \Delta t \sum_{k=0}^{\infty} D_k s_{i-k} - r_i \right) s_{i-j} \Delta t. \quad (2.50)$$

Rearranging and simplifying this expression gives the condition

$$\Delta t \sum_{k=0}^{\infty} D_k \left(\frac{\Delta t}{T} \sum_{i=0}^{T/\Delta t} s_{i-k} s_{i-j} \right) = \frac{\Delta t}{T} \sum_{i=0}^{T/\Delta t} (r_i - r_0) s_{i-j}. \quad (2.51)$$

If we take the limit $\Delta t \rightarrow 0$ and make the replacements $i\Delta t \rightarrow t$, $j\Delta t \rightarrow \tau$, and $k\Delta t \rightarrow \tau'$, the sums in equation 2.51 turn back into integrals, the indexed variables become functions, and we find

$$\int_0^\infty d\tau' D(\tau') \left(\frac{1}{T} \int_0^T dt s(t - \tau') s(t - \tau) \right) = \frac{1}{T} \int_0^T dt (r(t) - r_0) s(t - \tau). \quad (2.52)$$

The term proportional to r_0 on the right side of this equation can be dropped because the time integral of s is zero. The remaining term is the firing rate-stimulus correlation function evaluated at $-\tau$, $Q_{rs}(-\tau)$. The term in large parentheses on the left side of 2.52 is the stimulus autocorrelation function. By shifting the integration variable $t \rightarrow t + \tau$, we find that it is $Q_{ss}(\tau - \tau')$, so 2.52 can be re-expressed in the form of equation 2.4.

40 Neural Encoding II: Reverse Correlation and Visual Receptive Fields

Equation 2.6 provides the solution to equation 2.4 only for a white noise stimulus. For an arbitrary stimulus, equation 2.4 can be solved easily by the method of Fourier transforms if we ignore causality and allow the estimated rate at time t to depend on the stimulus at times later than t , so that

$$r_{\text{est}}(t) = r_0 + \int_{-\infty}^{\infty} d\tau D(\tau) s(t - \tau). \quad (2.53)$$

The estimate written in this acausal form, satisfies a slightly modified version of equation 2.4,

$$\int_{-\infty}^{\infty} d\tau' Q_{ss}(\tau - \tau') D(\tau') = Q_{rs}(-\tau). \quad (2.54)$$

We define the Fourier transforms (see the Mathematical Appendix)

$$\tilde{D}(\omega) = \int_{-\infty}^{\infty} dt D(t) \exp(i\omega t) \quad \text{and} \quad \tilde{Q}_{ss}(\omega) = \int_{-\infty}^{\infty} d\tau Q_{ss}(\tau) \exp(i\omega\tau) \quad (2.55)$$

as well as $\tilde{Q}_{rs}(\omega)$ defined analogously to $\tilde{Q}_{ss}(\omega)$.

Equation 2.54 is solved by taking the Fourier transform of both sides and using the convolution identity (Mathematical Appendix)

$$\int_{-\infty}^{\infty} dt \exp(i\omega t) \int_{-\infty}^{\infty} d\tau' Q_{ss}(\tau - \tau') D(\tau') = \tilde{D}(\omega) \tilde{Q}_{ss}(\omega) \quad (2.56)$$

In terms of the Fourier transforms, equation 2.54 then becomes

$$\tilde{D}(\omega) \tilde{Q}_{ss}(\omega) = \tilde{Q}_{rs}(-\omega) \quad (2.57)$$

which can be solved directly to obtain $\tilde{D}(\omega) = \tilde{Q}_{rs}(-\omega)/\tilde{Q}_{ss}(\omega)$. The inverse Fourier transform from which $D(\tau)$ is recovered is (Mathematical Appendix)

$$D(\tau) = \frac{1}{2\pi} \int_{-\infty}^{\infty} d\omega \tilde{D}(\omega) \exp(-i\omega\tau), \quad (2.58)$$

so the optimal acausal kernel when the stimulus is temporally correlated is given by

$$D(\tau) = \frac{1}{2\pi} \int_{-\infty}^{\infty} d\omega \frac{\tilde{Q}_{rs}(-\omega)}{\tilde{Q}_{ss}(\omega)} \exp(-i\omega\tau). \quad (2.59)$$

B) The Most Effective Stimulus

We seek the stimulus that produces the maximum predicted responses at time t subject to the fixed energy constraint

$$\int_0^T dt' (s(t'))^2 = \text{constant}. \quad (2.60)$$

We impose this constraint by the method of Lagrange multipliers (see the Mathematical Appendix), which means that we must find the unconstrained maximum value with respect to s of

$$r_{\text{est}}(t) + \lambda \int_0^T dt' s^2(t') = r_0 + \int_0^\infty d\tau D(\tau)s(t-\tau) + \lambda \int_0^T dt' (s(t'))^2 \quad (2.61)$$

where λ is the Lagrange multiplier. Setting the derivative of this expression with respect to the function s to zero (using the same methods used in appendix A) gives

$$D(\tau) = -2\lambda s(t-\tau). \quad (2.62)$$

The value of λ (which is less than zero) is determined by requiring that condition 2.60 is satisfied, but the precise value is not important for our purposes. The essential result is the proportionality between the optimal stimulus and $D(\tau)$.

C) Bussgang's Theorem

Bussgang (1952 & 1975) proved that an estimate based on the optimal kernel for linear estimation can still be self-consistent (although not necessarily optimal) when nonlinearities are present. The self-consistency condition is that when the nonlinear estimate $r_{\text{est}} = r_0 + F(L(t))$ is substituted into equation 2.6, the relationship between the linear kernel and the firing rate-stimulus correlation function should still hold. In other words, we require that

$$D(\tau) = \frac{1}{\sigma_s^2 T} \int_0^T dt r_{\text{est}}(t)s(\tau-t) = \frac{1}{\sigma_s^2 T} \int_0^T dt F(L(t))s(\tau-t). \quad (2.63)$$

We have dropped the r_0 term because the time integral of s is zero. In general, equation 2.63 does not hold, but if the stimulus used to extract D is Gaussian white noise, equation 2.63 reduces to a simple normalization condition on the function F . This result is based on the identity, valid for a Gaussian white-noise stimulus,

$$\frac{1}{\sigma_s^2 T} \int_0^T dt F(L(t))s(\tau-t) = \frac{D(\tau)}{T} \int_0^T dt \frac{dF(L(t))}{dL}. \quad (2.64)$$

For the right side of this equation to be $D(\tau)$, the remaining expression, involving the integral of the derivative of F , must be equal to one. This can be achieved by appropriate scaling of F . The critical identity 2.64 is based on integration by parts for a Gaussian weighted integral. A simplified proof is left as an exercise.

2.10 Annotated Bibliography

Marmarelis & Marmarelis (1978), Rieke et al. (1997) and Gabbiani & Koch (1998) provide general discussions of reverse correlation methods. A useful reference relevant to our presentation of their application to the visual system is Carandini et al. (1996). Volterra and Wiener functional expansions are discussed in Wiener (1958) and Marmarelis & Marmarelis (1978).

General introductions to the visual system include Hubel & Wiesel (1962, 1977), Orban (1984), Hubel (1988), Wandell (1995), and De Valois & De Valois (1990). Our treatment follows Dowling (1987) on processing in the retina, and Schwartz (1977), Van Essen et al. (1984), and Rovamo & Virsu (1984) on aspects of the retinotopic map from the eye to the brain. Properties of this map are used to account for aspects of visual hallucinations in Ermentrout & Cowan (1979). We also follow Movshon et al. (1978a & b) for definitions of simple and complex cells; Daugman (1985) and Jones & Palmer (1987b) on the use of Gabor functions (Gabor, 1946) to describe visual receptive fields; and DeAngelis et al. (1995) on space-time receptive fields. Our description of the energy model of complex cells is based on Adelson & Bergen (1985), which is related to work by Pollen & Ronner (1982), Van Santen & Sperling (1984), and Watson & Ahumada (1985), and to earlier ideas of Reichardt (1961) and Barlow & Levick (1965). Heeger's (1992; 1993) model of contrast saturation is reviewed in Carandini et al. (1996) and has been applied in a approach more closely related to the representational learning models of chapter 10 by Simoncelli & Schwartz (1999). The difference-of-Gaussians model for retinal and LGN receptive fields is due to Rodieck (1965) and Enroth-Cugell and Robson (1966). A useful reference to modeling of the early visual system is Wörgötter & Koch (1991). The issue of linearity and non-linearity in early visual processing is reviewed by Ferster (1994).

Chapter 3

Neural Decoding

3.1 Encoding and Decoding

In chapters 1 and 2, we considered the problem of predicting neural responses to known stimuli. The nervous system faces the reverse problem, determining what is going on in the real world from neuronal spiking patterns. It is interesting to attempt such computations ourselves, using the responses of one or more neurons to identify a particular stimulus or to extract the value of a stimulus parameter. We will assess the accuracy with which this can be done primarily by using optimal decoding techniques, regardless of whether the computations involved seem biologically plausible. Some biophysically realistic implementations are discussed in chapter 7. Optimal decoding allows us to determine limits on the accuracy and reliability of neuronal encoding. In addition, it is useful for estimating the information content of neuronal spike trains, an issue addressed in chapter 4.

As we discuss in chapter 1, neural responses, even to a single repeated stimulus, are typically described by stochastic models due to their inherent variability. In addition, the stimuli themselves are often described stochastically. For example, the stimuli used in an experiment might be drawn randomly from a specified probability distribution. Natural stimuli can also be modeled stochastically as a way of capturing the statistical properties of complex environments.

Given this two-fold stochastic model, encoding and decoding are related through a basic identity of probability theory called Bayes theorem. Let \mathbf{r} represent the response of a neuron or a population of neurons to a stimulus characterized by a parameter s . Throughout this chapter, $\mathbf{r} = (r_1, r_2, \dots, r_N)$ for N neurons is a list of spike-count firing rates, although, for the present discussion, it could be any other set of parameters describing the neuronal response. Several different probabilities and con-

conditional probability

ditional probabilities enter into our discussion. A conditional probability is just an ordinary probability of an event occurring except that its occurrence is subject to an additional condition. The conditional probability of an event A occurring subject to the condition B is denoted by $P[A|B]$. The probabilities we need are:

- prior probability*
- $P[s]$, the probability of stimulus s being presented. This is often called the prior probability,
 - $P[r]$, the probability of response r being recorded,
 - $P[r,s]$, the probability of stimulus s being presented and response r being recorded,
 - $P[r|s]$, the conditional probability of evoking response r given that stimulus s was presented, and
 - $P[s|r]$, the conditional probability that stimulus s was presented given that the response r was recorded.

Note that $P[r|s]$ is the probability of observing the rates r given that the stimulus took the value s , while $P[r]$ is the probability of the rates taking the values r independent of what stimulus was used. $P[r]$ can be computed from $P[r|s]$ by summing over all stimulus values weighted by their probabilities,

$$P[r] = \sum_s P[r|s]P[s] \text{ and similarly } P[s] = \sum_r P[s|r]P[r]. \quad (3.1)$$

An additional relationship between the probabilities listed above can be derived by noticing that $P[r,s]$ can be expressed as either the conditional probability $P[r|s]$ times the probability of the stimulus, or as $P[s|r]$ times the probability of the response,

$$P[r,s] = P[r|s]P[s] = P[s|r]P[r]. \quad (3.2)$$

Bayes theorem

This is the basis of Bayes theorem relating $P[s|r]$ to $P[r|s]$,

$$P[s|r] = \frac{P[r|s]P[s]}{P[r]}, \quad (3.3)$$

assuming that $P[r] \neq 0$. Encoding is characterized by the set of probabilities $P[r|s]$ for all stimuli and responses. Decoding a response, on the other hand, amounts to determining the probabilities $P[s|r]$. According to Bayes theorem, $P[s|r]$ can be obtained from $P[r|s]$, but the stimulus probability $P[s]$ is also needed. As a result, decoding requires knowledge of the statistical properties of experimentally or naturally occurring stimuli.

In the above discussion, we have assumed that both the stimulus and response are characterized by discrete values so that ordinary probabilities,

not probability densities, are used to describe their distributions. For example, firing rates obtained by counting spikes over the duration of a trial take discrete values and can be described by a probability. However, we sometimes treat the response firing rates or the stimulus values as continuous variables. In this case, the probabilities listed must be replaced by the corresponding probability densities, $p[r]$, $p[r|s]$, etc. Nevertheless, the relationships discussed above are equally valid.

In the following sections, we present examples of decoding that involve both single neurons and neuronal populations. We first study a restricted case of single-cell decoding, discrimination between two different stimulus values. We then consider extracting the value of a parameter that characterizes a static stimulus from the responses of a population of neurons. As a final example, we return to single neurons and discuss spike-train decoding in which an estimate of a time-varying stimulus is constructed from the spike train it evokes.

3.2 Discrimination

To introduce the notion of discriminability and the receiver operating characteristic that lie at the heart of discrimination analysis, we will discuss a fascinating study performed by Britten, Shadlen, Newsome and Movshon (1992). In their experiments, a monkey was trained to discriminate between two directions of motion of a visual stimulus. The stimulus was a pattern of dots on a video monitor that jump from random initial locations to new locations every 45 ms. To introduce a sense of directed movement at a particular velocity, a percentage of the dots move together by a fixed amount in a fixed direction (figure 3.1). The coherently moving dots are selected randomly at each time step, and the remaining dots move to random new locations. The percentage of dots that move together in the fixed direction is called the coherence level. At 0% coherence, the image appears chaotic with no sense of any particular direction of motion. As the coherence increases, a sense of movement in a particular direction appears in the image, until, at 100% coherence, the entire array of dots moves together on the monitor. By varying the degree of coherence, the task of detecting the movement direction can be made more or less difficult.

The experiments combined neural recording with behavioral measurements. In the behavioral part, the monkey had to report the direction of motion in the random dot images. During the same task, recordings were made from neurons in area MT. Only two different possible directions of coherent movement of the dots were used while a particular neuron was being recorded; either the direction that produced the maximum response in that neuron, or the opposite direction. The monkey's task was to discriminate between these two directions. The filled circles and solid curve in figure 3.2A show the proportion of correct responses in a typical experiment. Below 1% coherence, the responses were near chance (fraction

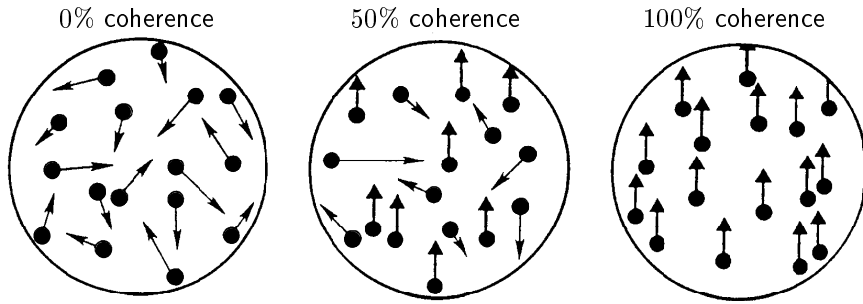


Figure 3.1: The moving random-dot stimulus for different levels of coherence. The visual image consists of randomly placed dots that jump every 45 ms according to the scheme described in the text. At 0% coherence the dots move randomly. At 50% coherence, half the dots move randomly and half move together (upwards in this example). At 100% coherence all the dots move together. (Adapted from Britten et al., 1992.)

correct = 0.5), but the monkey approached perfect performance (fraction correct = 1) above 10% coherence.

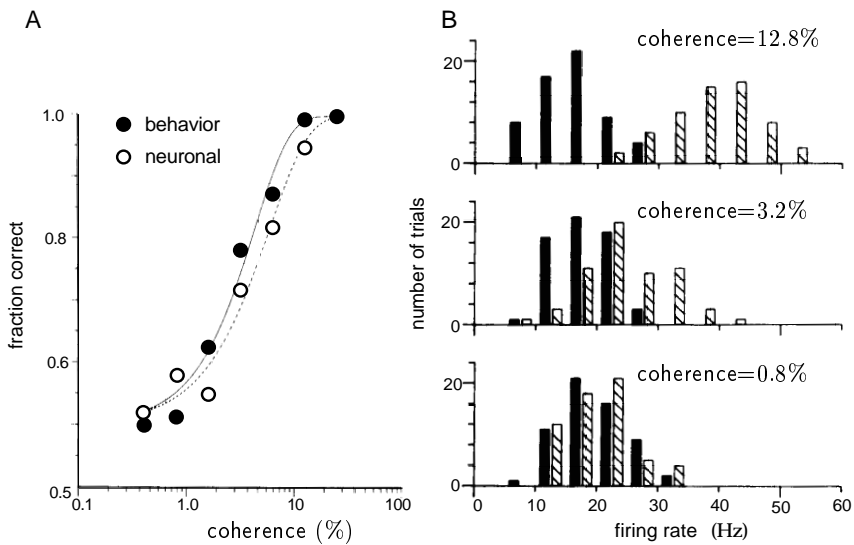


Figure 3.2: Behavioral and electrophysiological results from a random dot motion discrimination task. A) The filled circles show the fraction of correct discriminations made by the monkey as a function of the degree of coherence of the motion. The open circles show the discrimination accuracy that an ideal observer could achieve on the analogous two-alternative forced choice discrimination task given the neural responses. B) Firing rate histograms for three different levels of coherence. Hatched rectangles show the results for motion in the plus direction and solid rectangles for motion in the minus direction. The histograms have been thinned for clarity so that not all the bins are shown. (Adapted from Britten et al., 1992.)

Figure 3.2B shows histograms of average firing rates in response to different levels of movement coherence. The firing rates plotted are the number of spikes recorded during the 2 s period that the stimulus was presented, divided by 2 s. The neuron shown tended to fire more spikes when the motion was in its preferred direction, which we will call the plus (or '+') direction (hatched histogram), than in the other, minus (or '-') direction (solid histogram). At high coherence levels, the firing-rate distributions corresponding to the two directions are fairly well separated, while at low coherence levels, they merge. Although spike count rates only take discrete values, it is more convenient to treat r as a continuous variable for our discussion. Treated as probability densities, these two distributions are approximately Gaussian with the same variance, σ_r^2 , but different means, $\langle r \rangle_+$ for the plus direction and $\langle r \rangle_-$ for the minus direction. A convenient measure of the separation between the distributions is the discriminability

$$d' = \frac{\langle r \rangle_+ - \langle r \rangle_-}{\sigma_r} \quad (3.4)$$

which is the distance between the means in units of their common standard deviation. The larger d' , the more separated the distributions.

In the example we are considering, decoding involves using the neural response to determine in which of the two possible directions the stimulus moved. A simple decoding procedure is to determine the firing rate r during a trial and compare it to a threshold number z . If $r \geq z$, we report plus; otherwise we report minus. Figure 3.2B suggests that if we choose z to lie somewhere between the two distributions, this procedure will give the correct answer at high coherence, but will have difficulty distinguishing the two directions for low coherence. This difficulty is clearly related to the degree to which the two distributions in figure 3.2B overlap, and thus to the discriminability.

The probability that the procedure outlined in the previous paragraph will generate the correct answer (called a hit) when the stimulus is moving in the plus direction is the conditional probability that $r \geq z$ given a plus stimulus, $P[r \geq z|+]$. The probability that it will give the answer plus when the stimulus is actually moving in the minus direction (called a false alarm) is similarly $P[r \geq z|-]$. These two probabilities completely determine the performance of the decoding procedure because the probabilities for the other two cases, i.e. reporting minus when the correct answer is plus, and reporting minus when the correct answer is minus, are $1 - P[r \geq z|+]$ and $1 - P[r \geq z|-]$ respectively. In signal detection theory, the quantity used to perform the discrimination, r in our case, is called the test, and the two probabilities corresponding to reporting a plus answer have specific names:

$$\begin{aligned} \alpha(z) &= P[r \geq z|-] \text{ is the size or false alarm rate of the test, and} \\ \beta(z) &= P[r \geq z|+] \text{ is the power or hit rate of the test.} \end{aligned} \quad (3.5)$$

discriminability d'

*test size and power
or false alarm and
hit rate*

The following table shows how the probabilities of the test giving correct and incorrect answers in the different cases depend on α and β .

stimulus	probability	
	correct	incorrect
+	β	$1 - \beta$
-	$1 - \alpha$	α

The performance of the decoding procedure we have been discussing depends critically on the value of the threshold z to which the rate r is compared. Obviously, we would like to use a threshold for which the size is near 0 and the power near 1. In general, it is impossible to choose the threshold so that both the size and power of the test are optimized; a compromise must be made. A logical optimization criterion is to maximize the probability of getting a correct answer, which is equal to $(\beta(z) + 1 - \alpha(z))/2$ if the plus and minus stimuli occur with equal probability. While this is a possible approach for the experiment we are studying, the analysis we present introduces a powerful technique that makes better use of the full range of recorded data and can be generalized to tasks where the optimal strategy is unknown. This approach makes use of ROC curves, which indicate how the size and power of a test trade off as the threshold is varied.

ROC Curves

receiver operating characteristic, ROC

The receiver operating characteristic (ROC) curve provides a way of evaluating how test performance depends on the choice of the threshold z . Each point on an ROC curve corresponds to a different value of z . The x coordinate of the point is α , the size of the test for this value of z , and the y coordinate is β , its power. As the threshold is varied continuously, these points trace out the ROC plot. If $z=0$, the firing rate will always be greater than or equal to z , so the decoding procedure will always give the answer plus. Thus, for $z=0$, $\alpha=\beta=1$, producing a point at the upper-right corner of the ROC plot. At the other extreme, if z is very large, r will always be less than z , the test will always report minus, and $\alpha=\beta=0$. This produces a point at the bottom-left corner of the plot. Between these extremes, a curve is traced out as a function of z .

Figure 3.3 shows ROC curves computed by Britten et al. for several different values of the stimulus coherence. At high coherence levels, when the task is easy, the ROC curve rises rapidly from $\alpha(z)=0$, $\beta(z)=0$ as the threshold is lowered from a very high value, and the probability $\beta(z)$ of a correct plus answer quickly approaches 1 without a concomitant increase in $\alpha(z)$. As the threshold is lowered further, the probability of giving the answer ‘plus’ when the correct answer is ‘minus’ also rises, and $\alpha(z)$ increases. When the task is difficult, the curve rises more slowly as z is lowered; and if the task is impossible, in that the test merely gives random

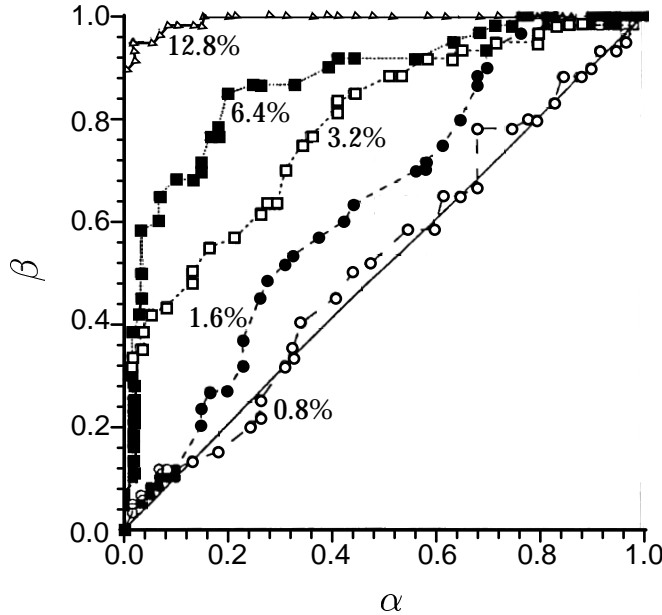


Figure 3.3: ROC curves for a variety of motion coherence levels. Each curve is the locus of points $(\alpha(z), \beta(z))$ for all z values. The values of α and β were computed from histograms such as those in figure 3.2B. The diagonal line is the ROC curve for random guessing. (Adapted from Britten et al., 1992.)

answers, the curve will lie along the diagonal $\alpha = \beta$, because the probabilities of answers being correct and incorrect are equal. This is exactly the trend of the ROC curves at different coherence levels shown in figure 3.3.

Examination of figure 3.3 suggests a relationship between the area under the ROC curve and the level of performance on the task. When the ROC curve in figure 3.3 lies along the diagonal, the area underneath it is $1/2$, which is the probability of a correct answer in this case (given any threshold). When the task is easy and the ROC curve hugs the left axis and upper limit in figure 3.3, and the area under it approaches one, which is again the probability of a correct answer (given an appropriate threshold). However, the precise relationship between task performance and the area under the ROC curve is complicated by the fact that different threshold values can be used. This ambiguity can be removed by considering a slightly different task, called two-alternative forced choice. Here, the stimulus is presented twice, once with motion in the plus direction and once in the minus direction. The task is to decide which presentation corresponded to the plus direction given the firing rates on both trials, r_1 and r_2 . A natural extension of the test procedure we have been discussing is to answer trial 1 if $r_1 \geq r_2$ and otherwise answer trial 2. This removes the threshold variable from consideration.

In the two-alternative forced choice task, the value of r on one trial serves

*two-alternative
forced choice test*

as the threshold for the other trial. For example, if the order of stimulus presentation is plus then minus, the comparison procedure we have outlined will report the correct answer if $r_1 \geq z$ where $z = r_2$, and this has probability $P[r_1 \geq z|+] = \beta(z)$ with $z = r_2$. To determine the probability of getting the correct answer in a two-alternative forced choice task, we need to integrate this probability over all possible values of r_2 weighted by their probability of occurrence. For small Δz , the probability that r_2 takes a value in the range between z and $z + \Delta z$ when the second trial has a minus stimulus is $p[z| -] \Delta z$, where $p[z| -]$ is the conditional firing rate probability density for a firing rate $r = z$. Integrating over all values of z gives the probability of getting the correct answer,

$$P[\text{correct}] = \int_0^\infty dz p[z| -] \beta(z). \quad (3.6)$$

Because the two-alternative forced choice test is symmetric, this is also the probability of being correct if the order of the stimuli is reversed.

The probability that $r \geq z$ for a minus stimulus, which is just $\alpha(z)$, can be written as an integral of the conditional firing-rate probability density $p[r| -]$,

$$\alpha(z) = \int_z^\infty dr p[r| -]. \quad (3.7)$$

Taking the derivative of this equation with respect to z we find that

$$\frac{d\alpha}{dz} = -p[z| -]. \quad (3.8)$$

This allows us to make the replacement $dz p[z| -] \rightarrow -d\alpha$ in the integral of equation 3.6 and to change the integration variable from z to α . Noting that $\alpha = 1$ when $z = 0$ and $\alpha = 0$ when $z = \infty$, we find

$$P[\text{correct}] = \int_0^1 d\alpha \beta. \quad (3.9)$$

The ROC curve is just β plotted as a function of α , so this integral is exactly the area under the ROC curve. Thus, the area under the ROC curve is exactly the probability of error in the two-alternative forced choice test.

Suppose that $p[r| +]$ and $p[r| -]$ are both Gaussian functions with means $\langle r \rangle_+$ and $\langle r \rangle_-$, and a common variance σ_r^2 . The reader is invited to show that, in this case,

$$P[\text{correct}] = \frac{1}{2} \operatorname{erfc} \left(\frac{\langle r \rangle_- - \langle r \rangle_+}{2\sigma_r} \right) = \frac{1}{2} \operatorname{erfc} \left(-\frac{d'}{2} \right) \quad (3.10)$$

*complementary
error function*

where d' is the discriminability defined in equation 3.4 and $\operatorname{erfc}(x)$ is the complementary error function (whose values are closely related to the area under the tail of a Gaussian distribution) defined as

$$\operatorname{erfc}(x) = \frac{2}{\sqrt{\pi}} \int_x^\infty dy \exp(-y^2). \quad (3.11)$$

In the case that the distributions are equal-variance Gaussians, the relationship between the discriminability and the area under the ROC curve is invertible because the complementary error function is monotonic. It is common to quote d' values even for non-Gaussian distributions by inverting the relationship between $P[\text{correct}]$ and d' in equation 3.10.

ROC Analysis of Motion Discrimination

To interpret their experiment as a two-alternative forced choice task, Britten et al. imagined that, in addition to being given the firing rate of the recorded neuron during stimulus presentation, the observer is given the firing rate of a hypothetical ‘anti-neuron’ having exactly the opposite response characteristics from the recorded neuron. In reality, the responses of this anti-neuron to a plus stimulus were just those of the recorded neuron to a minus stimulus, and vice versa. The idea of using the responses of a single neuron to opposite stimuli as if they were the simultaneous responses of two different neurons reappears again in our discussion of spike train decoding. An observer predicting motion directions on the basis of just these two neurons at a level equal to the area under the ROC curve is termed an ideal observer.

Figure 3.2A shows a typical result for the performance of an ideal observer using one recorded neuron and its anti-neuron partner. The open circles in figure 3.2A were obtained by calculating the areas under the ROC curves for this neuron. Amazingly, the ability of the ideal observer to perform the discrimination task using a single neuron/anti-neuron pair is equal to the ability of the monkey to do the task. Although the choices of the ideal observer and the monkey do not necessarily match on a trial-to-trial basis, their performances are comparable when averaged over trials. This seems remarkable because the monkey presumably has access to a large population of neurons, while the ideal observer uses only two. One speculation is that correlations in the response variability between neurons limit the performance of the monkey.

The Likelihood Ratio Test

The discrimination test we have considered compares the firing rate to a threshold value. Could an observer do better than this already remarkable performance by comparing some other function of the firing rate to a threshold? What is the best test function to use for this purpose? The Neyman-Pearson lemma (proven in appendix A) shows that it is impossible to do better than to chose the test function to be the ratio of probability densities (or, where appropriate, probabilities),

$$l(r) = \frac{p[r|+]}{p[r|-]}, \quad (3.12)$$

*Neyman-Pearson
lemma*

likelihood ratio

which is known as the likelihood ratio. The test function r used above is not equal to the likelihood ratio. However, if the likelihood is a monotonically increasing function of r , as it is for the data of Britten et al., the firing-rate threshold test is equivalent to using the likelihood ratio and is indeed optimal. Similarly, any monotonic function of the likelihood ratio will provide as good a test as the likelihood itself, and the logarithm is frequently used.

There is a direct relationship between the likelihood ratio and the ROC curve. As in equations 3.7 and 3.8, we can write

$$\beta(z) = \int_z^\infty dr p[r|+] \frac{d\beta}{dz} = -p[z|+]. \quad (3.13)$$

Combining this result with 3.8, we find that

$$\frac{d\beta}{d\alpha} = \frac{d\beta}{dz} \frac{dz}{d\alpha} = \frac{p[z|+]}{p[z|-]} = l(z), \quad (3.14)$$

so the slope of the ROC curve is equal to the likelihood ratio.

Another way of seeing that comparing the likelihood ratio to a threshold value is an optimal decoding procedure for discrimination uses a Bayesian approach based on associating a cost or penalty with getting the wrong answer. Suppose that the penalty associated with answering minus when the correct answer is plus is quantified by the loss parameter L_- . Similarly, quantify the loss for answering plus when the correct answer is minus as L_+ . For convenience, we assume that there is neither loss nor gain for answering correctly. The probabilities that the correct answer is plus or minus given the firing rate r are $P[+|r]$ and $P[-|r]$ respectively. These probabilities are related to the conditional firing-rate probability densities by Bayes Theorem,

$$P[+|r] = \frac{p[r|+]P[+]}{p[r]} \quad \text{and} \quad P[-|r] = \frac{p[r|-]P[-]}{p[r]}. \quad (3.15)$$

The average loss expected for a plus answer when the firing rate is r is the loss associated with being wrong times the probability of being wrong, $\text{Loss}_+ = L_+ P[-|r]$. Similarly the expected loss when answering minus is $\text{Loss}_- = L_- P[+|r]$. A reasonable strategy is to ‘cut the losses’, answering plus if $\text{Loss}_+ \leq \text{Loss}_-$ and minus otherwise. Using equation 3.15, we find that this strategy gives the response plus if

$$l(r) = \frac{p[r|+]}{p[r|-]} \geq \frac{L_+}{L_-} \frac{P[-]}{P[+]}. \quad (3.16)$$

This shows that the strategy of comparing the likelihood ratio to a threshold is a way of minimizing the expected loss. The right hand side of this inequality gives an explicit formula for the value of the threshold that should be used, and reflects two factors. One is the relative losses for the two sorts of possible errors. The other is the prior probabilities that the stimulus is

plus or minus. Interestingly, it is possible to change the thresholds that human subjects use in discrimination tasks by manipulating these two factors.

If the conditional probability densities $p[r|+]$ and $p[r|-]$ are Gaussians with means r_+ and r_- and identical variances σ_r^2 , and $P[+] = P[-] = 1/2$, the probability $P[+|r]$ is a sigmoidal function of r

$$P[+|r] = \frac{1}{1 + \exp(-d'(r - r_{\text{ave}})/\sigma_r)} \quad (3.17)$$

where $r_{\text{ave}} = (r_+ + r_-)/2$. This provides an alternate interpretation of the parameter d' that is often used in the psychophysics literature; it determines the slope of a sigmoidal fit to $P[+|r]$.

We have so far considered discriminating between two quite distinct stimulus values, plus and minus. Often we are interested in discriminating between two stimulus values $s + \Delta s$ and s that are very close to each other. In this case, the likelihood ratio is

$$\begin{aligned} \frac{p[r|s + \Delta s]}{p[r|s]} &\approx \frac{p[r|s] + \Delta s \partial p[r|s]/\partial s}{p[r|s]} \\ &= 1 + \Delta s \frac{\partial \ln p[r|s]}{\partial s}. \end{aligned}$$

For small Δs , a test that compares

$$Z(r) = \frac{\partial \ln p[r|s]}{\partial s} \quad (3.18)$$

to a threshold $(z - 1)/\Delta s$ is equivalent to the likelihood ratio test. The function $Z(r)$ is sometimes called the score.

score $Z(r)$

3.3 Population Decoding

The use of large numbers of neurons to perform tasks is one of the basic operating principles of most nervous systems. Population coding has a number of advantages, including reduction of uncertainty due to neuronal variability and the ability to represent a number of different stimulus attributes simultaneously. Individual neurons in such a population typically have different but overlapping selectivities so that many neurons, but not necessarily all, respond to a given stimulus. In the previous section, we discussed discrimination between stimuli on the basis of the response of a single neuron. The responses of a population of neurons can also be used for discrimination, with the only essential difference being that terms such as $p[r|s]$ are replaced by $p[\mathbf{r}|s]$, the conditional probability density of the population response \mathbf{r} . ROC analysis, likelihood ratio tests, and the

Neyman-Pearson lemma continue to apply in exactly the same way. Discrimination is a special case of decoding in which only few different stimulus values are considered. A more general problem is the extraction of a continuous stimulus parameter from one or more neuronal responses. In this section, we study how the value of a continuous parameter associated with a static stimulus can be decoded from the spike-count firing rates of a population of neurons.

Encoding and Decoding Direction

The cercal system of the cricket, used to report the direction of incoming air currents as a warning of approaching predators, is an interesting example of population coding involving a relatively small number of neurons. Crickets and other related insects have two appendages called cerci extending from their hind ends. These are covered with hairs that are deflected by air currents. Each hair is attached to a neuron that fires when the hair is deflected. Thousands of these primary sensory neurons send axons to a set of interneurons that relay the sensory information to the rest of the cricket's nervous system. No single interneuron of the cercal system responds to all wind directions, and multiple interneurons respond to any given wind direction. This implies that the interneurons encode the wind direction collectively as a population.

Theunissen and Miller (1991) measured both the mean and the variance of responses of cercal interneurons while blowing air currents at the cerci. At low wind velocities, information about wind direction is encoded by just four interneurons. Figure 3.4 shows average firing rate tuning curves for the four relevant interneurons as a function of wind direction. These neurons are sensitive primarily to the angle of the wind around the ver-

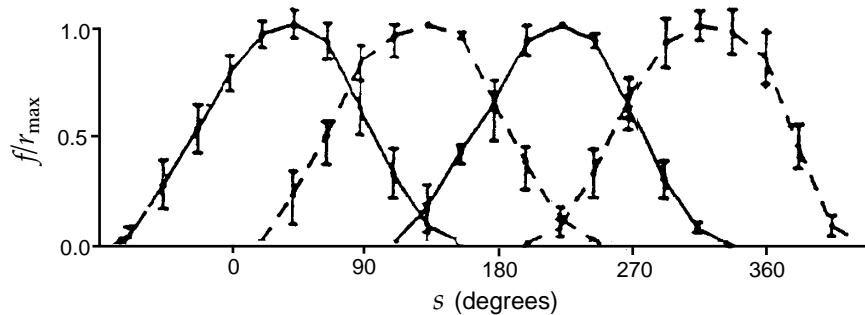


Figure 3.4: Tuning curves for the four low-velocity interneurons of the cricket cercal system plotted as a function of the wind direction s . Each neuron responds with a firing rate that closely approximated by a half-wave rectified cosine function. The preferred directions of the neurons are located 90° from each other, and r_{\max} values are typically around 40 Hz. Error bars show standard deviations. (Adapted from Theunissen and Miller, 1991.)

tical axis and not to its elevation above the horizontal plane. Wind speed was held constant in these experiments so we do not discuss how it is encoded. The interneuron tuning curves are well approximated by half-wave rectified cosine functions. Neuron a (where $a = 1, 2, 3, 4$) responds with a maximum average firing rate when the angle of the wind direction is s_a , the preferred direction angle for that neuron. The tuning curve for interneuron a in response to wind direction s , $\langle r_a \rangle = f_a(s)$, normalized to its maximum, can be written as

cosine tuning

$$\left(\frac{f(s)}{r_{\max}} \right)_a = [(\cos(s - s_a))]_+ \quad (3.19)$$

where the half-wave rectification eliminates negative firing rates. Here r_{\max} , which may be different for each neuron, is a constant equal to the maximum average firing rate. The fit can be improved somewhat by introducing a small offset rate, but the simple cosine is adequate for our purposes.

To determine the wind direction from the firing rates of the cercal interneurons it is useful to change the notation somewhat. In place of the angle s , we can represent wind direction by a spatial vector \vec{v} pointing parallel to the wind velocity and having unit length, $|\vec{v}|=1$ (we use over-arrows to denote spatial vectors). Similarly, we can represent the preferred wind direction for each interneuron by a vector \vec{c}_a of unit length pointing in the direction specified by the angle s_a . In this case, we can use the vector dot product to write $\vec{v} \cdot \vec{c}_a = \cos(s - s_a)$. In terms of these vectors, the average firing rate is proportional to a half-wave rectified projection of the wind direction vector onto the preferred direction axis of the neuron,

dot product

$$\left(\frac{f(s)}{r_{\max}} \right)_a = [\vec{v} \cdot \vec{c}_a]_+ . \quad (3.20)$$

Decoding the cercal system is particularly easy because of the close relationship between the representation of wind direction it provides and a two-dimensional Cartesian coordinate system. In a Cartesian system, vectors are parameterized by their projections onto x and y axes, v_x and v_y . These projections can be written as dot products of the vector being represented, \vec{v} , with vectors of unit length \vec{x} and \vec{y} lying along the x and y axes, $v_x = \vec{v} \cdot \vec{x}$ and $v_y = \vec{v} \cdot \vec{y}$. Except for the half-wave rectification, these equations are identical to 3.20. Furthermore, the preferred directions of the four interneurons, like the x and y axes of a Cartesian coordinate system, lie along two perpendicular directions (figure 3.5A). Four neurons are required, rather than two, because firing rates cannot represent negative projections. The cricket discovered the Cartesian coordinate system long before Descartes, but failed to invent negative numbers! Perhaps credit should also be given to the leech, for Lewis and Kristan (1998) have shown that the direction of touch sensation in its body segments is encoded by four neurons in a virtually identical arrangement.

A vector \vec{v} can be reconstructed from its Cartesian components through the component-weighted vector sum $\vec{v} = v_x \vec{x} + v_y \vec{y}$. Because the firing rates of

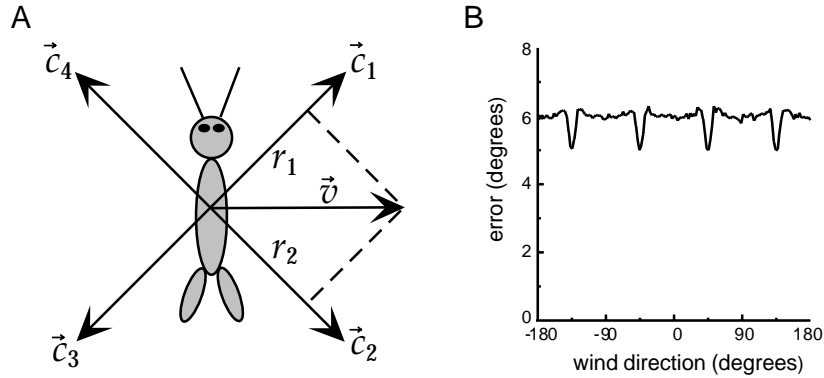


Figure 3.5: A) Preferred directions of four cercal interneurons in relation to the cricket's body. The firing rate of each neuron for a fixed wind speed is proportional to the projection of the wind velocity vector \vec{v} onto the preferred direction axis of the neuron. The projection directions \vec{c}_1 , \vec{c}_2 , \vec{c}_3 and \vec{c}_4 for the four neurons are separated by 90° , and they collectively form a Cartesian coordinate system. B) The root-mean-square error in the wind direction determined by vector decoding of the firing rates of four cercal interneurons. These results were obtained through simulation by randomly generating interneuron responses to a variety of wind directions, with the average values and trial-to-trial variability of the firing rates matched to the experimental data. The generated rates were then decoded using equation 3.21 and compared to the wind direction used to generate them. (B adapted from Salinas and Abbott, 1994.)

the cercal interneurons we have been discussing are proportional to the Cartesian components of the wind direction vector, a similar sum should allow us to reconstruct the wind direction from a knowledge of the interneuron firing rates, except that four, not two, terms must be included. If r_a is the spike-count firing rate of neuron a , an estimate of the wind direction on any given trial can be obtained from the direction of the vector

$$\vec{v}_{\text{pop}} = \sum_{a=1}^4 \left(\frac{r}{r_{\max}} \right)_a \vec{c}_a. \quad (3.21)$$

population vector

vector method

This vector is known as the population vector, and the associated decoding method is called the vector method. This decoding scheme works quite well. Figure 3.5B shows the root-mean-square difference between the direction determined by equation 3.21 and the actual wind direction that evoked the firing rates. The difference between the decoded and actual wind directions is around 6° except for dips at the angles corresponding to the preferred directions of the neurons. These dips are not due to the fact that one of the neurons responds maximally, but rather arise because the two neurons with tuning curves adjacent to the maximally responding neuron are most sensitive to wind direction at these points.

As discussed in chapter 1, tuning curves of certain neurons in the primary motor cortex (M1) of the monkey can be described by cosine functions of

arm movement direction. Thus, a vector decomposition similar to that of the cercal system appears to take place in M1. Many M1 neurons have nonzero offset rates so they can represent the cosine function over most or all of its range. When an arm movement is made in the direction represented by a vector of unit length, \vec{v} , the average firing rates for such an M1 neuron, labeled by an index a , (assuming that it fires over the entire range of angles) can be written as

$$\left(\frac{\langle r \rangle - r_0}{r_{\max}} \right)_a = \left(\frac{f(s) - r_0}{r_{\max}} \right)_a = \vec{v} \cdot \vec{c}_a \quad (3.22)$$

where \vec{c}_a is the preferred direction vector that defines the selectivity of this neuron. Because these firing rates represent the full cosine function, it would, in principle, be possible to encode all movement directions in three dimensions using just three neurons. Instead, many thousands of M1 neurons have arm-movement related tuning curves resulting in a highly redundant representation. Of course, these neurons encode additional movement-related quantities, for example, their firing rates depend on the initial position of the arm relative to the body as well as on movement velocity and acceleration. This complicates the interpretation of their activity as reporting movement direction in a particular coordinate system.

Unlike the cercal interneuron, M1 neurons do not have orthogonal preferred directions that form a Cartesian coordinate system. Instead, the preferred directions of the neurons appear to point in all directions with roughly equal probability. If the projection axes are not orthogonal, the Cartesian sum of equation 3.21 is not the correct way to reconstruct \vec{v} . Nevertheless, if the preferred directions point uniformly in all directions and the number of neurons N is sufficiently large, the population vector

$$\vec{v}_{\text{pop}} = \sum_{a=1}^N \left(\frac{r - r_0}{r_{\max}} \right)_a \vec{c}_a \quad (3.23)$$

will, on average, point in a direction parallel to the arm movement direction vector \vec{v} . If we average equation 3.23 over trials and use equation 3.22, we find

$$\langle \vec{v}_{\text{pop}} \rangle = \sum_{a=1}^N (\vec{v} \cdot \vec{c}_a) \vec{c}_a. \quad (3.24)$$

We leave as an exercise the proof that $\langle \vec{v}_{\text{pop}} \rangle$ is approximately parallel to \vec{v} if a large enough number of neurons is included in the sum, and if their preferred direction vectors point randomly in all directions with equal probability. Later in this chapter, we discuss how corrections can be made if the distribution of preferred directions is not uniform or the number of neurons is not large. The population vectors constructed from equation 3.23 on the basis of responses of neurons in primary motor cortex recorded while a monkey performed a reaching task are compared with the actual directions of arm movements in figure 3.6.

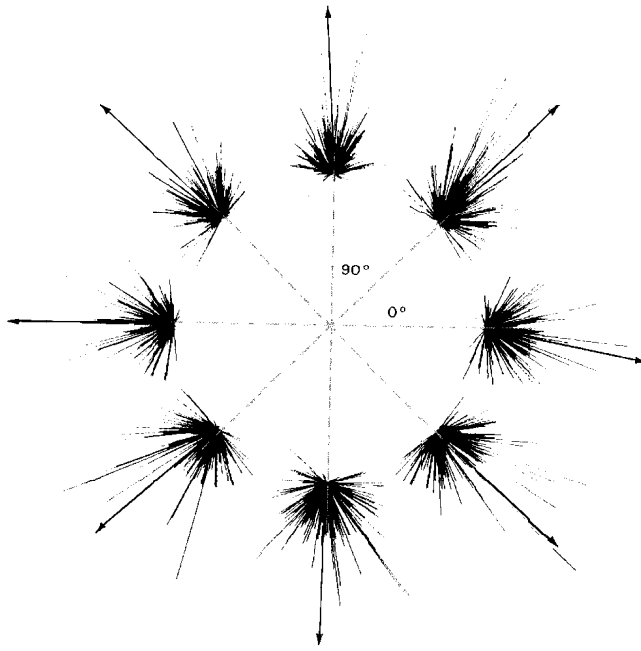


Figure 3.6: Comparison of population vectors with actual arm movement directions. Results are shown for eight different movement directions. Actual arm movement directions are radially outward at angles that are multiples of 45° . The groups of lines without arrows show the preferred direction vectors of the recorded neurons multiplied by their firing rates. Vector sums of these terms for each movement direction are indicated by the arrows. The fact that the arrows point approximately radially outward shows that the population vector reconstructs the actual movement direction fairly accurately. (Figure adapted from Kandel et al., 1991 based on data from Kalaska et al., 1983.)

Optimal Decoding Methods

The vector method is a simple decoding method that can perform quite well in certain cases, but it is neither a general nor an optimal way to reconstruct a stimulus from the firing rates of a population of neurons. In this section, we discuss two methods that can, by some measure, be considered optimal. These are called Bayesian and maximum *a posteriori* or MAP inference. We also discuss a special case of MAP called maximum likelihood or ML inference. The Bayesian approach involves finding the minimum of a loss function that expresses the cost of estimation errors. MAP and ML inference generally produce estimates that are as accurate, in terms of the variance of the estimate, as any that can be achieved by a wide class of estimation methods (so-called unbiased estimates), at least when large numbers of neurons are used in the decoding. Bayesian and MAP estimates use the conditional probability that a stimulus parameter takes a value between s and $s + \Delta s$ given that the set of N encoding neurons

fired at rates given by \mathbf{r} . The probability density needed for a continuous stimulus parameter, $p[s|\mathbf{r}]$, can be obtained from the encoding probability density $p[\mathbf{r}|s]$ by the continuous version of Bayes theorem (equation 3.3),

$$p[s|\mathbf{r}] = \frac{p[\mathbf{r}|s]p[s]}{p[\mathbf{r}]} . \quad (3.25)$$

A disadvantage of these methods is that extracting $p[s|\mathbf{r}]$ from experimental data can be difficult. In contrast, the vector method only requires us to know the preferred stimulus values of the encoding neurons,

As mentioned in the previous paragraph, Bayesian inference is based on the minimization of a particular loss function $L(s, s_{\text{bayes}})$ that quantifies the ‘cost’ of reporting the estimate s_{bayes} when the correct answer is s . The loss function provides a way of defining the optimality criterion for decoding analogous to the loss computation discussed previously for optimal discrimination. The value of s_{bayes} is chosen to minimize the expected loss averaged over all stimuli for a given set of rates, i.e. to minimize the function $\int ds L(s, s_{\text{bayes}})p[s|\mathbf{r}]$. If the loss function is the squared difference between the estimate and the true value, $L(s, s_{\text{bayes}}) = (s - s_{\text{bayes}})^2$, the estimate that minimizes the expected loss is the mean

$$s_{\text{bayes}} = \int ds p[s|\mathbf{r}]s . \quad (3.26)$$

If the loss function is the absolute value of the difference, $L(s, s_{\text{bayes}}) = |s - s_{\text{bayes}}|$, then s_{bayes} is the median rather than the mean of the distribution $p[s|\mathbf{r}]$.

Maximum *a posteriori* (MAP) inference does not involve a loss function but instead simply chooses the stimulus value, s_{MAP} , that maximizes the conditional probability density of the stimulus, $p[s_{\text{MAP}}|\mathbf{r}]$. The MAP approach is thus to choose as the estimate s_{MAP} the most likely stimulus value for a given set of rates. If the prior or stimulus probability density $p[s]$ is independent of s , $p[s|\mathbf{r}]$ and $p[\mathbf{r}|s]$ have the same dependence on s , because the factor $p[s]/p[\mathbf{r}]$ in equation 3.25 is independent of s . In this case, the MAP algorithm is equivalent to maximizing the likelihood function, i.e. choosing s_{ML} to maximize $p[\mathbf{r}|s_{\text{ML}}]$, which is called maximum likelihood (ML) inference.

Bayesian inference

MAP inference

ML inference

Previously we applied the vector decoding method to the cercal system of the cricket. Figure 3.7 shows the root-mean-square difference between the true and estimated wind directions for the cercal system using ML and Bayesian methods. For the cercal interneurons, the response probability density $p[\mathbf{r}|s]$ is a product of four Gaussians with means and variances given by the data points and error bars in figure 3.4. The Bayesian estimate in figure 3.7 is based on the squared-difference loss function. Both estimates use a constant stimulus probability density $p[s]$, so the ML and MAP estimates are identical. The maximum likelihood estimate is either more or less accurate than the Bayesian estimate, depending on the angle.

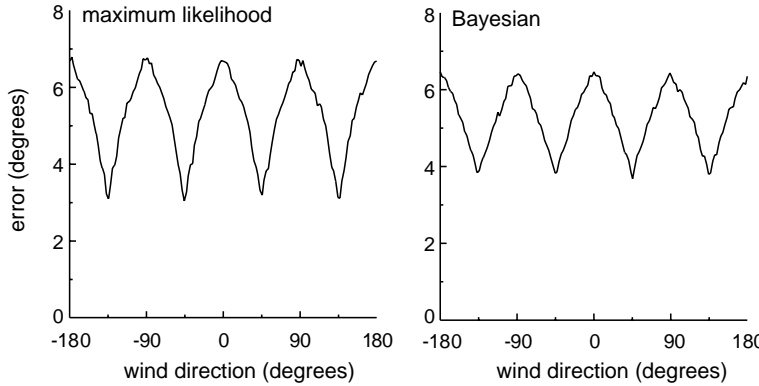


Figure 3.7: Maximum likelihood and Bayesian estimation errors for the cricket cercal system. ML and Bayesian estimates of the wind direction were compared with the actual stimulus value for a large number of simulated firing rates. Firing rates were generated as for figure 3.5B. The error shown is the root-mean-squared difference between the estimated and actual stimulus angles. (Adapted from Salinas and Abbott, 1994.)

The Bayesian result has a slightly smaller average error across all angles. The dips in the error curves in figure 3.7, as in the curve of figure 3.5B, appear at angles where one tuning curve peaks and two others rise from threshold (see figure 3.4). As in figure 3.5B these dips are due to the two neurons responding near threshold, not to the maximally responding neuron. They occur because neurons are most sensitive at points where their tuning curves have maximum slopes which, in this case, is near threshold (see figure 3.11). Comparing these results with figure 3.5B shows the improved performance of these methods relative to the vector method. The vector method performs extremely well for this system, so the degree of improvement is not large. This is because the cercal responses are well described by cosine functions and their preferred directions are 90° apart. Much more dramatic differences occur when the tuning curves are not cosines or the preferred stimulus directions are not perpendicular.

Up to now, we have considered the decoding of a direction angle. We now turn to the more general case of decoding an arbitrary continuous stimulus parameter. An instructive example is provided by an array of N neurons with preferred stimulus values distributed uniformly across the full range of possible stimulus values. An example of such an array for Gaussian tuning curves,

$$f_a(s) = r_{\max} \exp \left(-\frac{1}{2} \left(\frac{s - s_a}{\sigma_a} \right)^2 \right) \quad (3.27)$$

is shown in figure 3.8. In this example, each neuron has a tuning curve with a different preferred value s_a and potentially a different width σ_a (although all the curves in figure 3.8 have the same width). If the tuning curves are evenly and densely distributed across the range of s values, the

sum of all tuning curves $\sum f_a(s)$ is approximately independent of s . The roughly flat line in figure 3.8 is proportional to this sum. The constancy of the sum over tuning curves will be useful in the following analysis.

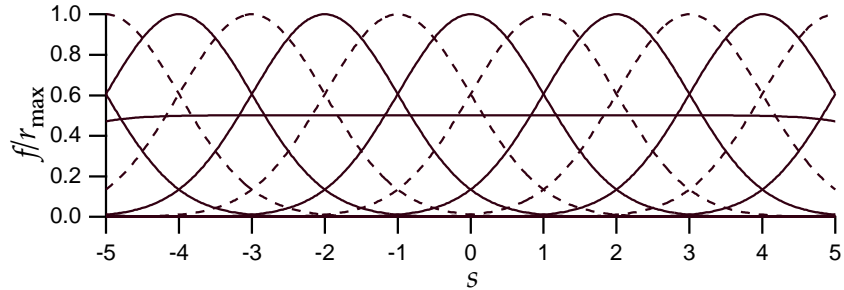


Figure 3.8: An array of Gaussian tuning curves spanning stimulus values from -5 to 5 . The peak values of the tuning curves fall on the integer values of s and the tuning curves all have $\sigma_a = 1$. For clarity, the curves are drawn alternately with dashed and solid lines. The approximately flat curve with value near 0.5 is $1/5$ the sum of the tuning curves shown, indicating that this sum is approximately independent of s .

Tuning curves give the mean firing rates of the neurons across multiple trials. In any single trial, measured firing rates will vary from their mean values. To implement the Bayesian, MAP, or ML approaches, we need to know the conditional firing-rate probability density $p[\mathbf{r}|s]$ that describes this variability. We assume that the firing rate r_a of neuron a is determined by counting n_a spikes over a trial of duration T (so that $r_a = n_a/T$), and that the variability can be described by the homogeneous Poisson model discussed in chapter 1. In this case, the probability of stimulus s evoking $n_a = r_a T$ spikes, when the average firing rate is $\langle r_a \rangle = f_a(s)$ is given by (see chapter 1)

$$P[r_a|s] = \frac{(f_a(s)T)^{r_a T}}{(r_a T)!} \exp(-f_a(s)T). \quad (3.28)$$

If we assume that each neuron fires independently, the firing-rate probability for the population is the product of the individual probabilities,

$$P[\mathbf{r}|s] = \prod_{a=1}^N \frac{(f_a(s)T)^{r_a T}}{(r_a T)!} \exp(-f_a(s)T). \quad (3.29)$$

The assumption of independence simplifies the calculations considerably.

The filled circles in figure 3.9 show a set of randomly generated firing rates for the array of Gaussian tuning curves in figure 3.8 for $s=0$. This figure also illustrates a useful way of visualizing population responses; plotting the responses as a function of the preferred stimulus values. The dashed curve in figure 3.9 is the tuning curve for the neuron with $s_a=0$. Because

the tuning curves are functions of $|s - s_a|$, the values of the dashed curve at $s_a = -5, -4, \dots, 5$ are the mean activities of the cells with preferred values at those locations for a stimulus at $s=0$.

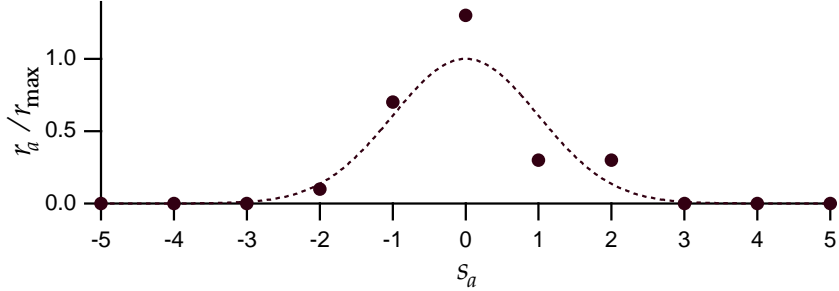


Figure 3.9: Simulated responses of 11 neurons with the Gaussian tuning curves shown in figure 3.8 to a stimulus value of zero. Firing rates for a single trial, generated using the Poisson model, are plotted as a function of the preferred stimulus values of the different neurons in the population (filled circles). The dashed curve shows the tuning curve for the neuron with $s_a = 0$. Its heights at integer values of s_a are the average responses of the corresponding cells. It is possible to have $r_a > r_{\max}$ (point at $s_a = 0$) because r_{\max} is the maximum average firing rate, not the maximum firing rate.

To apply the ML estimation algorithm, we only need to consider the terms in $P[\mathbf{r}|s]$ that depend on s . Because equation 3.29 involves a product, it is convenient to take its logarithm and write

$$\ln P[\mathbf{r}|s] = T \sum_{a=1}^N r_a \ln(f_a(s)) + \dots \quad (3.30)$$

where the ellipsis represents terms that are independent or approximately independent of s , including, as discussed above, $\sum f_a(s)$. Because maximizing a function and maximizing its logarithm are equivalent, we can use the logarithm of the conditional probability in place of the actual probability in ML decoding.

The ML estimated stimulus, s_{ML} , is the stimulus that maximizes the right-hand side of equation 3.30. Setting the derivative to zero, we find that s_{ML} is determined by

$$\sum_{a=1}^N r_a \frac{f'_a(s_{\text{ML}})}{f_a(s_{\text{ML}})} = 0 \quad (3.31)$$

where the prime denotes a derivative. If the tuning curves are the Gaussians of equation 3.27, this equation can be solved explicitly using the result $f'_a(s)/f_a(s) = (s_a - s)/\sigma_a^2$,

$$s_{\text{ML}} = \frac{\sum r_a s_a / \sigma_a^2}{\sum r_a / \sigma_a^2}. \quad (3.32)$$

If all the tuning curves have the same width, this reduces to

$$s_{\text{ML}} = \frac{\sum r_a s_a}{\sum r_a}, \quad (3.33)$$

which is a simple estimation formula with an intuitive interpretation as the firing-rate weighted average of the preferred values of the encoding neurons. The numerator of this expression is reminiscent of the population vector.

Although equation 3.33 gives the ML estimate for a population of neurons with Poisson variability, it has some undesirable properties as a decoding algorithm. Consider a neuron with a preferred stimulus value s_a that is much greater than the actual stimulus value s . Because $s_a \gg s$, the average firing rate of this neuron is essentially zero. For a Poisson distribution, zero rate implies zero variability. If, however, this neuron fires one or more spikes on a trial due to a non-Poisson source of variability, this will cause a large error in the estimate because of the large weighting factor s_a .

The MAP estimation procedure is similar in spirit to the ML approach, but the MAP estimate, s_{MAP} , may differ from s_{ML} if the probability density $p[s]$ depends on s . The MAP algorithm allows us to include prior knowledge about the distribution of stimulus values into the decoding estimate. As noted above, if the $p[s]$ is constant, the MAP and ML estimates are identical. In addition, if many neurons are observed, or if a small number of neurons is observed over a long trial period, even a non-constant stimulus distribution has little effect and $s_{\text{MAP}} \approx s_{\text{ML}}$.

The MAP estimate is computed from the distribution $p[s|r]$ determined by Bayes theorem. In terms of the logarithms of the probabilities, $\ln p[s|r] = \ln P[r|s] + \ln p[s] - \ln P[r]$. The last term in this expression is independent of s and can be absorbed into the ignored s -independent terms, so we can write

$$\ln p[s|r] = T \sum_{a=1}^N r_a \ln(f_a(s)) + \ln p[s] + \dots \quad (3.34)$$

Maximizing this determines the MAP estimate,

$$T \sum_{a=1}^N \frac{r_a f'_a(s_{\text{MAP}})}{f_a(s_{\text{MAP}})} + \frac{p'[s_{\text{MAP}}]}{p[s_{\text{MAP}}]} = 0. \quad (3.35)$$

If the stimulus or prior distribution is itself Gaussian with mean s_{prior} and variance σ_{prior}^2 , and we use the Gaussian array of tuning curves, equation 3.35 yields

$$s_{\text{MAP}} = \frac{T \sum r_a s_a / \sigma_a^2 + s_{\text{prior}} / \sigma_{\text{prior}}^2}{T \sum r_a / \sigma_a^2 + 1 / \sigma_{\text{prior}}^2}. \quad (3.36)$$

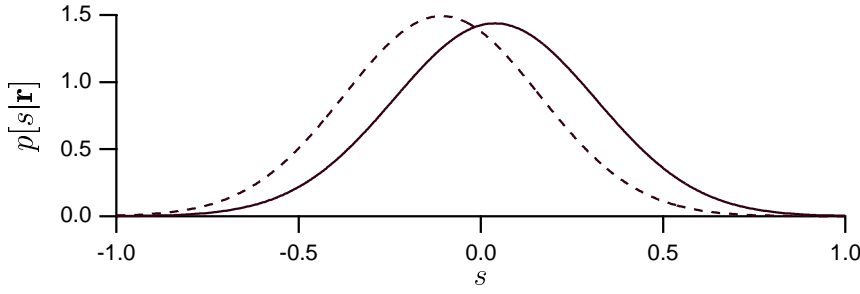


Figure 3.10: Probability densities for the stimulus given the firing rates shown in figure 3.9 and assuming the tuning curves of figure 3.8. The solid curve is $p[s|r]$ when the prior distribution of stimulus values is constant and the true value of the stimulus is $s = 0$. The dashed curve is for a Gaussian prior distribution with a mean of -2 and variance of 1 , again with the true stimulus being $s = 0$. The peak of the solid and dashed curves are at 0.0385 and -0.107 respectively.

Figure 3.10 compares the conditional stimulus probability densities $p[s|r]$ for a constant stimulus distribution (solid curve) and for a Gaussian stimulus distribution with $s_{\text{prior}} = -2$ and $\sigma_{\text{prior}}^2 = 1$, using the firing rates given by the filled circles in figure 3.9. If the stimulus distribution is constant, $p[s|r]$ is peaked near the true stimulus value of zero. The effect of a non-constant stimulus distribution is to shift the curve toward the value -2 where the stimulus probability density has its maximum, and to decrease its width by a small amount. The estimate is shifted to the left because the prior distribution suggests that the stimulus is more likely to take negative values than positive ones, independent of the evoked response. The decreased width is due to the added information that the prior distribution provides. The curves in figure 3.10 can be computed from equations 3.27 and 3.34 as Gaussians with variances $1/(T \sum r_a/\sigma_a^2)$ (constant prior) and $1/(T \sum r_a/\sigma_a^2 + 1/\sigma_{\text{prior}}^2)$ (Gaussian prior).

The accuracy with which an estimate s_{est} describes a stimulus s can be characterized by two important quantities; its bias $b_{\text{est}}(s)$ and its variance $\sigma_{\text{est}}^2(s)$. The bias is the difference between the average of s_{est} across trials that use the stimulus s and the true value of the stimulus, namely s ,

$$b_{\text{est}}(s) = \langle s_{\text{est}} \rangle - s. \quad (3.37)$$

Note that the bias depends on the true value of the stimulus. An estimate is termed unbiased if $b_{\text{est}}(s) = 0$ for all stimulus values.

The variance of the estimator, which quantifies how much the estimate varies about its mean value, is defined as

$$\sigma_{\text{est}}^2(s) = \langle (s_{\text{est}} - \langle s_{\text{est}} \rangle)^2 \rangle. \quad (3.38)$$

The bias and variance together can be used to compute the trial-average squared estimation error, $\langle (s_{\text{est}} - s)^2 \rangle$. This is measure of the spread of

the estimated values about the true value of the stimulus. Because $s = \langle s_{\text{est}} \rangle + b_{\text{est}}(s)$, we can write the squared estimation error as

$$\langle (s_{\text{est}} - s)^2 \rangle = \langle (s_{\text{est}} - \langle s_{\text{est}} \rangle - b_{\text{est}}(s))^2 \rangle = \sigma_{\text{est}}^2(s) + b_{\text{est}}^2(s). \quad (3.39)$$

In other words, the average squared estimation error is the sum of the variance and the square of the bias. For an unbiased estimate, the average squared estimation error is equal to the variance of the estimator.

Fisher Information

Decoding can be used to limit the accuracy with which a neural system encodes the value of a stimulus parameter because the encoding accuracy cannot exceed the accuracy of an optimal decoding method. Of course, we must be sure that the decoding technique used to establish such a bound is truly optimal, or else the result will reflect the limitations of the decoding procedure, not bounds on the neural system being studied. The Fisher information is a quantity that provides one such measure of encoding accuracy. Through a bound known as the Cramér-Rao bound, the Fisher information limits the accuracy with which any decoding scheme can extract an estimate of an encoded quantity.

The Cramér-Rao bound limits the variance of any estimate s_{est} according to (appendix B) *Cramér-Rao bound*

$$\sigma_{\text{est}}^2(s) \geq \frac{(1 + b'_{\text{est}}(s))^2}{I_F(s)} \quad (3.40)$$

where $b'_{\text{est}}(s)$ is the derivative of $b_{\text{est}}(s)$. If we assume here that the firing rates take continuous values and that their distribution in response to a stimulus s is described by the conditional probability density $p[\mathbf{r}|s]$, the quantity $I_F(s)$ is the Fisher information of the firing-rate distribution, which is related to $p[\mathbf{r}|s]$ (assuming the latter is sufficiently smooth) by

$$I_F(s) = \left\langle -\frac{\partial^2 \ln p[\mathbf{r}|s]}{\partial s^2} \right\rangle = \int d\mathbf{r} p[\mathbf{r}|s] \left(-\frac{\partial^2 \ln p[\mathbf{r}|s]}{\partial s^2} \right). \quad (3.41)$$

The reader can verify that the Fisher information can also be written as

$$I_F(s) = \left\langle \left(\frac{\partial \ln p[\mathbf{r}|s]}{\partial s} \right)^2 \right\rangle = \int d\mathbf{r} p[\mathbf{r}|s] \left(\frac{\partial \ln p[\mathbf{r}|s]}{\partial s} \right)^2. \quad (3.42)$$

The Cramér-Rao bound sets a limit on the accuracy of any unbiased estimate of the stimulus. When $b_{\text{est}}(s) = 0$, equation 3.39 indicates that the average squared estimation error is equal to σ_{est}^2 and, by equation 3.40, this satisfies the bound $\sigma_{\text{est}}^2 \geq 1/I_F(s)$. Provided that we restrict ourselves to unbiased decoding schemes, the Fisher information sets an absolute limit

Fisher information

on decoding accuracy, and it thus provides a useful limit on encoding accuracy. Although imposing zero bias on the decoding estimate seems reasonable, the restriction is not trivial. In general, minimizing the decoding error in equation 3.39 involves a trade-off between minimizing the bias and the variance of the estimator. In some cases, biased schemes may produce more accurate results than unbiased ones. For a biased estimator, the average squared estimation error and the variance of the estimate are not equal, and the estimation error can be either larger or smaller than $1/I_F(s)$.

The limit on decoding accuracy set by the Fisher information can be attained by a decoding scheme we have studied, the maximum likelihood method. In the limit of large numbers of encoding neurons ($N \rightarrow \infty$), and for most firing rate distributions, the ML estimate satisfies a number of desirable properties. First, it is asymptotically consistent, in the sense that $P[|s_{ML} - s| > \epsilon] \rightarrow 0$ for any $\epsilon > 0$; it is also unbiased and saturates the Cramér-Rao bound. In other words, the variance of the ML estimate is given asymptotically (for large N) by $\sigma_{ML}^2(s) = 1/I_F(s)$. Any unbiased estimator that saturates the Cramér-Rao lower bound is called efficient. Furthermore, $I_F(s)$ grows linearly with N , and the ML estimate obeys a central limit theorem, so that $N^{1/2}(s_{ML} - s)$ is Gaussian distributed with a variance that is independent of N in the large N limit.

As equation 3.41 shows, the Fisher information is a measure of the expected curvature of the log likelihood at the stimulus value s . Curvature is important because the likelihood is expected to be at a maximum near to the true stimulus value s that caused the responses. If the likelihood is very curved and thus the Fisher information is large, typical responses to the stimulus s are much less likely for other slightly different stimuli. Therefore, the typical response provides a strong indication of the value of the stimulus. If the likelihood is fairly flat and thus the Fisher information is small, typical responses to s are likely to occur for slightly different stimuli as well. Thus, the response does not as clearly determine the stimulus value. The Fisher information is purely local in the sense that it does not reflect the existence of stimulus values completely different from s that are likely to evoke the same responses as those evoked by s itself. However, this does not happen for the sort of simple population codes we consider. Shannon's mutual information measure, discussed in chapter 4, takes such possibilities into account.

The Fisher information for a population of neurons with uniformly arrayed tuning curves (the Gaussian array in figure 3.8, for example) and Poisson statistics can be computed from the conditional firing-rate probability in equation 3.30. Because the spike-count rate is described here by a probability rather than a probability density, we use the discrete analog of equation 3.41,

$$I_F(s) = \left\langle -\frac{d^2 \ln P[\mathbf{r}|s]}{ds^2} \right\rangle = T \sum_{a=1}^N \langle r_a \rangle \left(\left(\frac{f'_a(s)}{f_a(s)} \right)^2 - \frac{f''_a(s)}{f_a(s)} \right). \quad (3.43)$$

If we assume that the array of tuning curves is symmetric, like the Gaus-

asymptotic consistency

efficiency

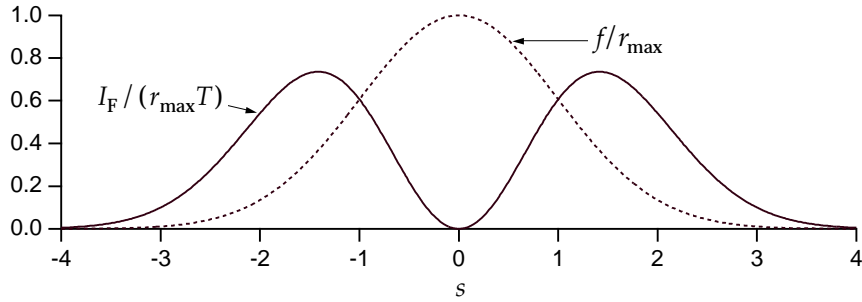


Figure 3.11: The Fisher information for a single neuron with a Gaussian tuning curve with $s=0$ and $\sigma_a=1$, and Poisson variability. The Fisher information (solid curve) has been divided by $r_{\max} T$, the peak firing rate of the tuning curve times the duration of the trial. The dashed curve shows the tuning curve scaled by r_{\max} . Note that the Fisher information is greatest where the slope of the tuning curve is highest, and vanishes at $s=0$ where the tuning curve peaks.

sian array of figure 3.8, the second term in the parentheses of the last expression is zero. We can also make the replacement $\langle r_a \rangle = f_a(s)$, producing the final result

$$I_F(s) = T \sum_{a=1}^N \frac{(f'_a(s))^2}{f_a(s)}. \quad (3.44)$$

In this expression, each neuron contributes an amount to the Fisher information proportional to the square of its tuning curve slope and inversely proportional to the average firing rate for the particular stimulus value being estimated. Highly sloped tuning curves give firing rates that are sensitive to the precise value of the stimulus. Figure 3.11 shows the contribution to the sum in equation 3.44 from a single neuron with a Gaussian tuning curve, the neuron with $s_a=0$ in figure 3.8. For comparison purposes, a dashed curve proportional to the tuning curve is also plotted. Note that the Fisher information vanishes for the stimulus value that produces the maximum average firing rate, because $f'_a(s)=0$ at this point. The firing rate of a neuron at the peak of its tuning curve is relatively unaffected by small changes in the stimulus. Individual neurons carry the most Fisher information in regions of their tuning curves where average firing rates are rapidly varying functions of the stimulus value, not where the firing rate is highest.

The Fisher information can be used to derive an interesting result on the optimal widths of response tuning curves (Zhang and Sejnowski, 1998). Consider a population of neurons with tuning curves of identical shapes, distributed evenly over a range of stimulus values as in figure 3.8. Equation 3.44 indicates that the Fisher information will be largest if the tuning curves of individual neurons are rapidly varying (making the square of their derivatives large), and if many neurons respond (making the sum over neurons large). For typical neuronal response tuning curves, these

two requirements are in conflict with each other. If the population of neurons has narrow tuning curves, individual neural responses are rapidly varying functions of the stimulus, but few neurons respond. Broad tuning curves allow many neurons to respond, but the individual responses are not as sensitive to the stimulus value. To determine whether narrow or broad tuning curves produce the most accurate encodings, we consider a dense distribution of Gaussian tuning curves, all with $\sigma_a = \sigma_r$. Using such curves in equation 3.44, we find

$$I_F(s) = T \sum_{a=1}^N \frac{r_{\max}(s - s_a)^2}{\sigma_r^4} \exp\left(-\frac{1}{2}\left(\frac{s - s_a}{\sigma_r}\right)^2\right). \quad (3.45)$$

This expression can be approximated by replacing the sum over neurons by an integral over their preferred stimulus values and multiplying by a density factor ρ_s . The factor ρ_s is the density with which the neurons cover the range of stimulus values, and it is equal to the number of neurons with preferred stimulus values lying within a unit range of s values. Replacing the sum over a with an integral over a continuous preferred stimulus parameter ξ (which replaces s_a), we find

$$\begin{aligned} I_F(s) &\approx \rho_s T \int_{-\infty}^{\infty} d\xi \frac{r_{\max}(s - \xi)^2}{\sigma_r^4} \exp\left(-\frac{1}{2}\left(\frac{s - \xi}{\sigma_r}\right)^2\right) \\ &= \frac{\sqrt{2\pi} \rho_s \sigma_r r_{\max} T}{\sigma_r^2}. \end{aligned} \quad (3.46)$$

We have expressed the final result in this form because the number of neurons that respond to a given stimulus value is roughly $\rho_s \sigma_r$, and the Fisher information is proportional to this number divided by the square of the tuning curve width. Combining these factors, the Fisher information is inversely proportional to σ_r , and the encoding accuracy increases with narrower tuning curve widths.

The advantage of using narrow tuning curves goes away if the stimulus is characterized by more than one parameter. Consider a stimulus with D parameters and suppose that the response tuning curves are products of identical Gaussians for each of these parameters. If the tuning curves cover the D -dimensional space of stimulus values with a uniform density ρ_s , the number of responding neurons for any stimulus value is proportional to $\rho_s \sigma_r^D$ and, using the same integral approximation as in equation 3.46, the Fisher information is

$$I_F = \frac{(2\pi)^{D/2} D \rho_s \sigma_r^D r_{\max} T}{\sigma_r^2} = (2\pi)^{D/2} D \rho_s \sigma_r^{D-2} r_{\max} T. \quad (3.47)$$

This equation, which reduces to the result given above if $D = 1$, allows us to examine the effect tuning curve width on encoding accuracy. The trade-off between the encoding accuracy of individual neurons and the number of responding neurons depends on the dimension of the stimulus space. Narrowing the tuning curves (making σ_r smaller) increases the Fisher information for $D = 1$, decreases it for $D > 2$, and has no impact if $D = 2$.

Optimal Discrimination

In the first part of this chapter, we considered discrimination between two values of a stimulus. An alternative to the procedures discussed there is simply to decode the responses and discriminate on the basis of the estimated stimulus values. Consider the case of discriminating between s and $s + \Delta s$ for small Δs . For large N , the average value of the difference between the ML estimates for the two stimulus values is equal to Δs (because the estimate is unbiased) and the variance of each estimate (for small Δs) is $1/I_F(s)$. Thus, the discriminability, defined in equation 3.4, for the ML based test is

*ML
discriminability*

$$d' = \Delta s \sqrt{I_F(s)}. \quad (3.48)$$

The larger the Fisher information, the higher the discriminability. We leave as an exercise the proof that for small Δs , this discriminability is the same as that of the likelihood ratio test $Z(\mathbf{r})$ defined in equation 3.18.

Discrimination by ML estimation requires maximizing the likelihood, and this may be computationally challenging. The likelihood ratio test described previously may be simpler, especially for Poisson variability, because, for small Δs , the likelihood ratio test Z defined in equation 3.18 is a linear function of the firing rates,

$$Z = T \sum_{a=1}^N r_a \frac{f'_a(s)}{f_a(s)}. \quad (3.49)$$

Figure 3.12 shows an interesting comparison of the Fisher information for orientation tuning in the primary visual cortex with human orientation discrimination thresholds. Agreement like this can occur for difficult tasks, like discrimination at threshold, where the performance of a subject may be limited by basic constraints on neuronal encoding accuracy.

3.4 Spike Train Decoding

The decoding methods we have considered estimate or discriminate static stimulus values on the basis of spike-count firing rates. Spike-count firing rates do not provide sufficient information for reconstructing a stimulus that varies during the course of a trial. Instead, we can estimate such a stimulus from the sequence of firing times t_i for $i = 1, 2, \dots, n$ of the spikes that it evokes. One method for doing this is similar to the Wiener kernel approach used to estimate the firing rate from the stimulus in chapter 2, and to the approximation of a firing rate using a sliding window function introduced in chapter 1. For simplicity, we restrict our discussion to the decoding of a single neuron. We assume, as we did in chapter 2, that the time average of the stimulus being estimated is zero.

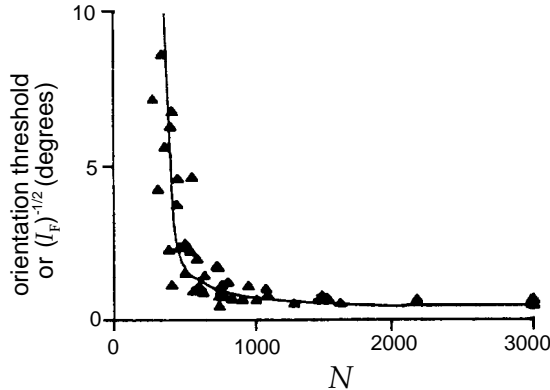


Figure 3.12: Comparison of Fisher information and discrimination thresholds for orientation tuning. The solid curve is the minimum standard deviation of an estimate of orientation angle from the Cramér-Rao bound, plotted as a function of the number of neurons (N) involved in the estimation. The triangles are data points from an experiment that determined the threshold for discrimination of the orientation of line images by human subjects as a function of line length and eccentricity. An effective number of neurons involved in the task was estimated for the different line lengths and eccentricities using the cortical magnification factor discussed in chapter 2. (Adapted from Paradiso, 1988.)

In spike train decoding, we attempt to construct an estimate of the stimulus at time t from the sequence of spikes evoked up to that time. There are paradoxical aspects of this procedure. The firing of an action potential at time t_i is only affected by the stimulus $s(t)$ prior to that time, $t < t_i$, and yet, in spike decoding, we attempt to extract information from this action potential about the value of the stimulus at a later time $t > t_i$. That is, the evoked spikes tell us about the past behavior of the stimulus and, in spike decoding, we attempt to use this information to predict the current stimulus value. Clearly, this requires that the stimulus have some form of temporal correlation so that past behavior provides information about the current stimulus value. To make the decoding task easier, we can introduce a prediction delay, τ_0 , and attempt to construct from spikes occurring prior to time t , an estimate of the stimulus at time $t - \tau_0$ (see figure 3.13A). Such a delayed estimate uses a combination of spikes that could have been fired in response to the stimulus $s(t - \tau_0)$ being estimated (those for which $t - \tau_0 < t_i < t$; spike 7 in figure 3.13A), and spikes that occurred too early to be affected by the value of $s(t - \tau_0)$ (those for which $t_i < t - \tau_0$; spikes 1-6 in figure 3.13A), but that can contribute to its estimation on the basis of stimulus correlations. The estimation task gets easier as τ_0 is increased, but this delays the decoding and makes the result less behaviorally relevant. We will consider decoding with an arbitrary delay and later discuss how to set a specific value for τ_0 .

prediction delay τ_0

stimulus estimate The stimulus estimate is constructed as a linear sum over all spikes. A spike occurring at time t_i contributes a kernel $K(t - t_i)$, and the total esti-

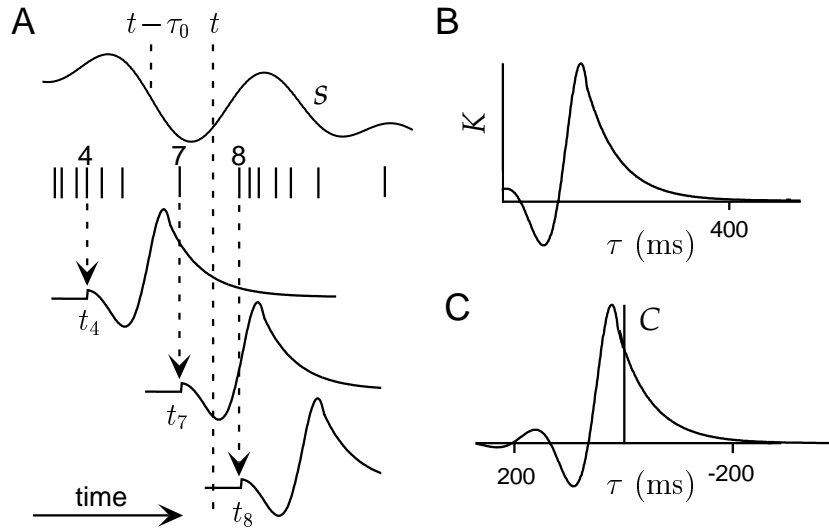


Figure 3.13: Cartoon illustrating spike train decoding. A) The top trace denotes a stimulus that evokes the spike train appearing below it. At time t an estimate is being made of the stimulus at time $t - \tau_0$. The estimate is obtained by summing the values of the kernels where they cross the dashed line labeled t , for spikes up to and including spike 7. Two such kernels are shown in the third and fourth traces from the top. The real estimate is obtained by summing similar contributions from all of the spikes. The kernel is zero for negative values of its argument, so spikes for $i \geq 8$ do not contribute to the estimate at this time. B) The kernel used in A. This has been truncated to zero value for negative values of τ . C) The spike triggered average corresponding to the kernel in B, assuming no spike train correlations. Note that C has been plotted with the τ axis reversed, following the convention established in chapter 1. With this convention, K in panel B is simply a shifted and truncated version of the curve appearing here. In this case $\tau_0 = 160$ ms.

mate is obtained by summing over all spikes,

$$s_{\text{est}}(t - \tau_0) = \sum_{i=1}^n K(t - t_i) - \langle r \rangle \int_{-\infty}^{\infty} d\tau K(\tau). \quad (3.50)$$

The last term, with $\langle r \rangle = \langle n \rangle / T$ the average firing rate over the trial, is included to impose the condition that the time average of s_{est} is zero, in agreement with the time-average condition on s . The sum in equation 3.50 includes all spikes so the constraint that only those spikes occurring prior to the time t (spikes 1-7 in figure 3.13A) should be included must be imposed by requiring $K(t - t_i) = 0$ for $t - t_i \leq 0$. A kernel satisfying this constraint is termed causal. We ignore the causality constraint for now and construct an acausal kernel, but we will return to issues of causality later in the discussion. Figure 3.13A shows how spikes contribute to a stimulus estimate using the kernel shown in figure 3.13B.

Equation 3.50 can be written in a compact way by using the neural re-

sponse function $\rho(t) = \sum \delta(t - t_i)$ introduced in chapter 1,

$$s_{\text{est}}(t - \tau_0) = \int_{-\infty}^{\infty} d\tau (\rho(t - \tau) - \langle r \rangle) K(\tau). \quad (3.51)$$

Using this form of the estimate, the construction of the optimal kernel K proceeds very much like the construction of the optimal kernel for predicting firing rates in chapter 2. We choose K so that the squared difference between the estimated stimulus and the actual stimulus, averaged over both time and trials,

$$\frac{1}{T} \int_0^T dt \left\langle \left(\int_{-\infty}^{\infty} d\tau (\rho(t - \tau) - \langle r \rangle) K(\tau) - s(t - \tau_0) \right)^2 \right\rangle, \quad (3.52)$$

is minimized. The calculation proceeds as in appendix A of chapter 2, and the result is that K obeys the equation

$$\int_{-\infty}^{\infty} d\tau' Q_{\rho\rho}(\tau - \tau') K(\tau') = Q_{rs}(\tau - \tau_0). \quad (3.53)$$

where $Q_{\rho\rho}$ is the spike-train autocorrelation function,

$$Q_{\rho\rho}(\tau - \tau') = \frac{1}{T} \int_0^T dt \langle (\rho(t - \tau) - \langle r \rangle)(\rho(t - \tau') - \langle r \rangle) \rangle, \quad (3.54)$$

as defined in chapter 1, and Q_{rs} is the correlation of the firing rate and the stimulus, which is related to the spike-triggered average C , both introduced in chapter 1,

$$Q_{rs}(\tau - \tau_0) = \langle r \rangle C(\tau_0 - \tau) = \frac{1}{T} \left\langle \sum_{i=1}^n s(t_i + \tau - \tau_0) \right\rangle. \quad (3.55)$$

At this point in the derivation of the optimal linear kernel for firing-rate prediction in chapter 2, we chose the stimulus to be uncorrelated so that an integral equation similar to 3.53 simplified. This could always be done because we have complete control over the stimulus in this type of experiment. However, we do not have similar control of the neuron, and must deal with whatever spike train autocorrelation function it gives us. If the spike train is uncorrelated, which tends to happen at low rates,

$$Q_{\rho\rho}(\tau) = \langle r \rangle \delta(\tau), \quad (3.56)$$

and we find from equation 3.53 that

$$K(\tau) = \frac{1}{\langle r \rangle} Q_{rs}(\tau - \tau_0) = C(\tau_0 - \tau) = \frac{1}{\langle n \rangle} \left\langle \sum_{i=1}^n s(t_i + \tau - \tau_0) \right\rangle. \quad (3.57)$$

This is the average value of the stimulus at time $\tau - \tau_0$ relative to the appearance of a spike. Because $\tau - \tau_0$ can be either positive or negative,

stimulus estimation, unlike firing rate estimation, involves both forward and backward correlation and the average values of the stimulus both before and after a spike. Decoding in this way follows a simple rule; every time a spike appears, we replace it with the average stimulus surrounding a spike, shifted by an amount τ_0 (figure 3.13).

The need for either stimulus correlations or a nonzero prediction delay is clear from equation 3.57. Correlations between a spike and subsequent stimuli can only arise, in a causal system, from correlations between the stimulus and itself. If these are absent, as for white noise, $K(\tau)$ will be zero for $\tau > \tau_0$. For causal decoding, we must also have $K(\tau) = 0$ for $\tau < 0$. Thus, if $\tau_0 = 0$ and the stimulus is uncorrelated, $K(\tau) = 0$ for all values of τ .

When the spike train autocorrelation function is not a δ function, the solution for K can be expressed as an inverse Fourier transform,

$$K(\tau) = \frac{1}{2\pi} \int d\omega \tilde{K}(\omega) \exp(-i\omega\tau) \quad (3.58)$$

where, as shown in appendix C,

$$\tilde{K}(\omega) = \frac{\tilde{Q}_{rs}(\omega) \exp(i\omega\tau_0)}{\tilde{Q}_{\rho\rho}(\omega)}. \quad (3.59)$$

Here \tilde{Q}_{rs} and $\tilde{Q}_{\rho\rho}$ are the Fourier transforms of Q_{rs} and $Q_{\rho\rho}$. The numerator in this expression reproduces the expression $Q_{rs}(\tau - \tau_0)$ in equation 3.57. The role of the denominator is to correct for any autocorrelations in the response spike train. Such correlations introduce a bias in the decoding, and the denominator in equation 3.59 corrects for this bias.

If we ignore the constraint of causality, then, because the occurrence of a spike cannot depend on the behavior of a stimulus in the very distant past, we can expect $K(\tau)$ from equation 3.57 or 3.58 and 3.59 to vanish for sufficiently negative values of $\tau - \tau_0$. For most neurons, this will occur for $\tau - \tau_0$ more negative than minus a few hundred ms. The decoding kernel given by equation 3.57 can therefore be made small for negative values of τ by choosing τ_0 large enough, but this may require a fairly large prediction delay. We can force exact adherence to the causality constraint for $\tau < 0$ by replacing $K(\tau)$ by $\Theta(\tau)K(\tau)$ where $\Theta(\tau)$ is defined such that $\Theta(\tau) = 1$ for $\tau > 0$ and $\Theta(\tau) = 0$ for $\tau < 0$. The causality constraint was imposed in this way in figure 3.13B. When it is multiplied by $\Theta(\tau)$, the restricted K is no longer the optimal decoding kernel, but it may be close to optimal.

causality constraint

Another way of imposing causality on the decoding kernel is to expand $K(\tau)$ as a weighted sum of causal basis functions (functions that vanish for negative arguments and span the space of functions satisfying the causal constraint). The optimal weights are then determined by minimizing the estimation error. This approach has the advantage of producing a truly optimal kernel for any desired value of τ_0 . A simpler but non-optimal

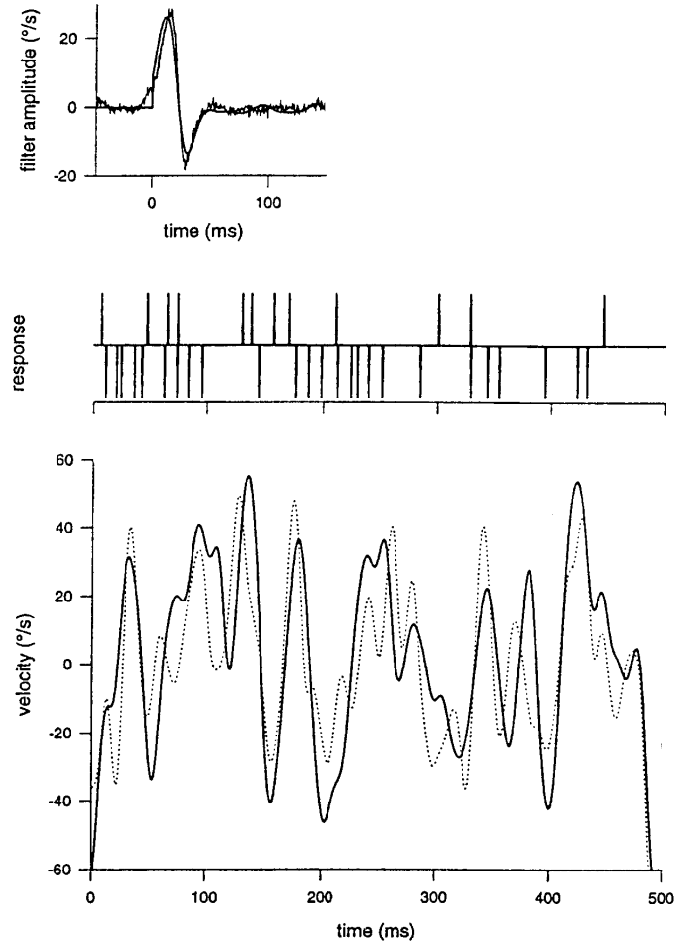


Figure 3.14: Decoding the stimulus from an H1 neuron of the fly. The upper panel is the decoding kernel. The jagged curve is the optimal acausal filter and the smooth curve is a kernel obtained by expanding in a causal set of basis functions. In both cases, the kernels are shifted by $\tau_0 = 40$ ms. The middle panel shows typical responses of the H1 neuron to the stimulus $s(t)$ (upper trace) and $-s(t)$ (bottom trace). The dashed line in the lower panel shows the actual stimulus and the solid line is the estimated stimulus from the optimal linear reconstruction using the acausal filter. (Adapted from Rieke et al., 1997.)

approach is to consider a fixed functional form for $K(\tau)$ that vanishes for $\tau \leq 0$ and is characterized by a number of free parameters that can be determined by minimizing the decoding error. Finally, the optimal causal kernel, also called the Wiener-Hopf filter, can be obtained by a technique

that involves so-called spectral factorization of $\tilde{Q}_{\rho\rho}(\omega)$.

Figure 3.14 shows an example of spike train decoding for the H1 neuron of the fly discussed in chapter 2. The top panel gives two reconstruction kernels, one acausal and one causal, that can be used in the decoding, and the bottom panel compares the reconstructed stimulus velocity with the actual stimulus velocity. The middle panel in figure 3.14 points out one further wrinkle in the procedure. Flies have two H1 neurons, one on each side of the body, that respond to motion in opposite directions. As is often the case, half-wave rectification prevents a single neuron from encoding both directions of motion. In the experiment described in the figure, rather than recording from both H1 neurons, Bialek et al. (1991) recorded from a single H1 neuron, but presented both the stimulus $s(t)$ and its negative, $-s(t)$. The two rows of spikes in the middle panel show sample traces for each of these presentations. This procedure provides a reasonable approximation of recording both H1 neurons, and produces a neuron/anti-neuron pair of recordings similar to the one that we discussed in connection with motion discrimination from area MT neurons. The stimulus is then decoded by summing the kernel $K(t - t_i)$ for all spike times t_i of the recorded H1 neuron and summing $-K(t - t_j)$ for all spike times t_j of its anti-neuron partner.

The fly only has two H1 neurons from which it must extract information about visual motion, so it seems reasonable that stimulus reconstruction using the spike-train decoding technique can produce quite accurate results (figure 3.14). It is perhaps more surprising that accurate decoding, at least in the sense of percent correct, can be obtained from single neurons out of the large population of MT neurons responding to visual motion in the monkey. Of course, the reconstruction of a time-dependent stimulus from H1 responses is more challenging than the binary discrimination done with MT neurons. Furthermore, it is worth remembering that in all the examples we have considered, including decoding wind direction from the cercal system and arm movement direction from a population of M1 neurons, the stimuli used are extremely simple compared to the naturally occurring stimuli that must be interpreted during normal behavior.

3.5 Chapter Summary

We have considered the decoding of stimulus characteristics from the responses they evoke, including discrimination between stimulus values, the decoding of static stimuli on the basis of population responses, and the decoding of dynamic stimulus parameters from spike trains. Discrimination was studied using the receiver operating characteristic, likelihood ratio tests, and the Neyman-Pearson lemma. For static parameter decoding we introduced the vector method, Bayesian, maximum *a posteriori* and maximum likelihood inference, the Fisher information and the Cramér-Rao lower bound. We also showed how to use ideas from Wiener filtering

to reconstruct an approximation to a time-varying stimulus from the spike trains it evokes.

3.6 Appendices

A) The Neyman-Pearson Lemma

Consider the difference $\Delta\beta$ in the power of two tests that have identical sizes α . One uses the likelihood ratio $l(r)$, and the other uses a different test function $h(r)$. For the test $h(r)$ using the threshold z_h ,

$$\alpha_h(z_h) = \int dr p[r| -] \Theta(h(r) - z_h) \quad \text{and} \quad \beta_h(z_h) = \int dr p[r| +] \Theta(h(r) - z_h). \quad (3.60)$$

Similar equations hold for the $\alpha_l(z_l)$ and $\beta_l(z_l)$ values for the test $l(r)$ using the threshold z_l . We use the Θ function, which is one for positive and zero for negative values of its argument, to impose the condition that the test is greater than the threshold. Comparing the β values for the two tests, we find

$$\Delta\beta = \beta_l(z_l) - \beta_h(z_h) = \int dr p[r| +] \Theta(l(r) - z_l) - \int dr p[r| +] \Theta(h(r) - z_h). \quad (3.61)$$

The range of integration where both $l(r) \geq z_l$ and $h(r) \geq z_h$ cancels between these two integrals, so, in a more compact notation, we can write

$$\Delta\beta = \int dr p[r| +] (\Theta(l(r) - z_l) \Theta(z_h - h(r)) - \Theta(z_l - l(r)) \Theta(h(r) - z_h)). \quad (3.62)$$

Using the definition $l(r) = p[r| +]/p[r| -]$ we can replace $p[r| +]$ by $l(r)p[r| -]$ in this equation, giving

$$\Delta\beta = \int dr l(r) p[r| -] \left(\Theta(l(r) - z_l) \Theta(z_h - h(r)) - \Theta(z_l - l(r)) \Theta(h(r) - z_h) \right). \quad (3.63)$$

Then, due to the conditions on $l(r)$ imposed by the Θ functions within the integrals, replacing $l(r)$ by z cannot decrease the value of the integral resulting from the first term in the large parentheses, nor increase the value arising from the second. This leads to the inequality

$$\Delta\beta \geq z \int dr p[r| -] (\Theta(l(r) - z_l) \Theta(z_h - h(r)) - \Theta(z_l - l(r)) \Theta(h(r) - z_h)). \quad (3.64)$$

Putting back the region of integration that cancels between these two terms (for which $l(r) \geq z_l$ and $h(r) \geq z_h$), we find

$$\Delta\beta \geq z \left[\int dr p[r] - \Theta(l(r) - z_l) - \int dr p[r] - \Theta(h(r) - z_h) \right]. \quad (3.65)$$

By definition, these integrals are the sizes of the two tests, which are equal by hypothesis. Thus $\Delta\beta \geq 0$, showing that no test can be better than the likelihood ratio $l(r)$, at least in the sense of maximizing the power for a given size.

B) The Cramér-Rao Bound

The Cramér-Rao lower bound for an estimator s_{est} is based on the Cauchy-Schwarz inequality, which states that for any two quantities A and B

Cauchy-Schwarz
inequality

$$\langle A^2 \rangle \langle B^2 \rangle \geq \langle AB \rangle^2. \quad (3.66)$$

To prove this inequality, note that

$$\left\langle \left(\langle B^2 \rangle A - \langle AB \rangle B \right)^2 \right\rangle \geq 0 \quad (3.67)$$

because it is the average value of a square. Computing the square gives

$$\langle B^2 \rangle^2 \langle A^2 \rangle - \langle AB \rangle^2 \langle B^2 \rangle \geq 0 \quad (3.68)$$

from which the inequality follows directly.

Consider the inequality of equation 3.66 with $A = \partial \ln p / \partial s$ and $B = s_{\text{est}} - \langle s_{\text{est}} \rangle$. From equations 3.42 and 3.38, we have $\langle A^2 \rangle = I_F$ and $\langle B^2 \rangle = \sigma_{\text{est}}^2$. The Cauchy-Schwarz inequality then gives

$$\sigma_{\text{est}}^2(s) I_F \geq \left\langle \frac{\partial \ln p[\mathbf{r}|s]}{\partial s} (s_{\text{est}} - \langle s_{\text{est}} \rangle) \right\rangle^2. \quad (3.69)$$

To evaluate the expression on the right side of the inequality 3.69, we differentiate the defining equation for the bias (equation 3.37),

$$s + b_{\text{est}}(s) = \langle s_{\text{est}} \rangle = \int d\mathbf{r} p[\mathbf{r}|s] s_{\text{est}}, \quad (3.70)$$

with respect to s to obtain

$$\begin{aligned} 1 + b'_{\text{est}}(s) &= \int d\mathbf{r} \frac{\partial p[\mathbf{r}|s]}{\partial s} s_{\text{est}} \\ &= \int d\mathbf{r} p[\mathbf{r}|s] \frac{\partial \ln p[\mathbf{r}|s]}{\partial s} s_{\text{est}} \\ &= \int d\mathbf{r} p[\mathbf{r}|s] \frac{\partial \ln p[\mathbf{r}|s]}{\partial s} (s_{\text{est}} - \langle s_{\text{est}} \rangle). \end{aligned}$$

The last equality follows from the identity

$$\int d\mathbf{r} p[\mathbf{r}|s] \frac{\partial \ln p[\mathbf{r}|s]}{\partial s} \langle s_{\text{est}} \rangle = \langle s_{\text{est}} \rangle \int d\mathbf{r} \frac{\partial p[\mathbf{r}|s]}{\partial s} = 0 \quad (3.71)$$

because $\int d\mathbf{r} p[\mathbf{r}|s] = 1$. The last line of equation 3.71 is just another way of writing the expression on the right side of the inequality 3.69, so combining this result with the inequality gives

$$\sigma_{\text{est}}^2(s) I_F \geq (1 + b'_{\text{est}}(s))^2 \quad (3.72)$$

which, when rearranged, is the Cramér-Rao bound of equation 3.40.

C) The Optimal Spike-Decoding Filter

The optimal linear kernel for spike train decoding is determined by solving equation 3.53. This is done by taking the Fourier transform of both sides of the equation, that is, multiplying both sides by $\exp(i\omega\tau)$ and integrating over τ ,

$$\int_{-\infty}^{\infty} d\tau \exp(i\omega\tau) \int_{-\infty}^{\infty} d\tau' Q_{\rho\rho}(\tau - \tau') K(\tau') = \int_{-\infty}^{\infty} d\tau \exp(i\omega\tau) Q_{rs}(\tau - \tau_0). \quad (3.73)$$

By making the replacement of integration variable $\tau \rightarrow \tau + \tau_0$, we find that the right side of this equation is

$$\exp(i\omega\tau_0) \int_{-\infty}^{\infty} d\tau \exp(i\omega\tau) Q_{rs}(\tau) = \exp(i\omega\tau_0) \tilde{Q}_{rs}(\omega) \quad (3.74)$$

where $\tilde{Q}_{rs}(\omega)$ is the Fourier transform of $Q_{rs}(\tau)$. The integral of the product of two functions that appears on the left side of equations 3.53 and 3.73 is called a convolution. To evaluate the Fourier transform on the left side of equation 3.73, we make use of an important theorem stating that the Fourier transform of a convolution is the product of the Fourier transforms of the two functions involved (see the Mathematical Appendix). According to this theorem

$$\int_{-\infty}^{\infty} d\tau \exp(i\omega\tau) \int_{-\infty}^{\infty} d\tau' Q_{\rho\rho}(\tau - \tau') K(\tau') = \tilde{Q}_{\rho\rho}(\omega) \tilde{K}(\omega) \quad (3.75)$$

where $\tilde{Q}_{\rho\rho}(\omega)$ and $\tilde{K}(\omega)$ are the Fourier transforms of $Q_{\rho\rho}(\tau)$ and $K(\tau)$ respectively,

$$\tilde{Q}_{\rho\rho}(\omega) = \int_{-\infty}^{\infty} d\tau \exp(i\omega\tau) Q_{\rho\rho}(\tau) \quad \text{and} \quad \tilde{K}(\omega) = \int_{-\infty}^{\infty} d\tau \exp(i\omega\tau) K(\tau). \quad (3.76)$$

Putting the left and right sides of equation 3.73 together as we have evaluated them, we find that

$$\tilde{Q}_{\rho\rho}(\omega)\tilde{K}(\omega) = \exp(i\omega\tau_0)\tilde{Q}_{rs}(\omega). \quad (3.77)$$

Equation 3.59 follows directly from this result, and equation 3.58 then determines $K(\tau)$ as the inverse Fourier transform of $\tilde{K}(\omega)$.

3.7 Annotated Bibliography

Statistical analysis of discrimination, various forms of decoding, the Neyman-Pearson lemma, the Fisher information and the Cramér-Rao lower bound can be found in Cox & Hinckley (1974). Receiver operator characteristics and signal detection theory are described comprehensively in Green & Swets (1966) and Graham (1989); and our account of spike train decoding follows that of Rieke et al. (1997). Newsome et al. (1989) and Salzman et al. (1992) present important results concerning visual motions discrimination and recordings from area MT, and Shadlen et al. (1996) provide a theoretically oriented review.

The vector method of population decoding has been considered in the context of a number of systems and references include Humphrey et al. (1970), Georgopoulos, Schwartz & Kettner (1986), Georgopoulos, Kettner & Schwartz (1988), van Gisbergen et al. (1987), and Lee et al. (1988). Various theoretical aspects of population decoding such as vector and ML decoding and the Fisher information that comprise our account were developed by Paradiso (1988); Baldi and Heiligenberg (1988); Vogels (1990), Snippe & Koenderink (1992); Zohary (1992), Seung & Sompolinsky (1993); Touretzky et al. (1993), Salinas & Abbott (1994); Sanger (1994, 1996), Snippe (1996), and Oram et al. (1998). Zhang & Sejnowski (1999) treat the effect of narrowing or broadening tuning curves on the Fisher information. Population codes are also known as coarse codes in the connectionist literature (Hinton, 1981).

Chapter 4

Information Theory

4.1 Entropy and Mutual Information

Neural encoding and decoding focus on the question: "What does the response of a neuron tell us about a stimulus". In this chapter we consider a related but different question: "How much does the neural response tell us about a stimulus". The techniques of information theory allow us to answer this question in a quantitative manner. Furthermore, we can use them to ask what forms of neural response are optimal for conveying information about natural stimuli.

Shannon invented information theory as a general framework for quantifying the ability of a coding scheme or a communication channel (such as the optic nerve) to convey information. It is assumed that the code involves a number of symbols (such as neuronal responses), and that the coding and transmission processes are stochastic and noisy. The quantities we consider in this chapter, the entropy and the mutual information, depend on the probabilities with which these symbols, or combinations of them, are used. Entropy is a measure of the theoretical capacity of a code to convey information. Mutual information measures how much of that capacity is actually used when the code is employed to describe a particular set of data. Communication channels, if they are noisy, have only limited capacities to convey information. The techniques of information theory are used to evaluate these limits and find coding schemes that saturate them.

In neuroscience applications, the symbols we consider are neuronal responses, and the data sets they describe are stimulus characteristics. In the most complete analyses, which are considered at the end of the chapter, the neuronal response is characterized by a list of action potential firing times. The symbols being analyzed in this case are sequences of action potentials. Computing the entropy and mutual information for spike sequences can

be difficult because the frequency of occurrence of many different spike sequences must be determined. This typically requires a large amount of data. For this reason, many information theory analyses use simplified descriptions of the response of a neuron that reduce the number of possible ‘symbols’ (i.e. responses) that need to be considered. We discuss cases in which the symbols consist of responses described by spike-count firing rates. We also consider the extension to continuous-valued firing rates. Because a reduced description of a spike train can carry no more information than the full spike train itself, this approach provides a lower bound on the actual information carried by the spike train.

Entropy

Entropy is a quantity that, roughly speaking, measures how ‘interesting’ or ‘surprising’ a set of responses is. Suppose that we are given a set of neural responses. If each response is identical, or if only a few different responses appear, we might conclude that this data set is relatively uninteresting. A more interesting set might show a larger range of different responses, perhaps in a highly irregular and unpredictable sequence. How can we quantify this intuitive notion of an interesting set of responses?

We begin by characterizing the responses in terms of their spike-count firing rates, i.e. the number of spikes divided by the trial duration, which can take a discrete set of different values. The methods we discuss are based on the probabilities $P[r]$ of observing a response with a spike-count rate r . The most widely used measure of entropy, due to Shannon, expresses the ‘surprise’ associated with seeing a response rate r as a function of the probability of getting that response, $h(P[r])$, and quantifies the entropy as the average of $h(P[r])$ over all possible responses. The function $h(P[r])$, which acts as a measure of surprise, is chosen to satisfy a number of conditions. First, $h(P[r])$ should be a decreasing function of $P[r]$ because low probability responses are more surprising than high probability responses. Further, the surprise measure for a response that consists of two independent spike counts should be the sum of the measures for each spike count separately. This assures that the entropy and information measures we ultimately obtain will be additive for independent sources. Suppose we record rates r_1 and r_2 from two neurons that respond independently of each other. Because the responses are independent, the probability of getting this pair of responses is the product of their individual probabilities, $P[r_1]P[r_2]$, so the additivity condition requires that

$$h(P[r_1]P[r_2]) = h(P[r_1]) + h(P[r_2]). \quad (4.1)$$

The logarithm is the only function that satisfies such an identity for all P . Thus, it only remains to decide what base to use for the logarithm. By convention, base 2 logarithms are used so that information can be compared easily with results for binary systems. To indicate that the base 2 logarithm

is being used, information is reported in units of ‘bits’, with

$$h(P[r]) = -\log_2 P[r]. \quad (4.2)$$

The minus sign makes h a decreasing function of its argument as required. Note that information is really a dimensionless number. The bit, like the radian for angles, is not a dimensional unit but a reminder that a particular system is being used.

Expression (4.2) quantifies the surprise or unpredictability associated with a particular response. Shannon’s entropy is just this measure averaged over all responses

$$H = -\sum_r P[r] \log_2 P[r]. \quad (4.3)$$

In the sum that determines the entropy, the factor $h = -\log_2 P[r]$ is multiplied by the probability that the response with rate r occurs. Responses with extremely low probabilities may contribute little to the total entropy, despite having large h values, because they occur so rarely. In the limit when $P[r] \rightarrow 0$, $h \rightarrow \infty$, but an event that does not occur does not contribute to the entropy because the problematic expression $-0 \log_2 0$ is evaluated as $-\epsilon \log_2 \epsilon$ in the limit $\epsilon \rightarrow 0$ and is zero. Very high probability responses also contribute little because they have $h \approx 0$. The responses that contribute most to the entropy have high enough probabilities so that they appear with a fair frequency, but not high enough to make h too small.

Computing the entropy in some simple cases helps provide a feel for what it measures. First, imagine the least interesting situation, when a neuron responds every time by firing at the same rate. In this case, all of the probabilities $P[r]$ are zero, except for one of them which is one. This means that every term in the sum of equation (4.3) is zero because either $P[r] = 0$ or $\log_2 1 = 0$. Thus, a set of identical responses has zero entropy. Next, imagine that the neuron responds in only two possible ways, either with rate r_+ or r_- . In this case, there are only two nonzero terms in equation (4.3), and, using the fact that $P[r_-] = 1 - P[r_+]$, the entropy is

$$H = -(1 - P[r_+]) \log_2 (1 - P[r_+]) - P[r_+] \log_2 P[r_+]. \quad (4.4)$$

This entropy, plotted in figure 4.1A, takes its maximum value of one bit when $P[r_-] = P[r_+] = 1/2$. Thus, a code consisting of two equally likely responses has one bit of entropy.

Mutual Information

To convey information about a set of stimuli, neural responses must be different for different stimuli. Entropy is a measure of response variability, but it does not tell us anything about the source of that variability. A neuron can only provide information about a stimulus if its response variability is correlated with changes in that stimulus, rather than being purely

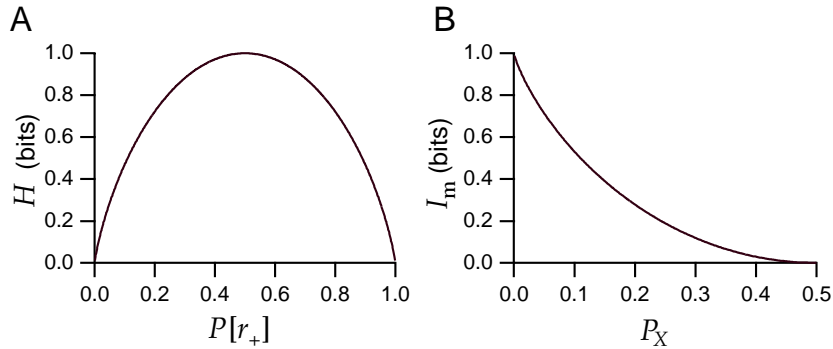


Figure 4.1: A) The entropy of a binary code. $P[r_+]$ is the probability of a response at rate r_+ . $P[r_-] = 1 - P[r_+]$ is the probability of the other response, r_- . The entropy is maximum when $P[r_-] = P[r_+] = 1/2$. B) The mutual information for a binary encoding of a binary stimulus. P_X is the probability of an incorrect response being evoked. The plot only shows $P_X \leq 1/2$ because values of $P_X > 1/2$ correspond to an encoding in which the relationship between the two responses and the two stimuli is reversed and the error probability is $1 - P_X$.

random or correlated with other unrelated factors. One way to determine whether response variability is correlated with stimulus variability is to compare the responses obtained using a different stimulus on every trial with those measured in trials involving repeated presentations of the same stimulus. Responses that are informative about the identity of the stimulus should exhibit larger variability for trials involving different stimuli than for trials that use the same stimulus repetitively. Mutual information is an entropy-based measure related to this idea.

The mutual information is the difference between the total response entropy and the average response entropy on trials that involve repetitive presentation of the same stimulus. Subtracting the entropy when the stimulus does not change removes from the total entropy the contribution from response variability that is not associated with the identity of the stimulus. When the responses are characterized by a spike-count rate, the total response entropy is given by equation 4.3. The entropy of the responses evoked by repeated presentations of a given stimulus s is computed using the conditional probability $P[r|s]$, the probability of a response at rate r given that stimulus s was presented, instead of the response probability $P[r]$ in equation 4.3. The entropy of the responses to a given stimulus is thus

$$H_s = - \sum_r P[r|s] \log_2 P[r|s]. \quad (4.5)$$

If we average this quantity over all the stimuli, we obtain a quantity called *noise entropy*

$$H_{\text{noise}} = \sum_s P[s] H_s = - \sum_{s,r} P[s] P[r|s] \log_2 P[r|s]. \quad (4.6)$$

This is the entropy associated with that part of the response variability that is not due to changes in the stimulus, but arises from other sources. The mutual information is obtained by subtracting the noise entropy from the full response entropy, which from equations 4.3 and 4.6 gives

mutual information

$$I_m = H - H_{\text{noise}} = - \sum_r P[r] \log_2 P[r] + \sum_{s,r} P[s] P[r|s] \log_2 P[r|s]. \quad (4.7)$$

The probability of a response r is related to the conditional probability $P[r|s]$ and the probability $P[s]$ that stimulus s is presented by the identity (chapter 3)

$$P[r] = \sum_s P[s] P[r|s]. \quad (4.8)$$

Using this, and writing the difference of the two logarithms in equation 4.7 as the logarithm of the ratio of their arguments, we can rewrite the mutual information as

$$I_m = \sum_{s,r} P[s] P[r|s] \log_2 \left(\frac{P[r|s]}{P[r]} \right). \quad (4.9)$$

Recall from chapter 3 that,

$$P[r,s] = P[s] P[r|s] = P[r] P[s|r] \quad (4.10)$$

where $P[r,s]$ is the joint probability of stimulus s appearing and response r being evoked. Equation 4.10 can be used to derive yet another form for the mutual information

$$I_m = \sum_{s,r} P[r,s] \log_2 \left(\frac{P[r,s]}{P[r] P[s]} \right). \quad (4.11)$$

This equation reveals that the mutual information is symmetric with respect to interchange of s and r , which means that the mutual information that a set of responses conveys about a set of stimuli is identical to the mutual information that the set of stimuli conveys about the responses. To see this explicitly, we apply equation 4.10 again to write

$$I_m = - \sum_s P[s] \log_2 P[s] + \sum_{s,r} P[r] P[s|r] \log_2 P[s|r]. \quad (4.12)$$

This result is the same as equation 4.7 except that the roles of the stimulus and the response have been interchanged. Equation 4.12 shows how response variability limits the ability of a spike train to carry information. The second term on the right side, which is negative, is the average uncertainty about the identity of the stimulus given the response, and reduces the total stimulus entropy represented by the first term.

To provide some concrete examples, we compute the mutual information for a few simple cases. First, suppose that the responses of the neuron are completely unaffected by the identity of the stimulus. In this case, $P[r|s] = P[r]$, and from equation 4.9 it follows immediately that $I_m = 0$. At the other extreme, suppose that each stimulus s produces a unique and distinct response r_s . Then, $P[r_s] = P[s]$ and $P[r|s] = 1$ if $r = r_s$ and $P[r|s] = 0$ otherwise. This causes the sum over r in equation 4.9 to collapse to just one term, and the mutual information becomes

$$I_m = \sum_s P[s] \log_2 \left(\frac{1}{P[r_s]} \right) = - \sum_s P[s] \log_2 P[s]. \quad (4.13)$$

The last expression, which follows from the fact that $P[r_s] = P[s]$, is the entropy of the stimulus. Thus, with no variability and a one-to-one map from stimulus to response, the mutual information is equal to the full stimulus entropy.

Finally, imagine that there are only two possible stimulus values, which we label + and −, and that the neuron responds with just two rates, r_+ and r_- . We associate the response r_+ with the + stimulus, and the response r_- with the − stimulus, but the encoding is not perfect. The probability of an incorrect response is P_X , meaning that for the correct responses $P[r_+|+] = P[r_-|-] = 1 - P_X$, and for the incorrect responses $P[r_+|-] = P[r_-|+] = P_X$. We assume that the two stimuli are presented with equal probability so that $P[r_+] = P[r_-] = 1/2$ which, from equation 4.4, makes the full response entropy one bit. The noise entropy is $-(1 - P_X) \log_2 (1 - P_X) - P_X \log_2 P_X$. Thus, the mutual information is

$$I_m = 1 + (1 - P_X) \log_2 (1 - P_X) + P_X \log_2 P_X. \quad (4.14)$$

This is plotted in figure 4.1B. When the encoding is error free ($P_X = 0$), the mutual information is one bit, which is equal to both the full response entropy and the stimulus entropy. When the encoding is random ($P_X = 1/2$), the mutual information goes to zero.

It is instructive to consider this example from the perspective of decoding. We can think of the neuron as being a communication channel that reports noisily on the stimulus. From this perspective, we want to know the probability that a + was presented given that the response r_+ was recorded. By Bayes theorem, this is $P[+|r_+] = P[r_+|+]P[+]/P[r_+] = 1 - P_X$. Before the response is recorded, the prior expectation was that + and − were equally likely. If the response r_+ is recorded, this expectation changes to $1 - P_X$. The mutual information measures the corresponding reduction in uncertainty, or equivalently, the tightening of the posterior distribution due to the response.

The mutual information is related to a measure used in statistics called the Kullback-Leibler (KL) divergence. The KL divergence between one

probability distribution $P[r]$ and another distribution $Q[r]$ is

$$D_{\text{KL}}(P, Q) = \sum_r P[r] \log_2 \left(\frac{P[r]}{Q[r]} \right). \quad (4.15)$$

The KL divergence has a property normally associated with a distance measure, $D_{\text{KL}}(P, Q) \geq 0$ with equality if and only if $P = Q$ (proven in appendix A). However, unlike a distance, it is not symmetric with respect to interchange of P and Q . Comparing the definition 4.15 with equation 4.11, we see that the mutual information is the KL divergence between the distributions $P[r, s]$ and $P[r]P[s]$. If the stimulus and the response were independent of each other, $P[r, s]$ would be equal to $P[r]P[s]$. Thus, the mutual information is the KL divergence between the actual probability distribution $P[r, s]$, and the value it would take if the stimulus and response were independent. The fact that $D_{\text{KL}} \geq 0$ proves that the mutual information cannot be negative. In addition, it can never be larger than either the full response entropy or the entropy of the stimulus set.

Entropy and Mutual Information for Continuous Variables

Up to now we have characterized neural responses using discrete spike-count rates. As in chapter 3, it is often convenient to treat these rates instead as continuous variables. There is a complication associated with entropies that are defined in terms of continuous response variables. If we could measure the value of a continuously defined firing rate with unlimited accuracy, it would be possible to convey an infinite amount of information using the endless sequence of decimal digits of this single variable. Of course, practical considerations always limit the accuracy with which a firing rate can be measured or conveyed.

To define the entropy associated with a continuous measure of a neural response, we must include some limit on the measurement accuracy. The effects of this limit typically cancel in computations of mutual information because these involve taking differences between two entropies. In this section, we show how entropy and mutual information are computed for responses characterized by continuous firing rates. For completeness, we also treat the stimulus parameter s as a continuous variable. This means that the probability $P[s]$ is replaced by the probability density $p[s]$, and sums over s are replaced by integrals.

For a continuously defined firing rate, the probability of the firing rate lying in the range between r and $r + \Delta r$, for small Δr , is expressed in terms of a probability density as $p[r]\Delta r$. Summing over discrete bins of size Δr we find, by analogy with equation (4.3),

$$\begin{aligned} H &= -\sum p[r]\Delta r \log_2(p[r]\Delta r) \\ &= -\sum p[r]\Delta r \log_2 p[r] - \log_2 \Delta r. \end{aligned} \quad (4.16)$$

To extract the last term we have expressed the logarithm of a product as the sum of two logarithms and used the fact the the sum of the response probabilities is one. We would now like to take the limit $\Delta r \rightarrow 0$ but we cannot because the $\log_2 \Delta r$ term diverges in this limit. This divergence reflects the fact that a continuous variable measured with perfect accuracy has infinite entropy. However, for reasonable (i.e. Riemann integrable) $p[r]$, everything works out fine for the first term because the sum becomes an integral in the limit $\Delta r \rightarrow 0$. In this limit, we can write

$$\lim_{\Delta r \rightarrow 0} \{H + \log_2 \Delta r\} = - \int dr p[r] \log_2 p[r]. \quad (4.17)$$

Δr is best thought of as a limit on the resolution with which the firing rate can be measured. Unless this limit is known, the entropy of a probability density for a continuous variable can only be determined up to an additive constant. However, if two entropies computed with the same resolution are subtracted, the troublesome term involving Δr cancels and we can proceed without knowing its precise value. All of the cases where we use equation 4.17 are of this form. The integral on the right side of equation 4.17 is sometimes called the differential entropy.

The noise entropy, for a continuous variable like the firing rate, can be written in a manner similar to the response entropy 4.17, except that the conditional probability density $p[r|s]$ is used

$$\lim_{\Delta r \rightarrow 0} \{H_{\text{noise}} + \log_2 \Delta r\} = - \int ds \int dr p[s] p[r|s] \log_2 p[r|s]. \quad (4.18)$$

The mutual information is the difference between the expression in equation 4.17 and 4.18,

$$I_m = \int ds \int dr p[s] p[r|s] \log_2 \left(\frac{p[r|s]}{p[r]} \right). \quad (4.19)$$

Note that the factor of $\log_2 \Delta r$ has canceled in the expression for the mutual information because both entropies were evaluated at the same resolution.

In chapter 3, we described the Fisher information as a local measure of how tightly the responses determine the stimulus. The Fisher information is local because it depends on the expected curvature of the likelihood $P[\mathbf{r}|s]$ (typically for the responses of many cells) evaluated at the true stimulus value. The mutual information is a global measure in the sense that it depends on the average overall uncertainty in the decoding distribution $P[s|\mathbf{r}]$, including values of s both close and far from the true stimulus. If the decoding distribution $P[s|\mathbf{r}]$ has a single peak about the true stimulus, the Fisher information and the mutual information are closely related. In particular, for large numbers of neurons, the maximum likelihood estimator tends to have a Gaussian distribution, as discussed in chapter 3. In this case, the mutual information between stimulus and response is essentially, up to an additive constant, the logarithm of the Fisher information.

4.2 Information and Entropy Maximization

Entropy and mutual information are useful quantities for characterizing the nature and efficiency of neural encoding and selectivity. Often, in addition to such characterizations, we seek to understand the computational implications of an observed response selectivity. For example, we might ask whether neural responses to natural stimuli are optimized to convey as much information as possible. This hypothesis can be tested by computing the response characteristics that maximize the mutual information conveyed about naturally occurring stimuli and comparing the results with responses observed experimentally.

Because the mutual information is the full response entropy minus the noise entropy, maximizing the information involves a compromise. We must make the response entropy as large as possible without allowing the noise entropy to get too big. If the noise entropy is small, which means that the mutual information is limited by the resolution with which the response can be read out rather than by extraneous sources of noise, maximizing the response entropy, subject to an appropriate constraint, maximizes the mutual information to a good approximation. We therefore begin our discussion by studying how response entropy can be maximized. Later in the discussion, we will consider the effects of noise entropy.

Constraints play a crucial role in this analysis. We have already seen that the theoretical information carrying capacity associated with a continuous firing rate is limited only by the resolution with which the firing rate can be defined. Even with a finite resolution, a firing rate could convey an infinite amount of information if it could take arbitrarily high values. Thus, we must impose some constraint that limits the firing rate to a realistic range. Possible constraints include limiting the maximum allowed firing rate or holding the average firing rate or its variance fixed.

Entropy Maximization for a Single Neuron

To maximize the response entropy we must find a probability density $p[r]$ that makes the integral in equation 4.17 as large as possible while satisfying whatever constraints we impose. During the maximization process, the resolution Δr is held fixed, so the $\log_2 \Delta r$ term remains constant, and it can be ignored. As a result, it will not generally appear in the following equations. One constraint that always applies in entropy maximization is that the integral of the probability density must be one. Suppose that the neuron in question has a maximum firing rate of r_{\max} . Then, the integrals in question extend from 0 to r_{\max} . To find the $p[r]$ producing the maximum entropy, we must maximize

$$-\int_0^{r_{\max}} dr p[r] \log_2 p[r] \quad (4.20)$$

subject to the constraint

$$\int_0^{r_{\max}} dr p[r] = 1. \quad (4.21)$$

The result is that the probability density that maximizes the entropy subject to this constraint is a constant,

$$p[r] = \frac{1}{r_{\max}}, \quad (4.22)$$

independent of r . The entropy for this probability density is

$$H = \log_2 r_{\max} - \log_2 \Delta r = \log_2 \left(\frac{r_{\max}}{\Delta r} \right). \quad (4.23)$$

Note that the factor Δr , expressing the resolution for firing rates makes the argument of the logarithm dimensionless.

histogram equalization

Equation 4.22 is the basis of a signal processing technique called histogram equalization. Applied to neural responses, this is a procedure for tailoring the neuronal selectivity so that $p[r] = 1/r_{\max}$ in response to a set of stimuli over which the entropy is to be maximized. Suppose a neuron responds to a stimulus characterized by the parameter s by firing at a rate $r = f(s)$, where $f(s)$ is the response tuning curve. For small Δs , the probability that the continuous stimulus variable falls in the range between s and $s + \Delta s$ is given in terms of the stimulus probability density by $p[s]\Delta s$. This produces a response that falls in the range between $f(s + \Delta s)$ and $f(s)$. If the response probability density takes its optimal value, $p[r] = 1/r_{\max}$, the probability that the response falls within this range is $|f(s + \Delta s) - f(s)|/r_{\max}$. Setting these two probabilities equal to each other, we find that $|f(s + \Delta s) - f(s)|/r_{\max} = p[s]\Delta s$. Consider the case of a monotonically increasing response so that $f(s + \Delta s) > f(s)$ for positive Δs . Then, in the limit $\Delta s \rightarrow 0$, the condition becomes

$$\frac{df}{ds} = r_{\max} p[s] \quad (4.24)$$

which has the solution

$$f(s) = r_{\max} \int_{s_{\min}}^s ds' p[s'] \quad (4.25)$$

where s_{\min} is the minimum value of s , which is assumed to generate no response. Thus, entropy maximization requires that the tuning curve of the responding neuron be proportional to the integral of the probability density of the stimulus.

Laughlin (1981) has provided evidence that responses of the large monopolar cell (LMC) in the visual system of the fly satisfy the entropy maximizing condition. The LMC responds to contrast, and Laughlin measured the probability distribution of contrasts of natural scenes in habitats where the

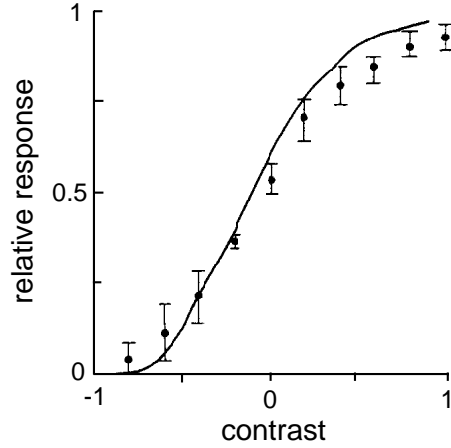


Figure 4.2: Contrast response of the fly LMC (data points) compared to the integral of the natural contrast probability distribution (solid curve). The relative response is the amplitude of the membrane potential fluctuation produced by the onset of a light or dark image with a given level of contrast divided by the maximum response. Contrast is defined relative to the background level of illumination, I_b , as $(I - I_b)/I_b$. (Adapted from Laughlin, 1981.)

flies he studied live. The solid curve in figure 4.2 is the integral of this measured distribution. The data points in figure 4.2 are LMC responses as a function of contrast. These responses are measured as membrane potential fluctuation amplitudes, not as firing rates, but the analysis presented above applies equally to this case. As figure 4.2 indicates, the response tuning curve as a function of contrast is very close to the integrated probability density, suggesting that the LMC is using a maximum entropy encoding.

Even though neurons have maximum firing rates, the constraint $r \leq r_{\max}$ may not always be the factor that limits the entropy. For example, the average firing rate of the neuron may be constrained to values much less than r_{\max} , or the variance of the firing rate might be constrained. The reader is invited to show that the entropy maximizing probability density if the average firing rate is constrained to a fixed value is an exponential. A related calculation shows that the probability density that maximizes the entropy subject to constraints on the firing rate and its variance is a Gaussian.

Populations of Neurons

When a population of neurons encodes a stimulus, optimizing their individual response properties will not necessarily lead to an optimized population response. Optimizing individual responses could result in a highly redundant population representation in which different neurons encode the same information. Entropy maximization for a population requires

that the neurons convey independent pieces of information, i.e. they must have different response selectivities. Let the vector \mathbf{r} with components r_a for $a = 1, 2, \dots, N$ denote the firing rates for a population of N neurons, measured with resolution Δr . If $p[\mathbf{r}]$ is the probability of evoking a population response characterized by the vector \mathbf{r} , the entropy for the entire population response is

$$H = - \int d\mathbf{r} p[\mathbf{r}] \log_2 p[\mathbf{r}] - N \log_2 \Delta r. \quad (4.26)$$

Along with the full population entropy of Equation 4.26, we can also consider the entropy associated with individual neurons within the population. If $p[r_a] = \int \prod_{b \neq a} dr_b p[\mathbf{r}]$ is the probability density for response r_a from neuron a , its entropy is

$$H_a = - \int dr_a p[r_a] \log_2 p[r_a] - \log_2 \Delta r = - \int d\mathbf{r} p[\mathbf{r}] \log_2 p[r_a] - \log_2 \Delta r. \quad (4.27)$$

The true population entropy can never be greater than the sum of these individual neuron entropies over the entire population,

$$H \leq \sum_a H_a. \quad (4.28)$$

To prove this, we note that the difference between the full entropy and the sum of individual neuron entropies is

$$\sum_a H_a - H = \int d\mathbf{r} p[\mathbf{r}] \log_2 \left(\frac{p[\mathbf{r}]}{\prod_a p_a[r_a]} \right) \geq 0. \quad (4.29)$$

The inequality follows from the fact that the middle expression is the KL divergence between the probability distributions $p[\mathbf{r}]$ and $\prod_a p_a[r_a]$, and a KL divergence is always non-negative. Equality holds only if

$$p[\mathbf{r}] = \prod_a p[r_a], \quad (4.30)$$

i.e. the responses of the neurons are statistically independent. Thus, the full response entropy is never greater than the sum of the entropies of the individual neurons in the population, and it reaches the limiting value when equation 4.30 is satisfied. A code that satisfies this condition is called a factorial code because the probability factorizes into a product of single neuron probabilities. The entropy difference in equation 4.29 has been suggested as a measure of redundancy. When the population response probability density factorizes, this implies that the individual neurons respond independently.

Combining this result with the results of the previous section, we conclude that the maximum population response entropy can be achieved

factorial code

factorization

by satisfying two conditions. First, the individual neurons must respond independently, i.e. $p[\mathbf{r}] = \prod_a p[r_a]$ must factorize. Second, they must all have response probabilities that are optimal for whatever constraints are imposed, for example flat, exponential, or Gaussian. If the same constraint is imposed on every neuron, the second condition implies that every neuron must have the same response probability density. In other words $p[r_a]$ must be the same for all a values, a property called probability equalization. This does not imply that all the neurons respond identically to every stimulus. Indeed, the conditional probabilities $p[r_a|s]$ must be different for different neurons if they are to act independently. We proceed by considering factorization and probability equalization as general principles of entropy maximization, without imposing explicit constraints.

Exact factorization and probability equalization are difficult to achieve, especially if the form of the neural response is restricted. These goals are likely to be impossible to achieve, for example, if the neural responses are modeled as having a linear relation to the stimulus. A more modest goal is to require that the lowest order moments of the population response probability distribution match those of a fully factorized and equalized distribution. If the individual response probability distributions are equal, the average firing rates and firing rate variances will be the same for all neurons, $\langle r_a \rangle = \langle r \rangle$ and $\langle (r_a - \langle r \rangle)^2 \rangle = \sigma_r^2$ for all a . The covariance matrix for a factorized and probability equalized population distribution is thus proportional to the identity matrix,

$$Q_{ab} = \int d\mathbf{r} p[\mathbf{r}] (r_a - \langle r \rangle)(r_b - \langle r \rangle) = \sigma_r^2 \delta_{ab}. \quad (4.31)$$

Finding response distributions that satisfy only the decorrelation and variance equalization condition of equation 4.31 is usually tractable. In the following examples, we will restrict ourselves to this easier task. This maximizes the entropy only if the statistics of the responses are Gaussian, but it is a reasonable procedure even in a non-Gaussian case, because it typically reduces the redundancy in the population code and spreads the load of information transmission equally among the neurons.

*probability
equalization**decorrelation and
variance
equalization*

Application to Retinal Ganglion Cell Receptive Fields

Entropy and information maximization have been used to explain properties of visual receptive fields in the retina, LGN, and primary visual cortex. The basic assumption is that these receptive fields serve to maximize the amount of information that the associated neural responses convey about natural visual scenes in the presence of noise. Information theoretical analyses are sensitive to the statistical properties of the stimuli being represented, so the statistics of natural scenes play an important role in these studies. Natural scenes exhibit substantial spatial and temporal redundancy. Maximizing the information conveyed requires removing this redundancy from the neural responses.

It should be kept in mind that the information maximization approach sets limited goals and requires strong assumptions about the nature of the constraints relevant to the nervous system. In addition, the approach only analyzes the representational properties of neural responses and ignores the computational goals of the visual system, such as object recognition or target tracking. Finally, maximizing other measures of performance, different from the mutual information, may give similar results. Nevertheless, the principal of information maximization is quite successful at accounting for properties of receptive fields early in the visual pathway.

In chapter 2, a visual image was defined by a contrast function $s(x, y, t)$ with an average value over trials of zero. For the calculations we present here, it is more convenient to express the x and y coordinates for locations on the viewing screen in terms of a single vector $\vec{x} = (x, y)$, or sometimes $\vec{y} = (x, y)$. Using this notation, the linear estimate of the response of a visual neuron discussed in chapter 2 can be written as

$$L(t) = \int_0^\infty d\tau \int d\vec{x} D(\vec{x}, \tau) s(\vec{x}, t - \tau). \quad (4.32)$$

If the space-time receptive field $D(\vec{x}, \tau)$ is separable, $D(\vec{x}, \tau) = D_s(\vec{x})D_t(\tau)$ and we can rewrite $L(t)$ as the product of integrals involving temporal and spatial filters. To keep the notation simple, we assume that the stimulus can also be separated, so that $s(\vec{x}, t) = s_s(\vec{x})s_t(t)$. Then, $L(t) = L_s L_t(t)$ where

$$L_s = \int d\vec{x} D_s(\vec{x}) s_s(\vec{x}) \quad (4.33)$$

and

$$L_t(t) = \int_0^\infty d\tau D_t(\tau) s_t(t - \tau). \quad (4.34)$$

In the following, we analyze the spatial and temporal components, D_s and D_t , separately by considering the information carrying capacity of L_s and L_t . We study the spatial receptive fields of retinal ganglion cells in this section, and the temporal response properties of LGN cells in the next. Later, we discuss the application of information maximization ideas to primary visual cortex.

To derive appropriately optimal spatial filters, we consider an array of retinal ganglion cells with receptive fields covering a small patch of the retina. We assume that the statistics of the input are spatially (and temporally) stationary or translation invariant. This means that all locations and directions in space (and all times), at least within the patch we consider, are equivalent. This equivalence allows us to give all of the receptive fields the same spatial structure, with the receptive fields of different cells merely being shifted to different points within the visual field. As a result, we write the spatial kernel describing a retinal ganglion cell with receptive

field centered at the point \vec{a} as $D_s(\vec{x} - \vec{a})$. The linear response of this cell is then

$$L_s(\vec{a}) = \int d\vec{x} D_s(\vec{x} - \vec{a}) s_s(\vec{x}). \quad (4.35)$$

Note that we are labeling the neurons by the locations \vec{a} of the centers of their receptive fields rather than by an integer index such as i . This is a convenient labeling scheme that allows sums over neurons to be replaced by sums over parameters describing their receptive fields. The vectors \vec{a} for the different neurons take on discrete values corresponding to the different neurons in the population. If many neurons are being considered, these discrete vectors may fill the range of receptive field locations quite densely. In this case, it is reasonable to approximate the large but discrete set of \vec{a} values, with a vector \vec{a} that is allowed to vary continuously. In other words, as an approximation, we proceed as if there were a neuron corresponding to every continuous value of \vec{a} . This allows us to treat $L(\vec{a})$ as a function of \vec{a} and to replace sums over neurons with integrals over \vec{a} . In the case we are considering, the receptive fields of retinal ganglion cells cover the retina densely, with many receptive fields overlapping each point on the retina, so the replacement of discrete sums over neurons with continuous integrals over \vec{a} is quite accurate.

The Whitening Filter

We will not attempt a complete entropy maximization for the case of retinal ganglion cells, but rather will follow the approximate procedure of setting the correlation matrix between different neurons within the population proportional to the identity matrix (equation 4.31). The relevant correlation, in this case, is the average over all stimuli of the product of the linear responses of two cells, one with receptive field centered at \vec{a} and the other at \vec{b} ,

$$Q_{LL}(\vec{a}, \vec{b}) = \langle L_s(\vec{a}) L_s(\vec{b}) \rangle = \int d\vec{x} d\vec{y} D_s(\vec{x} - \vec{a}) D_s(\vec{y} - \vec{b}) \langle s_s(\vec{x}) s_s(\vec{y}) \rangle. \quad (4.36)$$

The average here, denoted by angle brackets, is not over trials but over the set of natural scenes for which we believe the receptive field is optimized. By analogy with equation 4.31, decorrelation and variance equalization of the different retinal ganglion cells, when \vec{a} and \vec{b} are taken to be continuous variables, require that we set this correlation function proportional to a δ function,

$$Q_{LL}(\vec{a}, \vec{b}) = \sigma_L^2 \delta(\vec{a} - \vec{b}). \quad (4.37)$$

This is the continuous variable analog of making a discrete correlation matrix proportional to the identity matrix (equation 4.31). The δ function with

vector arguments is only non-zero when all of the components of \vec{a} and \vec{b} are identical.

The quantity $\langle s_s(\vec{x})s_s(\vec{y}) \rangle$ in equation 4.36 is the correlation function of the stimulus averaged over natural scenes. Our assumption of homogeneity implies that this quantity is only a function of the vector difference $\vec{x} - \vec{y}$ (actually, if all directions are equivalent, it is only a function of the magnitude $|\vec{x} - \vec{y}|$), and we write it as

$$Q_{ss}(\vec{x} - \vec{y}) = \langle s_s(\vec{x})s_s(\vec{y}) \rangle. \quad (4.38)$$

To determine the form of the receptive field filter that is optimal, we must solve equation 4.37 for D_s . This is done by expressing D_s and Q_{ss} in terms of their Fourier transforms \tilde{D}_s and \tilde{Q}_{ss} ,

$$D_s(\vec{x} - \vec{a}) = \frac{1}{4\pi^2} \int d\vec{k} \exp(-i\vec{k} \cdot (\vec{x} - \vec{a})) \tilde{D}_s(\vec{k}) \quad (4.39)$$

$$Q_{ss}(\vec{x} - \vec{y}) = \frac{1}{4\pi^2} \int d\vec{k} \exp(-i\vec{k} \cdot (\vec{x} - \vec{y})) \tilde{Q}_{ss}(\vec{k}). \quad (4.40)$$

\tilde{Q}_{ss} , which is real and non-negative, is also called the stimulus power spectrum (see chapter 1). In terms of these Fourier transforms, equation 4.37 becomes

$$|\tilde{D}_s(\vec{k})|^2 \tilde{Q}_{ss}(\vec{k}) = \sigma_L^2 \quad (4.41)$$

from which we find

$$|\tilde{D}_s(\vec{k})| = \frac{\sigma_L}{\sqrt{\tilde{Q}_{ss}(\vec{k})}}. \quad (4.42)$$

whitening filter

The linear kernel described by equation 4.42 exactly compensates for whatever dependence the Fourier transform of the stimulus correlation function has on the spatial frequency \vec{k} such that the product $\tilde{Q}_{ss}(\vec{k})|\tilde{D}_s(\vec{k})|^2$ is independent of \vec{k} . This product is the power spectrum of L . The output of the optimal filter has a power spectrum that is independent of spatial frequency, and therefore has the same characteristics as white noise. Therefore, the kernel in equation 4.42 is called a whitening filter. Different spatial frequencies act independently in a linear system, so decorrelation and variance equalization require them to be utilized at equal signal strength. The calculation we have performed only determines the amplitude $|\tilde{D}_s(\vec{k})|$ and not $\tilde{D}_s(\vec{k})$ itself. Thus, decorrelation and variance equalization do not uniquely specify the form of the linear kernel. We study some consequences of the freedom to choose different linear kernels satisfying equation 4.42 later in the chapter.

The spatial correlation function for natural scenes has been measured, with the result that $\tilde{Q}_{ss}(\vec{k})$ is proportional to $1/|\vec{k}|^2$ over the range it has

been evaluated. The behavior near $\vec{k} = 0$ is not well established, but the divergence of $1/|\vec{k}|^2$ near $\vec{k} = 0$ can be removed by setting $\tilde{Q}_{ss}(\vec{k})$ proportional to $1/(|\vec{k}|^2 + k_0^2)$ where k_0 is a constant. The stimuli of interest in the calculation of retinal ganglion receptive fields are natural images as they appear on the retina, not in the photographs from which the natural scenes statistics are measured. An additional factor must be included in $\tilde{Q}_{ss}(\vec{k})$ to account for filtering introduced by the optics of the eye (the optical modulation transfer function). A simple model of the optical modulation transfer function results in an exponential correction to the stimulus correlation function

optical modulation transfer function

$$\tilde{Q}_{ss}(\vec{k}) \propto \frac{\exp(-\alpha|\vec{k}|)}{|\vec{k}|^2 + k_0^2}. \quad (4.43)$$

Putting this into equation 4.42 gives a rather peculiar result; the amplitude $|\tilde{D}_s(\vec{k})|$, being proportional to the inverse of the square root of \tilde{Q}_{ss} , is predicted to grow exponentially for large $|\vec{k}|$. Whitening filters maximize entropy by equalizing the distribution of response power over the entire spatial frequency range. High spatial frequency components of images are relatively rare in natural scenes and, even as they occur, are greatly attenuated by the eye. The whitening filter compensates for this by boosting the responses to high spatial frequencies. Although this is the result of the entropy maximization calculation, it is not a good strategy to use in an unrestricted way for visual processing. Real inputs to retinal ganglion cells involve a mixture of true signal and noise coming from biophysical sources in the retina. At high spatial frequencies, for which the true signal is weak, inputs to retinal ganglion cells are likely to be dominated by noise, especially in low-light conditions. Boosting the amplitude of this noise-dominated input and transmitting it to the brain is not an efficient visual encoding strategy.

The problem of excessive boosting of responses at high spatial frequency arises in the entropy maximization calculation because no distinction has been made between the entropy coming from true signals and that coming from noise. To correct this problem, we should maximize the information transmitted by the retinal ganglion cells about natural scenes, rather than maximize the entropy. A full information maximization calculation of the receptive field properties of retinal ganglion cells can be performed, but this requires introducing a number of assumptions about the constraints that are relevant, and it is not entirely obvious what these constraints should be. Instead, we will follow an approximate procedure that pre-filters the input to eliminate as much noise as possible, and then uses the results of this section to maximize the entropy of a linear filter acting on the pre-filtered input signal.

Filtering Input Noise

Suppose that the visual stimulus on the retina is the sum of the true stimulus $s_s(\vec{x})$ that should be conveyed to the brain and a noise term $\eta(\vec{x})$ that reflects image distortion, photoreceptor noise, and other signals that are not worth conveying beyond the retina. To deal with such a mixed input signal, we express the Fourier transform of the linear kernel $\tilde{D}_s(\vec{k})$ as a product of two terms, a noise filter, $\tilde{D}_\eta(\vec{k})$, that eliminates as much of the noise as possible, and a whitening filter, $\tilde{D}_w(\vec{k})$, that satisfies equation 4.42. The Fourier transform of the complete filter is then $\tilde{D}_s(\vec{k}) = \tilde{D}_w(\vec{k})\tilde{D}_\eta(\vec{k})$.

To determine the form of the noise filter, we demand that when it is applied to the total input $s_s(\vec{x}) + \eta(\vec{x})$, the result is as close to the signal part of the input, $s_s(\vec{x})$, as possible. As in the previous section, it is easiest to perform the necessary calculations in the Fourier-transformed spatial frequency domain. Thus, we express the difference between the filtered input and the true signal in terms of the Fourier transforms of the signal and noise, $\tilde{s}(\vec{k})$ and $\tilde{\eta}(\vec{k})$. The Fourier transform of the output of the noise filter is $\tilde{D}_\eta(\vec{k})(\tilde{s}(\vec{k}) + \tilde{\eta}(\vec{k}))$, and we want to make this as close as possible to the Fourier transform of the pure signal, $\tilde{s}(\vec{k})$. To do this, we minimize the integral over \vec{k} of the squared amplitude of the difference between these two quantities, averaged over natural scenes,

$$\left\langle \int d\vec{k} \left| \tilde{D}_\eta(\vec{k}) (\tilde{s}(\vec{k}) + \tilde{\eta}(\vec{k})) - \tilde{s}(\vec{k}) \right|^2 \right\rangle. \quad (4.44)$$

Note that the squared amplitude of a complex quantity such as $\tilde{s}(\vec{k})$ is $|\tilde{s}(\vec{k})|^2 = \tilde{s}(\vec{k})\tilde{s}^*(\vec{k})$ where $\tilde{s}^*(\vec{k})$ is the complex conjugate of $\tilde{s}(\vec{k})$. Setting the derivative of equation 4.44 with respect to $\tilde{D}_\eta^*(\vec{k}')$ to zero gives

$$\int d\vec{k} \tilde{D}_\eta(\vec{k}) \left(\left\langle \tilde{s}(\vec{k}) \tilde{s}^*(\vec{k}') \right\rangle + \left\langle \tilde{\eta}(\vec{k}) \tilde{\eta}^*(\vec{k}') \right\rangle \right) = \int d\vec{k} \left\langle \tilde{s}(\vec{k}) \tilde{s}^*(\vec{k}') \right\rangle. \quad (4.45)$$

In evaluating this expression, we have assumed that the signal and noise terms are uncorrelated so that $\langle \tilde{s}(\vec{k}) \tilde{\eta}^*(\vec{k}') \rangle = \langle \tilde{\eta}(\vec{k}) \tilde{s}^*(\vec{k}') \rangle = 0$. The remaining averages are related to the Fourier transforms of the stimulus-stimulus and noise-noise correlation functions (assuming spatial stationarity in both the stimulus and the noise) by the identities

$$\langle \tilde{s}(\vec{k}) \tilde{s}^*(\vec{k}') \rangle = \tilde{Q}_{ss}(\vec{k})\delta(\vec{k} - \vec{k}') \text{ and } \langle \tilde{\eta}(\vec{k}) \tilde{\eta}^*(\vec{k}') \rangle = \tilde{Q}_{\eta\eta}(\vec{k})\delta(\vec{k} - \vec{k}'). \quad (4.46)$$

Substituting these expressions into equation 4.45 gives

$$\tilde{D}_\eta(\vec{k}) \left(\tilde{Q}_{ss}(\vec{k}) + \tilde{Q}_{\eta\eta}(\vec{k}) \right) = \tilde{Q}_{ss}(\vec{k}), \quad (4.47)$$

noise filter

which has the solution

$$\tilde{D}_\eta(\vec{k}) = \frac{\tilde{Q}_{ss}(\vec{k})}{\tilde{Q}_{ss}(\vec{k}) + \tilde{Q}_{\eta\eta}(\vec{k})}. \quad (4.48)$$

This determines both the phase and magnitude of the noise filter. Because the noise filter is designed so that its output matches the signal as closely as possible, we make the approximation of using the same whitening filter as before (equation 4.42). Combining the two, we find that

$$|\tilde{D}_s(\vec{k})| \propto \frac{\sigma_L \sqrt{\tilde{Q}_{ss}(\vec{k})}}{\tilde{Q}_{ss}(\vec{k}) + \tilde{Q}_{\eta\eta}(\vec{k})}. \quad (4.49)$$

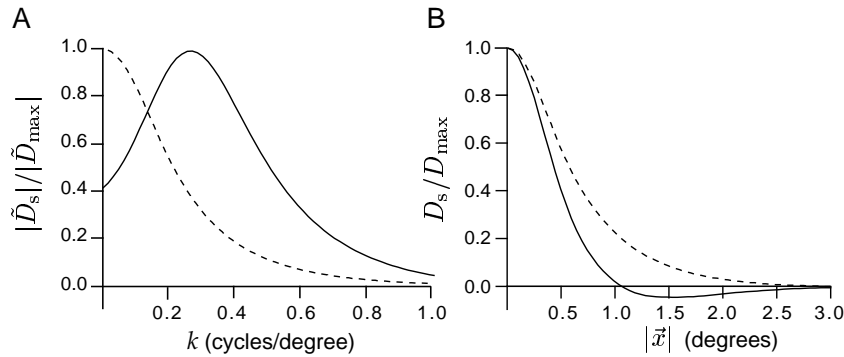


Figure 4.3: Receptive field properties predicted by entropy maximization and noise suppression of responses to natural images. A) The amplitude of the predicted Fourier-transformed linear filters for low (solid curve) and high (dashed curve) input noise. $|\tilde{D}_s(\vec{k})|$ is plotted relative to its maximum value. B) The linear kernel as a function of the distance from the center of the receptive field for low (solid curve) and high (dashed curve) input noise. Note the center-surround structure at low noise. $\tilde{D}_s(\vec{k})$ is taken to be real, and $D_s(|\vec{x}|)$ is plotted relative to its maximum value. Parameter values used were $\alpha = 0.16$ cycles/degree, $k_0 = 0.16$ cycles/degree, and $\tilde{Q}_{\eta\eta}/\tilde{Q}_{ss}(0) = 0.05$ for the low-noise case and 1 for the high-noise case.

Linear kernels resulting from equation 4.49 using equation 4.43 for the stimulus correlation function are plotted in figure 4.3. For this figure, we have assumed that the input noise is white so that $\tilde{Q}_{\eta\eta}$ is independent of \vec{k} . Both the amplitude of the Fourier transform of the kernel (figure 4.3A), and the actual spatial kernel $D_s(\vec{x})$ (figure 4.3B) are plotted under conditions of low and high noise. The linear kernels in figure 4.3B have been constructed by assuming that $\tilde{D}_s(\vec{k})$ satisfies equation 4.49 and is real, which minimizes the spatial extent of the resulting receptive field. The resulting function $D_s(\vec{x})$ is radially symmetric so it only depends on the distance $|\vec{x}|$ from the center of the receptive field to the point \vec{x} , and this radial dependence is plotted in figure 4.3B. Under low noise conditions (solid lines in figure 4.3), the linear kernel has a bandpass character and the

predicted receptive field has a center-surround structure, which matches the retinal ganglion receptive fields shown in chapter 2. This structure eliminates one major source of redundancy in natural scenes; the strong similarity of neighboring inputs owing to the predominance of low spatial frequencies in images.

When the noise level is high (dashed lines in figure 4.3), the structure of the optimal receptive field is different. In spatial frequency terms, the filter is now low-pass, and the receptive field loses its surround. This structure averages over neighboring pixels to extract the true signal obscured by the uncorrelated noise. In the retina, we expect the signal-to-noise ratio to be controlled by the level of ambient light, with low levels of illumination corresponding to the high noise case. The predicted change in the receptive fields at low illumination (high noise) matches what actually happens in the retina. At low light levels, circuitry changes within the retina remove the opposing surrounds from retinal ganglion cell receptive fields.

Temporal Processing in the LGN

Just as many aspects of the visual world vary gradually across space, natural images also tend to change slowly over time. This means that there is substantial redundancy in the succession of natural images, suggesting an opportunity for efficient temporal filtering to complement efficient spatial filtering. An analysis similar to that of the previous section can be performed to account for the temporal receptive fields of visually responsive neurons early in the visual pathway. Recall that the predicted linear temporal response is given by $L_t(t)$ as expressed in equation 4.34. The analog of equation 4.37 for temporal decorrelation and variance equalization is

$$\langle L_t(t)L_t(t') \rangle = \sigma_L^2 \delta(t - t'). \quad (4.50)$$

This is mathematically identical to equation 4.37 except that the role of the spatial variables \vec{a} and \vec{b} has been replaced by the temporal variables t and t' . The analysis proceeds exactly as above and the optimal filter is the product of a noise filter and a temporal whitening filter as before. The temporal linear kernel $D_t(\tau)$ is written in terms of its Fourier transform

$$D_t(\tau) = \frac{1}{2\pi} \int d\omega \exp(-i\omega\tau) \tilde{D}_t(\omega) \quad (4.51)$$

and $\tilde{D}_t(\omega)$ is given by an equation similar to 4.49,

$$|\tilde{D}_t(\omega)| \propto \frac{\sigma_L \sqrt{\tilde{Q}_{ss}(\omega)}}{\tilde{Q}_{ss}(\omega) + \tilde{Q}_{\eta\eta}(\omega)}. \quad (4.52)$$

In this case, $\tilde{Q}_{ss}(\omega)$ and $\tilde{Q}_{\eta\eta}(\omega)$ are the power spectra of the signal and the noise in the temporal domain.

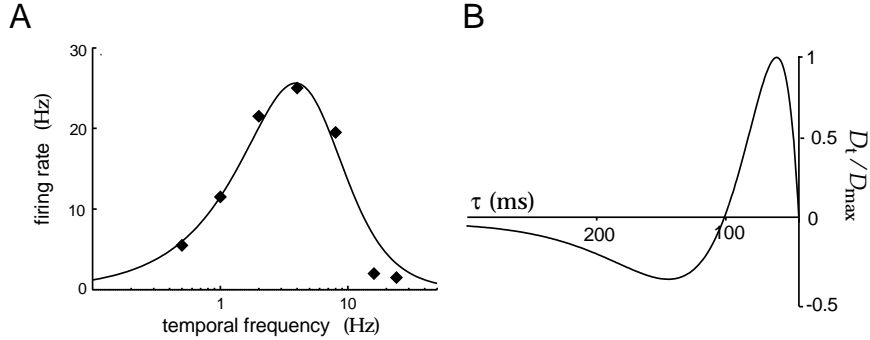


Figure 4.4: A) Predicted (curve) and actual (diamonds) selectivity of an LGN cell as a function of temporal frequency. The predicted curve is based on the optimal linear filter $\tilde{D}_t(\omega)$ with $\omega_0 = 5.5$ Hz. B) Causal, minimum phase, temporal form of the optimal filter. (Adapted from Dong and Atick, 1995; data in A from Saul and Humphrey, 1990.)

Dong and Atick (1995) analyzed temporal receptive fields in the LGN in this way under the assumption that a substantial fraction of the temporal redundancy of visual stimuli is removed in the LGN rather than in the retina. They determined that the temporal power spectrum of natural scenes has the form

$$\tilde{Q}_{ss}(\omega) \propto \frac{1}{\omega^2 + \omega_0^2} \quad (4.53)$$

where ω_0 is a constant. The resulting filter, in both the temporal frequency and time domains, is plotted in figure 4.4. Figure 4.4A shows the predicted and actual frequency responses of an LGN cell. This is similar to the plot in figure 4.3A except that the result has been normalized to a realistic response level so that it can be compared with data. Because the optimization procedure only determines the amplitude of the Fourier transform of the linear kernel, $D_t(\tau)$ is not uniquely specified. To uniquely specify the temporal kernel we require it to be causal ($D_t(\tau) = 0$ for $\tau < 0$) and impose a technical condition known as minimum phase, which assures that the output changes as rapidly as possible when the stimulus varies. Figure 4.4B shows the resulting form of the temporal filter. The space-time receptive fields shown in chapter 2 tend to change sign as a function of τ . The temporal filter in figure 4.4B has exactly this property.

An interesting test of the notion of optimal coding was carried out by Dan, Atick, and Reid (1996). They used both natural scene and white-noise stimuli while recording cat LGN cells. Figure 4.5A shows the power spectra of spike trains of cat LGN cells in response to natural scenes (the movie *Casablanca*), and figure 4.5B shows power spectra for white-noise stimuli. The power spectra of the responses to natural scenes are quite flat above about $\omega = 3$ Hz. In response to white noise, on the other hand, they rise with ω . This is exactly what we would expect if LGN cells are acting as

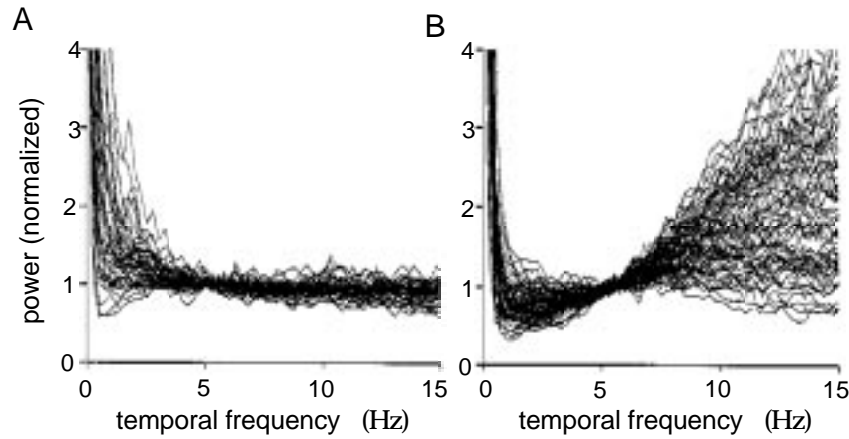


Figure 4.5: A) Power spectra of the spike trains of 51 cat LGN cells in response to presentation of the movie *Casablanca*, normalized to their own values between 5 and 6 Hz. B) Equivalently normalized power spectra of the spike trains of 75 LGN cells in response to white-noise stimuli. (Adapted from Dan et al., 1996.)

temporal whitening filters. In the case of natural stimuli, the whitening filter evenly distributes the output power over a broad frequency range. Responses to white-noise stimuli increase at high frequencies due to the boosting of inputs at these frequencies by the whitening filter.

Cortical Coding

Computational concerns beyond mere linear information transfer are likely to be relevant at the level of cortical processing of visual images. For one thing, the primary visual cortex has many more neurons than the LGN, yet they can collectively convey no more information about the visual world than they receive. As we saw in chapter 2, neurons in primary visual cortex are selective for quantities such as spatial frequency and orientation that are of particular importance in relation to object recognition but not for information transfer. Nevertheless, the methods described in the previous section can be used to understand restricted aspects of receptive fields of neurons in primary visual cortex, namely the way that the multiple selectivities are collectively assigned. For example, cells that respond best at high spatial frequencies tend to respond more to low temporal frequency components of images, and vice-versa.

The stimulus power spectrum written as a function of both spatial and temporal frequency has been estimated as

$$Q_{ss}(\vec{k}, \omega) \propto \frac{1}{|\vec{k}|^2 + \alpha^2 \omega^2} \quad (4.54)$$

where $\alpha = 0.4$ cycle seconds/degree. This correlation function decreases

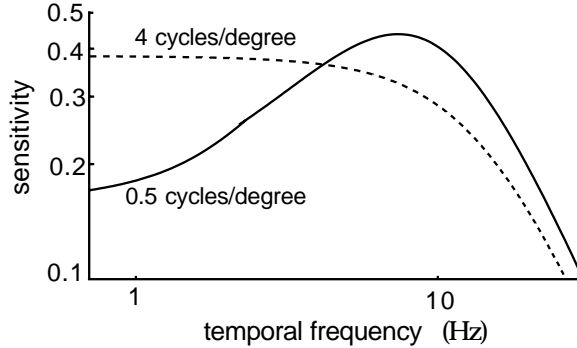


Figure 4.6: Dependence of temporal frequency tuning on preferred spatial frequency for space-time receptive fields derived from information maximization in the presence of noise. The curves show a transition from partial whitening in temporal frequency for low preferred spatial frequency (solid curve, 0.5 cycles/degree) to temporal summation for high preferred spatial frequency (dashed curve, 4 cycles/degree). (Adapted from Li, 1996.)

both for high spatial and high temporal frequencies. Figure 4.6 shows how temporal selectivity for a combined noise and whitening filter constructed using this stimulus power spectrum changes for different preferred spatial frequencies. The basic idea is that components with fairly low stimulus power are boosted by the whitening filter, while those with very low stimulus power get suppressed by the noise filter. As shown by Li (1996), if a cell is selective for high spatial frequencies, the input signal rapidly falls below the noise (treated as white) as the temporal frequency of the input is increased. As a result, the noise filter of equation 4.48 causes the temporal response to be largest at zero temporal frequency (dashed curve of figure 4.6). If instead, the cell is selective for low spatial frequencies, the signal dominates the noise up to higher temporal frequencies, and the whitening filter causes the response to increase as a function of temporal frequency up to a maximum value where the noise filter begins to suppress the response (solid curve in figure 4.6). Model receptive fields with preference for high spatial frequency thus act as low-pass temporal filters, and receptive fields with selectivity for low spatial frequency act as band-pass temporal filters.

Similar conclusions can be drawn concerning other joint selectivities. For instance, color selective (chrominance) cells tend to be selective for low temporal frequencies, because their input signal to noise ratio is lower than that for broad-band (luminance) cells. There is also an interesting predicted relationship between ocular dominance and spatial frequency tuning due to the nature of the correlations between the two eyes. Optimal receptive fields with low spatial frequency tuning (for which the input signal-to-noise ratio is high) have enhanced sensitivity to differences between inputs coming from the two eyes. Receptive fields tuned to intermediate and high spatial frequencies suppress ocular differences.

4.3 Entropy and Information for Spike Trains

Computing the entropy or information content of a neuronal response characterized by spike times is much more difficult than computing these quantities for responses described by firing rates. Nevertheless, these computations are important, because firing rates are incomplete descriptions that can lead to serious underestimates of the entropy and information. In this section, we discuss how the entropy and mutual information can be computed for spike trains. Extensive further discussion can be found in the book by Rieke et al. (1997).

Spike-train entropy calculations are typically based on the study of long-duration recordings consisting of many action potentials. The entropy or mutual information typically grows linearly with the length of the spike train being considered. For this reason, the entropy and mutual information of spike trains are reported as entropy or information rates. These are the total entropy or information divided by the duration of the spike train. We write the entropy rate as h rather than H . Alternately, entropy and mutual information can be divided by the total number of action potentials and reported as bits per spike rather than bits per second.

To compute entropy and information rates for a spike train, we need to determine the probabilities that various temporal patterns of action potentials appear. These probabilities replace the factors $P[r]$ or $p[r]$ that occur when discrete or continuous firing rates are used to characterize a neural response. The temporal pattern of a group of action potentials can be specified by listing either the individual spike times or the sequence of intervals between successive spikes. The entropy and mutual information calculations we present are based on a spike-time description, but as an initial example we consider an approximate computation of entropy using interspike intervals.

The probability of an interspike interval falling in the range between τ and $\tau + \Delta\tau$ is given in terms of the interspike interval probability density by $p[\tau]\Delta\tau$. Because the interspike interval is a continuous variable, we must specify a resolution $\Delta\tau$ with which it is measured to define the entropy. If the different interspike interval are statistically independent, the entropy associated with the interspike intervals in a spike train of average rate $\langle r \rangle$ and of duration T is the number of intervals, $\langle r \rangle T$, times the integral over τ of $-p[\tau] \log_2(p[\tau]\Delta\tau)$. The entropy rate is obtained by dividing this result by T , and the entropy per spike requires dividing by the number of spikes, $\langle r \rangle T$. The assumption of independent interspike intervals is critical for obtaining the spike-train entropy solely in terms of $p[\tau]$. Correlations between different interspike intervals reduce the total entropy, so the result obtained by assuming independent intervals provides an upper bound on the true entropy of a spike train. Thus, in general, the entropy rate h for a spike train with interspike interval distribution $p[\tau]$ and average rate $\langle r \rangle$

*entropy and
information rates*

satisfies

$$\langle h \rangle \leq -\langle r \rangle \int_0^\infty d\tau p[\tau] \log_2(p[\tau]\Delta\tau). \quad (4.55)$$

If a spike train is described by a homogeneous Poisson process with rate $\langle r \rangle$, we have $p[\tau] = \langle r \rangle \exp(-\langle r \rangle \tau)$, and the interspikes are statistically independent (chapter 1). Equation 4.55 is then an equality and, performing the integrals,

$$\langle h \rangle = \frac{\langle r \rangle}{\ln(2)} (1 - \ln(\langle r \rangle \Delta\tau)). \quad (4.56)$$

Poisson entropy rate

We now turn to a more general calculation of the spike-train entropy. To make entropy calculations practical, a long spike train is broken into statistically independent subunits, and the total entropy is written as the sum of the entropies for the individual subunits. In the case of equation 4.55, the subunit was the interspike interval. If interspike intervals are not independent and we wish to compute a result and not merely a bound, we must work with larger subunit descriptions. Strong, Koberle, de Ruyter van Steveninck, and Bialek (1998) proposed a scheme that uses spike sequences of duration T_s as these basic subunits. Note that the variable T_s is used here to denote the duration of the spike sequence being considered, while T , which is much larger than T_s , is the duration of the entire spike train.

The time that a spike occurs is a continuous variable so, as in the case of interspike intervals, a resolution must be specified when spike train entropies are computed. This can be done by dividing time into discrete bins of size Δt . We assume that the bins are small enough so that not more than one spike appears in a bin. Depending on whether or not a spike occurred within it, each bin is labeled by a zero (no spike) or a one (spike). A spike sequence defined over a block of duration T_s is thus represented by a string of $T_s/\Delta t$ zeros and ones. We denote such a sequence by $B(t)$, where B is a $T_s/\Delta t$ bit binary number, and t specifies the time of the first bin in the sequence being considered. Both T_s and t are integer multiples of the bin size Δt .

The probability of a sequence B occurring at any time during the entire response is denoted by $P[B]$. This can be obtained by counting the number of times the sequence B occurs anywhere within the spike trains being analyzed (including overlapping cases). The spike-train entropy rate implied by this distribution is

$$h = -\frac{1}{T_s} \sum_B P[B] \log_2 P[B], \quad (4.57)$$

where the sum is over all the sequences B found in the data set, and we have divided by the duration T_s of a single sequence.

If the spike sequences in non-overlapping intervals of duration T_s are independent, the full spike-train entropy rate is also given by equation 4.57. However, any correlations between successive intervals (if $B(t + T_s)$ is correlated with $B(t)$, for example) reduce the total spike-train entropy, causing equation 4.57 to overestimate the true entropy rate. Thus, for finite T_s , this equation provides an upper bound on the true entropy rate. If T_s is too small, $B(t + T_s)$ and $B(t)$ are likely to be correlated, and the overestimate may be severe. As T_s increases, we expect the correlations to get smaller, and equation 4.57 should provide a more accurate value. For any finite data set, T_s cannot be increased past a certain point, because there will not be enough spike sequences of duration T_s in the data set to determine their probabilities. Thus, in practice, T_s must be increased until the point where the extraction of probabilities becomes problematic, and some form of extrapolation to $T_s \rightarrow \infty$ must be made.

Statistical mechanics arguments suggest that the difference between the entropy for finite T_s and the true entropy for $T_s \rightarrow \infty$ should be proportional to $1/T_s$ for large T_s . Therefore, the true entropy can be estimated, as in figure 4.7, by linearly extrapolating a plot of the entropy rate versus $1/T_s$ to the point $1/T_s = 0$. In figure 4.7 (upper line), this has been done for data from the motion sensitive H1 neuron of the fly visual system. The plotted points show entropy rates computed for different values of $1/T_s$, and they vary linearly over most of the range of the plot. However, when $1/T_s$ goes below about 20/s (or $T_s = 50$ ms), the variation suddenly increases. This is the point at which the amount of data is insufficient to extract even an overestimate of the entropy. By linearly extrapolating the linear part of the series of computed points in figure 4.7, Strong et al. estimated that the H1 spike trains had an entropy rate of 157 bits/s for a resolution of $\Delta t = 3$ ms.

To compute the mutual information rate for a spike train, we must subtract the noise entropy rate from the full spike-train entropy rate. The noise entropy rate is determined from the probabilities of finding various sequences B given that they were evoked by the same stimulus. This is done by considering sequences $B(t)$ that start at a fixed time t . If the same stimulus is used in repeated trials, sequences that begin at time t in every trial are generated by the same stimulus. Therefore, the conditional probability of the response given the stimulus is, in this case, the distribution $P[B(t)]$ for response sequences beginning at the time t . This is obtained by determining the fraction of trials on which $B(t)$ was evoked. Note that $P[B(t)]$ is the probability of finding a given sequence at time t within a set of spike trains obtained on trials using the same stimulus. In contrast, $P[B]$, used in the spike-train entropy calculation, is the probability of finding the sequence B at any time within these trains. Determining $P[B(t)]$ for a sufficient number of spike sequences may take a large number of trials using the same stimulus.

The full noise entropy is computed by averaging the noise entropy at time t over all t values. The average over t plays the role of the average over

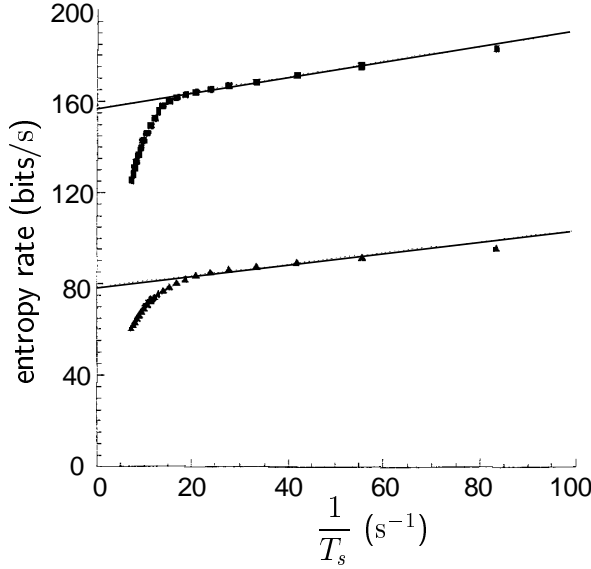


Figure 4.7: Entropy and noise entropy rates for the H1 visual neuron in the fly responding to a randomly moving visual image. The filled circles in the upper trace show the full spike-train entropy rate computed for different values of $1/T_s$. The straight line is a linear extrapolation to $1/T_s = 0$, which corresponds to $T_s \rightarrow \infty$. The lower trace shows the spike train noise entropy rate for different values of $1/T_s$. The straight line is again an extrapolation to $1/T_s = 0$. Both entropy rates increase as functions of $1/T_s$, and the true spike-train and noise entropy rates are overestimated at large values of $1/T_s$. At $1/T_s \approx 20/\text{s}$, there is a sudden shift in the dependence. This occurs when there is insufficient data to compute the spike sequence probabilities. The difference between the y intercepts of the two straight lines plotted is the mutual information rate. The resolution is $\Delta t = 3\text{ ms}$. (Adapted from Strong et al., 1998.)

stimuli in equation 4.6. The result is

$$h_{\text{noise}} = -\frac{\Delta t}{T} \sum_t \left(\frac{1}{T_s} \sum_B P[B(t)] \log_2 P[B(t)] \right) \quad (4.58)$$

where $T/\Delta t$ is the number of different t values being summed.

If equation 4.58 is based on finite-length spike sequences, it provides an upper bound on the noise entropy rate. The true noise entropy rate is estimated by performing a linear extrapolation in $1/T_s$ to $1/T_s = 0$, as was done for the spike-train entropy rate. This is done for the H1 data in figure 4.7. The result is a noise entropy of 79 bits/s for $\Delta t = 3\text{ ms}$. The information rate is obtained by taking the difference between the extrapolated values for the spike-train and noise entropy rates. The result for the fly H1 neuron used in figure 4.7, is an information rate of $157 - 79 = 78\text{ bits/s}$ or 1.8 bits/spike . Values in the range 1 to 3 bits/spike are typical results of such calculations for a variety of preparations.

Both the spike-train and noise entropy rates depend on Δt . The leading dependence, coming from the $\log_2 \Delta t$ term discussed previously, cancels in the computation of the information rate, but the information can still depend on Δt through non-divergent terms. This reflects the fact that more information can be extracted from accurately measured spike times than from poorly measured spike times. Thus, we expect the information rate to increase with decreasing Δt , at least over some range of Δt values. At some critical value of Δt that matches the natural degree of noise jitter in the spike timings, we expect the information rate to stop increasing. This value of Δt is interesting because it tells us about the degree of spike timing accuracy in neural encoding.

The information conveyed by spike trains can be used to compare responses to different stimuli and thereby reveal stimulus-specific aspects of neural encoding. For instance, Rieke, Bodnar and Bialek (1995) compared the information conveyed by single neurons in a peripheral auditory organ (the amphibian papilla) of the bullfrog in response to broad-band noise or to noise filtered to have an amplitude spectrum close to that of natural bullfrog calls (although the phases for each frequency component were chosen randomly). They determined that the cells conveyed on average 46 bits per second (1.4 bits per spike) for broad-band noise and 133 bits per second (7.8 bits per spike) for stimuli with call-like spectra, despite the fact that the broad-band noise had a higher entropy. The spike trains in response to the call-like stimuli conveyed information with near maximal efficiency.

4.4 Chapter Summary

Shannon's information theory can be used to determine how much a neural response tells both us, and presumably the animal in which the neuron lives, about a stimulus. Entropy is a measure of the uncertainty or surprise associated with a stochastic variable, such as a stimulus. Mutual information quantifies the reduction in uncertainty associated with the observation of another variable, such as a response. The mutual information is related to the Kullback-Leibler divergence between two probability distributions. We defined the response and noise entropies for probability distributions of discrete and continuous firing rates and considered how the information transmitted about a set of stimuli might be optimized. The principles of entropy and information maximization were used to account for features of the receptive fields of cells in the retina, LGN, and primary visual cortex. This analysis introduced probability factorization and equalization and whitening and noise filters. Finally, we discussed how the information conveyed about dynamic stimuli by spike sequences can be estimated.

Information theoretic principles also lie at the heart of many of the unsupervised learning methods that are discussed in chapters 8 and 10 which

suggest how to adjust synaptic weights so that single neurons or networks of neurons code their inputs in ways that come to be appropriately sensitive to the information they contain.

4.5 Appendix

Positivity of the Kullback-Leibler Divergence

The logarithm is a concave function which means that $\log_2 \langle z \rangle \geq \langle \log_2 z \rangle$, where the angle brackets denote averaging with respect to some probability distribution and z is any positive quantity. The equality holds only if z is a constant. If we consider this relation, known as Jensen's inequality, with $z = P[r]/Q[r]$ and the average defined over the probability distribution $P[r]$, we find

$$-D_{\text{KL}}(P, Q) = \sum_r P[r] \log \left(\frac{Q[r]}{P[r]} \right) \leq \log \left(\sum_r P[r] \frac{Q[r]}{P[r]} \right) = 0. \quad (4.59)$$

The last equality holds because $Q[r]$ is a probability distribution and thus satisfies $\sum_r Q[r] = 1$. The equations in 4.59 implies that $D_{\text{KL}}(P, Q) \geq 0$, with equality holding if and only if $P[r] = Q[r]$. A similar result holds for the Kullback-Leibler divergence between two probability densities,

$$D_{\text{KL}}(p, q) = \int dr p[r] \ln \left(\frac{p[r]}{q[r]} \right) \geq 0. \quad (4.60)$$

Jensen's inequality

4.6 Annotated Bibliography

Information theory was created by Shannon (see [Shannon & Weaver, 1949](#)) largely as a way of understanding communication in the face of noise. [Cover & Thomas \(1991\)](#) provide a recent review, and [Rieke et al. \(1997\)](#) give a treatment specialized to neural coding. Information theory, and theories inspired by it, such as histogram equalization, were quickly adopted in neuroscience and psychology as a way of understanding sensory transduction and coding, as discussed by [Barlow \(1961\)](#) and [Uttley \(1979\)](#). We followed a more recent set of studies, inspired by [Linkser \(1988\)](#) and [Barlow \(1989\)](#), which have particularly focused on optimal coding in early vision; [Atick & Redlich \(1990\)](#), [Plumbley \(1991\)](#), [Atick, Li & Redlich \(1992\)](#), [Atick \(1992\)](#), [van Hateren \(1992; 1993\)](#), [Li & Atick \(1994a\)](#), [Dong & Atick \(1995\)](#), and [Dan et al. \(1996\)](#). [Li & Atick \(1994b\)](#) discuss the extension to joint selectivities of cells in V1 and [Li & Atick \(1994a\)](#); [Li \(1996\)](#) treat stereo and motion sensitivities as examples.

The statistics of natural sensory inputs is reviewed by [Field \(1987\)](#). [Campbell & Gubisch \(1966\)](#) estimated the optimal modulation transfer function.

We followed the technique of Strong et al. (1998) for computing the mutual information about a dynamical stimulus in spike trains. Bialek et al. (1993) present an earlier approach based on stimulus reconstruction.

Chapter 5

Model Neurons I: Neuroelectronics

5.1 Introduction

A great deal is known about the biophysical mechanisms responsible for generating neuronal activity, and these provide a basis for constructing neuron models. Such models range from highly detailed descriptions involving thousands of coupled differential equations to greatly simplified caricatures useful for studying large interconnected networks. In this chapter, we discuss the basic electrical properties of neurons and the mathematical models by which they are described. We present a simple but nevertheless useful model neuron, the integrate-and-fire model, in a basic version and with added membrane and synaptic conductances. We also discuss the Hodgkin-Huxley model, which describes the conductances responsible for generating action potentials. In chapter 6, we continue by presenting more complex models, both in terms of their conductances and their morphology. Circuits and networks of model neurons are discussed in chapter 7. This chapter makes use of basic concepts of electrical circuit theory, which are reviewed in the Mathematical Appendix.

5.2 Electrical Properties of Neurons

Like other cells, neurons are packed with a huge number and variety of ions and molecules. A cubic micron of cytoplasm might contain, for example, 10^{10} water molecules, 10^8 ions, 10^7 small molecules such as amino acids and nucleotides, and 10^5 proteins. Many of these molecules carry charges, either positive or negative. Most of the time, there is an excess concentration of negative charge inside a neuron. Excess charges that are

mobile, like ions, repel each other and build up on the inside surface of the cell membrane. Electrostatic forces attract an equal density of positive ions from the extracellular medium to the outside surface of the membrane.

cell membrane

The cell membrane is a lipid bilayer 3 to 4 nm thick that is essentially impermeable to most charged molecules. This insulating feature causes the cell membrane to act as a capacitor by separating the charges lying along its interior and exterior surfaces. Numerous ion-conducting channels embedded in the cell membrane (figure 5.1) lower the effective membrane resistance for ion flow to a value about 10,000 times smaller than that of a pure lipid bilayer. The resulting membrane conductance depends on the density and types of ion channels. A typical neuron may have a dozen or more different types of channels, anywhere from a few to hundreds of channels in a square micron of membrane, and hundreds of thousands to millions of channels in all. Many, but not all, channels are highly selective, allowing only a single type of ion to pass through them (to an accuracy of about 1 ion in 10^4). The capacity of channels for conducting ions across the cell membrane can be modified by many factors including the membrane potential (voltage-dependent channels), the internal concentration of various intracellular messengers (Ca^{2+} -dependent channels, for example), and the extracellular concentration of neurotransmitters or neuromodulators (synaptic receptor channels, for example). The membrane also contains selective pumps that expend energy to maintain differences in the concentrations of ions inside and outside the cell.

ion channels

channel selectivity

ion pumps

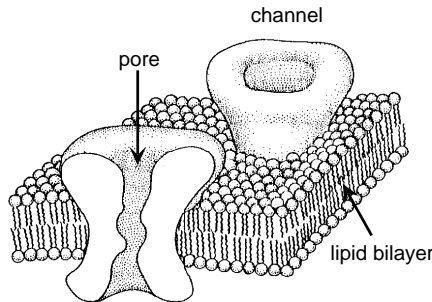


Figure 5.1: A schematic diagram of a section of the lipid bilayer that forms the cell membrane with two ion channels embedded in it. The membrane is 3 to 4 nm thick and the ion channels are about 10 nm long. (Adapted from Hille, 1992.)

membrane potential

By convention, the potential of the extracellular fluid outside a neuron is defined to be zero. When a neuron is inactive, the excess internal negative charge causes the potential inside the cell membrane to be negative. This potential is an equilibrium point at which the flow of ions into the cell matches that out of the cell. The potential can change if the balance of ion flow is modified by the opening or closing of ion channels. Under normal conditions, neuronal membrane potentials vary over a range from about -90 to +50 mV. The order of magnitude of these potentials can be estimated from basic physical principles.

Membrane potentials are small enough to allow neurons to take advantage of thermal energy to help transport ions across the membrane, but are large enough so that thermal fluctuations do not swamp the signaling capabilities of the neuron. These conditions imply that potential differences across the cell membrane must lie in a range so that the energy gained or lost by an ion traversing the membrane is the same order of magnitude as its thermal energy. The thermal energy of an ion is about $k_B T$ where k_B is the Boltzmann constant and T is the temperature on an absolute Kelvin scale. For chemists and biologists (though not for physicists), it is more customary to discuss moles of ions rather than single ions. A mole of ions has Avagadro's number times as much thermal energy as a single ion, or RT , where R is the universal gas constant, equal to 8.31 joules/mol K° = 1.99 cal/mol K°. RT is about 2500 joules/mol or 0.6 kCal/mol at normal temperatures. To estimate the size of typical membrane potentials, we equate this to the energy gained or lost when a mole of ions crosses a membrane with a potential difference V_T across it. This energy is FV_T where F is the Faraday constant, $F = 96,480$ Coulombs/mol, equal to Avagadro's number times the charge of a single proton, q . Setting $FV_T = RT$ gives

$$V_T = \frac{RT}{F} = \frac{k_B T}{q}. \quad (5.1)$$

This is an important parameter that enters into a number of calculations. V_T is between 24 and 27 mV for the typical temperatures of cold and warm-blooded animals. This sets the overall scale for membrane potentials across neuronal membranes, which range from about -3 to +2 times V_T .

 V_T

Intracellular Resistance

Membrane potentials measured at different places within a neuron can take different values. For example, the potentials in the soma, dendrite, and axon can all be different. Potential differences between different parts of a neuron cause ions to flow within the cell, which tends to equalize these differences. The intracellular medium provides a resistance to such flow. This resistance is highest for long and narrow stretches of dendritic or axonal cable, such as the segment shown in figure 5.2. The longitudinal current I_L flowing along such a cable segment can be computed from Ohm's law. For the cylindrical segment of dendrite shown in figure 5.2, the longitudinal current flowing from right to left satisfies $V_2 - V_1 = I_L R_L$. Here, R_L is the longitudinal resistance, which grows in proportion to the length of the segment (long segments have higher resistances than short ones) and is inversely proportional to the cross-sectional area of the segment (thin segments have higher resistances than fat ones). The constant of proportionality is called the intracellular resistivity, r_L , and it typically falls in a range from 1 to 3 kΩ·mm. The longitudinal resistance of the segment in figure 5.2 is r_L times the length L divided by the cross-sectional

longitudinal current I_L *longitudinal resistance R_L* *intracellular resistivity r_L*

area πa^2 , $R_L = r_L L / \pi a^2$. A segment 100 μm long with a radius of 2 μm has a longitudinal resistance of about 8 $\text{M}\Omega$. A voltage difference of 8 mV would be required to force 1 nA of current down such a segment.

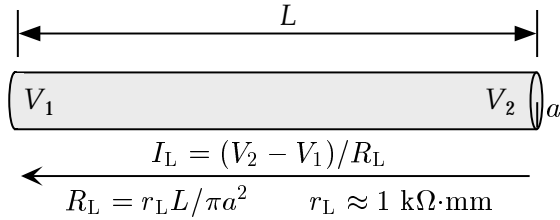


Figure 5.2: The longitudinal resistance of a cylindrical segment of neuronal cable with length L and radius a . The difference between the membrane potentials at either end of this segment is related to the longitudinal current within the segment by Ohm's law, with R_L the longitudinal resistance of the segment. The arrow indicates the direction of positive current flow. The constant r_L is the intracellular resistivity, and a typical value is given.

We can also use the intracellular resistivity to estimate crudely the conductance of a single channel. The conductance, being the inverse of a resistance, is equal to the cross-sectional area of the channel pore divided by its length and by r_L . We approximate the channel pore as a tube of length 6 nm and opening area 0.15 nm^2 . This gives an estimate of $0.15 \text{ nm}^2 / (1 \text{ k}\Omega \text{ mm} \times 6 \text{ nm}) \approx 25 \text{ pS}$, which is the right order of magnitude for a channel conductance.

Membrane Capacitance and Resistance

The intracellular resistance to current flow can cause substantial differences in the membrane potential measured in different parts of a neuron, especially during rapid transient excursions of the membrane potential from its resting value, such as action potentials. Neurons that have few of the long and narrow cable segments that produce high longitudinal resistance may have relatively uniform membrane potentials across their surfaces. Such neurons are termed electrotonically compact. For electrotonically compact neurons, or for less compact neurons in situations where spatial variations in the membrane potential are not thought to play an important functional role, the entire neuron may be adequately described by a single membrane potential. Here, we discuss the membrane capacitance and resistance using such a description. An analysis for the case of spatially varying membrane potentials is presented in chapter 6.

We have mentioned that there is typically an excess negative charge on the inside surface of the cell membrane of a neuron, and a balancing positive charge on its outside surface (figure 5.3). In this arrangement, the cell membrane creates a capacitance C_m , and the voltage across the mem-

single-channel conductance

electrotonic compactness

membrane capacitance C_m

brane V and the amount of this excess charge Q are related by the standard equation for a capacitor, $Q = C_m V$. The membrane capacitance is proportional to the total amount of membrane or, equivalently, to the surface area of the cell. The constant of proportionality, called the specific membrane capacitance, is the capacitance per unit area of membrane, and is approximately the same for all neurons, $c_m \approx 10 \text{ nF/mm}^2$. The total capacitance C_m is the membrane surface area A times the specific capacitance, $C_m = c_m A$. Neuronal surface areas tend to be in the range 0.01 to 0.1 mm^2 , so the membrane capacitance for a whole neuron is typically 0.1 to 1 nF. For a neuron with a total membrane capacitance of 1 nF, $7 \times 10^{-11} \text{ C}$ or about 10^9 singly charged ions are required to produce a resting potential of -70 mV. This is about a hundred-thousandth of the total number of ions in a neuron and is the amount of charge delivered by a 0.7 nA current in 100 ms.

*specific membrane
capacitance c_m*

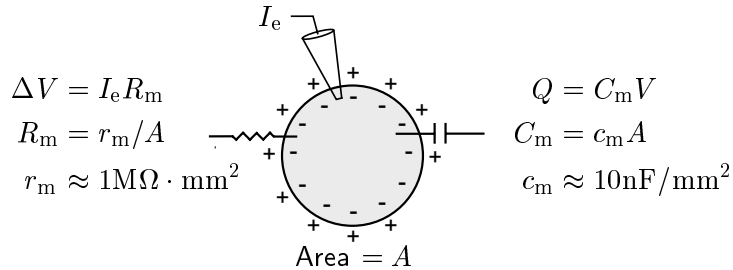


Figure 5.3: The capacitance and membrane resistance of a neuron considered as a single compartment. The membrane capacitance determines how the membrane potential V and excess internal charge Q are related. The membrane resistance R_m determines the size of the membrane potential deviation ΔV caused by a small current I_e entering through an electrode, for example. Equations relating the total membrane capacitance and resistance, C_m and R_m , to the specific membrane capacitance and resistance, c_m and r_m , are given along with typical values of c_m and r_m . The value of r_m may vary considerably under different conditions and for different neurons.

We can use the membrane capacitance to determine how much current is required to change the membrane potential at a given rate. The time derivative of the basic equation relating the membrane potential and charge,

$$C_m \frac{dV}{dt} = \frac{dQ}{dt}, \quad (5.2)$$

plays an important role in the mathematical modeling of neurons. The time derivative of the charge dQ/dt is equal to the current passing into the cell, so the amount of current needed to change the membrane potential of a neuron with a total capacitance C_m at a rate dV/dt is $C_m dV/dt$. For example, 1 nA will change the membrane potential of a neuron with a capacitance of 1 nF at a rate of 1 mV/ms.

membrane resistance R_m

The capacitance of a neuron determines how much current is required to make the membrane potential change at a given rate. Holding the membrane potential steady at a level different from its resting value also requires current, but this current is determined by the membrane resistance rather than by the capacitance of the cell. For example, if a small constant current I_e is injected into a neuron through an electrode, as in figure 5.3, the membrane potential will shift away from its resting value by an amount ΔV given by Ohm's law, $\Delta V = I_e R_m$. R_m is known as the membrane or input resistance. The restriction to small currents and small ΔV is required because membrane resistances can vary as a function of voltage, whereas Ohm's law assumes R_m is constant over the range ΔV .

membrane conductance

The membrane resistance is the inverse of the membrane conductance, and, like the capacitance, the conductance of a piece of cell membrane is proportional to its surface area. The constant of proportionality is the membrane conductance per unit area, but we write it as $1/r_m$, where r_m is called the specific membrane resistance. Conversely, the membrane resistance R_m is equal to r_m divided by the surface area. When a neuron is in a resting state, the specific membrane resistance is around $1 \text{ M}\Omega \cdot \text{mm}^2$. This number is much more variable than the specific membrane capacitance. Membrane resistances vary considerably among cells and under different conditions and at different times for a given neuron, depending on the number, type, and state of its ion channels. For total surface areas between 0.01 and 0.1 mm, the membrane resistance is typically in the range 10 to $100 \text{ M}\Omega$. With a $100 \text{ M}\Omega$ membrane resistance, a constant current of 0.1 nA is required to hold the membrane potential 10 mV away from its resting value.

membrane time constant τ_m

The product of the membrane capacitance and the membrane resistance is a quantity with the units of time called the membrane time constant, $\tau_m = R_m C_m$. Because C_m and R_m have inverse dependences on the membrane surface area, the membrane time constant is independent of area and equal to the product of the specific membrane capacitance and resistance, $\tau_m = r_m c_m$. The membrane time constant sets the basic time scale for changes in the membrane potential and typically falls in the range between 10 and 100 ms.

Equilibrium and Reversal Potentials

Electric forces and diffusion are responsible for driving ions through channel pores. Voltage differences between the exterior and interior of the cell produce forces on ions. Negative membrane potentials attract positive ions into the neuron and repel negative ions. In addition, ions diffuse through channels because the ion concentrations differ inside and outside the neuron. These differences are maintained by the ion pumps within the cell membrane. The concentrations of Na^+ and Ca^{2+} are higher outside the cell than inside, so these ions are driven into the neuron by diffusion. K^+

is more concentrated inside the neuron than outside, so it tends to diffuse out of the cell.

It is convenient to characterize the current flow due to diffusion in terms of an equilibrium potential. This is defined as the membrane potential at which current flow due to electric forces cancels the diffusive flow. For channels that conduct a single type of ion, the equilibrium potential can be computed easily. The potential difference across the cell membrane biases the flow of ions into or out of a neuron. Consider, for example, a positively charged ion and a negative membrane potential. In this case, the membrane potential opposes the flow of ions out of the the cell. Ions can only cross the membrane and leave the interior of the cell if they have sufficient thermal energy to overcome the energy barrier produced by the membrane potential. If the ion has an electric charge zq where q is the charge of one proton, it must have a thermal energy of at least $-zqV$ to cross the membrane (this is a positive energy for $z > 0$ and $V < 0$). The probability that an ion has a thermal energy greater than or equal to $-zqV$, when the temperature (on an absolute scale) is T , is $\exp(zqV/k_B T)$. This is determined by integrating the Boltzmann distribution for energies greater than or equal to $-zqV$. In molar units, this result can be written as $\exp(zFV/RT)$, which is equal to $\exp(zV/V_T)$ by equation 5.1.

equilibrium potential

The biasing effect of the electrical potential can be overcome by an opposing concentration gradient. A concentration of ions inside the cell, [inside], that is sufficiently greater than the concentration outside the cell, [outside], can compensate for the Boltzmann probability factor. The rate at which ions flow into the cell is proportional to [outside]. The flow of ions out of the cell is proportional to [inside] times the Boltzmann factor, because in this direction only those ions that have sufficient thermal energy can leave the cell. The net flow of ions will be zero when the inward and outward flows are equal. We use the letter E to denote the particular potential that satisfies this balancing condition, which is then

$$[\text{outside}] = [\text{inside}] \exp(zE/V_T). \quad (5.3)$$

Solving this equation for E , we find

$$E = \frac{V_T}{z} \ln\left(\frac{[\text{outside}]}{[\text{inside}]}\right). \quad (5.4)$$

Nernst equation

Equation 5.4 is the Nernst equation. The reader can check that, if the result is derived for either sign of ionic charge or membrane potential, the result is identical to 5.4, which thus applies in all cases. Equilibrium potentials for K^+ channels, labeled E_K , typically fall in the range between -70 and -90 mV. Na^+ equilibrium potentials, E_{Na} , are 50 mV or higher, and E_{Ca} for Ca^{2+} channels is higher still, around 150 mV. Finally, Cl^- equilibrium potentials are typically around -60 to -65 mV, near the resting potential of many neurons.

The Nernst equation (5.4) applies when the channels that generate a particular conductance allow only one type of ion to pass through them. Some

*Goldman equation
reversal potential*

channels are not so selective, and in this case the potential E is not determined by equation 5.4, but rather takes a value intermediate between the equilibrium potentials of the individual ion types that it conducts. An approximate formula known as the Goldman equation (see Tuckwell, 1988; or Johnston and Wu, 1995) can be used to estimate E for such conductances. In this case, E is often called a reversal potential, rather than an equilibrium potential, because the direction of current flow through the channel switches as the membrane potential passes through E .

depolarization

A conductance with an equilibrium or reversal potential E tends to move the membrane potential of the neuron toward the value E . When $V > E$ this means that positive current will flow outward, and when $V < E$ positive current will flow inward. Because Na^+ and Ca^{2+} conductances have positive reversal potentials, they tend to depolarize a neuron (make its membrane potential less negative). K^+ conductances, with their negative E values, normally hyperpolarize a neuron (make its membrane potential more negative). Cl^- conductances with reversal potentials near the resting potential, may pass little net current. Instead, their primary impact is to change the membrane resistance of the cell. Such conductances are sometimes called shunting, although all conductances ‘shunt’, that is, increase the total conductance of a neuron. Synaptic conductances are also characterized by reversal potentials and are termed excitatory or inhibitory on this basis. Synapses with reversal potentials less than the threshold for action potential generation are typically called inhibitory, while those with more depolarizing reversal potentials are called excitatory.

hyperpolarization

*shunting
conductances*

*inhibitory and
excitatory synapses*

*membrane current
per unit area i_m*

*driving force
conductance per
unit area g_i*

The Membrane Current

The total current flowing across the membrane through all of its ion channels is called the membrane current of the neuron. By convention, the membrane current is defined as positive when positive ions leave the neuron and negative when positive ions enter the neuron. The total membrane current is determined by summing currents due to all of the different types of channels within the cell membrane, including voltage-dependent and synaptic channels. To facilitate comparisons between neurons of different sizes, it is convenient to use the membrane current per unit area of cell membrane, which we call i_m . The total membrane current is obtained from i_m by multiplying it by A the total surface area of the cell.

We label the different types of channels in a cell membrane with an index i . As discussed in the last section, the current carried by a set of channels of type i with reversal potential E_i , vanishes when the membrane potential satisfies $V = E_i$. For many types of channels, the current increases or decreases approximately linearly when the membrane potential deviates from this value. The difference $V - E_i$ is called the driving force, and the membrane current per unit area due to the type i channels is written as $g_i(V - E_i)$. The factor g_i is the conductance per unit area due to these

channels. Summing over the different types of channels, we obtain the total membrane current

$$i_m = \sum_i g_i(V - E_i). \quad (5.5)$$

Sometimes a more complicated expression called the Goldman-Hodgkin-Katz formula is used to relate the membrane current to g_i and membrane potential (see Tuckwell, 1988; or Johnston and Wu, 1995), but we will restrict our discussion to the simpler relationship used in equation 5.5.

Much of the complexity and richness of neuronal dynamics arises because membrane conductances change over time. However, some of the factors that contribute to the total membrane current can be treated as relatively constant, and these are typically grouped together into a single term called the leakage current. The currents carried by ion pumps that maintain the concentration gradients that make equilibrium potentials nonzero typically fall into this category. For example, one type of pump uses the energy of ATP hydrolysis to move three Na^+ ions out of the cell for every two K^+ ions it moves in. It is normally assumed that these pumps work at relatively steady rates so that the currents they generate can be included in a time-independent leakage conductance. Sometimes, this assumption is dropped and explicit pump currents are modeled. In either case, all of the time-independent contributions to the membrane current can be lumped together into a single leakage term $\bar{g}_L(V - E_L)$. Because this term hides many sins, its reversal potential E_L is not usually equal to the equilibrium potential of any specific ion. Instead it is often kept as a free parameter and adjusted to make the resting potential of the model neuron match that of the cell being modeled. Similarly, \bar{g}_L is adjusted to match the membrane conductance at rest. The line over the parameter \bar{g}_L is used to indicate that it has constant value. A similar notation is used later in this chapter to distinguish variable conductances from the fixed parameters that describe them. The leakage conductance is called a passive conductance to distinguish it from variable conductances that are termed active.

membrane current

leakage current

resting potential

5.3 Single-Compartment Models

Models that describe the membrane potential of a neuron by a single variable V are called single-compartment models. This chapter deals exclusively with such models. Multi-compartment models, which can describe spatial variations in the membrane potential, are considered in chapter 6. The equations for single-compartment models, like those of all neuron models, describe how charges flow into and out of a neuron and affect its membrane potential.

Equation 5.2 provides the basic relationship that determines the membrane potential for a single-compartment model. This equation states that the rate of change of the membrane potential is proportional to the rate

single-compartment model

at which charge builds up inside the cell. The rate of charge buildup is, in turn, equal to the total amount of current entering the neuron. The relevant currents are those arising from all the membrane and synaptic conductances plus, in an experimental setting, any current injected into the cell through an electrode. From equation 5.2, the sum of these currents is equal to $C_m dV/dt$, the total capacitance of the neuron times the rate of change of the membrane potential. Because the membrane current is usually characterized as a current per unit area, i_m , it is more convenient to divide this relationship by the surface area of the neuron. Then, the total current per unit area is equal to $c_m dV/dt$, where $c_m = C_m/A$ is the specific membrane capacitance. One complication in this procedure is that the electrode current, I_e is not typically expressed as a current per unit area, so we must divide it by the total surface area of the neuron, A . Putting all this together, the basic equation for all single-compartment models is

$$c_m \frac{dV}{dt} = -i_m + \frac{I_e}{A}. \quad (5.6)$$

By convention, current that enters the neuron through an electrode is defined as positive-inward, whereas membrane current is defined as positive-outward. This explains the different signs for the currents in equation 5.6. The membrane current in equation 5.6 is determined by

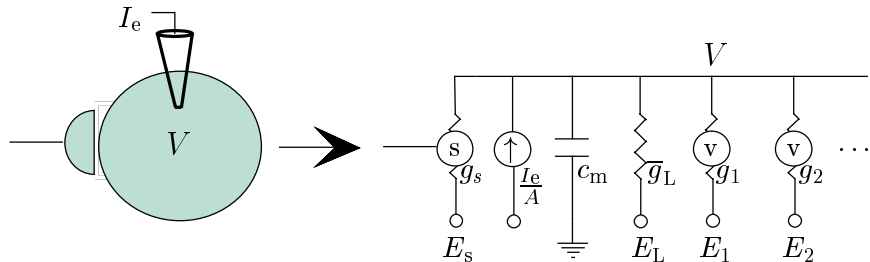


Figure 5.4: The equivalent circuit for a one-compartment neuron model. The neuron is represented, at the left, by a single compartment of surface area A with a synapse and a current injecting electrode. At right is the equivalent circuit. The circled (s) indicates a synaptic conductance that depends on the activity of a presynaptic neuron. A single synaptic conductance g_s is indicated, but, in general, there may be several different types. The circled (v) indicates a voltage-dependent conductance, and I_e is the current passing through the electrode, The dots stand for possible additional membrane conductances.

equivalent circuit

equation 5.5 and additional equations that specify the conductance variables g_i . The structure of such a model is the same as that of an electrical circuit, called the equivalent circuit, consisting of a capacitor and a set of variable and non-variable resistors corresponding to the different membrane conductances. Figure 5.4 shows the equivalent circuit for a generic one-compartment model.

5.4 Integrate-and-Fire Models

A neuron will typically fire an action potential when its membrane potential reaches a threshold value of about -55 to -50 mV. During the action potential, the membrane potential follows a rapid stereotyped trajectory and then returns to a value that is hyperpolarized relative to the threshold potential. As we will see, the mechanisms by which voltage-dependent K⁺ and Na⁺ conductances produce action potentials are well-understood and can be modeled quite accurately. On the other hand, neuron models can be simplified and simulations can be accelerated dramatically if the biophysical mechanisms responsible for action potentials are not explicitly included in the model. Integrate-and-fire models do this by stipulating that an action potential occurs whenever the membrane potential of the model neuron reaches a threshold value V_{th} . After the action potential, the potential is reset to a value V_{reset} below the threshold potential, $V_{\text{reset}} < V_{\text{th}}$.

*integrate and fire
model*

The basic integrate-and-fire model was proposed by Lapicque in 1907, long before the mechanisms that generate action potentials were understood. Despite its age and simplicity, the integrate-and-fire model is still an extremely useful description of neuronal activity. By avoiding a biophysical description of the action potential, integrate-and-fire models are left with the simpler task of modeling only subthreshold membrane potential dynamics. This can be done with various levels of rigor. In the simplest version of these models, all active membrane conductances are ignored, including, for the moment, synaptic inputs, and the entire membrane conductance is modeled as a single passive leakage term, $i_m = \bar{g}_L(V - E_L)$. This version is called the passive or leaky integrate-and-fire model. For small fluctuations about the resting membrane potential, neuronal conductances are approximately constant, and the passive integrate-and-fire model assumes that this constancy holds over the entire subthreshold range. For some neurons this is a reasonable approximation, and for others it is not. With these approximations, the model neuron behaves like an electric circuit consisting of a resistor and a capacitor in parallel (figure 5.4), and the membrane potential is determined by equation 5.6 with $i_m = \bar{g}_L(V - E_L)$,

$$c_m \frac{dV}{dt} = -\bar{g}_L(V - E_L) + \frac{I_e}{A}. \quad (5.7)$$

It is convenient to multiply equation 5.7 by the specific membrane resistance r_m , which in this case is given by $r_m = 1/\bar{g}_L$. This cancels the factor of \bar{g}_L on the right side of the equation and leaves a factor $c_m r_m = \tau_m$ on the left side, where τ_m is the membrane time constant of the neuron. The electrode current ends up being multiplied by r_m/A which is the total membrane resistance R_m . Thus, the basic equation of the passive integrate-and-fire models is

$$\tau_m \frac{dV}{dt} = E_L - V + R_m I_e. \quad (5.8)$$

*passive
integrate-and-fire
model*

To generate action potentials in the model, equation 5.8 is augmented by the rule that whenever V reaches the threshold value V_{th} , an action potential is fired and the potential is reset to V_{reset} . Equation 5.8 indicates that when $I_e = 0$, the membrane potential relaxes exponentially with time constant τ_m to $V = E_L$. Thus, E_L is the resting potential of the model cell.

The membrane potential for the passive integrate-and-fire model is determined by integrating equation 5.8 (a numerical method for doing this is described in appendix A) and applying the threshold and reset rule for action potential generation. The response of a passive integrate-and-fire model neuron to a time-varying electrode current is shown in figure 5.5.

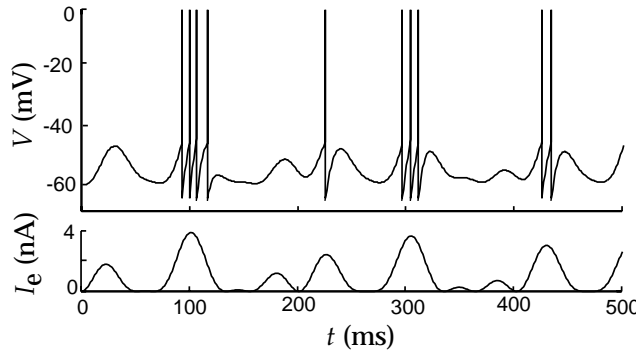


Figure 5.5: A passive integrate-and-fire model driven by a time-varying electrode current. The upper trace is the membrane potential and the bottom trace the driving current. The action potentials in this figure are simply pasted onto the membrane potential trajectory whenever it reaches the threshold value. The parameters of the model are $E_L = V_{\text{reset}} = -65$ mV, $V_{\text{th}} = -50$ mV, $\tau_m = 10$ ms, and $R_m = 10$ MΩ.

The firing rate of an integrate-and-fire model in response to a constant injected current can be computed analytically. When I_e is independent of time, the subthreshold potential $V(t)$ can easily be computed by solving equation 5.8 and is

$$V(t) = E_L + R_m I_e + (V(0) - E_L - R_m I_e) \exp(-t/\tau_m) \quad (5.9)$$

where $V(0)$ is the value of V at time $t = 0$. This solution can be checked simply by substituting it into equation 5.8. It is valid for the integrate-and-fire model only as long as V stays below the threshold. Suppose that at $t = 0$, the neuron has just fired an action potential and is thus at the reset potential, so that $V(0) = V_{\text{reset}}$. The next action potential will occur when the membrane potential reaches the threshold, that is, at a time $t = t_{\text{isi}}$ when

$$V(t_{\text{isi}}) = V_{\text{th}} = E_L + R_m I_e + (V_{\text{reset}} - E_L - R_m I_e) \exp(-t_{\text{isi}}/\tau_m). \quad (5.10)$$

By solving this for t_{isi} , the time of the next action potential, we can determine the interspike interval for constant I_e , or equivalently its inverse,

which we call the interspike-interval firing rate of the neuron,

$$r_{\text{isi}} = \frac{1}{t_{\text{isi}}} = \left[\tau_m \ln \left(\frac{R_m I_e + E_L - V_{\text{reset}}}{R_m I_e + E_L - V_{\text{th}}} \right) \right]^{-1}. \quad (5.11)$$

This expression is valid if $R_m I_e > V_{\text{th}} - E_L$, otherwise $r_{\text{isi}} = 0$. For sufficiently large values of I_e , we can use the linear approximation of the logarithm ($\ln(1 + z) \approx z$ for small z) to show that

$$r_{\text{isi}} \approx \left[\frac{E_L - V_{\text{th}} + R_m I_e}{\tau_m (V_{\text{th}} - V_{\text{reset}})} \right]_+, \quad (5.12)$$

which shows that the firing rate grows linearly with I_e for large I_e .

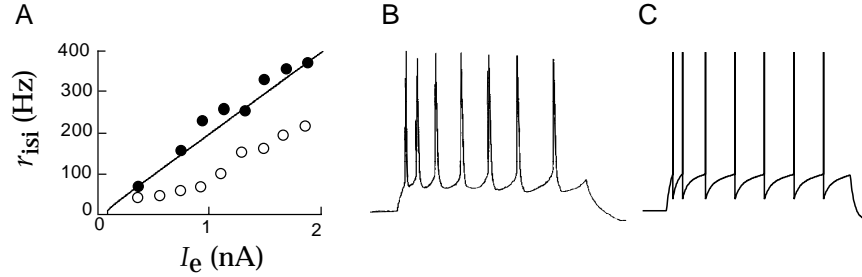


Figure 5.6: A) Comparison of interspike-interval firing rates as a function of injected current for an integrate-and-fire model and a cortical neuron measure *in vivo*. The line gives r_{isi} for a model neuron with $\tau_m = 30$ ms, $E_L = V_{\text{reset}} = -65$ mV, $V_{\text{th}} = -50$ mV and $R_m = 90$ MΩ. The data points are from a pyramidal cell in the primary visual cortex of a cat. The filled circles show the inverse of the interspike interval for the first two spikes fired, while the open circles show the steady-state interspike-interval firing rate after spike-rate adaptation. B) A recording of the firing of a cortical neuron under constant current injection showing spike-rate adaptation. C) Membrane voltage trajectory and spikes for an integrate-and-fire model with an added current with $r_m \Delta g_{\text{sra}} = 0.06$, $\tau_{\text{sra}} = 100$ ms, and $E_K = -70$ mV (see equations 5.13 and 5.14). (Data in A from Ahmed et al., 1998, B from McCormick, 1990.)

Figure 5.6A compares r_{isi} as a function of I_e , using appropriate parameter values, with data from current injection into a cortical neuron *in vivo*. The firing rate of the cortical neuron in figure 5.6A has been defined as the inverse of the interval between pairs of spikes. The rates determined in this way using the first two spikes fired by the neuron in response to the injected current (filled circles in figure 5.6A) agree fairly well with the results of the integrate-and-fire model with the parameters given in the figure caption. However, the real neuron exhibits spike-rate adaptation, in that the interspike intervals lengthen over time when a constant current is injected into the cell (figure 5.6B) before settling to a steady-state value. The steady-state firing rate in figure 5.6A (open circles) could also be fit by an integrate-and-fire model, but not using the same parameters as were used to fit the initial spikes. Spike-rate adaptation is a common feature of

spike-rate adaptation

cortical pyramidal cells, and consideration of this phenomenon allows us to show how an integrate-and-fire model can be modified to incorporate more complex dynamics.

Spike-Rate Adaptation and Refractoriness

The passive integrate-and-fire model that we have described thus far is based on two separate approximations, a highly simplified description of the action potential and a linear approximation for the total membrane current. If details of the action potential generation process are not important for a particular modeling goal, the first approximation can be retained while the membrane current is modeled in as much detail as is necessary. We will illustrate this process by developing a heuristic description of spike-rate adaptation using a model conductance that has characteristics similar to measured neuronal conductances known to play important roles in producing this effect.

We model spike-rate adaptation by including an additional current in the model,

$$\tau_m \frac{dV}{dt} = E_L - V - r_m g_{sra}(V - E_K) + R_m I_e . \quad (5.13)$$

The spike-rate adaptation conductance g_{sra} has been modeled as a K^+ conductance so, when activated, it will hyperpolarize the neuron, slowing any spiking that may be occurring. We assume that this conductance relaxes to zero exponentially with time constant τ_{sra} through the equation

$$\tau_{sra} \frac{dg_{sra}}{dt} = -g_{sra} . \quad (5.14)$$

Whenever the neuron fires a spike, g_{sra} is increased by an amount Δg_{sra} , that is, $g_{sra} \rightarrow g_{sra} + \Delta g_{sra}$. During repetitive firing, the current builds up in a sequence of steps causing the firing rate to adapt. Figures 5.6B and 5.6C compare the adapting firing pattern of a cortical neuron with the output of the model.

As discussed in chapter 1, the probability of firing for a neuron is significantly reduced for a short period of time after the appearance of an action potential. Such a refractory effect is not included in the basic integrate-and-fire model. The simplest way of including an absolute refractory period in the model is to add a condition to the basic threshold crossing rule forbidding firing for a period of time immediately after a spike. Refractoriness can be incorporated in a more realistic way by adding a conductance similar to the spike-rate adaptation conductance discussed above, but with a faster recovery time and a larger conductance increment following an action potential. With a large increment, the current can essentially clamp the neuron to E_K following a spike, temporarily preventing further firing and producing an absolute refractory period. As this conductance relaxes

back to zero, firing will be possible but initially less likely, producing a relative refractory period. When recovery is completed, normal firing can resume. Another scheme that is sometimes used to model refractory effects is to raise the threshold for action potential generation following a spike and then to allow it to relax back to its normal value. Spike-rate adaptation can also be described by using an integrated version of the integrate-and-fire model known as the spike-response model in which membrane potential wave forms are determined by summing pre-computed postsynaptic potentials and after-spike hyperpolarizations. Finally, spike-rate adaptation and other effects can be incorporated into the integrate-and-fire framework by allowing the parameters \bar{g}_L and E_L in equation 5.7 to vary with time.

5.5 Voltage-Dependent Conductances

Most of the interesting electrical properties of neurons, including their ability to fire and propagate action potentials, arise from nonlinearities associated with active membrane conductances. Recordings of the current flowing through single channels indicate that channels fluctuate rapidly between open and closed states in a stochastic manner (figure 5.7). Models of membrane and synaptic conductances must describe how the probability that a channel is in an open, ion-conducting state at any given time depends on the membrane potential (for a voltage-dependent conductance), the presence or absence of a neurotransmitter (for a synaptic conductance), or a number of other factors such as the concentration of Ca^{2+} or other messenger molecules inside the cell. In this chapter, we consider two classes of active conductances, voltage-dependent membrane conductances and transmitter-dependent synaptic conductances. An additional type, the Ca^{2+} -dependent conductance, is considered in chapter 6.

*stochastic channel
voltage-dependent,
synaptic, and
 Ca^{2+} -dependent
conductances*

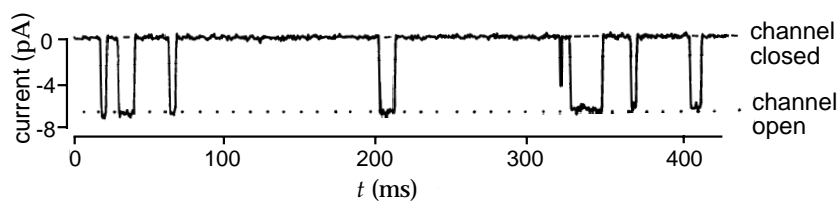


Figure 5.7: Recording of the current passing through a single ion channel. This is a synaptic receptor channel sensitive to the neurotransmitter acetylcholine. A small amount of acetylcholine was applied to the preparation to produce occasional channel openings. In the open state, the channel passes 6.6 pA at a holding potential of -140 mV. This is equivalent to more than 10^7 charges per second passing through the channel and corresponds to an open channel conductance of 47 pS. (From Hille, 1992.)

In a later section of this chapter, we discuss stochastic models of individual channels based on state diagrams and transition rates. However, most neuron models use deterministic descriptions of the conductances arising from many channels of a given type. This is justified because of the large number of channels of each type in the cell membrane of a typical neuron. If large numbers of channels are present, and if they act independently of each other (which they do, to a good approximation), then, from the law of large numbers, the fraction of channels open at any given time is approximately equal to the probability that any one channel is in an open state. This allows us to move between single-channel probabilistic formulations and macroscopic deterministic descriptions of membrane conductances.

We have denoted the conductance per unit area of membrane due to a set of ion channels of type i by g_i . The value of g_i at any given time is determined by multiplying the conductance of an open channel by the density of channels in the membrane and by the fraction of channels that are open at that time. The product of the first two factors is a constant called the maximal conductance and denoted by \bar{g}_i . It is the conductance per unit area of membrane if all the channels of type i are open. Maximal conductance parameters tend to range from $\mu\text{S}/\text{mm}^2$ to mS/mm^2 . The fraction of channels in the open state is equivalent to the probability of finding any given channel in the open state, and it is denoted by P_i . Thus, $g_i = \bar{g}_i P_i$. The dependence of a conductance on voltage, transmitter concentration, or other factors arises through effects on the open probability.

The open probability of a voltage-dependent conductance depends, as its name suggests, on the membrane potential of the neuron. In this chapter, we discuss models of two such conductances, the so-called delayed-rectifier K^+ and fast Na^+ conductances. The formalism we present, which is almost universally used to describe voltage-dependent conductances, was developed by Hodgkin and Huxley (1952) as part of their pioneering work showing how these conductances generate action potentials in the squid giant axon. Other conductances are modeled in chapter 6.

Persistent Conductances

Figure 5.8 shows cartoons of the mechanisms by which voltage-dependent channels open and close as a function of membrane potential. Channels are depicted for two different types of conductances termed persistent (figure 5.8A) and transient (figure 5.8B). We begin by discussing persistent conductances. Figure 5.8A shows a swinging gate attached to a voltage sensor that can open or close the pore of the channel. In reality, channel gating mechanisms involve complex changes in the conformational structure of the channel, but the simple swinging gate picture is sufficient if we are only interested in the current carrying capacity of the channel. A channel that acts as if it had a single type of gate (although, as we will see, this is actually modeled as a number of identical sub-gates), like the channel in figure 5.8A, produces what is called a persistent or noninactivating

activation gate

conductance. Opening of the gate is called activation of the conductance and gate closing is called deactivation. For this type of channel, the probability that the gate is open, P_K , increases when the neuron is depolarized and decreases when it is hyperpolarized. The delayed-rectifier K^+ conductance that is responsible for repolarizing a neuron after an action potential is such a persistent conductance.

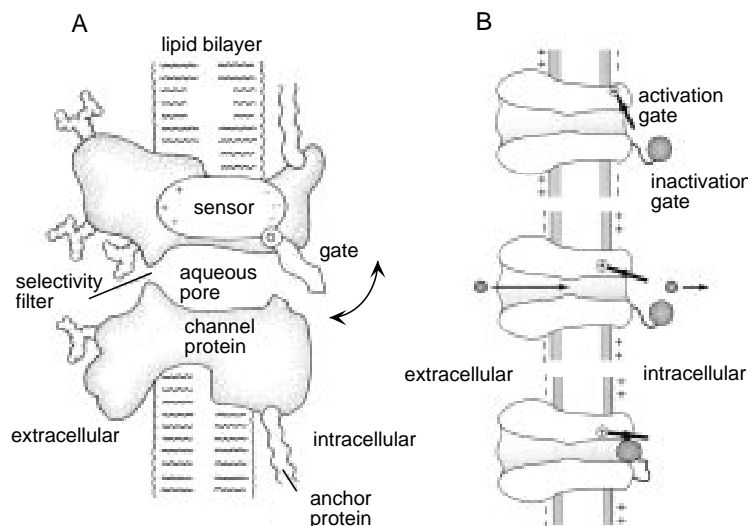


Figure 5.8: Gating of membrane channels. In both figures, the interior of the neuron is to the right of the membrane, and the extracellular medium is to the left. A) A cartoon of gating of a persistent conductance. A gate is opened and closed by a sensor that responds to the membrane potential. The channel also has a region that selectively allows ions of a particular type to pass through the channel, for example, K^+ ions for a potassium channel. B) A cartoon of the gating of a transient conductance. The activation gate is coupled to a voltage sensor (denoted by a circled +) and acts like the gate in A. A second gate, denoted by the ball, can block that channel once it is open. The top figure shows the channel in a deactivated (and deinactivated) state. The middle panel shows an activated channel, and the bottom panel shows an inactivated channel. Only the middle panel corresponds to an open, ion-conducting state. (A from Hille, 1992; B from Kandel et al., 1991.)

The opening of the gate that describes a persistent conductance may involve a number of conformational changes. For example, the delayed-rectifier K^+ conductance is constructed from four identical subunits, and it appears that all four must undergo a structural change for the channel to open. In general, if k independent, identical events are required for a channel to open, P_K can be written as

$$P_K = n^k \quad (5.15)$$

where n is the probability that any one of the k independent gating events has occurred. Here, n , which varies between 0 and 1, is called a gating

*activation variable
n*

or an activation variable, and a description of its voltage and time dependence amounts to a description of the conductance. We can think of n as the probability of an individual subunit gate being open, and $1 - n$ as the probability that it is closed.

Although using the value of $k = 4$ is consistent with the four subunit structure of the delayed-rectifier conductance, in practice k is an integer chosen to fit the data, and should be interpreted as a functional definition of a subunit rather than a reflection of a realistic structural model of the channel. Indeed, the structure of the channel was not known at the time that Hodgkin and Huxley chose the form of equation 5.15 and suggested that $k = 4$.

channel kinetics

We describe the transition of each subunit gate by a simple kinetic scheme in which the gating transition closed \rightarrow open occurs at a voltage-dependent rate $\alpha_n(V)$, and the reverse transition open \rightarrow closed occurs at a voltage-dependent rate $\beta_n(V)$. The probability that a subunit gate opens over a short interval of time is proportional to the probability of finding the gate closed, $1 - n$, multiplied by the opening rate $\alpha_n(V)$. Likewise, the probability that a subunit gate closes during a short time interval is proportional to the probability of finding the gate open, n , multiplied by the closing rate $\beta_n(V)$. The rate at which the open probability for a subunit gate changes is given by the difference of these two terms

$$\frac{dn}{dt} = \alpha_n(V)(1 - n) - \beta_n(V)n. \quad (5.16)$$

gating equation

The first term describes the opening process and the second term the closing process (hence the minus sign) that lowers the probability of being in the configuration with an open subunit gate. Equation 5.16 can be written in another useful form by dividing through by $\alpha_n(V) + \beta_n(V)$,

$$\tau_n(V) \frac{dn}{dt} = n_\infty(V) - n, \quad (5.17)$$

$\tau_n(V)$

where

$$\tau_n(V) = \frac{1}{\alpha_n(V) + \beta_n(V)} \quad (5.18)$$

$n_\infty(V)$

and

$$n_\infty(V) = \frac{\alpha_n(V)}{\alpha_n(V) + \beta_n(V)}. \quad (5.19)$$

Equation 5.17 indicates that for a fixed voltage V , n approaches the limiting value $n_\infty(V)$ exponentially with time constant $\tau_n(V)$.

The key elements in the equation that determines n are the opening and closing rate functions $\alpha_n(V)$ and $\beta_n(V)$. These are obtained by fitting experimental data. It is useful to discuss the form that we expect these rate functions to take on the basis of thermodynamic arguments. The state

transitions described by α_n , for example, are likely to be rate-limited by barriers requiring thermal energy. These transitions involve the movement of charged components of the gate across part of the membrane, so the height of these energy barriers should be affected by the membrane potential. The transition requires the movement of an effective charge, which we denote by qB_α , through the potential V . This requires an energy $qB_\alpha V$. The constant B_α reflects both the amount of charge being moved and the distance over which it travels. The probability that thermal fluctuations will provide enough energy to surmount this energy barrier is proportional to the Boltzmann factor, $\exp(-qB_\alpha V/k_B T)$. Based on this argument, we expect α_n to be of the form

$$\alpha_n(V) = A_\alpha \exp(-qB_\alpha/k_B T) = A_\alpha \exp(-B_\alpha V/V_T) \quad (5.20)$$

for some constant A_α . The closing rate β_n should be expressed similarly, except with different constants A_β and B_β . From equation 5.19, we then find that $n_\infty(V)$ is expected to be a sigmoidal function

$$n_\infty(V) = \frac{1}{1 + (A_\beta/A_\alpha) \exp((B_\alpha - B_\beta)V/V_T)} . \quad (5.21)$$

For a voltage-activated conductance, depolarization causes n to grow toward one, and hyperpolarization causes them to shrink toward zero. Thus, we expect that the opening rate, α_n should be an increasing function of V (and thus $B_\alpha < 0$) and β_n should be a decreasing function of V (and thus $B_\beta > 0$). Examples of the functions we have discussed are plotted in figure 5.9.

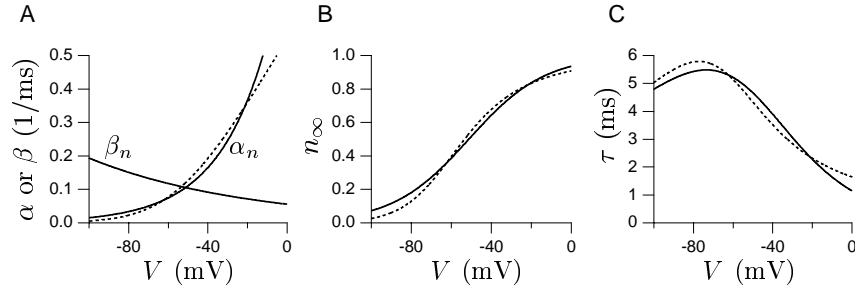


Figure 5.9: Generic voltage-dependent gating functions compared with Hodgkin-Huxley results for the delayed-rectifier K⁺ conductance. A) The exponential α_n and β_n functions expected from thermodynamic arguments are indicated by the solid curves. Parameter values used were $A_\alpha = 1.22 \text{ ms}^{-1}$, $A_\beta = 0.056 \text{ ms}^{-1}$, $B_\alpha/V_T = -0.04/\text{mV}$, and $B_\beta/V_T = 0.0125/\text{mV}$. The fit of Hodgkin and Huxley for β_n is identical to the solid curve shown. The Hodgkin-Huxley fit for α_n is the dashed curve. B) The corresponding function $n_\infty(V)$ of equation 5.21 (solid curve). The dashed curve is obtained using the α_n and β_n functions of the Hodgkin-Huxley fit (equation 5.22). C) The corresponding function $\tau_n(V)$ obtained from equation 5.18 (solid curve). Again the dashed curve is the result of using the Hodgkin-Huxley rate functions.

voltage clamping

While thermodynamic arguments support the forms we have presented, they rely on simplistic assumptions. Not surprisingly, the resulting functional forms do not always fit the data and various alternatives are often employed. The data upon which these fits are based are typically obtained using a technique called voltage clamping. In this techniques, an amplifier is configured to inject the appropriate amount of electrode current to hold the membrane potential at a constant value. By current conservation, this current is equal to the membrane current of the cell. Hodgkin and Huxley fit the rate functions for the delayed-rectifier K⁺ conductance they studied using the equations

$$\alpha_n = \frac{.01(V + 55)}{1 - \exp(-.1(V + 55))} \quad \text{and} \quad \beta_n = 0.125 \exp(-0.0125(V + 65)) \quad (5.22)$$

where V is expressed in mV, and α_n and β_n are both expressed in units of 1/ms. The fit for β_n is exactly the exponential form we have discussed with $A_\beta = 0.125 \exp(-0.0125 \cdot 65) \text{ ms}^{-1}$ and $B_\beta/V_T = 0.0125 \text{ mV}^{-1}$, but the fit for α_n uses a different functional form. The dashed curves in figure 5.9 plot the formulas of equation 5.22.

Transient Conductances

activation variable m
inactivation variable h

Some channels only open transiently when the membrane potential is depolarized because they are gated by two processes with opposite voltage-dependences. Figure 5.8B is a schematic of a channel that is controlled by two gates and generates a transient conductance. The swinging gate in figure 5.8B behaves exactly like the gate in figure 5.8A. The probability that it is open is written as m^k where m is an activation variable similar to n , and k is an integer. Hodgkin and Huxley used $k = 3$ for their model of the fast Na⁺ conductance. The ball in figure 5.8B acts as the second gate. The probability that the ball does not block the channel pore is written as h and called the inactivation variable. The activation and inactivation variables m and h are distinguished by having opposite voltage dependences. Depolarization causes m to increase and h to decrease, and hyperpolarization decreases m while increasing h .

For the channel in figure 5.8B to conduct, both gates must be open, and, assuming the two gates act independently, this has probability

$$P_{\text{Na}} = m^k h, \quad (5.23)$$

This is the general form used to describe the open probability for a transient conductance. We could raise the h factor in this expression to an arbitrary power as we did for m , but we leave out this complication to streamline the discussion. The activation m and inactivation h , like all gating variables, vary between zero and one. They are described by equations identical to 5.16, except that the rate functions α_n and β_n are replaced by

either α_m and β_m or α_h and β_h . These rate functions were fit by Hodgkin and Huxley using the equations (in units of 1/ms with V in mV)

$$\begin{aligned}\alpha_m &= \frac{.1(V + 40)}{1 - \exp[-.1(V + 40)]} & \beta_m &= 4 \exp[-.0556(V + 65)] \\ \alpha_h &= .07 \exp[-.05(V + 65)] & \beta_h &= 1/(1 + \exp[-.1(V + 35)]). \quad (5.24)\end{aligned}$$

Functions $m_\infty(V)$ and $h_\infty(V)$ describing the steady-state activation and inactivation levels, and voltage-dependent time constants for m and h can be defined as in equations 5.19 and 5.18. These are plotted in figure 5.10. For comparison, $n_\infty(V)$ and $\tau_n(V)$ for the K^+ conductance are also plotted. Note that $h_\infty(V)$, because it corresponds to an inactivation variable, is flipped relative to $m_\infty(V)$ and $n_\infty(V)$, so that it approaches one at hyperpolarized voltages and zero at depolarized voltages.

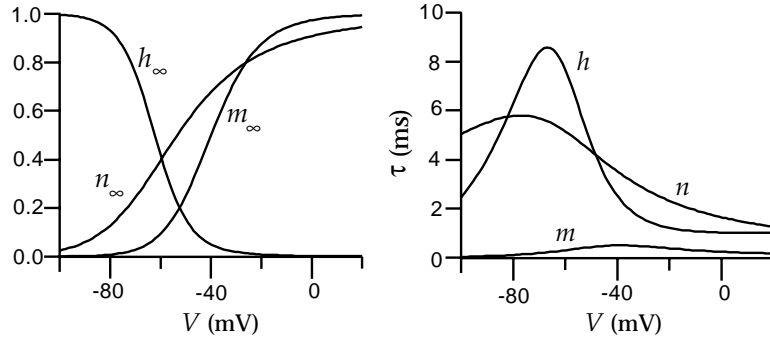


Figure 5.10: The voltage-dependent functions of the Hodgkin-Huxley model. The left panel shows $m_\infty(V)$, $h_\infty(V)$, and $n_\infty(V)$, the steady-state levels of activation and inactivation of the Na^+ conductance and activation of the K^+ conductance. The right panel shows the voltage-dependent time constants that control the rates at which these steady-state levels are approached for the three gating variables.

The presence of two factors in equation (5.23) gives a transient conductance some interesting properties. To turn on a transient conductance maximally, it may first be necessary to hyperpolarize the neuron below its resting potential and then to depolarize it. Hyperpolarization raises the value of the inactivation h , a process called deinactivation. The second step, depolarization, increases the value of m , a process known as activation. Only when m and h are both nonzero is the conductance turned on. Note that the conductance can be reduced in magnitude either by decreasing m or h . Decreasing h is called inactivation to distinguish it from decreasing m , which is called deactivation.

deinactivation
activation

inactivation
deactivation

Hyperpolarization-Activated Conductances

Persistent currents act as if they are controlled by an activation gate, while transient currents act as if they have both an activation and an inactiva-

tion gate. Another class of conductances, the hyperpolarization-activated conductances, behave as if they are controlled solely by an inactivation gate. They are thus persistent conductances, but they open when the neuron is hyperpolarized rather than depolarized. The opening probability for such channels is written solely of an inactivation variable similar to h . Strictly speaking these conductances deinactivate when they turn on and inactivate when they turn off. However, most people cannot bring themselves to say deinactivate all the time, so they say instead that these conductances are activated by hyperpolarization.

5.6 The Hodgkin-Huxley Model

The Hodgkin-Huxley model for the generation of the action potential, in its single-compartment form, is constructed by writing the membrane current in equation 5.6 as the sum of a leakage current, a delayed-rectified K⁺ current and a transient Na⁺ current,

$$i_m = \bar{g}_L(V - E_L) + \bar{g}_K n^4(V - E_K) + \bar{g}_{Na} m^3 h(V - E_{Na}). \quad (5.25)$$

The maximal conductances and reversal potentials used in the model are $\bar{g}_L = 0.003 \text{ mS/mm}^2$, $\bar{g}_K = 0.036 \text{ mS/mm}^2$, $\bar{g}_{Na} = 1.2 \text{ mS/mm}^2$, $E_L = -54.402 \text{ mV}$, $E_K = -77 \text{ mV}$ and $E_{Na} = 50 \text{ mV}$. The full model consists of equation 5.6 with equation 5.25 for the membrane current, and equations of the form 5.17 for the gating variables n , m , and h . These equations can be integrated numerically using the methods described in appendices A and B.

The temporal evolution of the dynamic variables of the Hodgkin-Huxley model during a single action potential is shown in figure 5.11. The initial rise of the membrane potential, prior to the action potential, seen in the upper panel of figure 5.11, is due to the injection of a positive electrode current into the model starting at $t = 5 \text{ ms}$. When this current drives the membrane potential up to about about -50 mV, the m variable that describes activation of the Na⁺ conductance suddenly jumps from nearly zero to a value near one. Initially, the h variable, expressing the degree of inactivation of the Na⁺ conductance, is around 0.6. Thus, for a brief period both m and h are significantly different from zero. This causes a large influx of Na⁺ ions producing the sharp downward spike of inward current shown in the second trace from the top. The inward current pulse causes the membrane potential to rise rapidly to around 50 mV (near the Na⁺ equilibrium potential). The rapid increase in both V and m is due to a positive feedback effect. Depolarization of the membrane potential causes m to increase, and the resulting activation of the Na⁺ conductance causes V to increase. The rise in the membrane potential causes the Na⁺ conductance to inactivate by driving h toward zero. This shuts off the Na⁺ current. In addition, the rise in V activates the K⁺ conductance by driving n toward one. This increases the K⁺ current which drives the membrane

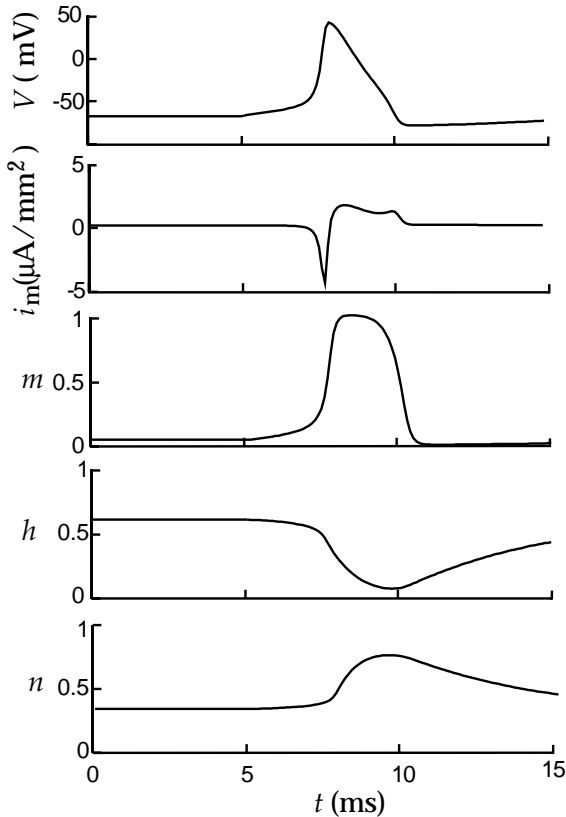


Figure 5.11: The dynamics of V , m , h , and n in the Hodgkin-Huxley model during the firing of an action potential. The upper trace is the membrane potential, the second trace is the membrane current produced by the sum of the Hodgkin-Huxley K^+ and Na^+ conductances, and subsequent traces show the temporal evolution of m , h , and n . Current injection was initiated at $t = 5$ ms.

potential back down to negative values. The final recovery involves the re-adjustment of m , h , and n to their initial values.

The Hodgkin-Huxley model can also be used to study propagation of an action potential down an axon, but for this purpose a multi-compartment model must be constructed. Methods for constructing such a model, and results from it, are described in chapter 6.

5.7 Modeling Channels

In previous sections, we described the Hodgkin-Huxley formalism for describing voltage-dependent conductances arising from a large number of channels. With the advent of single channel studies, microscopic de-

scriptions of the transitions between the conformational states of channel molecules have been developed. Because these models describe complex molecules, they typically involve many states and transitions. Here, we discuss simple versions of these models that capture the spirit of single-channel modeling without getting mired in the details.

Models of single channels are based on state diagrams that indicate the possible conformational states that the channel can assume. Typically, one of the states in the diagram is designated as open and ion-conducting, while the other states are non-conducting. The current conducted by the channel is written as $\bar{g}P(V - E)$, where E is the reversal potential, \bar{g} is the single-channel open conductance and P is one whenever the open state is occupied and zero otherwise. Channel models can be instantiated directly from state diagrams simply by keeping track of the state of the channel and allowing stochastic changes of state to occur at appropriate transition rates. If the model is updated in short time steps of duration Δt , the probability that the channel makes a given transition during an update interval is the transition rate times Δt .

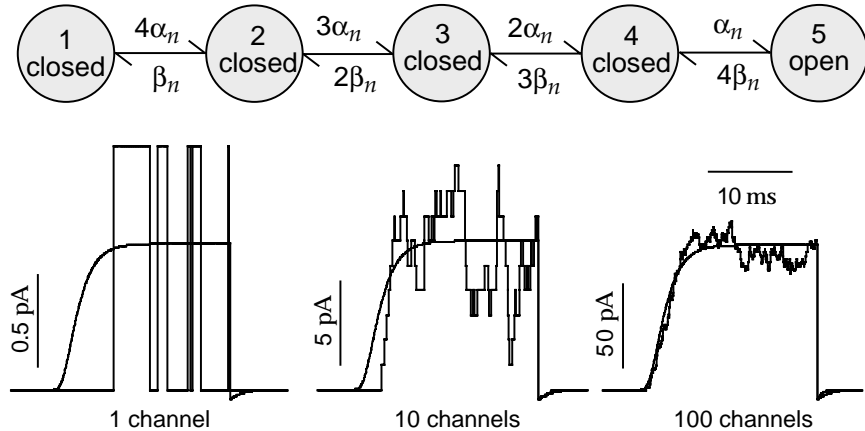


Figure 5.12: A model of the delayed-rectifier K^+ channel. The upper diagram shows the states and transition rates of the model. In the simulations shown in the lower panels, the membrane potential was initially held at -100 mV, then held at 10 mV for 20 ms, and finally returned to a holding potential of -100 mV. The smooth curves in these panels show the membrane current predicted by the Hodgkin-Huxley model in this situation. The left panel shows a simulation of a single channel that opened several times during the depolarization. The middle panel shows the total current from 10 simulated channels and the right panel corresponds to 100 channels. As the number of channels increases, the Hodgkin-Huxley model provides a more accurate description of the current.

Figure 5.12 shows the state diagram and simulation results for a model of a single delayed-rectifier K^+ channel that is closely related to the Hodgkin-Huxley description of the macroscopic delayed-rectifier conductance. The factors α_n and β_n in the transition rates shown in the state diagram of fig-

ure 5.12 are the voltage-dependent rate functions of the Hodgkin-Huxley model. The model uses the same four subunit structure assumed in the Hodgkin-Huxley model. We can think of state 1 in this diagram as a state in which all the subunit gates are closed. States 2, 3, 4, and 5 have 1, 2, 3, and 4 open subunit gates respectively. State 5 is the sole open state. The factors of 1, 2, 3, and 4 in the transition rates in figure 5.12 correspond to the number of subunit gates that can make a given transition. For example, the transition rate from state 1 to state 2 is four times faster than the rate from state 4 to state 5. This is because any one of the 4 subunit gates can open to get from state 1 to state 2, but the transition from state 4 to state 5 requires the single remaining closed subunit gate to open.

The lower panels in figure 5.12 show simulations of this model involving 1, 10, and 100 channels. The sum of currents from all of these channels is compared with the current predicted by the Hodgkin-Huxley model (scaled by the appropriate maximal conductance). For each channel, the pattern of opening and closing is random, but when enough channels are summed, the total current matches that of the Hodgkin-Huxley model quite well.

To see how the channel model in figure 5.12 reproduces the results of the Hodgkin-Huxley model when the currents from many channels are summed, we must consider a probabilistic description of the channel model. We denote the probability that a channel is in state a of figure 5.12 by p_a , with $a = 1, 2, \dots, 5$. Dynamic equations for these probabilities are easily derived by setting the rate of change for a given p_a equal to the probability per unit time of entry into state a from other states minus the rate for leaving a state. The entry probability per unit time is the product of the appropriate transition rate times the probability that the state making the transition is occupied. The probability per unit time for leaving is p_a times the sum of all the rates for possible transitions out of the state. Following this reasoning, the equations for the state probabilities are

$$\begin{aligned}\frac{dp_1}{dt} &= \beta_n p_2 - 4\alpha_n p_1 \\ \frac{dp_2}{dt} &= 4\alpha_n p_1 + 2\beta_n p_3 - (\beta_n + 3\alpha_n) p_2 \\ \frac{dp_3}{dt} &= 3\alpha_n p_2 + 3\beta_n p_4 - (2\beta_n + 2\alpha_n) p_3 \\ \frac{dp_4}{dt} &= 2\alpha_n p_3 + 4\beta_n p_5 - (3\beta_n + \alpha_n) p_4 \\ \frac{dp_5}{dt} &= \alpha_n p_4 - 4\beta_n p_5.\end{aligned}\tag{5.26}$$

A solution for these equations can be constructed if we recall that, in the Hodgkin-Huxley model, n is the probability of a subunit gate being in the open state and $1 - n$ the probability of it being closed. If we use that same notation here, state 1 has 4 closed subunit gates, and thus $p_1 = (1 - n)^4$. State 5, the open state, has 4 open subunit gates so $p_5 = n^4 = P$. State

2 has one open subunit gate, which can be any one of the four subunit gates, and three closed states making $p_2 = 4n(1 - n)^3$. Similar arguments yield $p_3 = 6n^2(1 - n)^2$ and $p_4 = 4n^3(1 - n)$. These expressions generate a solution to the above equations provided that n satisfies equation 5.16, as the reader can verify.

In the Hodgkin-Huxley model of the Na^+ conductance, the activation and inactivation processes are assumed to act independently. The schematic in figure 5.8B, which cartoons the mechanism believed to be responsible for inactivation, suggests that this assumption is incorrect. The ball that inactivates the channel is located inside the cell membrane where it cannot be affected directly by the potential across the membrane. Furthermore, in this scheme, the ball cannot occupy the channel pore until the activation gate has opened, making the two processes inter-dependent.

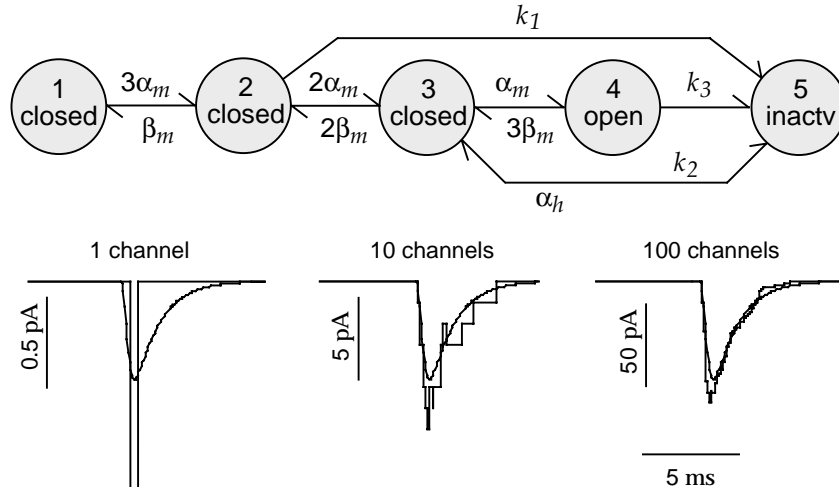


Figure 5.13: A model of the fast Na^+ channel. The upper diagram shows the states and transitions rates of the model. The values $k_1 = 0.24/\text{ms}$, $k_2 = 0.4/\text{ms}$, and $k_3 = 1.5/\text{ms}$ were used in the simulations shown in the lower panels. For these simulations, the membrane potential was initially held at -100 mV , then held at 10 mV for 20 ms , and finally returned to a holding potential of -100 mV . The smooth curves in these panels show the current predicted by the Hodgkin-Huxley model in this situation. The left panel shows a simulation of a single channel that opened once during the depolarization. The middle panel shows the total current from 10 simulated channels and the right panel corresponds to 100 channels. As the number of channels increases, the Hodgkin-Huxley model provides a fairly accurate description of the current, but it is not identical to the channel model in this case.

*state-dependent
inactivation*

The state diagram in figure 5.13 reflects this by having a state-dependent, voltage-independent inactivation mechanism. This diagram is a simplified version of a Na^+ channel model due to Patlak (1991). The sequence of transitions that lead to channel opening through states 1, 2, 3, and 4 is identical to that of the Hodgkin-Huxley model with transition rates deter-

mined by the Hodgkin-Huxley functions $\alpha_m(V)$ and $\beta_m(V)$ and appropriate combinatoric factors. State 4 is the open state. The transition to the inactivated state 5, however, is quite different from the inactivation process in the Hodgkin-Huxley model. Inactivation transitions to state 5 can only occur from states 2, 3, and 4, and the corresponding transition rates k_1 , k_2 , and k_3 are constants, independent of voltage. The deactivation process occurs at the Hodgkin-Huxley rate $\alpha_h(V)$ from state 5 to state 3.

Figure 5.13 shows simulations of this Na^+ channel model. In contrast to the K^+ channel model shown in figure 5.12, this model does not reproduce exactly the results of the Hodgkin-Huxley model when large numbers of channels are summed. Nevertheless, the two models agree quite well, as seen in the lower right panel of figure 5.13. The agreement, despite the different mechanisms of inactivation, is due to the speed of the activation process for the Na^+ conductance. The inactivation rate function $\beta_h(V)$ in the Hodgkin-Huxley model has a sigmoidal form similar to the asymptotic activation function $m_\infty(V)$ (see equation 5.24). This is indicative of the actual dependence of inactivation on m and not V . However, the activation variable m of the Hodgkin-Huxley model reaches its voltage-dependent asymptotic value $m_\infty(V)$ so rapidly that it is difficult to distinguish inactivation processes that depend on m from those that depend on V . Differences between the two models are only apparent during a sub-millisecond time period while the conductance is activating. Experiments that can resolve this time scale support the channel model over the original Hodgkin-Huxley description.

5.8 Synaptic Conductances

Synaptic transmission at a spike-mediated chemical synapse begins when an action potential invades the presynaptic terminal and activates voltage-dependent Ca^{2+} channels leading to a rise in the concentration of Ca^{2+} within the terminal. This causes vesicles containing transmitter molecules to fuse with the cell membrane and release their contents into the synaptic cleft between the pre- and postsynaptic sides of the synapse. The transmitter molecules then diffuse across the cleft and bind to receptors on the postsynaptic neuron. Binding of transmitter molecules leads to the opening of ion channels that modify the conductance of the postsynaptic neuron, completing the transmission of the signal from one neuron to the other. Postsynaptic ion channels can be activated directly by binding to the transmitter, or indirectly when the transmitter binds to a distinct receptor that affects ion channels through an intracellular second-messenger signaling pathway.

As with a voltage-dependent conductance, a synaptic conductance can be written as the product of a maximal conductance and an open channel probability, $g_s = \bar{g}_s P$. The open probability for a synaptic conductance can be expressed as a product of two terms that reflect processes occurring on

synaptic open probability P_s

the pre- and postsynaptic sides of the synapse, $P = P_s P_{\text{rel}}$. The factor P_s is the probability that a postsynaptic channel opens given that the transmitter was released by the presynaptic terminal. Because there are typically many postsynaptic channels, this can also be taken as the fraction of channels opened by the transmitter.

transmitter release probability P_{rel}

P_{rel} is related to the probability that transmitter is released by the presynaptic terminal following the arrival of an action potential. This reflects the fact that transmitter release is a stochastic process. Release of transmitter at a presynaptic terminal does not necessarily occur every time an action potential arrives, and, conversely, spontaneous release can occur even in the absence of action potential induced depolarization. The interpretation of P_{rel} is a bit subtle because a synaptic connection between neurons may involve multiple anatomical synapses, and each of these may have multiple independent transmitter release sites. The factor P_{rel} , in our discussion, is the average of the release probabilities at each release site. If there are many release sites, the total amount of transmitter released by all the sites is proportional to P_{rel} . If there is a single release site, P_{rel} is the probability that it releases transmitter. We will restrict our discussion to these two interpretations of P_{rel} . For a modest number of release sites with widely varying release probabilities, the current we discuss only describes an average over multiple trials.

*ionotropic synapse
metabotropic
synapse*

Synapses can exert their effects on the soma, dendrites, axon spike-initiation zone, or presynaptic terminals of their postsynaptic targets. There are two broad classes of synaptic conductances that are distinguished by whether the transmitter binds to the synaptic channel and activates it directly, or the transmitter binds to a distinct receptor that activates the conductance indirectly through an intracellular signaling pathway. The first class is called ionotropic and the second metabotropic. Ionotropic conductances activate and deactivate more rapidly than metabotropic conductances. Metabotropic receptors can, in addition to opening channels, cause long-lasting changes inside a neuron. They typically operate through pathways that involve G-protein mediated receptors and various intracellular signalling molecules known as second messengers. A large number of neuromodulators including serotonin, dopamine, norepinephrine, and acetylcholine can act through metabotropic receptors. These have a wide variety of important effects on the functioning of the nervous system.

*glutamate, GABA
AMPA, NMDA*

Glutamate and GABA (γ -aminobutyric acid) are the major excitatory and inhibitory transmitters in the brain. Both act ionotropically and metabotropically. The principal ionotropic receptor types for glutamate are called AMPA and NMDA. Both AMPA and NMDA receptors produce mixed-cation conductances with reversal potentials around 0 mV. The AMPA current is fast activating and deactivating. The NMDA receptor is somewhat slower to activate and deactivates considerably more slowly. In addition, NMDA receptors have an unusual voltage dependence that we discuss in a later section, and are rather more permeable to Ca^{2+} than

AMPA receptors.

GABA activates two important inhibitory synaptic conductances in the brain. GABA_A receptors produce a relatively fast ionotropic Cl⁻ conductance. GABA_B receptors are metabotropic and act to produce a slower and longer lasting K⁺ conductance.

In addition to chemical synapses, neurons can be coupled through electrical synapses (gap junctions) that produce a synaptic current proportional to the difference between the pre- and postsynaptic membrane potentials. Some gap junctions rectify so that positive and negative current flow is not equal for potential differences of the same magnitude.

GABA_A, GABA_B

gap junctions

The Postsynaptic Conductance

In a simple model of a directly activated receptor channel, the transmitter interacts with the channel through a binding reaction in which k transmitter molecules bind to a closed receptor and open it. In the reverse reaction, the transmitter molecules unbind from the receptor and it closes. These processes are analogous to the opening and closing involved in the gating of a voltage-dependent channel, and the same type of equation is used to describe how the open probability P_s changes with time,

$$\frac{dP_s}{dt} = \alpha_s(1 - P_s) - \beta_s P_s. \quad (5.27)$$

Here, β_s determines the closing rate of the channel and is usually assumed to be a constant. The opening rate, α_s , on the other hand, depends on the concentration of transmitter available for binding to the receptor. If the concentration of transmitter at the site of the synaptic channel is [transmitter], the probability of finding k transmitter molecules within binding range of the channel is proportional to [transmitter] ^{k} , and α_s is some constant of proportionality times this factor.

When an action potential invades the presynaptic terminal, the transmitter concentration rises and α_s grows rapidly causing P_s to increase. Following the release of transmitter, diffusion out of the cleft, enzyme-mediated degradation, and presynaptic uptake mechanisms can all contribute to a rapid reduction of the transmitter concentration. This sets α_s to zero, and P_s follows suit by decaying exponentially with a time constant $1/\beta_s$. Typically, the time constant for channel closing is considerably larger than the opening time.

As a simple model of transmitter release, we assume that the transmitter concentration in the synaptic cleft rises extremely rapidly after vesicle release, remains at a high value for a period of duration T , and then falls rapidly to zero. Thus, the transmitter concentration is modeled as a square pulse. While the transmitter concentration is nonzero, α_s takes a constant value much greater than β_s , otherwise $\alpha_s = 0$. Suppose that vesicle release

occurs at time $t = 0$ and that the synaptic channel open probability takes the value $P_s(0)$ at this time. While the transmitter concentration in the cleft is nonzero, α_s is so much larger than β_s that we can ignore the term involving β_s in equation 5.27. Integrating equation 5.27 under this assumption, we find that

$$P_s(t) = 1 + (P_s(0) - 1) \exp(-\alpha_s t) \quad \text{for } 0 \leq t \leq T. \quad (5.28)$$

The open probability takes its maximum value at time $t = T$ and then, for $t \geq T$, decays exponentially at a rate determined by the constant β_s ,

$$P_s(t) = P_s(T) \exp(-\beta_s(t - T)) \quad \text{for } t \geq T. \quad (5.29)$$

If $P_s(0) = 0$, as it will if there is no synaptic release immediately before the release at $t = 0$, equation 5.28 simplifies to $P_s(t) = 1 - \exp(-\alpha_s t)$ for $0 \leq t \leq T$, and this reaches a maximum value $P_{\max} = P_s(T) = 1 - \exp(-\alpha_s T)$. In terms of this parameter, a simple manipulation of equation 5.28 shows that we can write, in the general case,

$$P_s(T) = P_s(0) + P_{\max}(1 - P_s(0)). \quad (5.30)$$

Figure 5.14 shows a fit to a recorded postsynaptic current using this formalism. In this case, β_s was set to 0.19 ms^{-1} . The transmitter concentration was modeled as a square pulse of duration $T = 1 \text{ ms}$ during which $\alpha_s = 0.93 \text{ ms}^{-1}$. Inverting these values, we find that the time constant determining the rapid rise seen in figure 5.14A is 0.9 ms , while the fall of the current is an exponential with a time constant of 5.26 ms .

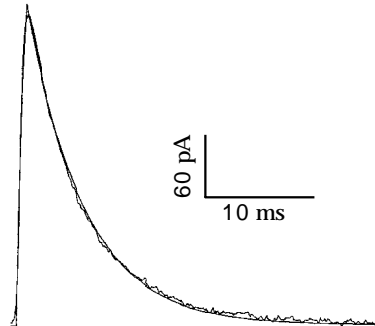


Figure 5.14: A fit of the model discussed in the text to the average EPSC (excitatory postsynaptic current) recorded from mossy fiber input to a CA3 pyramidal cell in a hippocampal slice preparation. The smooth line is the theoretical curve and the wiggly line is the result of averaging recordings from a number of trials. (Adapted from Destexhe et al., 1994.)

For a fast synapse like the one shown in figure 5.14, the rise of the conductance following a presynaptic action potential is so rapid that it can be approximated as instantaneous. In this case, the synaptic conductance

due to a single presynaptic action potential occurring at $t = 0$ is often written as an exponential, $P_s = P_{\max} \exp(-t/\tau_s)$ (see the AMPA trace in figure 5.15A) where, from equation 5.29, $\tau_s = 1/\beta_s$. The synaptic conductance due to a sequence of action potentials at arbitrary times can be modeled by allowing P_s to decay exponentially to zero according to the equation

$$\tau_s \frac{dP_s}{dt} = -P_s, \quad (5.31)$$

and, on the basis of the equation 5.30, making the replacement

$$P_s \rightarrow P_s + P_{\max}(1 - P_s) \quad (5.32)$$

immediately after each presynaptic action potential.

Equations 5.28 and 5.29 can also be used to model synapses with slower rise times, but other functional forms are often used. One way of describing both the rise and the fall of a synaptic conductance is to express P_s as the difference of two exponentials (see the GABA_A and NMDA traces in figure 5.15). For an isolated presynaptic action potential occurring at $t = 0$, the synaptic conductance is written as

$$P_s = P_{\max} B (\exp(-t/\tau_1) - \exp(-t/\tau_2)) \quad (5.33)$$

where $\tau_1 > \tau_2$, and B is a normalization factor that assures that the peak value of P_s is equal to one,

$$B = \left(\left(\frac{\tau_2}{\tau_1} \right)^{\tau_{\text{rise}}/\tau_1} - \left(\frac{\tau_2}{\tau_1} \right)^{\tau_{\text{rise}}/\tau_2} \right)^{-1}. \quad (5.34)$$

The rise time of the synapse is determined by $\tau_{\text{rise}} = \tau_1 \tau_2 / (\tau_1 - \tau_2)$, while the fall time is set by τ_1 . This conductance reaches its peak value $\tau_{\text{rise}} \ln(\tau_1/\tau_2)$ after the presynaptic action potential.

Another way of describing a synaptic conductance is to use the expression

$$P_s = \frac{P_{\max} t}{\tau_s} \exp(1 - t/\tau_s) \quad (5.35)$$

for an isolated presynaptic release that occurs at time $t = 0$. This expression, called an alpha function, starts at zero, reaches its peak value at $t = \tau_s$, and then decays with a time constant τ_s .

alpha function

We mentioned earlier in this chapter that NMDA receptor conductance has an additional dependence on the postsynaptic potential not normally seen in other conductances. To incorporate this dependence, the current due to the NMDA receptor can be described using an additional factor that depends on the postsynaptic potential, V . The NMDA current is written as $\bar{g}_{\text{NMDA}} G_{\text{NMDA}}(V) P(V - E_{\text{NMDA}})$. P is the usual open probability factor. The factor $G_{\text{NMDA}}(V)$ describes an extra voltage dependence due to the fact that, when the postsynaptic neuron is near its resting potential,

NMDA receptor

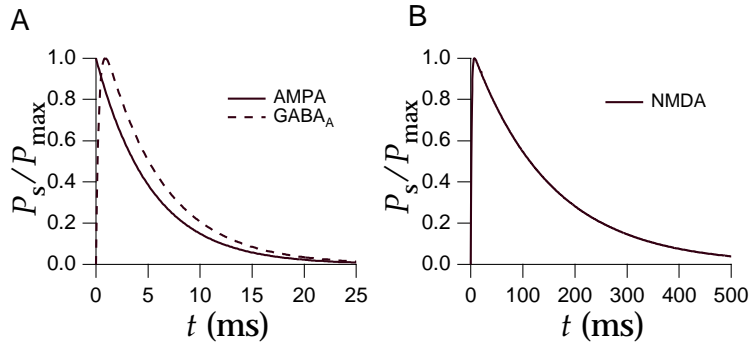


Figure 5.15: Time-dependent open probabilities fit to match AMPA, GABA_A, and NMDA synaptic conductances. A) The AMPA curve is a single exponential described by equation 5.31 with $\tau_s = 5.26$ ms. The GABA_A curve is a difference of exponentials with $\tau_1 = 5.6$ ms and $\tau_{rise} = 0.3$ ms. B) The NMDA curve is the differences of two exponentials with $\tau_1 = 152$ ms and $\tau_{rise} = 1.5$ ms. (Parameters are from Destexhe et al., 1994.)

NMDA receptors are blocked by Mg²⁺ ions. To activate the conductance, the postsynaptic neuron must be depolarized to knock out the blocking ions. Jahr and Stevens (1990) have fit this dependence by (figure 5.16)

$$G_{\text{NMDA}} = \left(1 + \frac{[\text{Mg}^{2+}]}{3.57 \text{ mM}} \exp(V/16.13 \text{ mV}) \right)^{-1}. \quad (5.36)$$

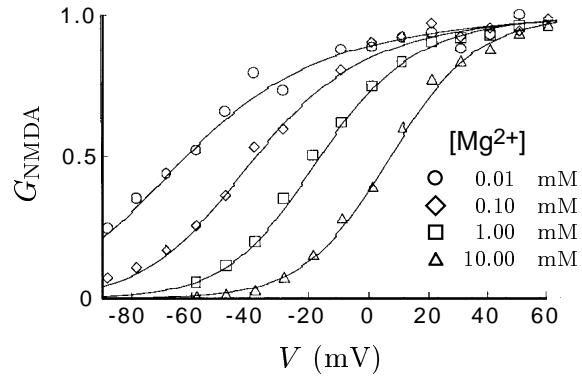


Figure 5.16: Dependence of the NMDA conductance on the extracellular Mg²⁺ concentration. Normal extracellular Mg²⁺ concentrations are in the range of 1 to 2 mM. The solid lines are the factors G_{NMDA} of equation 5.36 for different values of [Mg²⁺] and the symbols indicate the data points. (Adapted from Jahr and Stevens, 1990.)

NMDA receptors conduct Ca²⁺ ions as well as monovalent cations. Entry of Ca²⁺ ions through NMDA receptors is a critical event for long-term

modification of synaptic strength. The fact that the opening of NMDA receptor channels requires both pre- and postsynaptic depolarization means that they can act as coincidence detectors of simultaneous pre- and postsynaptic activity. This plays an important role in connection with the Hebb rule for synaptic modification discussed in chapter 8.

coincidence detection

Release Probability and Short-Term Plasticity

The probability of transmitter release and the magnitude of the resulting conductance change in the postsynaptic neuron can depend on the history of activity at a synapse. The effects of activity on synaptic conductances are termed short- and long-term. Short-term plasticity refers to a number of phenomena that affect the probability that a presynaptic action potential opens postsynaptic channels and that last anywhere from milliseconds to tens of seconds. The effects of long-term plasticity are extremely persistent, lasting, for example, as long as the preparation being studied can be kept alive. The modeling and implications of long-term plasticity are considered in chapter 8. Here we describe a simple way of describing short-term synaptic plasticity as a modification in the release probability for synaptic transmission. Short-term modifications of synaptic transmission can involve other mechanisms than merely changes in the probability of transmission, but for simplicity we absorb all these effects into a modification of the factor P_{rel} introduced previously. Thus, P_{rel} can be interpreted more generally as a presynaptic factor affecting synaptic transmission.

short-term plasticity

long-term plasticity

Figure 5.17 illustrates two principal types of short-term plasticity, depression and facilitation. Figure 5.17A shows trial-averaged postsynaptic current pulses produced in one cortical pyramidal neuron by evoking a regular series of action potentials in a second pyramidal neuron presynaptic to the first. The pulses decrease in amplitude dramatically upon repeated activation of the synaptic conductance, revealing short-term synaptic depression. Figure 5.17B shows a similar series of averaged postsynaptic current pulses recorded in a cortical inhibitory interneuron when a sequence of action potentials was evoked in a presynaptic pyramidal cell. In this case, the amplitude of the pulses increases, and thus the synapse facilitates. In general, synapses can exhibit facilitation and depression over a variety of time scales, and multiple components of short-term plasticity can be found at the same synapse. To keep the discussion simple, we consider synapses that exhibit either facilitation or depression described by a single time constant.

depression facilitation

Facilitation and depression can both be modeled as presynaptic processes that modify the probability of transmitter release. We describe them using a simple non-mechanistic model that has similarities to the model of P_s presented in the previous subsection. For both facilitation and depression, the release probability after a long period of presynaptic silence is $P_{\text{rel}} = P_0$. Activity at the synapse causes P_{rel} to increase in the case of facilitation

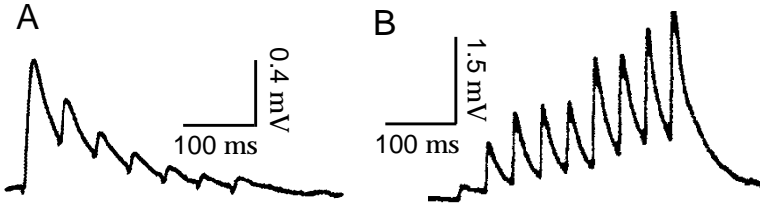


Figure 5.17: Depression and facilitation of excitatory intracortical synapses. A) Depression of an excitatory synapse between two layer 5 pyramidal cells recorded in a slice of rat somatosensory cortex. Spikes were evoked by current injection into the presynaptic neuron and postsynaptic currents were recorded with a second electrode. B) Facilitation of an excitatory synapse from a pyramidal neuron to an inhibitory interneuron in layer 2/3 of rat somatosensory cortex. (A from Markram and Tsodyks, 1996; B from Markram et al., 1998.)

and to decrease for depression. Between presynaptic action potentials, the release probability decays exponentially back to its ‘resting’ value P_0 ,

$$\tau_P \frac{dP_{\text{rel}}}{dt} = P_0 - P_{\text{rel}}. \quad (5.37)$$

The parameter τ_P controls the rate at which the release probability decays to P_0 .

The models of facilitation and depression differ in how the release probability is changed by presynaptic activity. In the case of facilitation, P_{rel} is augmented by making the replacement $P_{\text{rel}} \rightarrow P_{\text{rel}} + f_F(1 - P_{\text{rel}})$ immediately after a presynaptic action potential (as in equation 5.32). The parameter f_F (with $0 \leq f_F \leq 1$) controls the degree of facilitation, and the factor $(1 - P_{\text{rel}})$ prevents the release probability from growing larger than one. To model depression, the release probability is reduced after a presynaptic action potential by making the replacement $P_{\text{rel}} \rightarrow f_D P_{\text{rel}}$. In this case, the parameter f_D (with $0 \leq f_D \leq 1$) controls the amount of depression, and the factor P_{rel} prevents the release probability from becoming negative.

We begin by analyzing the effects of facilitation on synaptic transmission for a presynaptic spike train with Poisson statistics. In particular, we compute the average release probability, denoted by $\langle P_{\text{rel}} \rangle$. $\langle P_{\text{rel}} \rangle$ is determined by requiring that the facilitation that occurs after each presynaptic action potential is exactly canceled by the average exponential decrement that occurs between presynaptic spikes. Consider two presynaptic action potentials separated by an interval τ , and suppose that the release probability takes its average value value $\langle P_{\text{rel}} \rangle$ at the time of the first spike. Immediately after this spike, it is augmented to $\langle P_{\text{rel}} \rangle + f_F(1 - \langle P_{\text{rel}} \rangle)$. By the time of the second spike, this will have decayed to $P_0 + (\langle P_{\text{rel}} \rangle + f_F(1 - \langle P_{\text{rel}} \rangle)) - P_0 \exp(-\tau/\tau_P)$, which is obtained by integrating equation 5.37. The average value of the exponential decay factor in this expression is the integral over all positive τ values of $\exp(-\tau/\tau_P)$ times the probability density for a Poisson spike train with a firing rate r to produce an interspike inter-

val of duration τ , which is $r \exp(-r\tau)$ (see chapter 1). Thus, the average exponential decrement is

$$r \int_0^\infty d\tau \exp(-r\tau - \tau/\tau_p) = \frac{r\tau_p}{1 + r\tau_p}. \quad (5.38)$$

In order for the release probability to return, on average, to its steady-state value between presynaptic spikes, we must therefore require that

$$\langle P_{\text{rel}} \rangle = P_0 + (\langle P_{\text{rel}} \rangle + f_F(1 - \langle P_{\text{rel}} \rangle) - P_0) \frac{r\tau_p}{1 + r\tau_p}. \quad (5.39)$$

Solving for $\langle P_{\text{rel}} \rangle$ gives

$$\langle P_{\text{rel}} \rangle = \frac{P_0 + f_F r \tau_p}{1 + r f_F \tau_p}. \quad (5.40)$$

This equals P_0 at low rates and rises toward the value one at high rates (figure 5.18A). As a result, isolated spikes in low-frequency trains are transmitted with lower probability than spikes occurring within high-frequency bursts. The synaptic transmission rate when the presynaptic neuron is firing at rate r is the firing rate times the release probability. This grows linearly as $P_0 r$ for small rates and approaches r at high rates (figure 5.18A).

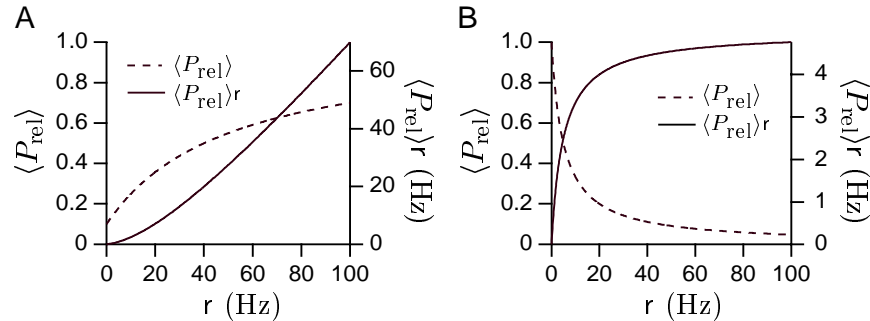


Figure 5.18: The effects of facilitation and depression on synaptic transmission. A) Release probability and transmission rate for a facilitating synapse as a function of the firing rate of a Poisson presynaptic spike train. The dashed curve shows the rise of the average release probability as the presynaptic rate increases. The solid curve is the average rate of transmission, which is the average release probability times the presynaptic firing rate. The parameters of the model are $P_0 = 0.1$, $f_F = 0.4$, and $\tau_p = 50$ ms. B) Same as A, but for the case of depression. The parameters of the model are $P_0 = 1$, $f_D = 0.4$, and $\tau_p = 500$ ms.

The value of $\langle P_{\text{rel}} \rangle$ for a Poisson presynaptic spike train can also be computed in the case of depression. The only difference from the above derivation is that following a presynaptic spike $\langle P_{\text{rel}} \rangle$ is decreased to $f_D \langle P_{\text{rel}} \rangle$. Thus, the consistency condition 5.39 is replaced by

$$\langle P_{\text{rel}} \rangle = P_0 + (f_D \langle P_{\text{rel}} \rangle - P_0) \frac{r\tau_p}{1 + r\tau_p} \quad (5.41)$$

giving

$$\langle P_{\text{rel}} \rangle = \frac{P_0}{1 + (1 - f_D)r\tau_P} \quad (5.42)$$

This equals P_0 at low rates and goes to zero as $1/r$ at high rates (figure 5.18B), which has some interesting consequences. As noted above, the average rate of successful synaptic transmissions is equal to $\langle P_{\text{rel}} \rangle$ times the presynaptic rate r . Because $\langle P_{\text{rel}} \rangle$ is proportional to $1/r$ at high rates, the average transmission rate is independent of r in this range. This can be seen by the flattening of the solid curve in figure 5.18B. As a result, synapses that depress do not convey information about the values of constant, high presynaptic firing rates to their postsynaptic targets. The presynaptic firing rate at which transmission starts to become independent of r is around $1/(1 - f_D)\tau_P$.

Figure 5.19 shows the average transmission rate, $\langle P_{\text{rel}} \rangle r$, in response to a series of steps in the presynaptic firing rate. Note first that the transmission rates during the 25, 100, 10 and 40 Hz periods are quite similar. This is a consequence of the $1/r$ dependence of the average release probability, as discussed above. The largest transmission rates in the figure occur during the sharp upward transitions between different presynaptic rates. This illustrates the important point that depressing synapses amplify transient signals relative to steady-state inputs. The transients corresponding to the 25 to 100 Hz transition and the 10 to 40 Hz transition are of roughly equal amplitudes, but the transient for the 10 to 40 Hz transition is broader than that for the 25 to 100 Hz transition.

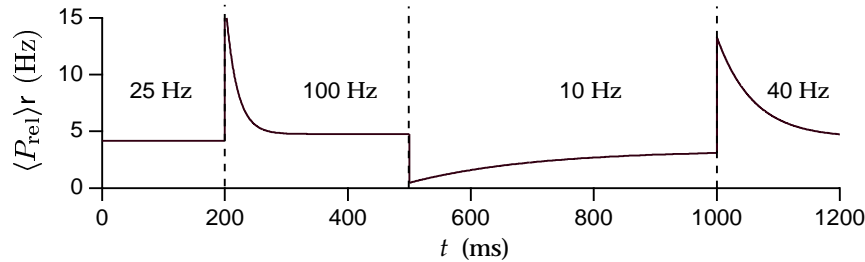


Figure 5.19: The average rate of transmission for a synapse with depression when the presynaptic firing rate changes in a sequence of steps. The firing rates were held constant at the values 25, 100, 10 and 40 Hz, except for abrupt changes at the times indicated by the dashed lines. The parameters of the model are $P_0 = 1$, $f_D = 0.6$, and $\tau_P = 500$ ms.

The equality of amplitudes of the two upward transients in figure 5.19 is a consequence of the $1/r$ behavior of $\langle P_{\text{rel}} \rangle$. Suppose that the presynaptic firing rate makes a sudden transition from a steady value r to a new value $r + \Delta r$. Before the transition, the average release probability is given by equation 5.42. Immediately after the transition, before the release probability has had time to adjust to the new input rate, the average transmis-

sion rate will be this previous value of $\langle P_{\text{rel}} \rangle$ times the new rate $r + \Delta r$, which is $P_0(r + \Delta r)/(1 + (1 - f_D)r\tau_P)$. For sufficiently high rates, this is approximately proportional to $(r + \Delta r)/r$. The size of the change in the transmission rate is thus proportional to $\Delta r/r$, which means that depressing synapses not only amplify transient inputs, they transmit them in a scaled manner. The amplitude of the transient transmission rate is proportional to the fractional change, not the absolute change, in the presynaptic firing rate. The two transients seen in figure 5.19 have similar amplitudes because in both cases $\Delta r/r = 3$. The difference in the recovery time for the two upward transients in figure 5.19 is due to the fact that the effective time constant governing the recovery to a new steady-state level r is $\tau_P/(1 + (1 - f_D)\tau_P r)$.

5.9 Synapses On Integrate-and-Fire Neurons

Synaptic inputs can be incorporated into an integrate-and-fire model by including synaptic conductances in the membrane current appearing in equation 5.8,

$$\tau_m \frac{dV}{dt} = E_L - V - r_m \bar{g}_s P_s (V - E_s) + R_m I_e. \quad (5.43)$$

For simplicity, we assume that $P_{\text{rel}} = 1$ in this example. The synaptic current is multiplied by r_m in equation 5.43 because equation 5.8 was multiplied by this factor. To model synaptic transmission, P_s changes whenever the presynaptic neuron fires an action potential using one of the schemes described previously.

Figures 5.20A and 5.20B show examples of two integrate-and-fire neurons driven by electrode currents and connected by identical excitatory or inhibitory synapses. The synaptic conductances in this example are described by the α function model. This means that the synaptic conductance a time t after the occurrence of a presynaptic action potential is given by $P_s = (t/\tau_s) \exp(-t/\tau_s)$. The figure shows a non-intuitive effect. When the synaptic time constant is sufficiently long ($\tau_s = 10$ ms in this example), excitatory connections produce a state in which the two neurons fire alternately, out of phase with each other, while inhibitory synapses produce synchronous firing. It is normally assumed that excitation produces synchrony. Actually, inhibitory connections can be more effective in some cases than excitatory connections at synchronizing neuronal firing.

*synchronous and
asynchronous
firing*

Synapses have multiple effects on their postsynaptic targets. In equation 5.43, the term $r_m \bar{g}_s P_s E_s$ acts as a source of current to the neuron, while the term $r_m \bar{g}_s P_s V$ changes the membrane conductance. The effects of the latter term are referred to as shunting, and they can be identified most easily if

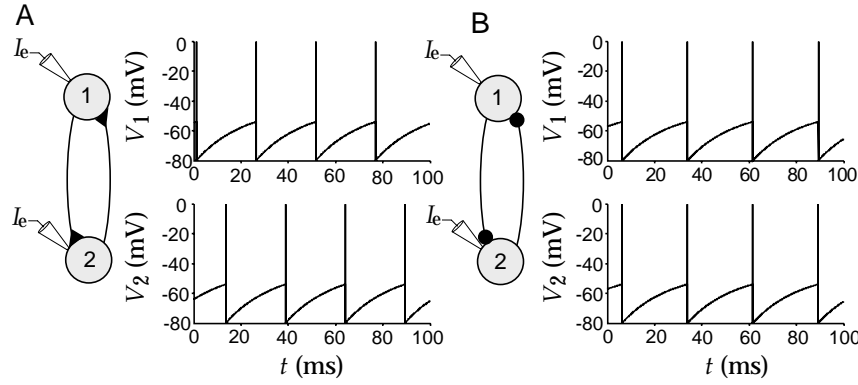


Figure 5.20: Two synaptically coupled integrate-and-fire neurons. A) Excitatory synapses ($E_s = 0 \text{ mV}$) produce an alternating, out-of-phase pattern of firing. B) Inhibitory synapses ($E_s = -80 \text{ mV}$) produce synchronous firing. Both model neurons have $E_L = -70 \text{ mV}$, $V_{\text{th}} = -54 \text{ mV}$, $V_{\text{reset}} = -80 \text{ mV}$, $r_m \bar{g}_s = 0.05$, $P_{\max} = 1$, $R_m I_e = 25 \text{ mV}$, and $\tau_s = 10 \text{ ms}$.

we divide equation 5.43 by $1 + r_m \bar{g}_s P_s$ to obtain

$$\frac{\tau_m}{1 + r_m \bar{g}_s P_s} \frac{dV}{dt} = -V + \frac{E_L + r_m \bar{g}_s P_s E_s + R_m I_e}{1 + r_m \bar{g}_s P_s}. \quad (5.44)$$

The shunting effects of the synapse are seen in this equation as a decrease in the effective membrane time constant and a divisive reduction in the impact of the leakage and synaptic reversal potentials, and of the electrode current.

The shunting effects seen in equation 5.44 have been proposed as a possible basis for neural computations involving division. However, shunting only has a divisive effect on the membrane potential of an integrate-and-fire neuron; its effect on the firing rate is subtractive. To see this, assume that synaptic input is arriving at a sufficient rate to maintain a relatively constant value of P_s . In this case, shunting amounts to changing the value of the membrane resistance from R_m to $R_m / (1 + r_m \bar{g}_s P_s)$. Recalling equation 5.12 for the firing rate of the integrate-and-fire model and the fact that $\tau_m = C_m R_m$, we can write the firing rate in a form that reveals its dependence on R_m ,

$$r_{\text{isi}} \approx \left[\frac{E_L - V_{\text{th}}}{C_m R_m (V_{\text{th}} - V_{\text{reset}})} + \frac{I_e}{C_m (V_{\text{th}} - V_{\text{reset}})} \right]_+. \quad (5.45)$$

Changing R_m only modifies the constant term in this equation, it has no effect on the dependence of the firing rate on I_e .

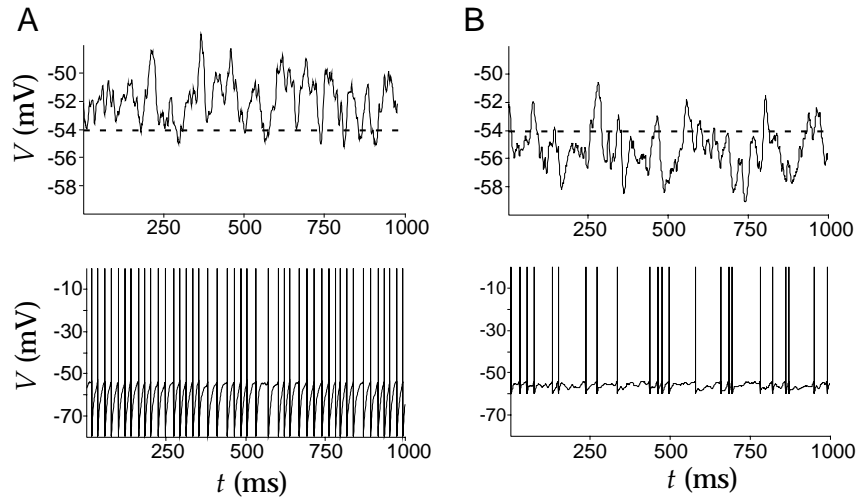


Figure 5.21: The regular and irregular firing modes of an integrate-and-fire model neuron. A) The regular firing mode. Upper panel: The membrane potential of the model neuron when the spike generation mechanism is turned off. The average membrane potential is above the spiking threshold (dashed line). Lower panel: When the spike generation mechanism is turned on, it produces a regular spiking pattern. B) The irregular firing mode. Upper panel: The membrane potential of the model neuron when the spike generation mechanism is turned off. The average membrane potential is below the spiking threshold (dashed line). Lower panel: When the spike generation mechanism is turned on, it produces an irregular spiking pattern. In order to keep the firing rates from differing too greatly between these two examples, the value of the reset voltage is higher in B than in A.

Regular and Irregular Firing Modes

Integrate-and-fire models are useful for studying how neurons sum large numbers of synaptic inputs and how networks of neurons interact. One issue that has received considerable attention is the degree of variability in the firing output of integrate-and-fire neurons receiving synaptic input. This work has led to the realization that neurons can respond to multiple synaptic inputs in two different modes of operation depending on the balance that exists between excitatory and inhibitory contributions.

The two modes of operation are illustrated in figure 5.21, which shows membrane potentials of an integrate-and-fire model neuron responding to 1000 excitatory and 200 inhibitory inputs. Each input consists of an independent Poisson spike train driving a synaptic conductance. The upper panels of figure 5.21 show the membrane potential with the action potential generation mechanism of the model turned off, and figures 5.21A and 5.21B illustrate the two different modes of operation. In figure 5.21A, the effect of the excitatory inputs is strong enough, relative to that of the inhibitory inputs, to make the average membrane potential, when action potential generation is blocked, more depolarized than the spiking thresh-

old of the model (the dashed line in the figure). When the action potential mechanism is turned on (lower panel of figure 5.21A), this produces a fairly regular pattern of action potentials.

The irregularity of a spike train can be quantified using the coefficient of variation (C_V), the ratio of the standard deviation to the mean of the interspike intervals (see chapter 1). For the Poisson inputs being used in this example, $C_V = 1$, while for the spike train in the lower panel of figure 5.21A, $C_V = 0.3$. Thus, the output spike train is much more regular than the input trains. This is not surprising, because the model neuron effectively averages its many synaptic inputs. In the regular firing mode, the total synaptic input attempts to charge the neuron above the threshold, but every time the potential reaches the threshold it gets reset and starts charging again. In this mode of operation, the timing of the action potentials is determined primarily by the charging rate of the cell, which is controlled by its membrane time constant.

Figure 5.21B shows the other mode of operation that produces an irregular firing pattern. In the irregular firing mode, the average membrane potential is more hyperpolarized than the threshold for action potential generation (upper panel of figure 5.21B). Action potentials are only generated when there is a fluctuation in the total synaptic input strong enough to make the membrane potential reach the threshold. This produces an irregular spike train, such as that seen in the lower panel of figure 5.21B which has a C_V value of 0.84.

The high degree of variability seen in the spiking patterns of *in vivo* recordings of cortical neurons (see chapter 1) suggests that they are better approximated by an integrate-and-fire model operating in an irregular-firing mode. There are advantages to operating in the irregular-firing mode that may compensate for its increased variability. One is that neurons firing in the irregular mode reflect in their outputs the temporal properties of fluctuations in their total synaptic input. In the regular firing mode, the timing of output spikes is only weakly related to the temporal character of the input spike trains. In addition, neurons operating in the irregular firing mode can respond more quickly to changes in presynaptic spiking patterns and firing rates than those operating in the regular firing mode.

5.10 Chapter Summary

In this chapter, we considered the basic electrical properties of neurons including their intracellular and membrane resistances, capacitances, and active voltage-dependent and synaptic conductances. We introduced the Nernst equation for equilibrium potentials and the formalism of Hodgkin and Huxley for describing persistent, transient, and hyperpolarization-activated conductances. Methods were introduced for modeling stochastic channel opening and stochastic synaptic transmission, including the

effects of synaptic facilitation and depression. We discussed a number of ways of describing synaptic conductances following the release of a neurotransmitter. Two models of action potential generation were discussed, the simple integrate-and-fire scheme and the more realistic Hodgkin-Huxley model.

5.11 Appendices

A) Integrating the Membrane Potential

We begin by considering the numerical integration of equation 5.8. It is convenient to rewrite this equation in the form

$$\tau_V \frac{dV}{dt} = V_\infty - V. \quad (5.46)$$

where $\tau_V = \tau_m$ and $V_\infty = E_L + R_m I_e$. When the electrode current I_e is independent of time, the solution of this equation is

$$V(t) = V_\infty + (V(t_0) - V_\infty) \exp(-(t - t_0)/\tau_V) \quad (5.47)$$

where t_0 is any time prior to t and $V(t_0)$ is the value of V at time t_0 . Equation 5.9 is a special case of this result with $t_0 = 0$.

If I_e depends on time, the solution 5.47 is not valid. An analytic solution can still be written down in this case, but it is not particularly useful except in special cases. Over a small enough time period Δt , we can approximate $I_e(t)$ as constant and use the solution 5.47 to step from a time t to $t + \Delta t$. This requires replacing the variable t_0 in equation 5.47 with t and t with $t + \Delta t$ so that

$$V(t + \Delta t) = V_\infty + (V(t) - V_\infty) \exp(-\Delta t/\tau_V). \quad (5.48)$$

This equation provides an updating rule for the numerical integration of equation 5.46. Provided that Δt is sufficiently small, repeated application of the update rule 5.48 provides an accurate way of determining the membrane potential. Furthermore, this method is stable because, if Δt is too large, it will only move V toward V_∞ and not, for example, make it grow without bound.

The equation for a general single-compartment conductance-based model, equation 5.6 with 5.5, can be written in the same form as equation 5.46 with

$$V_\infty = \frac{\sum_i g_i E_i + I_e / A}{\sum_i g_i} \quad (5.49)$$

and

$$\tau_V = \frac{C_m}{\sum_i g_i}. \quad (5.50)$$

Note that if c_m is in units of nF/mm^2 and the conductances are in the units $\mu\text{S}/\text{mm}^2$, τ_V comes out in ms units. Similarly, if the reversal potentials are given in units of mV, I_e is in nA, and A is in mm^2 , V_∞ will be in mV units.

If we take the time interval Δt to be small enough so that the gating variables can be approximated as constant during this period, the membrane potential can again be integrated over one time step using equation 5.48. Of course, the gating variables are not fixed, so once V has been updated by this rule, the gating variables must be updated as well.

B) Integrating the Gating Variables

All the gating variables in a conductance-based model satisfy equations of the same form,

$$\tau_z \frac{dz}{dt} = z_\infty - z \quad (5.51)$$

where we use z to denote a generic variable. Note that this equation has the same form as equation 5.46, and it can be integrated in exactly the same way. We assume that Δt is sufficiently small so that V does not change appreciably over this time interval (and similarly $[\text{Ca}^{2+}]$ is approximated as constant over this interval if any of the conductances are Ca^{2+} -dependent). Then, τ_z and z_∞ , which are functions of V (and possibly $[\text{Ca}^{2+}]$) can be treated as constants over this period and z can be updated by a rule identical to 5.48,

$$z(t + \Delta t) = z_\infty + (z(t) - z_\infty) \exp(-\Delta t / \tau_z). \quad (5.52)$$

An efficient integration scheme for conductance-based models is to alternate using rule (5.48) to update the membrane potential and rule (5.52) to update all the gating variables. It is important to alternate the updating of V with that of the gating variables, rather than doing them all simultaneously, as this keeps the method accurate to second order in Δt . If Ca^{2+} -dependent conductances are included, the intracellular Ca^{2+} concentration should be computed simultaneously with the membrane potential. By alternating the updating, we mean that the membrane potential is computed at times $0, \Delta t, 2\Delta t, \dots$, while the gating variables are computed at times $\Delta t/2, 3\Delta t/2, 5\Delta t/2, \dots$. A discussion of the second-order accuracy of this scheme is given in Mascagni and Sherman (1998).

5.12 Annotated Bibliography

Jack et al. (1975); Tuckwell (1988); Johnston & Wu (1995); Koch & Segev (1998); Koch (1998) cover much of the material in this chapter and chapter 6. Hille (1992) provides a comprehensive treatment of ion channels.

Hodgkin & Huxley (1952) present the classic biophysical model of the action potential, and **Sakmann & Neher (1983)** describe patch clamp recording techniques allowing single channels to be studied electrophysiologically.

The integrate-and-fire model was introduced by Lapicque in 1907. **DesTexhe et al. (1994)** describe kinetic models of both ion channels and short-term postsynaptic effects at synapses. Marom & Abbott (1994) show how the Na^+ channel model of Patlak (1991) can be reconciled with typical macroscopic conductance models. For a review of the spike-response model, the integrated version of the integrate-and-fire model, see **Gerstner (1998)**. Wang (1994) has analyzed a spike-rate adaptation similar to the one we presented, and Stevens & Zador (1998) introduce an integrate-and-fire model with time-dependent parameters.

The dynamic aspects of synaptic transmission are reviewed in **Magelby (1987)** and **Zucker (1989)**. Our presentation followed Abbott et al. (1997), Varela et al. (1997), and Tsodyks & Markram (1997). Wang & Rinzel (1992) noted that inhibitory synapses can synchronize coupled cells, and in our discussion we followed the treatment in Van Vreeswijk et al. (1994). Our analysis of the regular and irregular firing mode regimes of integrate-and-fire cells was based on Troyer & Miller (1997). Numerical methods for integrating the equations of neuron models are discussed in **Mascagni & Sherman (1998)**.

Chapter 6

Model Neurons II: Conductances and Morphology

6.1 Levels of Neuron Modeling

In modeling neurons, we must deal with two types of complexity; the intricate interplay of active conductances that makes neuronal dynamics so rich and interesting, and the elaborate morphology that allows neurons to receive and integrate inputs from so many other neurons. The first part of this chapter extends the material presented in chapter 5, by examining single-compartment models with a wider variety of voltage-dependent conductances, and hence a wider range of dynamic behaviors, than the Hodgkin-Huxley model. In the second part of the chapter, we introduce methods that allow us to study the effects of morphology on the electrical characteristics of neurons. An analytic approach known as cable theory is presented first, followed by a discussion of multi-compartment models that permit numerical simulation of complex neuronal structures.

Model neurons range from greatly simplified caricatures to highly detailed descriptions involving thousands of differential equations. Choosing the most appropriate level of modeling for a given research problem requires a careful assessment of the experimental information available and a clear understanding of the research goals. Oversimplified models can, of course, give misleading results, but excessively detailed models can obscure interesting results beneath inessential and unconstrained complexity.

6.2 Conductance-Based Models

The electrical properties of neurons arise from membrane conductances with a wide variety of properties. The basic formalism developed by Hodgkin and Huxley to describe the Na^+ and K^+ conductances responsible for generating action potentials (discussed in chapter 5) is also used to represent most of the additional conductances encountered in neuron modeling. Models that treat these aspects of ionic conductances, known as conductance-based models, can reproduce the rich and complex dynamics of real neurons quite accurately. In this chapter, we discuss both single- and multi-compartment conductance-based models, beginning with the single-compartment case.

conductance-based model

To review from chapter 5, the membrane potential of a single-compartment neuron model, V , is determined by integrating the equation

$$c_m \frac{dV}{dt} = -i_m + \frac{I_e}{A}. \quad (6.1)$$

with I_e the electrode current, A the membrane surface area of the cell, and i_m the membrane current. In the following subsections, we present expressions for the membrane current in terms of the reversal potentials, maximal conductance parameters, and gating variables of the different conductances of the models being considered. The gating variables and V comprise the dynamic variables of the model. All the gating variables are determined by equations of the form

$$\tau_z(V) \frac{dz}{dt} = z_\infty(V) - z \quad (6.2)$$

where we have used the letter z to denote a generic gating variable. The functions $\tau_z(V)$ and $z_\infty(V)$ are determined from experimental data. For some conductances, these are written in terms of the open and closing rates $\alpha_z(V)$ and $\beta_z(V)$ (see chapter 5) as

$$\tau_z(V) = \frac{1}{\alpha_z(V) + \beta_z(V)} \quad \text{and} \quad z_\infty(V) = \frac{\alpha_z(V)}{\alpha_z(V) + \beta_z(V)}. \quad (6.3)$$

We have written $\tau_z(V)$ and $z_\infty(V)$ as functions of the membrane potential, but for Ca^{2+} -dependent currents they also depend on the internal Ca^{2+} concentration. We call the $\alpha_z(V)$, $\beta_z(V)$, $\tau_z(V)$, and $z_\infty(V)$ collectively gating functions. A method for numerically integrating equations 6.1 and 6.2 is described in the appendices of chapter 5.

In the following subsections, some basic features of conductance-based models are presented in a sequence of examples of increasing complexity. We do this to illustrate the effects of various conductances and combinations of conductances on neuronal activity. Different cells (and even the same cell held at different resting potentials) can have quite different response properties due to their particular combinations of conductances.

Research on conductance-based models focuses on understanding how neuronal response dynamics arises from the properties of membrane and synaptic conductances, and how the characteristics of different neurons interact when they are coupled to each other in networks.

The Connor-Stevens Model

The Hodgkin-Huxley model of action potential generation, discussed in chapter 5, was developed on the basis of data from the giant axon of the squid, and we present a multi-compartment simulation of action potential propagation using this model in a later section. The Connor-Stevens model (Connor and Stevens, 1971; Connor et al. 1977) provides an alternative description of action potential generation. Like the Hodgkin-Huxley model, it contains fast Na^+ , delayed-rectifier K^+ , and leakage conductances. The fast Na^+ and delayed-rectifier K^+ conductances have somewhat different properties from those of the Hodgkin-Huxley model, in particular faster kinetics, so the action potentials are briefer. In addition, the Connor-Stevens model contains an extra K^+ conductance, called the A-current, that is transient. K^+ conductances come in wide variety of different forms, and the Connor-Stevens model involves two of them.

A-type potassium current

The membrane current in the Connor-Stevens model is

$$i_m = \bar{g}_L(V - E_L) + \bar{g}_{\text{Na}}m^3h(V - E_{\text{Na}}) + \bar{g}_Kn^4(V - E_K) + \bar{g}_Aa^3b(V - E_A) \quad (6.4)$$

where $\bar{g}_L = 0.003 \text{ mS/mm}^2$ and $E_L = -17 \text{ mV}$ are the maximal conductance and reversal potential for the leak conductance, and $\bar{g}_{\text{Na}} = 1.2 \text{ mS/mm}^2$, $\bar{g}_K = 0.2 \text{ mS/mm}^2$, $\bar{g}_A = 0.477 \text{ mS/mm}^2$, $E_{\text{Na}} = 55 \text{ mV}$, $E_K = -72 \text{ mV}$, and $E_A = -75 \text{ mV}$ (although the A-current is carried by K^+ , the model does not require $E_A = E_K$) and are similar parameters for the active conductances. The gating variables, m , h , n , a , and b , are determined by equations of the form 6.2 with the gating functions given in appendix A.

The fast Na^+ and delayed-rectifier K^+ conductances generate action potentials in the Connor-Stevens model just as they do in the Hodgkin-Huxley model (see chapter 5). What is the role of the additional A-current? Figure 6.1 illustrates action potential generation in the Connor-Stevens model. In the absence of an injected electrode current or synaptic input, the membrane potential of the model remains constant at a resting value of -68 mV . For a constant electrode current greater than a threshold value, the model neuron generates action potentials. Figure 6.1A shows how the firing rate of the model depends on the magnitude of the electrode current relative to the threshold value. The firing rate rises continuously from zero and then increases roughly linearly for currents over the range shown. Figure 6.1B shows an example of action potential generation for one particular value of the electrode current.

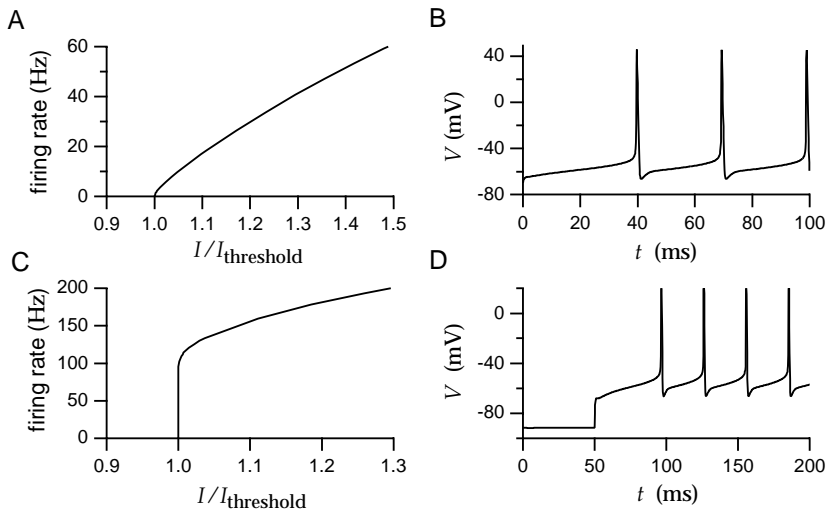


Figure 6.1: Firing of action potentials in the Connor-Stevens model. A) Firing rate as a function of electrode current. The firing rate rises continuously from zero as the current increases beyond the threshold value. B) An example of action potentials generated by constant current injection. C) Firing rate as a function of electrode current when the A-current is turned off. The firing rate now rises discontinuously from zero as the current increases beyond the threshold value. D) Delayed firing due to hyperpolarization. The neuron was held hyperpolarized for a prolonged period by injection of negative current. At $t = 50$ ms, the negative electrode current was switched to a positive value. The A-current delays the occurrence of the first action potential.

Figure 6.1C shows the firing rate as a function of electrode current for the Connor-Stevens model with the maximal conductance of the A-current set to zero. The leakage conductance and reversal potential have been adjusted to keep the resting potential and membrane resistance the same as in the original model. The firing rate is clearly much higher with the A-current turned off. This is because the deactivation rate of the A-current limits the rise time of the membrane potential between action potentials. In addition, the transition from no firing for currents less than the threshold value to firing with suprathreshold currents is different when the A-current is eliminated. Without the A-current, the firing rate jumps discontinuously to a nonzero value rather than rising continuously. Neurons with firing rates that rise continuously from zero as a function of electrode current are called type I, and those with discontinuous jumps in their firing rates at threshold are called type II. An A-current is not the only mechanism that can produce a type I response but, as figures 6.1A and 6.1C show, it plays this role in the Connor-Stevens model. The Hodgkin-Huxley model produces a type II response.

type I, type II

Another effect of the A-current is illustrated in figure 6.1D. Here the model neuron was held hyperpolarized by negative current injection for an ex-

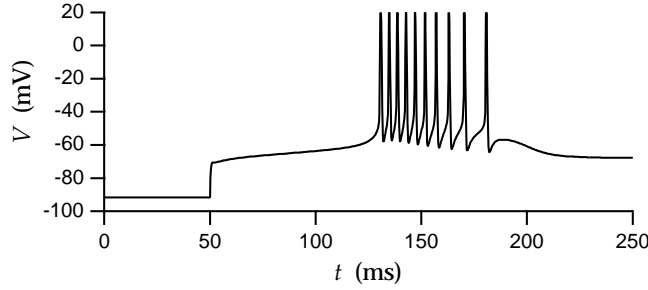


Figure 6.2: A burst of action potentials due to rebound from hyperpolarization. The model neuron was held hyperpolarized for an extended period (until the conductances came to equilibrium) by injection of constant negative electrode current. At $t = 50$ ms, the electrode current was set to zero, and a burst of Na^+ spikes was generated due to an underlying Ca^{2+} spike. The delay in the firing is caused by the presence of the A-current in the model.

tended period of time, and then the current was switched to a positive value. While the neuron was hyperpolarized, the A-current deinactivated, that is, the variable b increased toward one. When the electrode current switched sign and the neuron depolarized, the A-current first activated and then inactivated. This delayed the first spike following the change in the electrode current.

Postinhibitory Rebound and Bursting

The range of responses exhibited by the Connor-Stevens model neuron can be extended by including a transient Ca^{2+} conductance. The conductance we use was modeled by Huguenard and McCormick (1992) on the basis of data from thalamic relay cells. The membrane current due to the transient Ca^{2+} conductance is expressed as

$$i_{\text{CaT}} = \bar{g}_{\text{CaT}} M^2 H(V - E_{\text{Ca}}) \quad (6.5)$$

with, for the example given here, $\bar{g}_{\text{CaT}} = 13 \mu\text{S}/\text{mm}^2$ and $E_{\text{Ca}} = 120 \text{ mV}$. The gating variables for the transient Ca^{2+} conductance are determined from the gating functions in appendix A.

Several different Ca^{2+} conductances are commonly expressed in neuronal membranes. These are categorized as L, T, N, and P types. L-type Ca^{2+} currents are persistent as far as their voltage dependence is concerned, and they activate at a relatively high threshold. They deactivate due to a Ca^{2+} -dependent rather than voltage-dependent process. T-type Ca^{2+} currents have lower activation thresholds and are transient. N- and P-type Ca^{2+} conductances have intermediate thresholds and are respectively transient and persistent. They may be responsible for the Ca^{2+} entry that causes the release of transmitter at presynaptic terminals. Entry of Ca^{2+} into a neuron

transient Ca^{2+} conductance

L, T, N and P type Ca^{2+} channels

has many secondary consequences ranging from gating Ca^{2+} -dependent channels to inducing long-term modifications of synaptic conductances.

Ca²⁺ spike burst

A transient Ca^{2+} conductance acts, in many ways, like a slower version of the transient Na^+ conductance that generates action potentials. Instead of producing an action potential, a transient Ca^{2+} conductance generates a slower transient depolarization sometimes called a Ca^{2+} spike. This transient depolarization causes the neuron to fire a burst of action potentials, which are Na^+ spikes riding on the slower Ca^{2+} spike. Figure 6.2 shows such a burst and illustrates one way to produce it. In this example, the model neuron was hyperpolarized for an extended period and then released from hyperpolarization by setting the electrode current to zero. During the prolonged hyperpolarization, the transient Ca^{2+} conductance deinactivated. When the electrode current was set to zero, the resulting depolarization activated the transient Ca^{2+} conductance and generated a burst of action potentials. The burst in figure 6.2 is delayed due to the presence of the A-current in the original Connor-Stevens model, and it terminates when the Ca^{2+} conductance inactivates. Generation of action potentials in response to release from hyperpolarization is called postinhibitory rebound because, in a natural setting, the hyperpolarization would be caused by inhibitory synaptic input, not by current injection.

postinhibitory rebound

thalamic relay neuron

The transient Ca^{2+} current is an important component of models of thalamic relay neurons. These neurons exhibit different firing patterns in sleep and wakeful states. Action potentials tend to appear in bursts during sleep. Figure 6.3 shows an example of three states of activity of a model thalamic relay cell due to Wang (1994) that has, in addition to fast Na^+ , delayed-rectifier K^+ , and transient Ca^{2+} conductances, a hyperpolarization activated mixed-cation conductance, and a persistent Na^+ conductance. The cell is silent or fires action potentials in a regular pattern or in bursts depending on the level of current injection. In particular, injection of small amounts of negative current leads to bursting. This occurs because the hyperpolarization due to the current injection deinactivates the transient Ca^{2+} current and activates the hyperpolarization activated current. The regular firing mode of the middle plot of figure 6.3 is believed to be relevant during wakeful states when the thalamus is faithfully reporting input from the sensory periphery to the cortex.

stomatogastric ganglion

Neurons can fire action potentials either at a steady rate or in bursts even in the absence of current injection or synaptic input. Periodic bursting is a common feature of neurons in central patterns generators, which are neural circuits that produce periodic patterns of activity to drive rhythmic motor behaviors such as walking, running, or chewing. To illustrate periodic bursting, we consider a model constructed to match the activity of neurons in the crustacean stomatogastric ganglion (STG), a neuronal circuit that controls chewing and digestive rhythms in the foregut of lobsters and crabs. The model contains fast Na^+ , delayed-rectifier K^+ , A-type K^+ , and transient Ca^{2+} conductances similar to those discussed above, although the formulae and parameters used are somewhat different. In addition,

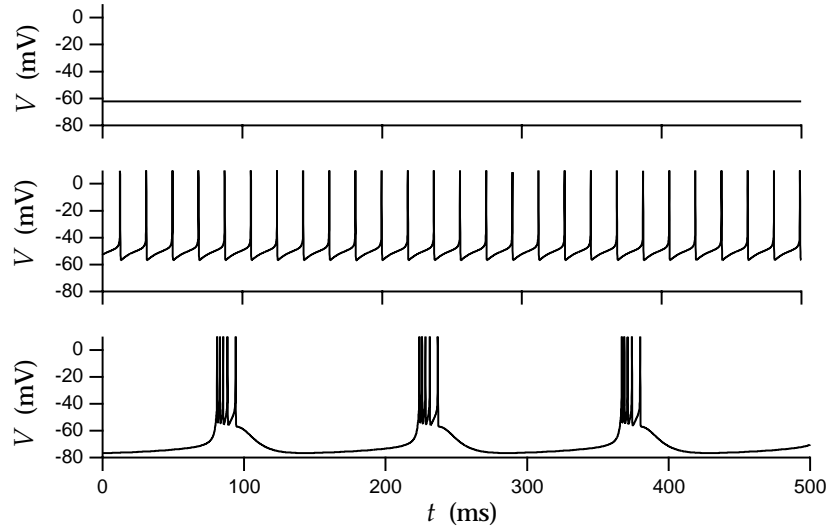


Figure 6.3: Three activity modes of a model thalamic neuron. Upper panel: with no electrode current the model is silent. Middle panel: when a positive current is injected into the model neuron, it fires action potentials in a regular periodic pattern. Lower panel: when negative current is injected into the model neuron, it fires action potentials in periodic bursts. (Adapted from Wang, 1994.)

the model has a Ca^{2+} -dependent K^+ conductance. Due to the complexity of the model, we do not provide complete descriptions of its conductances except for the Ca^{2+} -dependent K^+ conductance which plays a particularly significant role in the model.

The repolarization of the membrane potential after an action potential is often carried out both by the delayed-rectifier K^+ conductance and by a fast Ca^{2+} -dependent K^+ conductance. Ca^{2+} -dependent K^+ conductances may be voltage dependent, but they are primarily activated by a rise in the level of intracellular Ca^{2+} . A slow Ca^{2+} -dependent K^+ conductance called the after-hyperpolarization (AHP) conductance builds up during sequences of action potentials and typically contributes to the spike-rate adaptation discussed and modeled in chapter 5.

*Ca^{2+} -dependent
 K^+ conductance*

*after-
hyperpolarization
conductance*

The Ca^{2+} -dependent K^+ current in the model STG neuron is given by

$$i_{\text{KCa}} = \bar{g}_{\text{KCa}} c^4 (V - E_{\text{K}}) \quad (6.6)$$

where c_∞ depends on both the membrane potential and the intracellular Ca^{2+} concentration, $[\text{Ca}^{2+}]$ (see appendix A). The intracellular Ca^{2+} concentration is computed in this model using a simplified description in which rises in intracellular Ca^{2+} are caused by influx through membrane Ca^{2+} channels, and Ca^{2+} removal is described by an exponential process.

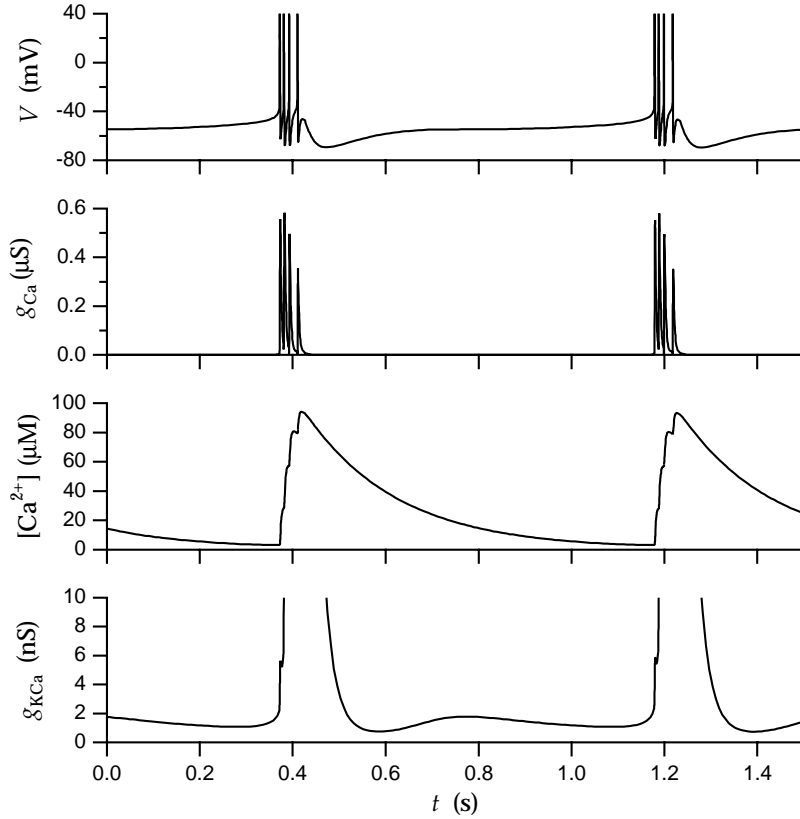


Figure 6.4: Periodic bursting in a model of a crustacean stomatogastric ganglion neuron. From the top, the panels show the membrane potential, the Ca^{2+} conductance, the intracellular Ca^{2+} concentration, and the Ca^{2+} -dependent K^+ conductance. The Ca^{2+} -dependent K^+ conductance is shown at an expanded scale so the reduction of the conductance due to the falling intracellular Ca^{2+} concentration during the interburst intervals can be seen. In this example, $\tau_{\text{Ca}} = 200$ ms. (Simulation by M. Goldman based on a variant of a model of Turrigiano et al., 1995 due to Z. Liu and M. Goldman.)

The resulting equation for the intracellular Ca^{2+} concentration, $[\text{Ca}^{2+}]$, is

$$\frac{d[\text{Ca}^{2+}]}{dt} = -\gamma i_{\text{Ca}} - \frac{[\text{Ca}^{2+}]}{\tau_{\text{Ca}}}. \quad (6.7)$$

Here i_{Ca} is the total Ca^{2+} current per unit area of membrane, τ_{Ca} is the time constant determining the rate at which intracellular Ca^{2+} is removed, and γ is a factor that converts from the electric current due to Ca^{2+} ion flow to the rate at which the Ca^{2+} ion concentration changes within the cell. Because the Ca^{2+} concentration is determined by dividing the number of Ca^{2+} ions in a cell by the total cellular volume and the Ca^{2+} influx is computed by multiplying i_{Ca} by the membrane surface area, γ is proportional

to the surface to volume ratio for the cell. It also contains a factor that converts from Coulombs per second of electrical current to moles per second of Ca^{2+} ions. This factor is $1/(zF)$ where z is the number of charges on the ion ($z = 2$ for Ca^{2+}), and F is the Faraday constant. If, as is normally the case, $[\text{Ca}^{2+}]$ is in mols/liter, γ should also contain a factor that converts the volume measure to liters, $10^6 \text{ mm}^3/\text{liter}$. Finally, γ must be multiplied by the additional factor that reflects fast intracellular Ca^{2+} buffering. Most of the Ca^{2+} ions that enter a neuron are rapidly bound to intracellular buffers, so only a fraction of the Ca^{2+} current through membrane channels is actually available to change the concentration $[\text{Ca}^{2+}]$ of free Ca^{2+} ions in the cell. This factor is about 1%. The minus sign in front of the γ factor in equation 6.7 is due to the definition of membrane currents as positive in the outward direction.

Figure 6.4 shows the model STG neuron firing action potentials in bursts. As in the models of figures 6.2 and 6.3, the bursts are transient Ca^{2+} spikes with action potentials riding on top of them. The Ca^{2+} current during these bursts causes a dramatic increase in the intracellular Ca^{2+} concentration. This activates the Ca^{2+} -dependent K^+ current which, along with the inactivation of the Ca^{2+} current, terminates the burst. The interburst interval is determined primarily by the time it takes for the intracellular Ca^{2+} concentration to return to a low value, which deactivates the Ca^{2+} -dependent K^+ current, allowing another burst to be generated. Although figure 6.4 shows that the conductance of the Ca^{2+} -dependent K^+ current reaches a low value immediately after each burst (due to its voltage dependence), this initial dip is too early for another burst to be generated at that point in the cycle.

The STG is a model system for investigating the effects of neuromodulators, such as amines and neuropeptides, on the activity patterns of a neural network. Neuromodulators modify neuronal and network behavior by activating, deactivating, or otherwise altering the properties of membrane and synaptic channels. Neuromodulation has a major impact on virtually all neural networks ranging from peripheral motor pattern generators like the STG to the sensory, motor, and cognitive circuits of the brain.

6.3 The Cable Equation

Single-compartment models describe the membrane potential over an entire neuron with a single variable. Membrane potentials can vary considerably over the surface of the cell membrane, especially for neurons with long and narrow processes or if we consider rapidly changing membrane potentials. Figure 6.5A shows the delay and attenuation of an action potential as it propagates from the soma out to the dendrites of a cortical pyramidal neuron. Figure 6.5B shows the delay and attenuation of an excitatory postsynaptic potential (EPSP) initiated in the dendrite by synaptic input as it spreads to the soma. Understanding these features is crucial for

determining whether and when a given synaptic input will cause a neuron to fire an action potential.

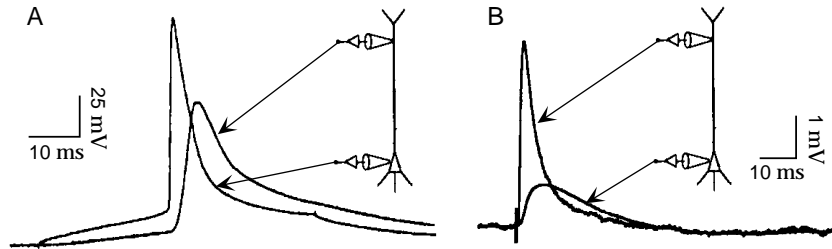


Figure 6.5: Simultaneous intracellular recordings from the soma and apical dendrite of a cortical pyramidal neuron in slice preparations. A) A pulse of current was injected into the soma of the neuron to produce the action potential seen in the somatic recording. The action potential appears delayed and with smaller amplitude in the dendritic recording. B) A set of axon fibers was stimulated producing an excitatory synaptic input. The excitatory postsynaptic potential is larger and peaks earlier in the dendrite than in the soma. Note that the scale for the potential is smaller than in A. (A adapted from Stuart and Sakmann, 1994; B adapted from Stuart and Spruston, 1998.)

The attenuation and delay within a neuron are most severe when electrical signals travel down the long and narrow, cable-like structures of dendritic or axonal branches. For this reason, the mathematical analysis of signal propagation within neurons is called cable theory. Dendritic and axonal cables are typically narrow enough that variations of the potential in the radial or axial directions are negligible compared to longitudinal variations. Therefore, the membrane potential along a neuronal cable is expressed as a function of a single longitudinal spatial coordinate x and time, $V(x, t)$, and the basic problem is to solve for this potential.

Current flows within a neuron due to voltage gradients. In chapter 5, we discussed how the potential difference across a segment of neuronal cable is related to the longitudinal current flowing down the cable. The longitudinal resistance of a cable segment of length Δx and radius a is given by multiplying the intracellular resistivity r_L by Δx and dividing by the cross-sectional area, πa^2 , so that $R_L = r_L \Delta x / (\pi a^2)$. The voltage drop across this length of cable, ΔV , is then related to the amount of longitudinal current flow by Ohm's law. In chapter 5, we discussed the magnitude of this current flow, but for the present purposes, we also need to define a sign convention for its direction. We define currents flowing in the direction of increasing x as positive. By this convention, the relationship between ΔV and I_L given by Ohm's law is $\Delta V = -R_L I_L$ or $\Delta V = -r_L \Delta x I_L / (\pi a^2)$. Solving this for the longitudinal current, we find $I_L = -\pi a^2 \Delta V / (r_L \Delta x)$. It is useful to take the limit of this expression for infinitesimally short cable segments, that is as $\Delta x \rightarrow 0$. In this limit, the ratio of ΔV to Δx becomes the derivative $\partial V / \partial x$. We use a partial derivative here, because V can also

cable theory

depend on time. Thus, for at any point along a cable of radius a and intracellular resistivity r_L , the longitudinal current flowing in the direction of increasing x is

$$I_L = -\frac{\pi a^2}{r_L} \frac{\partial V}{\partial x}. \quad (6.8)$$

The membrane potential $V(x, t)$ is determined by solving a partial differential equation, the cable equation, that describes how the currents entering, leaving, and flowing within a neuron affect the rate of change of the membrane potential. To derive the cable equation, we consider the currents within the small segment shown in figure 6.6. This segment has a radius a and a short length Δx . The rate of change of the membrane potential due to currents flowing into and out of this region is determined by its capacitance. Recall from chapter 5 that the capacitance of a membrane is determined by multiplying the specific membrane capacitance c_m by the area of the membrane. The cylinder of membrane shown in figure 6.6 has a surface area of $2\pi a \Delta x$ and hence a capacitance of $2\pi a \Delta x c_m$. The amount of current needed to change the membrane potential at a rate $\partial V / \partial t$ is $2\pi a \Delta x c_m \partial V / \partial t$.

cable equation

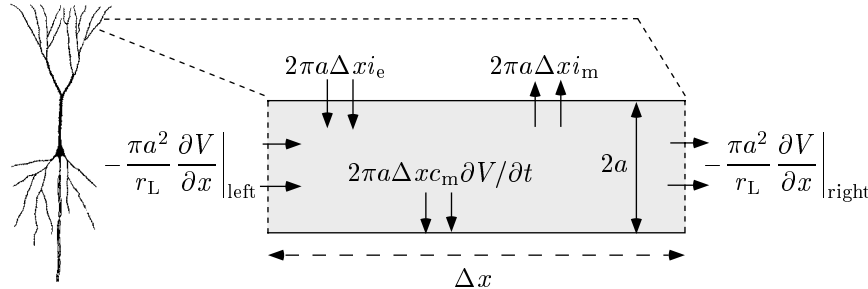


Figure 6.6: The segment of neuron used in the derivation of the cable equation. The longitudinal, membrane, and electrode currents that determine the rate of change of the membrane potential within this segment are denoted. The segment has length Δx and radius a . The expression involving the specific membrane capacitance refers to the rate at which charge builds up on the cell membrane generating changes in the membrane potential.

All of the currents that can change the membrane potential of the segment being considered are shown in figure 6.6. Current can flow longitudinally into the segment from neighboring segments, and expression 6.8 has been used in figure 6.6 to specify the longitudinal currents at both ends of the segment. Current can flow across the membrane of the segment we are considering through ion and synaptic receptor channels, or through an electrode. The contribution from ion and synaptic channels is expressed as a current per unit area of membrane i_m times the surface area of the segment, $2\pi a \Delta x$. The electrode current is not normally expressed as a current per unit area, but, for the present purposes, it is convenient to

define i_e to be the total electrode current flowing into a given region of the neuronal cable divided by the surface area of that region. The total amount of electrode current being injected into the cable segment of figure 6.6 is then $i_e 2\pi a \Delta x$. Because the electrode current is normally specified by I_e , not by a current per unit area, all the results we obtain will ultimately be re-expressed in terms of I_e . Following the standard convention, membrane and synaptic currents are defined as positive when they are outward, and electrode currents are defined as positive when they are inward.

The cable equation is derived by setting the sum of all the currents shown in figure 6.6 equal to the current needed to charge the membrane. The total longitudinal current entering the cylinder is the difference between the current flowing in on the left and that flowing out on the right. Thus,

$$2\pi a \Delta x c_m \frac{\partial V}{\partial t} = - \left(\frac{\pi a^2}{r_L} \frac{\partial V}{\partial x} \right) \Big|_{\text{left}} + \left(\frac{\pi a^2}{r_L} \frac{\partial V}{\partial x} \right) \Big|_{\text{right}} - 2\pi a \Delta x (i_m - i_e). \quad (6.9)$$

Dividing both sides of this equation by $2\pi a \Delta x$, we note that the right side involves the term

$$\frac{1}{2ar_L \Delta x} \left[\left(a^2 \frac{\partial V}{\partial x} \right) \Big|_{\text{right}} - \left(a^2 \frac{\partial V}{\partial x} \right) \Big|_{\text{left}} \right] \rightarrow \frac{\partial}{\partial x} \left(\frac{\pi a^2}{r_L} \frac{\partial V}{\partial x} \right). \quad (6.10)$$

The arrow refers to the limit $\Delta x \rightarrow 0$, which we now take. We have moved r_L outside the derivative in this equation under the assumption that it is not a function of position. However, the factor of a^2 must remain inside the integral unless it is independent of x . Substituting the result 6.10 into 6.9, we obtain the cable equation

$$c_m \frac{\partial V}{\partial t} = \frac{1}{2ar_L} \frac{\partial}{\partial x} \left(a^2 \frac{\partial V}{\partial x} \right) - i_m + i_e. \quad (6.11)$$

*boundary
conditions on the
cable equation*

To determine the membrane potential, equation (6.11) must be augmented by appropriate boundary conditions. The boundary conditions specify what happens to the membrane potential when the neuronal cable branches or terminates. The point at which a cable branches or equivalently where multiple cable segments join is called a node. At such a branching node, the potential must be continuous, that is, the functions $V(x, t)$ defined along each of the segments must yield the same result when evaluated at the x value corresponding to the node. In addition, charge must be conserved, which means that the sum of the longitudinal currents entering (or leaving) a node along all of its branches must be zero. According to equation 6.8, the longitudinal current entering a node is proportional to the square of the cable radius times the derivative of the potential evaluated at that point, $a^2 \partial V / \partial x$. The sum of the longitudinal currents entering the node, computed by evaluating these derivatives along each cable segment at the point where they meet at the node, must be zero.

Several different boundary conditions can be imposed at the end of a terminating cable segment. A reasonable condition is that no current should flow out of the end of the cable. By equation 6.8, this means that the spatial derivative of the potential must vanish at a termination point.

Due to the complexities of neuronal membrane currents and morphologies, the cable equation is most often solved numerically using multi-compartmental techniques described later in this chapter. However, it is useful to study analytic solutions of the cable equation in simple cases to get a feel for how different morphological features such as long dendritic cables, branching nodes, changes in cable radii, and cable ends affect the membrane potential.

Linear Cable Theory

Before we can solve the cable equation by any method, the membrane current i_m must be specified. We discussed models of various ion channel contributions to the membrane current in chapter 5 and earlier in this chapter. These models typically produce nonlinear expressions that are too complex to allow analytic solution of the cable equation. The analytic solutions we discuss use two rather drastic approximations; synaptic currents are ignored, and the membrane current is written as a linear function of the membrane potential. Eliminating synaptic currents requires us to examine how a neuron responds to the electrode current i_e . In some cases, electrode current can mimic the effects of a synaptic conductance, although the two are not equivalent. Nevertheless, studying responses to electrode current allows us to investigate the effects of different morphologies on membrane potentials.

Typically, a linear approximation for the membrane current is only valid if the membrane potential stays within a limited range, for example close to the resting potential of the cell. The resting potential is defined as the potential where no net current flows across the membrane. Near this potential, we approximate the membrane current per unit area as

$$i_m = (V - V_{\text{rest}})/r_m \quad (6.12)$$

where V_{rest} is the resting potential, and the factor of r_m follows from the definition of the membrane resistance. It is convenient to define v as the membrane potential relative to the resting potential, $v = V - V_{\text{rest}}$, so that $i_m = v/r_m$.

If the radii of the cable segments used to model a neuron are constant except at branches and abrupt junctions, the factor a^2 in equation 6.11 can be taken out of the derivative and combined with the prefactor $1/2ar_L$ to produce a factor $a/2r_L$ that multiplies the second spatial derivative. With this modification and use of the linear expression for the membrane current,

the cable equation for v is

$$c_m \frac{\partial v}{\partial t} = \frac{a}{2r_L} \frac{\partial^2 v}{\partial x^2} - \frac{v}{r_m} + i_e. \quad (6.13)$$

It is convenient to multiply this equation by r_m , turning the factor that multiplies the time derivative on the left side into the membrane time constant $\tau_m = r_m c_m$. This also changes the expression multiplying the spatial second derivative on the right side of equation 6.13 to $ar_m/2r_L$. This factor has the dimensions of length squared, and it defines a fundamental length constant for a segment of cable of radius a , the electrotonic length,

λ electrotonic length

$$\lambda = \sqrt{\frac{ar_m}{2r_L}}. \quad (6.14)$$

Using the values $r_m = 1 \text{ M}\Omega \cdot \text{mm}^2$ and $r_L = 1 \text{ k}\Omega \cdot \text{mm}$, a cable of radius $a = 2 \mu\text{m}$ has an electrotonic length of 1 mm. A segment of cable with radius a and length λ has a membrane resistance that is equal to its longitudinal resistance, as can be seen from equation 6.14,

$$R_\lambda = \frac{r_m}{2\pi a \lambda} = \frac{r_L \lambda}{\pi a^2}. \quad (6.15)$$

The resistance R_λ defined by this equation is a useful quantity that enters into a number of calculations.

Expressed in terms of τ_m and λ , the cable equation becomes

$$\tau_m \frac{\partial v}{\partial t} = \lambda^2 \frac{\partial^2 v}{\partial x^2} - v + r_m i_e. \quad (6.16)$$

Equation 6.16 is a linear equation for v similar to the diffusion equation, and it can be solved by standard methods of mathematical analysis. The constants τ_m and λ set the scale for temporal and spatial variations in the membrane potential. For example, the membrane potential requires a time of order τ_m to settle down after a transient, and deviations in the membrane potential due to localized electrode currents decay back to zero over a length of order λ .

The membrane potential is affected both by the form of the cable equation and by the boundary conditions imposed at branching nodes and terminations. To isolate these two effects, we consider two idealized cases: an infinite cable that does not branch or terminate, and a single branching node that joins three semi-infinite cables. Of course, real neuronal cables are not infinitely long, but the solutions we find are applicable for long cables far from their ends. We determine the potential for both of these morphologies when current is injected at a single point. Because the equation we are studying is linear, the membrane potential for any other spatial distribution of electrode current can be determined by summing solutions corresponding to current injection at different points. The use of point injection to build more general solutions is a standard method of linear analysis. In this context, the solution for a point source of current injection is called a Green's function.

Green's function

An Infinite Cable

In general, solutions to the linear cable equation are functions of both position and time. However, if the current being injected is held constant, the membrane potential settles to a steady-state solution that is independent of time. Solving for this time-independent solution is easier than solving the full time-dependent equation, because the cable equation reduces to an ordinary differential equation in the static case,

$$\lambda^2 \frac{d^2 v}{dx^2} = v - r_m i_e . \quad (6.17)$$

For the localized current injection we wish to study, i_e is zero everywhere except within a small region of size Δx around the injection site, which we take to be $x = 0$. Eventually we will let $\Delta x \rightarrow 0$. Away from the injection site, the linear cable equation is $\lambda^2 d^2 v / dx^2 = v$, which has the general solution $v(x) = B_1 \exp(-x/\lambda) + B_2 \exp(x/\lambda)$ with as yet undetermined coefficients B_1 and B_2 . These constant coefficients are determined by imposing boundary conditions appropriate to the particular morphology being considered. For an infinite cable, on physical grounds, we simply require that the solution does not grow without bound when $x \rightarrow \pm\infty$. This means that we must choose the solution with $B_1 = 0$ for the region $x < 0$ and the solution with $B_2 = 0$ for $x > 0$. Because the solution must be continuous at $x = 0$, we must require $B_1 = B_2 = B$, and these two solutions can be combined into a single expression $v(x) = B \exp(-|x|/\lambda)$. The remaining task is to determine B , which we do by balancing the current injected with the current that diffuses away from $x = 0$.

In the small region of size Δx around $x = 0$ where the current is injected, the full equation $\lambda^2 d^2 v / dx^2 = v - r_m i_e$ must be solved. If the total amount of current injected by the electrode is I_e , the current per unit area injected into this region is $I_e / 2\pi a \Delta x$. This grows without bound as $\Delta x \rightarrow 0$. The first derivative of the membrane potential $v(x) = B \exp(-|x|/\lambda)$ is discontinuous at the point $x = 0$. For small Δx , the derivative at one side of the region we are discussing (at $x = -\Delta x/2$) is approximately B/λ , while at the other side (at $x = +\Delta x/2$) it is $-B/\lambda$. In these expressions, we have used the fact that Δx is small to set $\exp(-|\Delta x|/2\lambda) \approx 1$. For small Δx , the second derivative is approximately the difference between these two first derivatives divided by Δx , which is $-2B/\lambda \Delta x$. We can ignore the term v in the cable equation within this small region, because it is not proportional to $1/\Delta x$. Substituting the expressions we have derived for the remaining terms in the equation, we find that $-2\lambda^2 B/\lambda \Delta x = -r_m I_e / 2\pi a \Delta x$, which means that $B = I_e R_\lambda / 2$, using R_λ from equation 6.15. Thus, the membrane potential for static current injection at the point $x = 0$ along an infinite cable is

$$v(x) = \frac{I_e R_\lambda}{2} \exp\left(-\frac{|x|}{\lambda}\right) . \quad (6.18)$$

According to this result, the membrane potential away from the site of current injection ($x = 0$) decays exponentially with length constant λ (see

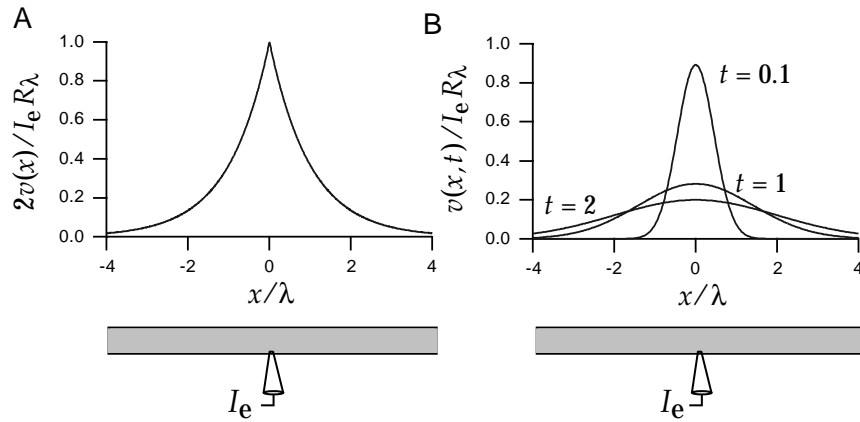


Figure 6.7: The potential for current injection at the point $x = 0$ along an infinite cable. A) Static solution for a constant electrode current. The potential decays exponentially away from the site of current injection. B) Time-dependent solution for a δ function pulse of current. The potential is described by a Gaussian function centered at the site of current injection that broadens and shrinks in amplitude over time.

figure 6.7A). The ratio of the membrane potential at the injection site to the magnitude of the injected current is called the input resistance of the cable. The value of the potential at $x = 0$ is $I_e R_\lambda / 2$ indicating that the infinite cable has an input resistance of $R_\lambda / 2$. Each direction of the cable acts like a resistance of R_λ and these two act in parallel to produce a total resistance half as big. Note that each semi-infinite cable extending from the point $x = 0$ has a resistance equal to a finite cable of length λ .

We now consider the membrane potential produced by an instantaneous pulse of current injected at the point $x = 0$ at the time $t = 0$. Specifically, we consider $i_e = I_e \delta(x) \delta(t) / 2\pi a$. We do not derive the solution for this case (see Tuckwell, 1988, for example), but simply state the answer

$$v(x, t) = \frac{I_e R_\lambda}{\sqrt{4\pi\lambda^2 t/\tau_m}} \exp\left(-\frac{\tau_m x^2}{4\lambda^2 t}\right) \exp\left(-\frac{t}{\tau_m}\right). \quad (6.19)$$

In this case, the spatial dependence of the potential is determined by a Gaussian, rather than an exponential function. The Gaussian is always centered around the injection site, so the potential is always largest at $x = 0$. The width of the Gaussian curve around $x = 0$ is proportional to $\lambda\sqrt{t/\tau_m}$. As expected, λ sets the scale for this spatial variation, but the width also grows as the square root of the time measured in units of τ_m . The factor $(4\pi\lambda^2 t/\tau_m)^{-1/2}$ in equation 6.19 preserves the total area under this Gaussian curve, but the additional exponential factor $\exp(-t/\tau_m)$ reduces the integrated amplitude over time. As a result, the spatial dependence of the membrane potential is described by a spreading Gaussian function with an integral that decays exponentially (figure 6.7B).

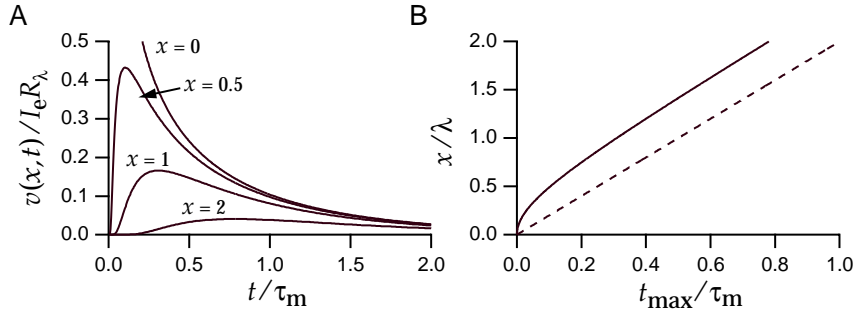


Figure 6.8: Time-dependence of the potential on an infinite cable in response to a pulse of current injected at the point $x = 0$ at time $t = 0$. A) The potential is always largest at the site of current injection. At any fixed point, it reaches its maximum value as a function of time later for measurement sites located further away from the current source. B) Movement of the temporal maximum of the potential. The solid line shows the relationship between the measurement location x , and the time t_{\max} when the potential reaches its maximum value at that location. The dashed line corresponds to a constant velocity $2\lambda/\tau_m$.

Figure 6.8 illustrates the properties of the solution 6.19 plotted at various fixed positions as a function of time. Figure 6.8A shows that the membrane potential measured further from the injection site reaches its maximum value at later times. It is important to keep in mind that the membrane potential spreads out from the region $x = 0$, it does not propagate like a wave. Nevertheless, we can define a type of ‘velocity’ for this solution by computing the time t_{\max} when the maximum of the potential occurs at a given spatial location. This is done by setting the time derivative of $v(x, t)$ in equation 6.19 to zero, giving

$$t_{\max} = \frac{\tau_m}{4} \left(\sqrt{1 + 4(x/\lambda)^2} - 1 \right). \quad (6.20)$$

For large x , $t_{\max} \approx x\tau_m/2\lambda$ corresponding to a velocity of $2\lambda/\tau_m$. For smaller x values, the location of the maximum moves faster than this ‘velocity’ would imply (figure 6.8B).

An Isolated Branching Node

To illustrate the effects of branching on the membrane potential in response to a point source of current injection, we consider a single isolated junction of three semi-infinite cables as shown in the bottom panels of figure 6.9. For simplicity, we discuss the solution for static current injection at a point, but the results generalize directly to the case of time-dependent currents. We label the potentials along the three segments by v_1 , v_2 , and v_3 , and label the distance outward from the junction point along any given segment by the coordinate x . The electrode injection site is located a distance y away from the junction along segment 2. The solution for the three

segments is then

$$\begin{aligned} v_1(x) &= p_1 I_e R_{\lambda_1} \exp(-x/\lambda_1 - y/\lambda_2) \\ v_2(x) &= \frac{I_e R_{\lambda_2}}{2} [\exp(-|y-x|/\lambda_2) + (2p_2 - 1) \exp(-(y+x)/\lambda_2)] \\ v_3(x) &= p_3 I_e R_{\lambda_3} \exp(-x/\lambda_3 - y/\lambda_2), \end{aligned} \quad (6.21)$$

where, for $i = 1, 2$, and 3 ,

$$p_i = \frac{a_i^{3/2}}{a_1^{3/2} + a_2^{3/2} + a_3^{3/2}}, \quad \lambda_i = \sqrt{\frac{r_m a_i}{2 r_L}}, \quad \text{and} \quad R_{\lambda_i} = \frac{r_L \lambda_i}{\pi a_i^2}. \quad (6.22)$$

Note that the distances x and y appearing in the exponential functions are divided by the electrotonic length of the segment along which the potential is measured or the current is injected. This solution satisfies the cable equation, because it is constructed by combining solutions of the form 6.18. The only term that has a discontinuous first derivative within the range being considered is the first term in the expression for v_2 , and this solves the cable equation at the current injection site because it is identical to 6.18. We leave it to the reader to verify that this solution satisfies the boundary conditions $v_1(0) = v_2(0) = v_3(0)$ and $\sum a_i^2 \partial v_i / \partial x = 0$.

Figure 6.9 shows the potential near a junction where a cable of radius 2μ breaks into two thinner cables of radius 1μ . In figure 6.9A, current is injected along the thicker cable, while in figure 6.9B it is injected along one of the thinner branches. In both cases, the site of current injection is one electrotonic length constant away from the junction. The two daughter branches have little effect on the fall-off of the potential away from the electrode site in figure 6.9A. This is because the thin branches do not represent a large current sink. The thick branch has a bigger effect on the attenuation of the potential along the thin branch receiving the electrode current in figure 6.9B. This can be seen as an asymmetry in the fall-off of the potential on either side of the electrode. Loading by the thick cable segment contributes to a quite severe attenuation between the two thin branches in figure 6.9B. Comparison of figures 6.9A and B reveals a general feature of static attenuation in a passive cable. Attenuation near the soma due to potentials arising in the periphery is typically greater than attenuation in the periphery due to potentials arising near the soma.

The Rall Model

The infinite and semi-infinite cables we have considered are clearly mathematical idealizations. We now turn to a model neuron introduced by Rall (1959, 1977) that, while still highly simplified, captures some of the important elements that affect the responses of real neurons. Most neurons receive their synaptic inputs over complex dendritic trees. The integrated effect of these inputs is usually measured from the soma, and the spike-initiation region of the axon that determines whether the neuron fires an

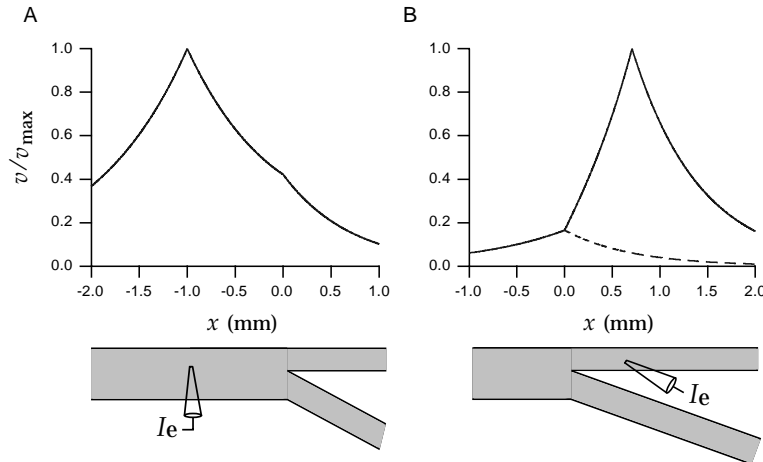


Figure 6.9: The potentials along the three branches of an isolated junction for a current injection site one electrotonic length constant away from the junction. The potential v is plotted relative to v_{\max} , which is v at the site of the electrode. The thick branch has a radius of 2μ and an electrotonic length constant $\lambda = 1$ mm, and the two thin branches have radii of 1μ and $\lambda = 2^{-1/2}$ mm. A) Current injection along the thick branch. The potentials along both of the thin branches, shown by the solid curve over the range $x > 0$, are identical. The solid curve over the range $x < 0$ shows the potential on the thick branch where current is being injected. B) Current injection along one of the thin branches. The dashed line shows the potential along the thin branch where current injection does not occur. The solid line shows the potential along the thick branch for $x < 0$ and along the thin branch receiving the injected current for $x > 0$.

action potential is typically located near the soma. In Rall's model, a compact soma region (represented by one compartment) is connected to a single equivalent cylindrical cable that replaces the entire dendritic region of the neuron (see the schematics in figures 6.10 and 6.12). The critical feature of the model is the choice of the radius and length for the equivalent cable to best match the properties of the dendritic structure being approximated.

The radius a and length L of the equivalent cable are determined by matching two important elements of the full dendritic tree. These are its average length in electrotonic units, which determines the amount of attenuation, and the total surface area, which determines the total membrane resistance and capacitance. The average electrotonic length of a dendrite is determined by considering direct paths from the soma to the terminals of the dendrite. The electrotonic lengths for these paths are constructed by measuring the distance traveled along each of the cable segments traversed in units of the electrotonic length constant for that segment. In general, the total electrotonic length measured by summing these electrotonic segment lengths depends on which terminal of the tree is used as the end point. However, an average value can be used to define an electrotonic length for the full dendritic structure. The length L of the equivalent ca-

ble is then chosen so that L/λ is equal to this average electrotonic length, where λ is the length constant for the equivalent cable. The radius of the equivalent cable, which is needed to compute λ , is determined by setting the surface area of the equivalent cable, $2\pi aL$, equal to the surface area of the full dendritic tree.

Under some restrictive circumstances the equivalent cable reproduces the effects of a full tree exactly. Among these conditions is the requirement $a_1^{3/2} = a_2^{3/2} + a_3^{3/2}$ on the radii of any three segments being joined at a nodes within the tree. Note from equation 6.22 that this conditions makes $p_1 = p_2 + p_3 = 1/2$. However, even when the so-called 3/2 law is not exact, the equivalent cable is an extremely useful and often reasonably accurate simplification.

Figures 6.10 and 6.12 depict static solutions of the Rall model for two different recording configurations expressed in the form of equivalent circuits. The equivalent circuits are an intuitive way of describing the solution of the cable equation. In figure 6.10, constant current is injected into the soma. The circuit diagram shows an arrangement of resistors that replicates the results of solving the time-independent cable equation (equation 6.17) for the purposes of voltage measurements at the soma, v_{soma} , and at a distance x along the equivalent cable, $v(x)$. The values for these resistances (and similarly the values of R_3 and R_4 given below) are set so that the equivalent circuit reconstructs the solution of the cable equation obtained using standard methods (see for example Tuckwell, 1988). R_{soma} is the membrane resistance of the soma, and

$$R_1 = \frac{R_\lambda (\cosh(L/\lambda) - \cosh((L-x)/\lambda))}{\sinh(L/\lambda)} \quad (6.23)$$

$$R_2 = \frac{R_\lambda \cosh((L-x)/\lambda)}{\sinh(L/\lambda)}. \quad (6.24)$$

Expressions for v_{soma} and $v(x)$, arising directly from the equivalent circuit using standard rules of circuit analysis (see the Mathematical Appendix), are given at the right side of figure 6.10.

The input resistance of the Rall model neuron, as measured from the soma, is determined by the somatic resistance R_{soma} acting in parallel with the effective resistance of the cable and is $(R_1 + R_2)R_{\text{soma}}/(R_1 + R_2 + R_{\text{soma}})$. The effective resistance of the cable, $R_1 + R_2 = R_\lambda / \tanh(L)$, approaches the value R_λ when $L \gg \lambda$. The effect of lengthening a cable saturates when it gets much longer than its electrotonic length. The voltage attenuation caused by the cable is defined as the ratio of the dendritic to somatic potentials, and it is given in this case by

$$\frac{v(x)}{v_{\text{soma}}} = \frac{R_2}{R_1 + R_2} = \frac{\cosh((L-x)/\lambda)}{\cosh(L/\lambda)}. \quad (6.25)$$

This result is plotted in figure 6.11.

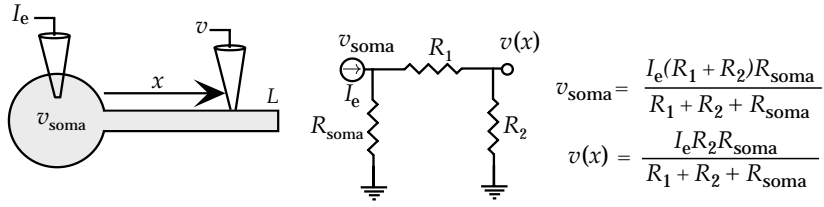


Figure 6.10: The Rall model with static current injected into the soma. The schematic at left shows the recording set up. The potential is measured at the soma and at a distance x along the equivalent cable. The central diagram is the equivalent circuit for this case, and the corresponding formulas for the somatic and dendritic voltages are given at the right. The symbols at the bottom of the resistances R_{soma} and R_2 indicate that these points are held at zero potential. R_{soma} is the membrane resistance of the soma, and R_1 and R_2 are the resistances given in equations 6.23 and 6.24.

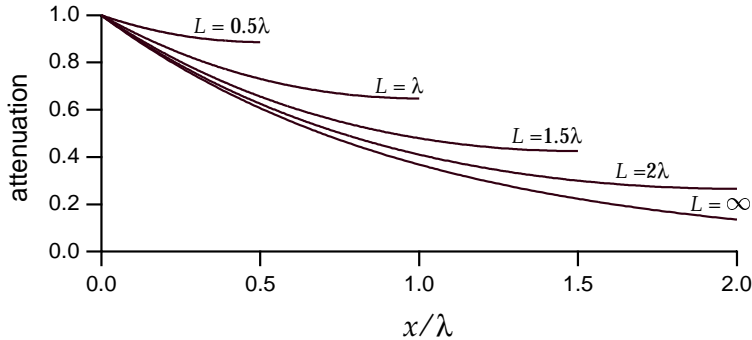


Figure 6.11: Voltage and current attenuation for the Rall model. The attenuation plotted is the ratio of the dendritic to somatic voltages for the recording setup of figure 6.10, or the ratio of the somatic current to the electrode current for the arrangement in figure 6.12. Attenuation is plotted as a function of x/λ for different equivalent cable lengths.

Figure 6.12 shows the equivalent circuit for the Rall model when current is injected at a location x along the dendritic tree and the soma is clamped at $v_{\text{soma}} = 0$ (or equivalently $V = V_{\text{rest}}$). The equivalent circuit can be used to determine the current entering the soma and the voltage at the site of current injection. In this case, the somatic resistance is irrelevant because the soma is clamped at its resting potential. The other resistances are

$$R_3 = R_\lambda \sinh(x/\lambda) \quad (6.26)$$

and

$$R_4 = \frac{R_\lambda \sinh(x/\lambda) \cosh((L-x)/\lambda)}{\cosh(L/\lambda) - \cosh((L-x)/\lambda)}. \quad (6.27)$$

The input resistance for this configuration, as measured from the dendrite, is determined by R_3 and R_4 acting in parallel and is $R_3 R_4 / (R_3 + R_4) =$

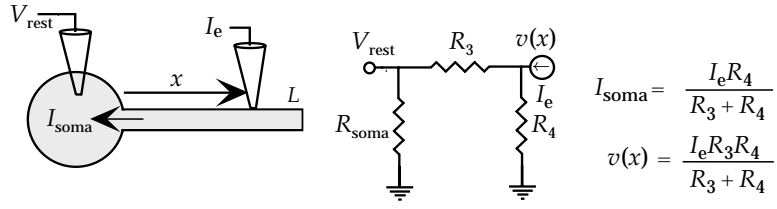


Figure 6.12: The Rall model with static current injected a distance x along the equivalent cable while the soma is clamped at its resting potential. The schematic at left shows the recording set up. The potential at the site of the current injection and the current entering the soma are measured. The central diagram is the equivalent circuit for this case, and the corresponding formulas for the somatic current and dendritic voltage are given at the right. R_{soma} is the membrane resistance of the soma, and R_3 and R_4 are the resistances given in equations 6.26 and 6.27.

$R_\lambda \sinh(x/\lambda) \cosh((L-x)/\lambda) / \cosh(L/\lambda)$. When L and x are both much larger than λ , this approaches the limiting value R_λ . The current attenuation is defined as the ratio of the somatic to electrode currents and is given by

$$\frac{I_{\text{soma}}}{I_e} = \frac{R_4}{R_3 + R_4} = \frac{\cosh((L-x)/\lambda)}{\cosh(L/\lambda)}. \quad (6.28)$$

The inward current attenuation (plotted in figure 6.11) for the recording configuration of figure 6.12 is identical to the outward voltage attenuation for figure 6.10 given by equation 6.25. Equality of the voltage attenuation measured in one direction and the current attenuation measured in the opposite direction is a general feature of linear cable theory.

The Morphoelectrotonic Transform

The membrane potential for a neuron of complex morphology is obviously much more difficult to compute than the simple cases we have considered. Fortunately, efficient numerical schemes (discussed later in this chapter) exist for generating solutions for complex cable structures. However, even when the solution is known, it is still difficult to visualize the effects of a complex morphology on the potential. Zador, Agmon-Snir, and Segev (1995; see also Tsai et al., 1994) devised a scheme for depicting the attenuation and delay of the membrane potential for complex morphologies. The voltage attenuation, as plotted in figure 6.11, is not an appropriate quantity to represent geometrically because it is not additive. Consider three points along a cable satisfying $x_1 > x_2 > x_3$. The attenuation between x_1 and x_3 is the product of the attenuation from x_1 to x_2 and from x_2 to x_3 , $v(x_1)/v(x_3) = (v(x_1)/v(x_2))(v(x_2)/v(x_3))$. An additive quantity can be obtained by taking the logarithm of the attenuation, due to the identity $\ln(v(x_1)/v(x_3)) = \ln(v(x_1)/v(x_2)) + \ln(v(x_2)/v(x_3))$. The morphoelectrotonic transform is a diagram of a neuron in which the distance between

morphoelectrotonic
transform

any two points is determined by the logarithm of the ratio of the membrane potentials at these two locations, not by the actual size of the neuron.

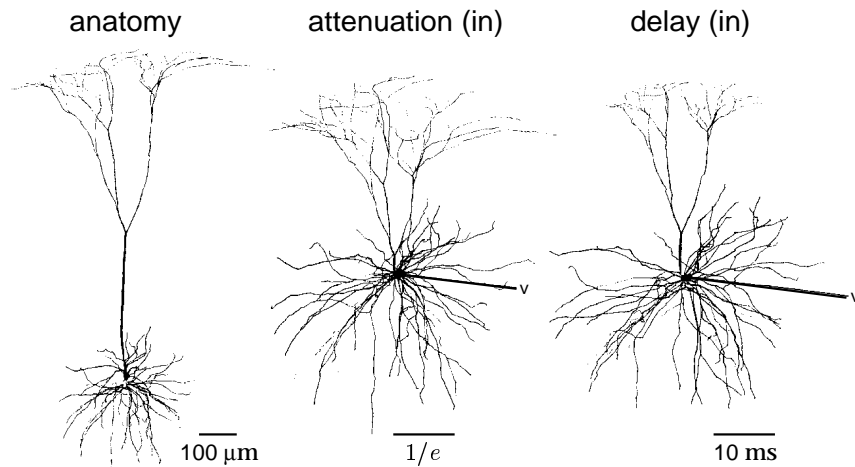


Figure 6.13: The morphoelectrotonic transform of a cortical neuron. The left panel is a normal drawing of the neuron. The central panel is a diagram in which the distance between any point and the soma is proportional to the logarithm of the steady-state attenuation between the soma and that point for static current injected at the terminals of the dendrites. The scale bar denotes the distance corresponding to an attenuation of $\exp(-1)$. In the right panel, the distance from the soma to a given point is proportional to the inward delay, which is the centroid of the soma potential minus the centroid at the periphery when a pulse of current is injected peripherally. The arrows in the diagrams indicate that the reference potential in these cases is the somatic potential. (Adapted from Zador et al, 1995.)

Another morphoelectrotonic transform can be used to indicate the amount of delay in the voltage waveform produced by a transient input current. The morphoelectrotonic transform uses a different definition of delay than that used in Figure 6.8B. The delay between any two points is defined as the difference between the centroid, or center of ‘gravity’, of the voltage response at these points. Specifically, the centroid at point x is defined as $\int dt tv(x, t) / \int dt v(x, t)$. Like the log-attenuation, the delay between any two points on a neuron is represented in the morphoelectrotonic transform as a distance.

Morphoelectrotonic transforms of a pyramidal cell from layer 5 of cat visual cortex are shown in figures 6.13 and 6.14. The left panel of figure 6.13 is a normal drawing of the neuron being studied, the middle panel shows the steady-state attenuation, and the right panel shows the delay. The transformed diagrams correspond to current being injected peripherally, with somatic potentials being compared to dendritic potentials. These figures indicate that, for potentials generated in the periphery, the apical and basal dendrites are much more uniform than the morphology would

suggest.

The small neuron diagram at the upper left of figure 6.14 shows attenuation for the reverse situation from figure 6.13, when DC current is injected into the soma and dendritic potentials are compared with the somatic potential. Note how much smaller this diagram is than the one in the central panel of figure 6.13. This illustrates the general feature mentioned previously that potentials are attenuated much less in the outward than in the inward direction. This is because the thin dendrites provide less of a current sink for potentials arising from the soma than the soma provides for potentials coming from the dendrites.

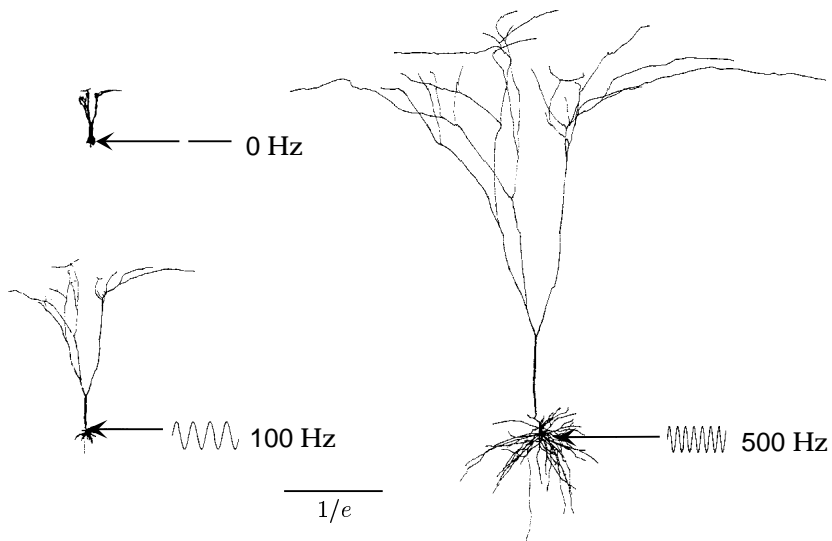


Figure 6.14: Morphoelectrotonic transforms of the same neuron as in figure 6.13 but showing the outward log-attenuation for DC and oscillating input currents. Distances in these diagrams are proportional to the logarithm of the amplitude of the voltage oscillations at a given point divided by the amplitude of the oscillations at the soma when a sinusoidal current is injected into the soma. The upper left panel corresponds to DC current injection, the lower left panel to sinusoidal current injection at a frequency of 100 Hz, and the right panel to an injection frequency of 500 Hz. The scale bar denotes the distance corresponding to an attenuation of $\exp(-1)$. (Adapted from Zador et al, 1995.)

The capacitance of neuronal cables causes the voltage attenuation for time-dependent current injection to increase as a function of frequency. Figure 6.14 compares the attenuation of dendritic potentials relative to the somatic potential when DC or sinusoidal current of two different frequencies is injected into the soma. Clearly, attenuation increases dramatically as a function of frequency. Thus, a neuron that appears electrotonically compact for static or low frequency current injection may be not compact when higher frequencies are considered. For example, action potential

waveforms, that correspond to frequencies around 500 Hz, are much more severely attenuated within neurons than slower varying potentials.

6.4 Multi-Compartment Models

The cable equation can only be solved analytically in relatively simple cases. When the complexities of real membrane conductances are included, the membrane potential must be computed numerically. This is done by splitting the neuron being modeled into separate regions or compartments and approximating the continuous membrane potential $V(x, t)$ by a discrete set of values representing the potentials within the different compartments. This assumes that each compartment is small enough so that there is negligible variation of the membrane potential across it. The precision of such a multi-compartmental description depends on the number of compartments used and on their size relative to the length constants that characterize their electrotonic compactness. Figure 6.15 shows a schematic diagram of a cortical pyramidal neuron, along with a series of compartmental approximations of its structure. The number of compartments used can range from thousands, in some models, to one, for the description at the extreme right of figure 6.15.

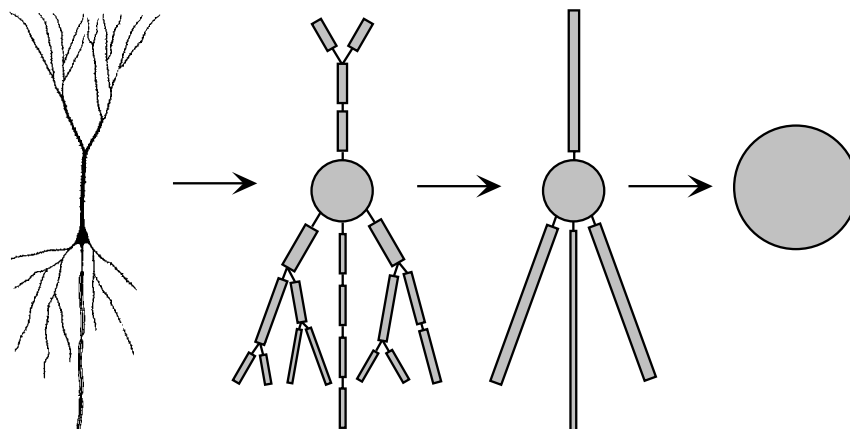


Figure 6.15: A sequence of approximations of the structure of a neuron. The neuron is represented by a variable number of discrete compartments each representing a region that is described by a single membrane potential. The connectors between compartments represent resistive couplings. The simplest description is the single-compartment model furthest to the right. (Neuron diagram from Haberly, 1990.)

In a multi-compartment model, each compartment has its own membrane potential V_μ (where μ labels compartments), and its own gating variables

that determine the membrane current for compartment μ , i_m^μ . Each membrane potential V_μ satisfies an equation similar to 6.1 except that the compartments couple to their neighbors in the multi-compartment structure (figure 6.16). For a non-branching cable, each compartment is coupled to two neighbors, and the equations for the membrane potentials of the compartments are

$$c_m \frac{dV_\mu}{dt} = -i_m^\mu + \frac{I_e^\mu}{A_\mu} + g_{\mu,\mu+1}(V_{\mu+1} - V_\mu) + g_{\mu,\mu-1}(V_{\mu-1} - V_\mu). \quad (6.29)$$

Here I_e^μ is the total electrode current flowing into compartment μ , and A_μ is its surface area. Compartments at the ends of a cable have only one neighbor and thus only a single term replacing the last two terms in equation 6.29. For a compartment where a cable branches in two, there are three such terms corresponding to coupling of the branching node to the first compartment in each of the daughter branches.

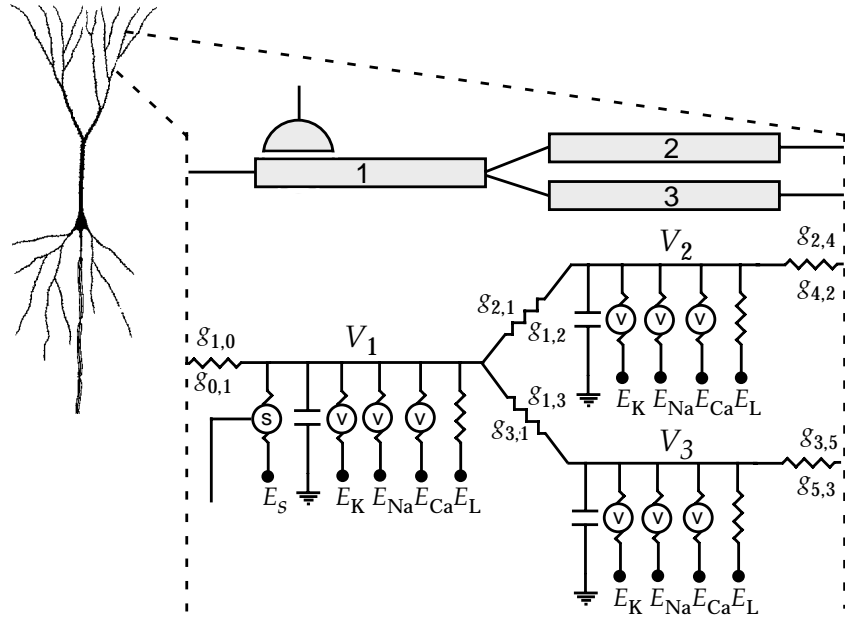


Figure 6.16: A multi-compartment model of a neuron. The expanded region shows three compartments at a branch point where a single cable splits into two. Each compartment has membrane and synaptic conductances, as indicated by the equivalent electrical circuit, and the compartments are coupled together by resistors. Although a single resistor symbol is drawn, note that $g_{\mu,\mu'}$ is not necessarily equal to $g_{\mu',\mu}$.

The constant $g_{\mu,\mu'}$ that determines the resistive coupling from neighboring compartment μ' to compartment μ is determined by computing the current that flows from one compartment to its neighbor due to Ohm's law. For simplicity, we begin by computing the coupling between two compartments that have the same length L and radius a . Using the results of

chapter 5, the resistance between two such compartments, measured from their centers, is the intracellular resistivity, r_L times the distance between the compartment centers divided by the cross-sectional area, $r_L L / \pi a^2$. The total current flowing from compartment $\mu + 1$ to compartment μ is then $\pi a^2 (V_{\mu+1} - V_\mu) / r_L L$. Equation 6.29 for the potential within a compartment μ refers to currents per unit area of membrane. Thus, we must divide the total current from compartment μ' by the surface area of compartment μ , $2\pi a_\mu L$. Thus, we find that $g_{\mu,\mu'} = a / (2r_L L^2)$.

The value of $g_{\mu,\mu'}$ is given by a more complex expression if the two neighboring compartments have different lengths or radii. This can occur when a tapering cable is approximated by a sequence of cylindrical compartments, or at a branch point where a single compartment connects with two other compartments as in figure 6.16. In either case, suppose that compartment μ has length L_μ and radius a_μ and compartment μ' has length $L_{\mu'}$ and radius $a_{\mu'}$. The resistance between these two compartments is the sum of the two resistances from the middle of each compartment to the junction between them, $r_L L_\mu / (2\pi a_\mu^2) + r_L L_{\mu'} / (2\pi a_{\mu'}^2)$. To compute $g_{\mu,\mu'}$ we invert this expression and divide the result by the total surface area of compartment μ , $2\pi a_\mu L_\mu$, which gives

$$g_{\mu,\mu'} = \frac{a_\mu a_{\mu'}^2}{r_L L_\mu (L_\mu a_{\mu'}^2 + L_{\mu'} a_\mu^2)} . \quad (6.30)$$

Equations 6.29 for all of the compartments of a model determine the membrane potential throughout the neuron with a spatial resolution given by the compartment size. An efficient method for integrating the coupled multi-compartment equations is discussed in appendix B. Using this scheme, models can be integrated numerically with excellent efficiency, even those involving large numbers of compartments. Such integration schemes are built into neuron simulation software packages such as Neuron and Genesis.

Action Potential Propagation Along an Unmyelinated Axon

As an example of multi-compartment modeling, we simulate the propagation of an action potential along an unmyelinated axon. In this model, each compartment has the same membrane conductances as the single-compartment Hodgkin-Huxley model discussed in chapter 5. The different compartments are joined together in a single non-branching cable representing a length of axon. Figure 6.17 shows an action potential propagating along an axon modeled in this way. The action potential extends over more than 1 mm of axon and it travels about 2 mm in 5 ms for a speed of 0.4 m/s.

Although action potentials typically move along axons in a direction outward from the soma (called orthodromic propagation), the basic process

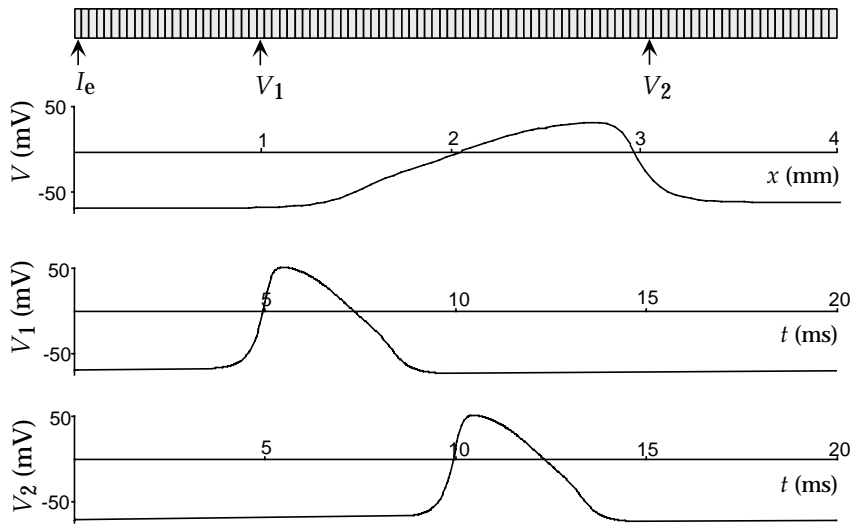


Figure 6.17: Propagation of an action potential along a multi-compartment model axon. The upper panel shows the multi-compartment representation of the axon with 100 compartments. The axon segment shown is 4 mm long and has a radius of $1 \mu\text{m}$. An electrode current sufficient to initiate action potentials is injected at the point marked I_e . The panel beneath this shows the membrane potential as a function of position along the axon, at $t = 9.75 \text{ ms}$. The spatial position in this panel is aligned with the axon depicted above it. The action potential is moving to the right. The bottom two panels show the membrane potential as a function of time at the two locations denoted by the arrows and symbols V_1 and V_2 in the upper panel.

*orthodromic;
antidromic
propagation*

of action potential propagation does not favor one direction over the other. Propagation in the reverse direction, called antidromic propagation, is possible under certain stimulation conditions. For example, if an axon is stimulated in the middle of its length, action potentials will propagate in both directions away from the point of stimulation. Once an action potential starts moving along an axon, it does not generate a second action potential moving in the opposite direction because of refractory effects. The region in front of a moving action potential is ready to generate a spike as soon as enough current moves longitudinally down the axon from the region currently spiking to charge the next region up to spiking threshold. However, Na^+ conductances in the region just behind the moving action potential are still partially inactivated, so this region cannot generate another spike until after a recovery period. By the time the trailing region has recovered, the action potential has moved too far away to generate a second spike.

Refractoriness following spiking has a number of other consequences for action potential propagation. Two action potentials moving in opposite directions that collide annihilate each other because they cannot pass through each other's trailing refractory regions. Refractoriness also keeps

action potentials from reflecting off the ends of axon cables, which avoids the impedance matching needed to prevent reflection from the ends of ordinary electrical cables.

The propagation velocity for an action potential along an unmyelinated axon is proportional to the ratio of the electrotonic length constant to the membrane time constant, $\lambda/\tau_m = (a/(c_m^2 r_L r_m))^{1/2}$. This is proportional to the square root of the axon radius. The square-root dependence of the propagation speed on the axon radius means that thick axons are required to achieve high action potential propagation speeds, and the squid giant axon is an extreme example. Action potential propagation can also be sped up by covering the axon with an insulating myelin wrapping, as we discuss next.

Propagation Along a Myelinated Axon

Many axons in vertebrates are covered with an insulating sheath of myelin, except at gaps, called the nodes of Ranvier, where there is a high density of fast voltage-dependent Na^+ channels and other ion channels (see figure 6.18A). The myelin sheath consists of many layers of (glial cell) membrane wrapped around the axon. This gives the myelinated region of the axon a very high membrane resistance and a small membrane capacitance. This results in what is called saltatory propagation, in which membrane potential depolarization is transferred passively down the myelin-covered sections of the axon, and action potentials are actively regenerated at the nodes of Ranvier. The cell membrane at the nodes of Ranvier has a high density of fast Na^+ channels. Figure 6.18A shows an equivalent circuit for a multi-compartment model of a myelinated axon.

saltatory propagation

We can compute the capacitance of a myelin-covered axon by treating the myelin sheath as an extremely thick cell membrane. Consider the geometry shown in the cross-sectional diagram of figure 6.18B. The myelin sheath extends from the radius a_1 of the axon core to the outer radius a_2 . For calculational purposes, we can think of the myelin sheath as being made of a series of thin concentric cylindrical shells. The capacitances of these shells combine in series to make up the full capacitance of the myelinated axon. If a single layer of cell membrane has thickness d_m and capacitance per unit area c_m , the capacitance of a cylinder of membrane of radius a , thickness Δa , and length L is $c_m 2\pi d_m L a / \Delta a$. According to the rule for capacitors in series, the inverse of the total capacitance is obtained by adding the inverses of the individual capacitances. The capacitance of a myelinated cylinder of length L and the dimensions in figure 6.18B is then obtained by taking the limit $\Delta a \rightarrow 0$ and integrating,

$$\frac{1}{C_m} = \frac{1}{c_m 2\pi d_m L} \int_{a_1}^{a_2} \frac{da}{a} = \frac{\ln(a_2/a_1)}{c_m 2\pi d_m L}. \quad (6.31)$$

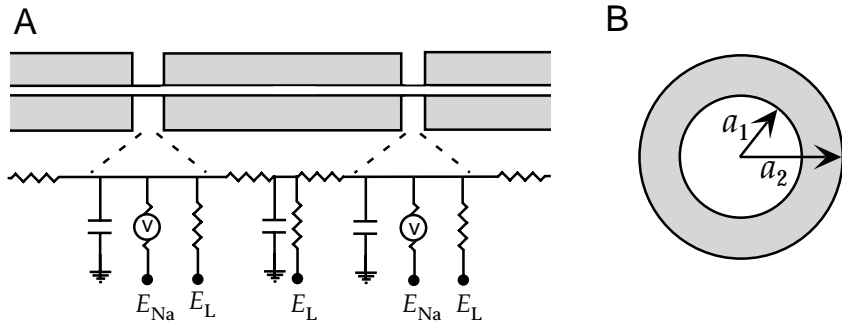


Figure 6.18: A myelinated axon. A) The equivalent circuit for a multi-compartment representation of a myelinated axon. The myelinated segments are represented by a membrane capacitance, a longitudinal resistance, and a leakage conductance. The nodes of Ranvier also contain a voltage-dependent Na^+ conductance. B) A cross-section of a myelinated axon consisting of a central axon core of radius a_1 and a myelin sheath making the outside radius a_2 .

A re-evaluation of the derivation of the linear cable equation earlier in this chapter indicates that the equation describing the membrane potential along the myelinated sections of an axon, in the limit of infinite resistance for the myelinated membrane and with $i_e = 0$, is

$$\frac{C_m}{L} \frac{\partial v}{\partial t} = \frac{\pi a_1^2}{r_L} \frac{\partial^2 v}{\partial x^2}. \quad (6.32)$$

This is equivalent to the diffusion equation, $\partial v / \partial t = D \partial^2 v / \partial x^2$ with diffusion constant $D = \pi a_1^2 L / (C_m r_L) = a_1^2 \ln(a_2/a_1) / (2c_m r_L d_m)$. It is interesting to compute the inner core radius, a_1 , that maximizes this diffusion constant for a fixed outer radius a_2 . Setting the derivative of D with respect to a_1 to zero gives the optimal inner radius $a_1 = a_2 \exp(-1/2)$ or $a_1 \approx 0.6a_2$. An inner core fraction of 0.6 is typical for myelinated axons. This indicates that, for a given outer radius, the thickness of myelin maximizes the diffusion constant along the myelinated axon segment.

At the optimal ratio of radii, $D = a_2^2 / (4ec_m r_L d_m)$, which is proportional to the square of the axon radius. Because of the form of the diffusion equation it obeys with this value of D , v can be written as a function of x/a_2 and t . This scaling implies that the propagation velocity for a myelinated cable is proportional to a_2 , that is, to the axon radius not its square root as in the case of an unmyelinated axon. Increasing the axon radius by a factor of four, for example, increases the propagation speed of an unmyelinated cable only by a factor of two, while it increases the speed for a myelinated cable fourfold.

6.5 Chapter Summary

We continued the discussion of neuron modeling that began in chapter 5 by considering models with more complete sets of conductances and techniques for incorporating neuronal morphology. We introduced A-type K⁺, transient Ca²⁺, and Ca²⁺-dependent K⁺ conductances and noted their effect on neuronal activity. The cable equation and its linearized version were introduced to examine the effects of morphology on membrane potentials. Finally, multi-compartment models were presented and used to discuss propagation of action potentials along unmyelinated and myelinated axons.

6.6 Appendices

A) Gating Functions for Conductance-Based Models

Connor-Stevens Model

The rate functions used for the gating variables n , m , and h of the Connor-Stevens model, in units of 1/ms with V in units of mV, are

$$\begin{aligned}\alpha_m &= \frac{0.38(V + 29.7)}{1 - \exp[-0.1(V + 29.7)]} & \beta_m &= 15.2 \exp[-0.0556(V + 54.7)] \\ \alpha_h &= 0.266 \exp[-0.05(V + 48)] & \beta_h &= 3.8 / (1 + \exp[-0.1(V + 18)]) \\ \alpha_n &= \frac{0.02(V + 45.7)}{1 - \exp[-0.1(V + 45.7)]} & \beta_n &= 0.25 \exp[-0.0125(V + 55.7)].\end{aligned}\quad (6.33)$$

The A-current is described directly in terms of the asymptotic values and τ functions for its gating variables (with τ_a and τ_b in units of ms and V in units of mV),

$$a_\infty = \left[\frac{0.0761 \exp[0.0314(V + 94.22)]}{1 + \exp[0.0346(V + 1.17)]} \right]^{1/3} \quad (6.34)$$

$$\tau_a = 0.3632 + 1.158 / (1 + \exp[0.0497(V + 55.96)]) \quad (6.35)$$

$$b_\infty = \left[\frac{1}{1 + \exp[0.0688(V + 53.3)]} \right]^4 \quad (6.36)$$

and

$$\tau_b = 1.24 + 2.678 / (1 + \exp[0.0624(V + 50)]). \quad (6.37)$$

Transient Ca^{2+} Conductance

The gating functions used for the variables M and H in the transient Ca^{2+} conductance model we discussed, with V in units of mV and τ_M and τ_H in ms, are

$$M_\infty = \frac{1}{1 + \exp(-(V + 57)/6.2)} \quad (6.38)$$

$$H_\infty = \frac{1}{1 + \exp((V + 81)/4)} \quad (6.39)$$

$$\tau_M = 0.612 + (\exp(-(V + 132)/16.7) + \exp((V + 16.8)/18.2))^{-1} \quad (6.40)$$

and

$$\tau_H = \begin{cases} \exp((V + 467)/66.6) & \text{if } V < -80 \text{ mV} \\ 28 + \exp(-(V + 22)/10.5) & \text{if } V \geq -80 \text{ mV.} \end{cases} \quad (6.41)$$

Ca^{2+} -dependent K^+ Conductance

The gating functions used for the Ca^{2+} -dependent K^+ conductance we discussed, with V in units of mV and τ_c in ms, are

$$c_\infty = \left(\frac{[\text{Ca}^{2+}]}{[\text{Ca}^{2+}] + 3\mu\text{M}} \right) \frac{1}{1 + \exp(-(V + 28.3)/12.6)} \quad (6.42)$$

and

$$\tau_c = 90.3 - \frac{75.1}{1 + \exp(-(V + 46)/22.7)}. \quad (6.43)$$

B) Integrating Multi-Compartment Models

Multi-compartmental models are defined by a coupled set of differential equations (equation 6.29), one for each compartment. There are also gating variables for each compartment, but these only involve the membrane potential (and possibly Ca^{2+} concentration) within that compartment, and integrating their equations can be handled as in the single-compartment case using the approach discussed in appendix B of chapter 5. Integrating the membrane potentials for the different compartments is more complex because they are coupled to each other.

Equation 6.29 for the membrane potential within compartment μ can be written in the form

$$\frac{dV_\mu}{dt} = A_\mu V_{\mu-1} + B_\mu V_\mu + C_\mu V_{\mu+1} + D_\mu \quad (6.44)$$

where

$$\begin{aligned} A_\mu &= c_m^{-1} g_{\mu,\mu-1}, & B_\mu &= -c_m^{-1} \left(\sum_i g_i^\mu + g_{\mu,\mu+1} + g_{\mu,\mu-1} \right), \\ C_\mu &= c_m^{-1} g_{\mu,\mu+1}, & \text{and } D_\mu &= c_m^{-1} \left(\sum_i g_i^\mu E_i + I_e^\mu / A_\mu \right). \end{aligned} \quad (6.45)$$

Note that the gating variables and other parameters have been absorbed into the values of A_μ , B_μ , C_μ , and D_μ in this equation. Equation 6.44, with μ running over all of the compartments of the model, generates a set of coupled differential equations. Because of the coupling between compartments, we cannot use the method discussed in appendix A of chapter 5 to integrate these equations. Instead, we present another method that shares some of the positive features of that method.

Two of the most important features of an integration method are accuracy and stability. Accuracy refers to how closely numerical finite-difference methods reproduce the exact solution of a differential equation as a function of the integration step size Δt . Stability refers to what happens when Δt is chosen to be excessively large and the method starts to become inaccurate. A stable integration method will degrade smoothly as Δt is increased, producing results of steadily decreasing accuracy. An unstable method, on the other hand, will, at some point, display a sudden transition and generate wildly inaccurate results. Given the tendency of impatient modelers to push the limits on Δt , it is highly desirable to have a method that is stable.

Defining

$$V_\mu(t + \Delta t) = V_\mu(t) + \Delta V_\mu, \quad (6.46)$$

the finite difference form of equation 6.44 gives the update rule

$$\Delta V_\mu = (A_\mu V_{\mu-1}(t) + B_\mu V_\mu(t) + C_\mu V_{\mu+1}(t) + D_\mu) \Delta t \quad (6.47)$$

which is how ΔV_μ is computed using the so-called Euler method. This method is both inaccurate and unstable. The stability of the method can be improved dramatically by evaluating the membrane potentials on the right side of equation 6.47 not at time t , but at a later time $t + z\Delta t$, so that

$$\Delta V_\mu = (A_\mu V_{\mu-1}(t + z\Delta t) + B_\mu V_\mu(t + z\Delta t) + C_\mu V_{\mu+1}(t + z\Delta t) + D_\mu) \Delta t. \quad (6.48)$$

Two such methods are predominantly used, the reverse Euler method for which $z = 1$ and the Crank-Nicholson method with $z = 0.5$. The reverse Euler method is the more stable of the two and the Crank-Nicholson is the more accurate. In either case, ΔV_μ is determined from equation 6.48. These methods are called implicit because equation 6.48 must be solved to determine ΔV_μ . To do this, we write $V_\mu(t + z\Delta t) \approx V_\mu(t) + z\Delta V_\mu$ and likewise for $V_{\mu\pm 1}$. Substituting this into equation 6.48 gives

$$\Delta V_\mu = a_\mu \Delta V_{\mu-1} + b_\mu \Delta V_\mu + c_\mu \Delta V_{\mu+1} + d_\mu \quad (6.49)$$

where

$$\begin{aligned} a_\mu &= A_\mu z \Delta t, & b_\mu &= B_\mu z \Delta t, & c_\mu &= C_\mu z \Delta t, & \text{and} \\ d_\mu &= (D_\mu + A_\mu V_{\mu-1}(t) + B_\mu V_\mu(t) + C_\mu V_{\mu+1}(t)) \Delta t. \end{aligned} \quad (6.50)$$

Equation 6.49 for all μ values provides a set of coupled linear equations for the quantities ΔV_μ . An efficient method exists for solving these equations (Hines 1984, Tuckwell 1988). We illustrate the method for a single, non-branching cable that begins with at compartment $\mu = 1$, so that $a_1 = 0$, and ends at compartment $\mu = N$, so $c_N = 0$. The method consists of solving equation 6.49 for ΔV_μ in terms of $\Delta V_{\mu+1}$ sequentially starting at one end of the cable and proceeding to the other end. For example, if we start the procedure at compartment one, ΔV_1 can be expressed as

$$\Delta V_1 = \frac{c_1 \Delta V_2 + d_1}{1 - b_1}. \quad (6.51)$$

Substituting this into the equation 6.49 for $\mu = 2$ gives

$$\Delta V_2 = b'_2 \Delta V_2 + c_2 \Delta V_3 + d'_2 \quad (6.52)$$

where $b'_2 = b_2 + a_2 c_1 / (1 - b_1)$ and $d'_2 = d_2 + a_2 d_1 / (1 - b_1)$. We now repeat the procedure going down the cable. At each stage, we solve for $\Delta V_{\mu-1}$ in terms of ΔV_μ finding

$$\Delta V_{\mu-1} = \frac{c_{\mu-1} \Delta V_\mu + d'_{\mu-1}}{1 - b'_{\mu-1}}. \quad (6.53)$$

where

$$b'_{\mu+1} = b_{\mu+1} + \frac{a_{\mu+1} c_\mu}{1 - b'_\mu} \quad (6.54)$$

and

$$d'_{\mu+1} = d_{\mu+1} + \frac{a_{\mu+1} d'_\mu}{1 - b'_\mu}. \quad (6.55)$$

Finally, when we get to the end of the cable we can solve for

$$\Delta V_N = \frac{d'_N}{1 - b'_N} \quad (6.56)$$

because $c_N = 0$.

The procedure for computing all the ΔV_μ is the following. Define $b'_1 = b_1$ and $d'_1 = d_1$ and iterate equations 6.54 and 6.55 down the length of the cable to define all the b' and d' parameters. Then, solve for ΔV_N from equation 6.56 and iterate back up the cable solving for the ΔV 's using 6.53. This process takes only $2N$ steps.

We leave the extension of this method to the case of a branched cable as an exercise for the reader. The general procedure is similar to the one we presented for an non-branching cable. The equations are solved starting at the ends of the branches and moving in toward their branching node, then continuing on as for an non-branching cable, and finally reversing direction and completing the solution moving in the opposite direction along the cable and its branches.

6.7 Annotated Bibliography

Many of the references for chapter 5 apply to this chapter as well, including **Jack et al. (1975)**; **Tuckwell (1988)**; **Johnston & Wu (1995)**; **Koch & Segev (1998)**; **Koch (1998)**; **Hille (1992)**; **Mascagni & Sherman (1998)**. **Rall (1977)** describes cable theory, the equivalent cable model of dendritic trees, and the $3/2$ law. **Marder & Calabrese, (1996)** review neuromodulation.

Two freely available modeling packages for detailed neural models are in wide use, **Neuron** (see Hines & Carnevale, 1997) and **Genesis** (see Bower & Beeman, 1998). These are available at <http://www.neuron.yale.edu> and <http://genesis.bbb.caltech.edu/GENESIS/genesis.html>.

Chapter 7

Network Models

7.1 Introduction

Extensive synaptic connectivity is a hallmark of neural circuitry. For example, neurons in the mammalian neocortex each receive thousands of synaptic inputs. Network models allow us to explore the computational potential of such connectivity, using both analysis and simulations. As illustrations, we study in this chapter how networks can perform the following tasks: coordinate transformations needed in visually guided reaching, selective amplification leading to models of simple and complex cells in primary visual cortex, integration as a model of short-term memory, noise reduction, input selection, gain modulation, and associative memory. Networks that undergo oscillations are also analyzed, with application to the olfactory bulb. Finally, we discuss network models based on stochastic rather than deterministic dynamics, using the Boltzmann machine as an example.

Neocortical circuits are a major focus of our discussion. In the neocortex, which forms the convoluted outer surface of the (for example) human brain, neurons lie in six vertical layers highly coupled within cylindrical columns. Such columns have been suggested as basic functional units, and stereotypical patterns of connections both within a column and between columns are repeated across cortex. There are three main classes of interconnections within cortex, and in other areas of the brain as well. Feed-forward connections bring input to a given region from another region located at an earlier stage along a particular processing pathway. Recurrent synapses interconnect neurons within a particular region that are considered to be at the same stage along the processing pathway. These may include connections within a cortical column as well as connections between both nearby and distant cortical columns within a region. Top-down connections carry signals back from areas located at later stages. These definitions depend on the how the region being studied is specified and on the

cortical columns

*feedforward,
recurrent, and
top-down
connections*

hierarchical assignment of regions along a pathway. In general, neurons within a given region send top-down projections back to the areas from which they receive feedforward input, and receive top-down input from the areas to which they project feedforward output. The numbers, though not necessarily the strengths, of feedforward and top-down fibers between connected regions are typically comparable, and recurrent synapses typically outnumber feedforward or top-down inputs. We begin this chapter by studying networks with purely feedforward input and then study the effects of recurrent connections. The analysis of top-down connections, for which it is more difficult to establish clear computational roles, is left until chapter 10.

The most direct way to simulate neural networks is to use the methods discussed in chapters 5 and 6 to synaptically connect model spiking neurons. This is a worthwhile and instructive enterprise, but it presents significant computational, calculational, and interpretational challenges. In this chapter, we follow a simpler approach and construct networks of neuron-like units with outputs consisting of firing rates rather than action potentials. Spiking models involve dynamics over time scales ranging from channel openings that can take less than a millisecond, to collective network processes that may be several orders of magnitude slower. Firing-rate models avoid the short time scale dynamics required to simulate action potentials and thus are much easier to simulate on computers. Firing-rate models also allow us to present analytic calculations of some aspects of network dynamics that could not be treated in the case of spiking neurons. Finally, spiking models tend to have more free parameters than firing-rate models, and setting these appropriately can be difficult.

There are two additional arguments in favor of firing-rate models. The first concerns the apparent stochasticity of spiking. The models discussed in chapters 5 and 6 produce spike sequences deterministically in response to injected current or synaptic input. Deterministic models can only predict spike sequences accurately if all their inputs are known. This is unlikely to be the case for the neurons in a complex network, and network models typically include only a subset of the many different inputs to individual neurons. Therefore, the greater apparent precision of spiking models may not actually be realized in practice. If necessary, firing-rate models can be used to generate stochastic spike sequences from a deterministically computed rate, using the methods discussed in chapters 1 and 2.

The second argument comes involves a complication with spiking models that arises when they are used to construct simplified networks. Although cortical neurons receive many inputs, the probability of finding a synaptic connection between a randomly chosen pair of neurons is actually quite low. Capturing this feature, while retaining a high degree of connectivity through polysynaptic pathways, requires including a large number of neurons in a network model. A standard way of dealing with this problem is to use a single model unit to represent the average response of several neurons that have similar selectivities. These ‘averaging’ units can then

be interconnected more densely than the individual neurons of the actual network, and so fewer of them are needed to build the model. If neural responses are characterized by firing rates, the output of the model unit is simply the average of the firing rates of the neurons it represents collectively. However, if the response is a spike, it is not clear how the spikes of the represented neurons can be averaged. The way spiking models are typically constructed, an action potential fired by the model unit duplicates the effect of all the neurons it represents firing synchronously. Not surprisingly, such models tend to exhibit large-scale synchronization unlike anything seen in a healthy brain.

Firing-rate models also have their limitations. Most importantly, they cannot account for aspects of spike timing and spike correlations that may be important for understanding nervous system function. Firing-rate models are restricted to cases where the firing of neurons in a network is uncorrelated, with little synchronous firing, and where precise patterns spike timing are unimportant. In such cases, comparisons of spiking network models with models that use firing-rate descriptions have shown that they produce similar results. Nevertheless, the exploration of neural networks undoubtedly requires the use of both firing-rate and spiking models.

7.2 Firing-Rate Models

As discussed in chapter 1, the sequence of spikes generated by a neuron is completely characterized by the neural response function $\rho(t)$, which consists of δ function spikes located at times when the neuron fired action potentials. In firing-rate models, the exact description of a spike sequence provided by the neural response function $\rho(t)$ is replaced by the approximate description provided by the firing rate $r(t)$. Recall from chapter 1 that $r(t)$ is defined as the probability density of firing and is obtained from $\rho(t)$ by averaging over trials. The validity of a firing-rate model depends on how well the trial-averaged firing rate of network units approximates the effect of actual spike sequences on the dynamic behavior of the network.

The replacement of the neural response function by the corresponding firing rate is typically justified by the fact that each network neuron has a large number of inputs. Replacing $\rho(t)$, which describes an actual spike train, by the trial-averaged firing rate $r(t)$ is justified if the quantities of relevance for network dynamics are relatively insensitive to the trial-to-trial fluctuations in the spike sequences represented by $\rho(t)$. In a network model, the relevant quantities that must be modeled accurately are the total inputs to all the neurons in the network. For any single synaptic input, the trial-to-trial variability is likely to be large. However, if we sum the input over many synapses activated by uncorrelated presynaptic spike trains, the mean of the total input typically grows linearly with the number of synapses, while its standard deviation grows only as the square root of the number of synapses. Thus, for uncorrelated presynaptic spike trains,

using presynaptic firing rates in place of the actual presynaptic spike trains may not significantly modify the dynamics of the network. Conversely, a firing-rate model will fail to describe a network adequately if the presynaptic inputs to a substantial fraction of its neurons are correlated. This can occur, for example, if the presynaptic neurons fire synchronously.

The synaptic input arising from a presynaptic spike train is effectively filtered by the dynamics of the conductance changes that each presynaptic action potential evokes in the postsynaptic neuron (see chapter 5), and the dynamics of propagation of the current from the synapse to the soma. The temporal averaging provided by slow synaptic or membrane dynamics can reduce the effects of spike train variability and help justify the approximation of using firing rates instead of presynaptic spike trains. Firing-rate models are more accurate if the network being modeled has a significant amount of synaptic transmission that is slow relative to typical presynaptic interspike intervals.

The construction of a firing-rate model proceeds in two steps. First, we determine how the total synaptic input to a neuron depends on the firing rates of its presynaptic afferents. This is where we use firing rates to approximate neural response functions. Second, we model how the firing rate of the postsynaptic neuron depends on its total synaptic input. Firing-rate response curves are typically measured by injecting current into the soma of a neuron. We therefore find it most convenient to define the total synaptic input as the total current delivered to the soma as a result of all the synaptic conductance changes resulting from presynaptic action potentials. We denote this total synaptic current by I_s . We then determine the postsynaptic firing rate from I_s . In general, I_s depends on the spatially inhomogeneous membrane potential of the neuron, but we assume that, other than during action potentials or transient hyperpolarizations, the membrane potential remains close to, but slightly below, the threshold for action potential generation. An example of this type of behavior is seen in the upper panels of figure 7.2. I_s is then approximately equal to the synaptic current that would be measured from the soma in a voltage-clamp experiment, except for a reversal of sign. In the next section, we model how I_s depends on presynaptic firing rates.

In the network models we consider, both the output from, and input to, a neuron are characterized by firing rates. To avoid a proliferation of sub- and superscripts on the quantity $r(t)$, we use the letter u to denote a presynaptic firing rate, and v to denote a postsynaptic rate. Note that v is used here to denote a firing rate, not a membrane potential. In addition, we use these two letters to distinguish input and output firing rates in network models, a convention we retain through the remaining chapters. When we consider multiple input or output neurons, we use vectors \mathbf{u} and \mathbf{v} to represent their firing rates collectively, with the components of these vectors representing the firing rates of the individual input and output units.

input rate u
output rate v

input rate vector \mathbf{u}
output rate vector \mathbf{v}

The Total Synaptic Current

Consider a neuron receiving N_u synaptic inputs labeled by $b = 1, 2, \dots, N_u$ (figure 7.1). The firing rate of input b is denoted by u_b , and the input rates are represented collectively by the N_u -component vector \mathbf{u} . We model how the synaptic current I_s depends on presynaptic firing rates by first considering how it depends on presynaptic spikes. If an action potential arrives at input b at time zero, we write the synaptic current generated in the soma of the postsynaptic neuron at time t as $w_b K_s(t)$ where w_b is the synaptic weight and $K_s(t)$ is called the synaptic kernel. Collectively, the synaptic weights are represented by a synaptic weight vector \mathbf{w} , which has N_u components w_b . The amplitude and sign of the synaptic current generated by input b are determined by w_b . For excitatory synapses, $w_b > 0$, and for inhibitory synapses, $w_b < 0$. In this formulation of the effect of presynaptic spikes, the probability of transmitter release from a presynaptic terminal is absorbed into the synaptic weight factor w_b , and we do not include short-term plasticity in the model (although this can be done by making w_b a dynamic variable).

synaptic weights \mathbf{w}

The synaptic kernel, $K_s(t) \geq 0$, describes the time course of the synaptic current in response to a presynaptic spike arriving at time $t=0$. This time course depends on the dynamics of the synaptic conductance activated by the presynaptic spike and also on both the passive and active properties of the dendritic cables that carry the synaptic current to the soma. For example, long passive cables broaden the synaptic kernel and slow its rise from zero. Cable calculations or multicompartment simulations, such as those discussed in chapter 6, can be used to compute $K_s(t)$ for a specific dendritic structure. To avoid ambiguity, we normalize $K_s(t)$ by requiring its integral over all positive times to be one. At this point, for simplicity, we use the same function $K_s(t)$ to describe all synapses.

*synaptic kernel
 $K_s(t)$*

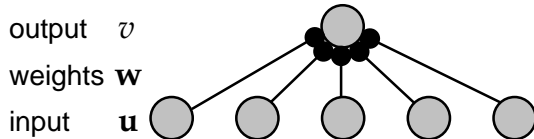


Figure 7.1: Feedforward inputs to a single neuron. Input rates \mathbf{u} drive a neuron at an output rate v through synaptic weights given by the vector \mathbf{w} .

Assuming that the spikes at a single synapse act independently, the total synaptic current at time t arising from a sequence of presynaptic spikes occurring at input b at times t_i is given by the sum

$$w_b \sum_{t_i < t} K_s(t - t_i) = w_b \int_{-\infty}^t d\tau K_s(t - \tau) \rho_b(\tau). \quad (7.1)$$

In the second expression, we have used the neural response function, $\rho_b(\tau) = \sum_i \delta(\tau - t_i)$, to describe the sequence of spikes fired by presy-

naptic neuron b . The equality follows from integrating over the sum of δ functions in the definition of $\rho_b(\tau)$. If there is no nonlinear interaction between different synaptic currents, the total synaptic current coming from all presynaptic inputs is obtained simply by summing,

$$I_s = \sum_{b=1}^{N_u} w_b \int_{-\infty}^t d\tau K_s(t - \tau) \rho_b(\tau). \quad (7.2)$$

As discussed previously, the critical step in the construction of a firing-rate model is the replacement of the neural response function $\rho_b(\tau)$ in equation 7.2 by the firing rate of neuron b , namely $u_b(\tau)$, so that we write

$$I_s = \sum_{b=1}^{N_u} w_b \int_{-\infty}^t d\tau K_s(t - \tau) u_b(\tau). \quad (7.3)$$

The synaptic kernel most frequently used in firing-rate models is an exponential, $K_s(t) = \exp(-t/\tau_r)/\tau_r$. With this kernel, we can describe I_s by a differential equation if we take the derivative of equation 7.3 with respect to t ,

$$\tau_s \frac{dI_s}{dt} = -I_s + \sum_{b=1}^{N_u} w_b u_b = -I_s + \mathbf{w} \cdot \mathbf{u}. \quad (7.4)$$

In the second equality, we have expressed the sum $\sum w_b u_b$ as the dot product of the weight and input vectors, $\mathbf{w} \cdot \mathbf{u}$. In this and the following chapters, we primarily use the vector versions of equations such as equation 7.4, but when we first introduce an important new equation, we often write it in its subscripted form as well.

Recall that K describes the temporal evolution of the synaptic current due to both synaptic conductance and dendritic cable effects. For an electrotonically compact dendritic structure, τ_s will be close to the time constant that describes the decay of the synaptic conductance. For fast synaptic conductances such as those due to AMPA glutamate receptors, this may be as short as a few milliseconds. For a long, passive dendritic cable, τ_s may be larger than this, but its measured value is typically quite small.

The Firing-Rate

Equation 7.4 determines the synaptic current entering the soma of a postsynaptic neuron in terms of the firing rates of the presynaptic neurons. To finish formulating a firing-rate model, we must determine the postsynaptic firing rate from our knowledge of I_s . For constant synaptic current, the firing rate of the postsynaptic neuron can be expressed as $v = F(I_s)$, where F is the steady-state firing rate as a function of somatic input current. F is also called an activation function. F is sometimes taken to be a saturating function such as a sigmoid function. This is useful in cases where

*activation
function $F(I_s)$*

the derivative of F is needed in the analysis of network dynamics. It is also bounded from above, which can be important in stabilizing a network against excessively high firing rates. More often, we use a threshold linear function $F(I_s) = [I_s - \gamma]_+$, where γ is the threshold and the notation $[]_+$ denotes half-wave rectification as in previous chapters. For convenience, we treat I_s in this expression as if its were measured in units of a firing rate (Hz), i.e. as if I_s is multiplied by a constant that converts its units from nA to Hz. This makes the synaptic weights dimensionless. The threshold γ also has units of Hz.

threshold γ

For time-independent inputs, the relation $v = F(I_s)$ is all we need to know to complete the firing-rate model. The total steady-state synaptic current predicted by equation 7.4 for time-independent \mathbf{u} is $I_s = \mathbf{w} \cdot \mathbf{u}$. This generates a steady-state output firing rate $v = v_\infty$ given by

$$v_\infty = F(\mathbf{w} \cdot \mathbf{u}). \quad (7.5)$$

The steady-state firing rate tells us how a neuron responds to constant current, but not to a current that changes with time. To model time-dependent inputs, we need to know the firing rate in response to a time-dependent synaptic current $I_s(t)$. The simplest assumption is that this is still given by the activation function, so $v = F(I_s(t))$ even when the total synaptic current varies with time. This leads to a firing-rate model in which all the dynamics arise exclusively from equation 7.4,

$$\tau_s \frac{dI_s}{dt} = -I_s + \mathbf{w} \cdot \mathbf{u} \quad \text{with} \quad v = F(I_s). \quad (7.6)$$

firing-rate model
with current
dynamics

An alternative formulation of a firing-rate model can be constructed by assuming that the firing rate does not follow changes in the total synaptic current instantaneously, as was assumed for the model of equation 7.6. Action potentials are generated by the synaptic current through its effect on the membrane potential of the neuron. Due to the membrane capacitance and resistance, the membrane potential is, roughly speaking, a low-pass filtered version of I_s (see the Mathematical Appendix). For this reason, the time-dependent firing rate is often modeled as a low-pass filtered version of the steady-state firing rate,

$$\tau_r \frac{dv}{dt} = -v + F(I_s(t)). \quad (7.7)$$

The constant τ_r in this equation determines how rapidly the firing rate approaches its steady-state value for constant I_s , and how closely v can follow rapid fluctuations for a time-dependent $I_s(t)$. Equivalently, it measures the time-scale over which v averages $F(I_s(t))$. The low-pass filtering effect of equation 7.7 is described in the Mathematical Appendix in the context of electrical circuit theory. The argument we have used to motivate equation 7.7 would suggest that τ_r should be approximately equal to the membrane time constant of the neuron. However, this argument really

applies to the membrane potential not the firing rate, and the dynamics of the two are not the same. Most network models use a value of τ_r that is considerably less than the membrane time constant. We re-examine this issue in the following section.

The second model that we have described involves the pair of equations 7.4 and 7.7. If one of these equations relaxes to its equilibrium point much more rapidly than the other, the pair can be reduced to a single equation. For example, if $\tau_r \ll \tau_s$, we can make the approximation that equation 7.7 rapidly sets $v = F(I_s(t))$, and then the second model reduces to the first model that is defined by equation 7.6. If instead, $\tau_r \gg \tau_s$, we can make the approximation that equation 7.4 comes to equilibrium quickly compared to equation 7.7. Then, we can make the replacement $I_s = \mathbf{w} \cdot \mathbf{u}$ in equation 7.7 and write

$$\tau_r \frac{dv}{dt} = -v + F(\mathbf{w} \cdot \mathbf{u}). \quad (7.8)$$

For most of this chapter, we analyze network models described by the firing-rate dynamics of equation 7.8, although occasionally we consider networks based on equation 7.6.

Firing-Rate Dynamics

The firing-rate models described by equations 7.6 and 7.8 differ in their assumptions about how firing rates respond to and track changes in the input current to a neuron. In one case (equation 7.6), it is assumed that firing rates follow time varying input currents instantaneously without attenuation or delay. In the other case (equation 7.8), the firing rate is a low-pass filtered version of the input current. To study the relationship between input current and firing rate, it is useful to examine the firing rate of a spiking model neuron in response to a time-varying injected current, $I(t)$. The model used for this purpose in figure 7.2 is an integrate-and-fire neuron receiving balanced excitatory and inhibitory synaptic input along with a current injected into the soma that is the sum of constant and oscillating components. This model was discussed in chapter 5. The balanced synaptic input is used to represent background input not included in the computation of I_s , and it acts as a source of noise. The noise prevents effects such as locking of the spiking to the oscillations of the injected current that would invalidate a firing-rate description.

Figure 7.2 shows the firing rates of the model integrate-and-fire neuron in response to an input current $I(t) = I_0 + I_1 \cos(\omega t)$. The firing rate is plotted at different times during the cycle of the input current oscillations for ω corresponding to frequencies of 1, 50, and 100 Hz. For the panels on the left side, the constant component of the injected current (I_0) was adjusted so the neuron never stopped firing during the cycle. In this case, the relation $v(t) = F(I(t))$ (solid curves) provides an accurate description

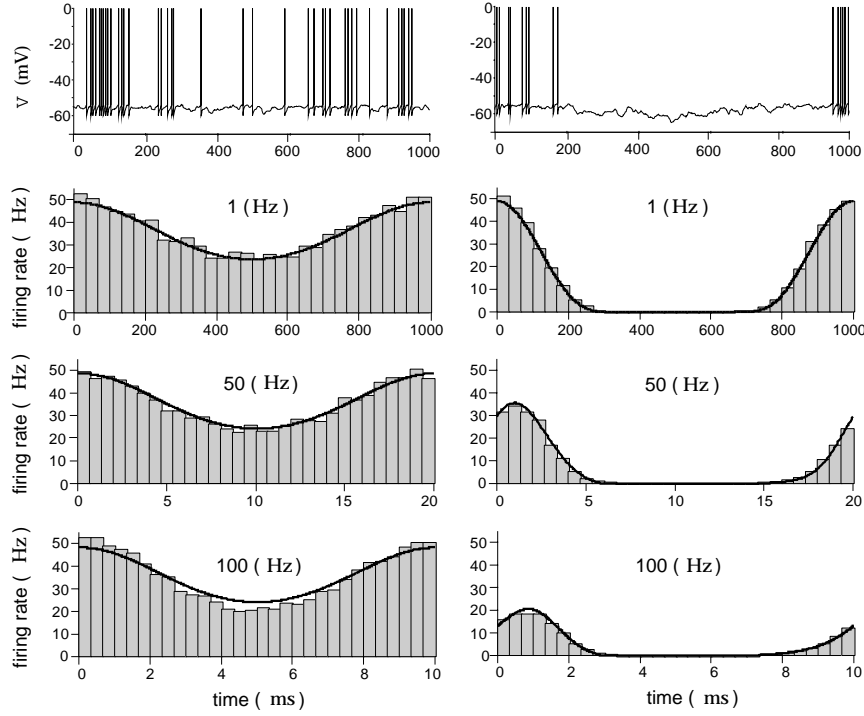


Figure 7.2: Firing rate of an integrate-and-fire neuron receiving balanced excitatory and inhibitory synaptic input and an injected current consisting of a constant and a sinusoidally varying term. For the left panels, the constant component of the injected current was adjusted so the firing never stopped during the oscillation of the varying part of the injected current. For the right panel, the constant component was lowered so the firing stopped during part of the cycle. The upper panels show two representative voltage traces of the model cell. The histograms beneath these traces were obtained by binning spikes generated over multiple cycles. They show the firing rate as a function of the time during each cycle of the injected current oscillations. The different rows show 1, 50, and 100 Hz oscillation frequencies for the injected current. The solid curves show the fit of a firing-rate model that involves both instantaneous and low-pass filtered effects of the injected current. For the left panel, this reduces to the simple prediction $v = F(I(t))$. (Adapted from Chance et al., 2000.)

of the firing rate for all of the oscillation frequencies shown. As long as the neuron keeps firing fairly rapidly, the low-pass filtering properties of the membrane potential are not relevant for the dynamics of the firing rate. Low-pass filtering is irrelevant in this case, because the neuron is continually being shuttled between the threshold and reset values, and so it never has a chance to settle exponentially anywhere near its steady-state value.

The right panels in figure 7.2 show that the situation is different if the input current is below the threshold for firing through a significant part of the oscillation cycle. In this case, the firing is delayed and attenuated

at high frequencies as would be predicted by equation 7.7. In this case, the membrane potential stays below threshold for long enough periods of time that its dynamics become relevant for the firing of the neuron.

The essential message from figure 7.2 is that neither equation 7.6 nor 7.8 provides a completely accurate prediction of the dynamics of the firing rate at all frequencies and for all levels of injected current. A more complex model can be constructed that accurately describes the firing rate over the entire range of input currents amplitudes and frequencies. The solid curves in figure 7.2 were generated by a model that expresses the firing rate as a function of both $F(I)$ and of v computed from equation 7.8 (although it reduces to $v = F(I(t))$ in the case of the left panel of figure 7.2). In other words, it is a combination of the two models discussed in the previous section. This compound model provides quite an accurate description of the firing rate of the integrate-and-fire model, but it is more complex than the models used in this chapter.

Feedforward and Recurrent Networks

Figure 7.3 shows examples of network models with feedforward and recurrent connectivity. The feedforward network of figure 7.3A has N_v output units with rates v_a ($a = 1, 2, \dots, N_v$), denoted collectively by the vector \mathbf{v} , driven by N_u input units with rates \mathbf{u} . Equations 7.8 and 7.6 can easily be extended to cover this case by replacing the vector of synaptic weights \mathbf{w} by a matrix \mathbf{W} , with the matrix component W_{ab} representing the strength of the synapse from input unit b to output unit a . Using the formulation of equation 7.8, the output firing rates are then determined by

$$\tau_r \frac{d\mathbf{v}}{dt} = -\mathbf{v} + \mathbf{F}(\mathbf{W} \cdot \mathbf{u}) \quad \text{or} \quad \tau_r \frac{dv_a}{dt} = -v_a + F \left(\sum_{b=1}^{N_u} W_{ab} u_b \right). \quad (7.9)$$

We use the notation $\mathbf{W} \cdot \mathbf{u}$ to denote the vector with components $\sum_b W_{ab} u_b$. The use of the dot to represent a sum of a product of two quantities over a shared index is borrowed from the notation for the dot product of two vectors. The expression $\mathbf{F}(\mathbf{W} \cdot \mathbf{u})$ represents the vector with components $F(\sum W_{ab} u_b)$ for $a = 1, 2, \dots, N_v$.

The recurrent network of figure 7.3B also has two layers of neurons with rates \mathbf{u} and \mathbf{v} , but in this case the neurons of the output layer are interconnected with synaptic weights described by a matrix \mathbf{M} . Matrix element $M_{aa'}$ describes the strength of the synapse from output unit a' to output unit a . The output rates in this case are determined by

$$\tau_r \frac{d\mathbf{v}}{dt} = -\mathbf{v} + \mathbf{F}(\mathbf{W} \cdot \mathbf{u} + \mathbf{M} \cdot \mathbf{v}). \quad (7.10)$$

It is often convenient to define the total feedforward input to each neuron in the network of figure 7.3B as $\mathbf{h} = \mathbf{W} \cdot \mathbf{u}$. Then, the output rates are

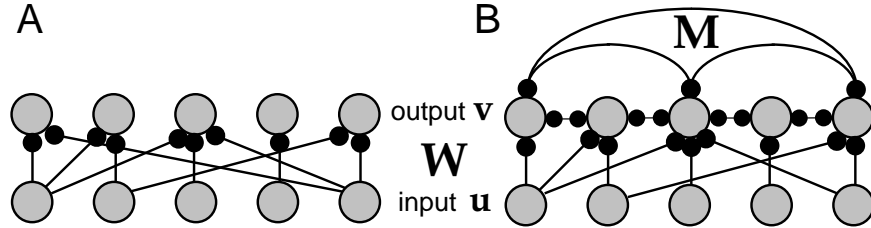


Figure 7.3: Feedforward and recurrent networks. A) A feedforward network with input rates u , output rates v , and a feedforward synaptic weight matrix W . B) A recurrent network with input rates u , output rates v , a feedforward synaptic weight matrix W , and a recurrent synaptic weight matrix M . Although we have drawn the connections between the output neurons as bidirectional, this does not necessarily imply connections of equal strength in both directions.

determined by the equation

$$\tau_r \frac{dv}{dt} = -v + F(h + M \cdot v). \quad (7.11)$$

Neurons are typically classified as either excitatory or inhibitory, meaning that they have either excitatory or inhibitory effects on all of their postsynaptic targets. This property is formalized in Dale's law, which states that a neuron cannot excite some of its postsynaptic targets and inhibit others. In terms of the elements of M , this means that for each presynaptic neuron a' , $M_{aa'}$ must have the same sign for all postsynaptic neurons a . To impose this restriction, it is convenient to describe excitatory and inhibitory neurons separately. The firing-rate vectors v_E and v_I for the excitatory and inhibitory neurons are then described by a coupled set of equations identical in form to equation 7.11,

$$\tau_E \frac{dv_E}{dt} = -v_E + F_E (h_E + M_{EE} \cdot v_E + M_{EI} \cdot v_I) \quad (7.12)$$

and

$$\tau_I \frac{dv_I}{dt} = -v_I + F_I (h_I + M_{IE} \cdot v_E + M_{II} \cdot v_I). \quad (7.13)$$

There are now four synaptic weight matrices describing the four possible types of neuronal interactions. The elements of M_{EE} and M_{IE} are greater than or equal to zero, and those of M_{EI} and M_{II} are less than or equal to zero. These equations allow the excitatory and inhibitory neurons to have different time constants, activation functions, and feedforward inputs.

In this chapter, we consider several recurrent network models described by equation 7.11 with a symmetric weight matrix, $M_{aa'} = M_{a'a}$ for all a and a' . Requiring M to be symmetric simplifies the mathematical analysis, but it violates Dale's law. Suppose, for example, that neuron a , which is excitatory, and neuron a' , which is inhibitory, are mutually connected. Then,

Dale's law

excitatory-inhibitory network

symmetric coupling

$M_{aa'}$ should be negative and $M_{a'a}$ positive, so they cannot be equal. Equation 7.11 with symmetric \mathbf{M} can be interpreted as a special case of equations 7.12 and 7.13 in which the inhibitory dynamics are instantaneous ($\tau_I \rightarrow 0$) and the inhibitory rates are given by $v_I = M_{IE}v_E$. This produces an effective recurrent weight matrix $\mathbf{M} = \mathbf{M}_{EE} + \mathbf{M}_{EI} \cdot \mathbf{M}_{IE}$, which can be made symmetric by the appropriate choice of the dimension and form of the matrices \mathbf{M}_{EI} and \mathbf{M}_{IE} . The dynamic behavior of equation 7.11 is restricted by requiring the matrix \mathbf{M} to be symmetric. For example symmetric coupling typically does not allow for network oscillations. In the latter part of this chapter, we consider the richer dynamics of models described by equations 7.12 and 7.13.

Continuously Labeled Networks

It is often convenient to identify each neuron in a network using a parameter that describes some aspect of its selectivity rather than the integer label a or b . For example, neurons in primary visual cortex can be characterized by their preferred orientation angles, preferred spatial phases and frequencies, or other stimulus-related parameters (see chapter 2). In many of the examples in this chapter, we consider stimuli characterized by a single angle Θ , which represents, for example, the orientation of a visual stimulus. Individual neurons are identified by their preferred stimulus angles, which are typically the values of Θ for which they fire at maximum rates. Thus, neuron a is identified by an angle θ_a . The weight of the synapse from neuron b or neuron a' to neuron a is then expressed as a function of the preferred stimulus angles θ_b , $\theta_{a'}$ and θ_a of the pre- and postsynaptic neurons, $W_{ab} = W(\theta_a, \theta_b)$ or $M_{aa'} = M(\theta_a, \theta_{a'})$. We often consider cases in which these synaptic weight functions depend only on the difference between the pre- and postsynaptic angles, so that $W_{ab} = W(\theta_a - \theta_b)$ or $M_{aa'} = M(\theta_a - \theta_{a'})$.

In large networks, the preferred stimulus parameters for different neurons will typically take a wide range of values. In the models we consider, the number of neurons is large and the angles θ_a , for different values of a cover the range from 0 to 2π densely. For simplicity, we assume that this coverage is uniform so that the density of coverage, the number of neurons with preferred angles falling within a unit range, which we denote by ρ_θ , is constant. For mathematical convenience in these cases, we allow the preferred angles to take continuous values rather than restricting them to the actual discrete values θ_a for $a = 1, 2, \dots, N$. Thus, we label the neurons by a continuous angle θ and express the firing rate as a function of θ , so that $u(\theta)$ and $v(\theta)$ describe the firing rates of neurons with preferred angles θ . Similarly, the synaptic weight matrices \mathbf{W} and \mathbf{M} are replaced by functions $W(\theta, \theta')$ and $M(\theta, \theta')$ that characterizes the strength of synapses from a presynaptic neuron with preferred angle θ' to a postsynaptic neuron with preferred angle θ in the feedforward and recurrent case, respectively.

If the number of neurons in a network is large and the density of cover-

ρ_θ density of coverage

age of preferred stimulus values is high, we can approximate the sums in equation 7.10 by integrals over θ' . The number of postsynaptic neurons with preferred angles within a range $\Delta\theta'$ is $\rho_\theta\Delta\theta'$, so, when we take the limit $\Delta\theta' \rightarrow 0$, the integral over θ' appears multiplied by the density factor ρ_θ . Thus, in the case of continuous labeling of neurons, equation 7.10 becomes (for constant ρ_θ)

$$\tau_r \frac{dv(\theta)}{dt} = -v(\theta) + F \left(\rho_\theta \int_{-\pi}^{\pi} d\theta' W(\theta, \theta') u(\theta') + M(\theta, \theta') v(\theta') \right). \quad (7.14)$$

As we did previously in equation 7.11, we can write the first term inside the integral of this expression as an input function $h(\theta)$. We make frequent use of continuous labeling for network models, and we often approximate sums over neurons by integrals over their preferred stimulus parameters.

continuous model

7.3 Feedforward Networks

Substantial computations can be performed by feedforward networks in the absence of recurrent connections. Much of the work done on feedforward networks centers on plasticity and learning, as discussed in the following chapters. Here, we present an example of the computational power of feedforward circuits, the calculation of the coordinate transformations needed in visually guided reaching tasks.

Neural Coordinate Transformations

Reaching for a viewed object requires a number of coordinate transformations that turn information about where the image of the object falls on the retina into movement commands in shoulder-, arm-, or hand-based coordinates. To perform a transformation from retinal to body-based coordinates, information about the retinal location of an image and about the direction of gaze relative to the body must be combined. Figure 7.4A and B illustrate, in a one-dimensional example, how a rotation of the eyes affects the relationship between gaze direction, retinal location, and location relative to the body. Figure 7.4C introduces the notation we use. The angle g describes the orientation of a line extending from the head to the point of visual fixation. The visual stimulus in retinal coordinates is given by the angle s between this line and a line extending out to the target. The angle describing the reach direction, the direction to the target relative to the body, is the sum $s + g$.

Visual neurons have receptive fields fixed to specific locations on the retina. Neurons in motor areas can display visually evoked responses that are not tied to specific retinal locations, but rather depend on the relationship of a visual image to various parts of the body. Figures 7.5A and B show tuning curves of a neuron in the premotor cortex of a monkey that

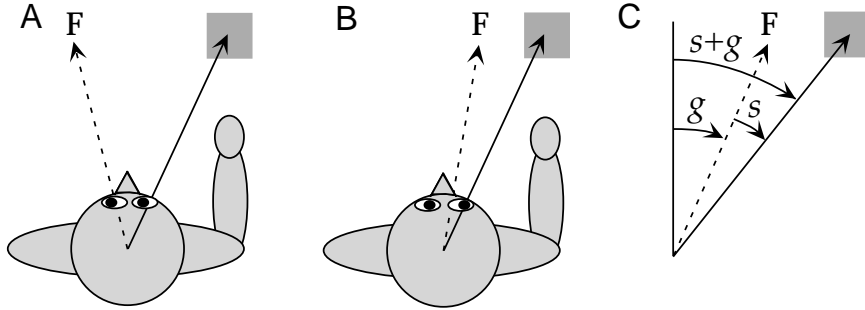


Figure 7.4: Coordinate transformations during a reaching task. A, B) The location of the target (the grey square) relative to the body is the same in A and B, and thus the movements required to reach toward it are identical. However, the image of the object falls on different parts of the retina in A and B due to a shift in the gaze direction produced by an eye rotation that shifts the fixation point F. C) The angles used in the analysis: s is the angle describing the location of the stimulus (the target) in retinal coordinates, that is, relative to a line directed to the fixation point; g is the gaze angle, indicating the direction of gaze relative to an axis straight out from the body. The direction of the target relative to the body-based axis is $s + g$.

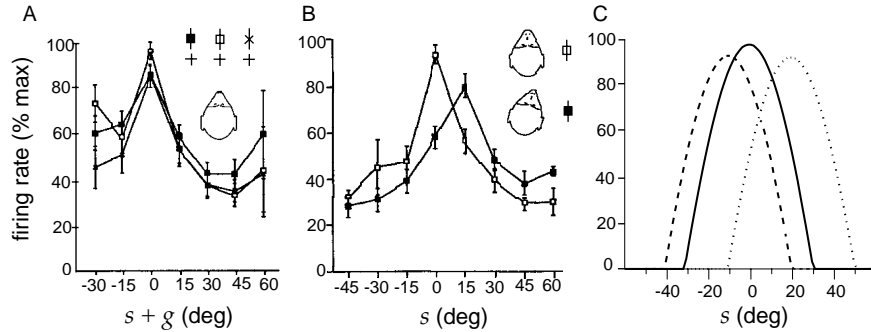


Figure 7.5: Tuning curves of a visually responsive neuron in the premotor cortex of a monkey. Incoming objects approaching at various angles provided the visual stimulation. A) When the monkey fixated on the three points denoted by the cross symbols, the response tuning curve did not shift with the eyes. In this panel, unlike B and C, the horizontal axis refers to the stimulus location in head-based, not retinal, coordinates ($s + g$, not s). B) Turning the monkey's head by 15° produced a 15° shift in the response tuning curve as a function of retinal location, indicating that this neuron encoded the stimulus direction in head-based coordinates. C) Model tuning curves based on equation 7.15 shift their retinal tuning to remain constant in body-based coordinates. The solid, heavy dashed, and light dashed curves refer to $g = 0^\circ$, 10° , and -20° respectively. The small changes in amplitude arise from the limited range of preferred retinal location and gaze angles in the model. (A,B adapted from Graziano et al., 1997; C adapted from Salinas and Abbott, 1995.)

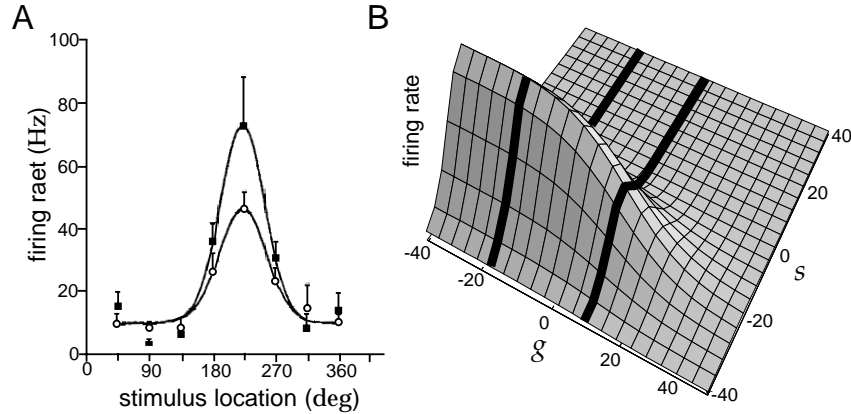


Figure 7.6: Gaze-dependent gain modulation of visual responses of neurons in posterior parietal cortex. A) Average firing-rate tuning curves of an area 7a neuron as a function of the location of the spot of light used to evoke the response. Stimulus location is measured as an angle around a circle of possible locations on the screen and is related to, but not equal to, our stimulus variable s . The two curves correspond to the same visual image but with two different gaze directions. B) A three-dimensional plot of the activity of a model neuron as a function of both retinal position and gaze direction. The striped bands correspond to tuning curves with different gains similar to those shown in A. (A adapted from Brotchie et al., 1995; B adapted from Pouget and Sejnowski, 1995.)

responded to visual images of approaching objects. Surprisingly, when the head of the monkey was held stationary during fixation on three different targets, the tuning curves did not shift as the eyes rotated (figure 7.5A). Although the recorded neurons respond to visual stimuli, the responses do not depend directly on the location of the image on the retina. When the head of the monkey is rotated but the fixation point remains the same, the tuning curves shift by precisely the amount of the head rotation (figure 7.5B). Thus, these neurons encode the location of the image in head- or body-based, not retinal, coordinates.

To account for these data, we need to construct a model neuron that is driven by visual input, but that nonetheless has a tuning curve for image location that is not a function of s , the retinal location of the image, but of $s + g$, the location of the object in body-based coordinates. A possible basis for this construction is provided by a combined representation of s and g by neurons in area 7a in the posterior parietal cortex of the monkey. Recordings made in area 7a reveal neurons that fire at rates that depend on both the location of the stimulating image on the retina and on the direction of gaze (figure 7.6A). The response tuning curves, expressed as functions of the retinal location of the stimulus, do not shift when the direction of gaze is varied. However, shifts of gaze direction affect the magnitude of the visual response. Thus, responses in area 7a exhibit gaze-dependent gain modulation of a retinotopic visual receptive field.

gain modulation

Figure 7.6B shows a mathematical description of a gain-modulated tuning curve. The response tuning curve is expressed as a product of a Gaussian function of $s - \xi$, where ξ is the preferred retinal location ($\xi = -20^\circ$ in figure 7.6B), and a sigmoid function of $g - \gamma$, where γ is the gaze direction producing half of the maximum gain ($\gamma = 20^\circ$ in figure 7.6B). Although it does not correspond to the maximum neural response, we refer to γ as the ‘preferred’ gaze direction.

To model a neuron with a body-centered response tuning curve, we construct a feedforward network with a single output unit representing, for example, the premotor neuron shown in figure 7.5. The input layer of the network consists of a population of area 7a neurons with gain-modulated responses similar to those shown in figure 7.6B. Neurons with gains that both increase and decrease as a function of g are included in the model. The average firing rates of the input layer neurons are described by tuning curves $u = f_u(s - \xi, g - \gamma)$ with the different neurons taking a range of ξ and γ values.

We use continuous labeling of neurons, and replace the sum over presynaptic neurons by an integral over their ξ and γ values, inserting the appropriate density factors ρ_ξ and ρ_γ , which we assume are constant. The steady-state response of the single output neuron is determined by the continuous analog of equation 7.5. The synaptic weight from a presynaptic neuron with preferred stimulus location ξ and preferred gaze direction γ is denoted by $w(\xi, \gamma)$, so the steady-state response of the output neurons is given by

$$v_\infty = F \left(\rho_\xi \rho_\gamma \int d\xi d\gamma w(\xi, \gamma) f_u(s - \xi, g - \gamma) \right). \quad (7.15)$$

For the output neuron to respond to stimulus location in body-based coordinates, its firing rate must be a function of $s + g$. To see if this is possible, we shift the integration variables in 7.15 by $\xi \rightarrow \xi - g$ and $\gamma \rightarrow \gamma + g$. Ignoring effects from the end points of the integration (which is valid if s and g are not too close to these limits), we find

$$v_\infty = F \left(\rho_\xi \rho_\gamma \int d\xi d\gamma w(\xi - g, \gamma + g) f_u(s + g - \xi, -\gamma) \right). \quad (7.16)$$

This is a function of $s + g$ provided that $w(\xi - g, \gamma + g) = w(\xi, \gamma)$, which holds if $w(\xi, \gamma)$ is a function of the sum $\xi + \gamma$. Thus, the coordinate transformation can be accomplished if the synaptic weight from a given neuron depends only the sum of its preferred retinal and gaze angles. It has been suggested that weights of this form can arise naturally from random hand and gaze movements through correlation-based synaptic modification of the type discussed in chapter 8.

Figure 7.5C shows responses predicted by equation 7.15 when the synaptic weights are given by a function $w(\xi + \gamma)$. The retinal location of the tuning curve shifts as a function of gaze direction, but would remain stationary if

it were plotted instead as a function of $s + g$. This can be seen by noting that the peaks of all three curves in figure 7.5C occur at $s + g = 0$.

Gain-modulated neurons provide a general basis for combining two different input signals in a nonlinear way. In the network we studied, it is possible to find appropriate synaptic weights $w(\xi, \gamma)$ to construct output neurons with a wide range of response tuning curves expressed as functions of s and g . The mechanism by which sensory and modulatory inputs combine in a multiplicative way in gain-modulated neurons is not known. Later in this chapter, we discuss a recurrent network model for generating gain-modulated responses.

7.4 Recurrent Networks

Recurrent networks have richer dynamics than feedforward networks, but they are more difficult to analyze. To get a feel for recurrent circuitry, we begin by analyzing a linear model, that is, a model for which the relationship between firing rate and synaptic current is linear, $F(\mathbf{h} + \mathbf{M} \cdot \mathbf{r}) = \mathbf{h} + \mathbf{M} \cdot \mathbf{r}$. The linear approximation is a drastic one that allows, among other things, the components of \mathbf{v} to become negative, which is impossible for real firing rates. Furthermore, some of the features we discuss in connection with linear, as opposed to nonlinear, recurrent networks can also be achieved by a feedforward architecture. Nevertheless, the linear model is extremely useful for exploring properties of recurrent circuits, and this approach will be used both here and in the following chapters. In addition, the analysis of linear networks forms the basis for studying the stability properties of nonlinear networks. We augment the discussion of linear networks with results from simulations of nonlinear networks.

Linear Recurrent Networks

Under the linear approximation, the recurrent model of equation 7.11 takes the form

$$\tau_r \frac{d\mathbf{v}}{dt} = -\mathbf{v} + \mathbf{h} + \mathbf{M} \cdot \mathbf{v}. \quad (7.17)$$

Because the model is linear, we can solve analytically for the vector of output rates \mathbf{v} in terms of the feedforward inputs \mathbf{h} and the initial values $\mathbf{v}(0)$. The analysis is simplest when the recurrent synaptic weight matrix is symmetric, and we assume this to be the case. Equation 7.17 can be solved by expressing \mathbf{v} in terms of the eigenvectors of \mathbf{M} . The eigenvectors \mathbf{e}_μ for $\mu = 1, 2, \dots, N_v$ satisfy

$$\mathbf{M} \cdot \mathbf{e}_\mu = \lambda_\mu \mathbf{e}_\mu \quad (7.18)$$

for some value of the constant λ_μ which is called the eigenvalue. For a

*linear recurrent
model*

eigenvector \mathbf{e}

eigenvalue λ

symmetric matrix, the eigenvectors are orthogonal, and they can be normalized to unit length so that $\mathbf{e}_\mu \cdot \mathbf{e}_v = \delta_{\mu v}$. Such eigenvectors define an orthogonal coordinate system or basis that can be used to represent any N_v -dimensional vector. In particular, we can write

$$\mathbf{v}(t) = \sum_{\mu=1}^{N_v} c_\mu(t) \mathbf{e}_\mu \quad (7.19)$$

where $c_\mu(t)$ for $\mu = 1, 2, \dots, N_v$ are a set of time-dependent coefficients describing $\mathbf{v}(t)$.

It is easier to solve equation 7.17 for the coefficients c_μ than for \mathbf{v} directly. Substituting the expansion 7.19 into equation 7.17 and using property 7.18, we find that

$$\tau_r \sum_{\mu=1}^{N_v} \frac{dc_\mu}{dt} \mathbf{e}_\mu = - \sum_{\mu=1}^{N_v} (1 - \lambda_\mu) c_\mu(t) \mathbf{e}_\mu + \mathbf{h}. \quad (7.20)$$

The sum over μ can be eliminated by taking the dot product of each side of this equation with one of the eigenvectors, \mathbf{e}_v , and using the orthogonality property $\mathbf{e}_\mu \cdot \mathbf{e}_v = \delta_{\mu v}$ to obtain

$$\tau_r \frac{dc_v}{dt} = -(1 - \lambda_v) c_v(t) + \mathbf{e}_v \cdot \mathbf{h}. \quad (7.21)$$

The critical feature of this equation is that it involves only one of the coefficients, c_v . For time-independent inputs \mathbf{h} , the solution of equation 7.44 is

$$c_v(t) = \frac{\mathbf{e}_v \cdot \mathbf{h}}{1 - \lambda_v} \left(1 - \exp \left(-\frac{t(1 - \lambda_v)}{\tau_r} \right) \right) + c_v(0) \exp \left(-\frac{t(1 - \lambda_v)}{\tau_r} \right) \quad (7.22)$$

where $c_v(0)$ is the value of c_v at time zero, which is given in terms of the initial firing-rate vector $\mathbf{v}(0)$ by $c_v(0) = \mathbf{e}_v \cdot \mathbf{v}(0)$.

Equation 7.22 has several important characteristics. If $\lambda_v > 1$, the exponential functions grow without bound as time increases, reflecting a fundamental instability of the network. If $\lambda_v < 1$, c_v approaches the steady-state value $\mathbf{e}_v \cdot \mathbf{h}/(1 - \lambda_v)$ exponentially with time constant $\tau_r/(1 - \lambda_v)$. This steady-state value is proportional to $\mathbf{e}_v \cdot \mathbf{h}$, which is the projection of the input vector onto the relevant eigenvector. For $0 < \lambda_v < 1$, the steady-state value is amplified relative to this projection by the factor $1/(1 - \lambda_v)$, which is greater than one. The approach to equilibrium is slowed relative to the basic time constant τ_r by an identical factor. The steady-state value of $\mathbf{v}(t)$, which we call \mathbf{v}_∞ , can be derived from equation 7.19 as

$$\mathbf{v}_\infty = \sum_{v=1}^{N_v} \frac{(\mathbf{e}_v \cdot \mathbf{h})}{1 - \lambda_v} \mathbf{e}_v. \quad (7.23)$$

steady state \mathbf{v}_∞

This steady-state response can also arise from a purely feedforward scheme if the feedforward weight matrix is chosen appropriately, as we invite the reader to verify as an exercise.

We have considered amplification when $0 < \lambda_1 < 1$. The linear network becomes unstable if $\lambda_1 > 1$. The case $\lambda_1 = 1$ is special and will be discussed in a later section.

Selective Amplification

Suppose that one of the eigenvalues of a recurrent weight matrix, denoted by λ_1 , is very close to one, and all the others are significantly smaller than 1. In this case, the denominator of the $v=1$ term on the right side of equation 7.23 is near zero, and, unless $e_1 \cdot h$ is extremely small, this single term will dominate the sum. As a result, we can write

$$v_\infty \approx \frac{(e_1 \cdot h)e_1}{1 - \lambda_1}. \quad (7.24)$$

Such a network performs selective amplification. The response is dominated by the projection of the input vector along the axis defined by e_1 , and the amplitude of the response is amplified by the factor $1/(1 - \lambda_1)$, which may be quite large if λ_1 is near one. The steady-state response of such a network, which is proportional to e_1 , therefore encodes an amplified projection of the input vector onto e_1 .

Further information can be encoded if more eigenvalues are close to one. Suppose, for example, that two eigenvectors, e_1 and e_2 have the same eigenvalue, $\lambda_1 = \lambda_2$, close to but less than one. Then, equation 7.24 is replaced by

$$v_\infty \approx \frac{(e_1 \cdot h)e_1 + (e_2 \cdot h)e_2}{1 - \lambda_1} \quad (7.25)$$

which shows that the network now amplifies and encodes the projection of the input vector onto the plane defined by e_1 and e_2 . In this case, the activity pattern of the network is not simply scaled when the input changes. Instead, changes in the input shift both the magnitude and pattern of network activity. Eigenvectors that share the same eigenvalue are termed degenerate, and degeneracy is often the result of a symmetry. In the examples considered in this chapter, degeneracy arises from invariance to shifts of the parameter θ by a constant amount. Degeneracy is not limited to just two eigenvectors. A recurrent network with n degenerate eigenvalues near one can amplify and encode a projection of the input vector from the N -dimensional space in which it is defined onto the n -dimensional subspace spanned by the degenerate eigenvectors.

Input Integration

If the recurrent weight matrix has an eigenvalue exactly equal to one, $\lambda_1 = 1$, and all the other eigenvalues satisfy $\lambda_v < 1$, a linear recurrent network can act as an integrator of its input. In this case, c_1 satisfies the equation

$$\tau_r \frac{dc_1}{dt} = \mathbf{e}_1 \cdot \mathbf{h} \quad (7.26)$$

obtained by setting $\lambda_1 = 1$ in equation 7.44. For arbitrary time-dependent inputs, the solution of this equation is

$$c_1(t) = c_1(0) + \frac{1}{\tau_r} \int_0^t dt' \mathbf{e}_1 \cdot \mathbf{h}(t') . \quad (7.27)$$

If $\mathbf{h}(t)$ is constant, $c_1(t)$ grows linearly with t . This explains why equation 7.24 diverges as $\lambda_1 \rightarrow 1$. Suppose, instead, that $\mathbf{h}(t)$ is nonzero for a while, and then is set to zero for an extended period of time. When $\mathbf{h} = 0$, equation 7.22 shows that $c_v \rightarrow 0$ for all $v \neq 1$, because for these eigenvectors $\lambda_v < 1$. Assuming that $c_1(0) = 0$, this means that, after such a period, the firing-rate vector is given, from equation 7.27 and 7.19, by

$$\mathbf{v}(t) \approx \frac{\mathbf{e}_1}{\tau_r} \int_0^t dt' \mathbf{e}_1 \cdot \mathbf{h}(t') . \quad (7.28)$$

This shows that the network activity provides a measure of the running integral of the projection of the input vector onto \mathbf{e}_1 . One consequence of this is that the activity of the network does not cease if $\mathbf{h} = 0$, provided that the integral up to that point in time is nonzero. The network thus exhibits sustained activity in the absence of input, which provides a memory of the integral of prior input.

Networks in the brain stem of vertebrates responsible for maintaining eye position appear to act as integrators, and networks similar to the one we have been discussing have been suggested as models of this system. As outlined in figure 7.7, eye position changes in response to bursts of activity in ocular motor neurons located in the brain stem. Neurons in the medial vestibular nucleus and prepositus hypoglossi appear to integrate these motor signals to provide a persistent memory of eye position. The sustained firing rates of these neurons are approximately proportional to the angular orientation of the eyes in the horizontal direction, and activity persists at an approximately constant rate when the eyes are held fixed (bottom trace in figure 7.7).

The ability of a linear recurrent network to integrate and display persistent activity relies on one of the eigenvalues of the recurrent weight matrix being exactly one. Any deviation from this value will cause the persistent activity to change over time. Eye position does indeed drift, but matching the performance of the ocular positioning system requires fine tuning of the eigenvalue to a value extremely close to one. Including nonlinear interactions does not alleviate the need for a precisely tuned weight matrix.

*network
integration*

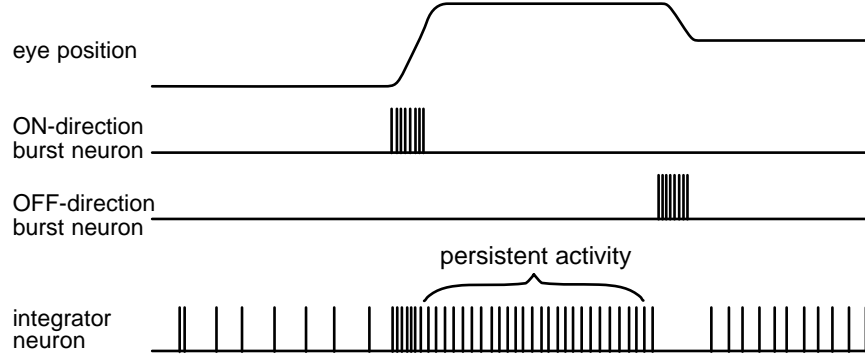


Figure 7.7: Cartoon of burst and integrator neurons involved in horizontal eye positioning. The upper trace represents horizontal eye position during two saccadic eye movements. Motion of the eye is driven by burst neurons that move the eyes in opposite directions (second and third traces from top). The steady-state firing rate (labeled persistent activity) of the integrator neuron is proportional to the time integral of the burst rates, integrated positively for the ON-direction burst neuron and negatively for the OFF-direction burst neuron, and thus provides a memory trace of the maintained eye position. (Adapted from Seung et al., 2000.)

Synaptic modification rules can be used to establish the necessary synaptic weights, but it is not clear how such precise tuning is accomplished in the biological system.

Continuous Linear Recurrent Networks

For a linear recurrent network with continuous labeling, the equation for the firing rate $v(\theta)$ of a neuron with preferred stimulus angle θ is a linear version of equation 7.14,

$$\tau_r \frac{dv(\theta)}{dt} = -v(\theta) + h(\theta) + \rho_\theta \int_{-\pi}^{\pi} d\theta' M(\theta - \theta') v(\theta') \quad (7.29)$$

where $h(\theta)$ is the feedforward input to a neuron with preferred stimulus angle θ , and we have assumed a constant density ρ_θ . Because θ is an angle, h , M , and v must all be periodic functions with period 2π . By making M a function of $\theta - \theta'$, we are imposing a symmetry with respect to translations or shifts of the angle variables on the network. In addition, we assume that M is an even function, $M(\theta - \theta') = M(\theta' - \theta)$. This is the analog, in a continuously labeled model, of a symmetric synaptic weight matrix.

Equation 7.29 can be solved by methods similar to those used for discrete networks. We introduce eigenfunctions that satisfy

$$\rho_\theta \int_{-\pi}^{\pi} d\theta' M(\theta - \theta') e_\mu(\theta') = \lambda_\mu e_\mu(\theta) . \quad (7.30)$$

We leave it as an exercise to show that the eigenfunctions (normalized so that ρ_θ times the integral from $-\pi$ to π of their square is one) are $1/\sqrt{2\pi\rho_\theta}$, corresponding to $\mu = 0$, and $\cos(\mu\theta)/\sqrt{\pi\rho_\theta}$ and $\sin(\mu\theta)/\sqrt{\pi\rho_\theta}$ for $\mu = 1, 2, \dots$. The eigenvalues are identical for the sine and cosine eigenfunctions and are given (including the case $\mu = 0$) by

$$\lambda_\mu = \rho_\theta \int_{-\pi}^{\pi} d\theta' M(\theta') \cos(\mu\theta'). \quad (7.31)$$

The identity of the eigenvalues for the cosine and sine eigenfunctions reflects a degeneracy that arises from the invariance of the network to shifts of the angle labels.

The steady-state firing rates for a constant input are given by the continuous analog of equation 7.23,

$$\begin{aligned} v_\infty(\theta) &= \frac{1}{1 - \lambda_0} \int_{-\pi}^{\pi} \frac{d\theta'}{2\pi} h(\theta') \\ &+ \sum_{\mu=1}^{\infty} \frac{\cos(\mu\theta)}{1 - \lambda_\mu} \int_{-\pi}^{\pi} \frac{d\theta'}{\pi} h(\theta') \cos(\mu\theta') \\ &+ \sum_{\mu=1}^{\infty} \frac{\sin(\mu\theta)}{1 - \lambda_\mu} \int_{-\pi}^{\pi} \frac{d\theta'}{\pi} h(\theta') \sin(\mu\theta'). \end{aligned} \quad (7.32)$$

Fourier series

The integrals in this expression are the coefficients in a Fourier series for the function h and are known as cosine and sine Fourier integrals (see the Mathematical Appendix).

Figure 7.8 shows an example of selective amplification by a linear recurrent network. The input to the network, shown in panel A of figure 7.8, is a cosine function that peaks at 0° to which random noise has been added. Figure 7.8C shows Fourier amplitudes for this input. The Fourier amplitude is the square root of the sum of the squares of the cosine and sine Fourier integrals. No particular μ value is overwhelmingly dominant. In this and the following examples, the recurrent connections of the network are given by

$$M(\theta - \theta') = \frac{\lambda_1}{\pi\rho_\theta} \cos(\theta - \theta') \quad (7.33)$$

which has all eigenvalues except λ_1 equal to zero. The network model shown in figure 7.8 has $\lambda_1 = 0.9$, so that $1/(1 - \lambda_1) = 10$. Input amplification can be quantified by comparing the Fourier amplitude of v_∞ , for a given μ value, with the analogous amplitude for the input h . According to equation 7.32, the ratio of these quantities is $1/(1 - \lambda_\mu)$, so, in this case, the $\mu = 1$ amplitude should be amplified by a factor of ten while all other amplitudes are unamplified. This factor of ten amplification can be seen by comparing the $\mu = 1$ Fourier amplitudes in figures 7.8C and D (note the different scales for the vertical axes). All the other components are unamplified. As a result, the output of the network is primarily in the form of a cosine function with $\mu = 1$, as seen in figure 7.8B.

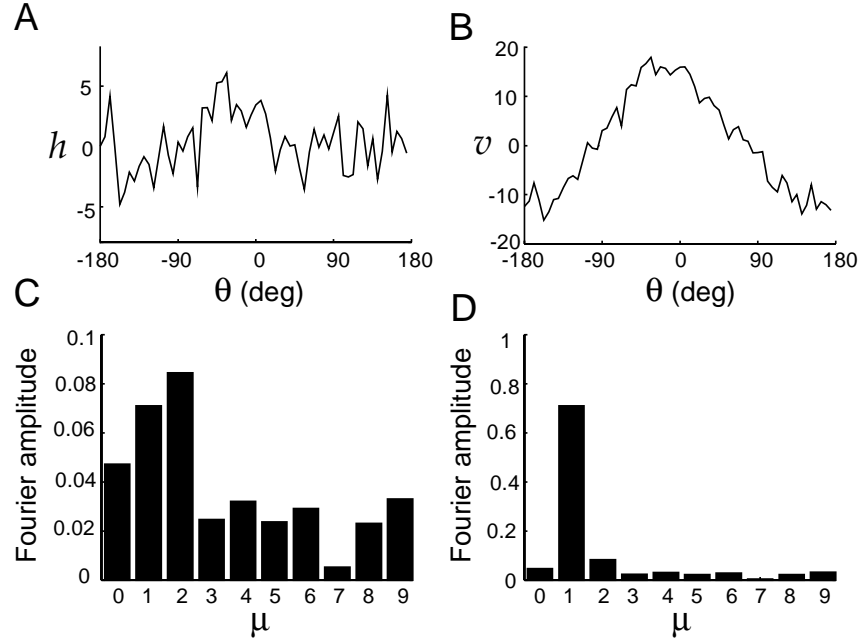


Figure 7.8: Selective amplification in a linear network. A) The input to the neurons of the network as a function of their preferred stimulus angle. B) The activity of the network neurons plotted as a function of their preferred stimulus angle in response to the input of panel A. C) The Fourier transform amplitudes of the input shown in panel A. D) The Fourier transform amplitudes of the output shown in panel B. The recurrent coupling of this network model took the form of equation 7.33 with $\lambda_1 = 0.9$. (This figure, and figures 7.9, 7.12, 7.13, and 7.14, were generated using software from Carandini and Ringach, 1998.)

Nonlinear Recurrent Networks

A linear model does not provide an adequate description of the firing rates of a biological neural network. The most significant problem is that the firing rates in a linear network can take negative values. This problem can be fixed by introducing rectification into equation 7.11 by choosing

rectification

$$\mathbf{F}(\mathbf{h} + \mathbf{M} \cdot \mathbf{r}) = [\mathbf{h} + \mathbf{M} \cdot \mathbf{r} - \boldsymbol{\gamma}]_+ . \quad (7.34)$$

where $\boldsymbol{\gamma}$ is a vector of threshold values that we often take to be $\mathbf{0}$. In this section, we show some examples illustrating the effect of including such a rectifying nonlinearity. Some of the features of linear recurrent networks remain when rectification is included, but several new features also appear.

In the examples given below, we consider a continuous model, similar to that of equation 7.29, with recurrent couplings given by equation 7.33, but

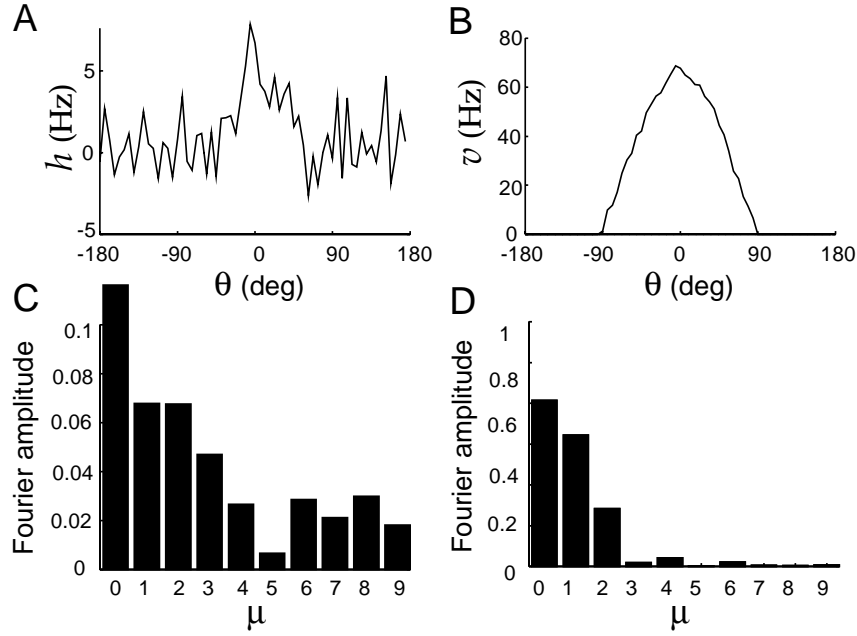


Figure 7.9: Selective amplification in a recurrent network with rectification. A) The input $h(\theta)$ of the network plotted as a function of preferred angle. B) The steady-state output $v(\theta)$ as a function of preferred angle. C) Fourier transform amplitudes of the input $h(\theta)$. D) Fourier transform amplitudes of the output $v(\theta)$. The recurrent coupling took the form 7.33 with $\lambda_1 = 1.9$.

now including a rectification nonlinearity, so that

$$\tau_r \frac{dv(\theta)}{dt} = -v(\theta) + \left[h(\theta) + \frac{\lambda_1}{\pi} \int_{-\pi}^{\pi} d\theta' \cos(\theta - \theta') v(\theta') \right]_+. \quad (7.35)$$

If λ_1 is not too large, this network converges to a steady state for any constant input (we consider conditions for steady-state convergence in a later section), and therefore we often limit the discussion to the steady-state activity of the network.

Nonlinear Amplification

Figure 7.9 shows the nonlinear analog of the selective amplification shown for a linear network in figure 7.8. Once again, a noisy input (figure 7.9A) generates a much smoother output response profile (figure 7.9B). The output response of the rectified network corresponds roughly to the positive part of the sinusoidal response profile of the linear network (figure 7.8B). The negative output has been eliminated by the rectification. Because fewer neurons in the network have nonzero responses than in the linear case, the value of the parameter λ_1 in equation 7.33 has been increased to

1.9. This value, being larger than one, would lead to an unstable network in the linear case. While nonlinear networks can also be unstable, the restriction to eigenvalues less than one is no longer the relevant condition.

In a nonlinear network, the Fourier analysis of the input and output responses is no longer as informative as it is for a linear network. Due to the rectification, the $v = 0, 1$, and 2 Fourier components are all amplified (figure 7.9D) compared to their input values (figure 7.9C). Nevertheless, except for rectification, the nonlinear recurrent network amplifies the input signal selectively in a similar manner as the linear network.

A Recurrent Model of Simple Cells in Primary Visual Cortex

In chapter 2, we discussed a feedforward model in which the elongated receptive fields of simple cells in primary visual cortex were formed by summing the inputs from lateral geniculate (LGN) neurons with their receptive fields arranged in alternating rows of ON and OFF cells. While this model quite successfully accounts for a number of features of simple cells, such as orientation tuning, it is difficult to reconcile with the anatomy and circuitry of the cerebral cortex. By far the majority of the synapses onto any cortical neuron arise from other cortical neurons, not from thalamic afferents. Therefore, feedforward models account for the response properties of cortical neurons while ignoring the inputs that are numerically most prominent. The large number of intracortical connections suggests, instead, that recurrent circuitry might play an important role in shaping the responses of neurons in primary visual cortex.

Ben-Yishai, Bar-Or, and Sompolinsky (1995) developed a model at the other extreme, for which recurrent connections are the primary determinants of orientation tuning. The model is similar in structure to the model of equations 7.35 and 7.33, except that it includes a global inhibitory interaction. In addition, because orientation angles are defined over the range from $-\pi/2$ to $\pi/2$, rather than over the full 2π range, the cosine functions in the model have extra factors of 2 in them. The basic equation of the model, as we implement it, is

$$\tau_r \frac{dv(\theta)}{dt} = -v(\theta) + \left[h(\theta) + \int_{-\pi/2}^{\pi/2} \frac{d\theta'}{\pi} (-\lambda_0 + \lambda_1 \cos(2(\theta - \theta'))) v(\theta') \right]_+ \quad (7.36)$$

where $v(\theta)$ is the firing rate of a neuron with preferred orientation θ .

The input to the model represents the orientation-tuned feedforward input arising from ON-center and OFF-center LGN cells responding to an oriented image. As a function of preferred orientation, the input for an image with orientation angle $\Theta = 0$ is

$$h(\theta) = Ac (1 - \epsilon + \epsilon \cos(2\theta)) \quad (7.37)$$

where A sets the overall amplitude and c is equal to the image contrast. The factor ϵ controls how strongly the input is modulated by the orientation angle. For $\epsilon = 0$, all neurons receive the same input, while $\epsilon = 0.5$ produces the maximum modulation consistent with a positive input. We study this model in the case when ϵ is small, which means that the input is only weakly tuned for orientation and any strong orientation selectivity must arise through recurrent interactions.

To study orientation selectivity, we want to examine the tuning curves of individual neurons in response to stimuli with different orientation angles Θ . The plots of network responses that we have been using show the firing rates $v(\theta)$ of all the neurons in the network as a function of their preferred stimulus angles θ when the input stimulus has a fixed value, typically $\Theta = 0$. As a consequence of the translation invariance of the network model, the response for other values of Θ can be obtained simply by shifting this curve so that it plots $v(\theta - \Theta)$. Furthermore, except for the asymmetric effects of noise on the input, $v(\theta - \Theta)$ is a symmetric function. These features follow from the fact that the network we are studying is invariant with respect to translations and sign changes of the angle variables that characterize the stimulus and response selectivities. An important consequence of this result is that the curve $v(\theta)$, showing the response of the entire population, can also be interpreted as the tuning curve of a single neuron. If the response of the population to a stimulus angle Θ is $v(\theta - \Theta)$, the response of a single neuron with preferred angle $\theta = 0$ is $v(-\Theta) = v(\Theta)$ from the symmetry of v . Because $v(\Theta)$ is the tuning curve of a single neuron with $\theta = 0$ to a stimulus angle Θ , the plots we show of $v(\theta)$ can be interpreted in a dual way, as both population responses and individual neuronal tuning curves.

Figure 7.10A shows the feedforward input to the model network for four different levels of contrast. Because the parameter ϵ was chosen to be 0.1, the modulation of the input as a function of orientation angle is small. Due to network amplification, the response of the network is much more strongly tuned to orientation (figure 7.10B). This is the result of the selective amplification of the tuned part of the input by the recurrent network. The modulation and overall height of the input curve in figure 7.10A increase linearly with contrast. The response shown in figure 7.10B, interpreted as a tuning curve, increases in amplitude for higher contrast, but does not broaden. This can be seen by noting that all four curves in figure 7.10B go to zero at the same two points. This effect, which occurs because the shape and width of the response tuning curve are determined primarily by the recurrent interactions within the network, is a feature of orientation curves of real simple cells, as seen in figure 7.10C. The width of the tuning curve can be reduced by including a positive threshold in the response function of equation 7.34, or by changing the amount of inhibition, but it stays roughly constant as a function of stimulus strength.

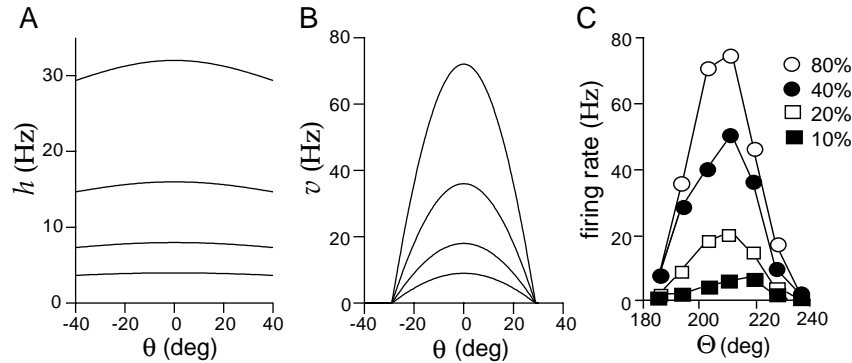


Figure 7.10: The effect of contrast on orientation tuning. A) The feedforward input as a function of preferred orientation. The four curves, from top to bottom, correspond to contrasts of 80%, 40%, 20%, and 10%. B) The output firing rates in response to different levels of contrast as a function of orientation preference. These are also the response tuning curves of a single neuron with preferred orientation zero. As in A, the four curves, from top to bottom, correspond to contrasts of 80%, 40%, 20%, and 10%. The recurrent model had $\lambda_0 = 7.3$, $\lambda_1 = 11$, $A = 40$ Hz, and $\epsilon = 0.1$. C) Tuning curves measure experimentally at four contrast levels as indicated in the legend. (C adapted from Sompolinsky and Shapley, 1997; based on data from Sclar and Freeman, 1982.)

A Recurrent Model of Complex Cells in Primary Visual Cortex

In the model of orientation tuning discussed in the previous section, recurrent amplification enhances selectivity. If the pattern of network connectivity amplifies nonselective rather than selective responses, recurrent interactions can also decrease selectivity. Recall from chapter 2 that neurons in the primary visual cortex are classified as simple or complex depending on their sensitivity to the spatial phase of a grating stimulus. Simple cells respond maximally when the spatial positioning of the light and dark regions of a grating matches the locations of the ON and OFF regions of their receptive fields. Complex cells do not have distinct ON and OFF regions in their receptive fields and respond to gratings of the appropriate orientation and spatial frequency relatively independently of where their light and dark stripes fall. In other words, complex cells are insensitive to spatial phase.

Chance, Nelson, and Abbott (1999) showed that complex cell responses could be generated from simple cell responses by a recurrent network. As in chapter 2, we label spatial phase preferences by the angle ϕ . The feed-forward input $h(\phi)$ in the model is set equal to the rectified response of a simple cell with preferred spatial phase ϕ (figure 7.11A). Each neuron in the network is labeled by the spatial phase preference of its feedforward input. The network neurons also receive recurrent input given by the weight function $M(\phi - \phi') = \lambda_1 / (2\pi\rho_\phi)$ that is the same for all con-

nected neuron pairs. As a result, their firing rates are determined by

$$\tau_r \frac{dv(\phi)}{dt} = -v(\phi) + \left[h(\phi) + \frac{\lambda_1}{2\pi} \int_{-\pi}^{\pi} d\phi' v(\phi') \right]_+. \quad (7.38)$$

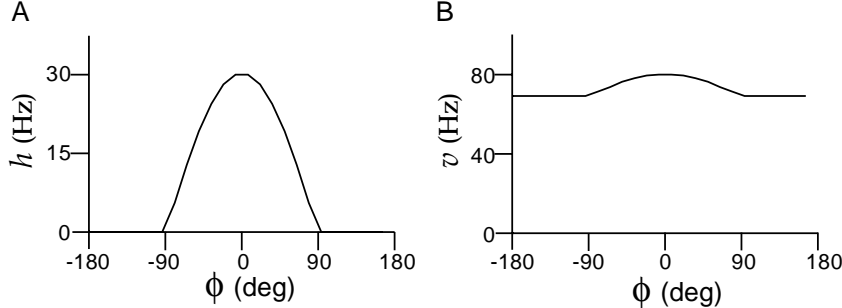


Figure 7.11: A recurrent model of complex cells. A) The input to the network as a function of spatial phase preference. The input $h(\phi)$ is equivalent to that of a simple cell with spatial phase preference ϕ responding to a grating of zero spatial phase. B) Network response, which can also be interpreted as the spatial phase tuning curve of a network neuron. The network was given by equation 7.38 with $\lambda_1 = 0.95$. (Adapted from Chance et al., 1999.)

In the absence of recurrent connections ($\lambda_1 = 0$), the response of a neuron labeled by ϕ is $v(\phi) = h(\phi)$, which is equal to the response of a simple cell with preferred spatial phase ϕ . However, for λ_1 sufficiently close to one, the recurrent model produces responses that resemble those of complex cells. Figure 7.11B shows the population response, or equivalently the single-cell response tuning curve, of the model in response to the tuned input shown in Figure 7.11A. The input, being the response of a simple cell, shows strong tuning for spatial phase. The output tuning curve, however, is almost constant as a function of spatial phase, like that of a complex cell. The spatial-phase insensitivity of the network response is due to the fact that the network amplifies the component of the input that is independent of spatial phase, because the eigenfunction of M with the largest eigenvalue is spatial-phase invariant. This changes simple cell inputs into complex cell outputs.

Winner-Take-All Input Selection

For a linear network, the response to two superimposed inputs is simply the sum of the responses to each input separately. Figure 7.12 shows one way in which a rectifying nonlinearity modifies this superposition property. In this case, the input to the recurrent network consists of activity centered around two preferred stimulus angles, $\pm 90^\circ$. The output of the nonlinear network shown in figure 7.12B is not of this form, but instead

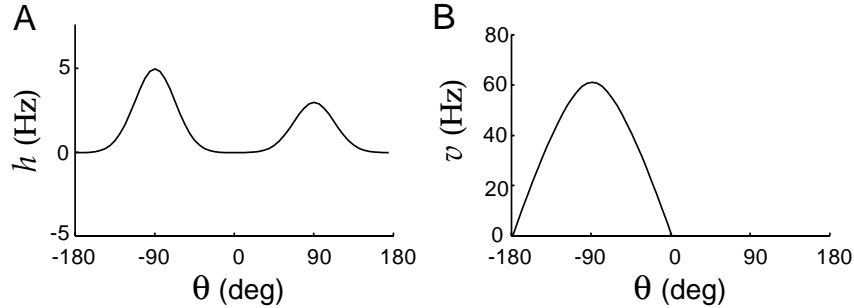


Figure 7.12: Winner-take-all input selection by a nonlinear recurrent network. A) The input to the network consisting of two peaks. B) The output of the network has a single peak at the location of the higher of the two peaks of the input. The model is the same as that used in figure 7.9.

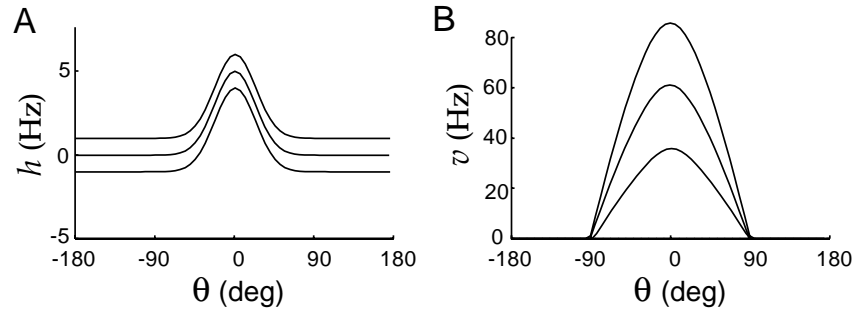


Figure 7.13: Effect of adding a constant to the input of a nonlinear recurrent network. A) The input to the network consists of a single peak to which a constant factor has been added. B) The gain-modulated output of the nonlinear network. The three curves correspond to the three input curves in panel A, in the same order. The model is the same as that used in figures 7.9 and 7.12.

has a single peak at the location of the input bump with the larger amplitude (the one at -90°). This occurs because the nonlinear recurrent network supports the stereotyped unimodal activity pattern seen in figure 7.12B, so a multimodal input tends to generate a unimodal output. The height of the input peak has a large effect in determining where the single peak of the network output is located, but it is not the only feature that determines the response. For example, the network output can favor a broader, lower peak over a narrower, higher one.

Gain Modulation

A nonlinear recurrent network can generate an output that resembles the gain-modulated responses of posterior parietal neurons shown in figure 7.6, as noted by Salinas and Abbott (1996). To obtain this result, we interpret the angle θ as a preferred direction in the visual field in retinal

coordinates (the variable we called s earlier in the chapter). The signal corresponding to gaze direction (what we called g before) is represented as a constant input to all neurons irrespective of their preferred stimulus angle. Figure 7.13 shows the effect of adding such a constant term to the input of the nonlinear network. The input shown in figure 7.13A corresponds to a visual target located at a retinal position of 0° . The different lines show different values of the constant input, representing three different gaze directions. The responses shown in figure 7.13B all have localized activity centered around $\theta=0^\circ$, indicating that the individual neurons have fixed tuning curves expressed in retinal coordinates. The effect of the constant input, representing gaze direction, is to scale up or gain modulate these tuning curves, producing a result similar to that shown in figure 7.6. The additive constant in the input shown in figure 7.13A has a multiplicative effect on the output activity shown in 7.13B. This is primarily due to the fact that the width of the activity profiles is fixed by the recurrent network interaction, so a constant positive input raises (and a negative input lowers) the peak of the response curve without broadening the base of the curve.

Sustained Activity

The effects illustrated in figures 7.12 and 7.13 arise because the nonlinear recurrent network has a stereotyped pattern of activity that is largely determined by interactions with other neurons in the network rather than by the feedforward input. If the recurrent connections are strong enough, the pattern of population activity, once established, can become independent of the structure of the input. For example, the recurrent network we have been studying can support a pattern of activity localized around a given preferred stimulus value, even when the input is uniform. This is seen in figure 7.14. The neurons of the network initially receive inputs that depend on their preferred angles, as seen in figure 7.14A. This produces a localized pattern of network activity (figure 7.14B). When the input is switched to the same constant value for all neurons (figure 7.14C), the network activity does not become uniform. Instead, it stays localized around the value $\theta=0$ (figure 7.14D). This means that constant input can maintain a state that provides a memory of previous localized input activity. Networks similar to this have been proposed as models of sustained activity in the head-direction system of the rat and in prefrontal cortex during tasks involving working memory.

This memory mechanism is related to the integration seen in the linear model of eye position maintenance discussed previously. The linear network has an eigenvector e_1 with eigenvalue $\lambda_1=1$. This allows $v=c_1e_1$ to be a static solution of the equations of the network (7.17) in the absence of input for any value of c_1 . As a result, the network can preserve any initial value of c_1 as a memory. In the case of figure 7.14, the steady-state activity in the absence of tuned input is a function of $\theta - \Theta$, for any value

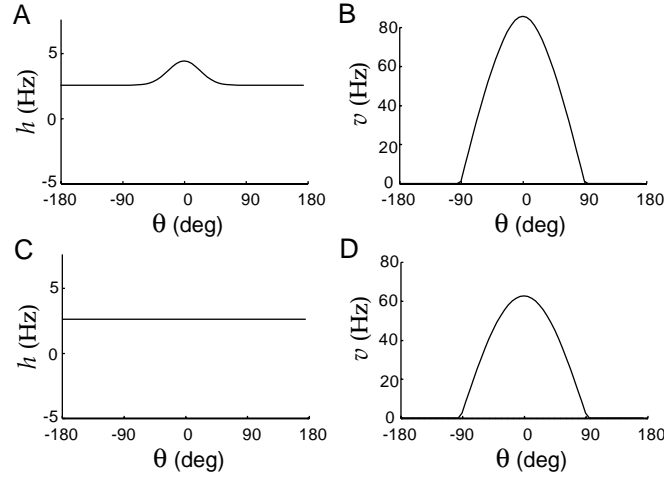


Figure 7.14: Sustained activity in a recurrent network. A) Input to the neurons of the network consisting of localized excitation and a constant background. B) The activity of the network neurons in response to the input of panel A. C) Constant network input. D) Response to the constant input of panel C when it immediately followed the input in A. The model is the same as that used in figures 7.9, 7.12, and 7.13.

of the angle Θ . As a result, the network can preserve any initial value of Θ as a memory ($\Theta = 0^\circ$ in the figure). The activities of the units $v(\theta)$ depend on Θ in an essentially nonlinear manner, but, if we consider linear perturbations around this nonlinear solution, there is an eigenvector with eigenvalue $\lambda_1 = 1$ associated with shifts in the value of Θ . In this case, it can be shown that $\lambda_1 = 1$ because the network was constructed to be translationally invariant.

Maximum Likelihood and Network Recoding

Recurrent networks can generate characteristic patterns of activity even when they receive complex inputs (figure 7.9) and can maintain these patterns while receiving constant input (figure 7.14). Pouget, Zhang, Deneve and Latham (1998) suggested that the location of the characteristic pattern (i.e. the value of Θ associated with the peak of the population activity profile) could be interpreted as a match of a fixed template curve to the input activity profile. This curve fitting operation is at the heart of the maximum likelihood decoding method we described in chapter 3 for estimating a stimulus variable such as Θ . In the maximum likelihood method, the fitting curve is determined by the tuning functions of the neurons, and the curve fitting procedure is defined by the characteristics of the noise perturbing the input activities. If the properties of the recurrent network match these optimal characteristics, the network can approximate maximum likelihood decoding. Once the activity of the population of neurons

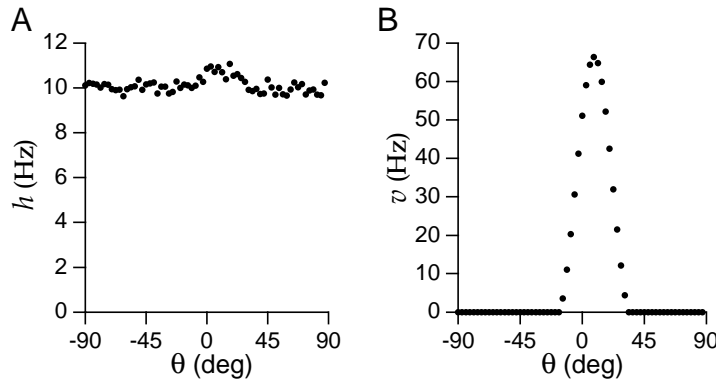


Figure 7.15: Recoding by a network model. A) The noisy initial inputs $h(\theta)$ to 64 network neurons are shown as dots. The standard deviation of the noise is 0.25 Hz. After a short settling time, the input is set to a constant value of $h(\theta) = 10$. B) The smooth activity profile that results from the recurrent interactions. The network model was similar to that used in figure 7.9 except that the recurrent synaptic weights were in the form of a Gabor-like function rather than a cosine, and the recurrent connections had short-range excitation and long-range inhibition. (see Pouget et al., 1998.)

has stabilized to its stereotyped shape, a simple decoding method such as vector decoding can be applied to extract the estimated value of Θ . This allows the accuracy of a vector decoding method to approach that of more complex optimal methods, because the computational work of curve fitting has been performed by the nonlinear recurrent interactions.

Figure 7.15 shows how this idea works in a network of 64 neurons receiving inputs that have Gaussian (rather than cosine) tuning curves as a function of Θ . Vector decoding applied to the reconstruction of Θ from the activity of the network or its inputs turns out to be almost unbiased. The way to judge decoding accuracy is therefore to compute the standard deviation of the decoded Θ values (chapter 3). The noisy input activity shown in figure 7.15A shows a slight bump around the value $\theta = 10^\circ$. Vector decoding applied to input activities with this level of noise gives a standard deviation in the decoded angle of 4.5° . Figure 7.15B shows the output of the network obtained by starting with initial activities $v(\theta) = 0$ and input $h(\theta)$ as in figure 7.15A, and then setting $h(\theta)$ to a constant (θ -independent) value to maintain sustained activity. This generates a smooth pattern of sustained population activity. Vector decoding applied to the output activities generated in this way gives a standard deviation in the decoded angle of 1.7° . This is not too far from the Cramér-Rao bound that gives the maximum possible accuracy for any unbiased decoding scheme applied to this system (see chapter 3), which is 0.88° .

Network Stability

When a network responds to a constant input by relaxing to a steady state with $dv/dt = \mathbf{0}$, it is said to exhibit fixed-point behavior. Almost all the network activity we have discussed thus far involves such fixed points. This is by no means the only type of long-term activity that a network model can display. In a later section of this chapter, we discuss networks that oscillate, and chaotic behavior is also possible. But if certain conditions are met, a network will inevitably reach a fixed point in response to constant input. The theory of Lyapunov functions, to which we give an informal introduction, can be used to prove when this occurs.

It is easier to discuss the Lyapunov function for a network if we use the firing-rate dynamics of equation 7.6 rather than equation 7.8. For a network model, this means expressing the vector of network firing rates as $\mathbf{v} = \mathbf{F}(\mathbf{I})$, where \mathbf{I} is the total synaptic current vector, i.e. I_a represents the total synaptic current for unit a . \mathbf{I} obeys the dynamic equation derived from generalizing equation 7.6 to a network situation,

$$\tau_s \frac{d\mathbf{I}}{dt} = -\mathbf{I} + \mathbf{h} + \mathbf{M} \cdot \mathbf{F}(\mathbf{I}). \quad (7.39)$$

Note that we have made the substitution $\mathbf{v} = \mathbf{F}(\mathbf{I})$ in the last term of the right side of this equation. Equation 7.39 is sometimes used instead of equation 7.11 as the dynamical equation governing recurrent firing-rate model networks. For this form of firing-rate model with a symmetric recurrent weight matrix satisfying $M_{aa} = 0$ for all a , Cohen and Grossberg (1983) showed that the function

$$L(\mathbf{I}) = \sum_{a=1}^{N_v} \left(\int_0^{I_a} dz_a z_a F'(z_a) - h_a F(I_a) - \frac{1}{2} \sum_{a'=1}^{N_v} F(I_a) M_{aa'} F(I_{a'}) \right) \quad (7.40)$$

has $dL/dt < 0$ whenever $d\mathbf{I}/dt \neq \mathbf{0}$. To see this, take the time derivative of equation 7.40 and use 7.39 to obtain

$$\frac{dL(\mathbf{I})}{dt} = -\frac{1}{\tau_s} \sum_{a=1}^{N_v} F'(I_a) \left(\frac{dI_a}{dt} \right)^2. \quad (7.41)$$

Because $F' > 0$, L decreases unless $d\mathbf{I}/dt = \mathbf{0}$. If L is bounded from below, it cannot decrease indefinitely, so $\mathbf{I} = \mathbf{h} + \mathbf{M} \cdot \mathbf{v}$ must converge to a fixed point. This implies that \mathbf{v} must converge to a fixed point as well.

We have required that $F'(I) > 0$ for all values of its argument I . However, with some technical complications, it can be shown that the Lyapunov function we have presented also applied to the case of the rectifying activation function $F(I) = [I]_+$, even though it is not differentiable at $I = 0$ and $F'(I) = 0$ for $I < 0$. Convergence to a fixed point, or one of a set of fixed points, requires the Lyapunov function to be bounded from below. One way to ensure this is to use a saturating activation function F , so that $F(I)$ is bounded as $I \rightarrow \infty$. Another way is to keep the eigenvalues of \mathbf{M} sufficiently small.

fixed-point behavior

*recurrent model
with current
dynamics*

*Lyapunov
function L*

Associative Memory

In an associative memory, a partial or approximate representation of a stored item is used to recall the full item. Unlike a standard random access memory, recall in an associative memory is based on content rather than on an address. For this reason, associative memory is also known as content-addressable memory. An example would be recalling every digit of a known phone number given a few of its digits as an initial clue. Associative memory networks have been suggested as models of various parts of the mammalian brain in which there is substantial recurrent feedback. These include area CA3 of the hippocampus and parts of the prefrontal cortex, structures which have long been implicated in various forms of memory. A number of network models exhibit associative memory, the best known being the so-called Hopfield networks (Hopfield, 1982 & 1984).

The models of memory we discussed previously in this chapter store information by means of persistent activity, with a particular item represented by the position of a stereotyped population activity profile. The idea underlying an associative (more strictly, auto-associative) memory is to extend persistent activity to a broader set of different population profiles, which are called memory patterns. Each of these is a fixed point of the dynamics of the network. The memory patterns are determined by and stored within the recurrent synaptic weights of the network, so memory retention does not require persistent activity. Rather, persistent activity is used to signal memory recall and to retain the identity of the most recently retrieved item.

During recall, an associative memory performs the computational operation of pattern matching, finding the memory pattern that most closely matches a distorted or partial activity pattern. This is achieved by initializing the network with an activity profile similar (but not identical) to one of the memory patterns, letting it relax to a fixed point, and treating the network activity at the fixed point as the best matching pattern. This is exactly the analog of the way that the recurrent model of maximum likelihood decoding executes a curve fitting procedure. Each memory pattern has a basin of attraction, defined as the set of initial states for which the network relaxes to that fixed point. The structure of these basins of attraction defines the matching properties of the network. The network dynamics is governed by a Lyapunov function of the form described above, and therefore the network will always relax to a fixed point. Provided that not too many memories are stored, the fixed points will closely resemble the stored memory patterns.

The associative network satisfies the dynamic equation 7.11, with the saturating activation function

$$F(I_s) = 150 \text{ Hz} \left[\tanh \left(\frac{I_s - \gamma}{150 \text{ Hz}} \right) \right]_+ \quad (7.42)$$

chosen to ensure that the Lyapunov function 7.40 is bounded from below. This is similar to a half-wave rectified activation function with threshold γ , except that it saturates at a firing rate of 150 Hz, which is outside the normal operating range of the units. We use a negative threshold, $\gamma = -20$ Hz, which corresponds to a constant source of excitation rather than a conventional threshold and generates background activity.

When this model is used for memory storage, a number of patterns, denoted by \mathbf{v}^m with $m = 1, 2, \dots, N_{\text{mem}}$, are stored. Associative recall is achieved by starting the network in an initial state that is almost, but not exactly, proportional to one of the memory patterns, $\mathbf{v}(0) \approx c\mathbf{v}^m$ for some value of m and constant c . In this case, approximately proportional means that a significant number, but not all, of the elements of $\mathbf{v}(0)$ are close to the corresponding elements of $c\mathbf{v}^m$. The network then evolves according to equation 7.11 (with $\mathbf{h} = \mathbf{0}$). If the recall is successful, the dynamics converge to a fixed point proportional to the memory pattern associated with the initial state, that is $\mathbf{v}(t) \rightarrow c'\mathbf{v}^m$ for large t , where c' is another constant. Failure of recall occurs if the fixed point reached by the network is not proportional to the memory state \mathbf{v}^m .

In the example we consider, the components of the patterns to be stored are set to either 0 or 1. The assignment of these two values to the components of a given \mathbf{v}^m is usually random with the probability of assigning a 1 equal to α and of assigning a 0 equal to $1 - \alpha$. However, in the example we show, two of the patterns have been assigned non-randomly to make them easier to detect in the figures. The parameter α is known as the sparseness of the memory patterns. The sparser the patterns, the more can be stored, but the less information each contains. We are interested in the limit of large N_v , in which case the maximum number of patterns that can be stored, N_{mem} , is proportional to N_v .

The key to successful recall is in the choice of the matrix \mathbf{M} , which is given by

$$\mathbf{M} = \frac{1.25}{(1 - \alpha)\alpha N_v} \sum_{m=1}^{N_{\text{mem}}} (\mathbf{v}^m - \alpha \mathbf{n})(\mathbf{v}^m - \alpha \mathbf{n})^T - \frac{1}{\alpha N_v} \mathbf{n} \mathbf{n}^T. \quad (7.43)$$

Here \mathbf{n} is defined as a vector that has each of its N_v components equal to one. This form of coupling is called a covariance rule, because the first term on the right side is proportional to the covariance matrix of the collection of patterns. In chapter 8, we study synaptic plasticity rules that lead to this term. The second term introduces inhibition between the units.

Figure 7.16 shows an example of a network of $N_v = 50$ units exhibiting associative memory. This network stores 4 patterns with $\alpha = 0.25$. Recall of two of these patterns is shown in figure 7.16B and 7.16C. From an initial activity pattern only vaguely resembling one of the stored patterns, the network is able to attain a fixed activity pattern approximately proportional to the best matching memory pattern. Similar results would apply

*memory
sparseness α*
*number of
memories N_{mem}*

*vector of ones \mathbf{n}
covariance rule*

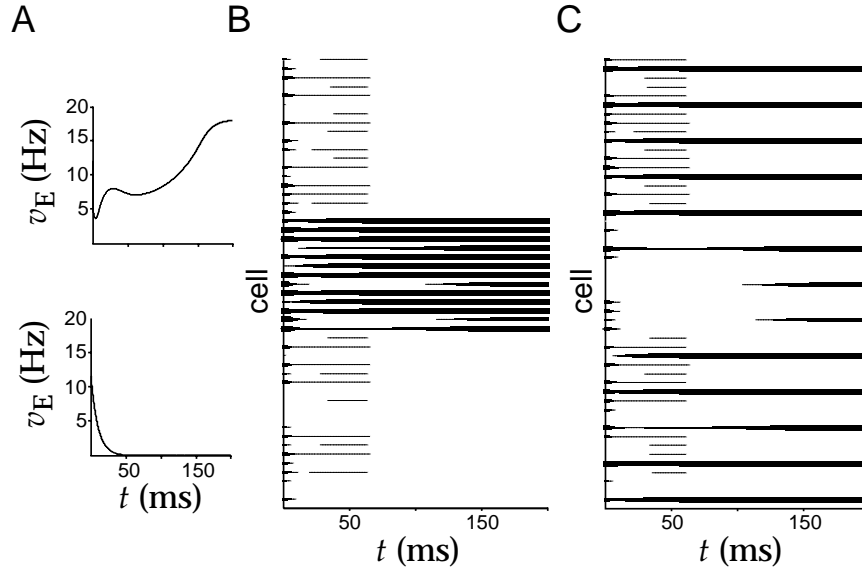


Figure 7.16: Associative recall of memory patterns in a network model. Panel A shows two representative model neurons, while panels B and C show the firing rates of all 50 cells plotted against time. The thickness of the horizontal lines in these plots is proportional to the firing rate of the corresponding neuron. A) Firing rates of representative neurons. The upper panel shows the firing rate of one of the excitatory neurons corresponding to a nonzero component of the recalled memory pattern. The firing rate achieves a nonzero steady-state value. The lower panel shows the firing rate of another excitatory neuron corresponding to a zero component of the recalled memory pattern. This firing rate goes to zero. B) Recall of one of the stored memory patterns. The stored pattern had nonzero values only for cells 18 through 31. The initial state of the network was random but with a bias toward this particular pattern. The final state is similar to the memory pattern. C) Recall of another of the stored memory patterns. The stored pattern had nonzero values only for every fourth cell. The initial state of the network was again random but biased toward this pattern. The final state is similar to the memory pattern.

for the other two memory patterns stored by the network, but it would be more difficult to see these patterns in the figure because they are random.

The rationale behind the weight matrix comes from considering the effect of the recurrent interactions if the activities match one of the memories, $\mathbf{v} = c'\mathbf{v}^1$ for example. A network activity pattern $\mathbf{v} = c'\mathbf{v}^1$ can only be a fixed point if

$$c'\mathbf{v}^1 = \mathbf{F}(c'\mathbf{M} \cdot \mathbf{v}^1), \quad (7.44)$$

which ensures that the right side of equation 7.11 (with $\mathbf{h} = \mathbf{0}$) vanishes. We assume that αN_v components of \mathbf{v}^1 are equal to one and the remaining $(1 - \alpha)N_v$ are zero. In this case,

$$\mathbf{M} \cdot \mathbf{v}^1 = 1.25\mathbf{v}^1 - (1 + 1.25\alpha)\mathbf{n} + \epsilon \quad (7.45)$$

where

$$\epsilon = \frac{1.25}{(1-\alpha)\alpha N_v} \sum_{m=2}^{N_{\text{mem}}} (\mathbf{v}^m - \alpha \mathbf{n})(\mathbf{v}^m - \alpha \mathbf{n}) \cdot \mathbf{v}^1 \quad (7.46)$$

is a term of order of magnitude $\sqrt{N_{\text{mem}}/N_v}$. To begin, suppose that ϵ is small enough to be ignored. Then, equation 7.44 amounts to two conditions, one arising from the nonzero components of \mathbf{v}^1 and the other from the zero components,

$$c' = F((0.25 - 1.25\alpha)c') \quad \text{and} \quad -(1 + 1.25\alpha)c' - \gamma < 0. \quad (7.47)$$

The inequality follows from the requirement that the total synaptic current plus the threshold is less than zero so that $F(I_s) = 0$ for these components. On the other hand, the first equation requires that $(0.25 - 1.25\alpha)c' - \gamma > 0$ so that $F > 0$ for the nonzero components of \mathbf{v}^1 . If ϵ can be ignored and these two conditions are satisfied, $\mathbf{v} = c'\mathbf{v}^1$ will be a fixed point of the network dynamics.

The term ϵ in equation 7.45, which we have been ignoring, is only negligible if $N_{\text{mem}} \ll N_v$. If $N_{\text{mem}} \approx N$, ϵ can become large enough to destabilize the memory states as fixed points. This limits the number of memories that can be stored in the network. Detailed analysis of the maximum value of N_{mem} is complicated by correlations among the terms that contribute to ϵ , but rigorous evaluations can be made of the capacity of the network, both for binary stored patterns (as here), and for real-valued patterns for which the activities of each element are drawn from a probability distribution. Different network architectures can also be considered, including ones with very sparse connectivity between units.

The basic conclusions from studies of associative memory models with threshold linear or saturating units is that large networks can store even larger numbers of patterns, particularly if the patterns are sparse (α is near 0) and if a few errors in recall can be tolerated. Nevertheless, the information stored per synapse is typically quite small. However, the simple covariance prescription for the weights in equation 7.43 is far from optimal. More sophisticated methods (such as the delta rule discussed in chapter 8) can achieve significantly higher storage densities.

7.5 Excitatory-Inhibitory Networks

In this section, we discuss models in which excitatory and inhibitory neurons are described separately by equations 7.12 and 7.13. These models exhibit richer dynamics than the single population models with symmetric coupling matrices we have analyzed up to this point. In models with excitatory and inhibitory sub-populations, the full synaptic weight matrix

is not symmetric, and network oscillations can arise. We begin by analyzing a model of homogeneous coupled excitatory and inhibitory populations. We introduce methods for determining whether this model exhibits constant or oscillatory activity. We then present two network models in which oscillations appear. The first is a model of the olfactory bulb, and the second displays selective amplification in an oscillatory mode.

Homogeneous Excitatory and Inhibitory Populations

As an illustration of the dynamics of excitatory-inhibitory network models, we analyze a simple model in which all of the excitatory neurons are described by a single firing rate v_E , and all of the inhibitory neurons are described by a second rate v_I . Although we think of this example as a model of interacting neuronal populations, it is constructed as if it consists of just two neurons. Equations 7.12 and 7.13 with threshold linear response functions are used to describe the two firing rates, so that

$$\tau_E \frac{dv_E}{dt} = -v_E + [M_{EE}v_E + M_{EI}v_I - \gamma_E]_+ \quad (7.48)$$

and

$$\tau_I \frac{dv_I}{dt} = -v_I + [M_{II}v_I + M_{IE}v_E - \gamma_I]_+ . \quad (7.49)$$

The synaptic weights M_{EE} , M_{IE} , M_{EI} , and M_{II} are numbers rather than matrices in this model. In the example we consider, we set $M_{EE} = 1.25$, $M_{IE} = 1$, $M_{II} = 0$, $M_{EI} = -1$, $\gamma_E = -10$ Hz, $\gamma_I = 10$ Hz, $\tau_E = 10$ ms, and we vary the value of τ_I . The negative value of γ_E means that this parameter serves as a source of constant background activity rather than as a threshold.

Phase-Plane Methods and Stability Analysis

The model of interacting excitatory and inhibitory populations given by equations 7.48 and 7.49 provides an opportunity for us to illustrate some of the techniques used to study the dynamics of nonlinear systems. This model exhibits both static (constant v_E and v_I) and oscillatory activity depending on the values of its parameters. Stability analysis can be used to determine the parameter values where transitions between these two types of activity take place.

The firing rates $v_E(t)$ and $v_I(t)$ arising from equations 7.48 and 7.49 can be displayed by plotting them as functions of time, as in figures 7.18A and 7.19A. Another useful way of depicting these results, illustrated in figures 7.18B and 7.19B, is to plot pairs of points $(v_E(t), v_I(t))$ for a range of t values. As the firing rates change, these points trace out a curve or trajectory in the v_E - v_I plane, which is called the phase plane of the model.

phase plane

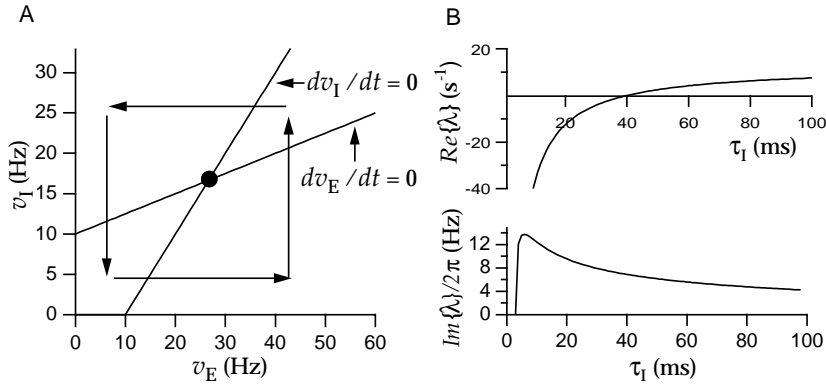


Figure 7.17: A) Nullclines, flow directions, and fixed point for the firing-rate model of interacting excitatory and inhibitory neurons. The two straight lines are the nullclines along which $dv_E/dt = 0$ or $dv_I/dt = 0$. The filled circle is the fixed point of the model. The horizontal and vertical arrows indicate the directions that v_E (horizontal arrows) and v_I (vertical arrows) flow in different regions of the phase plane relative to the nullclines. B) Real (upper panel) and imaginary (lower panel) parts of the eigenvalue determining the stability of the fixed point. To the left of the point where the imaginary part of the eigenvalue goes to zero, both eigenvalues are real. The imaginary part has been divided by 2π to give the frequency of oscillations near the fixed point.

Phase-plane plots can be used to give a geometric picture of the dynamics of a model.

Values of v_E and v_I for which the right sides of either equation 7.48 or equation 7.49 vanish are of particular interest in phase-plane analysis. Sets of such values form two curves in the phase plane known as nullclines. The nullclines for equations 7.48 and 7.49 are the straight lines drawn in figure 7.17A. The nullclines are important because they divide the phase plane into regions with opposite flow patterns. This is because dv_E/dt and dv_I/dt are positive on one side of their nullclines and negative on the other. Above the nullcline along which $dv_E/dt = 0$, $dv_E/dt < 0$, and below it $dv_E/dt > 0$. Similarly, $dv_I/dt > 0$ to the right of the nullcline where $dv_I/dt = 0$, and $dv_I/dt < 0$ to the left of it. This determines the direction of flow in the phase plane, as denoted by the horizontal and vertical arrows in figure 7.17A.

At a fixed point of a dynamic system, the dynamic variables remain at constant values. In the model being considered, a fixed point occurs when the firing rates v_E and v_I take values that make $dv_E/dt = dv_I/dt = 0$. Because a fixed point requires both derivatives to vanish, it can only occur at an intersection of nullclines. The model we are considering has a single fixed point (at $v_E = 26.67$, $v_I = 16.67$) denoted by the filled circle in figure 7.17A. A fixed point provides a potential static configuration for the system, but it is critically important whether the fixed point is stable

nullcline

fixed point

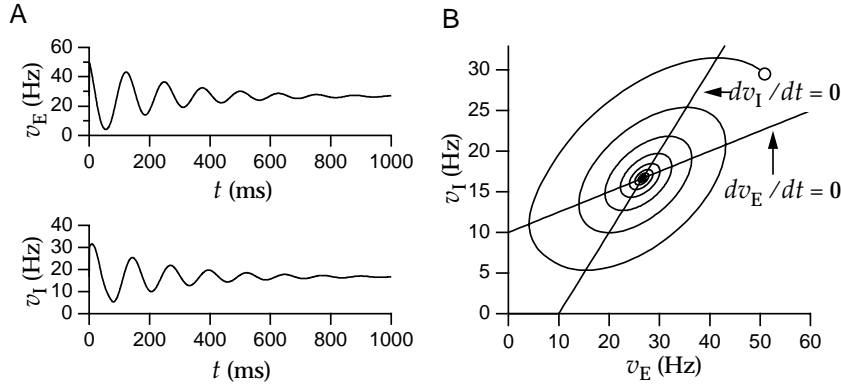


Figure 7.18: Activity of the excitatory-inhibitory firing-rate model when the fixed point is stable. A) The excitatory and inhibitory firing rates settle to the fixed point over time. B) The phase-plane trajectory is a counter-clockwise spiral collapsing to the fixed point. The open circle marks the initial values $v_E(0)$ and $v_I(0)$. For this example, $\tau_I = 30$ ms.

or unstable. If a fixed point is stable, initial values of v_E and v_I near the fixed point will be drawn toward it over time. If the fixed point is unstable, nearby configurations are pushed away from the fixed point, and the system will only remain at the fixed point indefinitely if the rates are set initially to the fixed-point values with infinite precision.

Linear stability analysis can be used to determine whether a fixed point is stable or unstable. This analysis starts by considering the first derivatives of the right sides of equations 7.48 and 7.49 with respect to v_E and v_I evaluated at the values of v_E and v_I that correspond to the fixed point. The four combinations of derivatives computed in this way can be arranged into a matrix

$$\begin{pmatrix} (M_{EE} - 1)/\tau_E & M_{EI}/\tau_E \\ M_{IE}/\tau_I & (M_{II} - 1)/\tau_I \end{pmatrix}. \quad (7.50)$$

As discussed in the Mathematical Appendix, the stability of the fixed point is determined by the real parts of the eigenvalues of this matrix. The eigenvalues are given by

$$\lambda = \frac{1}{2} \left(\frac{M_{EE} - 1}{\tau_E} + \frac{M_{II} - 1}{\tau_I} \pm \sqrt{\left(\frac{M_{EE} - 1}{\tau_E} - \frac{M_{II} - 1}{\tau_I} \right)^2 + \frac{4M_{EI}M_{IE}}{\tau_E\tau_I}} \right). \quad (7.51)$$

If the real parts of both eigenvalues are less than zero the fixed point is stable, while if either is greater than zero the fixed point is unstable. If the factor inside the square root in equation 7.51 is positive, both eigenvalues are real, and the behavior near the fixed point is exponential. This means that there is exponential movement toward the fixed point if both eigenvalues are negative, or away from the fixed point if either eigenvalue is

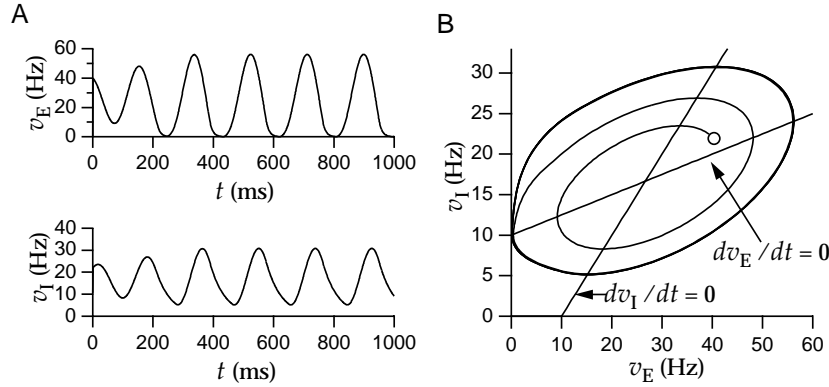


Figure 7.19: Activity of the excitatory-inhibitory firing-rate model when the fixed point is unstable. A) The excitatory and inhibitory firing rates settle into periodic oscillations. B) The phase-plane trajectory is a counter-clockwise spiral that joins the limit cycle, which is the closed orbit. The open circle marks the initial values $v_E(0)$ and $v_I(0)$. For this example, $\tau_I = 50$ ms.

positive. We focus on the case when the factor inside the square root is negative, so that the square root is imaginary and the eigenvalues form a complex conjugate pair. In this case, the behavior near the fixed point is oscillatory and the trajectory either spirals into the fixed point, if the real part of the eigenvalues is negative, or out from the fixed point if the real part of the eigenvalues is positive. The imaginary part of the eigenvalue determines the frequency of oscillations near the fixed point. The real and imaginary parts of one of these eigenvalues are plotted as a function of τ_I in figure 7.17B. This figure indicates that the fixed point is stable if $\tau_I < 40$ ms and unstable for larger values of τ_I .

Figures 7.18 and 7.19 show examples in which the fixed point is stable and unstable, respectively. In figure 7.18A, the oscillations in v_E and v_I are damped, and the firing rates settle down to the stable fixed point. The corresponding phase-plane trajectory is a collapsing spiral (figure 7.18B). In figure 7.19A the oscillations grow, and in figure 7.19B the trajectory is a spiral that expands outward until the system enters a limit cycle. A limit cycle is a closed orbit in the phase plane indicating periodic behavior. The fixed point is unstable in this case, but the limit cycle is stable. Without rectification, the phase-plane trajectory would spiral out from the unstable fixed point indefinitely. The rectification nonlinearity prevents the spiral trajectory from expanding past zero and thereby stabilizes the limit cycle.

limit cycle

There are a number of ways that a nonlinear system can make a transition from a stable fixed point to a limit cycle. Such transitions are called bifurcations. The transition seen between figures 7.18 and 7.19 is a Hopf bifurcation. In this case, a fixed point becomes unstable as a parameter is changed (in this case τ_I) when the real part of a complex eigenvalue changes sign. In a Hopf bifurcation, the limit cycle emerges at a finite fre-

Hopf bifurcation

saddle-node
bifurcation

mitral cells
tufted cells

granule cells

quency, which is similar to the behavior of a type II neuron when it starts firing action potentials, as discussed in chapter 6. Other types of bifurcations produce type I behavior with oscillations emerging at zero frequency (chapter 6). One example of this is a saddle-node bifurcation, which occurs when parameters are changed such that two fixed points, one stable and one unstable, meet at the same point in the phase plane.

The Olfactory Bulb

The olfactory bulb, and analogous olfactory areas in insects, provide examples where sensory processing involves oscillatory activity. The olfactory bulb represents the first stage of processing beyond the olfactory receptors in the vertebrate olfactory system. Olfactory receptor neurons respond to odor molecules and send their axons to the olfactory bulb. These axons terminate in glomeruli where they synapse onto mitral and tufted cells, and also local interneurons. The mitral and tufted cells provide the output of the olfactory bulb by sending projections to the primary olfactory cortex. They also synapse onto the larger population of inhibitory granule cells. The granule cells in turn inhibit the mitral and tufted cells.

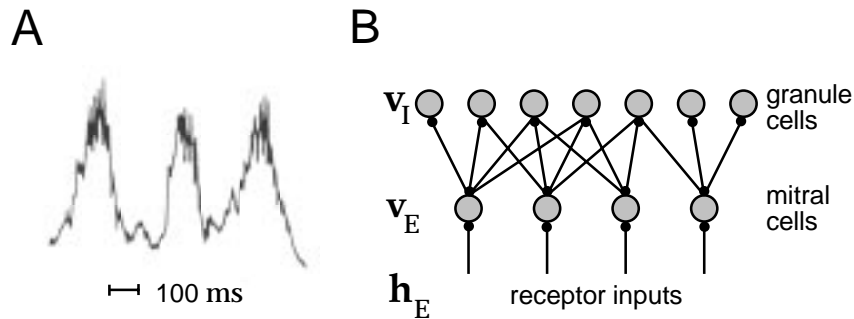


Figure 7.20: A) Extracellular field potential recorded in the olfactory bulb during respiratory waves representing three successive sniffs. B) Schematic diagram of the olfactory bulb model. (A adapted from Freeman and Schneider, 1982; B adapted from Li, 1995.)

The activity in the olfactory bulb of many vertebrates is strongly influenced by a sniff cycle in which a few quick sniffs bring odors past the olfactory receptors. Figure 7.20A shows an extracellular potential recorded during three successive sniffs. The three large oscillations in the figure are due to the sniffs. The oscillations we discuss in this section are the smaller, higher frequency oscillations seen around the peak of each sniff cycle. These arise from oscillatory neural activity. Individual mitral cells have quite low firing rates, and do not fire on each cycle of the oscillations. The oscillations are phase-locked across the bulb, but different odors induce oscillations of different amplitudes and phases.

Li and Hopfield (1989) modeled the mitral and granule cells of the olfactory bulb as a nonlinear input-driven network oscillator. Figure 7.20B shows the architecture of the model, which uses equations 7.12 and 7.13 with $M_{EE} = M_{II} = 0$. The absence of these couplings in the model is in accord with the anatomy of the bulb. The rates v_E and v_I refer to the mitral and granule cells, respectively (figure 7.20B). Figure 7.21A shows the activation functions of the model. The time constants for the two populations of cells are the same, $\tau_E = \tau_I = 6.7$ ms. h_E is the input from the receptors to the mitral cells, and h_I is a constant representing top-down input that exists from the olfactory cortex to the granule cells.

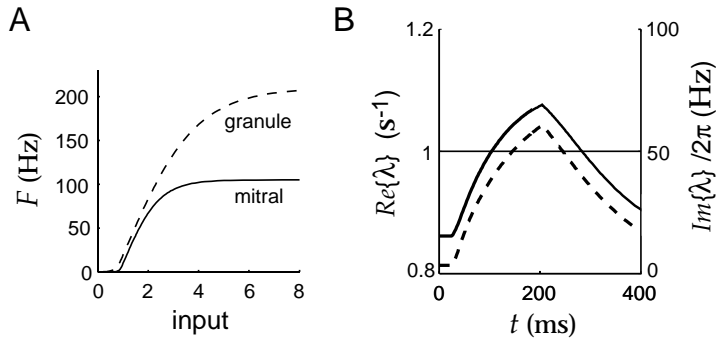


Figure 7.21: Activation functions and eigenvalues for the olfactory bulb model. A) The activation functions F_E (solid curve) for the mitral cells, and F_I (dashed curve) for the granule cells. B) The real (solid line, left axis) and imaginary (dashed line, right axis) parts of the eigenvalue that determines whether the network model exhibits fixed-point or oscillatory behavior. These are plotted as a function of time during a sniff cycle. When the real part of the eigenvalue becomes greater than one, it determines the growth rate away from the fixed point and the imaginary part divided by 2π determines the initial frequency of the resulting oscillations. (Adapted from Li, 1995.)

The field potential in figure 7.20A shows oscillations during each sniff, but not between sniffs. For the model to match this pattern of activity, the input from the olfactory receptors, h_E , must induce a transition between fixed-point and oscillatory activity. Before a sniff, the network must have a stable fixed point with low activities. As h_E increases during a sniff, this steady-state configuration must become unstable leading to oscillatory activity. The analysis of the stability of the fixed point and the onset of oscillations is closely related to our previous stability analysis of the model of homogeneous populations of coupled excitatory and inhibitory neurons. It is based on properties of the eigenvalues of the linear stability matrix (see the Mathematical Appendix). In this case, the stability matrix includes contributions from the derivatives of the activation functions evaluated at the fixed point. For the fixed point to become unstable, the real part of at least one of the eigenvalues that arise in this analysis must become larger than 1. To ensure oscillations, at least one of these destabilizing eigenval-

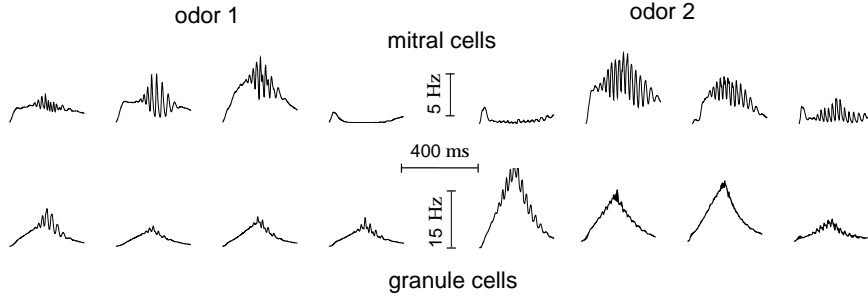


Figure 7.22: Activities of four of ten mitral (upper) and granule (lower) cells during a single sniff cycle for two different odors. (Adapted from Li and Hopfield, 1989.)

ues should have a non-zero imaginary part. These requirements impose constraints on the connections between the mitral and granule cells and on the inputs.

Figure 7.21B shows the real and imaginary parts of the relevant eigenvalue, labeled λ , during one sniff cycle. About 100 ms into the cycle the real part of λ gets bigger than 1. Reading off the imaginary part of λ at this point, we find that this sets off roughly 40 Hz oscillations in the network. These oscillations stop about 300 ms into the sniff cycle when the real part of λ drops below 1. The input h_E from the receptors plays two critical roles in this process. First, it makes the eigenvalue great than 1 by modifying where the fixed point lies on the activation function curves in figure 7.21A. Second, it affects which particular neurons are destabilized and thus, which begin to oscillate. The ultimate pattern of oscillatory activity is determined both by the input h_E and by the recurrent couplings of the network.

Figure 7.22 shows the behavior of the network during a single sniff cycle in the presence of two different odors, represented by two different values of h_E . The top rows show the activity of four mitral cells, and the bottom rows four granule cells. The amplitudes and phases of the oscillations seen in these traces, along with the identities of the mitral cells taking part in them, provide a signature of the identity of the odor that was presented.

Oscillatory Amplification

As a final example of network oscillations, we return to amplification of input signals by a recurrently connected network. Two factors control the amount of selective amplification that is viable in networks such as that shown in figure 7.9. The most important constraint on the recurrent weights is that the network must be stable, so the activity does not increase without bound. Another possible constraint is suggested by figure 7.14D where the output shows a tuned response even though the input to the net-

work is constant as a function of θ . Tuned output in the absence of tuned input can serve as a memory mechanism, but it would produce persistent perceptions if it occurs in a primary sensory area, for example. Avoiding this in the network limits the recurrent weights and the amount of amplification that can be supported.

Li and Dayan (1999) showed that this restriction can be significantly eased using the richer dynamics of networks of coupled inhibitory and excitatory neurons. Figure 7.23 shows an example with continuous neuron labeling based on a continuous version of equations 7.12 and 7.13. The input is either $h_E(\theta) = 8(1 + \frac{5}{8} \cos(2\theta))$ in the modulated case (figure 7.23B) or $h_E(\theta) = 8$ in the unmodulated case (figure 7.23C). Noise with standard deviation 0.4 corrupts this input. The input to the network is constant in time.

The network oscillates in response to either constant or tuned input. Figure 7.23A shows the time average of the oscillating activities of the neurons in the network as a function of their preferred angles for noisy tuned (solid curve) and untuned (dashed curve) inputs. Neurons respond to the tuned input in a highly tuned and amplified manner. Despite the high degree of amplification, the average response of the neurons to untuned input is almost independent of θ . Figures 7.23B and 7.23C show the activities of individual neurons with $\theta = 0^\circ$ ('o') and $\theta = -37^\circ$ ('x') over time for the tuned and untuned inputs respectively. The network does not produce persistent perception, because the output to an untuned input is itself untuned. In contrast, a non-oscillatory version of this network, with $\tau_I = 0$, exhibits tuned sustained activity in response to an untuned input for recurrent weights this strong. The oscillatory network can thus operate in a regime of high selective amplification without generating spurious tuned activity.

7.6 Stochastic Networks

Up to this point, we have considered models in which the output of a cell is a deterministic function of its input. In this section, we consider a network model called the Boltzmann machine in which the input-output relationship is stochastic. Boltzmann machines are interesting from the perspective of learning, and also because they offer an alternative interpretation of the dynamics of network models.

*Boltzmann
machine*

In the simplest form of Boltzmann machine, the neurons are treated as binary, so $v_a(t) = 1$ if unit a is active at time t (e.g. it fires a spike between times t and $t + \Delta t$ for some small value of Δt), and $v_a(t) = 0$ if it is inactive. The state of unit a is determined by its total input current,

$$I_a(t) = h_a(t) + \sum_{a'=1}^{N_v} M_{aa'} v_{a'}(t), \quad (7.52)$$

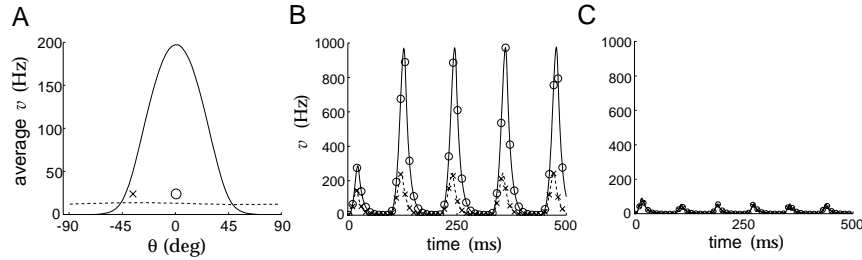


Figure 7.23: Selective amplification in an excitatory-inhibitory network. A) Time-averaged response of the network to a tuned input with $\Theta = 0^\circ$ (solid curve) and to an untuned input (dashed curve). Symbols 'o' and 'x' mark the 0° and -37° points seen in B and C. B) Activities over time of neurons with preferred angles of $\theta = 0^\circ$ (solid curve) and $\theta = -37^\circ$ (dashed curve) in response to a modulated input with $\Theta = 0^\circ$. C) Activities of the same units shown in B to a constant input. The lines lie on top of each other showing that the two units respond identically. The parameters are $\tau_E = \tau_I = 10$ ms, $h_I = 0$, $M_{EI} = -\delta(\theta - \theta')/\rho_\theta$, $M_{EE} = (1/\pi\rho_\theta)[5.9 + 7.8 \cos(2(\theta - \theta'))]_+$, $M_{IE} = 13.3/\pi\rho_\theta$, and $M_{II} = 0$. (After Li and Dayan, 1999.)

where $M_{aa'} = M_{a'a}$ and $M_{aa} = 0$ for all a and a' values, and h_a is the total feedforward input into unit a . In the model, units can only change state at integral multiples of Δt . At each time step, a single unit is selected, usually at random, to be updated. This update is based on a probabilistic rather than a deterministic rule. If unit a is selected, its state at the next time step is set stochastically to 1 with probability

$$P[v_a(t + \Delta t) = 1] = F(I_a(t)) \quad \text{with} \quad F(I_a) = \frac{1}{1 + \exp(-I_a)}. \quad (7.53)$$

Of course, it follows that $P[v_a(t + \Delta t) = 0] = 1 - F(I_a(t))$. F is a sigmoidal function, which has the property that the larger the value of I_a , the more likely unit a is to take the value one.

Markov chain

Under equation 7.53, the state of activity of the network evolves as a Markov chain. This means that the components of v at different times are sequences of random variables with the property that $v(t+1)$ depends only on $v(t)$, and not on the previous history of the network. The update of equation 7.53 is known as Glauber dynamics.

An advantage of using Glauber dynamics to define the evolution of a network model is that general results from statistical mechanics can be used to determine the equilibrium distribution of activities. Under Glauber dynamics, v does not converge to a fixed point, but can be described by a probability distribution associated with an energy function

$$E(v) = -\mathbf{h} \cdot v - \frac{1}{2} \mathbf{v} \cdot \mathbf{M} \cdot \mathbf{v}. \quad (7.54)$$

The probability distribution characterizing v , once the network has con-

verged to an equilibrium state, is

$$P[\mathbf{v}] = \frac{\exp(-E(\mathbf{v}))}{Z} \quad \text{where} \quad Z = \sum_{\mathbf{v}} \exp(-E(\mathbf{v})). \quad (7.55)$$

The notion of convergence as $t \rightarrow \infty$ can be formalized precisely, but informally, it means that after repeated updating according to equation 7.53, the states of the network are described statistically by equation 7.55. Z is called the partition function and $P[\mathbf{v}]$ the Boltzmann distribution. Under the Boltzmann distribution, states with lower energies are more likely. In this case, Glauber dynamics implements a statistical operation called Gibbs sampling for the distribution given in equation 7.55.

*partition function
Boltzmann
distribution
Gibbs sampling*

The Boltzmann machine is an inherently stochastic device. An approximation to the Boltzmann machine, known as the mean-field approximation, can be constructed on the basis of the deterministic synaptic current dynamics of a firing-rate model. In this case, I is determined by the dynamic equation 7.39 rather than by equation 7.52, and the model runs in continuous rather than discrete time. The function F in equation 7.39 is taken to be the same sigmoidal function as in equation 7.53. Although the mean-field formulation of the Boltzmann machine is inherently deterministic, $F(I_a)$ can be used to generate a probability distribution over a binary output vector \mathbf{v} . This is done by treating the output of each unit a , v_a , as an independent binary variable set to either 1 or 0 with probability $F(I_a)$ or $1 - F(I_a)$ respectively. This replaces the deterministic rule $v_a = F(I_a)$ used in the firing-rate version of the model. Because $v_a = 1$ has probability $F(I_a)$ and $v_a = 0$ probability $1 - F(I_a)$ and the units are independent, the probability distribution for the entire vector \mathbf{v} is

$$Q[\mathbf{v}] = \prod_{a=1}^{N_v} F(I_a)^{v_a} (1 - F(I_a))^{1-v_a}. \quad (7.56)$$

This is called the mean-field distribution for the Boltzmann machine. Note that this distribution (and indeed \mathbf{v} itself) plays no role in the dynamics of the mean-field formulation of the Boltzmann machine. It is rather a way of interpreting the outputs.

*mean field
distribution*

We have presented two formulations of the Boltzmann machine, Gibbs sampling and the mean-field approach, that lead to the two distributions $P[\mathbf{v}]$ and $Q[\mathbf{v}]$ (equations 7.55 and 7.56). The Lyapunov function of equation 7.40, that decreases steadily under the dynamics of equation 7.39 until a fixed point is reached, provides a key insight into the relationship between these two distributions. In the appendix, we show that this Lyapunov function can be expressed as

$$L(\mathbf{I}) = D_{\text{KL}}(Q, P) + K \quad (7.57)$$

where K is a constant, and D_{KL} is the Kullback-Liebler divergence defined in chapter 4. $D_{\text{KL}}(Q, P)$ is a measure of how different the two distributions Q and P are from each other. The fact that the dynamics of equation 7.39

reduces the Lyapunov function to a minimum value means that it also reduces the difference between Q and P , as measured by the Kullback-Liebler divergence. This offers an interesting interpretation of the mean-field dynamics; it modifies the current value of the vector \mathbf{I} until the distribution of binary output values generated by the mean-field formulation of the Boltzmann machine matches as closely as possible (to at least a local minimum of $D_{KL}(Q, P)$) the distribution generated by Gibbs sampling. In this way, the mean-field procedure can be viewed as an approximation of Gibbs sampling.

The power of the Boltzmann machine lies in the relationship between the distribution of output values, equation 7.55, and the quadratic energy function of equation 7.54. This makes it is possible to determine how changing the weights \mathbf{M} affects the distribution of output states. In chapter 8, we present a learning rule for the weights of the Boltzmann machine that allows $P[\mathbf{v}]$ to approximate a probability distribution extracted from a set of inputs. In chapter 10, we study other models that construct output distributions in this way.

Note that the mean field distribution $Q[\mathbf{v}]$ is simpler than the full Boltzmann distribution $P[\mathbf{v}]$ because the units are statistically independent. This prevents $Q[\mathbf{v}]$ from providing a good approximation in some cases, particularly if there are negative weights between units, which tend to make their activities mutually exclusive. Correlations such as these in the fluctuations of the states about their mean values can be important for learning. The mean-field analysis of the Boltzmann machine illustrates the limitations of rate-based descriptions in capturing the full extent of the correlations that can exist between spiking neurons.

7.7 Chapter Summary

The models in this chapter mark the start of our discussion of computation, as opposed to coding. Using a description of the firing rates of network neurons, we showed how to construct linear and nonlinear feedforward and recurrent networks that transform information from one coordinate system to another, selectively amplify input signals, integrate inputs over extended periods of time, select between competing inputs, sustain activity in the absence of input, exhibit gain modulation, allow simple decoding with performance near the Cramér-Rao bound, and act as content addressable memories. We used network responses to a continuous stimulus variable as an extended example. This led to models of simple and complex cells in primary visual cortex. We described a model of the olfactory bulb as an example of a system for which computation involves oscillations arising from asymmetric couplings between excitatory and inhibitory neurons. Linear stability analysis was applied to a simplified version of this model. We also considered a stochastic network model called the Boltzmann machine.

Appendix

Lyapunov Function for the Boltzmann Machine

Here, we show that the Lyapunov function of equation 7.40 can be reduced to equation 7.57 when applied to the mean-field version of the Boltzmann machine. Recall, from equation 7.40, that

$$L(\mathbf{I}) = \sum_{a=1}^{N_v} \left(\int_0^{I_a} dz_a z_a F'(z_a) - h_a F(I_a) - \frac{1}{2} \sum_{a'=1}^{N_v} F(I_a) M_{aa'} F(I_{a'}) \right) \quad (7.58)$$

When F is given by the sigmoidal function of equation 7.53,

$$\int_0^{I_a} dz_a z_a F'(z_a) = F(I_a) \ln F(I_a) + (1 - F(I_a)) \ln(1 - F(I_a)) + k \quad (7.59)$$

where k is a constant, as can be verified by differentiating the right side. The non-constant part of the right side of this equation is just the entropy associated with the binary variable v_a . In fact,

$$\sum_{a=1}^{N_v} \int_0^{I_a} dz_a z_a F'(z_a) = \langle \ln Q[\mathbf{v}] \rangle_Q + N_v k \quad (7.60)$$

where the average is over all values of \mathbf{v} with probabilities $Q[\mathbf{v}]$.

To evaluate the remaining terms in equation 7.58, we note that, because the components of \mathbf{v} are binary and independent, relations such as $\langle v_a \rangle_Q = F(I_a)$ and $\langle v_a v_b \rangle_Q = F(I_a)F(I_b)$ are valid. Then, using equation 7.54, we find

$$L(\mathbf{I}) = \sum_{a=1}^{N_v} \left(-h_a F(I_a) - \frac{1}{2} \sum_{a'=1}^{N_v} F(I_a) M_{aa'} F(I_{a'}) \right) = \langle -E(\mathbf{v}) \rangle_Q. \quad (7.61)$$

Similarly, from equation 7.55, we can show that

$$\langle \ln P[\mathbf{v}] \rangle_Q = \langle -E(\mathbf{v}) \rangle_Q - \ln Z. \quad (7.62)$$

Combining the results of equations 7.60, 7.61, and 7.62, we obtain

$$L(\mathbf{I}) = \langle \ln Q[\mathbf{v}] - \ln P[\mathbf{v}] \rangle_Q + N_v k - \ln Z. \quad (7.63)$$

which gives equation 7.57 with $K = N_v k - \log Z$ because $\langle \ln Q[\mathbf{v}] - \ln P[\mathbf{v}] \rangle_Q$ is, by definition, the Kullback-Liebler divergence $D_{KL}(Q, P)$ (see chapter 4, although there we use base 2 logarithms, while here we use base e logarithms in the definition of D_{KL} , but the difference is only an overall multiplicative constant).

7.8 Annotated Bibliography

Wilson & Cowan (1972, 1973) provide pioneering analyses of firing-rate models. Subsequent analyses related to the discussion in this chapter are presented in Abbott (1994), Ermentrout (1998), Amit & Tsodyks (1991a & b) and Bressloff & Coombes (2000). Rinzel and Ermentrout (1998) discuss phase-plane methods; XPP (see <http://www.pitt.edu/~phase>) provides a computer environment for performing phase-plane and other forms of mathematical analysis on neuron and network models.

Our discussion of the feedforward coordinate transformation model followed Pouget & Sejnowski (1995, 1997) and Salinas & Abbott (1995), which built on theoretical work by Zipser & Andersen (1988) to explain parietal gain fields (see Andersen, 1989).

We followed Seung's (1996) discussion of neural integration for eye position, which builds on Robinson (1989).

The notion of a regular repeating unit of cortical computation dates back to the earliest investigations of cortex (see Douglas & Martin 1998). We followed Seung (1996); Zhang (1996) in adopting the theoretical context of continuous line or surface attractors, that has the many applications discussed in the chapter (see also Hahnloser et al., 2000). Sompolinsky & Shapley 1997 review a recently active debate about the balance of control of orientation selectivity in primary visual cortex between feedforward input and a recurrent line attractor. We presented a model of a hypercolumn; the extension to multiple hypercolumns is used to link psychophysical and physiological data on contour integration and texture segmentation by Li (1998, 1999).

Network associative memories are described and analyzed by Hopfield (1982; 1984) and Cohen & Grossberg (1983), who described a general Lyapunov function. Grossberg (1988); Amit (1989); Hertz, et al. (1991) present a host of theory about associative networks, in particular about their capacity to store information. Associative memory in non-binary recurrent networks has been studied in particular by Treves and collaborators (see Rolls & Treves, 1998) and, in the context of line attractor networks, by Samsonovich & McNaughton (1997) and Battaglia & Treves (1998).

We followed Li's (1995) presentation of Li & Hopfield's (1989) oscillatory model of the olfactory bulb.

The Boltzmann machine was invented by Hinton & Sejnowski (1986), and is a stochastic generalization of the Hopfield net (Hopfield, 1982). The mean-field model is due to Hopfield (1984), and we followed the probabilistic discussion in Jordan et al. (1998).

Chapter 8

Plasticity and Learning

8.1 Introduction

Activity-dependent synaptic plasticity is widely believed to be the basic phenomenon underlying learning and memory, and it is also thought to play a crucial role in the development of neural circuits. To understand the functional and behavioral significance of synaptic plasticity, we must study how experience and training modify synapses, and how these modifications change patterns of neuronal firing to affect behavior. Experimental work has revealed ways in which neuronal activity can affect synaptic strength, and experimentally inspired synaptic plasticity rules have been applied to a wide variety of tasks including auto- and hetero-associative memory, pattern recognition, storage and recall of temporal sequences, and function approximation.

In 1949, Donald Hebb conjectured that if input from neuron A often contributes to the firing of neuron B, the synapse from A to B should be strengthened. Hebb suggested that such synaptic modification could produce neuronal assemblies that reflect the relationships experienced during training. The Hebb rule forms the basis of much of the research done on the role of synaptic plasticity in learning and memory. For example, consider applying this rule to neurons that fire together during training due to an association between a stimulus and a response. These neurons would develop strong interconnections, and subsequent activation of some of them by the stimulus could produce the synaptic drive needed to activate the remaining neurons and generate the associated response. Hebb's original suggestion concerned increases in synaptic strength, but it has been generalized to include decreases in strength arising from the repeated failure of neuron A to be involved in the activation of neuron B. General forms of the Hebb rule state that synapses change in proportion to the correlation or covariance of the activities of the pre- and postsynaptic neurons.

Hebb rule

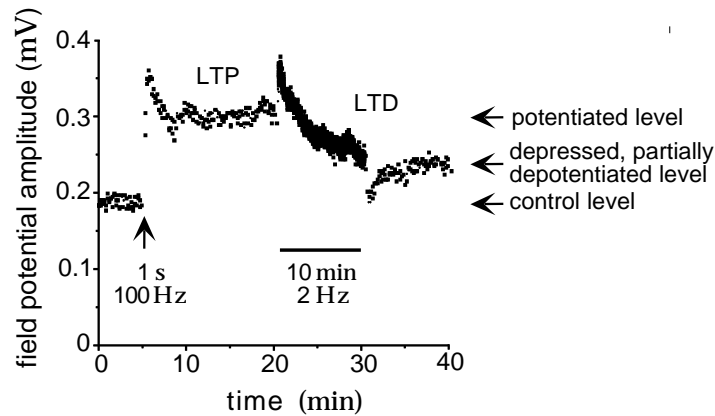


Figure 8.1: LTP and LTD at the Schaffer collateral inputs to the CA1 region of a rat hippocampal slice. The points show the amplitudes of field potentials evoked by constant amplitude stimulation. At the time marked by the arrow (at time 5 minutes), stimulation at 100 Hz for 1 s caused a significant increase in the response amplitude. Some of this increase decayed away following the stimulation, but most of it remained over the following 15 min test period, indicating LTP. Next, stimulation at 2 Hz was applied for 10 min (between times 20 and 30 minutes). This reduced that amplitude of the response. After a transient dip, the response amplitude remained at a reduced level approximately midway between the original and post-LTP values, indicating LTD. The arrows at the right show the levels initially (control), after LTP (potentiated), and after LTD (depressed, partially de-potentiated). (Unpublished data of J Fitzpatrick and J Lisman.)

Experimental work in a number of brain regions including hippocampus, neocortex, and cerebellum, has revealed activity-dependent processes that can produce changes in the efficacies of synapses that persist for varying amounts of time. Figure 8.1 shows an example in which the data points indicate amplitudes of field potentials evoked in the CA1 region of a slice of rat hippocampus by stimulation of the Schaffer collateral afferents. In experiments such as this, field potential amplitudes (or more often slopes) are used as a measure of synaptic strength. In Figure 8.1, high-frequency stimulation induced synaptic potentiation (an increase in strength), and then long-lasting, low-frequency stimulation resulted in synaptic depression (a decrease in strength) that partially removed the effects of the previous potentiation. This is in accord with a generalized Hebb rule because high-frequency presynaptic stimulation evokes a postsynaptic response, whereas low-frequency stimulation does not. Changes in synaptic strength involve both transient and long-lasting effects, as seen in figure 8.1. The longest-lasting forms appear to require protein synthesis. Changes that persist for tens of minutes or longer are generally called long-term potentiation (LTP) and long-term depression (LTD). Inhibitory synapses can also display plasticity, but this has been less thoroughly investigated both experimentally and theoretically, and we focus on the plas-

potentiation

depression

LTP and LTD

ticity of excitatory synapses in this chapter.

A wealth of data is available on the underlying cellular basis of activity-dependent synaptic plasticity. The postsynaptic concentration of calcium ions appears to play a critical role in the induction of both long-term potentiation and depression. However, we will not consider mechanistic models. Rather, we study synaptic plasticity at a functional level, attempting to relate the impact of synaptic plasticity on neurons and networks to the basic rules governing its induction.

Studies of plasticity and learning involve analyzing how synapses are affected by activity over the course of a training period. In this and the following chapters, we consider three types of training procedures. In unsupervised (or sometimes self-supervised) learning, a network responds to a series of inputs during training solely on the basis of its intrinsic connections and dynamics. The network then self-organizes in a manner that depends on the synaptic plasticity rule being applied and on the nature of inputs presented during training. We consider unsupervised learning in a more general setting called density estimation in chapter 10. In supervised learning, which we consider in the last section of this chapter, a desired set of input-output relationships is imposed on the network by a ‘teacher’ during training. Networks that perform particular tasks can be constructed in this way by letting a modification rule adjust the synapses until the desired computation emerges as a consequence of the training process. This is an alternative to explicitly specifying the synaptic weights, as was done in chapter 7. In this case, finding a biological plausible teaching mechanism may not be a concern, if the scientific question being addressed is whether any weights can be found that allow a network to implement a particular function. In more biologically plausible examples of supervised learning, one network can act as the teacher for another network. In chapter 9, we discuss a third form of learning, reinforcement learning, that is somewhat intermediate between these cases. In reinforcement learning, the network output is not constrained by a teacher, but evaluative feedback on network performance is provided in the form of reward or punishment. This can be used to control the synaptic modification process. We will see that the same synaptic plasticity rule can be used for different types of learning procedures.

In this chapter we focus on activity-dependent synaptic plasticity of the Hebbian type, meaning plasticity based on correlations of pre- and post-synaptic firing. To ensure stability and to obtain interesting results, we must often augment Hebbian plasticity with more global forms of synaptic modification that, for example, scale the strengths of all the synapses onto a given neuron. These can have a major impact on the outcome of development or learning. Non-Hebbian forms of synaptic plasticity, such as those that modify synaptic strengths solely on the basis of pre- or postsynaptic firing, are likely to play important roles in homeostatic, developmental, and learning processes. Activity can also modify the intrinsic excitability and response properties of neurons. Models of such intrinsic plasticity

*unsupervised
learning*

*supervised
learning*

*reinforcement
learning*

*non-Hebbian
plasticity*

show that neurons can be remarkably robust to external perturbations if they adjust their conductances to maintain specified functional characteristics. Intrinsic and synaptic plasticity can interact in interesting ways. For example, shifts in intrinsic excitability can compensate for changes in the level of input to a neuron caused by synaptic plasticity. It is likely that all of these forms of plasticity, and many others, are important elements of both the stability and adaptability of nervous systems.

In this chapter, we describe and analyze basic correlation- and covariance-based synaptic plasticity rules in the context of unsupervised learning, and discuss their extension to supervised learning. One running example is the development of ocular dominance in single cells in primary visual cortex and the ocular dominance stripes they collectively form.

Stability and Competition

Increasing synaptic strength in response to activity is a positive feedback process. The activity that modifies synapses is reinforced by Hebbian plasticity, which leads to more activity and further modification. Without appropriate adjustments of the synaptic plasticity rules or the imposition of constraints, Hebbian modification tends to produce uncontrolled growth of synaptic strengths.

The easiest way to control synaptic strengthening is to impose an upper limit on the value that a synaptic weight (defined as in chapter 7) can take. Such an upper limit is supported by LTP experiments. Further, it makes sense to prevent weights from changing sign, because the plasticity processes we are modeling cannot change an excitatory synapse into an inhibitory synapse or vice versa. We therefore impose the constraint, which we call a saturation constraint, that all excitatory synaptic weights must lie between zero and a maximum value w_{\max} , which is a constant. The simplest implementation of saturation is to set any weight that would cross a saturation bound due to application of a plasticity rule to the limiting value.

Uncontrolled growth is not the only problem associated with Hebbian plasticity. Synapses are modified independently under a Hebbian rule, which can have deleterious consequences. For example, all of the synaptic weights may be driven to their maximum allowed values w_{\max} , causing the postsynaptic neuron to lose selectivity to different patterns of input. The development of input selectivity typically requires competition between different synapses, so that some are forced to weaken when others become strong. We discuss a variety of synaptic plasticity rules that introduce competition between synapses. In some cases, the same mechanism that leads to competition also stabilizes growth of the synaptic weights. In other cases, it does not, and saturation constraints must also be imposed.

synaptic saturation

synaptic competition

8.2 Synaptic Plasticity Rules

Rules for synaptic modification take the form of differential equations describing the rate of change of synaptic weights as a function of the pre- and postsynaptic activity and other possible factors. In this section, we give examples of such rules. In later sections, we discuss their computational implications.

In the models of plasticity we study, the activity of each neuron is described by a continuous variable, not by a spike train. As in chapter 7, we use the letter u to denote the presynaptic level of activity and v to denote the postsynaptic activity. Normally, u and v represent the firing rates of the pre- and postsynaptic neurons, in which case they should be restricted to non-negative values. Sometimes, to simplify the analysis, we ignore this constraint. An activity variable that takes both positive and negative values can be interpreted as the difference between a firing rate and a fixed background rate, or between the firing rates of two neurons being treated as a single unit. Finally, to avoid extraneous conversion factors in our equations, we take u and v to be dimensionless measures of the corresponding neuronal firing rates or activities. For example, u and v could be the firing rates of the pre- and postsynaptic neurons divided by their maximum or average values.

In the first part of this chapter, we consider unsupervised learning as applied to a single postsynaptic neuron driven by N_u presynaptic inputs with activities represented by u_b for $b = 1, 2, \dots, N_u$, or collectively by the vector \mathbf{u} . Because we study unsupervised learning, the postsynaptic activity v is evoked directly by the presynaptic activity \mathbf{u} , not by an external agent. We use a linear version of the firing-rate model discussed in chapter 7,

$$\tau_r \frac{dv}{dt} = -v + \mathbf{w} \cdot \mathbf{u} = -v + \sum_{b=1}^{N_u} w_b u_b \quad (8.1)$$

where τ_r is a time constant that controls the firing rate response dynamics. Recall that w_b is the synaptic weight that describes the strength of the synapse from presynaptic neuron b to the postsynaptic neuron, and \mathbf{w} is the vector formed by all N_u synaptic weights. The individual synaptic weights can be either positive, representing excitation, or negative, representing inhibition. Equation 8.1 does not include any nonlinear dependence of the firing rate on the total synaptic input, not even rectification. Using such a linear firing-rate model considerably simplifies the analysis of synaptic plasticity. The restriction to non-negative v will either be imposed by hand, or sometimes it will be ignored to simplify the analysis.

w weight vector

The processes of synaptic plasticity are typically much slower than the dynamics characterized by equation 8.1. If, in addition, the stimuli are presented slowly enough to allow the network to attain its steady-state activity during training, we can replace the dynamic equation 8.1 by

$$v = \mathbf{w} \cdot \mathbf{u}, \quad (8.2)$$

which sets v instantaneously to the asymptotic, steady-state value determined by equation 8.1. This is the equation we primarily use in our analysis of synaptic plasticity in unsupervised learning. Synaptic modification is included in the model by specifying how the vector w changes as a function of the pre- and postsynaptic levels of activity. The complex time-course of plasticity seen in figure 8.1 is simplified by modeling only the longer-lasting changes.

The Basic Hebb Rule

The simplest plasticity rule that follows the spirit of Hebb's conjecture takes the form

$$\tau_w \frac{d\mathbf{w}}{dt} = v\mathbf{u}, \quad (8.3)$$

which implies that simultaneous pre- and postsynaptic firing increases synaptic strength. We call this the basic Hebb rule. If the activity variables represent firing rates, the right side of this equation can be interpreted as a measure of the probability that the pre- and postsynaptic neurons both fire spikes during a small time interval. Here, τ_w is a time constant that controls the rate at which the weights change.

Synaptic plasticity is generally modeled as a slow process that gradually modifies synaptic weights over a time period during which the components of \mathbf{u} take a variety of different values. Each set of \mathbf{u} values is called an input pattern. The direct way to compute the weight changes induced by a series of input patterns is to sum the small changes caused by each of them separately. A convenient alternative is to average over all of the different input patterns and compute the weight changes induced by this average. As long as the synaptic weights change slowly enough, the averaging method provides a good approximation of the weight changes produced by the set of input patterns.

In this chapter, we use angle brackets $\langle \rangle$ to denote averages over the ensemble of input patterns presented during training (which is a slightly different usage from earlier chapters). The Hebb rule of equation 8.3, when averaged over the inputs used during training, becomes

$$\tau_w \frac{d\mathbf{w}}{dt} = \langle v\mathbf{u} \rangle. \quad (8.4)$$

In unsupervised learning, v is determined by equation 8.2, and, if we replace v by $\mathbf{w} \cdot \mathbf{u}$, we can rewrite the averaged plasticity rule (equation 8.4) as

$$\tau_w \frac{d\mathbf{w}}{dt} = \mathbf{Q} \cdot \mathbf{w} \quad \text{or} \quad \tau_w \frac{dw_b}{dt} = \sum_{b'=1}^{N_u} Q_{bb'} w_{b'} \quad (8.5)$$

correlation-based rule

Q input correlation matrix where \mathbf{Q} is the input correlation matrix given by

$$\mathbf{Q} = \langle \mathbf{u}\mathbf{u} \rangle \quad \text{or} \quad Q_{bb'} = \langle u_b u_{b'} \rangle. \quad (8.6)$$

Equation 8.5 is called a correlation-based plasticity rule because of the presence of the input correlation matrix.

Whether or not the pre- and postsynaptic activity variables are restricted to non-negative values, the basic Hebb rule is unstable. To show this, we consider the square of the length of the weight vector, $|\mathbf{w}|^2 = \mathbf{w} \cdot \mathbf{w} = \sum_b w_b^2$. Taking the dot product of equation 8.3 with \mathbf{w} and noting that $d|\mathbf{w}|^2/dt = 2\mathbf{w} \cdot d\mathbf{w}/dt$ and that $\mathbf{w} \cdot \mathbf{u} = v$, we find that $\tau_w d|\mathbf{w}|^2/dt = 2v^2$, which is always positive (except in the trivial case $v = 0$). Thus, the length of the weight vector grows continuously when the rule 8.3 is applied. To avoid unbounded growth, we must impose an upper saturation constraint. A lower limit is also required if the activity variables are allowed to be negative. Even with saturation, the basic Hebb rule fails to induce competition between different synapses.

Sometimes, we think of the presentation of patterns over discrete rather than continuous time. In this case, the effect of equation 8.5, integrated over a time T while ignoring the weight changes that occur during this period, is approximated by making the replacement

$$\mathbf{w} \rightarrow \mathbf{w} + \frac{T}{\tau_w} \mathbf{Q} \cdot \mathbf{w}. \quad (8.7)$$

The Covariance Rule

If, as in Hebb's original conjecture, u and v are interpreted as representing firing rates (which must be positive), the basic Hebb rule only describes LTP. Experiments, such as the one shown in figure 8.1, indicate that synapses can depress in strength if presynaptic activity is accompanied by a low level of postsynaptic activity. High levels of postsynaptic activity, on the other hand, produce potentiation. These results can be modeled by a synaptic plasticity rule of the form

$$\tau_w \frac{d\mathbf{w}}{dt} = (v - \theta_v) \mathbf{u} \quad (8.8)$$

where θ_v is a threshold that determines the level of postsynaptic activity above which LTD switches to LTP. As an alternative to equation 8.8, we can impose the threshold on the input rather than output activity and write

$$\tau_w \frac{d\mathbf{w}}{dt} = v(\mathbf{u} - \boldsymbol{\theta}_u). \quad (8.9)$$

Here $\boldsymbol{\theta}_u$ is a vector of thresholds that determines the levels of presynaptic activities above which LTD switches to LTP. It is also possible to combine these two rules by subtracting thresholds from both the \mathbf{u} and v terms, but

θ_v postsynaptic
threshold

$\boldsymbol{\theta}_u$ presynaptic
threshold

this has the undesirable feature of predicting LTP when pre- and postsynaptic activity levels are both low.

A convenient choice for the thresholds is the average value of the corresponding variable over the training period. In other words, we set the threshold in equation 8.8 to the average postsynaptic activity, $\theta_v = \langle v \rangle$, or the threshold vector in equation 8.9 to the average presynaptic activity vector, $\theta_u = \langle u \rangle$. As we did for equation 8.5, we use the relation $v = w \cdot u$ and average over training inputs to obtain an averaged form of the plasticity rule. When the thresholds are set to their corresponding activity averages, equations 8.8 and 8.9 both produce the same averaged rule,

C input covariance matrix

covariance rules

$$\tau_w \frac{dw}{dt} = C \cdot w \quad (8.10)$$

where C is the input covariance matrix,

$$C = \langle (u - \langle u \rangle)(u - \langle u \rangle)^T \rangle = \langle uu^T \rangle - \langle u \rangle \langle u^T \rangle = \langle (u - \langle u \rangle)u^T \rangle. \quad (8.11)$$

Because of the presence of the covariance matrix in equation 8.10, equations 8.8 and 8.9 are known as covariance rules.

Although they both average to give equation 8.10, the rules in equations 8.8 and 8.9 have their differences. Equation 8.8 only modifies synapses with nonzero presynaptic activities. When $v < \theta_v$, this produces an effect called homosynaptic depression. In contrast, equation 8.9 reduces the strengths of inactive synapses if $v > 0$. This is called heterosynaptic depression. Note that the threshold in equation 8.8 must change as the weights are modified to keep $\theta_v = \langle v \rangle$, whereas the threshold in equation 8.9 is independent of the weights and does not need to change during the training period to keep $\theta_u = \langle u \rangle$.

Even though covariance rules include LTD, allowing weights to decrease, they are unstable because of the same positive feedback that makes the basic Hebb rule unstable. For either rule 8.8 with $\theta_v = \langle v \rangle$ or rule 8.9 with $\theta_u = \langle u \rangle$, $d|w|^2/dt = 2v(v - \langle v \rangle)$. The time average of the right side of this equation is proportional to the variance of the output, $\langle v^2 \rangle - \langle v \rangle^2$, which is positive except in the trivial case when v is constant. The covariance rules, like the Hebb rule, are non-competitive, but competition can be introduced by allowing the thresholds to slide, as described below.

The BCM Rule

The covariance-based rule of equation 8.8 does not require any postsynaptic activity to produce LTD, and rule 8.9 can produce LTD without presynaptic activity. Bienenstock, Cooper and Munro (1982), suggested an alternative plasticity rule, for which there is experimental evidence, that requires both pre- and postsynaptic activity to change a synaptic weight. This rule, which is called the BCM rule, takes the form

BCM rule

$$\tau_w \frac{d\mathbf{w}}{dt} = v\mathbf{u} (v - \theta_v) . \quad (8.12)$$

As in equation 8.8, θ_v acts as a threshold on the postsynaptic activity that determines whether synapses are strengthened or weakened.

If the threshold θ_v is held fixed, the BCM rule, like the basic Hebbian rule, is unstable. Synaptic modification can be stabilized against unbounded growth by allowing the threshold to vary. The critical condition for stability is that θ_v must grow more rapidly than v if the output activity grows large. In one instantiation of the BCM rule with a sliding threshold, θ_v follows v^2 according to the equation

$$\tau_\theta \frac{d\theta_v}{dt} = v^2 - \theta_v \quad (8.13)$$

sliding threshold

where τ_θ sets the time scale for modification of the threshold. This is usually slower than the presentation of individual presynaptic patterns, but faster than the rate at which the weights change, which is determined by τ_w . With a sliding threshold, the BCM rule implements competition between synapses because strengthening some synapses increases the postsynaptic firing rate, which raises the threshold and makes it more difficult for other synapses to be strengthened or even to remain at their current strengths.

Synaptic Normalization

The BCM rule stabilizes Hebbian plasticity by means of a sliding threshold that reduces synaptic weights if the postsynaptic neuron becomes too active. This amounts to using the postsynaptic activity as an indicator of the strengths of synaptic weights. A more direct way to stabilize a Hebbian plasticity rule is to add terms that depend explicitly on the weights. This typically leads to some form of weight normalization, the idea that postsynaptic neurons can only support a fixed total synaptic weight, so increases in some weights must be accompanied by decreases in others.

Normalization of synaptic weights involves imposing some sort of global constraint. Two types of constraints are typically used. If the synaptic weights are non-negative, their growth can be limited by holding the sum of all the weights of the synapses onto a given postsynaptic neuron to a constant value. An alternative, which also works for weights that can be either positive or negative, is to constrain the sum of the squares of the weights instead of their linear sum. In either case, the constraint can be imposed either rigidly, requiring that it be satisfied at all times during a training process, or dynamically, only requiring that it be satisfied asymptotically at the end of training. We discuss one example of each type; a rigid scheme for imposing a constraint on the sum of synaptic weights and a dynamic scheme for constraining the sum over their squares. Dynamic constraints can be applied in the former case and rigid constraints in the

latter, but we restrict our discussion to two widely used schemes. We discuss synaptic normalization in connection with the basic Hebb rule, but the results we present can be applied to covariance rules as well. Weight normalization can drastically alter the outcome of a training procedure, and different normalization methods may lead to different outcomes.

Subtractive Normalization

The sum over synaptic weights that is constrained by subtractive normalization can be written as $\sum w_b = \mathbf{n} \cdot \mathbf{w}$ where \mathbf{n} is an N_u -dimensional vector with all its components equal to one (as introduced in chapter 7). This sum can be constrained by replacing equation 8.3 with

$$\tau_w \frac{d\mathbf{w}}{dt} = v\mathbf{u} - \frac{v(\mathbf{n} \cdot \mathbf{u})\mathbf{n}}{N_u} \quad (8.14)$$

This rule imposes what is called subtractive normalization because the same quantity is subtracted from the change to each weight whether that weight is large or small. Subtractive normalization imposes the constraint on the sum of weights rigidly because it does not allow the Hebbian term to change $\mathbf{n} \cdot \mathbf{w}$. To see this, we take the dot product of equation 8.14 with \mathbf{n} to obtain

$$\tau_w \frac{d(\mathbf{n} \cdot \mathbf{w})}{dt} = v\mathbf{n} \cdot \mathbf{u} \left(1 - \frac{\mathbf{n} \cdot \mathbf{n}}{N_u} \right) = 0. \quad (8.15)$$

The last equality follows because $\mathbf{n} \cdot \mathbf{n} = N_u$. Hebbian modification with subtractive normalization is non-local in that it requires the value of the sum of all weights, $\mathbf{n} \cdot \mathbf{w}$ to be available to the mechanism that modifies any particular synapse. This scheme could conceivably be implemented by some form of intracellular signaling system.

Subtractive normalization must be augmented by a saturation constraint that prevents weights from becoming negative. If the rule 8.14 attempts to drive any of the weights below zero, the saturation constraint prevents this change. At this point, the rule is not applied to any saturated weights, and its effect on the other weights is modified. Both modifications can be achieved by setting the components of the vector \mathbf{n} corresponding to any saturated weights to zero and the factor of N_u in equation 8.14 equal to the sum of the components of this modified \mathbf{n} vector. Without any upper saturation limit, this procedure often results in a final outcome in which all weights but one have been set to zero. To avoid this, an upper saturation limit is also typically imposed. Hebbian plasticity with subtractive normalization is highly competitive because small weights are reduced by a larger proportion of their sizes than large weights.

*Hebb rule with
subtractive
normalization*

Multiplicative Normalization and the Oja Rule

A constraint on the sum of the squares of the synaptic weights can be imposed dynamically using a modification of the basic Hebb rule known as the Oja rule (Oja, 1982),

$$\tau_w \frac{d\mathbf{w}}{dt} = v\mathbf{u} - \alpha v^2 \mathbf{w} \quad (8.16)$$

where α is a positive constant. This rule only involves information that is local to the synapse being modified, namely the pre- and postsynaptic activities and the local synaptic weight, but its form is based more on theoretical arguments than on experimental data. The normalization it imposes is called multiplicative because the amount of modification induced by the second term in equation 8.16 is proportional to \mathbf{w} .

The stability of the Oja rule can be established by repeating the analysis of changes in length of the weight vector presented above to find that

$$\tau_w \frac{d|\mathbf{w}|^2}{dt} = 2v^2(1 - \alpha|\mathbf{w}|^2). \quad (8.17)$$

This indicates that $|\mathbf{w}|^2$ will relax over time to the value $1/\alpha$, which obviously prevents the weights from growing without bound, proving stability. It also induces competition between the different weights because, when one weight increases, the maintenance of a constant length for the weight vector forces other weights to decrease.

Timing-Based Rules

Experiments have shown that the relative timing of pre- and postsynaptic action potentials plays a critical role in determining the sign and amplitude of the changes in synaptic efficacy produced by activity. Figure 8.2 shows examples from an intracellular recording of a pair of cortical pyramidal cells in a slice experiment, and from an *in vivo* experiment on retinotectal synapses in a *Xenopus* tadpole. Both experiments involve repeated pairing of pre- and postsynaptic action potentials, and both show that the relative timing of these spikes is critical in determining the amount and type of synaptic modification that takes place. Synaptic plasticity only occurs if the difference in the pre- and postsynaptic spike times falls within a window of roughly ± 50 ms. Within this window, the sign of the synaptic modification depends on the order of stimulation. Presynaptic spikes that precede postsynaptic action potentials produce LTP. Presynaptic spikes that follow postsynaptic action potentials produce LTD. This is in accord with Hebb's original conjecture, because a synapse is strengthened only when a presynaptic action potential precedes a postsynaptic action potential and can therefore be interpreted as contributing to it. When the order is reversed and the presynaptic action potential could not have contributed

Oja rule

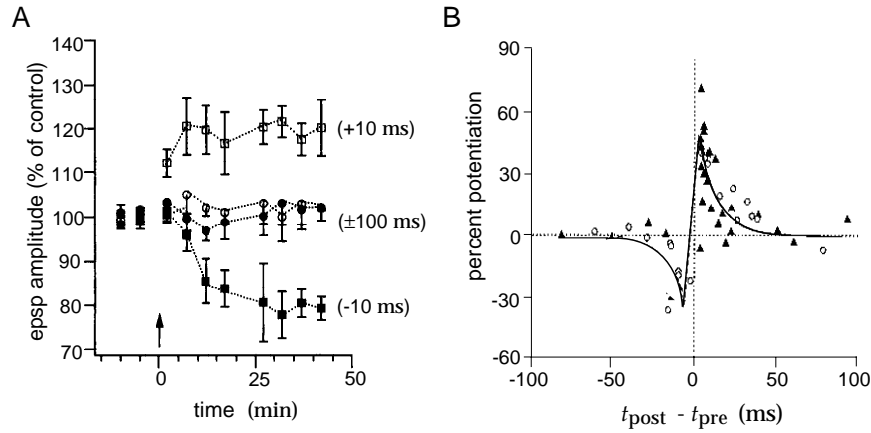


Figure 8.2: LTP and LTD produced by paired action potentials with various timings. A) The amplitude of excitatory postsynaptic potentials evoked by stimulation of the presynaptic neuron plotted as a percentage of the amplitude prior to paired stimulation. At the time indicated by the arrow, 50 to 75 paired stimulations of the presynaptic and postsynaptic neurons were performed. For the traces marked by open symbols, the presynaptic spike occurred either 10 or 100 ms before the postsynaptic neuron fired an action potential. The traces marked by solid symbols denote the reverse ordering in which the presynaptic spike occurred either 10 or 100 ms after the postsynaptic spike. Separations of 100 ms had no long-lasting effect. In contrast, the 10 ms delays produced effects that built up to a maximum over a 10 to 20 minute period and lasted for the duration of the experiment. Pairing a presynaptic action potential with a postsynaptic action potential 10 ms later produced LTP, while the reverse ordering generated LTD. B) LTP and LTD of retinotectal synapses recorded *in vivo* in *Xenopus* tadpoles. The percent change in synaptic strength produced by multiple pairs of action potentials is plotted as a function of their time difference. The filled symbols correspond to extracellular stimulation of the postsynaptic neuron and the open symbols to intracellular stimulation. The H function in equation 8.18 is proportional to the solid curve. (A adapted from Markram et al., 1997; B adapted from Zhang et al., 1998.)

to the postsynaptic response, the synapse is weakened. The maximum amount of synaptic modification occurs when the paired spikes are separated by only a few ms, and the evoked plasticity decreases to zero as this separation increases.

Simulating the spike-timing dependence of synaptic plasticity requires a spiking model. However, an approximate model can be constructed on the basis of firing rates. The effect of pre- and postsynaptic timing can be included in a synaptic modification rule by including a temporal difference τ between the times when the firing rates of the pre- and postsynaptic neurons are evaluated. A function $H(\tau)$ determines the rate of synaptic modification that occurs due to postsynaptic activity separated in time from presynaptic activity by an interval τ . The total rate of synaptic modification is determined by integrating over all time differences τ . If we assume that the rate of synaptic modification is proportional to the product of the

pre- and postsynaptic rates, as it is for a Hebbian rule, the rate of change of the synaptic weights at time t is given by

$$\tau_w \frac{d\mathbf{w}}{dt} = \int_0^\infty d\tau (H(\tau)v(t)\mathbf{u}(t-\tau) + H(-\tau)v(t-\tau)\mathbf{u}(t)) . \quad (8.18)$$

If $H(\tau)$ is positive for positive τ and negative for negative τ , the first term on the right side of this equation represents LTP and the second LTD. The solid curve in figure 8.2B is an example of such an H function. The temporal asymmetry of H has a dramatic effect on synaptic weight changes because it causes them to depend on the temporal order of the activity during training. Among other things, this allows synaptic weights to store information about temporal sequences.

Rules in which synaptic plasticity is based on the relative timing of pre- and postsynaptic action potentials still require saturation constraints for stability, but they can generate competition between synapses without further constraints or modifications, at least in nonlinear, spike-based models. This is because different synapses compete for control of the timing of postsynaptic spikes. Synapses that are able to evoke postsynaptic spikes rapidly get strengthened. These synapses then exert a more powerful influence on the timing of postsynaptic spikes, and they tend to generate spikes at times that lead to the weakening of other synapses less capable of controlling spike timing.

timing-based rule

8.3 Unsupervised Learning

We now consider the computational properties of the different synaptic modification rules we have introduced, in the context of unsupervised learning. Unsupervised learning provides a model for the effects of activity on developing neural circuits and the effects of experience on mature networks. We separate the discussion of unsupervised learning into cases involving a single postsynaptic neuron and cases in which there are multiple postsynaptic neurons.

Single Postsynaptic Neuron

Equation 8.5, which shows the consequence of averaging the basic Hebb rule over all the presynaptic training patterns, is a linear equation for \mathbf{w} . Provided that we ignore any constraints on \mathbf{w} , it can be analyzed using standard techniques for solving differential equations (see chapter 7 and the Mathematical Appendix). In particular, we use the method of matrix diagonalization, which involves expressing \mathbf{w} in terms of the eigenvectors of \mathbf{Q} . These are denoted by \mathbf{e}_μ with $\mu = 1, 2, \dots, N_u$, and they satisfy $\mathbf{Q} \cdot \mathbf{e}_\mu = \lambda_\mu \mathbf{e}_\mu$. For correlation or covariance matrices, all the eigenvalues,

λ_μ for all μ , are real and non-negative, and, for convenience, we order them so that $\lambda_1 \geq \lambda_2 \geq \dots \geq \lambda_{N_u}$.

Any N_u -dimensional vector can be represented using the eigenvectors as a basis, so we can write

$$\mathbf{w}(t) = \sum_{\mu=1}^{N_u} c_\mu(t) \mathbf{e}_\mu \quad (8.19)$$

where the coefficients are equal to the dot products of the eigenvectors with \mathbf{w} . For example, at time zero $c_\mu(0) = \mathbf{w}(0) \cdot \mathbf{e}_\mu$. Writing \mathbf{w} as a sum of eigenvectors turns matrix multiplication into ordinary multiplication, making calculations easier. Substituting the expansion 8.19 into 8.5 and following the procedure presented in chapter 7 for isolating uncoupled equations for the coefficients, we find that $c_\mu(t) = c_\mu(0) \exp(\lambda_\mu t / \tau_w)$. Going back to equation 8.19, this means that

$$\mathbf{w}(t) = \sum_{\mu=1}^{N_u} \exp\left(\frac{\lambda_\mu t}{\tau_w}\right) (\mathbf{w}(0) \cdot \mathbf{e}_\mu) \mathbf{e}_\mu. \quad (8.20)$$

The exponential factors in 8.20 all grow over time, because the eigenvalues λ_μ are positive for all μ values. For large t , the term with the largest value of λ_μ (assuming it is unique) becomes much larger than any of the other terms and dominates the sum for \mathbf{w} . This largest eigenvalue has the label $\mu = 1$, and its corresponding eigenvector \mathbf{e}_1 is called the principal eigenvector. Thus, for large t , $\mathbf{w} \propto \mathbf{e}_1$ to a good approximation, provided that $\mathbf{w}(0) \cdot \mathbf{e}_1 \neq 0$. After training, the response to an arbitrary input vector \mathbf{u} is well-approximated by

$$v \propto \mathbf{e}_1 \cdot \mathbf{u}. \quad (8.21)$$

Because the dot product corresponds to a projection of one vector onto another, Hebbian plasticity can be interpreted as producing an output proportional to the projection of the input vector onto the principal eigenvector of the correlation matrix of the inputs used during training. We discuss the significance of this result in the next section.

The proportionality sign in equation 8.21 hides the large factor $\exp(\lambda_1 t / \tau_w)$, which is a result of the positive feedback inherent in Hebbian plasticity. One way to limit growth of the weight vector in equation 8.5 is to impose a saturation constraint. This can have significant effects on the outcome of Hebbian modification, including, in some cases, preventing the weight vector from ending up proportional to the principal eigenvector. Figure 8.3 shows examples of the Hebbian development of the weights in a case with just two inputs. For the correlation matrix used in this example, the principal eigenvector is $\mathbf{e}_1 = (1, -1)/\sqrt{2}$, so an analysis that ignored saturation would predict that one weight would increase while the other decreases. Which weight moves in which direction is controlled by the initial conditions. Given the constraints, this would suggest that

principal
eigenvector

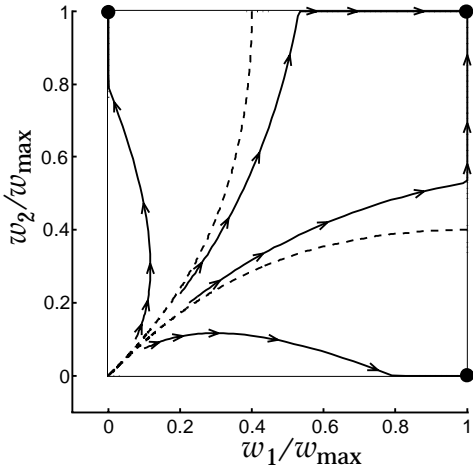


Figure 8.3: Hebbian weight dynamics with saturation. The correlation matrix of the input vectors had diagonal elements equal to 1 and off-diagonal elements of -0.4. The principal eigenvector, $\mathbf{e}_1 = (1, -1)/\sqrt{2}$, dominates the dynamics if the initial values of the weights are small enough (below and to the left of the dashed lines). This makes the weight vector move to the corners ($w_{\max}, 0$) or $(0, w_{\max})$. However, starting the weights with larger values (between the dashed lines) allows saturation to occur at the corner (w_{\max}, w_{\max}) . (Adapted from MacKay and Miller, 1990.)

$(w_{\max}, 0)$ and $(0, w_{\max})$ are the most likely final configurations. This analysis only gives the correct answer for the regions in figure 8.3 below or to the left of the dashed lines. Between the dashed lines, the final state is $\mathbf{w} = (w_{\max}, w_{\max})$ because the weights hit the saturation boundary before the exponential growth is large enough to allow the principal eigenvector to dominate.

Another way to eliminate the large exponential factor in the weights is to use the Oja rule, 8.16, instead of the basic Hebb rule. The weight vector generated by the Oja rule, in the example we have discussed, approaches $\mathbf{w} = \mathbf{e}_1 / (\alpha)^{1/2}$ as $t \rightarrow \infty$. In other words, the Oja rule gives a weight vector that is parallel to the principal eigenvector, but normalized to a length of $1/(\alpha)^{1/2}$ rather than growing without bound.

Finally, we examine the effect of including a subtractive constraint, as in equation 8.14. Averaging equation 8.14 over the training inputs, we find

$$\tau_w \frac{d\mathbf{w}}{dt} = \mathbf{Q} \cdot \mathbf{w} - \frac{(\mathbf{w} \cdot \mathbf{Q} \cdot \mathbf{n})\mathbf{n}}{N_u}. \quad (8.22)$$

averaged Hebb rule with subtractive constraint

If we once again express \mathbf{w} as a sum of eigenvectors of \mathbf{Q} , we find that the growth of each coefficient in this sum is unaffected by the extra term in equation 8.22 provided that $\mathbf{e}_\mu \cdot \mathbf{n} = 0$. However, if $\mathbf{e}_\mu \cdot \mathbf{n} \neq 0$, the extra term modifies the growth. In our discussion of ocular dominance, we consider a case in which the principal eigenvector of the correlation matrix is

proportional to \mathbf{n} . In this case, $\mathbf{Q} \cdot \mathbf{e}_1 - (\mathbf{e}_1 \cdot \mathbf{Q} \cdot \mathbf{n})\mathbf{n}/N = 0$ so the projection in the direction of the principal eigenvector is unaffected by the synaptic plasticity rule. Further, $\mathbf{e}_\mu \cdot \mathbf{n} = 0$ for $\mu \geq 2$ because the eigenvectors of the correlation matrix are mutually orthogonal, which implies that the evolution of the remaining eigenvectors is unaffected by the constraint. As a result,

$$\mathbf{w}(t) = (\mathbf{w}(0) \cdot \mathbf{e}_1) \mathbf{e}_1 + \sum_{\mu=2}^{N_u} \exp\left(\frac{\lambda_\mu t}{\tau_w}\right) (\mathbf{w}(0) \cdot \mathbf{e}_\mu) \mathbf{e}_\mu. \quad (8.23)$$

Thus, ignoring the effects of any saturation constraints, the synaptic weight matrix tends to become parallel to the eigenvector with the second largest eigenvalue as $t \rightarrow \infty$.

In summary, if weight growth is limited by some form of multiplicative normalization, as in the Oja rule, the configuration of synaptic weights produced by Hebbian modification will typically be proportional to the principal eigenvector of the input correlation matrix. When subtractive normalization is used and the principal eigenvector is proportional to \mathbf{n} , the eigenvector with the next largest eigenvalue provides an estimate of the configuration of final weights, again up to a proportionality factor. If, however, saturation constraints are used, as they must be in a subtractive scheme, this can invalidate the results of a simplified analysis based solely on these eigenvectors (as in figure 8.3). Nevertheless, we base our analysis of the Hebbian development of ocular dominance, and cortical maps in a later section on an analysis of the eigenvectors of the input correlation matrix. We present simulation results to verify that this analysis is not invalidated by the constraints imposed in the full models.

Principal Component Projection

If applied for a long enough time, both the basic Hebb rule (equation 8.3) and the Oja rule (equation 8.16) generate weight vectors that are parallel to the principal eigenvector of the correlation matrix of the inputs used during training. Figure 8.4A provides a geometric picture of the significance of this result. In this example, the basic Hebb rule was applied to a unit described by equation 8.2 with two inputs ($N_u = 2$). The constraint of positive u and v has been dropped to simplify the discussion. The inputs used during the training period were chosen from a two-dimensional Gaussian distribution with unequal variances, resulting in the elliptical distribution of points seen in the figure. The initial weight vector $\mathbf{w}(0)$ was chosen randomly. The two-dimensional weight vector produced by a Hebbian rule is proportional to the principal eigenvector of the input correlation matrix. The line in figure 8.4A indicates the direction along which the final \mathbf{w} lies, with the u_1 and u_2 axes used to represent w_1 and w_2 as well. The weight vector points in the direction along which the cloud of input points has the largest variance, a result with interesting implications.

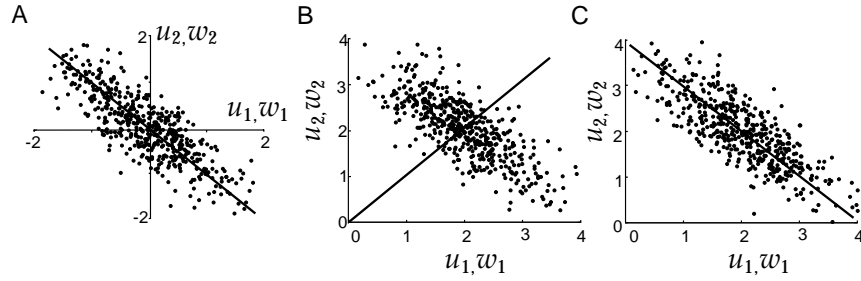


Figure 8.4: Unsupervised Hebbian learning and principal component analysis. The axes in these figures are used to represent the components of both \mathbf{u} and \mathbf{w} . A) The filled circles show the inputs $\mathbf{u} = (u_1, u_2)$ used during a training period while a Hebbian plasticity rule was applied. After training, the vector of synaptic weights was aligned parallel to the solid line. B) Correlation-based modification with non-zero mean input. Input vectors were generated as in A except that the distribution was shifted to produce an average value $\langle \mathbf{u} \rangle = (2, 2)$. After a training period during which a Hebbian plasticity rule was applied, the synaptic weight vector was aligned parallel to the solid line. C) Covariance-based modification. Points from the same distribution as in B were used while a covariance-based Hebbian rule was applied. The weight vector becomes aligned with the solid line.

Any unit that obeys equation 8.2 characterizes the state of its N_u inputs by a single number v , which is proportional to the projection of \mathbf{u} onto the weight vector \mathbf{w} . Intuition suggests, and a technique known as principal component analysis (PCA) formalizes, that this projection is often the optimal choice if a set of vectors is to be represented by, and reconstructed from, a set of single numbers. An information theoretic interpretation of this projection direction is also possible. The entropy of a Gaussian distributed random variable with variance σ^2 grows with increasing variance as $\log_2 \sigma$. If the input statistics and output noise are Gaussian, maximizing the variance of v by a Hebbian rule thus maximizes the amount of information v carries about \mathbf{u} . In chapter 10, we further consider the computational significance of finding the direction of maximum variance in the input data set, and we discuss the relationship between this and general techniques for extracting structure from input statistics.

PCA principal component analysis

Figure 8.4B shows the consequence of applying correlational Hebbian plasticity when the average activities of the inputs are not zero, as is inevitable if real firing rates are employed. In this example, correlation-based Hebbian modification aligns the weight vector parallel to a line from the origin to the point $\langle \mathbf{u} \rangle$. This clearly fails to capture the essence of the distribution of inputs. Figure 8.4C shows the result of applying a covariance-based Hebbian modification instead. Now the weight vector is aligned with the cloud of data points because this rule finds the direction of the principal eigenvector of the covariance matrix \mathbf{C} of equation 8.11 rather the correlation matrix \mathbf{Q} .

Hebbian Development of Ocular Dominance

The input to neurons in the adult primary visual cortex of many mammalian species tends to favor one eye over the other, a phenomenon known as ocular dominance. This is especially true for neurons in layer 4, which receives extensive innervation from the LGN. Neurons dominated by one eye or the other occupy different patches of cortex, and areas with left- or right-eye ocular dominance alternate across the cortex in fairly regular bands, forming a cortical map. The patterns of connections that give rise to neuronal selectivities and cortical maps are established during development by both activity-independent and activity-dependent processes. A conventional view is that activity-independent mechanisms control the initial targeting of axons, determine the appropriate layer for them to innervate, and establish a coarse topographic order in their projections. Other activity-independent and activity-dependent mechanisms then refine this order and help to create and preserve neuronal selectivities and cortical maps. Although the relative roles of activity-independent and activity-dependent processes in cortical development are the subject of extensive debate, developmental models based on activity-dependent plasticity rules have played an important role in suggesting key experiments and successfully predicting their outcomes. A detailed analysis of the more complex pattern-forming models that have been proposed is beyond the scope of this book. Instead, in this and later sections, we give a brief overview of the different approaches and results that have been obtained.

As an example of a developmental model of ocular dominance at the single neuron level, we consider the highly simplified case of a layer 4 cell that receives input from just two LGN afferents. One afferent is associated with the right eye and has activity u_R , and the other is from the left eye with activity u_L . Two synaptic weights $w = (w_R, w_L)$ describe the strengths of these projections, and the output activity v is determined by equation 8.2,

$$v = w_R u_R + w_L u_L. \quad (8.24)$$

The weights in this model are constrained to non-negative values. Initially, the weights for the right- and left-eye inputs are set to approximately equal values. Ocular dominance arises when one of the weights is pushed to zero while the other remains positive.

We can estimate the results of a Hebbian developmental process by considering the input correlation matrix. We assume that the two eyes are equivalent, so the correlation matrix of the right- and left-eye inputs takes the form

$$\mathbf{Q} = \langle \mathbf{u} \mathbf{u} \rangle = \begin{pmatrix} \langle u_R u_R \rangle & \langle u_R u_L \rangle \\ \langle u_L u_R \rangle & \langle u_L u_L \rangle \end{pmatrix} = \begin{pmatrix} q_S & q_D \\ q_D & q_S \end{pmatrix}. \quad (8.25)$$

The subscripts S and D denote same- and different-eye correlations. The

eigenvectors are $\mathbf{e}_1 = (1, 1)/\sqrt{2}$ and $\mathbf{e}_2 = (1, -1)/\sqrt{2}$ for this correlation matrix, and their eigenvalues are $\lambda_1 = q_S + q_D$ and $\lambda_2 = q_S - q_D$.

If the right- and left-eye weights evolve according to equation 8.5, it is straightforward to show that the eigenvector combinations $w_+ = w_R + w_L$ and $w_- = w_R - w_L$ obey the uncoupled equations

$$\tau_w \frac{dw_+}{dt} = (q_S + q_D)w_+ \quad \text{and} \quad \tau_w \frac{dw_-}{dt} = (q_S - q_D)w_- . \quad (8.26)$$

Positive correlations between the two eyes are likely to exist ($q_D > 0$) after eye opening has occurred. This means that $q_S + q_D > q_S - q_D$, so, according to equations 8.26, w_+ grows more rapidly than w_- . Equivalently, $\mathbf{e}_1 = (1, 1)/\sqrt{2}$ is the principal eigenvector. The basic Hebbian rule thus predicts a final weight vector proportional to \mathbf{e}_1 , which implies equal innervation from both eyes. This is not the observed outcome.

Figure 8.3 suggests that, for some initial weight configurations, saturation could ensure that the final configuration of weights is $(w_{\max}, 0)$ or $(0, w_{\max})$, reflecting ocular dominance, rather than (w_{\max}, w_{\max}) as the eigenvector analysis would suggest. However, this result would require the initial weights to be substantially unequal. To obtain a more robust prediction of ocular dominance, we can use the Hebbian rule with subtractive normalization, equation 8.14. This completely eliminates the growth of the weight vector in the direction of \mathbf{e}_1 (i.e. the increase of w_+) because, in this case, \mathbf{e}_1 is proportional to \mathbf{n} . On the other hand, it has no effect on growth in the direction \mathbf{e}_2 (i.e. the growth of w_-) because $\mathbf{e}_2 \cdot \mathbf{n} = 0$. Thus, with subtractive normalization, the weight vector grows parallel (or anti-parallel) to the direction $\mathbf{e}_2 = (1, -1)/\sqrt{2}$. The direction of this growth depends on initial conditions through the value of $\mathbf{w}(0) \cdot \mathbf{e}_2 = (w_R(0) - w_L(0))/\sqrt{2}$. If this is positive, w_R will increase and w_L will decrease, and if it is negative w_L will increase and w_R will decrease. Eventually, the decreasing weight will hit the saturation limit of zero, and the other weight will stop increasing due to the normalization constraint. At this point, total dominance by one eye or the other has been achieved. This simple model shows that ocular dominance can arise from Hebbian plasticity if there is sufficient competition between the growth of the left- and right-eye weights.

Hebbian Development of Orientation Selectivity

Hebbian models can also account for the development of the orientation selectivity displayed by neurons in primary visual cortex. The model of Hubel and Wiesel for generating an orientation-selective simple cell response by summing linear arrays of alternating ON and OFF LGN inputs was presented in chapter 2. The necessary pattern of LGN inputs can arise from Hebbian plasticity on the basis of correlations between the responses of different LGN cells and competition between ON and OFF units. Such

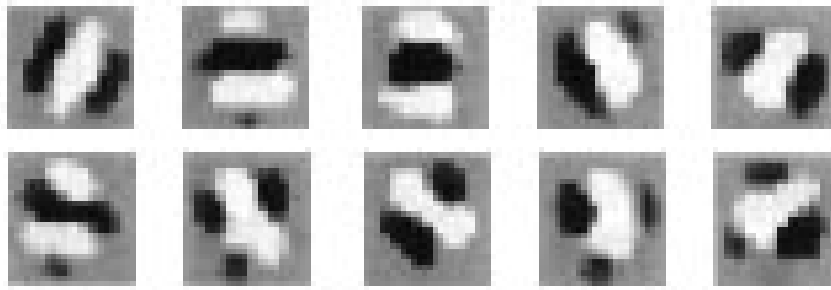


Figure 8.5: Different cortical receptive fields arising from a correlation-based developmental model. White and black regions correspond to areas in the visual field where ON-center cells (white regions) or OFF-center (black regions) LGN cells excite the cortical neuron being modeled. (Adapted from Miller, 1994.)

a model can be constructed by considering a simple cell receiving input from ON-center and OFF-center cells of the LGN and applying Hebbian plasticity, subject to appropriate constraints, to the feedforward weights of the model.

As in the case of ocular dominance, the development of orientation selectivity can be analyzed on the basis of properties of the correlation matrix driving Hebbian development. However, constraints must be taken into account and, in this case, the nonlinearities introduced by the constraints play a significant role. For this reason, we do not analyze this model mathematically, but simply present simulation results.

Neurons in primary visual cortex only receive afferents from LGN cells centered over a finite region of the visual space. This anatomical constraint can be included in developmental models by introducing what is called an arbor function. The arbor function, which is often taken to be Gaussian, characterizes the density of innervation from different visual locations to the cell being modeled. As a simplification, this density is not altered during the Hebbian developmental process, but that the strengths of synapses within the arbor are modified by the Hebbian rule. The outcome is oriented receptive fields of a limited spatial extent. Figure 8.5 shows the weights resulting from a simulation of receptive-field development using a large array of ON- and OFF-center LGN afferents. This illustrates a variety of oriented receptive field structures that can arise through a Hebbian developmental rule.

Temporal Hebbian Rules and Trace Learning

arbor function

trace learning

Temporal Hebbian rules exhibit a phenomenon called trace learning, because the changes to a synapse depend on a history or trace of the past activity across the synapse. Integrating equation 8.18 from $t = 0$ to a large final time $t = T$, assuming that $w = 0$ initially, and shifting the integration

variable, we can approximate the final result of this temporal plasticity rule as

$$\mathbf{w} = \frac{1}{\tau_w} \int_0^T dt v(t) \int_{-\infty}^{\infty} d\tau H(\tau) \mathbf{u}(t - \tau). \quad (8.27)$$

The approximation comes from ignoring both small contributions associated with the end points of the integral and the change in v produced during training by the modification of w . Equation 8.27 shows that temporally dependent Hebbian plasticity depends on the correlation between the postsynaptic activity and the presynaptic activity temporally filtered by the function H .

Equation 8.27 (with a suitably chosen H) can be used to model the development of invariant responses. Neurons in infero-temporal cortex, for example, can respond selectively to particular objects independent of their location within a wide receptive field. The idea underlying the application of equation 8.27 is that objects persist in the visual environment for characteristic lengths of time, while moving across the retina. If the plasticity rule in equation 8.27 filters presynaptic activity over this characteristic time scale, it tends to strengthen the synapses from the presynaptic units that are active for all the positions adopted by the object while it persists. As a result, the response of the postsynaptic cell comes to be independent of the position of the object, and position-invariant responses are generated.

Multiple Postsynaptic Neurons

To study the effect of plasticity on multiple neurons, we introduce the network of figure 8.6 in which N_v output neurons receive input from N_u feedforward connections and from recurrent interconnections. A vector \mathbf{v} represents the activities of the multiple output units, and the feedforward synaptic connections are described by a matrix \mathbf{W} with the element W_{ab} giving the strength and sign of the synapse from input unit b to output unit a .

\mathbf{W} *feedforward weight matrix*

It is important that different output neurons in a multi-unit network be selective for different aspects of the input, or else their responses will be completely redundant. For the case of a single cell, competition between different synapses could be used to ensure that synapse-specific plasticity rules did not make the same modifications to all of the synapses onto a postsynaptic neuron. For multiple output networks, fixed or plastic linear or nonlinear recurrent interactions can be used to ensure that the units do not all develop the same selectivity.

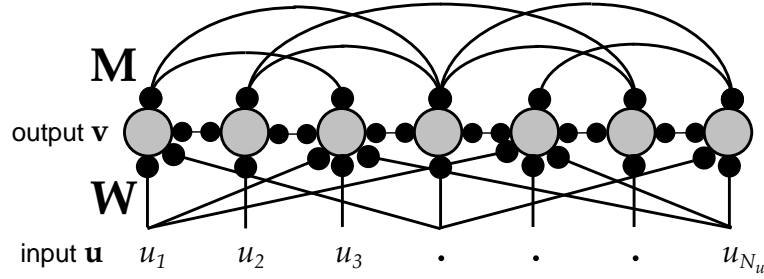


Figure 8.6: A network with multiple output units driven by feedforward synapses with weights W , and interconnected by recurrent synapses with weights M .

Fixed Linear Recurrent Connections

We first consider the case of linear recurrent connections from output cell a' to output cell a described by element $M_{aa'}$ of the matrix M . As in chapter 7, the output activity is determined by

$$\tau_r \frac{dv}{dt} = -v + W \cdot u + M \cdot v. \quad (8.28)$$

The steady-state output activity vector is then

$$v = W \cdot u + M \cdot v. \quad (8.29)$$

Provided that the real parts of the eigenvalues of M are less than 1, equation 8.29 can be solved by defining the matrix inverse $K = (I - M)^{-1}$, where I is the identity matrix, yielding

$$v = K \cdot W \cdot u. \quad (8.30)$$

With fixed recurrent weights M and plastic feedforward weights W , the effect of averaging Hebbian modifications over the training inputs is

$$\tau_w \frac{dW}{dt} = \langle vu \rangle = K \cdot W \cdot Q \quad (8.31)$$

where $Q = \langle uu \rangle$ is the input autocorrelation matrix. Equation 8.31 has the same form as the single unit equation 8.5, except that both K and Q affect the growth of W .

We illustrate the effect of fixed recurrent interactions using a model of the Hebbian development of ocular dominance. In the single-cell version of this model considered in a previous section, the ultimate ocular preference of the output cell depends on the initial conditions of its synaptic weights. A multiple-output version of the model without any recurrent connections would therefore generate a random pattern of selectivities across the cortex if it started with random weights. Figure 8.7B shows that ocular dominance is actually organized in a highly structured cortical map. Such structure can arise in the context of Hebbian development of the feedforward weights if we include a fixed intracortical connection matrix M .

M recurrent weight matrix

K effective recurrent interactions

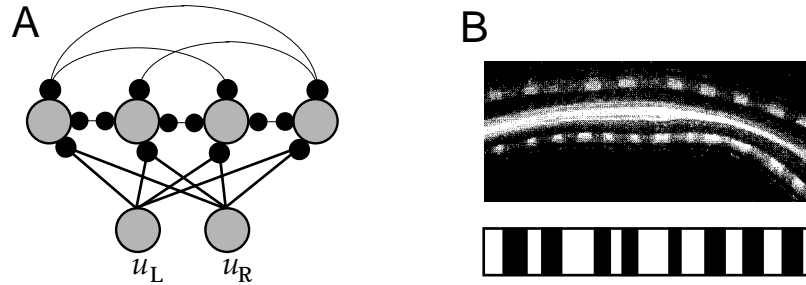


Figure 8.7: The development of ocular dominance in a Hebbian model. A) The simplified model in which right- and left- eye inputs from a single retinal location drive an array of cortical neurons. B) Ocular dominance maps. The upper panel shows an area of cat primary visual cortex radioactively labeled to distinguish regions activated by one eye or the other. The light and dark areas along the cortical regions at the top and bottom indicate alternating right- and left-eye innervation. The central region is white matter where fibers are not segregated by ocular dominance. The lower panel shows the pattern of innervation for a 512 unit model after Hebbian development. White and black regions denote units dominated by right- and left-eye projections respectively. (B data of S LeVay adapted from Nicholls et al. 1992.)

We consider a highly simplified model of the development of ocular dominance maps including only a single direction across the cortex and a single point in the visual field. Figure 8.7A shows the simplified model, which has only two input activities, u_R and u_L , with the correlation matrix of equation 8.25, connected to multiple output units through weight vectors w_R and w_L . The output units are connected to each other through weights M , so $v = w_R u_R + w_L u_L + M \cdot v$. The index a denoting the identity of a given output unit also represents its cortical location. This linking of a to locations and distances across the cortical surface allows us to interpret the results of the model in terms of a cortical map.

Writing $w_+ = w_R + w_L$ and $w_- = w_R - w_L$, the equivalent of equation 8.26 is

$$\tau_w \frac{d\mathbf{w}_+}{dt} = (q_S + q_D) \mathbf{K} \cdot \mathbf{w}_+ \quad \tau_w \frac{d\mathbf{w}_-}{dt} = (q_S - q_D) \mathbf{K} \cdot \mathbf{w}_- \quad (8.32)$$

As in the single-cell case we discussed, subtractive normalization, which holds the value of \mathbf{w}_+ fixed while leaving the growth of \mathbf{w}_- unaffected, eliminates the tendency for the cortical cells to become binocular. In this case, only the equation for \mathbf{w}_- is relevant, and its growth is dominated by the principal eigenvector of \mathbf{K} . The components of \mathbf{w}_- determine whether a particular region of the cortex is dominated by the right eye (if they are positive) or the left eye (if they are negative). Oscillations in sign of the components of this principal eigenvector translate into oscillations in ocular preference across the cortex, also known as ocular dominance stripes.

We assume that the connections between the output neurons are trans-

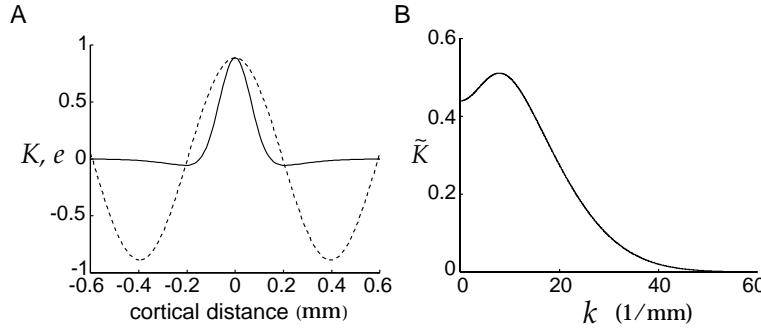


Figure 8.8: Hypothesized K function. A) The solid line is K given by the difference of two Gaussian functions. We have plotted this as a function of the distance between the cortical locations corresponding to the indices a and a' . The dotted line is the principal eigenvector plotted on the same scale. B) The Fourier transform \tilde{K} of K . This is also given by the difference of two Gaussians. As in A, we use cortical distance units and plot \tilde{K} in terms of the spatial frequency k rather than the integer index μ .

lation invariant, so that $K_{aa'} = K(|a - a'|)$ only depends on the separation between the cortical cells a and a' . We also use a convenient trick to remove edge effects, which is to impose periodic boundary conditions, requiring the activities of the units with $a = 0$ and $a = N_v$ to be identical. This means that all the input and output units have equivalent neighbors, a reasonable model of a patch of the cortex away from regional boundaries. Actually, edge effects can impose important constraints on the overall structure of maps such as that of ocular dominance stripes, but we do not analyze this here. In the case of periodic boundary conditions, the eigenvectors of K have the form

$$e_a^\mu = \cos\left(\frac{2\pi\mu a}{N_v} - \phi\right) \quad (8.33)$$

for $\mu = 0, 1, 2, \dots, N_v/2$. The eigenvalues are given by the discrete Fourier transform $\tilde{K}(\mu)$ of $K(|a - a'|)$ (see the Mathematical Appendix). The phase ϕ is arbitrary. The principal eigenvector is the eigenfunction from equation 8.33 with its μ value chosen to maximize the Fourier transform $\tilde{K}(\mu)$, which is real and non-negative in the case we consider. The functions K and \tilde{K} in figure 8.8 are each the difference of two Gaussian functions. \tilde{K} has been plotted as a function of the spatial frequency $k = 2\pi\mu/(N_v d)$, where d is the cortical distance between location a and $a + 1$. The value of μ to be used in equation 8.33, corresponding to the principal eigenvector, is determined by the k value of the maximum of the curve in figure 8.8B.

The oscillations in sign of the principal eigenvector, which is indicated by the dotted line in figure 8.8A, generate an alternating pattern of left- and right-eye innervation resembling the ocular dominance maps seen in primary visual cortex (upper panel figure 8.7B). The lower panel of figure

8.7B shows the result of a simulation of Hebbian development of an ocular dominance map for a one-dimensional line across cortex consisting of 512 units. In this simulation, constraints that limit the growth of synaptic weights have been included, but these do not dramatically alter the conclusions of our analysis.

Competitive Hebbian Learning

Linear recurrent connections can only produce a limited amount of differentiation among network neurons, because they only induce fairly weak competition between output units. As detailed in chapter 7, recurrent connections can lead to much stronger competition if the interactions are nonlinear.

One form of nonlinear competition represents the effect of cortical processing in two somewhat abstract stages. One stage, modeling the effects of long-range inhibition, involves competition among all the cortical cells for feedforward input in a scheme related to that used in chapter 2 for contrast saturation. The second stage, modeling shorter range excitation, involves cooperation in which neurons that receive feedforward input excite their neighbors.

nonlinear competition

In the first stage, the feedforward input for unit a , and that for all the other units, is fed through a nonlinear function to generate a competitive measure of the local excitation generated at location a ,

$$z_a = \frac{(\sum_b W_{ab} u_b)^\delta}{\sum_{a'} (\sum_b W_{a'b} u_b)^\delta}. \quad (8.34)$$

The activities and weights are all assumed to be positive. The parameter δ controls the degree of competition among units. For large δ , only the largest feedforward input survives. The case of $\delta = 1$ is closely related to the linear recurrent connections of the previous section.

In the cooperative stage, the local excitation of equation 8.34 is distributed across the cortex by the recurrent connections, so that the final level of activity in unit a is

$$v_a = \sum_{a'} M_{aa'} z_{a'}. \quad (8.35)$$

This ensures that the localized excitation characterized by z_a is spread across a local neighborhood of the cortex, rather than being concentrated entirely at location a . In this scheme, the recurrent connections are usually purely excitatory and fairly short-range, because the effect of longer range inhibition has been modeled by the competition.

Using the outputs of equation 8.35 in conjunction with a Hebbian rule for the feedforward weights is called competitive Hebbian learning. The com-

competitive Hebbian learning

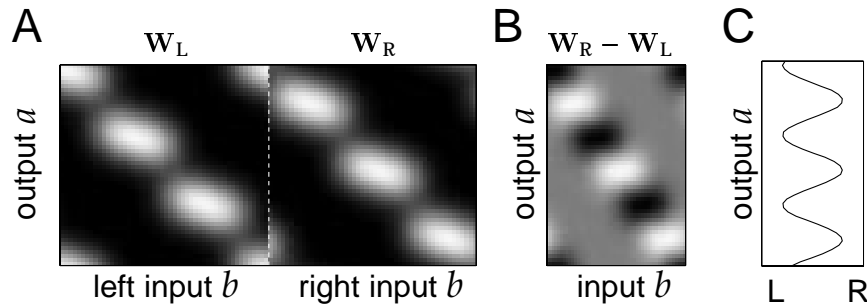


Figure 8.9: Ocular dominance patterns from a competitive Hebbian model. A) Final stable weights W_{ab} plotted as a function of a and b , showing the relative strengths and topography of the connections from left- and right-eye inputs. White represents a large positive value. B) The difference in the connections between right- and left- inputs. C) Difference in the connections summed across all the inputs b to each cortical cell a showing the net ocularity for each cell. The model used here has 100 input units for each eye and for the output layer, and a coarse initial topography was assumed. Circular (toroidal) boundary conditions were imposed to avoid edge effects. The input activity patterns during training represented single Gaussian illuminations in both eyes centered on a randomly chosen input unit b , with a larger magnitude for one eye (chosen randomly) than for the other. The recurrent weights M took the form of a Gaussian.

petition between neurons implemented by this scheme does not ensure competition among the synapses onto a given neuron, so some mechanism such as a normalization constraint is still required. Most importantly, the outcome of training cannot be analyzed simply by considering eigenvectors of the covariance or correlation matrix because the activation process is nonlinear. Rather, higher-order statistics of the input distribution are important. Nonlinear competition can lead to differentiation of the output units and the removal of redundancy beyond the second order.

An example of the use of competitive Hebbian learning is shown in figure 8.9, in the form of a one-dimensional cortical map of ocular dominance with inputs arising from LGN neurons with receptive fields covering an extended region of the visual field (rather than the single location of our simpler model). This example uses competitive Hebbian plasticity with non-dynamic multiplicative weight normalization. Two weight matrices, W_R and W_L , corresponding to right- and left-eye inputs, characterize the connectivity of the model. These are shown separately in figure 8.9A, which illustrates that the cortical cells develop retinotopically ordered receptive fields and segregate into alternating patches dominated by one eye or the other. The ocular dominance pattern is easier to see in figure 8.9B, which shows the difference between the right- and left-eye weights, $W_R - W_L$, and 8.9C which shows the net ocularity of the total input to each output neuron of the model ($\sum_b [W_R - W_L]_{ab}$, for each a). It is possible to analyze the structure shown in figure 8.9 and reveal the precise effect of the competition (i.e. the effect of changing the competition

parameter δ in equation 8.34). Such an analysis shows, for example, that subtractive normalization of the synaptic weight is not necessary to ensure the robust development of ocular dominance as it is in the non-competitive case.

Feature-Based Models

Models of cortical map formation can get extremely complex when multiple neuronal selectivities such as retinotopic location, ocular dominance and orientation preference are considered simultaneously. To deal with this, a class of more abstract models, called competitive feature-based models, has been developed. These use a general approach similar to the competitive Hebbian models discussed in the previous section. These models are further from the biophysical reality of neuronal firing rates and synaptic strengths, but they provide a compact description of map development.

*feature-based
models*

Feature-based models characterize neurons and their inputs by their selectivities rather than by their synaptic weights. The idea, evident from figure 8.9, is that the receptive field of cortical cell a for the weights shown in figure 8.9A (at the end point of development) can be characterized by just two numbers. One, the ocularity, ζ_a , is shown in the right hand plot of figure 8.9C, and is the summed difference of the connections from the left and right eyes to cortical unit a . The other, x_a , is the mean topographic location in the input of cell a . For many developmental models, the stimuli used during training, although involving the activities of a whole set of input units, can also be characterized abstractly using the same small number of feature parameters.

The matrix element W_{ab} in a feature-based model is equal to the variable characterizing the selectivity on neuron a to the feature parameter b . Thus, in a one-dimensional model of topography and ocular dominance, $W_{a1} = x_a$, $W_{a2} = \zeta_a$. Similarly, the inputs are considered in terms of the same feature parameters and are expressed as $\mathbf{u} = (x, \zeta)$. N_u is equal to the number of parameters being used to characterize the stimulus (here, $N_u = 2$). In the case of figure 8.9, the inputs are drawn from a distribution in which x is chosen randomly between 1 and 100, and ζ takes a fixed positive or negative value with equal probability. The description of the model is completed by specifying the feature-based equivalent of how a particular input activates the cortical cells, and how this leads to plasticity in the feature-based weights \mathbf{W} .

The response of a selective neuron depends on how closely the stimulus matches the characteristics of its preferred stimulus. The weights W_{ab} determine the preferred stimulus features, and thus we assume that the activation of neuron a is high if the components of the input u_b match the components of W_{ab} . A convenient way to achieve this is to express the activation for unit a as $\exp(-\sum_b(u_b - W_{ab})^2/(2\sigma_b^2))$, which has its maximum at $u_b = W_{ab}$ for all b , and falls off as a Gaussian function for less perfect matches of the stimulus to the selectivity of the cell. The param-

eter σ_b determines how selective the neuron is to characteristic b of the stimulus.

The Gaussian expression for the activation of neuron a is not used directly to determine its level of activity. Rather, as in the case of competitive Hebbian learning, we introduce a competitive activity variable for cortical site a ,

$$z_a = \frac{\exp(-\sum_b(u_b - W_{ab})^2/(2\sigma_b^2))}{\sum_{a'} \exp(-\sum_b(u_b - W_{a'b})^2/(2\sigma_b^2))}. \quad (8.36)$$

In addition, some cooperative mechanism must be included to keep the maps smooth, which means that nearby neurons should, as far as possible, have similar selectivities. The two algorithms we discuss, the self-organizing map and the elastic net, differ in how they introduce this second element.

self-organizing map

The self-organizing map spreads the activity defined by equation 8.36 to nearby cortical sites through equation 8.35, $v_a = \sum_{a'} M_{aa'} z_{a'}$. This gives cortical cells a and a' similar selectivities if they are nearby, because v_a and $v_{a'}$ are related through local recurrent connections. Hebbian development of the selectivities characterized by W is then generated by an activity dependent rule. In general, Hebbian plasticity adjusts the weights of activated units so that they become more responsive to and selective for the input patterns that excite them. Feature-based models achieve the same thing by modifying the selectivities W_{ab} so they more closely match the input parameters u_b when output unit a is activated by u . In the case of the self-organized map, this is achieved through the averaged rule

feature-based learning rule

$$\tau_w \frac{dW_{ab}}{dt} = \langle v_a(u_b - W_{ab}) \rangle. \quad (8.37)$$

elastic net

The other feature-based algorithm, the elastic net, sets the activity of unit a to the result of equation 8.36, $v_a = z_a$, which generates competition. Smoothness of the map is ensured not by spreading this activity, as in the self-organizing map, but by including an additional term in the plasticity rule that tends to make nearby selectivities the same. The elastic net modification rule is

$$\tau_w \frac{dW_{ab}}{dt} = \langle v_a(u_b - W_{ab}) \rangle + \beta \sum_{a' \text{ neighbor of } a} (W_{a'b} - W_{ab}) \quad (8.38)$$

where the sum is over all points a' that are neighbors of a , and β is a parameter that controls the degree of smoothness in the map. The elastic net makes W_{ab} similar to $W_{a'b}$, if a and a' are nearby on the cortex, by reducing $(W_{a'b} - W_{ab})^2$.

Figure 8.10A shows the results of an optical imaging experiment that reveals how ocularity and orientation selectivity are arranged across a region of the primary visual cortex of a macaque monkey. The dark lines

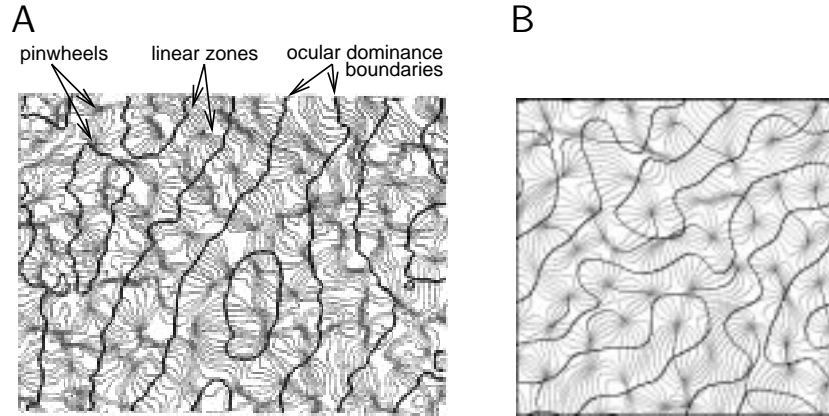


Figure 8.10: Orientation domains and ocular dominance. A) Contour map showing iso-orientation contours (grey lines) and the boundaries of ocular dominance stripes (black lines) in a 1.7×1.7 mm patch of macaque primary visual cortex. Iso-orientation contours are drawn at intervals of 11.25° . Pinwheels are singularities in the orientation map where all the orientations meet, and linear zones are extended patches over which the iso-orientation contours are parallel. B) Ocular dominance and orientation map produced by the elastic net model. The significance of the lines is the same as in A, except that the darker grey lines show orientation preferences of 0° . (A adapted from Obermayer and Blasdel, 1993; B from Erwin et al., 1995.)

show the boundaries of the ocular dominance stripes. The lighter lines show iso-orientation contours, i.e. locations where the preferred orientations are roughly constant and indicate, by the regions they enclose, that neighborhoods of cells favor similar orientations. They also show how these neighborhoods are arranged with respect to each other and with respect to the ocular dominance stripes. There are singularities, called pinwheels, in the orientation map where regions with different orientation preferences meet at a point. These tend to occur near the centers of the ocular dominance stripes. There are also linear zones where the iso-orientation domains run parallel to each other. These tend to occur at, and run perpendicular to, the boundaries of the ocular dominance stripes.

Figure 8.10B shows the result of an elastic net model plotted in the same form as the macaque map of figure 8.10A. The similarity is evident and striking. Here, 5 input feature dimensions were incorporated $\mathbf{u} = (x, y, o, e \cos \theta, e \sin \theta)$, two (x, y) for topographic location, one o for ocularity, and two $(e \cos \theta, e \sin \theta)$ for the direction and strength of orientation. The self-organizing map can produce almost identical results, and non-competitive and competitive Hebbian developmental algorithms can also lead to structures like this.

Anti-Hebbian Modification

We previously alluded to the problem of redundancy among multiple output neurons that can arise from feedforward Hebbian modification. The Oja rule of equation 8.16 for multiple output units, which takes the form

$$\tau_w \frac{dW_{ab}}{dt} = v_a u_b - \alpha v_a^2 W_{ab}, \quad (8.39)$$

provides a good illustration of this problem. In the absence of recurrent connections, this rule sets each row of the feedforward weight matrix to the principal eigenvector of the input correlation matrix, making each output unit respond identically.

*plastic recurrent
synapses
anti-Hebbian
plasticity*

One way to reduce redundancy in a linear model is to make the linear recurrent interactions of equation 8.29 plastic rather than fixed, using an anti-Hebbian modification rule. As the name implies, anti-Hebbian plasticity causes synapses to decrease (rather than increase) in strength when there is simultaneous pre- and postsynaptic activity. The recurrent interactions arising from an anti-Hebbian rule can prevent the output units from representing the same eigenvector. This occurs because the recurrent interactions tend to make the different output units less correlated by canceling the effects of common feedforward input. Anti-Hebbian modification is believed to be the predominant form of plasticity at synapses from parallel fibers to Purkinje cells in the cerebellum, although this may be a special case because Purkinje cells inhibit rather than excite their targets. A basic anti-Hebbian rule for $M_{aa'}$ can be created simply by changing the sign on the right side of equation 8.3. However, just as Hebbian plasticity tends to make weights increase without bound, anti-Hebbian modification tends to make them decrease, and for reasons of stability, it is necessary to use

$$\tau_M \frac{d\mathbf{M}}{dt} = -\mathbf{v}\mathbf{v} + \beta\mathbf{M} \quad \text{or} \quad \tau_M \frac{dM_{aa'}}{dt} = -v_a v_{a'} + \beta M_{aa'} \quad (8.40)$$

to modify the off-diagonal components of \mathbf{M} (the diagonal components are defined to be zero). Here, β is a positive constant. For suitably chosen β and τ_M , the combination of rules 8.39 and 8.40 produces a stable configuration in which the rows of the weight matrix \mathbf{W} are different eigenvectors of the correlation matrix \mathbf{Q} , and all the elements of the recurrent weight matrix \mathbf{M} are zero.

Goodall (1960) proposed an alternative scheme for decorrelating different output units. In his model, the feedforward weights \mathbf{W} are kept constant, while the recurrent weights adapt according to the anti-Hebbian rule

$$\tau_M \frac{d\mathbf{M}}{dt} = -(\mathbf{W} \cdot \mathbf{u})\mathbf{v} + \mathbf{I} - \mathbf{M} \quad (8.41)$$

The minus sign in the term $-(\mathbf{W} \cdot \mathbf{u})\mathbf{v}$ embodies the anti-Hebbian modification. This term is non-local, because the change in the weight of a given

Goodall rule

synapse depends on the total feedforward input to the postsynaptic neuron, not merely on the input at that particular synapse (recall that $v \neq W \cdot u$ in this case because of the recurrent connections). The term $I - M$ prevents the weights from going to zero by forcing them toward the identity matrix I . Unlike 8.40, this rule requires the existence of autapses, synapses that a neuron makes onto itself (i.e. the diagonal elements of M are not zero).

If the Goodall plasticity rule converges and stops changing M , the right side of equation 8.41 must vanish on average, which requires (using the definition of K)

$$\langle (W \cdot u)v \rangle = I - M = K^{-1}. \quad (8.42)$$

Multiplying both sides by K we find, using equation 8.30,

$$\langle (K \cdot W \cdot u)v \rangle = \langle vv \rangle = I. \quad (8.43)$$

This means that the outputs are decorrelated and also indicates histogram equalization in the sense, discussed in chapter 4, that all the elements of v have the same variance. Indeed, the Goodall algorithm can be used to implement the decorrelation and whitening discussed in chapter 4. Because the anti-Hebbian and Goodall rules are based on linear models, they are only capable of removing second-order redundancy, meaning redundancy characterized by the covariance matrix. In chapter 10, we consider models that are based on eliminating higher orders of redundancy as well.

Timing-Based Plasticity and Prediction

Temporal Hebbian rules have been used in the context of multi-unit networks to store information about temporal sequences. To illustrate this, we consider a network with the architecture of figure 8.6. We study the effect of time-dependent synaptic plasticity, as given by equation 8.18, on the recurrent synapses of the model, leaving the feedforward synapses constant. Suppose that, before training, the average response of output unit a to a stimulus characterized by a parameter s is given by the tuning curve $f_a(s)$, which reaches its maximum for the optimal stimulus $s = s_a$. Different neurons have different optimal stimulus values, as depicted by the dashed and thin solid curves in figure 8.11A. We now examine what happens when the plasticity rule 8.18 is applied throughout a training period during which the stimulus being presented is an increasing function of time. Such a stimulus excites the different neurons in the network sequentially. For example, the neuron with $s_a = -2$ is active before the neuron with $s_a = 0$, which in turn is active before the neuron with $s_a = 2$. If the stimulus changes rapidly enough, the interval between the firing of the neuron with $s_a = -2$ and that with $s_a = 0$ will fall within the window for LTP depicted in figure 8.2B. This means that a synapse from the neuron with $s_a = -2$ to the $s_a = 0$ neuron will be strengthened. On the other hand, because the neuron with $s_a = 2$ fires after the $s_a = 0$ neuron, a

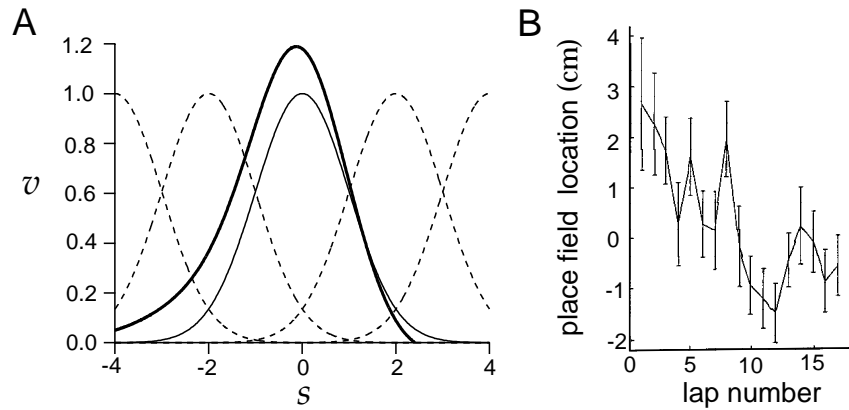


Figure 8.11: A) Predicted and experimental shift of place fields. A) Shift in a neuronal firing-rate tuning curve caused by repeated exposure to a time-dependent stimulus during training. The dashed curves and thin solid curve indicate the initial response tuning curves of a network of interconnected neurons. The thick solid curve is the response tuning curve of the neuron that initially had the thin solid tuning curve after a training period involving a time-dependent stimulus. The tuning curve increased in amplitude, broadened, and shifted as a result of temporally asymmetric Hebbian plasticity. The shift shown corresponds to a stimulus with a positive rate of change, that is, one that moved rightward on this plot as a function of time. The corresponding shift in the tuning curve is to the left. The shift has been calculated using more neurons and tuning curves than are shown in this plot. B) Location of place field centers while a rat traversed laps around a closed track (zero is defined as the average center location across the whole experiment). Over sequential laps, the place fields expanded (not shown) and shifted backward relative to the direction the rat moved. (B from Mehta et al., 1997.)

synapse from it to the $s_a = 0$ neuron will be weakened by the temporally asymmetric plasticity rule of equation 8.18.

The effect of this type of modification on the tuning curve in the middle of the array (the thin solid curve in figure 8.11A centered at $s = 0$) is shown by the thick solid curve in figure 8.11A. After the training period, the neuron with $s_a = 0$ receives strengthened input from the $s_a = -2$ neuron and weakened input from the neuron with $s_a = 2$. This broadens and shifts the tuning curve of the neuron with $s_a = 0$ to lower stimulus values. The leftward shift seen in figure 8.11A is a result of the temporal character of the plasticity rule and the temporal evolution of the stimulus during training. Note that the shift is in the direction opposite to the motion of the stimulus during training. This backward shift has an interesting interpretation. If the same time-dependent stimulus is presented again after training, the neuron with $s_a = 0$ will respond earlier than it did prior to training. The responses of other neurons will shift in a similar manner; we just chose the neuron with $s_a = 0$ as a representative example. Thus, the training experience causes neurons to develop responses that predict the behavior of the stimulus.

Enlargements and backward shifts of neural response tuning curves similar to those predicted from temporally asymmetric LTP and LTD induction have been seen in recordings of hippocampal place cells in rats. Figure 8.11B shows the average location of place fields recorded while a rat ran repeated laps around a closed track. Over time, the place field shifted backward along the track relative to the direction the rat moved.

8.4 Supervised Learning

In unsupervised learning, inputs are imposed during a training period, and the output is determined by the network dynamics using the current values of the weights. This means that the network and plasticity rule must uncover patterns and regularities in the input data (such as the direction of maximal variance) by themselves. In supervised learning, both a set of inputs and the corresponding desired outputs are imposed during training, so the network is essentially given the answer.

Two basic problems addressed in supervised learning are storage, which means learning the relationship between the input and output patterns provided during training, and generalization, which means being able to provide appropriate outputs for inputs that were not presented during training, but are similar to those that were. The main task we consider within the context of supervised learning is function approximation (or regression), in which the output of a network unit is trained to approximate a specified function of the input. We also consider classification of inputs into two categories. Understanding generalization in such settings has been a major focus of theoretical investigations in statistics and computer science but lies outside the scope of our discussion.

Supervised Hebbian Learning

In supervised learning, a set of paired inputs and output samples, \mathbf{u}^m and v^m for $m = 1 \dots N_S$, is presented during training. For a feedforward network, an averaged Hebbian plasticity rule for supervised learning can be obtained from equation 8.4 by averaging across all the input-output pairs,

$$\tau_w \frac{d\mathbf{w}}{dt} = \langle v\mathbf{u} \rangle = \frac{1}{N_S} \sum_{m=1}^{N_S} v^m \mathbf{u}^m. \quad (8.44)$$

Note that this is similar to the unsupervised Hebbian learning case, except that the output v^m is imposed on the network rather than being determined by it. This has the consequence that the input-input correlation is replaced by the input-output cross-correlation $\langle v\mathbf{u} \rangle$.

cross-correlation

Unless the cross-correlation is zero, equation 8.44 never stops changing the synaptic weights. The methods introduced to stabilize Hebbian modi-

fication in the case of unsupervised learning can be applied to supervised learning as well. However, stabilization is easier in the supervised case, because the right side of equation 8.44 does not depend on \mathbf{w} . Therefore, the growth is only linear, rather than exponential, in time, making a simple multiplicative synaptic weight decay term sufficient for stability. This is introduced by writing the supervised learning rule as

*supervised learning
with decay*

$$\tau_w \frac{d\mathbf{w}}{dt} = \langle v\mathbf{u} \rangle - \alpha \mathbf{w}, \quad (8.45)$$

for some positive constant α . Asymptotically, equation 8.45 makes $\mathbf{w} = \langle v\mathbf{u} \rangle / \alpha$, that is, the weights become proportional to the input-output cross-correlation.

We have discussed supervised Hebbian learning in the case of a single output unit, but the results can obviously be generalized to multiple outputs as well.

Classification and The Perceptron

*perceptron
binary classifier*

The perceptron is a nonlinear map that classifies inputs into one of two categories. It thus acts as a binary classifier. To make the model consistent when units are connected together in a network, we also require the inputs to be binary. We can think of the two possible states as representing units that are either active or inactive. As such, we would naturally assign them the values 1 and 0. However, the analysis is simpler while producing similar results if, instead, we require the inputs u_a and output v to take the two values +1 and -1.

The output of the perceptron is based on a modification of the linear rule of equation 8.2 to

$$v = \begin{cases} +1 & \text{if } \mathbf{w} \cdot \mathbf{u} - \gamma \geq 0 \\ -1 & \text{if } \mathbf{w} \cdot \mathbf{u} - \gamma < 0. \end{cases} \quad (8.46)$$

The threshold γ thus determines the dividing line between values of $\mathbf{w} \cdot \mathbf{u}$ that generate +1 and -1 outputs. The supervised learning task for the perceptron is to place each of N_S input patterns \mathbf{u}^m into one of two classes designated by the binary output v^m . How well the perceptron performs this task depends on the nature of the classification. The weight vector and threshold define a subspace (called a hyperplane) of dimension $N_u - 1$ (the subspace perpendicular to \mathbf{w}) that cuts the N_u -dimensional space of input vectors into two regions. It is only possible for a perceptron to classify inputs perfectly if a hyperplane exists that divides the input space into one half-space containing all the inputs corresponding to $v = +1$, and another half-space containing all those for $v = -1$. This condition is called linear separability. An instructive case to consider is when each component of each input vector and the associated output values are chosen randomly and independently with equal probabilities of being +1 and -1. For large

linear separability

N_u , the maximum number of random associations that can be described by a perceptron in this case is $2N_u$.

For linearly separable inputs, a set of weights exists that allows the perceptron to perform perfectly. However, this does not mean that a Hebbian modification rule can construct such weights. A Hebbian rule based on equation 8.45 with $\alpha = N_u/N_S$ constructs the weight vector

$$\mathbf{w} = \frac{1}{N_u} \sum_{m=1}^{N_S} v^m \mathbf{u}^m. \quad (8.47)$$

To see how well such weights allow the perceptron to perform, we compute the output generated by one input vector, \mathbf{u}^n , chosen from the training set. For this example, we set $\gamma = 0$. Nonzero threshold values are considered later in the chapter.

With $\gamma = 0$, the value of v for input \mathbf{u}^n is determined solely by the sign of $\mathbf{w} \cdot \mathbf{u}^n$. Using the weights of equation 8.47, we find

$$\mathbf{w} \cdot \mathbf{u}^n = \frac{1}{N_u} \left(v^n \mathbf{u}^n \cdot \mathbf{u}^n + \sum_{m \neq n} v^m \mathbf{u}^m \cdot \mathbf{u}^n \right). \quad (8.48)$$

If we set $\sum_{m \neq n} v^m \mathbf{u}^m \cdot \mathbf{u}^n / N_u = \eta^n$ (where the superscript is again a label not a power) and note that $1^2 = (-1)^2 = 1$ so $v^n \mathbf{u}^n \cdot \mathbf{u}^n / N_u = v^n$, we can write

$$\mathbf{w} \cdot \mathbf{u}^n = v^n + \eta^n. \quad (8.49)$$

Substituting this expression into equation 8.46 to determine the output of the perceptron for the input \mathbf{u}^n , we see that the term η^n acts as a source of noise, interfering with the ability of the perceptron to generate the correct answer $v = v^n$.

We can think of η^n as a sample drawn from a probability distribution of η values. Consider the case when all the components of \mathbf{u}^m and v^m for all m are chosen randomly with equal probabilities of being $+1$ or -1 . Including the dot product, the right side of the expression $N_u \eta^n = \sum_{m \neq n} v^m \mathbf{u}^m \cdot \mathbf{u}^n$ that defines η^n is the sum of $(N_S - 1)N_u$ terms, each of which is equally likely to be either $+1$ or -1 . For large N_u and N_S , the central limit theorem (see the Mathematical Appendix) tells us that the distribution of η values is Gaussian with zero mean and variance $(N_S - 1)/N_u$. This suggests that the perceptron with Hebbian weights should work well if the number of input patterns being learned is significantly less than the number of input vector components. We can make this more precise by noting from equations 8.46 with $\gamma = 0$ and equation 8.49 that, for $v^n = +1$, the perceptron will give the correct answer if $-1 < \eta^n < \infty$. Similarly, for $v^n = -1$, the perceptron will give the correct answer if $-\infty < \eta^n < 1$. If v^n has probability one half of taking either value, the probability of the perceptron giving the correct answer is one half the integral of the Gaussian distribution from -1 to ∞

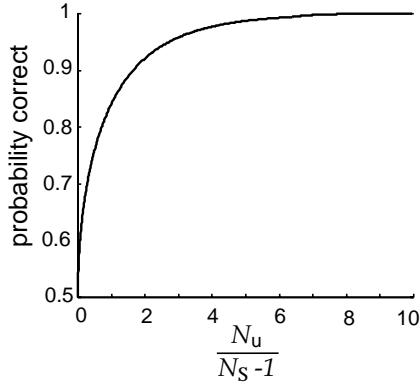


Figure 8.12: Percentage of correct responses for a perceptron with a Hebbian weight vector for a random binary input-output map. As the ratio of the number of inputs, N_u , to one less than the number of input vectors being learned, $N_S - 1$, grows, the percentage of correct responses goes to one. When this ratio is small, the percentage of correct responses approaches the chance level of $1/2$.

plus one half its integral from $-\infty$ to 1. Combining these two terms we find

$$P[\text{correct}] = \sqrt{\frac{N_u}{2\pi(N_S - 1)}} \int_{-\infty}^1 d\eta \exp\left(-\frac{N_u\eta^2}{2(N_S - 1)}\right). \quad (8.50)$$

This result is plotted in figure 8.12, which shows that the Hebbian perceptron performs fairly well if $N_S - 1$ is less than about $0.2N_u$. It is possible for the perceptron to perform considerably better than this if a non-Hebbian weight vector is used. We return to this in a later section.

Function Approximation

In chapter 1, we studied examples in which the firing rate of a neuron was given by a function of a stimulus parameter, namely the response tuning curve. When such a relationship exists, we can think of the neuronal firing rate as representing the function. Populations of neurons (labeled by an index $b = 1, 2, \dots, N_u$) that respond to a stimulus value s , by firing at average rates $f_b(s)$ can similarly represent an entire set of functions. However, a function $h(s)$ that is not equal to any of the single neuron tuning curves can only be represented by combining the responses of a number of units. This can be done using the network shown in figure 8.13. The average steady-state activity level of the output unit in this network, in response to stimulus value s , is given by equation 8.2,

*function
approximation*

$$v(s) = \mathbf{w} \cdot \mathbf{u} = \mathbf{w} \cdot \mathbf{f}(s) = \sum_{b=1}^N w_b f_b(s). \quad (8.51)$$

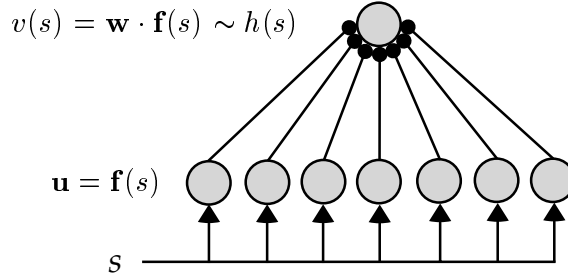


Figure 8.13: A network for representing functions. The value of an input variable s is encoded by the activity of a population of neurons with tuning curves $f(s)$. This activity drives an output neuron through a vector of weights w to create an output activity v that approximates the function $h(s)$.

Note that we have replaced u by $f(s)$ where $f(s)$ is the vector with components $f_b(s)$. The network presented in chapter 7 that performs coordinate transformation is an example of this type of function approximation.

In equation 8.51, the input tuning curves $f(s)$ act as a basis for representing the output function $h(s)$, and for this reason they are called basis functions. Different sets of basis functions can be used to represent a given set of output functions. A set of basis functions that can represent any member of a class of functions using a linear sum, as in equation 8.51, is called complete for this class. For the sets of complete functions typically used in mathematics, such as the sines and cosines used in a Fourier series, the weights in equation 8.51 are unique. When neural tuning curves are used to expand a function, the weights tend not to be unique, and the set of input functions is called overcomplete. In this chapter, we assume that the basis functions are held fixed, and only the weights are adjusted to improve output performance, although it is interesting to consider methods for learning the best basis functions for a particular application. One way of doing this is by applying backpropagation, which develops the basis functions guided by the output errors of the network. Other methods, which we consider in chapter 10, involve unsupervised learning.

basis functions

completeness

overcomplete

Suppose that the function-representation network of figure 8.13 is provided a sequence of N_S sample stimuli s^m for $m = 1, 2, \dots, N_S$, and the corresponding function values $h(s^m)$ during a training period. To make $v(s^m)$ match $h(s^m)$ as closely as possible for all m , we minimize the error

$$E = \frac{1}{2N_S} \sum_{m=1}^{N_S} (h(s^m) - v(s^m))^2 = \frac{1}{2} \langle (h(s) - w \cdot f(s))^2 \rangle. \quad (8.52)$$

We have made the replacement $v(s) = w \cdot f(s)$ in this equation and have used the bracket notation for the average over the training inputs. Equations for the weights that minimize this error, called the normal equations, are obtained by setting its derivative with respect to the weights to zero,

normal equations

yielding the condition

$$\langle \mathbf{f}(s)\mathbf{f}(s) \rangle \cdot \mathbf{w} = \langle \mathbf{f}(s)h(s) \rangle . \quad (8.53)$$

The supervised Hebbian rule of equation 8.45, applied in this case, ultimately sets the weight vector to $\mathbf{w} = \langle \mathbf{f}(s)h(s) \rangle / \alpha$. These weights must satisfy the normal equations 8.53 if they are to optimize function approximation. There are two circumstances under which this occurs. The obvious one is when the input units are orthogonal across the training stimuli, $\langle \mathbf{f}(s)\mathbf{f}(s) \rangle = \mathbf{I}$. In this case, the normal equations are satisfied with $\alpha = 1$. However, this condition is unlikely to hold for most sets of input tuning curves. An alternative possibility is that, for all pairs of stimuli s^m and $s^{m'}$ in the training set,

$$\mathbf{f}(s^m) \cdot \mathbf{f}(s^{m'}) = c\delta_{mm'} \quad (8.54)$$

tight frame

for some constant c . This is called a tight frame condition. If it is satisfied, the weights given by a supervised Hebbian learning with decay can satisfy the normal equations. To see this, we insert the weights $\mathbf{w} = \langle \mathbf{f}(s)h(s) \rangle / \alpha$ into equation 8.53 and use 8.54 to obtain

$$\begin{aligned} \langle \mathbf{f}(s)\mathbf{f}(s) \rangle \cdot \mathbf{w} &= \frac{\langle \mathbf{f}(s)\mathbf{f}(s) \rangle \cdot \langle \mathbf{f}(s)h(s) \rangle}{\alpha} = \frac{1}{\alpha N_S^2} \sum_{mm'} \mathbf{f}(s^m) \mathbf{f}(s^m) \cdot \mathbf{f}(s^{m'}) h(s^{m'}) \\ &= \frac{c}{\alpha N_S^2} \sum_m \mathbf{f}(s^m) h(s^m) = \frac{c}{\alpha N_S} \langle \mathbf{f}(s)h(s) \rangle . \end{aligned} \quad (8.55)$$

This shows that the normal equations are satisfied for $\alpha = c/N_S$. Thus, we have shown two ways that supervised Hebbian learning can solve the function approximation problem, but both require special conditions on the basis functions $\mathbf{f}(s)$. A more general scheme, discussed below, involves using an error-correcting rule.

Supervised Error-Correcting Rules

An essential limitation of supervised Hebbian rules is that synaptic modification does not depend on the actual performance of the network. An alternative learning strategy is to start with an initial guess for the weights, compare the output v in response to input \mathbf{u}^m with the desired output v^m , and change the weights to improve the performance. Two important error-correcting modification rules are the perceptron rule, which applies to binary classification, and the delta rule, which can be applied to function approximation and many other problems.

The Perceptron Learning Rule

Suppose that the perceptron of equation 8.46 incorrectly classifies an input pattern \mathbf{u}^m . If the output is $v(\mathbf{u}^m) = -1$ when $v^m = 1$, the weight vector

should be modified to make $\mathbf{w} \cdot \mathbf{u}^m - \gamma$ larger. Similarly, if $v(\mathbf{u}^m) = 1$ when $v^m = -1$, $\mathbf{w} \cdot \mathbf{u}^m - \gamma$ should be decreased. A plasticity rule that performs such an adjustment is the perceptron learning rule,

$$\mathbf{w} \rightarrow \mathbf{w} + \frac{\epsilon_w}{2} (v^m - v(\mathbf{u}^m)) \mathbf{u}^m \quad \gamma \rightarrow \gamma - \frac{\epsilon_w}{2} (v^m - v(\mathbf{u}^m)) \quad (8.56)$$

*perceptron
learning rule*

Here, and in subsequent sections in this chapter, we use discrete updates for the weights (indicated by the \rightarrow) rather than the differential equations used up to this point. This is due to the discrete nature of the presentation of the training patterns. Here, ϵ_w determines the modification rate and is analogous to $1/\tau_w$. In equation 8.56, we have assumed that the threshold γ is also plastic. The learning rule for γ is inverted compared with that for the weights, because γ enters equation 8.46 with a minus sign.

To verify that the perceptron learning rule makes appropriate weight adjustments, we note that it implies that

$$(\mathbf{w} \cdot \mathbf{u}^m - \gamma) \rightarrow (\mathbf{w} \cdot \mathbf{u}^m - \gamma) + \frac{\epsilon_w}{2} (v^m - v(\mathbf{u}^m)) (|\mathbf{u}^m|^2 + 1). \quad (8.57)$$

This result shows that if $v^m = 1$ and $v(\mathbf{u}^m) = -1$, the weight change increases $\mathbf{w} \cdot \mathbf{u}^m - \gamma$. If $v^m = -1$ and $v(\mathbf{u}^m) = 1$, $\mathbf{w} \cdot \mathbf{u}^m - \gamma$ is decreased. This is exactly what is needed to compensate for the error. Note that the perceptron learning rule does not modify the weights if the output is correct.

To learn a set of input pattern classifications, the perceptron learning rule is applied to each one sequentially. For fixed ϵ_w , the perceptron learning rule of equation 8.56 is guaranteed to find a set of weights \mathbf{w} and threshold γ that solve any linearly separable problem. This is proved in the appendix.

The Delta Rule

The perceptron learning rule is designed for binary outputs. The function approximation task with the error function E of equation 8.52 can also be solved using an error correcting scheme. A simple but extremely useful version of this is the gradient descent procedure, which modifies \mathbf{w} according to

$$\mathbf{w} \rightarrow \mathbf{w} - \epsilon_w \nabla_{\mathbf{w}} E \quad \text{or} \quad w_b \rightarrow w_b - \epsilon_w \frac{\partial E}{\partial w_b} \quad (8.58)$$

gradient descent

where $\nabla_{\mathbf{w}} E$ is the vector with components $\partial E / \partial w_b$. This rule is sensible because $-\nabla_{\mathbf{w}} E$ points in the direction along which E decreases most rapidly. This process tends to reduce E because, to first order in ϵ_w

$$E(\mathbf{w} - \epsilon_w \nabla_{\mathbf{w}} E) = E(\mathbf{w}) - \epsilon_w |\nabla_{\mathbf{w}} E|^2 \leq E(\mathbf{w}). \quad (8.59)$$

Note that, if ϵ_w is too large, or \mathbf{w} is very near to a point where $\nabla_{\mathbf{w}} E(\mathbf{w}) = \mathbf{0}$, then E can increase. We will take ϵ_w to be small, and ignore this concern.

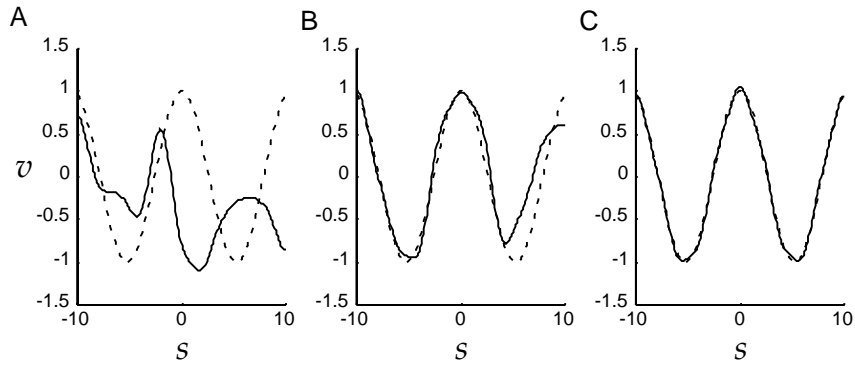


Figure 8.14: Eleven input neurons with Gaussian tuning curves drive an output neuron to approximate a sine function. The input tuning curves are $f_b(s) = \exp[-0.5(s - s_b)^2]$ with $s_b = -10, -8, -6, \dots, 8, 10$. A delta plasticity rule was used to set the weights. Sample points were chosen randomly in the range between -10 and 10. The firing rate of the output neuron is plotted as a solid curve and the sinusoidal target function as a dashed curve. A) The firing rate of the output neuron when random weights in the range between -1 and 1 were used. B) The output firing rate after weight modification using the delta rule for 20 sample points. C) The output firing rate after weight modification using the delta rule for 100 sample points.

Thus, E decreases until w is close to a minimum. If E has many minima, gradient descent will find only one of them (a local minimum), and not necessarily the one with the lowest value of E (the global minimum). In the case of linear function approximation using basis functions, as in equation 8.51, gradient descent finds a value of w that satisfies the normal equations, and therefore constructs an optimal function approximator, because there are no non-global minima.

For function approximation, the error E in equation 8.52 is an average over a set of examples. As for the perceptron learning rule of equation 8.56, it is possible to present randomly chosen input output pairs s^m and $h(s^m)$, and change w according to $-\nabla_w(h(s^m) - v(s^m))^2/2$. Using $\nabla_w v = u = f$, this produces what is called the delta rule,

$$w \rightarrow w + \epsilon_w (h(s^m) - v(s^m)) f(s^m). \quad (8.60)$$

The procedure of applying the delta rule to each pattern sequentially is called stochastic gradient descent, and it is particularly useful because it allows learning to take place continuously while sample inputs are presented. There are more efficient methods of searching for minima of functions than stochastic gradient descent, but many of them are complicated to implement. The weights w will typically not completely settle down to fixed values during the training period for a fixed value of ϵ_w . However, their averages will tend to satisfy the normal equations.

Figure 8.14 shows the result of modifying an initially random set of weights using the delta rule. Ultimately, an array of input neurons with

delta rule

stochastic gradient decent

Gaussian tuning curves drives an output neuron that quite accurately represents a sine function. The difference between figures 8.14B and C illustrates the difference between storage and generalization. Figure 8.14B is based on 20 pairs of training inputs and outputs, while figure 8.14C involves 100 pairs. It is clear that $v(s)$ in figure 8.14B does not match the sine function very well, at least for values of s that were not in the training set, while $v(s)$ in figure 8.14C provides a good approximation of the sine function for all s values. The ability of the network to approximate the function $h(s)$ for stimulus values not presented during training depends in a complicated way on its smoothness and the number and smoothness of the basis functions $f(s)$.

It is not obvious how the delta rule of equation 8.60 could be implemented biophysically, because the network has to compute the difference $h(s)f(s^m) - v(s^m)f(s^m)$. One possibility is that the two terms $h(s^m)f(s^m)$ and $v(s^m)f(s^m)$ could be computed in separate phases. First, the output of the network is clamped to the desired value $h(s^m)$ and Hebbian plasticity is applied. Then, the network runs freely to generate $v(s^m)$ and anti-Hebbian modifications are made. In the next section, we discuss a particular example of this in the case of the Boltzmann machine, and we show how learning rules intended for supervised learning can sometimes be used for unsupervised learning as well.

Contrastive Hebbian Learning

In chapter 7, we presented the Boltzmann machine, which is a stochastic network with binary units. One of the key innovations associated with the Boltzmann machine is a synaptic modification rule that has a sound foundation in probability theory. We start by describing the case of supervised learning, although the underlying theory is similar for both supervised and unsupervised learning with the Boltzmann machine.

We first consider a Boltzmann machine with only feedforward weights \mathbf{W} connecting \mathbf{u} to \mathbf{v} . Given an input \mathbf{u} , an output \mathbf{v} is computed by setting each component v_a to one with probability $F(\sum_b W_{ab}u_b)$ (and zero otherwise) where $F(I) = 1/(1 + \exp(-I))$. This is the Gibbs sampling procedure discussed in chapter 7 applied to the feedforward Boltzmann machine. Because there are no recurrent connections, the states of the output units are independent, and they can all be sampled simultaneously. Analogous to the discussion in chapter 7, this procedure gives rise to a conditional probability distribution $P[\mathbf{v}|\mathbf{u}; \mathbf{W}]$ for \mathbf{v} given \mathbf{u} that can be written as

$$P[\mathbf{v}|\mathbf{u}; \mathbf{W}] = \frac{\exp(-E(\mathbf{u}, \mathbf{v}))}{Z(\mathbf{u})} \quad \text{with} \quad Z(\mathbf{u}) = \sum_{\mathbf{v}} \exp(-E(\mathbf{u}, \mathbf{v})) \quad (8.61)$$

where $E(\mathbf{u}, \mathbf{v}) = -\mathbf{v} \cdot \mathbf{W} \cdot \mathbf{u}$.

Supervised learning in deterministic networks involves the development of a relationship between inputs \mathbf{u} and outputs \mathbf{v} that matches, as closely as

possible, a set of samples $(\mathbf{u}^m, \mathbf{v}^m)$ for $m = 1, 2, \dots, N_S$. An analogous task for a stochastic network is to match the distribution $P[\mathbf{v}|\mathbf{u}; \mathbf{W}]$ as closely as possible to a probability distribution $P[\mathbf{v}|\mathbf{u}]$ associated with the samples $(\mathbf{u}^m, \mathbf{v}^m)$. This is done by adjusting the feedforward weight matrix \mathbf{W} . Note that we are using the argument \mathbf{W} to distinguish between two different distributions, $P[\mathbf{u}|\mathbf{v}]$, which is provided externally and generates the sample data, and $P[\mathbf{u}|\mathbf{v}; \mathbf{W}]$, which is the distribution generated by the Boltzmann machine with weights \mathbf{W} . The idea of constructing networks that reproduce probability distributions inferred from sample data is central to the problem of density estimation covered more fully in chapter 10.

density estimation

The natural measure for determining how well the distribution generated by the network $P[\mathbf{v}|\mathbf{u}; \mathbf{W}]$ matches the sampled distribution $P[\mathbf{v}|\mathbf{u}]$ for a particular input \mathbf{u} is the Kullback-Leibler divergence,

$$\begin{aligned} D_{\text{KL}}(P[\mathbf{v}|\mathbf{u}], P[\mathbf{v}|\mathbf{u}; \mathbf{W}]) &= \sum_{\mathbf{v}} P[\mathbf{v}|\mathbf{u}] \ln \left(\frac{P[\mathbf{v}|\mathbf{u}]}{P[\mathbf{v}|\mathbf{u}; \mathbf{W}]} \right) \\ &= - \sum_{\mathbf{v}} P[\mathbf{v}|\mathbf{u}] \ln (P[\mathbf{v}|\mathbf{u}; \mathbf{W}]) + K, \end{aligned} \quad (8.62)$$

where K is a term that is proportional to the entropy of the distribution $P[\mathbf{v}|\mathbf{u}]$ (see chapter 4). We do not write out this term explicitly because it does not depend on the feedforward weight matrix, so it does not affect the learning rule used to modify \mathbf{W} . As in chapter 7, we have, for convenience, used natural rather than base 2 logarithms in the definition of the Kullback-Leibler divergence.

To estimate, from the samples, how well $P[\mathbf{v}|\mathbf{u}; \mathbf{W}]$ matches $P[\mathbf{v}|\mathbf{u}]$ across the different values of \mathbf{u} , we average the Kullback-Leibler divergence over all of the input samples \mathbf{u}^m . We also use the sample outputs \mathbf{v}^m to provide a stochastic approximation of the sum over all \mathbf{v} in equation 8.62 with weighting factor $P[\mathbf{v}|\mathbf{u}]$. Using brackets to denote the average over samples, this results in the measure

$$\langle D_{\text{KL}}(P[\mathbf{v}|\mathbf{u}], P[\mathbf{v}|\mathbf{u}; \mathbf{W}]) \rangle = - \frac{1}{N_S} \sum_{m=1}^{N_S} \ln (P[\mathbf{v}^m|\mathbf{u}^m; \mathbf{W}]) + \langle K \rangle \quad (8.63)$$

for comparing $P[\mathbf{v}|\mathbf{u}; \mathbf{W}]$ and $P[\mathbf{v}|\mathbf{u}]$. Each logarithmic term in the sum on the right side of this equation is the negative of the logarithm of the probability that a sample output \mathbf{v}^m would have been drawn from the distribution $P[\mathbf{v}|\mathbf{u}^m; \mathbf{W}]$, when in fact it is drawn from $P[\mathbf{v}|\mathbf{u}^m]$. A consequence of this approximate equality is that finding the network distribution $P[\mathbf{v}|\mathbf{u}^m; \mathbf{W}]$ that best matches $P[\mathbf{v}|\mathbf{u}^m]$ (in the sense of minimizing the Kullback-Leibler divergence) is equivalent to maximizing the conditional likelihood that the sample \mathbf{v}^m could have been drawn from $P[\mathbf{v}|\mathbf{u}^m; \mathbf{W}]$.

likelihood maximization

A learning rule that is equivalent to stochastic gradient ascent of the log likelihood can be derived by changing the weights by an amount proportion to the derivative of the logarithmic term in equation 8.63 with respect

to the weight being changed. In a stochastic gradient ascent scheme, the change in the weight matrix after sample m is presented only depends on the log likelihood for that sample, so we only need to take the derivative with respect to W_{ab} of the corresponding term in equation 8.63,

$$\begin{aligned} \frac{\partial \ln P[\mathbf{v}^m | \mathbf{u}^m; \mathbf{W}]}{\partial W_{ab}} &= \frac{\partial}{\partial W_{ab}} \left(-E(\mathbf{u}^m, \mathbf{v}^m) - \ln Z(\mathbf{u}^m) \right) \\ &= v_a^m u_b^m - \sum_v P[\mathbf{v} | \mathbf{u}^m; \mathbf{W}] v_a u_b^m. \end{aligned} \quad (8.64)$$

This derivative has a simple form for the Boltzmann machine because of equation 8.61.

Before we derive the stochastic gradient ascent learning rule, we need to evaluate the sum over \mathbf{v} in the last term of the bottom line of equation 8.64. For Boltzmann machines with recurrent connections like the ones we discuss below, this average cannot be calculated tractably. However, because the learning rule is used repeatedly, it can be estimated by stochastic sampling. In other words, we approximate the average over \mathbf{v} by a single instance of a particular output $\mathbf{v}(\mathbf{u}^m)$ generated by the Boltzmann machine in response to the input \mathbf{u}^m . Making this replacement and setting the change in the weight matrix proportional to the derivative in equation 8.64, we obtain the learning rule

$$W_{ab} \rightarrow W_{ab} + \epsilon_w (v_a^m u_b^m - v_a(\mathbf{u}^m) u_b^m). \quad (8.65)$$

Equation 8.65 is identical in form to the perceptron learning rule of equation 8.56, except that $\mathbf{v}(\mathbf{u}^m)$ is computed from the input \mathbf{u}^m by Gibbs sampling rather than by a deterministic rule. As discussed at the end of the previous section, equation 8.65 can also be interpreted as the difference of Hebbian and anti-Hebbian terms. The Hebbian term $v_a^m u_b^m$ is based on the sample input \mathbf{u}^m and output \mathbf{v}^m . The anti-Hebbian term $-v_a(\mathbf{u}^m) u_b^m$ involves the product of the sample input \mathbf{u}^m with an output $\mathbf{v}(\mathbf{u}^m)$ generated by the Boltzmann machine in response to this input, rather than the sample output \mathbf{v}^m . In other words, while \mathbf{v}^m is provided externally, $\mathbf{v}(\mathbf{u}^m)$ is obtained by Gibbs sampling using the input \mathbf{u}^m and the current values of the network weights. The overall learning rule is sometimes called a contrastive Hebbian rule because it depends on the difference between Hebbian and anti-Hebbian terms.

Supervised learning for the Boltzmann machine is run in two phases, both of which use a sample input \mathbf{u}^m . The first phase, sometimes called the wake phase, involves Hebbian plasticity between sample inputs and outputs. The dynamics of the Boltzmann machine play no role during this phase. The second phase, called the sleep phase, consists of the network ‘dreaming’ (i.e. internally generating) $\mathbf{v}(\mathbf{u}^m)$ in response to \mathbf{u}^m based on the current weights \mathbf{W} . Then, anti-Hebbian learning based on \mathbf{u}^m and $\mathbf{v}(\mathbf{u}^m)$ is applied to the weight matrix. Gibbs sampling is typically used to generate $\mathbf{v}(\mathbf{u}^m)$ from \mathbf{u}^m . It is also possible to use the mean field method we

*supervised
learning for \mathbf{W}*

*contrastive
Hebbian rule*

wake phase

sleep phase

discussed in chapter 7 to approximate the average over the distribution $P[\mathbf{v}|\mathbf{u}^m; \mathbf{W}]$ in equation 8.64.

Supervised learning can also be implemented in a Boltzmann machine with recurrent connections. When the output units are connected by a symmetric recurrent weight matrix \mathbf{M} (with $M_{aa} = 0$), the energy function is

$$E(\mathbf{u}, \mathbf{v}) = -\mathbf{v} \cdot \mathbf{W} \cdot \mathbf{u} - \frac{1}{2}\mathbf{v} \cdot \mathbf{M} \cdot \mathbf{v}. \quad (8.66)$$

Everything that has been described thus far applies to this case, except that the output $\mathbf{v}(\mathbf{u}^m)$ for the sample input \mathbf{u}^m must now be computed by repeated Gibbs sampling using $F(\sum_b W_{ab} u_b^m + \sum_{a'} M_{aa'} v_{a'})$ for the probability that $v_a = 1$ (see chapter 7). Repeated sampling is required to assure that the network relaxes to the equilibrium distribution of equation 8.61. Modification of the feedforward weight W_{ab} then proceeds as in equation 8.65. The contrastive Hebbian modification rule for recurrent weight $M_{aa'}$ is similarly given by

$$M_{aa'} \rightarrow M_{aa'} + \epsilon_m (v_a^m v_{a'}^m - v_a(\mathbf{u}^m) v_{a'}(\mathbf{u}^m)). \quad (8.67)$$

The Boltzmann machine was originally introduced in the context of unsupervised rather than supervised learning. In the supervised case, we tried to make the distribution $P[\mathbf{v}|\mathbf{u}; \mathbf{W}]$ match the probability distribution $P[\mathbf{v}|\mathbf{u}]$ that generates the samples pairs $(\mathbf{u}^m, \mathbf{v}^m)$. In the unsupervised case, no output sample \mathbf{v}^m is provided, and instead we try to make the network generate a probability distribution over \mathbf{u} that matches the distribution $P[\mathbf{u}]$ from which the samples \mathbf{u}^m are drawn. As we discuss in chapter 10, a common goal of probabilistic unsupervised learning is to generate network distributions that match the distributions of input data.

In addition to the distribution of equation 8.61 for \mathbf{v} given a specific input \mathbf{u} , the energy function of the Boltzmann machine can be used to define a distribution over both \mathbf{u} and \mathbf{v} defined by

$$P[\mathbf{u}, \mathbf{v}; \mathbf{W}] = \frac{\exp(-E(\mathbf{u}, \mathbf{v}))}{Z} \quad \text{with} \quad Z = \sum_{\mathbf{u}, \mathbf{v}} \exp(-E(\mathbf{u}, \mathbf{v})). \quad (8.68)$$

This can be used to construct a distribution for \mathbf{u} alone by summing over the possible values of \mathbf{v} ,

$$P[\mathbf{u}; \mathbf{W}] = \sum_{\mathbf{v}} P[\mathbf{u}, \mathbf{v}; \mathbf{W}] = \frac{1}{Z} \sum_{\mathbf{v}} \exp(-E(\mathbf{u}, \mathbf{v})). \quad (8.69)$$

The goal of unsupervised learning for the Boltzmann machine is to make this distribution match, as closely as possible, the distribution of inputs $P[\mathbf{u}]$.

The derivation of an unsupervised learning rule for a feedforward Boltzmann machine proceeds very much like the derivation we presented for

the supervised case. The equivalent of equation 8.64 is

$$\frac{\partial \ln P[\mathbf{u}^m; \mathbf{W}]}{\partial W_{ab}} = \sum_{\mathbf{v}} P[\mathbf{v}|\mathbf{u}^m; \mathbf{W}] v_a u_b^m - \sum_{\mathbf{u}, \mathbf{v}} P[\mathbf{u}, \mathbf{v}; \mathbf{W}] v_a u_b. \quad (8.70)$$

In this case, both terms must be evaluated by Gibbs sampling. The wake phase Hebbian term requires a stochastic output $\mathbf{v}(\mathbf{u}^m)$, which is calculated from the sample input \mathbf{u}^m just as it was for the anti-Hebbian term in equation 8.65. However, the sleep phase anti-Hebbian term in this case requires both an input \mathbf{u} and an output \mathbf{v} generated by the network. These are computed using a Gibbs sampling procedure in which both input and output states are stochastically generated through repeated Gibbs sampling. A randomly chosen component v_a is set to one with probability $F(\sum_b W_{ab} u_b)$ (or zero otherwise), and a random component u_b is set to one with probability $F(\sum_a v_a W_{ab})$ (or zero otherwise). Note that this corresponds to having the input units drive the output units in a feedforward manner through the weights \mathbf{W} and having the output units drive the input units in a reversed manner using feedback weights with the same values. Once the network has settled to equilibrium through repeated Gibbs sampling of this sort, and the stochastic inputs and outputs have been generated, the full learning rule is

$$W_{ab} \rightarrow W_{ab} + \epsilon_w (v_a(\mathbf{u}^m) u_b^m - v_a u_b). \quad (8.71)$$

*unsupervised
learning for \mathbf{W}*

The unsupervised learning rule can be extended to include recurrent connections by following the same general procedure.

8.5 Chapter Summary

We presented a variety of forms of Hebbian synaptic plasticity ranging from the basic Hebb rule to rules that involve multiplicative and subtractive normalization, a constant or sliding thresholds, and spike-timing effects. Two important features in synaptic plasticity were emphasized, stability and competition. We showed how the effects of unsupervised Hebbian learning could be estimated by computing the principal eigenvector of the correlation matrix of the inputs used during training. Unsupervised Hebbian learning could be interpreted as a process that produces weights that project the input vector onto the direction of maximal variance in the training data set. In some cases, this requires an extension from correlation-based to covariance-based rules. We used the principal eigenvector approach to analyze Hebbian models of the development of ocular dominance and its associated map in primary visual cortex. Plasticity rules based on the dependence of synaptic modification on spike timing were shown to implement temporal sequence and trace learning.

Forcing multiple outputs to have different selectivities requires them to be connected, either through fixed weights or by weights that are themselves

plastic. In the latter case, anti-Hebbian plasticity can ensure decorrelation of multiple output units. We also considered the role of competition and cooperation in models of activity-dependent development and described two examples of feature-based models, the self-organizing map and the elastic net.

Finally, we considered supervised learning applied to binary classification and function approximation, using supervised Hebbian learning, the perceptron learning rule, and gradient descent learning through the delta rule. We also treated contrastive Hebbian learning for the Boltzmann machine, involving Hebbian and anti-Hebbian updates in different phases.

8.6 Appendix

Convergence of the Perceptron Learning Rule

For convenience, we take $\epsilon_w = 1$ and start the perceptron learning rule with $\mathbf{w} = \mathbf{0}$ and $\gamma = 0$. Then, under presentation of the sample m , the changes in the weights and threshold are given by

$$\Delta \mathbf{w} = \frac{1}{2}(v^m - v(\mathbf{u}^m))\mathbf{u}^m \quad \text{and} \quad \Delta \gamma = -\frac{1}{2}(v^m - v(\mathbf{u}^m)). \quad (8.72)$$

Given a finite, linearly separable problem, there must be a set of weights \mathbf{w}^* and a threshold γ^* that are normalized ($|\mathbf{w}^*|^2 + (\gamma^*)^2 = 1$) and allow the perceptron to categorize correctly, for which we require the condition $(\mathbf{w}^* \cdot \mathbf{u}^m - \gamma^*)v^m > \delta$ for some $\delta > 0$ and for all m .

Consider the cosine of the angle between the current weights and threshold \mathbf{w}, γ and the solution \mathbf{w}^*, γ^*

$$\Phi(\mathbf{w}, \gamma) = \frac{\mathbf{w} \cdot \mathbf{w}^* + \gamma \gamma^*}{\sqrt{|\mathbf{w}|^2 + (\gamma)^2}} = \frac{\psi(\mathbf{w}, \gamma)}{|\mathbf{w}, \gamma|}, \quad (8.73)$$

to introduce some compact notation. Because it is a cosine, Φ must lie between -1 and 1 . The perceptron convergence theorem shows the perceptron learning rule must lead to a solution of the categorization problem or else Φ would grow larger than one, which is impossible.

To show this, we consider the change in ψ due to one step of perceptron learning during which \mathbf{w} and γ are modified because the current weights generated the wrong response. When an incorrect response is generated $v(\mathbf{u}^m) = -v^m$, so $(v^m - v(\mathbf{u}^m))/2 = v^m$, and thus

$$\Delta \psi = (\mathbf{w}^* \cdot \mathbf{u}^m - \gamma^*)v^m > \delta. \quad (8.74)$$

The inequality follows from the condition imposed on \mathbf{w}^* and γ^* as providing a solution of the categorization problem. Assuming that ψ is initially positive and iterating this result over n steps in which the weights

change, we find that

$$\psi(\mathbf{w}, \gamma) \geq n\delta. \quad (8.75)$$

Similarly, over one learning step in which some change is made

$$\Delta|\mathbf{w}, \gamma|^2 = 2(\mathbf{w} \cdot \mathbf{u}^m - \gamma)v^m + |\mathbf{u}^m|^2 + 1. \quad (8.76)$$

The first term on the right side is always negative when an error is made and, if we define D to be the maximum value of $|\mathbf{u}^m|^2$ over all the training samples, we find

$$\Delta|\mathbf{w}, \gamma|^2 < D + 1. \quad (8.77)$$

After n non-trivial learning iterations (iterations in which the weights and threshold are modified) starting from $|\mathbf{w}, \gamma|^2 = 0$, we therefore have

$$|\mathbf{w}, \gamma|^2 < n(D + 1) \quad (8.78)$$

Putting together equations 8.75 and 8.78, we find after n non-trivial training steps

$$\Phi(\mathbf{w}, \gamma) > \frac{n\delta}{\sqrt{n(D+1)}}. \quad (8.79)$$

To ensure that $\Phi(\mathbf{w}, \gamma) \leq 1$, we must have $n \leq (D+1)/\delta^2$. Therefore, after a finite number of weight changes, the perceptron learning rule must stop changing the weights, and the perceptron must classify all the patterns correctly.

8.7 Annotated Bibliography

Hebb's (1949) original proposal about learning set the stage for many of the subsequent investigations. We followed the treatments of Hebbian, BCM, anti-Hebbian and trace learning of Goodall (1960); Sejnowski (1977); Bienenstock, Cooper & Munro (1982); Oja (1982); Földiák (1989; 1991); Leen (1991); Atick & Redlich (1993); Wallis & Baddeley (1997); extensive coverage of these and related analyses can be found in Hertz et al. (1991). We followed Miller & MacKay (1994); Miller (1996b) in the analysis of weight constraints and normalization. Jolliffe (1986) treats principal components analysis theoretically; see also chapter 10; Intrator & Cooper (1992) treats BCM from the statistical perspective of projection pursuit (Huber, 1985).

Sejnowski (1999) comments on the relationship between Hebb's suggestions and recent experimental data and theoretical studies on temporal sensitivity in Hebbian plasticity (see Levy & Steward, 1983; Blum & Abbott, 1996; Kempter et al., 1999; Song et al., 2000).

Descriptions of relevant data on the patterns of responsivity across cortical areas and the development of these patterns include Hubener et al. (1997); Yuste & Sur (1999); Weliky (2000); Price & Willshaw (2000) offers a broad-based, theoretically informed review. There are various recent experimental challenges to plasticity-based models (e.g. Crair et al., 1998; Crowley & Katz, 1999). Neural pattern formation mechanisms involving chemical matching, which are likely important at least for establishing coarse maps, are reviewed from a theoretical perspective in Goodhill & Richards (1999). The use of learning algorithms to account for cortical maps is reviewed in Erwin et al. (1995), Miller (1996a) and Swindale (1996). The underlying mathematical basis of some rules is closely related to Turing (1952)'s reaction diffusion theory of morphogenesis; others are motivated on the basis of minimizing quantities such as wire length in cortex. We described Hebbian models for the development of ocular dominance and orientation selectivity due to Linsker (1986); Miller et al. (1989) and Miller (1994); a competitive Hebbian model closely related to that of Goodhill (1993) and Piepenbrock & Obermayer (1999); a self-organizing map model related to that of Obermayer et al. (1992); and the elastic net (Durbin & Willshaw, 1987) model of Durbin & Mitchison (1990); Goodhill & Willshaw (1990); Erwin et al. (1995). The first feature-based models were called noise models (see Swindale, 1996).

The perceptron learning rule is due to Rosenblatt (1958); see Minsky & Papert (1969). The delta rule was introduced by Widrow & Hoff (1960; see also Widrow & Stearns, 1985) and independently arose in various other fields. The widely used backpropagation algorithm is a form of delta rule learning that works in a larger class of networks. O'Reilly (1996) suggests a more biologically plausible implementation.

Supervised learning for classification and function approximation, and its ties to Bayesian and frequentist statistical theory, are reviewed in Duda & Hart, 1973; Kearns & Vazirani, 1994; Bishop, 1995. Poggio and colleagues have explored basis function models of various representational and learning phenomena (see Poggio, 1990). Tight frames are discussed in Daubechies et al. (1986) and applied to visual receptive fields by Salinas & Abbott (2000).

Contrastive Hebbian learning is due to Hinton & Sejnowski (1986). See Hinton (2000) for discussion of the particular Boltzmann machine without recurrent connections, and for an alternative learning rule.

Chapter 9

Classical Conditioning and Reinforcement Learning

9.1 Introduction

The ability of animals to learn to take appropriate actions in response to particular stimuli on the basis of associated rewards or punishments is a focus of behavioral psychology. The field is traditionally separated into classical (or Pavlovian) and instrumental (or operant) conditioning. In classical conditioning, the reinforcers (i.e. the rewards or punishments) are delivered independently of any actions taken by the animal. In instrumental conditioning, the actions of the animal determine what reinforcement is provided. Learning about stimuli or actions solely on the basis of the rewards and punishments associated with them is called reinforcement learning. As discussed in chapter 8, reinforcement learning is minimally supervised because animals are not told explicitly what actions to take in particular situations, but must work this out for themselves on the basis of the reinforcement they receive.

We begin this chapter with a discussion of aspects of classical conditioning and the models that have been developed to account for them. We first discuss various pairings of one or more stimuli with presentation or denial of a reward and present a simple learning algorithm that summarizes the results. We then present an algorithm, called temporal difference learning, that leads to predictions of both the presence and timing of rewards delivered after a delay following stimulus presentation. Two neural systems, the cerebellum and the midbrain dopamine system, have been particularly well studied from the perspective of conditioning. The cerebellum has been studied in association with eyeblink conditioning, a paradigm in which animals learn to shut their eyes just in advance of disturbances such as puffs of air that are signalled by cues. The midbrain dopaminergic

*classical and
instrumental
conditioning*

*reinforcement
learning*

system has been studied in association with reward learning. We focus on the latter, together with a small fraction of the extensive behavioral data on conditioning.

There are two broad classes of instrumental conditioning tasks. In the first class, which we illustrate with an example of foraging by bees, the reinforcer is delivered immediately after the action is taken. This makes learning relatively easy. In the second class, the reward or punishment depends on an entire sequence of actions and is partly or wholly delayed until the sequence is completed. Thus, learning the appropriate action at each step in the sequence must be based on future expectation, rather than immediate receipt, of reward. This makes learning more difficult. Despite the differences between classical and instrumental conditioning, we show how to use the temporal difference model we discuss for classical conditioning as the heart of a model of instrumental conditioning when rewards are delayed.

For consistency with the literature on reinforcement learning, throughout this chapter, the letter r is used to represent a reward rather than a firing rate. Also, for convenience, we consider discrete actions such as a choice between two alternatives, rather than a continuous range of actions. We also consider trials that consist of a number of discrete events and use an integer time variable $t = 0, 1, 2, \dots$ to indicate steps during a trial. We therefore also use discrete weight update rules (like those we discussed for supervised learning in chapter 8) rather than learning rules described by differential equations.

9.2 Classical Conditioning

Classical conditioning involves a wide range of different training and testing procedures and a rich set of behavioral phenomena. The basic procedures and results we discuss are summarized in table 9.1. Rather than going through the entries in the table at this point, we introduce a learning algorithm that serves to summarize and structure these results.

In the classic Pavlovian experiment, dogs are repeatedly fed just after a bell is rung. Subsequently, the dogs salivate whenever the bell sounds as if they expect food to arrive. The food is called the unconditioned stimulus. Dogs naturally salivate when they receive food, and salivation is thus called the unconditioned response. The bell is called the conditioned stimulus because it only elicits salivation under the condition that there has been prior learning. The learned salivary response to the bell is called the conditioned response. We do not use this terminology in the following discussion. Instead, we treat those aspects of the conditioned responses that mark the animal's expectation of the delivery of reward, and build models of how these expectations are learned. We therefore refer to stimuli, rewards, and expectation of reward.

*unconditioned stimulus and response
conditioned stimulus and response*

Paradigm	Pre-Train	Train	Result
Pavlovian		$s \rightarrow r$	$s \rightarrow 'r'$
Extinction	$s \rightarrow r$	$s \rightarrow \cdot$	$s \rightarrow \cdot \cdot$
Partial		$s \rightarrow r \quad s \rightarrow \cdot$	$s \rightarrow \alpha'r$
Blocking	$s_1 \rightarrow r$	$s_1 + s_2 \rightarrow r$	$s_1 \rightarrow 'r' \quad s_2 \rightarrow \cdot \cdot$
Inhibitory		$s_1 + s_2 \rightarrow \cdot \quad s_1 \rightarrow r$	$s_1 \rightarrow 'r' \quad s_2 \rightarrow -'r'$
Overshadow		$s_1 + s_2 \rightarrow r$	$s_1 \rightarrow \alpha_1'r \quad s_2 \rightarrow \alpha_2'r$
Secondary	$s_1 \rightarrow r$	$s_2 \rightarrow s_1$	$s_2 \rightarrow 'r'$

Table 9.1: Classical conditioning paradigms. The columns indicate the training procedures and results, with some paradigms requiring a pre-training as well as a training period. Both training and pre-training periods consist of a moderate number of training trials. The arrows represent an association between one or two stimuli (s , or s_1 and s_2) and either a reward (r) or the absence of a reward (\cdot). In Partial and Inhibitory conditioning, the two types of training trials that are indicated are alternated. In the Result column, the arrows represent an association between a stimulus and the expectation of a reward (' r ') or no reward (' \cdot '). The factors of α denote a partial or weakened expectation, and the minus sign indicates the suppression of an expectation of reward.

Predicting Reward - The Rescorla-Wagner Rule

The Rescorla-Wagner rule (Rescorla and Wagner, 1972), which is a version of the delta rule of chapter 8, provides a concise account of certain aspects of classical conditioning. The rule is based on a simple linear prediction of the award associated with a stimulus. We use a binary variable u to represent the presence or absence of the stimulus ($u = 1$ if the stimulus is present, $u = 0$ if it is absent). The expected reward, denoted by v , is expressed as this stimulus variable multiplied by a weight w ,

$$v = wu . \quad (9.1)$$

stimulus u
expected reward v

weight w

The value of the weight is established by a learning rule designed to minimize the expected squared error between the actual reward r and the prediction v , $\langle(r - v)^2\rangle$. The angle brackets indicate an average over the presentations of the stimulus and reward, either or both of which may be stochastic. As we saw in chapter 8, stochastic gradient descent in the form of the delta rule is one way of minimizing this error. This results in the trial-by-trial learning rule known as the Rescorla-Wagner rule,

$$w \rightarrow w + \epsilon \delta u \quad \text{with} \quad \delta = r - v . \quad (9.2)$$

Rescorla-Wagner
rule

Here ϵ is the learning rate, which can be interpreted in psychological terms as the associability of the stimulus with the reward. The crucial term in this learning rule is the prediction error, δ . In a later section, we interpret the activity of dopaminergic cells in the ventral tegmental area (VTA) as encoding a form of this prediction error. If ϵ is sufficiently small, the rule changes w systematically until the average value of δ is zero, at which point w fluctuates about the equilibrium value $w = \langle ur \rangle$.

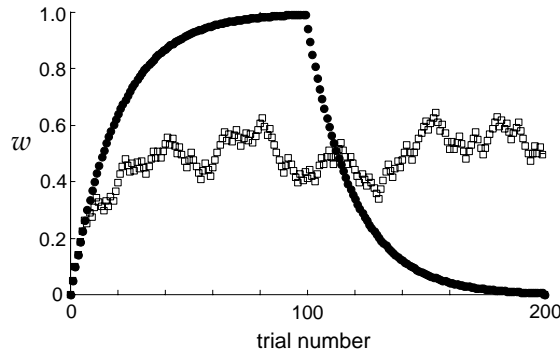


Figure 9.1: Acquisition and extinction curves for Pavlovian conditioning and partial reinforcement as predicted by the Rescorla-Wagner model. The filled circles show the time evolution of the weight w over 200 trials. In the first 100 trials, a reward of $r = 1$ was paired with the stimulus, while in trials 100–200 no reward was paired ($r = 0$). Open squares show the evolution of the weights when a reward of $r = 1$ was paired with the stimulus randomly on 50% of the trials. In both cases, $\epsilon = 0.05$.

Pavlovian
conditioning
extinction

The filled circles in figure 9.1 show how learning progresses according to the Rescorla-Wagner rule during Pavlovian conditioning and extinction. In this example, the stimulus and reward were both initially presented on each trial, but later the reward was removed. The weight approaches the asymptotic limit $w = r$ exponentially during the rewarded phase of training (conditioning), and exponentially decays to $w = 0$ during the unrewarded phase (extinction). Experimental learning curves are generally more sigmoidal in shape. There are various ways to account for this discrepancy, the simplest of which is to assume a nonlinear relationship between the expectation v and the behavior of the animal.

partial
reinforcement

The Rescorla-Wagner rule also accounts for aspects of the phenomenon of partial reinforcement, in which a reward is only associated with a stimulus on a random fraction of trials (table 9.1). Behavioral measures of the ultimate association of the reward with the stimulus in these cases indicate that it is weaker than when the reward is always presented. This is expected from the delta rule, because the ultimate steady-state average value of $w = \langle ur \rangle$ is smaller than r in this case. The open squares in figure 9.1 show what happens to the weight when the reward is associated with the stimulus 50% of the time. After an initial rise from zero, the weight varies randomly around an average value of 0.5.

stimulus vector \mathbf{u}
weight vector \mathbf{w}

To account for experiments in which more than one stimulus is used in association with a reward, the Rescorla-Wagner rule must be extended to include multiple stimuli. This is done by introducing a vector of binary variables \mathbf{u} , with each of its components representing the presence or absence of a given stimulus, together with a vector of weights \mathbf{w} . The expected reward is then the sum of each stimulus parameter multiplied by

its corresponding weight, written compactly as a dot product,

$$v = \mathbf{w} \cdot \mathbf{u} . \quad (9.3)$$

Minimizing the prediction error by stochastic gradient decent in this case gives the delta learning rule

$$\mathbf{w} \rightarrow \mathbf{w} + \epsilon \delta \mathbf{u} \quad \text{with} \quad \delta = r - v . \quad (9.4)$$

Various classical conditioning experiments probe the way that predictions are shared between multiple stimuli (see table 9.1). Blocking is the paradigm that first led to the suggestion of the delta rule in connection with classical conditioning. In blocking, two stimuli are presented together with the reward, but only after an association has already developed for one stimulus by itself. In other words, during the pre-training period, a stimulus is associated with a reward as in Pavlovian conditioning. Then, during the training period, a second stimulus is present along with the first in association with the same reward. In this case, the pre-existing association of the first stimulus with the reward blocks an association from forming between the second stimulus and the reward. Thus, after training, a conditioned response is only evoked by the first stimulus, not by the second. This follows from the vector form of the delta rule, because training with the first stimulus makes $w_1 = r$. When the second stimulus is presented along with the first, its weight starts out at $w_2 = 0$, but the prediction of reward $v = w_1 u_1 + w_2 u_2$ is still equal to r . This makes $\delta = 0$, so no further weight modification occurs.

delta rule

blocking

A standard way to induce inhibitory conditioning is to use trials in which one stimulus is shown in conjunction with the reward in alternation with trials in which that stimulus and an additional stimulus are presented in the absence of reward. In this case, the second stimulus becomes a conditioned inhibitor, predicting the absence of reward. This can be demonstrated by presenting a third stimulus that also predicts reward, in conjunction with the inhibitory stimulus, and showing that the net prediction of reward is reduced. It can also be demonstrated by showing that subsequent learning of an positive association between the inhibitory stimulus and reward is slowed. Inhibition emerges naturally from the delta rule. Trials in which the first stimulus is associated with a reward result in a positive value of w_1 . Over trials in which both stimuli are presented together, the net prediction $v = w_1 + w_2$ comes to be 0, so w_2 is forced to be negative.

inhibitory conditioning

A further example of the interaction between stimuli is overshadowing. If two stimuli are presented together during training, the prediction of reward is shared between them. After application of the delta rule, $v = w_1 + w_2 = r$. However, the prediction is often shared unequally, as if one stimulus is more salient than the other. Overshadowing can be encompassed by generalizing the delta rule so that the two stimuli have different learning rates (different values of ϵ), reflecting unequal associabilities.

overshadowing

Weight modification stops when $\langle \delta \rangle = 0$, at which point the faster growing weight will be larger than the slower growing weight. Various, more subtle, effects come from having different and modifiable associabilities, but they lie beyond the scope of our account.

The Rescorla-Wagner rule, binary stimulus parameters, and linear reward prediction are obviously gross simplifications of animal learning behavior. Yet they summarize and unify an impressive amount of classical conditioning data and are useful, provided their shortcomings are fully appreciated. As a reminder of this, we point out one experiment, namely secondary conditioning, that cannot be encompassed within this scheme. Secondary conditioning involves the association of one stimulus with a reward, followed by an association of a second stimulus with the first stimulus (table 9.1). This causes the second stimulus to evoke expectation of a reward with which it has never been paired (although if pairings of the two stimuli without the reward are repeated too many times, the result is extinction of the association of both stimuli with the reward). The delta rule cannot account for the positive expectation associated with the second stimulus. Indeed, because the reward does not appear when the second stimulus is presented, the delta rule would cause w_2 to become negative. In other words, in this case, the delta rule would predict inhibitory, not secondary, conditioning. Secondary conditioning is particularly important, because it lies at the heart of our solution to the problem of delayed rewards in instrumental conditioning tasks.

Secondary conditioning raises the important issue of keeping track of the time within a trial in which stimuli and rewards are present. This is evident because a positive association with the second stimulus is only reliably established if it precedes the first stimulus in the trials in which they are paired. If the two stimuli are presented simultaneous, the result may indeed be inhibitory rather than secondary conditioning.

Predicting Future Reward – Temporal Difference Learning

We measure time within a trial using a discrete time variable t , which falls in the range $0 \leq t \leq T$. The stimulus $u(t)$, the prediction $v(t)$, and the reward $r(t)$ are all expressed as functions of t .

In addition to associating stimuli with rewards and punishments, animals can learn to predict the future time within a trial at which a reinforcer will be delivered. We might therefore be tempted to interpret $v(t)$ as the reward predicted to be delivered at time step t . However, Sutton and Barto (1990) suggested an alternative interpretation of $v(t)$ that provides a better match to psychological and neurobiological data, and suggests how animals might use their predictions to optimize behavior in the face of delayed rewards. The suggestion is that the variable $v(t)$ should be interpreted as a prediction of the total future reward expected from time t onward to the end of the trial, namely

total future reward

$$\left\langle \sum_{\tau=0}^{T-t} r(t+\tau) \right\rangle. \quad (9.5)$$

The brackets denote an average over trials. This quantity is useful for optimization, because it summarizes the total expected worth of the current state. To compute $v(t)$, we generalize the linear relationship used for classical conditioning, equation 9.3. For the case of a single time-dependent stimulus $u(t)$, we write

$$v(t) = \sum_{\tau=0}^t w(\tau)u(t-\tau). \quad (9.6)$$

This is just a discrete time version of the sort of linear filter used in chapters 1 and 2.

Arranging for $v(t)$ to predict the total future reward would appear to require a simple alteration of the delta rule we have discussed previously,

$$w(\tau) \rightarrow w(\tau) + \epsilon \delta(t)u(t-\tau), \quad (9.7)$$

with $\delta(t)$ being the difference between the actual and predicted total future reward, $\delta(t) = \sum r(t+\tau) - v(t)$. However, there is a problem with applying this rule in a stochastic gradient descent algorithm. Computation of $\delta(t)$ requires knowledge of the total future reward on a given trial. Although $r(t)$ is known at this time, the succeeding $r(t+1), r(t+2) \dots$ have yet to be experienced, making it impossible to calculate $\delta(t)$. A possible solution is suggested by the recursive formula

$$\sum_{\tau=0}^{T-t} r(t+\tau) = r(t) + \sum_{\tau=0}^{T-t-1} r(t+1+\tau). \quad (9.8)$$

The temporal difference model of prediction is based on the observation that $v(t+1)$ provides an approximation of the trial-average value of the last term in equation 9.8,

$$v(t+1) \approx \left\langle \sum_{\tau=0}^{T-t-1} r(t+1+\tau) \right\rangle. \quad (9.9)$$

Substituting this approximation into the original expression for δ gives the temporal difference learning rule

$$w(\tau) \rightarrow w(\tau) + \epsilon \delta(t)u(t-\tau) \quad \text{with} \quad \delta(t) = r(t) + v(t+1) - v(t). \quad (9.10)$$

The name of the rule comes from the term $v(t+1) - v(t)$, which is the difference between two successive estimates. $\delta(t)$ is usually called the temporal difference error. There is an extensive body of theory showing circumstances under which this rule converges to make the correct predictions.

Figure 9.2 shows what happens when the temporal difference rule is applied during a training period in which a stimulus appears at time $t = 100$,

*temporal difference
rule*

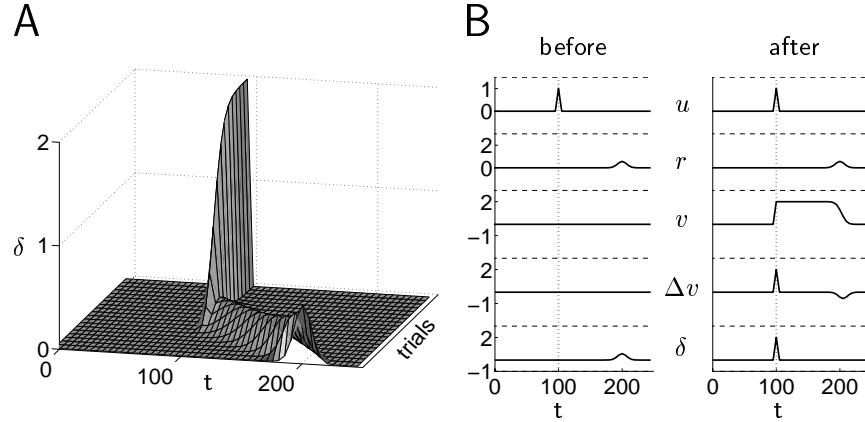


Figure 9.2: Learning to predict a reward. A) The surface plot shows the prediction error $\delta(t)$ as a function of time within a trial, across trials. In the early trials, the peak error occurs at the time of the reward ($t = 200$), while in later trials it occurs at the time of the stimulus ($t = 100$). (B) The rows show the stimulus $u(t)$, the reward $r(t)$, the prediction $v(t)$, the temporal difference between predictions $\Delta v(t - 1) = v(t) - v(t - 1)$, and the full temporal difference error $\delta(t - 1) = r(t - 1) + \Delta v(t - 1)$. The reward is presented over a short interval, and the prediction v sums the total reward. The left column shows the behavior before training, and the right column after training. $\Delta v(t - 1)$ and $\delta(t - 1)$ are plotted instead of $\Delta v(t)$ and $\delta(t)$ because the latter quantities cannot be computed until time $t + 1$ when $v(t + 1)$ is available.

and a reward is given for a short interval around $t = 200$. Initially, $w(\tau) = 0$ for all τ . Figure 9.2A shows that the temporal difference error starts off being non-zero only at the time of the reward, $t = 200$, and then, over trials, moves backward in time, eventually stabilizing around the time of the stimulus, where it takes the value 2. This is equal to the (integrated) total reward provided over the course of each trial. Figure 9.2B shows the behavior during a trial of a number of variables before and after learning. After learning, the prediction $v(t)$ is 2 from the time the stimulus is first presented ($t = 100$) until the time the reward starts to be delivered. Thus, the temporal difference prediction error has a spike at $t = 99$. This spike persists, because $u(t) = 0$ for $t < 100$. The temporal difference term $\Delta v(t)$ is negative around $t = 200$, exactly compensating for the delivery of reward, and so making $\delta = 0$.

As the peak in δ moves backwards from the time of the reward to the time of the stimulus, weights $w(\tau)$ for $\tau = 100, 99, \dots$ successively grow. This gradually extends the prediction of future reward, $v(t)$, from an initial transient at the time of the stimulus, to a broad plateau extending from the time of the stimulus to the time of the reward. Eventually, v predicts the correct total future reward from the time of the stimulus onward, and predicts the time of the reward delivery by dropping to zero when the reward is delivered. The exact shape of the ridge of activity that moves from $t = 200$ to $t = 100$ over the course of trials is sensitive to a number of fac-

tors, including the learning rate, and the exact form of the linear filter of equation 9.6.

Unlike the delta rule, the temporal difference rule provides an account of secondary conditioning. Suppose an association between stimulus s_1 and a future reward has been established, as in figure 9.2. When, as indicated in table 9.1, a second stimulus, s_2 , is introduced before the first stimulus, the positive spike in $\delta(t)$ at the time that s_1 is presented drives an increase in the value of the weight associated with s_2 and thus establishes a positive association between the second stimulus and the reward. This exactly mirrors the primary learning process for s_1 described above. Of course, because the reward is not presented in these trials, there is a negative spike in $\delta(t)$ at the time of the reward itself, and ultimately the association between both s_1 and s_2 and the reward extinguishes.

Dopamine and Predictions of Reward

The prediction error δ plays an essential role in both the Rescorla-Wagner and temporal difference learning rules, and we might hope to find a neural signal that represents this quantity. One suggestion is that the activity of dopaminergic neurons in the ventral tegmental area (VTA) in the midbrain plays this role.

There is substantial evidence that dopamine is involved in reward learning. Drugs of addiction, such as cocaine and amphetamines, act partly by increasing the longevity of the dopamine that is released onto target structures such as the nucleus accumbens. Other drugs, such as morphine and heroin, also affect the dopamine system. Further, dopamine delivery is important in self-stimulation experiments. Rats will compulsively press levers that cause current to be delivered through electrodes into various areas of their brains. One of the most effective self-stimulation sites is the medial forebrain ascending bundle, which is an axonal pathway. Stimulating this pathway is likely to cause increased delivery of dopamine to the nucleus accumbens because the bundle contains many fibers from dopaminergic cells in the VTA projecting to the nucleus accumbens.

ventral tegmental area VTA

dopamine

In a series of studies by Schultz and his colleagues (Schultz, 1998), monkeys were trained through instrumental conditioning to respond to stimuli such as lights and sounds to obtain food and drink rewards. The activities of cells in the VTA were recorded while the monkeys learned these tasks. Figure 9.3A shows histograms of the mean activities of dopamine cells over the course of learning in one example. The figure is based on a reaction time task in which the monkey keeps a finger resting on a key until a light comes on. The monkey then has to release the key and press another one to get a fruit juice reward. The reward is delivered a short time after the second key is pressed. The upper plot shows the response of the cells in early trials. The cells respond vigorously to the reward, but barely fire above baseline to the light. The lower plot shows the response

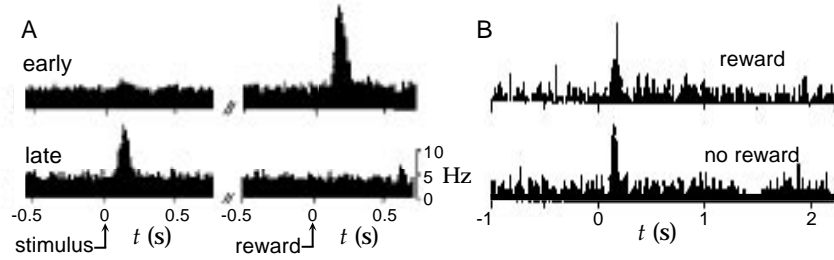


Figure 9.3: Activity of dopaminergic neurons in the VTA for a monkey performing a reaction time task. A) Histograms show the number of spikes per second for various time bins accumulated across trials and either time-locked to the light stimulus (left panels) or the reward (right panels) at the time marked zero. The top row is for early trials before the behavior is established. The bottom row is for late trials, when the monkey expects the reward on the basis of the light. B) Activity of dopamine neurons with and without reward delivery. The top row shows the normal behavior of the cells when reward is delivered. The bottom row shows the result of not delivering an expected reward. The basal firing rate of dopamine cells is rather low, but the inhibition at the time the reward would have been given is evident. (Adapted from Schultz, 1998.)

after a moderate amount of training. Now, the cell responds to the light, but not to the reward. The responses show a distinct similarity to the plots of $\delta(t)$ in figure 9.2.

The similarity between the responses of the dopaminergic neurons and the quantity $\delta(t)$ suggests that their activity provides a prediction error for reward, i.e. an ongoing difference between the amount of reward that is delivered and the amount that is expected. Figure 9.3B provides further evidence for this interpretation. It shows the activity of dopamine cells in a similar task to that of figure 9.3A. The top row of this figure shows normal performance, and is just like the bottom row of figure 9.3A. The bottom row shows what happens when the monkey is expecting reward, but it is not delivered. In this case, the cell's activity is inhibited below baseline at just the time it would have been activated by the reward in the original trials. This is in agreement with the prediction error interpretation of this activity.

Something similar to the temporal difference learning rule could be realized in a neural system if the dopamine signal representing δ acts to gate and regulate the plasticity associated with learning. We discuss this possibility further in a later section.

9.3 Static Action Choice

In classical conditioning experiments, rewards are directly associated with stimuli. In more natural settings, rewards and punishments are associated

with the actions an animal takes. Animals develop policies, or plans of action, that increase reward. In studying how this might be done, we consider two different cases. In static action choice, the reward or punishment immediately follows the action taken. In sequential action choice, reward may be delayed until several actions are completed.

As an example of static action choice, we consider bees foraging among flowers in search of nectar. We model an experiment in which single bees forage under controlled conditions among blue and yellow colored artificial flowers (small dishes of sugar water sitting on colored cards). In actual experiments, the bees learn within a single session (involving visits to 40 artificial flowers) about the reward characteristics of the yellow and blue flowers. All else being equal, they preferentially land on the color of flower that delivers more reward. This preference is maintained over multiple sessions. However, if the reward characteristics of the flowers are interchanged, the bees quickly swap their preferences.

We treat a simplified version of the problem, ignoring the spatial aspects of sampling, and assuming that a model bee is faced with repeated choices between two different flowers. If the bee chooses the blue flower on a trial, it receives a quantity of nectar r_b drawn from a probability density $p[r_b]$. If it chooses the yellow flower, it receives a quantity r_y , drawn from a probability density $p[r_y]$. The task of choosing between the flowers is a form of stochastic two-armed bandit problem (named after slot machines), and is formally equivalent to many instrumental conditioning tasks.

The model bee has a stochastic policy, which means that it chooses blue and yellow flowers with probabilities that we write as $P[b]$ and $P[y]$ respectively. A convenient way to parameterize these probabilities is to use the softmax distribution

$$P[b] = \frac{\exp(\beta m_b)}{\exp(\beta m_b) + \exp(\beta m_y)} \quad P[y] = \frac{\exp(\beta m_y)}{\exp(\beta m_b) + \exp(\beta m_y)} \quad (9.11)$$

Here, m_b and m_y are parameters, known as action values, that are adjusted by one of the learning processes described below. Note that $P[b] + P[y] = 1$, corresponding to the fact that the model bee invariably makes one of the two choices. Note that $P[b] = \sigma(\beta(m_b - m_y))$ where $\sigma(m) = 1/(1 + \exp(-m))$ is the standard sigmoid function, which grows monotonically from zero to one as m varies from $-\infty$ to ∞ . $P[y]$ is similarly a sigmoid function of $\beta(m_y - m_b)$. The parameters m_b and m_y determine the frequency at which blue and yellow flowers are visited. Their values must be adjusted during the learning process on the basis of the reward provided.

The parameter β determines the variability of the bee's actions and exerts a strong influence over exploration. For large β , the probability of an action rises rapidly to one, or falls rapidly to zero, as the difference between the action values increases or decreases. This makes the bee's action choice almost a deterministic function of the m variables. If β is small, the

policy

foraging

two-armed bandit

stochastic policy

softmax

action values m

exploration-exploitation dilemma

action value vector \mathbf{m}

softmax probability approaches one or zero more slowly, and the bee's actions are more variable and random. Thus, β controls the balance between exploration (small β) and exploitation (large β). The choice of whether to explore to determine if the current policy can be improved, or to exploit the available resources on the basis of the current policy, is known as the exploration-exploitation dilemma. Exploration is clearly critical, because the bee must sample from the two colors of flowers to determine which is better, and keep sampling to make sure that the reward conditions have not changed. But exploration is costly, because the bee has to sample flower it believes to be less beneficial, to check if this is really the case. Some algorithms adjust β over trials, but we will not consider this possibility.

There are only two possible actions in the example we study, but the extension to multiple actions, $a = 1, 2, \dots, N_a$, is straightforward. In this case, a vector \mathbf{m} of parameters controls the decision process, and the probability $P[a]$ of choosing action a is

$$P[a] = \frac{\exp(\beta m_a)}{\sum_{a'=1}^{N_a} \exp(\beta m_{a'})}. \quad (9.12)$$

We consider two simple methods of solving the bee foraging task. In the first method, called the indirect actor, the bee learns to estimate the expected nectar volumes provided by each flower using a delta rule. It then bases its action choice on these estimates. In the second method, called the direct actor, the choice of actions is based directly on maximizing the expected average reward.

The Indirect Actor

indirect actor

One course for the bee to follow is to learn the average nectar volumes provided by each type of flower and base its action choice on these. This is called an indirect actor scheme, because the policy is mediated indirectly by the expected volumes. Here, this means setting the action values to

$$m_b = \langle r_b \rangle \quad \text{and} \quad m_y = \langle r_y \rangle. \quad (9.13)$$

In our discussion of classical conditioning, we saw that the Rescorla-Wagner or delta rule develops weights that approximate the average value of a reward, just as required for equation 9.13. Thus if the bee chooses a blue flower on a trial and receives nectar volume r_b , it should update m_b according to the prediction error by

$$m_b \rightarrow m_b + \epsilon \delta \quad \text{with} \quad \delta = r_b - m_b, \quad (9.14)$$

and leave m_y unchanged. If it lands on a yellow flower, m_y is changed to $m_y + \epsilon \delta$ with $\delta = r_y - m_y$, and m_b is unchanged. If the probability densities

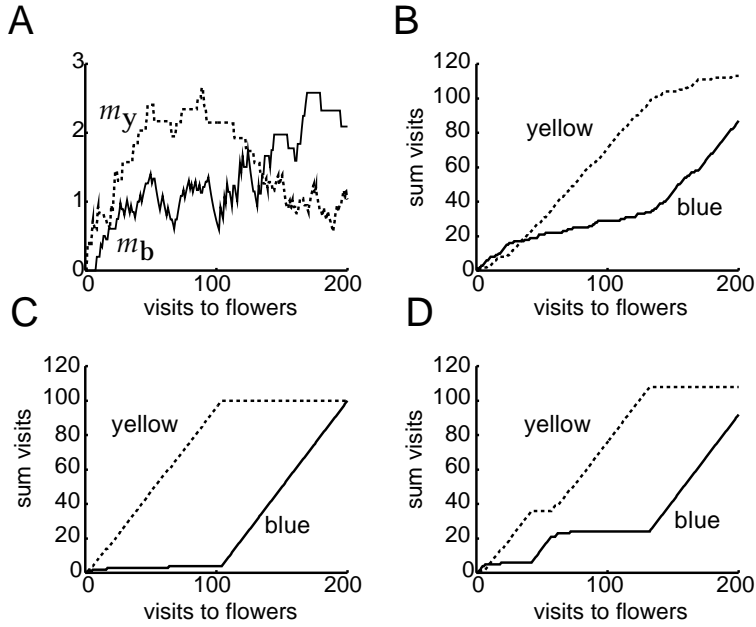


Figure 9.4: The indirect actor. Rewards were $\langle r_b \rangle = 1$, $\langle r_y \rangle = 2$ for the first 100 flower visits, and $\langle r_b \rangle = 2$, $\langle r_y \rangle = 1$ for the second 100 flower visits. Nectar was delivered stochastically on half the flowers of each type. A) Values of m_b (solid) and m_y (dashed) as a function of visits for $\beta = 1$. Because a fixed value of $\epsilon = 0.1$ was used, the weights do not converge perfectly to the corresponding average reward, but they fluctuates around these values. B-D) Cumulative visits to blue (solid) and yellow (dashed) flowers. B) When $\beta = 1$, learning is slow, but ultimately the change to the optimal flower color is made reliably. C;D) When $\beta = 50$, sometimes the bee performs well (C), and other times it performs poorly (D).

of reward $p[r_b]$ and $p[r_y]$ change slowly relative to the learning rate, m_b and m_y will track $\langle r_b \rangle$ and $\langle r_y \rangle$ respectively.

Figure 9.4 shows the performance of the indirect actor on the two-flower foraging task. Figure 9.4A shows the course of weight change due to the delta rule in one example run. Figures 9.4B-D indicate the quality of the action choice by showing cumulative sums of the number of visits to blue and yellow flowers in three different runs. For ideal performance in this task, the dashed line should have slope 1 until trial 100 and 0 thereafter, and the solid line would show the reverse behavior, close to what is seen in figure 9.4C. This reflects the consistent choice of the optimal flower in both halves of the trial. A value of $\beta = 1$ (figure 9.4B) allows for continuous exploration, but at the cost of slow learning. When $\beta = 50$ (figure 9.4C & D), the tendency to exploit sometimes leads to good performance (figure 9.4C), but other times, the associated reluctance to explore causes the policy to perform poorly (figure 9.4D).

Figure 9.5A shows action choices of real bumble bees in a foraging exper-

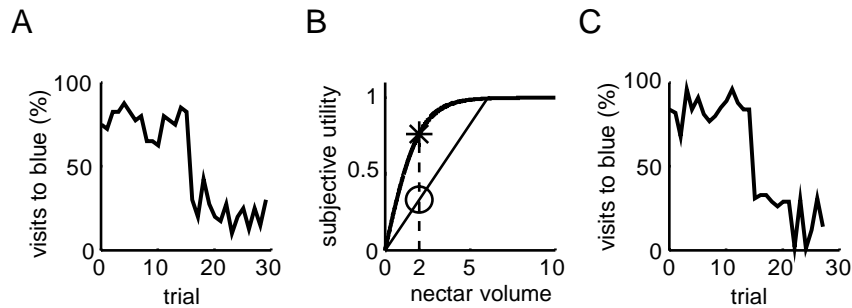


Figure 9.5: Foraging in bumble bees. A) The mean preference of five real bumble bees for blue flowers over 30 trials involving 40 flower visits. There is a rapid switch of flower preference following the interchange of characteristics after trial 15. Here, $\epsilon = 3/10$ and $\beta = 23/8$. B) Concave subjective utility function mapping nectar volume (in μl) to the subjective utility. The circle shows the average utility of the variable flowers, and the star shows the utility of the constant flowers. C) The preference of a single model bee on the same task as the bumble bees. (Data in A from Real, 1991; B & C adapted from Montague et al., 1995.)

iment. This experiment was designed to test risk aversion in the bees, so the blue and yellow flowers differed in the reliability rather than the quantity of their nectar delivery. For the first 15 trials (each involving 40 visits to flowers), blue flowers always provided $2 \mu\text{l}$ of nectar, whereas $\frac{1}{3}$ of the yellow flowers provided $6 \mu\text{l}$, and $\frac{2}{3}$ provided nothing (note that the mean reward is the same for the two flower types). Between trials 15 and 16, the delivery characteristics of the flowers were swapped. Figure 9.5A shows the average performance of five bees on this task in terms of their percentage visits to the blue flowers across trials. They exhibit a strong preference for the constant flower type and switch this preference within only a few visits to the flowers when the contingencies change.

To apply the foraging model we have been discussing to the experiment shown in figure 9.5A, we need to model the risk avoidance exhibited by the bees, that is, their reluctance to choose the unreliable flower. One way to do this is to assume that the bees base their policy on the subjective utility function of the nectar volume shown in figure 9.5B, rather than on the nectar volume itself. Because the function is concave, the mean utility of the unreliable flowers is less than that of the reliable flowers. Figure 9.5C shows that the choices of the model bee match quite well those of the real bees. The model bee is less variable than the actual bees (even more than it appears, because the curve in 9.5A is averaged over five bees), perhaps because the model bees are not sampling from a two-dimensional array of flowers.

subjective utility

The Direct Actor

An alternative to basing action choice on average rewards is to choose action values directly to maximize the average expected reward. The expected reward per trial is given in terms of the action values and average rewards per flower by

$$\langle r \rangle = P[b]\langle r_b \rangle + P[y]\langle r_y \rangle. \quad (9.15)$$

This can be maximized by stochastic gradient ascent. To see how this is done, we take the derivative of $\langle r \rangle$ with respect to m_b ,

$$\frac{\partial \langle r \rangle}{\partial m_b} = \beta (P[b]P[y]\langle r_b \rangle - P[y]P[b]\langle r_y \rangle). \quad (9.16)$$

In deriving this result, we have used the fact that

$$\frac{\partial P[b]}{\partial m_b} = \beta P[b]P[y] \quad \text{and} \quad \frac{\partial P[y]}{\partial m_b} = -\beta P[y]P[b]. \quad (9.17)$$

Using the relation $P[y] = 1 - P[b]$, we can rewrite equation 9.16 as

$$\frac{\partial \langle r \rangle}{\partial m_b} = \beta P[b](1 - P[b])\langle r_b \rangle - \beta P[y]P[b]\langle r_y \rangle. \quad (9.18)$$

Furthermore, we can include an arbitrary parameter \bar{r} in both these terms, because it cancels out. Thus,

$$\frac{\partial \langle r \rangle}{\partial m_b} = \beta P[b](1 - P[b])(\langle r_b \rangle - \bar{r}) - \beta P[y]P[b](\langle r_y \rangle - \bar{r}). \quad (9.19)$$

A similar expression applies to $\partial \langle r \rangle / \partial m_y$ except that the blue and yellow labels are interchanged.

In stochastic gradient ascent, the changes in the parameter m_b are determined such that, averaged over trials, they end up proportional to $\partial \langle r \rangle / \partial m_b$. We can derive a stochastic gradient ascent rule for m_b from equation 9.19 in two steps. First, we interpret the two terms on the right hand side as changes associated with the choice of blue and yellow flowers respectively. This accounts for the factors $P[b]$ and $P[y]$ respectively. Second, we note that over trials in which blue is selected, $r_b - \bar{r}$ averages to $\langle r_b \rangle - \bar{r}$, and over trials in which yellow is selected, $r_y - \bar{r}$ averages to $\langle r_y \rangle - \bar{r}$. Thus, if we change m_b according to

$$\begin{aligned} m_b &\rightarrow m_b + \epsilon(1 - P[b])(r_b - \bar{r}) && \text{if b is selected} \\ m_b &\rightarrow m_b - \epsilon P[b](r_y - \bar{r}) && \text{if y is selected,} \end{aligned}$$

the average change in m_b is proportional to $\partial \langle r \rangle / \partial m_b$. Note that m_b is changed even when the bee chooses the yellow flower. We can summarize this learning rule as

$$m_b \rightarrow m_b + \epsilon(\delta_{ab} - P[b])(r_a - \bar{r}) \quad (9.20)$$

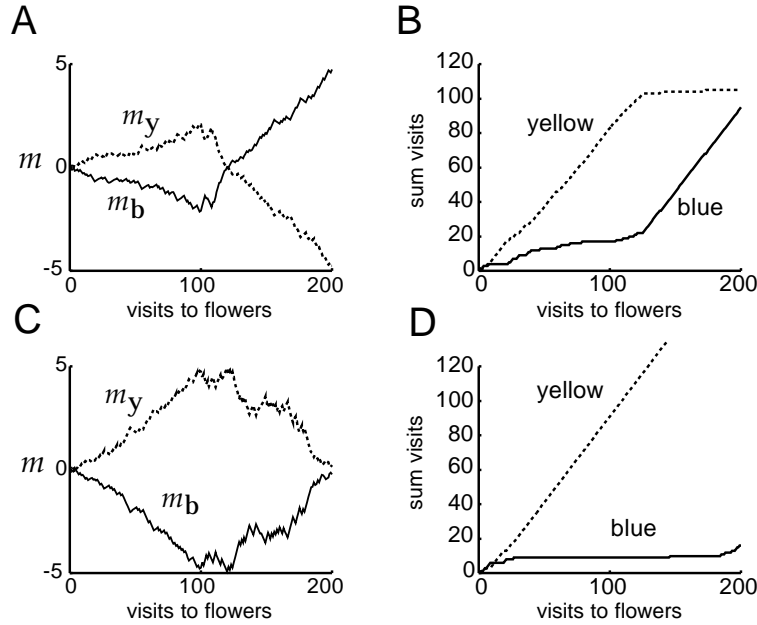


Figure 9.6: The direct actor. The statistics of the delivery of reward are the same as in figure 9.4, and $\epsilon = 0.1$, $\bar{r} = 1.5$, and $\beta = 1$. The evolution of the weights and cumulative choices of flower type (with yellow dashed and blue solid) are shown for two sample sessions, one with good performance (A & B) and one with poor performance (C & D).

where a is the action selected (either b or y) and δ_{ab} is the Kronecker delta, $\delta_{ab} = 1$ if $a = b$ and $\delta_{ab} = 0$ if $a = y$. Similarly, the rule for m_y is

$$m_y \rightarrow m_y + \epsilon(\delta_{ay} - P[y])(r_a - \bar{r}) \quad (9.21)$$

The learning rule of equations 9.20 and 9.21 performs stochastic gradient ascent on the average reward, whatever the value of \bar{r} . Different values of \bar{r} lead to different variances of the stochastic gradient terms, and thus different speeds of learning. A natural value for \bar{r} is the mean reward under the specified policy or some estimate of this quantity.

Figure 9.6 shows the consequences of using the direct actor in the stochastic foraging task shown figure 9.4. Two sample sessions are shown with widely differing levels of performance. Compared to the indirect actor, initial learning is quite slow, and the behavior after the reward characteristics of the flowers are interchanged can be poor. Explicit control of the trade-off between exploration and exploitation is difficult, because the action values can scale up to compensate for different values of β . Despite its comparatively poor performance in this task, the direct actor is important because it is used later as a model for how action choice can be separated from action evaluation.

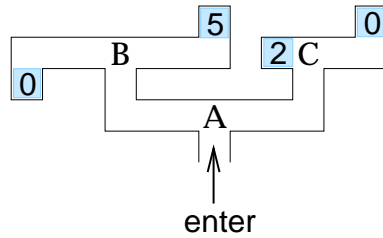


Figure 9.7: The maze task. The rat enters the maze from the bottom and has to move forward. Upon reaching one of the end points (the shaded boxes), it receives the number of food pellets indicated and the trial ends. Decision points are A, B, and C.

The direct actor learning rule can be extended to multiple actions, $a = 1, 2, \dots, N_a$, by using the multidimensional form of the softmax distribution (equation 9.12). In this case, when action a is taken, $m_{a'}$ for all values of a' is updated according to

$$m_{a'} \rightarrow m_{a'} + \epsilon (\delta_{aa'} - P[a']) (r_a - \bar{r}). \quad (9.22)$$

9.4 Sequential Action Choice

In the previous section, we considered ways that animals might learn to choose actions on the basis of immediate information about the consequences of those actions. A significant complication that arises when reward is based on a sequence of actions is illustrated by the maze task shown in figure 9.7. In this example, a hungry rat has to move through a maze, starting from point A, without retracing its steps. When it reaches one of the shaded boxes, it receives the associated number of food pellets and is removed from the maze. The rat then starts again at A. The task is to optimize the total reward, which in this case entails moving left at A and right at B. It is assumed that the animal starts knowing nothing about the structure of the maze or about the rewards.

If the rat started from point B or point C, it could learn to move right or left (respectively) using the methods of the previous section, because it experiences an immediate consequence of its actions in the delivery or non-delivery of food. The difficulty arises because neither action at the actual starting point, A, leads directly to a reward. For example, if the rat goes left at A and also goes left at B, it has to figure out that the former choice was good but the latter bad. This is a typical problem in tasks that involve delayed rewards. The reward for going left at A is delayed until after the rat also goes right at B.

There is an extensive body of theory in engineering, called dynamic programming, as to how systems of any sort can come to select appro-

*dynamic
programming*

policy iteration

priate actions in optimizing control problems similar to (and substantially more complicated than) the maze task. An important method on which we focus is called policy iteration. Our reinforcement learning version of policy iteration maintains and improves a stochastic policy, which determines the actions at each decision point (i.e. left or right turns at A, B, or C) through action values and the softmax distribution of equation 9.12. Policy iteration involves two elements. One, called the critic, uses temporal difference learning to estimate the total future reward that is expected when starting from A, B, or C, when the current policy is followed. The other element, called the actor, maintains and improves the policy. Adjustment of the action values at point A is based on predictions of the expected future rewards associated with points B and C that are provided by the critic. In effect, the rat learns the appropriate action at A using the same methods of static action choice that allow it to learn the appropriate actions at B and C. However, rather than using an immediate reward as the reinforcement signal, it uses the expectations about future reward that are provided by the critic.

critic

actor

The Maze Task

As we mentioned when discussing the direct actor, a stochastic policy is a way of assigning a probability distribution over actions (in this case choosing to turn either left or right) to each location (A, B, or C). The location is specified by a variable u that takes the values A, B, or C, and a two-component action value vector $\mathbf{m}(u)$ is associated with each location. The components of the action vector $\mathbf{m}(u)$ control the probability of taking a left or a right turn at u .

The immediate reward provided when action a is taken at location u is written as $r_a(u)$. This takes the values 0, 2, or 5 depending on the values of u and a . The predicted future reward expected at location u is given by $v(u) = w(u)$. This is an estimate of the total award that the rat expects to receive, on average, if it starts at the point u and follows its current policy through to the end of the maze. The average is taken over the stochastic choices of actions specified by the policy. In this case, the expected reward is simply equal to the weight. The learning procedure consists of two separate steps: policy evaluation, in which $w(u)$ is adjusted to improve the predictions of future reward, and policy improvement, in which $\mathbf{m}(u)$ is adjusted to increase the total reward.

Policy Evaluation

In policy evaluation, the rat keeps its policy fixed (i.e. keeps all the $\mathbf{m}(u)$ fixed) and uses temporal difference learning to determine the expected total future reward starting from each location. Suppose that, initially, the rat has no preference for turning left or right, that is, $\mathbf{m}(u) = 0$ for all u , so

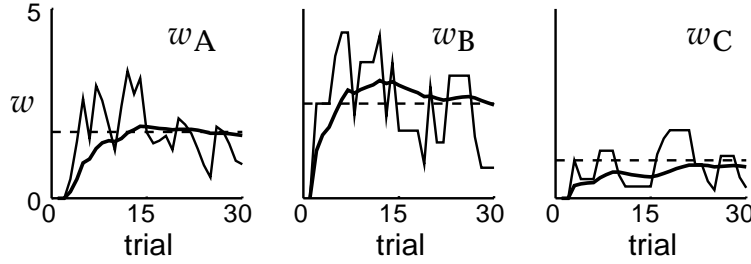


Figure 9.8: Policy evaluation. The thin lines show the course of learning of the weights $w(A)$, $w(B)$ and $w(C)$ over trials through the maze in figure 9.7 using a random unbiased policy ($m(u) = 0$). Here $\epsilon = 0.5$, so learning is fast but noisy. The dashed lines show the correct weight values from equation 9.23. The thick lines are running averages of the weight values.

the probability of left and right turns is $1/2$ at all locations. By inspection of the possible places the rat can go, we find that the values of the states are

$$\begin{aligned} v(B) &= \frac{1}{2}(0 + 5) = 2.5, & v(C) &= \frac{1}{2}(0 + 2) = 1, & \text{and} \\ v(A) &= \frac{1}{2}(v(B) + v(C)) = 1.75. \end{aligned} \quad (9.23)$$

These values are the average total future rewards that will be received during exploration of the maze when actions are chosen using the random policy. The temporal difference learning rule of equation 9.10 can be used to learn them. If the rat chooses action a at location u and ends up at location u' , the temporal difference rule modifies the weight $w(u)$ by

critic learning rule

$$w(u) \rightarrow w(u) + \epsilon \delta \quad \text{with} \quad \delta = r_a(u) + v(u') - v(u). \quad (9.24)$$

Here, a location index u substitutes for the time index t , and we only associate a single weight $w(u)$ with each state rather than a whole temporal kernel (this is equivalent to only using $\tau=0$ in equation 9.10). Figure 9.8 shows the result of applying the temporal difference rule to the maze task of figure 9.7. After a fairly short adjustment period, the weights $w(u)$ (and thus the predictions $v(u)$) fluctuate around the correct values for this policy, as given by equation 9.23. The size of the fluctuations could be reduced by making ϵ smaller, but at the expense of increasing the learning time.

In our earlier description of temporal difference learning, we included the possibility that the reward delivery might be stochastic. Here, that stochasticity is the result of a policy that makes use of the information provided by the critic. In the appendix, we discuss a Monte-Carlo interpretation of the terms in the temporal difference learning rule that justifies using its use.

Policy Improvement

In policy improvement, the expected total future rewards at the different locations are used as surrogate immediate rewards. Suppose the rat takes action a at location u and moves to location u' . The expected worth to the rat of that action is the sum of the actual reward received and the rewards that are expected to follow, which is $r_a(u) + v(u')$. The direct actor scheme of equation 9.22 uses the difference $r_a - \bar{r}$ between a sample of the worth of the action (r_a) and a reinforcement comparison term (\bar{r}), which might be the average value over all the actions that can be taken. Policy improvement uses $r_a(u) + v(u')$ as the equivalent of the sampled worth of the action, and $v(u)$ as the average value across all actions that can be taken at u . The difference between these is $\delta = r_a(u) + v(u') - v(u)$, which is exactly the same term as in policy evaluation (equation 9.24). The policy improvement or actor learning rule is then

$$m_{a'}(u) \rightarrow m_{a'}(u) + \epsilon (\delta_{aa'} - P[a'; u]) \delta \quad (9.25)$$

for all a' , where $P[a'; u]$ is the probability of taking action a' at location u given by the softmax distribution of equation 9.11 or 9.12 with action value $m_{a'}(u)$.

To look at this more concretely, consider the temporal difference error starting from location $u=A$, using the true values of the locations given by equation 9.23 (i.e. assuming that policy evaluation is perfect). Depending on the action, δ takes the two values

$$\begin{aligned} \delta &= 0 + v(B) - v(A) = 0.75 && \text{for a left turn} \\ \delta &= 0 + v(C) - v(A) = -0.75 && \text{for a right turn.} \end{aligned}$$

The learning rule of equation 9.25 increases the probability that the action with $\delta > 0$ is taken and decreases the probability that the action with $\delta < 0$ is taken. This increases the chance that the rat makes the correct turn (left) at A in the maze of figure 9.7.

As the policy changes, the values, and therefore the temporal difference terms, change as well. However, because the values of all locations can only increase if we choose better actions at those locations, this form of policy improvement inevitably leads to higher values and better actions. This monotonic improvement (or at least non-worsening) of the expected future rewards at all locations is proved formally in the dynamic programming theory of policy iteration for a class of problems called Markov decision problems (which includes the maze task), as discussed in the appendix.

Strictly speaking, policy evaluation should be complete before a policy is improved. It is also most straightforward to improve the policy completely before it is re-evaluated. A convenient (though not provably correct) alternative is to interleave partial policy evaluation and policy improvement steps. This is called the actor-critic algorithm. Figure 9.9 shows

Markov decision problems

actor-critic algorithm

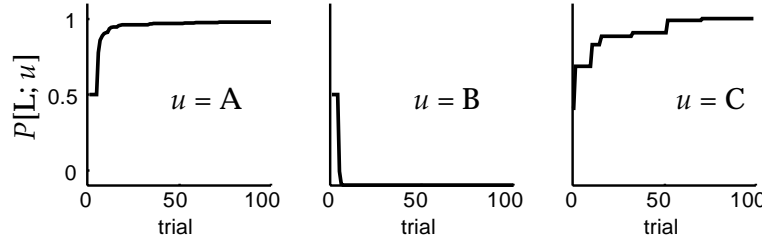


Figure 9.9: Actor-critic learning. The three curves show $P[L; u]$ for the three starting locations $u = A, B$, and C in the maze of figure 9.7. These rapidly converge to their optimal values, representing left turns and A and C and a right turn at B . Here, $\epsilon = 0.5$ and $\beta = 1$.

the result of applying this algorithm to the maze task. The plots show the development over trials of the probability of choosing to go left, $P[L; u]$, for all the three locations. The model rat quickly learns to go left at location A and right at B . Learning at location C is slow because the rat learns quickly that it is not worth going to C at all, so it rarely gets to try the actions there. The algorithm makes an implicit choice of exploration strategy.

Generalizations of Actor-Critic Learning

The full actor-critic model for solving sequential action tasks includes three generalizations of the maze learner that we have presented. The first involves additional information that may be available at the different locations. If, for example, sensory information is available at a location u , we associate a state vector $\mathbf{u}(u)$ with that location. The vector $\mathbf{u}(u)$ parameterizes whatever information is available at location u that might help the animal decide which action to take. For example, the state vector might represent a faint scent of food that the rat might detect in the maze task. When a state vector is available, the most straightforward generalization is to use the linear form $v(u) = \mathbf{w} \cdot \mathbf{u}(u)$ to define the value at location u . The learning rule for the critic (equation 9.24) is then generalized to include the information provided by the state vector,

$$\mathbf{w} \rightarrow \mathbf{w} + \epsilon \delta \mathbf{u}(u), \quad (9.26)$$

with δ given as in equation 9.24. The maze task we discussed could be formulated in this way using what is called a unary representation, $\mathbf{u}(A) = (1, 0, 0)$, $\mathbf{u}(B) = (0, 1, 0)$, and $\mathbf{u}(C) = (0, 0, 1)$.

state vector \mathbf{u}

unary representation

We must also modify the actor learning rule to make use of the information provided by the state vector. This is done by generalizing the action value vector \mathbf{m} to a matrix \mathbf{M} , called an action matrix. \mathbf{M} has as many columns as there are components of \mathbf{u} and as many rows as there are actions. Given input \mathbf{u} , action a is chosen at location u with the softmax probability of

action matrix \mathbf{M}

equation 9.12, but using component a of the action value vector

$$\mathbf{m} = \mathbf{M} \cdot \mathbf{u}(u) \quad \text{or} \quad m_a = \sum_b M_{ab} u_b(u). \quad (9.27)$$

In this case, the learning rule 9.25 must be generalized to specify how to change elements of the action matrix when action a is chosen at location u with state vector $\mathbf{u}(u)$, leading to location u' . A rule similar to equation 9.25 is appropriate, except that the change in \mathbf{M} depends on the state vector \mathbf{u} ,

$$M_{a'b} \rightarrow M_{a'b} + \epsilon (\delta_{aa'} - P[a'; u]) \delta u_b(u) \quad (9.28)$$

for all a' , with δ given again as in equation 9.24. This is called a three-term covariance learning rule.

We can speculate about the biophysical significance of the three-term covariance rule by interpreting $\delta_{aa'}$ as the output of cell a' when action a is chosen (which has mean value is $P[a'; u]$) and interpreting \mathbf{u} as the input to that cell. Compared with the Hebbian covariance rules studied in chapter 8, learning is gated by a third term, the reinforcement signal δ . It has been suggested that the dorsal striatum, which is part of the basal ganglia, is involved in the selection and sequencing of actions. Terminals of axons projecting from the substantia nigra pars compacta release dopamine onto synapses within the striatum, suggesting that they might play such a gating role. The activity of these dopamine neurons is similar to that of the VTA neurons discussed previously as a possible substrate for δ .

The second generalization is to the case that rewards and punishments received soon after an action are more important than rewards and punishments received later. One natural way to accommodate this is a technique called exponential discounting. In computing the expected future reward, this amounts to multiplying a reward that will be received τ time steps after a given action by a factor γ^τ , where $0 \leq \gamma \leq 1$ is the discounting factor. The smaller γ , the stronger the effect, i.e. the less important are temporally distant rewards. Discounting has a major influence on the optimal behavior in problems for which there are many steps to a goal. Exponential discounting can be accommodated within the temporal difference framework by changing the prediction error δ to

$$\delta = r_a(u) + \gamma v(u') - v(u), \quad (9.29)$$

which is then used in the learning rules of equations 9.26 and 9.28.

In computing the amount to change a weight or action value, we defined the worth of an action as the sum of the immediate reward delivered and the estimate of the future reward arising from the next state. A final generalization of actor-critic learning comes from basing the learning rules on the sum of the next two immediate rewards delivered and the estimate of the future reward from the next state but one, or the next three immediate rewards and the estimate from the next state but two, and so on. As in

three-term covariance rule

*dorsal striatum
basal ganglia*

discounting

discounting, we can use a factor λ to weight how strongly the expected future rewards from temporally distant points in the trial affect learning. Suppose that $\mathbf{u}(t) = \mathbf{u}(u(t))$ is the state vector used at time step t of a trial. Such generalized temporal difference learning can be achieved by computing new state vectors, defined by the recursive relation

$$\tilde{\mathbf{u}}(t) = \tilde{\mathbf{u}}(t-1) + (1 - \lambda)(\mathbf{u}(t) - \tilde{\mathbf{u}}(t-1)) \quad (9.30)$$

and using them instead of the original state vectors \mathbf{u} in equations 9.26 and 9.28. The resulting learning rule is called the $TD(\lambda)$ rule. Use of this rule with an appropriate value of λ can significantly speed up learning.

TD(λ) rule

Learning the Water Maze

As an example of generalized reinforcement learning, we consider the water maze task. This is a navigation problem in which rats are placed in a large pool of milky water and have to swim around until they find a small platform that is submerged slightly below the surface of the water. The opaqueness of the water prevents them from seeing the platform directly, and their natural aversion to water (although they are competent swimmers) motivates them to find the platform. After several trials, the rats learn the location of the platform and swim directly to it when placed in the water.

Figure 9.10A shows the structure of the model, with the state vector \mathbf{u} providing input to the critic and a collection of 8 possible actions for the actor, which are expressed as compass directions. The components of \mathbf{u} represent the activity of hippocampal place cells (which are discussed in chapter 1). Figure 9.10B shows the activation of one of the input units as a function of spatial position in the pool. The activity, like that of a place cell, is spatially restricted.

During training, each trial consists of starting the model rat from a random location at the outside of the maze and letting it run until it finds the platform indicated by a small circle in the lower part of figure 9.10C. At that point a reward of 1 is provided. The reward is discounted with $\gamma = 0.9975$ to model the incentive for the rat to find the goal as quickly as possible. Figure 9.10C indicates the course of learning (trials 1, 5 and 20) of the expected future reward as a function of location (upper figures) and the policy (lower figures with arrows). The lower figures also show sample paths taken by the rat (lower figures with wiggly lines). The final value function (at trial 20) is rather inaccurate, but, nevertheless, the policy learned is broadly correct, and the paths to the platform are quite short and direct.

Judged by measures such as path length, initial learning proceeds in the model in a manner comparable to that of actual rats. Figure 9.11A shows the average performance of 12 real rats in running the water maze on four

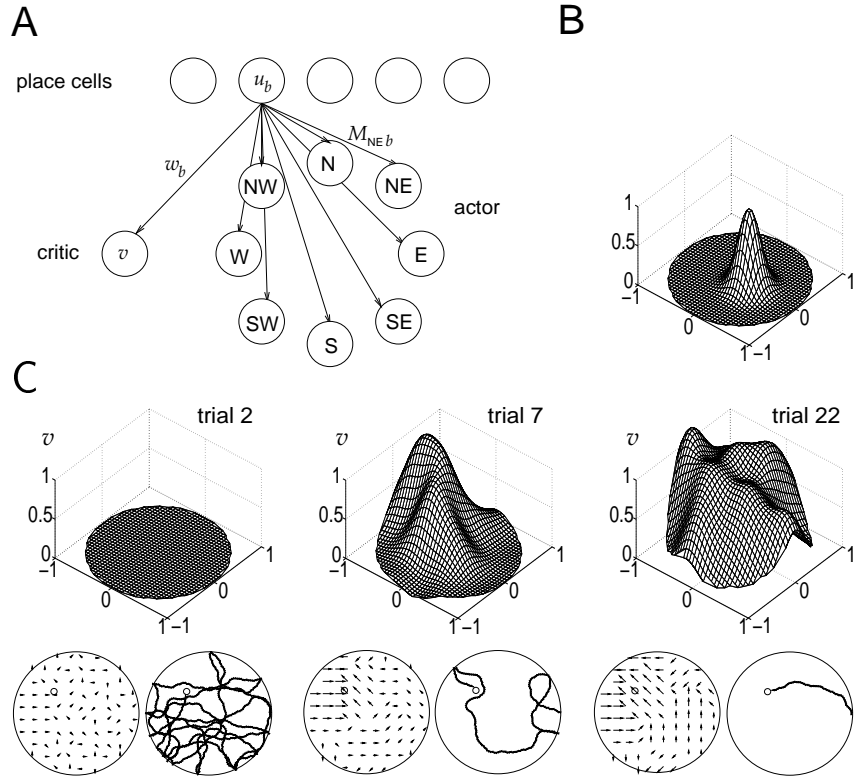


Figure 9.10: Reinforcement learning model of a rat solving a simple water maze task in a 2 m diameter circular pool. A) There are 493 place cell inputs and 8 actions. The rat moves at 0.3 m/s and reflects off the walls of the maze if it hits them. B) Gaussian place field for a single input cell with width $\sigma = 0.16$ m. The centers of the place fields for different cells are uniformly distributed across the pool. C) Upper: The development of the value function v as a function of the location in the pool over the first 20 trials, starting from $v=0$ everywhere. Lower arrow plots: The action with the highest probability for each location in the maze. Lower path plots: Actual paths taken by the model rat from random starting points to the platform, indicated by a small circle. A slight modification of the actor learning rule was used to enforce generalization between spatially similar actions. (Adapted from Foster et al., 2000.)

trials per day to a platform at a fixed location, starting from randomly chosen initial locations. The performance of the rats rapidly improves and levels off by about the sixth day. When the platform is moved on the eighth day, in what is called reversal training, the initial latency is long, because the rats search near the old platform position. However, they rapidly learn the new location. Figure 9.11B shows the performance of the model on the same task (though judged by path lengths rather than latencies). Initial learning is equally quick, with near perfect paths by the sixth day. However, performance during reversal training is poor, because the model has trouble forgetting the previous location of the platform. The rats are

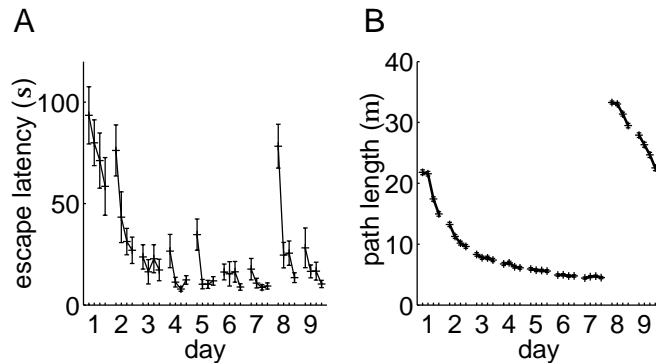


Figure 9.11: Comparison of rats and the model in the water maze task. A) Average latencies of 12 rats in getting to a fixed platform in the water maze, using four trials per day. On the 8th day, the platform was moved to a new location, which is called reversal. B) Average path length from 1000 simulations of the model performing the same task. Initial learning matches that of the rats, but performance is worse following reversal. (Adapted from Foster et al., 2000.)

clearly better at handling this transition. Nevertheless the model shows something of the power of a primitive, but general, learning method.

9.5 Chapter Summary

We discussed reinforcement learning models for classical and instrumental conditioning, interpreting the former in terms of learning predictions about total future rewards and the latter in terms of optimization of those rewards. We introduced the Rescorla-Wagner or delta learning rule for classical conditioning, together with its temporal difference extension, and indirect and direct actor rules for instrumental conditioning given immediate rewards. Finally, we presented the actor-critic version of the dynamic programming technique of policy iteration, evaluating policies using temporal difference learning and improving them using the direct actor learning rule, based on surrogate immediate rewards from the evaluation step. In the appendix, we show more precisely how temporal difference learning can be seen as a Monte-Carlo technique for performing policy iteration.

Appendix

Markov Decision Problems

Markov decision problems offer a simple formalism for describing tasks such as the maze. A Markov decision problem is comprised of states, ac-

absorbing state

Markov property

tions, transitions, and rewards. The states, labeled by u , are what we called locations in the maze task, and the actions, labeled by a , are the analogs of the choices of directions to run. In the maze, each action taken at state u led uniquely and deterministically to a new state u' . Markov decision problems generalize this to include the possibility that the transitions from u due to action a may be stochastic, leading to state u' with a transition probability $P[u'|u; a]$. $\sum_{u'} P[u'|u; a] = 1$ for all u and a , because the animal has to end up somewhere. There can be absorbing states (like the shaded boxes in figure 9.7), which are u for which $P[u|u; a] = 1$ for all actions a , i.e. there is no escape for the animal from these locations. Finally, the rewards r can depend both on the state u and the action executed a , and they might be stochastic. We write $\langle r_a(u) \rangle$ for the mean reward in this case. For convenience, we only consider Markov chains that are finite (finite numbers of actions and states), absorbing, (the animal always ends up in one of the absorbing states), and in which the rewards are bounded. We also require that $\langle r_a(u) \rangle = 0$ for all actions a at all absorbing states. The crucial Markov property is that, given the state at the current time step, the distribution over future states and rewards is independent of the past states.

The Bellman Equation

The task for a system or animal facing a Markov decision problem, starting in state u at time 0, is to choose a policy, denoted by M , that maximizes the expected total future reward

$$v^*(u) = \max_M \left\langle \sum_{t=0}^{\infty} r_{a(t)}(u(t)) \right\rangle_{u,M} \quad (9.31)$$

where $u(0) = u$, actions $a(t)$ are determined (either deterministically or stochastically) on the basis of the state $u(t)$ according to policy M , and the notation $\langle \cdot \rangle_{u,M}$ implies taking an expectation over the actions and the states to which they lead, starting at state u and using policy M .

The trouble with the sum in equation 9.31 is that the action $a(0)$ at time 0 affects not only $\langle r_{a(0)}(u(0)) \rangle$, but, by influencing the state of the system, also the subsequent rewards. It would seem that the animal would have to consider optimizing whole sequences of actions, the number of which grows exponentially with time. Bellman's (1957) insight was that the Markov property effectively solves this problem. He rewrote equation 9.31 to separate the first and subsequent terms, and used a recursive principle for the latter. The Bellman equation is

$$v^*(u) = \max_a \left\{ \langle r_a(u) \rangle + \sum_{u'} P[u'|u; a] v^*(u') \right\} \quad (9.32)$$

This says that maximizing reward at u requires choosing the action a that maximizes the sum of the mean immediate reward $\langle r_a(u) \rangle$ and the average of the largest possible values of all the states u' to which a can lead the system, weighted by their probabilities.

Policy Iteration

The actor-critic algorithm is a form of a dynamic programming technique called policy iteration. Policy iteration involves interleaved steps of policy evaluation (the role of the critic) and policy improvement (the role of the actor). Evaluation of policy M requires working out the values for all states u . We call these values $v^M(u)$, to reflect explicitly their dependence on the policy. Each value is analogous to the quantity in 9.5. Using the same argument that led to the Bellman equation, we can derive the recursive formula

$$v^M(u) = \sum_a P_M[a; u] \left\{ \langle r_a(u) \rangle + \sum_{u'} P[u'|u; a] v^M(u') \right\} \quad (9.33)$$

Equation 9.33 for all states u is a set of linear equations, that can be solved by matrix inversion. Reinforcement learning can be interpreted as a stochastic Monte-Carlo method for performing this operation (Barto and Duff, 1994).

Temporal difference learning uses an approximate Monte-Carlo method to evaluate the right side of equation 9.33, and uses the difference between this approximation and the estimate of $v^M(u)$ as the prediction error. The first idea underlying the method is that $r_a(u) + v^M(u')$ is a sample whose mean is exactly the right side of equation 9.33. The second idea is bootstrapping, using the current estimate $v(u')$ in place of $v^M(u')$ in this sample. Thus $r_a(u) + v(u')$ is used as a sampled approximation to $v^M(u)$, and

*Monte-Carlo
method*

$$\delta(t) = r_a(u) + v(u') - v(u) \quad (9.34)$$

is used as a sampled approximation to the discrepancy $v^M(u) - v(u)$ which is an appropriate error measure for training $v(u)$ to equal $v^M(u)$. Evaluating and improving policies from such samples without learning $P[u'|u; a]$ and $\langle r_a(u) \rangle$ directly is called an asynchronous, model-free, approach to policy evaluation. It is possible to guarantee the convergence of the estimate v to its true value v^M under a set of conditions discussed in the texts mentioned in the annotated bibliography.

The other half of policy iteration is policy improvement. This normally works by finding an action a^* that maximizes the expression in the curly brackets in equation 9.33 and making the new $P_M[a^*; u] = 1$. One can show that the new policy will be uniformly better than the old policy, making the expected long-term reward at every state no smaller than the old policy, or equally large, if it is already optimal. Further, because the number of different policies is finite, policy iteration is bound to converge.

Performing policy improvement like this requires knowledge of the transition probabilities and mean rewards. Reinforcement learning again uses an asynchronous, model-free approach to policy improvement, using Monte-Carlo samples. First, note that any policy M' that improves the

average value

$$\sum_a P_{\mathbf{M}'}[u; a] \left\{ \langle r_a(u) \rangle + \sum_{u'} P[u'|u; a] v^{\mathbf{M}'}(u') \right\}. \quad (9.35)$$

for every state u is guaranteed to be a better policy. The idea for a single state u is to treat equation 9.35 rather like equation 9.15, except replacing the average immediate reward $\langle r_a \rangle$ there by an effective average immediate reward $\langle r_a(u) \rangle + \sum_{u'} P[u'|u; a] v^{\mathbf{M}'}(u')$ to take long term as well as current reward into account. By the same reasoning as above, $r_a(u) + v(u')$ is used as an approximate Monte-Carlo sample of the effective immediate reward, and $v(u)$ as the equivalent of the reinforcement comparison term \bar{r} . This leads directly to the actor learning rule of equation 9.25.

Note that there is an interaction between the stochasticity in the reinforcement learning versions of policy evaluation and policy improvement. This means that it is not known whether the two together are guaranteed to converge. One could perform temporal difference policy evaluation (which can be proven to converge) until convergence before attempting policy improvement, and this would be sure to work.

9.6 Annotated Bibliography

Dickinson (1980); Mackintosh (1983); Shanks (1995) review animal and human conditioning behavior, including alternatives to Rescorla & Wagner's (1972) rule. **Gallistel (1990); Gallistel & Gibbon (2000)** discuss aspects of conditioning, in particular to do with timing, that we have omitted.

Our description of the temporal difference model of classical conditioning in this chapter is based on **Sutton (1988); Sutton & Barto (1990)**. The treatment of static action choice comes from **Narendra & Thatachar (1989)** and **Williams (1992)**, and of action choice in the face of delayed rewards and the link to dynamic programming from **Barto, Sutton & Anderson (1983); Watkins (1989); Barto, Sutton & Watkins (1989); Bertsekas & Tsitsiklis (1996); Sutton & Barto (1998)**. **Bertsekas & Tsitsiklis (1996); Sutton & Barto (1998)** describe some of the substantial theory of temporal difference learning that has been developed. Dynamic programming as a computational tool of ethology is elucidated by **Mangel & Clark (1988)**.

Schultz (1998) reviews the data on the activity of primate dopamine cells during appetitive conditioning tasks, together with the psychological and pharmacological rationale for studying these cells. The link with temporal difference learning was made by **Montague, Dayan & Sejnowski (1996); Friston et al. (1994); Houk et al. (1995)**. **Houk et al. (1995)** review the basal ganglia from a variety of perspectives. **Wickens (1993)** provides a theoretically motivated treatment. The model of **Montague et al. (1995)**

for Real's (1991) experiments in bumble bee foraging was based on Hammer's (1993) description of an octopaminergic neuron in honey bees that appears to play, for olfactory conditioning, a somewhat similar role to the primate dopaminergic cells.

The kernel representation of the weight between a stimulus and reward can be seen as a form of a serial compound stimulus (Kehoe, 1977) or a spectral timing model (Grossberg & Schmajuk, 1989). Grossberg and colleagues (see Grossberg, 1982, 1987 & 1988) have developed a sophisticated mathematical model of conditioning, including aspects of opponent processing (Konorski, 1967; Solomon & Corbit, 1974), which puts prediction of the absence of reward (or the presence of punishment) on a more equal footing with prediction of the presence of reward, and develops aspects of how animals pay differing amounts of attention to stimuli. There are many other biologically inspired models of conditioning, particularly of the cerebellum (e.g. Gluck et al., 1990; Gabriel & Moore, 1990; Raymond et al., 1996; Mauk & Donegan, 1997).

Chapter 10

Representational Learning

10.1 Introduction

The response selectivities of individual neurons, and the way they are distributed across neuronal populations, define how sensory information is represented by neural activity in a particular brain region. Sensory information is typically represented in multiple regions, the visual system being a prime example, with the nature of the representation shifting progressively along the sensory pathway. In previous chapters, we discuss how such representations can be generated by neural circuitry and developed by activity-dependent plasticity. In this chapter, we study neural representations from a computational perspective, asking what goals are served by particular representations and how appropriate representations might be developed on the basis of input statistics.

Constructing new representations of, or re-representing, sensory input is important because sensory receptors often deliver information in a form that is unsuitable for higher level cognitive tasks. For example, roughly 10^8 photoreceptors provide a pixelated description of the images that appear on our retinas. A list of the membrane potentials of each of these photoreceptors is a bulky and awkward representation of the visual world from which it is difficult to identify directly the underlying causes of visual images, such as the objects and people we typically see. Instead, the information provided by photoreceptor outputs is processed in a series of stages involving increasingly sophisticated representations of the visual world. In this chapter, we consider how to specify and learn these more complex and useful representations.

re-representation

The key to constructing useful representations lies in determining the structure of visual images and the constraints imposed on them by the natural world. Images have causes, such as objects with given locations, orientations, and scales, illuminated by particular lighting schemes, and

observed from particular viewing locations and directions. Because of this, the set of possible pixelated activities arising from natural scenes is richly structured. Sophisticated representations of images arise from ways of characterizing this structure.

In this chapter, we discuss one approach to identifying the structure in natural stimuli and using it as a basis for constructing useful and efficient representations. The basic goal in the models we discuss is to determine the causes that give rise to stimuli. These are assumed to be the sources of structure in the sensory input data. Causal representations are appropriate because inferences, decisions, and actions are typically based on underlying causes. In more abstract terms, causes are the natural coordinates for describing complex stimuli such as images. To account for the inevitable variability that arises when considering natural stimuli, many of the models we discuss are probabilistic, specifying the probabilities that various causes underlie particular stimuli.

Causal Models

Figure 10.1A provides a simple example of structured data that suggests underlying causes. In this case, each input is characterized by a two component vector $\mathbf{u} = (u_1, u_2)$. A collection of sample inputs that we wish to represent in terms of underlying causes is indicated by the 40 crosses in figure 10.1A. These inputs are drawn from a probability density $p[\mathbf{u}]$ that we call the input distribution. Clearly, there are two clusters of points in figure 10.1A, one centered near $(0, 1)$ and the other near $(1, 0)$. Many processes can generate such clustered data. For example, u_1 and u_2 might represent two characterizations of the voltage recorded on an extracellular electrode in response to an action potential. Interpreted in this way, these data suggest that we are looking at spikes produced by two neurons (called A and B), which are the underlying causes of the two clusters seen in figure 10.1A. A more compact and causal description of the data can be provided by a single output variable v that takes the value A or B for each data point, representing which of the two neurons was responsible for this input. The variable v , which we associate with a cause, is sometimes called a hidden or latent variable because, although it underlies \mathbf{u} , its value cannot necessarily be determined unambiguously from \mathbf{u} . For example, it may be impossible to determine definitively the value of v for an input \mathbf{u} near the boundary between the two clusters in figure 10.1A.

The ultimate goal of a causal model is recognition, in which the model tells us something about the causes underlying a particular input. Recognition can be either deterministic or probabilistic. In a causal model of the data in figure 10.1A with deterministic recognition, the output $v(\mathbf{u}) = A$ or B is the model's estimate of which neuron produced the spike associated with input \mathbf{u} . In probabilistic recognition, the model estimates the probability that the spike with input data \mathbf{u} was generated by either neuron A or neu-

input vector \mathbf{u}

input distribution $p[\mathbf{u}]$

cause v

hidden or latent variable

recognition

deterministic recognition
probabilistic recognition

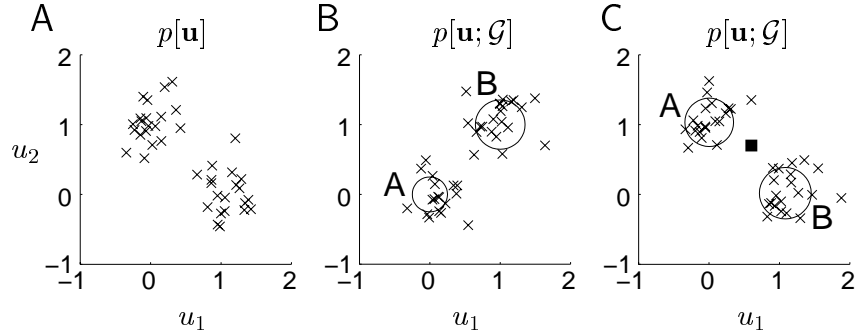


Figure 10.1: Clustering. A) Input data points drawn from the distribution $p[\mathbf{u}]$ are indicated by the crosses. B) Initialization for a generative model. The means and twice the standard deviations of the two Gaussians are indicated by the locations and radii of the circles. The crosses show synthetic data, which are samples from the distribution $p[\mathbf{u}; \mathcal{G}]$ of the generative model. C) Means, standard deviations, and synthetic data points generated by the optimal generative model. The square indicates a new input point that can be assigned to cluster A or B with probabilities computed from the recognition model.

ron B. In either case, the output v is taken as the model's re-representation of the input.

We consider models that infer causes in an unsupervised manner. In the example of figure 10.1A, this means that no indication is given about which neuron fired which action potential. The only information available is the statistical structure of the input data that is apparent in the figure. In the absence of supervisory information or even reinforcement, causes are judged by their ability to explain and reproduce, statistically, the inputs they are designed to represent. This is achieved by constructing a generative model that can be used to create synthetic input data from assumed causes. The generative model has a number of parameters that we collectively represent by \mathcal{G} , and an overall structure or form that determines how these parameters specify a distribution over the inputs. The parameters are adjusted until the distributions of synthetic and real inputs are as similar as possible. If the final statistical match is good, the causes are judged trustworthy, and the model can be used as a basis for recognition.

*generative model
parameters \mathcal{G}*

Generative Models

To illustrate the concept of a generative model, we construct one for the data in figure 10.1A. We begin by specifying the proportions (also known as mixing proportions) of action potentials that come from the two neurons. These are written as $P[v; \mathcal{G}]$ with $v = A$ or B . $P[v; \mathcal{G}]$, which is called the prior distribution over causes, is the probability that a given spike is generated by neuron v in the absence of any knowledge about the input \mathbf{u} associated with that spike. This might reflect the fact that one of the neu-

*mixing proportions
prior $P[v; \mathcal{G}]$*

rons has a higher firing rate than the other, for example. The two prior probabilities represent two of the model parameters contained in the list G , $P[v; G] = \gamma_v$ for $v = A$ and B . These parameters are not independent because they must sum to one. We start by assigning them random values consistent with this constraint.

To continue the construction of the generative model, we need to assume something about the distribution of \mathbf{u} values arising from the action potentials generated by each neuron. An examination of figure 10.1A suggests that Gaussian distributions (with the same variance in both dimensions) might be appropriate. We write the probability density of \mathbf{u} values given that neuron v fired as $p[\mathbf{u}|v; G]$, and set it equal to a Gaussian distribution with a mean and variance that, initially, we guess. The parameter list G now contains the prior probabilities for neurons A and B to fire, γ_v , and the means and variances of the Gaussian distributions over \mathbf{u} for $v = A$ and B , which we label \mathbf{g}_v and Σ_v respectively. Note that we use Σ_v for the variance of cluster v , not its standard deviation, and also that each cluster is characterized by a single variance because we only consider circularly symmetric Gaussian distributions.

Figure 10.1B shows synthetic data points (crosses) generated by this model. To create each point, we set $v = A$ with probability $P[v = A; G]$ (or otherwise set $v = B$) and then generated a point \mathbf{u} randomly from the distribution $p[\mathbf{u}|v; G]$. This generative model clearly has the capacity to create a data distribution with two clusters similar to the one in figure 10.1A. However, the values of the parameters G used in figure 10.1B are obviously inappropriate. They must be adjusted by a learning procedure that matches, as accurately as possible, the distribution of synthetic data points in figure 10.1B to the actual input distribution in figure 10.1A. We describe how this is done in a following section. After optimization, as seen in figure 10.1C, synthetic data points generated by the model (crosses) overlap well with the actual data points seen in figure 10.1A.

In summary, generative models are defined by a prior probability distribution over causes, $P[v; G]$, and a generative distribution for inputs given each particular cause, $p[\mathbf{u}|v; G]$, which collectively depend on a list of parameters G . Sometimes, we consider inputs that are discrete, in which case, following our convention for writing probabilities and probability densities, the probability distribution for the inputs is written as $P[\mathbf{u}]$ and the generative distribution as $P[\mathbf{u}|v; G]$. Alternatively, the causal variables can be continuous, and the generative model then has the prior probability density $p[v; G]$. Sometimes, the relationship between causes and synthetic inputs in the generative model is deterministic rather than being stochastic. This corresponds to setting $p[\mathbf{u}|v; G]$ to a δ function, $p[\mathbf{u}|v; G] = \delta(\mathbf{u} - \mathbf{f}(v; G))$, where \mathbf{f} is a vector of functions. Causes are sometimes described by a vector \mathbf{v} instead of a single variable v . A general problem that arises in the example of figure 10.1 is determining the number of possible causes, i.e. the number of clusters. Probabilistic methods can be used to make statistical inferences about the number of clusters in

generative distribution
 $p[\mathbf{u}|v; G]$

the data, but they lie beyond the scope of this text.

The distribution of synthetic data points in figures 10.1B and 10.1C is described by the density $p[\mathbf{u}; G]$ that the generative model synthesizes an input with the value \mathbf{u} . This density can be computed from the prior $P[v; G]$ and the conditional density $p[\mathbf{u}|v; G]$ that define the generative model,

$$p[\mathbf{u}; G] = \sum_v P[v; G] p[\mathbf{u}|v; G]. \quad (10.1)$$

*marginal distribution
 $p[\mathbf{u}; G]$*

The process of summing over all causes is called marginalization, and $p[\mathbf{u}; G]$ is called the marginal distribution over \mathbf{u} . As in chapter 8, we use the additional argument G to distinguish the distribution of synthetic inputs produced by the generative model, $p[\mathbf{u}; G]$, from the distribution of actual inputs, $p[\mathbf{u}]$. The process of adjusting the parameters G to make the distributions of synthetic and real input data points match, corresponds to making the marginal distribution $p[\mathbf{u}; G]$ approximate, as closely as possible, the distribution $p[\mathbf{u}]$ from which the input data points are drawn. Before we discuss the procedures used to adjusting the parameters of the generative model to their optimal values, we describe how a model of recognition can be constructed on the basis of the generative description.

Recognition Models

Once the optimal generative model has been constructed, the culmination of representational learning is recognition, in which new input data are interpreted in terms of the causes established during training. In probabilistic recognition models, this amounts to determining the probability that cause v is associated with input \mathbf{u} .

In the model of figure 10.1, and in many of the models discussed in this chapter, recognition falls directly out of the generative model. The probability of cause v given input \mathbf{u} is $P[v|\mathbf{u}; G]$, which is the statistical inverse of the distribution $p[\mathbf{u}|v; G]$ that defines the generative model. $P[v|\mathbf{u}; G]$ is called the posterior distribution over causes or the recognition distribution. Using Bayes theorem, it can be expressed in terms of the distributions that define the generative model as

$$P[v|\mathbf{u}; G] = \frac{p[\mathbf{u}|v; G] P[v; G]}{p[\mathbf{u}; G]}. \quad (10.2)$$

*recognition distribution
 $P[v|\mathbf{u}; G]$*

In the example of figure 10.1, equation 10.2 can be used to determine that the point indicated by the filled square in figure 10.1C has probability $P[v=A|\mathbf{u}; G] = 0.8$ of being associated with neuron A and $P[v=B|\mathbf{u}; G] = 0.2$ of being associated with neuron B.

Although equation 10.2 provides a direct solution of the recognition problem, it is sometimes impractically difficult to compute the right side of this equation. We call models in which the recognition distribution can be

invertible and non-invertible models

*approximate
recognition
distribution
 $Q[v; \mathbf{u}, W]$*

computed from equation 10.2, invertible, and those in which it cannot be computed tractably, non-invertible. In the latter case, recognition is based on an approximate recognition distribution. That is, recognition is based on a function $Q[v; \mathbf{u}, W]$, expressed in terms of a set of parameters collectively labeled W , that provides an approximation to the exact recognition distribution $P[v|\mathbf{u}; G]$. Like generative models, approximate recognition models can have different structures and parameters. In many cases, as we discuss in the next section, the best approximation of the recognition distribution comes from adjusting W through an optimization procedure. Once this is done, $Q[v; \mathbf{u}, W]$ provides the model's estimate of the probability that input \mathbf{u} is associated with cause v , performing the same role that $P[v|\mathbf{u}; G]$ does for invertible models.

*factorial coding
sparse coding
dimensionality
reduction*

The choice of a particular structure for a generative model reflects our notions and prejudices, collectively referred to as heuristics, about the properties of the causes that underlie a set of input data. Usually, the heuristics consist of biases toward certain types of representations, which are imposed through the choice of the prior distribution $p[v; G]$. For example, we may want the identified causes to be mutually independent (which leads to a factorial code) or sparse, or of lower dimension than the input data. Many heuristics can be formalized using the information theoretic ideas we discuss in chapter 4.

Once a causal model has been constructed, it is possible to check whether the biases imposed by the prior distribution of the generative model have actually been realized. This is done by examining the distribution of causes produced by the recognition model in response to actual data. This distribution should match the prior distribution over the causes, and thus share its desired properties, such as mutual independence. If the prior distribution of the generative model does not match the actual distribution of causes produced by the recognition model, this is an indication that the desired heuristic does not apply accurately to the input data.

Expectation Maximization

EM

There are various ways to adjust the parameters of a generative model to optimize the match between the synthetic data it generates and the actual input data. In this chapter (except for one case), we use a generalization of an approach called expectation maximization or EM. The general theory of EM is discussed in detail in the next section but, as an introduction to the method, we apply it here to the example of figure 10.1. Recall that the problem of optimizing the generative model in this case involves adjusting the mixing proportions, means, and variances of the two Gaussian distributions until the clusters of synthetic data points in figure 10.1B and C match the clusters of actual data points in figure 10.1A.

The parameters \mathbf{g}_v and Σ_v for $v=A$ and B of the Gaussian distributions of the generative model should equal the means and variances of the data

points associated with each cluster in figure 10.1A. If we knew which cluster each input point belonged to, it would be a simple matter to compute these means and variances and construct the optimal generative model. Similarly, we could set γ_v , the prior probability of a given spike being a member of cluster v , equal to the fraction of data points assigned to that cluster. Of course, we do know the cluster assignments of the input points; that would amount to knowing the answer to the recognition problem. However, we can make an informed guess about which point belongs to which cluster on the basis of equation 10.2. In other words, the recognition distribution $P[v|\mathbf{u}; G]$ of equation 10.2 provides us with our best current guess about the cluster assignment, and this can be used in place of the actual knowledge about which neuron produces which spike. The recognition distribution $P[v|\mathbf{u}; G]$ is thus used to assign the data point \mathbf{u} to cluster v in a probabilistic manner.

In EM algorithm, the mean and variance of the Gaussian distribution corresponding to cause v are set equal to a weighted mean and variance of all the data points, with the weight for point \mathbf{u} equal to the current estimate $P[v|\mathbf{u}; G]$ of the probability that it belongs to cluster v . In this context, the recognition probability $P[v|\mathbf{u}; G]$ is also called the responsibility of v for \mathbf{u} . A similar argument is applied to the mixing proportions, resulting in the equations

$$\gamma_v = \langle P[v|\mathbf{u}; G] \rangle, \quad \mathbf{g}_v = \frac{\langle P[v|\mathbf{u}; G]\mathbf{u} \rangle}{\gamma_v}, \quad \Sigma_v = \frac{\langle P[v|\mathbf{u}; G](\mathbf{u} - \mathbf{g}_v)^2 \rangle}{2\gamma_v}. \quad (10.3)$$

The angle brackets indicate averages over all the input data points. The factors of γ_v dividing the last two expressions correct for the fact that the number of points in cluster v is only expected to be γ_v times the total number of input data points, whereas the full averages denoted by the brackets involve dividing by the total number of data points.

The full EM algorithm consists of two phases that are applied in alternation. In the E (or expectation) phase, the responsibilities $P[v|\mathbf{u}; G]$ are calculated from equation 10.2. In the M (or maximization) phase, the generative parameters G are modified according to equation 10.3. The process of determining the responsibilities and then averaging according to them repeats because the responsibilities change when G is modified. Figure 10.2 shows intermediate results at three different times during the running of the EM procedure starting from the generative model in figure 10.1B and resulting in the fit shown in figure 10.1C.

E phase
M phase

The EM procedure for optimizing the generative model in the example of figure 10.1 makes intuitive sense, but it is not obvious that it will converge to an optimal model. Indeed, the process appears circular because the generative model defines the responsibilities used to construct itself. However, there are rigorous theoretical arguments justifying its use, which we discuss in the following section. These provide a framework for performing unsupervised learning in a wide class of models.

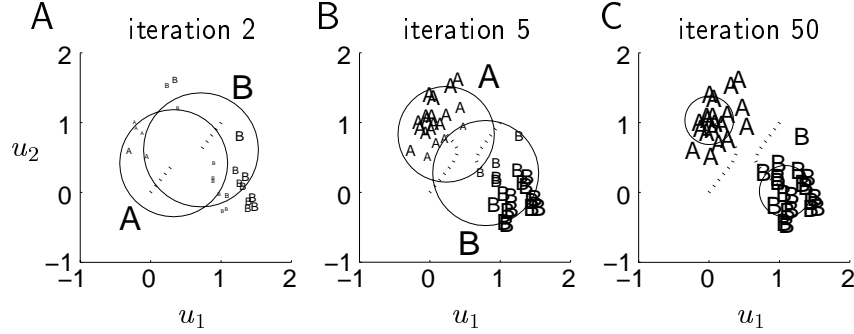


Figure 10.2: EM for clustering. Three iterations over the course of EM learning of a generative model. The circles show the Gaussian distributions for clusters A and B (labeled with the largest ‘A’ and ‘B’) as in figure 10.1B & C. The ‘trails’ behind the centers of the circles plot the change in the mean since the last iteration. The data from figure 10.1A are plotted using the small labels. Label ‘A’ is used if $P[v=A|\mathbf{u}; G] > 0.5$ (and otherwise label ‘B’), with the font size proportional to $|P[v=A|\mathbf{u}; G] - 0.5|$. This makes the fonts small in regions where the two distributions overlap, even inside one of the circles. The assignment of labels for the two Gaussians (i.e. which is ‘A’ and which ‘B’) is arbitrary, depending on initial conditions.

10.2 Density Estimation

The process of matching the distribution $p[\mathbf{u}; G]$ produced by the generative model to the actual input distribution $p[\mathbf{u}]$ is a form of density estimation. This technique is discussed in chapter 8 in connection with the Boltzmann machine. As mentioned in the introduction, the parameters G of the generative model are fit to the training data by minimizing the discrepancy between the probability density of the input data $p[\mathbf{u}]$ and the marginal probability density of equation 10.1. This discrepancy is measured using the Kullback-Leibler divergence (chapter 4)

$$\begin{aligned} D_{\text{KL}}(p[\mathbf{u}], p[\mathbf{u}; G]) &= \int d\mathbf{u} p[\mathbf{u}] \ln \frac{p[\mathbf{u}]}{p[\mathbf{u}; G]} \\ &\approx -\langle \ln p[\mathbf{u}; G] \rangle + K \end{aligned} \quad (10.4)$$

where K is a term proportional to the entropy of the distribution $p[\mathbf{u}]$ that is independent of G . In the second line, we have approximated the integral over all \mathbf{u} values weighted by $p[\mathbf{u}]$ by the average over input data points generated from the distribution $p[\mathbf{u}]$. We assume there are sufficient input data to justify this approximation.

Equation 10.4 and the following discussion are similar to our treatment of learning in the Boltzmann machine discussed in chapter 8. As in that case, equation 10.4 implies that minimizing the discrepancy between $p[\mathbf{u}]$ and $p[\mathbf{u}; G]$ amounts to maximizing the log likelihood that the training data could have been created by the generative model,

$$L(G) = \langle \ln p[\mathbf{u}; G] \rangle . \quad (10.5)$$

Here $L(G)$ is the average log likelihood, and the method is known as maximum likelihood density estimation. A theorem due to Shannon describes circumstances under which the generative model that maximizes the likelihood over input data also provides the most efficient way of coding those data, so density estimation is closely related to optimal coding.

maximum likelihood density estimation

Theory of EM

Although stochastic gradient ascent can be used to adjust the parameters of the generative model to maximize the likelihood in equation 10.5 (as it was for the Boltzmann machine), the EM algorithm discussed in the introduction is an alternative procedure that is often more efficient. We already applied this algorithm, on intuitive grounds, to the example of figure 10.1, but we now present a more general and rigorous discussion. This is based on the connection of EM with maximization of the function

$$F(Q, G) = \left\langle \sum_v Q[v; \mathbf{u}] \ln \frac{p[v, \mathbf{u}; G]}{Q[v; \mathbf{u}]} \right\rangle \quad (10.6)$$

where

$$p[v, \mathbf{u}; G] = p[\mathbf{u}|v; G]P[v; G] = P[v|\mathbf{u}; G]p[\mathbf{u}; G] \quad (10.7)$$

*joint distribution
 $p[v, \mathbf{u}; G]$*

is the joint probability distribution over both causes and inputs specified by the model. In equation 10.6, $Q[v; \mathbf{u}]$ is any non-negative function of the discrete argument v and continuous input \mathbf{u} that satisfies

$$\sum_v Q[v; \mathbf{u}] = 1 \quad (10.8)$$

for all \mathbf{u} . Although, in principle, $Q[v; \mathbf{u}]$ can be any function, we consider it to be an approximate recognition distribution. For some non-invertible models, we express Q in terms of a set of parameters W and write it as $Q[v; \mathbf{u}, W]$.

F is a useful quantity because, by a rearrangement of terms, it can be written as the difference of the average log likelihood and the average Kullback-Leibler divergence between $Q[v; \mathbf{u}]$ and $p[v|\mathbf{u}; G]$. This is done by substituting the second equality of equation 10.7 into equation 10.6 and using 10.8 and the definition of the Kullback-Leibler divergence to obtain

$$\begin{aligned} F(Q, G) &= \left\langle \sum_v Q[v; \mathbf{u}] \left(\ln p[\mathbf{u}; G] + \ln \frac{P[v|\mathbf{u}; G]}{Q[v; \mathbf{u}]} \right) \right\rangle \\ &= \langle \ln p[\mathbf{u}; G] \rangle - \left\langle \sum_v Q[v; \mathbf{u}] \left(\ln \frac{Q[v; \mathbf{u}]}{P[v|\mathbf{u}; G]} \right) \right\rangle \\ &= L(G) - \langle D_{\text{KL}}(Q[v; \mathbf{u}], P[v|\mathbf{u}; G]) \rangle . \end{aligned} \quad (10.9)$$

Because the Kullback-Leibler divergence is never negative,

$$L(G) \geq F(Q, G), \quad (10.10)$$

and because $D_{KL} = 0$ only if the two distributions being compared are identical, this inequality is saturated, becoming an equality, only if

$$Q[v; \mathbf{u}] = P[v|\mathbf{u}; G]. \quad (10.11)$$

The negative of F is related to an important quantity in statistical physics called the free energy.

Expressions 10.9, 10.10, and 10.11 are critical to the operation of EM. The two phases of EM are concerned with separately maximizing (or at least increasing) F with respect to its two arguments. When F increases, this increases a lower bound on the log likelihood of the input data (equation 10.10). In the M phase, F is increased with respect to G , keeping Q constant. For the generative model of figure 10.1, it is possible to maximize F with respect to G in a single step, through equation 10.3. For other generative models, this may require multiple steps that perform gradient ascent on F . In the E phase, F is increased with respect to Q , keeping G constant. From equation 10.9, we see that increasing F by changing Q is equivalent to reducing the average Kullback-Leibler divergence between $Q[v; \mathbf{u}]$ and $P[v|\mathbf{u}; G]$. The E phase can proceed in at least three possible ways, depending on the nature of the generative model being considered. We discuss these separately.

Invertible Models

If the causal model being considered is invertible, the E step of EM simply consists of solving equation 10.2 for the recognition distribution, and setting Q equal to the resulting $P[v|\mathbf{u}; G]$ as in equation 10.11. This maximizes F with respect to Q by setting the Kullback-Leibler term to zero, and it makes the function F equal to $L(G)$, the average log likelihood of the data points. However, the EM algorithm for maximizing F is not exactly the same as likelihood maximization. This is because the function Q is held constant during the M phase while the parameters G are modified. Although F is equal to L at the beginning of the M phase, exact equality ceases to be true as soon as G is modified, making $P[v|\mathbf{u}; G]$ different from Q . F is equal to $L(G)$ again only after the update of Q during the following E phase. At this point, $L(G)$ must have increased since the last E phase, because F has increased. This shows that the log likelihood increases monotonically during EM until the process converges, even though EM is not identical to likelihood maximization. One advantage of EM over likelihood maximization through gradient methods is that this monotonicity holds even if the successive changes to G are large. Thus, large steps toward the maximum can be taken during each M cycle of modification. Of course, the log likelihood may have multiple maxima, in which case

neither gradient ascent nor EM is guaranteed to find the globally optimal solution. Also, the process of maximizing a function one coordinate at a time (which is called coordinate ascent) is subject to local maxima that other optimization methods avoid (we encounter an example of this later in the chapter).

For the example of figure 10.1, the joint probability over causes and inputs is

$$p[v, \mathbf{u}; G] = \frac{\gamma_v}{2\pi\Sigma_v} \exp\left(-\frac{|\mathbf{u} - \mathbf{g}_v|^2}{2\Sigma_v}\right), \quad (10.12)$$

and thus

$$F = \left\langle \sum_v Q[v; \mathbf{u}] \left(\ln\left(\frac{\gamma_v}{2\pi}\right) - \ln \Sigma_v - \frac{|\mathbf{u} - \mathbf{g}_v|^2}{2\Sigma_v} - \ln Q[v; \mathbf{u}] \right) \right\rangle. \quad (10.13)$$

The E phase amounts to computing $P[v|\mathbf{u}; G]$ from equation 10.2 and setting Q equal to it, as in equation 10.11. The M phase involves maximizing F with respect to G for this Q . We leave it as an exercise for the reader to show that maximizing equation 10.13 with respect to the parameters γ_v (taking into account the constraint $\sum_v \gamma_v = 1$), \mathbf{g}_v , and Σ_v leads to the rules of equation 10.3.

Non-Invertible Deterministic Models

If the generative model is non-invertible, the E phase of the EM algorithm is more complex than simply setting Q equal to $P[v|\mathbf{u}; G]$, because it is not practical to compute the recognition distribution exactly. The steps taken during the E phase depend on whether the approximation to the inverse of the model is deterministic or probabilistic, although the basic argument is the same in either case.

The recognition process based on a deterministic approximation results in a prediction $v(\mathbf{u})$ of the cause underlying input \mathbf{u} . In terms of the function F , this amounts to retaining only the single term $v = v(\mathbf{u})$ in the sum in equation 10.6, and for this single term $Q[v(\mathbf{u}); \mathbf{u}] = 1$. Thus, in this case F is a functional of the function $v(\mathbf{u})$, and a function of the parameters G , given by

$$F(Q, G) = F(v(\mathbf{u}), G) = \langle \ln P[v(\mathbf{u}), \mathbf{u}; G] \rangle. \quad (10.14)$$

The M phase of EM consists, as always, of maximizing this expression with respect to G . During the E phase we try to find the function $v(\mathbf{u})$ that maximizes F . Because v is varied during the optimization procedure, the approach is sometimes called a variational method. The E and M steps make intuitive sense; we are finding the input-output relationship that maximizes the probability that the generative model would have simultaneously produced the cause $v(\mathbf{u})$ and the input \mathbf{u} .

variational method

The approximation that the recognition model is deterministic can be rather drastic, making it difficult, in the case of visual representations for example, to account for psychophysical aspects of sensory processing. We also encounter a case later in the chapter where this approximation requires us to introduce constraints on G .

Non-Invertible Probabilistic Models

The alternative to using a deterministic approximate recognition model is to treat $Q[v; \mathbf{u}]$ as a full probability distribution over v for each input example \mathbf{u} . In this case, we choose a specific functional form for Q , expressed in terms of a set of parameters collectively labeled W . Thus, we write the approximate recognition distribution as $Q[v; \mathbf{u}, W]$. F can now be treated as a function of W , rather than of Q , so we write it as $F(W, G)$. As in all cases, the M phase of EM consists of maximizing $F(W, G)$ with respect to G . The E phase now consists of maximizing $F(W, G)$ with respect to W . This has the effect of making $Q[v; \mathbf{u}, W]$ as similar as possible to $P[v|\mathbf{u}; G]$, in the sense that the KL divergence between them, averaged over the input data, is minimized (see equation 10.9).

Because each E and M step separately increases the value of F , the EM algorithm is guaranteed to converge to at least a local maximum of F (except in the rare cases that coordinate ascent induces extra local maxima). In general, this does not correspond to a local maximum of the likelihood function, because Q is not exactly equal to the actual recognition distribution (that is, F is only guaranteed to be a lower bound on $L(G)$). Nevertheless, a good generative model should be obtained if the lower bound is tight.

It is not necessary to maximize $F(W, G)$ completely with respect to W and then G during successive E and M phases. Instead, gradient ascent steps that modify W and G by small amounts can be taken in alternation, in which case the E and M phases effectively overlap.

10.3 Causal Models for Density Estimation

In this section, we present a number of models in which representational learning is achieved through density estimation. The mixture of Gaussians and factor analysis models that we discuss are examples of invertible generative models with probabilistic recognition. Principal components analysis is a limiting case of factor analysis with deterministic recognition. We consider two other models with deterministic recognition, independent components analysis, which is invertible, and sparse coding, which is non-invertible. Our final example, the Helmholtz machine, is non-invertible with probabilistic recognition. The Boltzmann machine,

discussed in chapters 7 and 8, is an additional example that is closely related to the causal models discussed here. We summarize and interpret general properties of representations derived from causal models at the end of the chapter. The table in the appendix summarizes the generative and recognition distributions and the learning rules for all the models we discuss.

Mixture of Gaussians

The model applied in the introduction to the data in figure 10.1A is a mixture of Gaussians model. That example involves two causes and two Gaussian distributions, but we now generalize this to N_v causes, each associated with a separate Gaussian distribution. The model is defined by the probability distributions

$$P[v; G] = \gamma_v \quad \text{and} \quad p[\mathbf{u}|v; G] = N(\mathbf{u}; \mathbf{g}_v, \Sigma_v) \quad (10.15)$$

where v takes N_v values representing the different causes and, for an N_u component input vector,

$$N(\mathbf{u}; \mathbf{g}, \Sigma) = \frac{1}{(2\pi\Sigma)^{N_u/2}} \exp\left(-\frac{|\mathbf{u} - \mathbf{g}|^2}{2\Sigma}\right) \quad (10.16)$$

is a Gaussian distribution with mean \mathbf{g} and variances for the individual components equal to Σ . The function $F(Q, G)$ for this model is given by an expression similar to equation 10.13 (with slightly different factors if $N_u \neq 2$), leading to the M-phase learning rules given in the appendix. Once the generative model has been optimized, the recognition distribution is constructed from equation 10.2 as

$$P[v|\mathbf{u}; G] = \frac{\gamma_v N(\mathbf{u}; \mathbf{g}_v, \Sigma_v)}{\sum_{v'} \gamma_{v'} N(\mathbf{u}; \mathbf{g}_{v'}, \Sigma_{v'})}. \quad (10.17)$$

K-Means Algorithm

A special case of mixture of Gaussians can be derived in the limit that the variances of the Gaussians are equal and tend toward 0, $\Sigma_v = \Sigma \rightarrow 0$. We discuss this limit for two clusters as in figure 10.1. When Σ is extremely small, the recognition distribution $P[v|\mathbf{u}; G]$ of equation 10.17 degenerates because it takes essentially two values, 0 or 1, depending on whether \mathbf{u} is closer to one cluster or the other. This provides a hard, rather than a probabilistic or soft, classification of \mathbf{u} . In the degenerate case, EM consists of choosing two random values for the centers of the two cluster distributions, finding all the inputs \mathbf{u} that are closest to a given center \mathbf{g}_v , and then moving \mathbf{g}_v to the average of these points. This is called the K -means algorithm (with $K = 2$ for two clusters). The mixing proportions γ_v do not play an important role for the K -means algorithm. New input points are recognized as belonging to the clusters to which they are closest.

Factor Analysis

The causes in the mixture of Gaussians model are discrete. Factor analysis uses a continuous vector of causes, \mathbf{v} , drawn from a Gaussian distribution. As in the mixture of Gaussians model, the distribution over inputs given a cause is Gaussian. However, the mean of this Gaussian is a linear function of \mathbf{v} , rather than a parameter of the model. We assume that the distribution $p[\mathbf{u}]$ has zero mean (non-zero means can be accommodated simply by shifting the input data). Then, the defining distributions for factor analysis are

$$p[\mathbf{v}; G] = N(\mathbf{v}; \mathbf{0}, 1) \quad \text{and} \quad p[\mathbf{u}|\mathbf{v}; G] = N(\mathbf{u}; \mathbf{G} \cdot \mathbf{v}, \Sigma) \quad (10.18)$$

where, the extension of equation 10.16 expressed in terms of the mean \mathbf{g} and covariance matrix Σ is

$$N(\mathbf{u}; \mathbf{g}, \Sigma) = \frac{1}{((2\pi)^{N_u} |\det \Sigma|)^{1/2}} \exp\left(-\frac{1}{2}(\mathbf{u} - \mathbf{g}) \cdot \Sigma^{-1} \cdot (\mathbf{u} - \mathbf{g})\right). \quad (10.19)$$

The expression $|\det \Sigma|$ indicates the absolute value of the determinant of Σ . In factor analysis, Σ is taken to be diagonal, $\Sigma = \text{diag}(\Sigma_1, \dots, \Sigma_{N_u})$ (see the Mathematical Appendix), with all the diagonal elements nonzero, so its inverse is simply $\Sigma^{-1} = \text{diag}(1/\Sigma_1, \dots, 1/\Sigma_{N_u})$ and $|\det \Sigma| = \Sigma_1 \Sigma_2 \dots \Sigma_{N_u}$.

According to equation 10.18, the individual components of \mathbf{v} are mutually independent. Furthermore, because Σ is diagonal, any correlations between the components of \mathbf{u} must arise from the mean values $\mathbf{G} \cdot \mathbf{v}$ of the generative distribution. The model requires \mathbf{v} to have fewer dimensions than \mathbf{u} ($N_v < N_u$). In terms of heuristics, factor analysis seeks a relatively small number of independent causes that account, in a linear manner, for collective Gaussian structure in the inputs.

The recognition distribution for factor analysis has the Gaussian form

$$p[\mathbf{v}|\mathbf{u}; G] = N(\mathbf{v}; \mathbf{W} \cdot \mathbf{u}, \Psi) \quad (10.20)$$

where expressions for \mathbf{W} and Ψ are given in the appendix. These do not depend on the input \mathbf{u} , so factor analysis involves a linear relation between the input and the mean of the recognition distribution. EM, as applied to an invertible model, can be used to adjust $G = (\mathbf{G}, \Sigma)$ on the basis of the input data. The resulting learning rules are given in the table in the appendix.

In this case, we can understand the goal of density estimation in an additional way. By direct calculation, as in equation 10.1, the marginal distribution for \mathbf{u} is

$$p[\mathbf{u}; G] = N(\mathbf{u}; \mathbf{0}, \mathbf{G} \cdot \mathbf{G}^T + \Sigma) \quad (10.21)$$

where $[G^T]_{ab} = [G]_{ba}$ and $[G \cdot G^T]_{ab} = \sum_c G_{ac}G_{bc}$ (see the Mathematical Appendix). Maximum likelihood density estimation requires determining the G that makes $G \cdot G^T + \Sigma$ match, as closely as possible, the covariance matrix of the input distribution.

Principal Components Analysis

In the same way that setting the parameters Σ_v to zero in the mixture of Gaussians model leads to the K -means algorithm, setting all the variances in factor analysis to zero leads to another well-known method, principal components analysis (which is also discussed in chapter 8). To see this, consider the case of a single factor. This means that v is a single number, and that the mean of the distribution $p[\mathbf{u}|v; G]$ is $v\mathbf{g}$, where the vector \mathbf{g} replaces the matrix G of the general case. The elements of the diagonal matrix Σ are set to a single variance Σ , which we shrink to zero.

As $\Sigma \rightarrow 0$, the Gaussian distribution $p[\mathbf{u}|v; G]$ in equation 10.18 approaches a δ function (see the Mathematical Appendix), and it can only generate the single vector $\mathbf{u}(v) = v\mathbf{g}$ from cause v . Similarly, the recognition distribution of equation 10.20 becomes a δ function, making the recognition process deterministic with $v(\mathbf{u}) = \mathbf{W} \cdot \mathbf{u}$ given by the mean of the recognition distribution of equation 10.20. Using the expression for \mathbf{W} in the appendix in the limit $\Sigma \rightarrow 0$, we find

$$v(\mathbf{u}) = \frac{\mathbf{g} \cdot \mathbf{u}}{|\mathbf{g}|^2}. \quad (10.22)$$

This is the result of the E phase of EM. In the M phase, we maximize

$$F(v(\mathbf{u}), G) = \langle \ln p[v(\mathbf{u}), \mathbf{u}; G] \rangle = K - \frac{N_u \ln \Sigma}{2} - \left\langle \frac{v^2(\mathbf{u})}{2} + \frac{|\mathbf{u} - \mathbf{g}v(\mathbf{u})|^2}{2\Sigma} \right\rangle \quad (10.23)$$

with respect to \mathbf{g} , without changing the expression for $v(\mathbf{u})$. Here, K is a term independent of \mathbf{g} and Σ . In this expression, the only term that depends on \mathbf{g} is proportional to $|\mathbf{u} - \mathbf{g}v(\mathbf{u})|^2$. Minimizing this in the M phase produces a new value of \mathbf{g} given by

$$\mathbf{g} = \frac{\langle v(\mathbf{u})\mathbf{u} \rangle}{\langle v^2(\mathbf{u}) \rangle}. \quad (10.24)$$

This only depends on the covariance matrix of the input distribution, as does the more general form given in the appendix. Under EM, equations 10.22 and 10.24 are alternated until convergence.

For principal components analysis, we can say more about the value of \mathbf{g} at convergence. We consider the case $|\mathbf{g}|^2 = 1$ because we can always multiply \mathbf{g} and divide $v(\mathbf{u})$ by the same factor to make this true without

affecting the dominant term in $F(v(\mathbf{u}), G)$ as $\Sigma \rightarrow 0$. Then, the \mathbf{g} that maximizes this dominant term must minimize

$$\langle |\mathbf{u} - \mathbf{g}(\mathbf{g} \cdot \mathbf{u})|^2 \rangle = \langle |\mathbf{u}|^2 - (\mathbf{g} \cdot \mathbf{u})^2 \rangle. \quad (10.25)$$

Here, we have used expression 10.22 for $v(\mathbf{u})$. Minimizing 10.25 with respect to \mathbf{g} , subject to the constraint $|\mathbf{g}|^2 = 1$, gives the result that \mathbf{g} is the eigenvector of the covariance matrix $\langle \mathbf{u}\mathbf{u} \rangle$ with maximum eigenvalue. This is just the principal component vector and is equivalent to finding the vector of unit length with the largest possible average projection onto \mathbf{u} .

The argument we have given shows that principal components analysis is a degenerate form of factor analysis. This is also true if more than one factor is considered, although maximizing F only constrains the projections $\mathbf{G} \cdot \mathbf{u}$ and therefore only forces \mathbf{G} to represent the principal components subspace of the data. The same subspace emerges from full factor analysis provided that the variances of all the factors are equal, even when they are nonzero.

Figure 10.3 illustrates an important difference between factor analysis and principal components analysis. In this figure, \mathbf{u} is a three-component input vector, $\mathbf{u} = (u_1, u_2, u_3)$. Samples of input data were generated on the basis of a ‘true’ cause, v_{true} according to

$$u_b = v_{\text{true}} + \epsilon_b \quad (10.26)$$

where ϵ_b represents noise on component b of the input. Input data points were generated from this equation by choosing a value of v_{true} from a Gaussian distribution with mean 0 and variance 1, and values of ϵ_b from independent Gaussian distributions with zero means. The variances of the distributions for ϵ_b , $b = 1, 2, 3$, were all equal to 0.25 in figures 10.3A & B. However, in figures 10.3C & D, the variance for ϵ_3 is much larger (equal to 9). We can think of this as representing the effect of a noisy sensor for this component of the input vector. The graphs plot the mean of the value of the cause v extracted from sample inputs by factor analysis, or the actual value of v for principal components analysis, as a function of the true value v_{true} used to generate the data. Perfect extraction of the underlying cause would find $v = v_{\text{true}}$. Here, perfect extraction is impossible because of the noise, and the absolute scale of v is arbitrary. Thus, the best we can expect is v values that are scattered but lie along a straight line when plotted as a function of v_{true} . When the input components are equally variable (figure 10.3A& B), this is exactly what happens for both factor and principal components analysis. However, when u_3 is much more variable than the other components, principal components analysis (figure 10.3D) is seduced by the extra variance and finds a cause v that does not correspond to v_{true} . By contrast, factor analysis (figure 10.3C) is only affected by the covariance between the input components and not by their individual variances (which are absorbed into Σ), so the cause it finds is not significantly perturbed (merely somewhat degraded) by the added sensor noise.

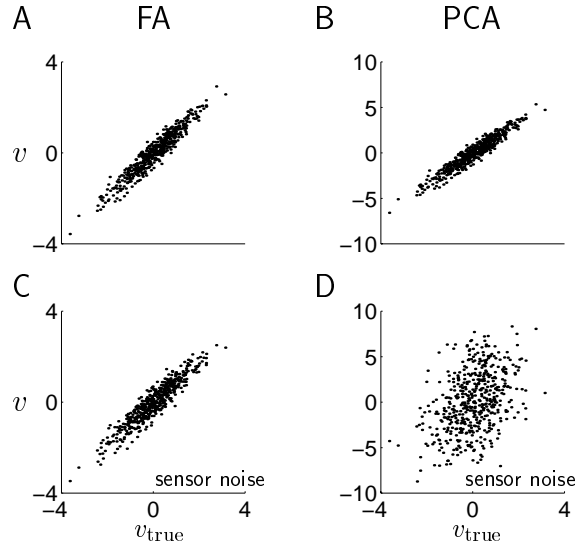


Figure 10.3: Factor analysis and principal components analysis applied to 500 samples noisy input reflecting a single underlying cause v_{true} . For A B, $\langle u_i u_j \rangle = 1 + 0.25 \delta_{ij}$, while for C & D, one sensor is corrupted by independent noise with standard deviation 3 rather than 0.5. The plots compare the true cause v_{true} with the cause v inferred by the model.

In chapter 8, we noted that principal components analysis maximizes the mutual information between the input and output under the assumption of a linear Gaussian model. This property, and the fact that principal components analysis minimizes the reconstruction error of equation 10.25, have themselves been suggested as goals for representational learning. We have now shown how they are also related to density estimation.

Both principal components analysis and factor analysis produce a marginal distribution $p[u; G]$ that is Gaussian. If the actual input distribution $p[u]$ is non-Gaussian, the best that these models can do is to match the mean and covariance of $p[u]$; they will fail to match higher-order moments. If the input is whitened to increase coding efficiency, as discussed in chapter 4, so that the covariance matrix $\langle uu \rangle$ is equal the identity matrix, neither method will extract any structure at all from the input data. By contrast, the generative models discussed in the following sections produce non-Gaussian marginal distributions and attempt to account for structure in the input data beyond merely the mean and covariance.

Sparse Coding

The prior distributions in factor analysis and principal components analysis are Gaussian and, if the model is sucessful, the distribution of v values in response to input should also be Gaussian. If we attempt to relate such

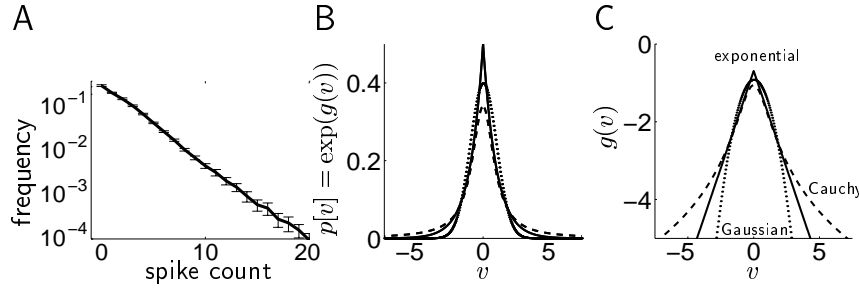


Figure 10.4: Sparse distributions. A) Log frequency distribution for the activity of a macaque IT cell in response to video images. The number of times that various numbers of spikes appeared in a spike-counting window is plotted against the number of spikes. The size of the window was adjusted so that, on average, there were two spikes per window. B) Three distributions $p[v] = \exp(g(v))$: double exponential ($g(v) = -|v|$, solid, kurtosis 3); Cauchy ($g(v) = -\ln(1 + v^2)$, dashed, kurtosis infinite); and Gaussian ($g(v) = -v^2/2$, dotted, kurtosis 0). C) The logarithms of the same three distributions. (A adapted from Baddeley et al., 1998.)

causal variables to the activities of cortical neurons, we find a discrepancy, because the activity distributions of cortical cells in response to natural inputs are not Gaussian. Figure 10.4A shows an example of the distribution of the numbers of spikes counted within a particular time window for a neuron in the infero-temporal (IT) area of the macaque brain recorded while a monkey freely viewed television shows. The distribution is close to being exponential. This means that the neurons are most likely to fire small numbers of spikes in the counting interval, but that they can occasionally fire a large number of spikes. Neurons in primary visual cortex exhibit similar patterns of activity in response to natural scenes.

sparse distributions

Distributions that generate values for the components of v close to zero most of the time, but occasionally far from zero, are called sparse. Sparse distributions are defined as being more likely than Gaussians of the same mean and variance to generate values near zero and also more likely to generate values far from zero. These occasional high values can convey substantial information. Distributions with this character are also called heavy-tailed. Figures 10.4B and C compare two sparse distributions to a Gaussian distribution.

kurtosis

Sparserness has been defined in a variety of different ways. Sparserness of a distribution is sometimes linked to a high value of a measure called kurtosis. Kurtosis of a distribution $p[v]$ is defined as

$$k = \frac{\int dv p[v](v - \bar{v})^4}{(\int dv p[v](v - \bar{v})^2)^2} - 3 \quad \text{with} \quad \bar{v} = \int dv p[v]v, \quad (10.27)$$

and it takes the value zero for a Gaussian distribution. Positive values of k are taken to imply sparse distributions, which are also called

super-Gaussian or leptokurtotic. Distributions with $k < 0$ are called sub-Gaussian or platykurtotic. This is a slightly different definition of sparseness from being heavy-tailed.

A sparse representation over a large population of neurons might more naturally be defined as one in which each input is encoded by a small number of the neurons in the population. Unfortunately, identifying this form of sparseness experimentally is difficult.

Unlike factor analysis and principal components analysis, sparse coding does not stress minimizing the number of representing units (i.e. components of \mathbf{v}). Indeed, sparse representations may require large numbers of units (though not necessarily). This is not a disadvantage when these models are applied to the visual system because representations in visual areas are greatly expanded at various steps along the pathway. For example, there are around 40 cells in primary visual cortex for each cell in the visual thalamus. Downstream processing can benefit greatly from sparse representations, because, for one thing, they minimize interference between different patterns of input.

Factor analysis and principal components analysis do not generate sparse representations because they have Gaussian priors. The mixture of Gaussians model is extremely sparse because each input is represented by a single cause (although the same cause could be deemed responsible for every input). This may be reasonable for relatively simple input patterns, but for complex stimuli such as images, we seek something between these extremes. Olshausen and Field (1996, 1997) suggested such a model by considering a nonlinear version of factor analysis. In this model, the distribution of \mathbf{u} given \mathbf{v} is a Gaussian with a diagonal covariance matrix, as for factor analysis, but the prior distribution over causes is sparse. Defined in terms of a function $g(v)$ (as in figure 10.4),

$$p[\mathbf{v}; G] \propto \prod_{a=1}^{N_v} \exp(g(v_a)) \quad \text{and} \quad p[\mathbf{u}|\mathbf{v}; G] = N(\mathbf{u}; \mathbf{G} \cdot \mathbf{v}, \boldsymbol{\Sigma}). \quad (10.28)$$

The prior $p[\mathbf{v}; G]$ should be normalized so that its integral over \mathbf{v} is one, but we omit the normalization factor to simplify the equations.

Because it is a product, the prior $p[\mathbf{v}; G]$ in equation 10.28 makes the components of \mathbf{v} mutually independent. If we took $g(v) = -v^2$, $p[\mathbf{v}; G]$ would be Gaussian (dotted lines in figures 10.4B & C), and the model would perform factor analysis. An example of a function that provides a sparse prior is $g(v) = -\alpha|v|$. This generates a double exponential distribution (solid lines in figures 10.4B & C) similar to the activity distribution in figure 10.4A. Another commonly used form is

$$g(v) = -\ln(\beta^2 + v^2) \quad (10.29)$$

with β a constant, which generates a Cauchy distribution (dashed lines in figures 10.4B & C).

double exponential distribution

Cauchy distribution

For $g(v)$ such as equation 10.29, it is difficult to compute the recognition distribution $p[v|u; G]$ exactly. This makes the sparse model non-invertible. Olshausen and Field chose a deterministic approximate recognition model. Thus, EM consists of finding $v(u)$ during the E phase, and using it to adjust the parameters G during the M phase. To simplify the discussion, we make the covariance matrix proportional to the identity matrix, $\Sigma = \Sigma I$. The function to be maximized is then

$$F(v(u), G) = \left\langle -\frac{1}{2\Sigma} |u - G \cdot v(u)|^2 + \sum_{a=1}^{N_v} g(v_a(u)) \right\rangle + K \quad (10.30)$$

where K is a term that is independent of G and v . For convenience in discussing the EM procedure, we further take $\Sigma = 1$ and do not allow it to vary. Similarly, we assume that β in equation 10.29 is predetermined and held fixed. Then, G consists only of the matrix G .

The E phase of EM involves maximizing F with respect to $v(u)$ for every u . This leads to the conditions (for all a)

$$\sum_{b=1}^{N_u} [u - G \cdot v(u)]_b G_{ba} + g'(v_a) = 0. \quad (10.31)$$

The prime on $g(v_a)$ indicates a derivative. One way to solve this equation is to let v evolve over time according to the equation

$$\tau_v \frac{dv_a}{dt} = \sum_{b=1}^{N_u} [u - G \cdot v(u)]_b G_{ba} + g'(v_a) \quad (10.32)$$

where τ_v is an appropriate time constant. This equation changes v so that it asymptotically approaches a value $v = v(u)$ that satisfies equation 10.31 and makes the right side of equation 10.32 zero. We assume that the evolution of v according to equation 10.32 is carried out long enough during the E phase for this to happen. This process is only guaranteed to find a local, not a global, maximum of F , and it is not guaranteed to find the same local maximum on each iteration.

Equation 10.32 resembles the equation used in chapter 7 for a firing-rate network model. The term $\sum_b u_b G_{ba}$, which can be written in vector form as $G^T \cdot u$, acts as the total input arising from units with activities u fed through a feedforward coupling matrix G^T . The term $-\sum_b [G \cdot v]_b G_{ba}$ can be interpreted as a recurrent coupling of the v units through the matrix $-G^T \cdot G$. Finally, the term $g'(v_a)$ plays the same role as the term $-v_a$ that would appear in the rate equations of chapter 7. If $g'(v) \neq -v$, this can be interpreted as a modified form of firing-rate dynamics. Figure 10.5 shows the resulting network. The feedback connections from the v units to the input units that determine the mean of the generative distribution, $G \cdot v$ (equation 10.28), are also shown in this figure.

After $v(u)$ has been determined during the E phase of EM, a delta rule (chapter 8) is used during the M phase to modify G and improve the generative model. The full learning rule is given in the appendix. The delta

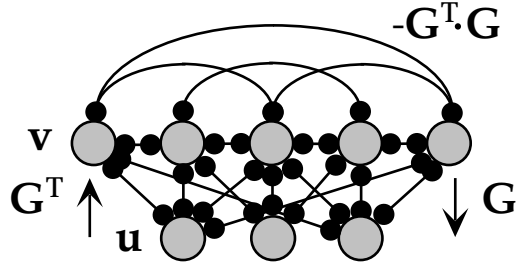


Figure 10.5: A network for sparse coding. This network reproduces equation (10.32) using recurrent weights $-G^T \cdot G$ in the v layer and weights connecting the input units to this layer that are given by the transpose of the matrix G . The reverse connections from the v layer to the input layer indicate how the mean of the recognition distribution is computed.

rule follows from maximizing $F(v(u), G)$ with respect to G . A complication arises here because the matrix G always appears multiplied by v . This means that the bias toward small values of v_a imposed by the prior can be effectively neutralized by scaling up G . This complication results from the approximation of deterministic recognition. To prevent the weights from growing without bound, constraints are applied on the lengths of the generative weights for each cause, $\sum_b G_{ba}^2$, to encourage the variances of all the different v_a to be approximately equal (see the appendix). Further, it is conventional to pre-condition the inputs before learning by whitening them so that $\langle u \rangle = 0$ and $\langle uu \rangle = I$. This typically makes learning faster, and it also ensures that the network is forced to find statistical structure beyond second order that would escape simpler methods such as factor analysis or principal components analysis. In the case that the input is created by sampling (e.g. pixelating an image), more sophisticated forms of pre-conditioning can be used to remove the resulting artifacts.

Applying the sparse coding model to inputs coming from the pixel intensities of small square patches of monochrome photographs of natural scenes leads to selectivities that resemble those of cortical simple cells. Before studying this result, we need to specify how the selectivities of generative models, such as the sparse coding model, are defined. The selectivities of sensory neurons are typically described by receptive fields, as in chapter 2. For a causal model, one definition of a receptive field for unit a is the set of inputs u for which v_a is likely to take large values. However, it may be impossible to construct receptive field by averaging over these inputs in nonlinear models, such as sparse coding models. Furthermore, generative models are most naturally characterized by projective fields rather than receptive fields. The projective field associated with a particular cause v_a can be defined as the set of inputs that it frequently generates. This consists of all the u values for which $P[u|v_a; G]$ is sufficiently large when v_a is large. For the model of figure 10.1, the projective fields are simply the circles in figure 10.1C. It is important to remember that projective fields can be quite different from receptive fields.

projective field

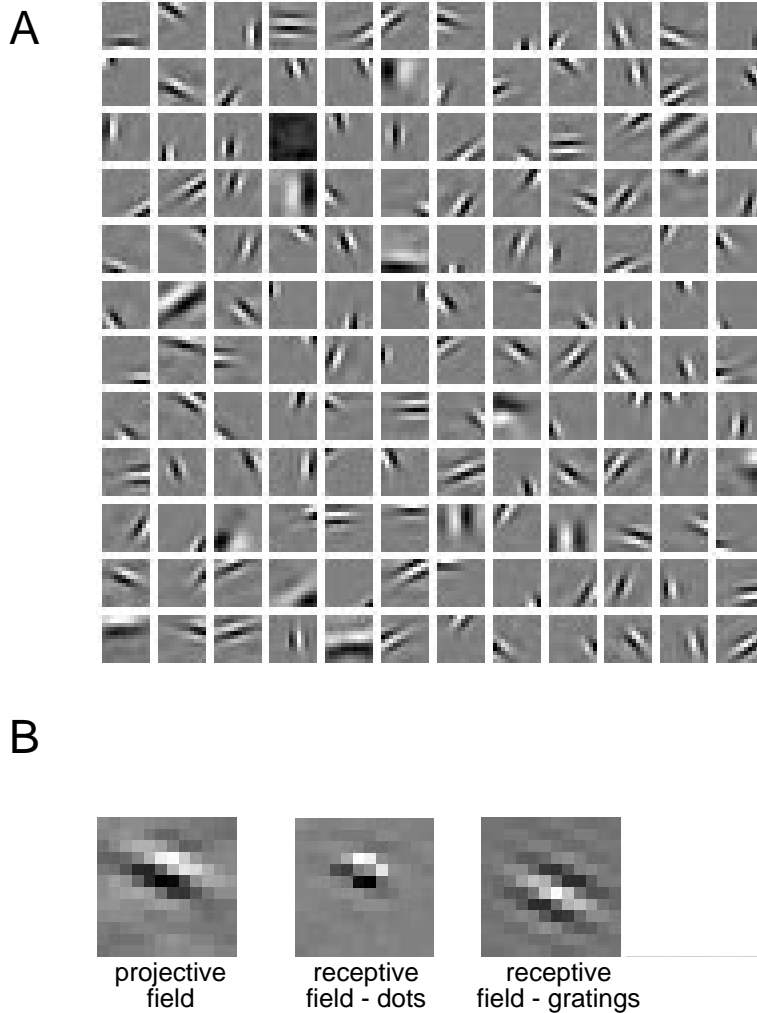


Figure 10.6: Projective and receptive fields for a sparse coding network with $N_u = N_v = 144$. A) Projective fields G_{ab} with a indexing representational units (the components of v), and b indexing input units u on a 12×12 pixel grid. Each box represents a different a value, and the b values are represented within the box by the corresponding input location. Weights are represented by the gray-scale level with gray indicating 0. B) The relationship between projective and receptive fields. The left panel shows the projective field of one of the units in A. The middle and right panels show its receptive field mapped using inputs generated by dots and gratings respectively. (Adapted from Olshausen and Field, 1997.)

Projective fields for the Olshausen and Field model trained on natural scenes are shown in figure 10.6A, with one picture for each component of \mathbf{v} . In this case, the projective field for v_a is simply the matrix elements G_{ab} plotted for all b values. In figure 10.6A, the index b is plotted over a two-dimensional grid representing the location of the input u_b within the visual field. The projective fields form a Gabor-like representation for images, covering a variety of spatial scales and orientations. The resemblance of this representation to the receptive fields of simple cells in primary visual cortex is quite striking, although these are the projective not the receptive fields of the model. Unfortunately, there is no simple form for the receptive fields of the \mathbf{v} units. Figure 10.6B compares the projective field of one unit to receptive fields determined by presenting either dots or gratings as inputs and recording the responses. The responses to the dots directly determine the receptive field, while responses to the gratings directly determine the Fourier transform of the receptive field. Differences between the receptive fields calculated on the basis of these two types of input are evident in the figure. In particular, the receptive field computed from gratings shows more spatial structure than the one mapped by dots. Nevertheless, both show a resemblance to the projective field and to a typical simple-cell receptive field.

In a generative model, projective fields are associated with the causes underlying the visual images presented during training. The fact that the causes extracted by the sparse coding model resemble Gabor patches within the visual field is somewhat strange from this perspective. It is difficult to conceive of images as arising from such low level causes, instead of causes couched in terms of objects within the images, for example. From the perspective of good representation, causes that are more like objects and less like Gabor patches would be more useful. To put this another way, although the prior distribution over causes biased them toward mutual independence, the causes produced by the recognition model in response to natural images are not actually independent. This is due to the structure in images arising from more complex objects than bars and gratings. It is unlikely that this high-order structure can be extracted by a model with only one set of causes. It is more natural to think of causes in a hierarchical manner, with causes at a higher level accounting for structure in the causes at a lower level. The multiple representations in areas along the visual pathway suggests such a hierarchical scheme, but the corresponding models are still in the rudimentary stages of development.

Independent Components Analysis

As for the case of the mixtures of Gaussians model and factor analysis, an interesting model emerges from sparse coding as $\Sigma \rightarrow 0$. In this limit, the generative distribution (equation 10.28) approaches a δ function and always generates $\mathbf{u}(\mathbf{v}) = \mathbf{G} \cdot \mathbf{v}$. Under the additional restriction that there are as many causes as inputs, the approximation we used for the sparse cod-

ing model of making the recognition distribution deterministic becomes exact, and the recognition distribution that maximizes F is

$$Q[\mathbf{v}; \mathbf{u}] = |\det \mathbf{W}|^{-1} \delta(\mathbf{u} - \mathbf{W}^{-1} \cdot \mathbf{v}) \quad (10.33)$$

where $\mathbf{W} = \mathbf{G}^{-1}$ is the matrix inverse of the generative weight matrix. The factor $|\det \mathbf{W}|$ comes from the normalization condition on Q , $\int d\mathbf{v} Q(\mathbf{v}; \mathbf{u}) = 1$. At the maximum with respect to Q , the function F is

$$F(Q, G) = \left\langle -\frac{1}{2\Sigma} |\mathbf{u} - \mathbf{G} \cdot \mathbf{W} \cdot \mathbf{u}|^2 + \sum_a g([\mathbf{W} \cdot \mathbf{u}]_a) \right\rangle + \ln |\det \mathbf{W}| + K \quad (10.34)$$

where K is independent of \mathbf{G} . Under the conventional EM procedure, we would maximize this expression with respect to \mathbf{G} , keeping \mathbf{W} fixed. However, the normal procedure fails in this case, because the minimum of the right side of equation 10.34 occurs at $\mathbf{G} = \mathbf{W}^{-1}$, and \mathbf{W} is being held fixed so \mathbf{G} cannot change. This is an anomaly of coordinate ascent in this particular limit.

Fortunately, it is easy to fix this problem, because we know that $\mathbf{W} = \mathbf{G}^{-1}$ provides an exact inversion of the generative model. Therefore, instead of holding \mathbf{W} fixed during the M phase of an EM procedure, we keep $\mathbf{W} = \mathbf{G}^{-1}$ at all times as we change \mathbf{G} . This sets F equal to the average log likelihood, and the process of optimizing with respect to \mathbf{G} is equivalent to likelihood maximization. Because $\mathbf{W} = \mathbf{G}^{-1}$, maximizing with respect to \mathbf{W} is equivalent to maximizing with respect to \mathbf{G} , and it turns out that this is easier to do. Therefore, we set $\mathbf{W} = \mathbf{G}^{-1}$ in equation 10.34, which causes the first term to vanish, and write the remaining terms as the log likelihood expressed as a function of \mathbf{W} instead of \mathbf{G} ,

$$L(\mathbf{W}) = \left\langle \sum_a g([\mathbf{W} \cdot \mathbf{u}]_a) \right\rangle + \ln |\det \mathbf{W}| + K. \quad (10.35)$$

Direct stochastic gradient ascent on this log likelihood can be performed using the update rule

$$\mathbf{W}_{ab} \rightarrow \mathbf{W}_{ab} + \epsilon ([\mathbf{W}^{-1}]_{ba} + g'(v_a) u_b) \quad (10.36)$$

where ϵ is a small learning rate parameter, and we have used the fact that $\partial \ln |\det \mathbf{W}| / \partial \mathbf{W}_{ab} = [\mathbf{W}^{-1}]_{ba}$.

The update rule of equation 10.36 can be simplified by using a clever trick. Because $\mathbf{W}^T \mathbf{W}$ is a positive definite matrix (see the Mathematical Appendix), the weight change can be multiplied by $\mathbf{W}^T \mathbf{W}$ without affecting the fixed points of the update rule. This means that the alternative learning rule

$$\mathbf{W}_{ab} \rightarrow \mathbf{W}_{ab} + \epsilon (\mathbf{W}_{ab} - g'(v_a) [\mathbf{v} \cdot \mathbf{W}]_b) \quad (10.37)$$

has the same potential final weight matrices as equation 10.36. This is called a natural gradient rule, and it avoids the matrix inversion of \mathbf{W} as well as providing faster convergence. Equation 10.37 can be interpreted as the sum of an anti-decay term that forces \mathbf{W} away from zero, and a generalized type of anti-Hebbian term. The choice of prior $p[v] \propto 1/\cosh(v)$ makes $g'(v) = -\tanh(v)$ and produces the rule

$$\mathbf{W}_{ab} \rightarrow \mathbf{W}_{ab} + \epsilon ([\mathbf{W}]_{ba} - \tanh(v_a) [\mathbf{v} \cdot \mathbf{W}]_b). \quad (10.38)$$

This algorithm is called independent components analysis. Just as the sparse coding network is a nonlinear generalization of factor analysis, independent components analysis is a nonlinear generalization of principal components analysis that attempts to account for non-Gaussian features of the input distribution. The generative model is based on the assumption that $\mathbf{u} = \mathbf{G} \cdot \mathbf{v}$. Some other technical conditions must be satisfied for independent components analysis to extract reasonable causes, specifically the prior distributions over causes $p[v] \propto \exp(g(v))$ must be non-Gaussian and, at least to the extent of being correctly super- or sub-Gaussian, must faithfully reflect the actual distribution over causes. The particular form $p[v] \propto 1/\cosh(v)$ is super-Gaussian, and thus generates a sparse prior. There are variants of independent components analysis in which the prior distributions are adaptive.

The independent components algorithm was suggested by Bell and Sejnowski (1995) from the different perspective of maximizing the mutual information between \mathbf{u} and \mathbf{v} when $v_a(\mathbf{u}) = f([\mathbf{W} \cdot \mathbf{u}]_a)$, with a particular, monotonically increasing nonlinear function f . Maximizing the mutual information in this context requires maximizing the entropy of the distribution over \mathbf{v} . This, in turn, requires the components of \mathbf{v} to be as independent as possible because redundancy between them reduces the entropy. In the case that $f(v) = g'(v)$, the expression for the entropy is the same as that for the log likelihood $L(\mathbf{W})$ in equation 10.35, up to constant factors, so maximizing the entropy and performing maximum likelihood density estimation are identical.

An advantage of independent components analysis over other sparse coding algorithms is that, because the recognition model is an exact inverse of the generative model, receptive as well as projective fields can be constructed. Just as the projective field for v_a can be represented by the matrix elements G_{ab} for all b values, the receptive field is given by W_{ab} for all b .

To illustrate independent components analysis, figure 10.7 shows an (admittedly bizarre) example of its application to the sounds created by tapping a tooth while adjusting the shape of the mouth to reproduce a tune by Beethoven. The input, sampled at 8 kHz, has the spectrogram shown in figure 10.7A. In this example, we have some idea about likely causes. For example, the plots in figures 10.7B & C show high- and low-frequency tooth taps, although other causes arise from the imperfect recording conditions. A close variant of the independent components analysis method described above was used to extract $N_v = 100$ independent components.

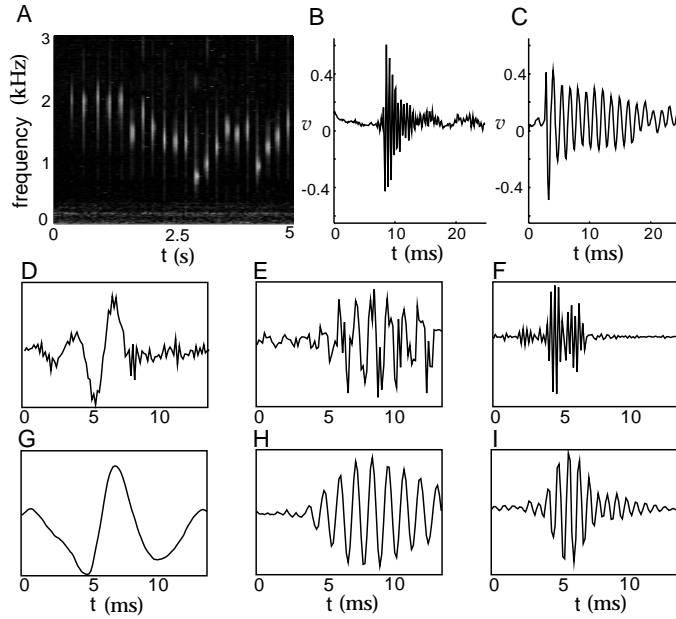


Figure 10.7: Independent components of tooth-tapping sounds. A) Spectrogram of the input. B & C) Waveforms for high- and low-frequency notes. The mouth acts as a damped resonant cavity in the generation of these tones. D, E, & F) Three independent components calculated on the basis of 1/80 s samples taken from the input at random times. The graphs show the receptive fields (from W) for three output units. D is reported as being sensitive to the sound of an air-conditioner. E & F extract tooth taps of different frequencies. G, H, & I) The associated projective fields (from G), showing the input activity associated with the causes in D, E, & F. (Adapted from Bell and Sejnowski, 1996.)

Figure 10.7D, E, & F show the receptive fields of three of these components. The last two extract particular frequencies in the input. Figure 10.7G, H, & I show projective fields. Note that the projective fields are much smoother than the receptive fields.

Bell and Sejnowski (1997) also used visual input data similar to those used in the example of figure 10.6, along with the prior $p[v] \propto 1/\cosh(v)$, and found that independent components analysis extracts Gabor-like receptive fields similar to the projective fields shown in figure 10.6A.

The Helmholtz Machine

The Helmholtz machine was designed to accommodate hierarchical architectures that construct complex multilayer representations. The model involves two interacting networks, one with parameters G that is driven in the top-down direction to implement the generative model, and the other, with parameters W , driven bottom-up to implement the recogni-

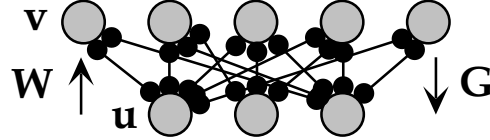


Figure 10.8: Network for the Helmholtz machine. In the bottom-up network, representational units v are driven by inputs u through feedforward weights W . In the top-down network, the inputs are driven by the v units through feedback weights G .

tion model. The parameters are determined by a modified EM algorithm that results in roughly symmetric updates for the two networks.

We consider a simple, two-layer, nonlinear Helmholtz machine with binary units, so that u_b and v_a for all b and a take the values 0 or 1. For this model,

$$P[\mathbf{v}; G] = \prod_a (f(g_a))^{v_a} (1 - f(g_a))^{1-v_a} \quad (10.39)$$

$$P[\mathbf{u}|\mathbf{v}; G] = \prod_b (f(h_b + [\mathbf{G} \cdot \mathbf{v}]_b))^{u_b} (1 - f(h_b + [\mathbf{G} \cdot \mathbf{v}]_b))^{1-u_b} \quad (10.40)$$

where g_a is a generative bias weight for output a that controls how frequently $v_a = 1$, h_b is the generative bias weight for u_b , and $f(g) = 1/(1 + \exp(-g))$ is the standard sigmoid function. The generative model is thus parameterized by $G = (\mathbf{g}, \mathbf{h}, \mathbf{G})$. According to these distributions, the components of \mathbf{v} are mutually independent, and the components of \mathbf{u} are independent given a fixed value of \mathbf{v} .

The generative model is non-invertible in this case, so an approximate recognition distribution must be constructed. This uses a similar form as equation 10.40, only using the bottom-up weights W and biases w

$$Q[\mathbf{v}; \mathbf{u}, W] = \prod_a (f(w_a + [\mathbf{W} \cdot \mathbf{u}]_a))^{v_a} (1 - f(w_a + [\mathbf{W} \cdot \mathbf{u}]_a))^{1-v_a}. \quad (10.41)$$

The parameter list for the recognition model is $W = (\mathbf{w}, \mathbf{W})$. This distribution is only an approximate inverse of the generative model because it implies that the components of \mathbf{v} are independent when, in fact, given a particular input \mathbf{u} , they are conditionally dependent, due to the way they can interact in equation 10.40 to generate \mathbf{u} .

The EM algorithm for this non-invertible model would consist of alternately maximizing the function F given by

$$F(W, G) = \left\langle \sum_{\mathbf{v}} Q[\mathbf{v}; \mathbf{u}, W] \ln \frac{P[\mathbf{v}, \mathbf{u}; G]}{Q[\mathbf{v}; \mathbf{u}, W]} \right\rangle \quad (10.42)$$

with respect to the parameters W and G . For the M phase of the Helmholtz machine, this is exactly what is done. However, during the

E phase, maximizing with respect to W is problematic because the function $Q[\mathbf{v}; \mathbf{u}, W]$ appears in two places in the expression for F . This also makes the learning rule during the E phase take a different form from that of the M phase rule. Instead, the Helmholtz machine uses a simpler and more symmetric approximation to EM.

The approximation to EM used by the Helmholtz machine is constructed by re-expressing F from equation 10.9, explicitly writing out the average over input data and then the expression for the Kullback-Leibler divergence,

$$\begin{aligned} F(W, G) &= L(G) - \sum_{\mathbf{u}} P[\mathbf{u}] D_{\text{KL}}(Q[\mathbf{v}; \mathbf{u}, W], P[\mathbf{v}|\mathbf{u}; G]) \quad (10.43) \\ &= L(G) - \sum_{\mathbf{u}} P[\mathbf{u}] \sum_{\mathbf{v}} Q[\mathbf{v}; \mathbf{u}, W] \ln \left(\frac{Q[\mathbf{v}; \mathbf{u}, W]}{P[\mathbf{v}|\mathbf{u}; G]} \right). \end{aligned}$$

This is the function that is maximized with respect to G during the M phase for the Helmholtz machine. However, the E phase is not based on maximizing equation 10.43 with respect to W . Instead, an approximate F function that we call \tilde{F} is used. This is constructed by using $P[\mathbf{u}; G]$ as an approximation for $P[\mathbf{u}]$ and $D_{\text{KL}}(P[\mathbf{v}|\mathbf{u}; G], Q[\mathbf{v}; \mathbf{u}, W])$ as an approximation for $D_{\text{KL}}(Q[\mathbf{v}; \mathbf{u}, W], P[\mathbf{v}|\mathbf{u}; G])$ in equation 10.43. These are likely to be good approximations if the generative and approximate recognition models are accurate. Thus, we write

$$\begin{aligned} \tilde{F}(W, G) &= L(G) - \sum_{\mathbf{u}} P[\mathbf{u}; G] D_{\text{KL}}(P[\mathbf{v}|\mathbf{u}; G], Q[\mathbf{v}; \mathbf{u}, W]) \quad (10.44) \\ &= L(G) - \sum_{\mathbf{u}} P[\mathbf{u}; G] \sum_{\mathbf{v}} P[\mathbf{v}|\mathbf{u}; G] \ln \left(\frac{P[\mathbf{v}|\mathbf{u}; G]}{Q[\mathbf{v}; \mathbf{u}, W]} \right). \end{aligned}$$

and maximize this, rather than F , with respect to W during the E phase. This amounts to averaging the ‘flipped’ Kullback-Leibler divergence over samples of \mathbf{u} created by the generative model, rather than real data samples. The advantage of making these approximations is that the E and M phases become highly symmetric, as can be seen by examining the second equalities in equations 10.43 and 10.44.

Learning in the Helmholtz machine proceeds using stochastic sampling to replace the weighted sums in equations 10.43 and 10.44. In the M phase, an input \mathbf{u} from $P[\mathbf{u}]$ is presented, and a sample \mathbf{v} is drawn from the current recognition distribution $Q[\mathbf{v}; \mathbf{u}, W]$. Then, the generative weights G are changed according to the discrepancy between \mathbf{u} and the generative or top-down prediction $f(\mathbf{h} + G \cdot \mathbf{v})$ of \mathbf{u} (see the appendix). Thus, the generative model is trained to make \mathbf{u} more likely to be generated by the cause \mathbf{v} associated with it by the recognition model. In the E phase, samples of both \mathbf{v} and \mathbf{u} are drawn from the generative model distributions $P[\mathbf{v}; G]$ and $P[\mathbf{u}|\mathbf{v}; G]$, and the recognition parameters W are changed according to the discrepancy between the sampled cause \mathbf{v} , and the recognition or bottom-up prediction $f(\mathbf{w} + W \cdot \mathbf{u})$ of \mathbf{v} (see the appendix). The rationale

for this is that the v that was used by the generative model to create u is a good choice for its cause in the recognition model.

The two phases of learning are sometimes called wake and sleep because learning in the first phase is driven by real inputs u from the environment, while learning in the second phase is driven by values v and u ‘fantasized’ by the generative model. This terminology is based on slightly different principles from the wake and sleep phases of the Boltzmann machine discussed in chapter 8. The sleep phase is only an approximation of the actual E phase, and general conditions under which learning converges appropriately are not known.

wake-sleep algorithm

10.4 Discussion

Because of the widespread significance of coding, transmitting, storing, and decoding visual images such as photographs and movies, substantial effort has been devoted to understanding the structure of this class of inputs. As a result, visual images provide an ideal testing ground for representational learning algorithms, allowing us to go beyond evaluating the representations they produce solely in terms of the log likelihood and qualitative similarities with cortical receptive fields.

Most modern image (and auditory) processing techniques are based on multi-resolution decompositions. In such decompositions, images are represented by the activity of a population of units with systematically varying spatial frequency preferences and different orientations, centered at various locations on the image. The outputs of the representational units are generated by filters (typically linear) that act as receptive fields and are partially localized in both space and spatial frequency. The filters usually have similar underlying forms, but they are cast at different spatial scales and centered at different locations for the different units. Systematic versions of such representations, in forms such as wavelets, are important signal processing tools, and there is an extensive body of theory about their representational and coding qualities. Representation of sensory information in separated frequency bands at different spatial locations has significant psychophysical consequences as well.

The projective fields of the units in the sparse coding network shown in figure 10.6 suggest that they construct something like a multi-resolution decomposition of inputs, with multiple spatial scales, locations, and orientations. Thus, multi-resolution analysis gives us a way to put into sharper focus the issues arising from models such as sparse coding and independent components analysis. After a brief review of multi-resolution decompositions, we use them to consider properties of representational learning from the perspective of information transmission and sparseness, overcompleteness, and residual dependencies between inferred causes.

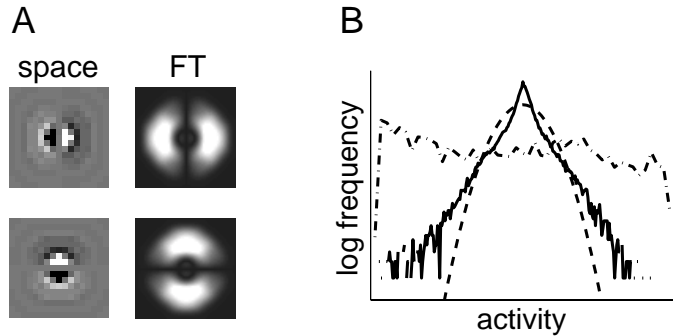


Figure 10.9: Multi-resolution filtering. A) Vertical and horizontal filters (left) and their Fourier transforms (right) that are used at multiple positions and spatial scales to generate a multi-resolution representation. The rows of the matrix \mathbf{W} are displayed here in grey-scale on a two-dimensional grid representing the location of the corresponding input. B) Log frequency distribution of the outputs of the highest spatial frequency filters (solid line) compared with a Gaussian distribution with the same mean and variance (dashed line) and the distribution of pixel values for the image shown in figure 10.10A (dot-dashed line). The pixel values of the image were rescaled to fit into the range. (Adapted from Simoncelli and Freeman, 1995; Karasidis and Simoncelli, 1996 & 1997.)

Multi-resolution decomposition

Many multi-resolution decompositions, with a variety of computational and representational properties, can be expressed as linear transformations $\mathbf{v} = \mathbf{W} \cdot \mathbf{u}$ where the rows of \mathbf{W} describe filters, such as those illustrated in figure 10.9A. Figure 10.10 shows the result of applying multi-resolution filters, constructed by scaling and shifting the filters shown in figure 10.9A, to the photograph in figure 10.10A. Vertical and horizontal filters similar to those in figure 10.9A, but with different sizes, produce the decomposition shown in figures 10.10B-D and F-H when translated across the image. The greyscale indicates the output generated by placing the different filters over the corresponding points on the image. These outputs, plus the low-pass image in figure 10.10E and an extra high-pass image that is not shown, can be used to reconstruct the whole photograph almost perfectly through a generative process that is the inverse of the recognition process.

Coding

One reason for using multi-resolution decompositions is that they offer efficient ways of encoding visual images. The raw values of input pixels provide an inefficient encoding of images. This is illustrated by the dot-dashed line in figure 10.9B, which shows that the distribution over the values of the input pixels of the image in figure 10.10A is approximately

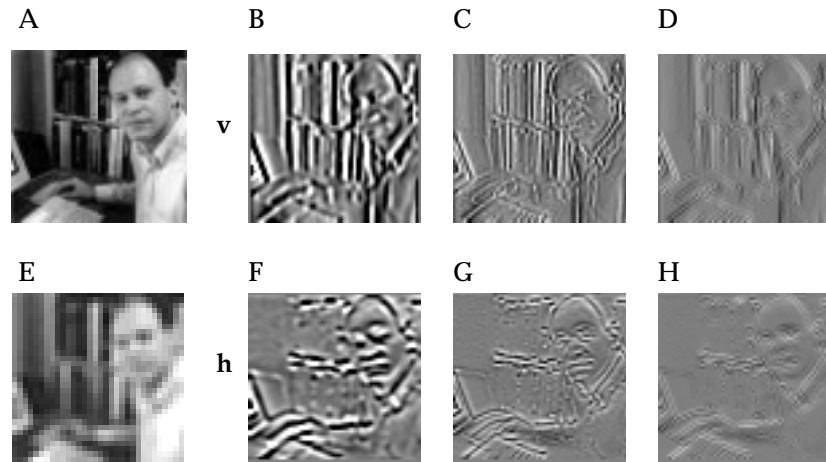


Figure 10.10: Multi-resolution image decomposition. A gray-scale image is decomposed using the pair of vertical and horizontal filters shown in figure 10.9. A) The original image. B, C, & D) The outputs of successively higher spatial frequency vertically oriented filters translated across the image. E) The image after passage through a low-pass filter. F, G, & H) The outputs of successively higher spatial frequency horizontally oriented filters translated across the image.

flat or uniform. Up to the usual additive constants related to the precision with which filter outputs are encoded, the contribution to the coding cost from a single unit is the entropy of the probability distribution of its output. The distribution over pixel intensities is flat, which is the maximum entropy distribution for a variable with a fixed range. Encoding the individual pixel values therefore incurs the maximum possible coding cost.

By contrast, the solid line in figure 10.9B shows the distribution of the outputs of the finest scale vertically and horizontally tuned filters (figures 10.10D & H) in response to figure 10.10A. The filter outputs have a sparse distribution similar to the double exponential distribution in figure 10.4B. This distribution has significantly lower entropy than the uniform distribution, so the filter outputs provide a more efficient encoding than pixel values.

In making these statements about the distributions of activities, we are equating the output distribution of a filter applied at many locations on a single image with the output distribution of a filter applied at a fixed location on many images. This assumes spatial translational invariance of the ensemble of visual images.

Images represented by multi-resolution filters can be further compressed by retaining only approximate values of the filter outputs. This is called lossy coding and may consist of reporting filter outputs as integer multiples of a basic unit. Making the multi-resolution code for an image lossy by coarsely quantizing the outputs of the highest spatial frequency filters generally has quite minimal perceptual consequences while saving sub-

lossy coding

stantial coding cost (because these outputs are most numerous). This fact illustrates the important point that trying to build generative models of all aspects of visual images may be unnecessarily difficult, because only certain aspects of images are actually relevant. Unfortunately, abstract principles are unlikely to tell us what information in the input can safely be discarded independent of details of how the representations are to be used.

Overcomplete Representations

Sparse representations often have more output units than input units. Such representations, called overcomplete, are the subject of substantial work in multi-resolution theory. Many reasons have been suggested for overcompleteness, although none obviously emerges from the requirement of fitting good probabilistic models to input data.

One interesting idea comes from the notion that the task of manipulating representations should be invariant to the groups of symmetry transformations of the input, which, for images, include rotation, translation, and scaling. Complete representations are minimal, and so do not densely sample orientations. This means that the operations required to manipulate images of objects presented at angles not directly represented by the filters are different from those required at the represented angles (such as horizontal and vertical for the example of figure 10.9). When a representation is overcomplete in such a way that different orientations are represented roughly equally, as in primary visual cortex, the computational operations required to manipulate images are more uniform as a function of image orientation. Similar ideas apply across scale, so that the operations required to manipulate large and small images of the same object (as if viewed from near or far) are likewise similar. It is impossible to generate representations that satisfy all these constraints perfectly.

In more realistic models that include noise, other rationales for overcompleteness come from considering population codes, in which many units redundantly report information about closely related quantities so that uncertainty can be reduced. Despite the ubiquity of overcomplete population codes in the brain, there are few representational learning models that produce them satisfactorily. The coordinated representations required to construct population codes are often incompatible with other heuristics such as factorial or sparse coding.

Interdependent Causes

One of the failings of multi-resolution decompositions for coding is that the outputs are not mutually independent. This makes encoding each of the redundant filter outputs wasteful. Figure 10.11 illustrates such an interdependence by showing the conditional distribution for the output v_c of

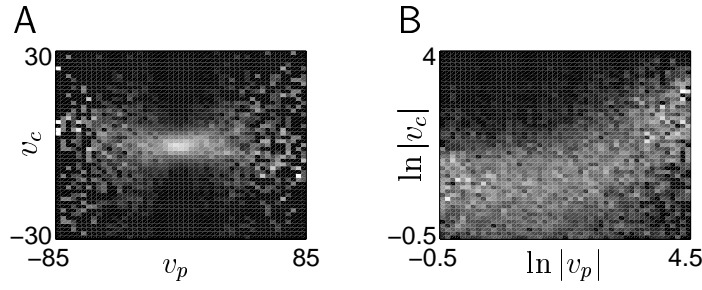


Figure 10.11: A) Gray-scale plot of the conditional distribution of the output of a filter at the finest spatial scale (v_c) given the output of a coarser filter (v_p) with the same position and orientation (using the picture in figure 10.10A as input data). Each column is separately normalized. The plot has a characteristic bow-tie shape. B) The same data plotted as the conditional distribution of $\ln|v_c|$ given $\ln|v_p|$. (Adapted from Simoncelli and Adelson, 1990; Simoncelli and Schwartz, 1999.)

a horizontally tuned filter at a fine scale, given the output v_p of a horizontally tuned unit at the next coarser scale. The plots show gray-scale values of the conditional probability density $p[v_c|v_p]$. The mean of this distribution is roughly 0, but there is a clear correlation between the magnitude of $|v_p|$ and the variance of v_c . This means that structure in the image is coordinated across different spatial scales, so that high outputs from a coarse scale filter are typically accompanied by substantial output (of one sign or the other) at a finer scale. Following Simoncelli (1997), we plot the conditional distribution of $\ln|v_c|$ given $\ln|v_p|$ in figure 10.11B. For small values of $\ln|v_p|$, the distribution of $\ln|v_c|$ is flat, but for larger values of $\ln|v_p|$ the growth in the value of $|v_c|$ is clear.

The interdependence shown in figure 10.11 suggests a failing of sparse coding to which we have alluded before. Although the prior distribution for sparse coding stipulates independent causes, the causes identified as underlying real images are not independent. The dependence apparent in figure 10.11 can be removed by a nonlinear transformation in which the outputs of the units normalize each other (similar to the model introduced to explain contrast saturation in chapter 2). This transformation can lead to more compact codes for images. However, the general problem suggests that something is amiss with the heuristic of seeking independent causes for representations early in the visual pathway.

The most important dependencies as far as causal models are concerned are those induced by the presence in images of objects with large-scale coordinated structure. Finding and building models of these dependencies is the goal for more sophisticated and hierarchical representational learning schemes aimed ultimately at object recognition within complex visual scenes.

10.5 Chapter Summary

We have presented a systematic treatment of exact and approximate maximum likelihood density estimation as a way of fitting probabilistic generative models and thereby performing representational learning. Recognition models, which are the statistical inverses of generative models, specify the causes underlying an input and play a crucial role in learning. We discussed the expectation maximization (EM) algorithm applied to invertible and non-invertible models, including the use of deterministic and probabilistic approximate recognition models and a lower bound to the log likelihood.

We presented a variety of models for continuous inputs with discrete, continuous, or vector-valued causes. These include mixture of Gaussians, K-means, factor analysis, principal components analysis, sparse coding, and independent components analysis. We also described the Helmholtz machines and discussed general issues of multi-resolution representation and coding.

10.6 Appendix

Summary of Causal Models

Model	Generative Model	Recognition Model	Learning Rules
mixture of Gaussians	$P[v; G] = \gamma_v$ $P[\mathbf{u} v; G] = N(\mathbf{u}; \mathbf{g}_v, \Sigma_v)$	$P[v \mathbf{u}; G] \propto \gamma_v N(\mathbf{u}; \mathbf{g}_v, \Sigma_v)$	$\mu_v = \langle P[v \mathbf{u}; G] \rangle$ $\mathbf{g}_v = \langle P[v \mathbf{u}; G \mathbf{u}] \rangle$ $\Sigma_v = \langle P[v \mathbf{u}; G \mathbf{u} - \mathbf{g}_v]^2 \rangle / (N_u \gamma_v)$
factor analysis	$P[\mathbf{v}; G] = N(\mathbf{v}; \mathbf{0}, \mathbf{I})$ $P[\mathbf{u} \mathbf{v}; G] = N(\mathbf{u}; \mathbf{G} \cdot \mathbf{v}, \Sigma)$ $\Sigma = \text{diag}(\Sigma_1, \Sigma_2, \dots, \Sigma_{N_u})$	$P[\mathbf{v} \mathbf{u}; G] = N(\mathbf{v}; \mathbf{W} \cdot \mathbf{u}, \Psi)$ $\Psi = (\mathbf{I} + \mathbf{G}^\top \cdot \Sigma^{-1} \cdot \mathbf{G})^{-1}$ $\mathbf{W} = \Psi \cdot \mathbf{G}^\top \cdot \Sigma^{-1}$	$\mathbf{G} = \mathbf{C} \cdot \mathbf{W}^\top \cdot (\mathbf{W} \cdot \mathbf{C} \cdot \mathbf{W}^\top + \Psi)^{-1}$ $\Sigma = \text{diag}(\mathbf{G} \cdot \Psi \cdot \mathbf{G}^\top + (\mathbf{I} - \mathbf{G} \cdot \mathbf{W}) \cdot \mathbf{C} \cdot (\mathbf{I} - \mathbf{G} \cdot \mathbf{W})^\top)$ $\mathbf{C} = \langle \mathbf{u}\mathbf{u} \rangle$
principal components analysis	$P[\mathbf{v}; G] = N(\mathbf{v}; \mathbf{0}, \mathbf{I})$ $\mathbf{u} = \mathbf{G} \cdot \mathbf{v}$	$\mathbf{v} = \mathbf{W} \cdot \mathbf{u}$ $\mathbf{W} = (\mathbf{G}^\top \cdot \mathbf{G})^{-1} \cdot \mathbf{G}^\top$	$\mathbf{G} = \mathbf{C} \cdot \mathbf{W}^\top \cdot (\mathbf{W} \cdot \mathbf{C} \cdot \mathbf{W}^\top)^{-1}$ $\mathbf{C} = \langle \mathbf{u}\mathbf{u} \rangle$
sparse coding	$P[\mathbf{v}; G] \propto \prod_a \exp(g(v_a))$ $P[\mathbf{u} \mathbf{v}; G] = N(\mathbf{u}; \mathbf{G} \cdot \mathbf{v}, \Sigma)$	$\mathbf{G}^\top \cdot (\mathbf{u} - \mathbf{G} \cdot \mathbf{v}) + \mathbf{g}'(\mathbf{v}) = 0$	$\mathbf{G} \rightarrow \mathbf{G} + \epsilon(\mathbf{u} - \mathbf{G} \cdot \mathbf{v})\mathbf{v}$ $(\sum_b G_{ba}^2) \rightarrow (\sum_b G_{ba}^2)((v_a^2 - (v_a)^2)/\sigma^2)^{0.01}$
independent components analysis	$P[\mathbf{v}; G] \propto \prod_a \exp(g(v_a))$ $\mathbf{u} = \mathbf{G} \cdot \mathbf{v}$	$\mathbf{v} = \mathbf{W} \cdot \mathbf{u}$ $\mathbf{W} = \mathbf{G}^{-1}$	$\mathbf{W}_{ab} \rightarrow \mathbf{W}_{ab} + \epsilon(\mathbf{W}_{ab} - g'(v_a))[\mathbf{v} \cdot \mathbf{W}]_b$ $g'(v) = \tanh(v) \text{ if } g(v) = -\ln \cosh(v)$
binary Helmholtz machine	$P[\mathbf{v}; G] = \prod_a (f(\mathbf{g}_a))^{v_a} (1 - f(\mathbf{g}_a))^{1-v_a}$ $P[\mathbf{u} \mathbf{v}; G] = \prod_b (f_b(\mathbf{h} + \mathbf{G} \cdot \mathbf{v}))^{u_b} (1 - f_b(\mathbf{h} + \mathbf{G} \cdot \mathbf{v}))^{1-u_b}$ $f_b(\mathbf{h} + \mathbf{G} \cdot \mathbf{v}) = f(h_b + [\mathbf{G} \cdot \mathbf{v}]_b)$	$Q[\mathbf{v}; \mathbf{u}, W] = \prod_a (f_a(\mathbf{w} + \mathbf{W} \cdot \mathbf{u}))^{u_a} \times (1 - f_a(\mathbf{w} + \mathbf{W} \cdot \mathbf{u}))^{1-u_a}$ $f_a(\mathbf{w} + \mathbf{W} \cdot \mathbf{u}) = f(w_a + [\mathbf{W} \cdot \mathbf{u}]_a)$	wake: $\mathbf{u} \sim P[\mathbf{u}]$, $\mathbf{v} \sim Q[\mathbf{v}; \mathbf{u}, W]$ $\mathbf{g} \rightarrow \mathbf{g} + \epsilon(\mathbf{v} - f(\mathbf{g}))$ $\mathbf{h} \rightarrow \mathbf{h} + \epsilon(\mathbf{u} - f(\mathbf{h} + \mathbf{G} \cdot \mathbf{v}))$ $\mathbf{G} \rightarrow \mathbf{G} + \epsilon(\mathbf{u} - f(\mathbf{h} + \mathbf{G} \cdot \mathbf{v}))\mathbf{v}$ sleep: $\mathbf{v} \sim P[\mathbf{v}; G]$, $\mathbf{u} \sim P[\mathbf{u}; \mathbf{v}, G]$ $\mathbf{w} \rightarrow \mathbf{w} + \epsilon(\mathbf{v} - f(\mathbf{w} + \mathbf{W} \cdot \mathbf{u}))$ $\mathbf{W} \rightarrow \mathbf{W} + \epsilon(\mathbf{v} - f(\mathbf{w} + \mathbf{W} \cdot \mathbf{u}))\mathbf{u}$

Table 1: All models are discussed in detail in the text, and the forms quoted are just for the simplest cases. $N(\mathbf{u}; \mathbf{g}, \Sigma)$ is a multivariate Gaussian distribution with mean \mathbf{g} and covariance matrix Σ (for $N(\mathbf{u}; \mathbf{g}, \Sigma)$, the variance of each component is Σ). For the sparse coding network, σ^2 is a target for the variances of each output unit. For the Helmholtz machine, $f(c) = 1/(1 + \exp(-c))$, and the symbol \sim indicates that the indicated variable is drawn from the indicated distribution. Other symbols and distributions are defined in the text.

10.7 Annotated Bibliography

The literature on unsupervised representational learning models is extensive. Recent reviews, from which we have borrowed, include Hinton (1989); Bishop (1995); Hinton & Ghahramani (1997); and Becker & Plumbley (1996), which also describes unsupervised learning methods such as IMAX (Becker & Hinton (1992)) that find statistical structure in the inputs directly rather than through causal models (see also projection pursuit, Huber, 1985). The field of belief networks or graphical statistical models (Pearl (1988); Lauritzen (1996); Jordan (1998)) provides an even more general framework for probabilistic generative models. Apart from Barlow (1961; 1989), early inspiration for unsupervised learning models came from Uttley (1979) and Marr (1970) and the adaptive resonance theory (ART) of Carpenter & Grossberg (see 1991).

Analysis by synthesis (e.g. Neisser, 1967), to which generative and recognition models are closely related, was developed in a statistical context by Grenander (1995), and was suggested by Mumford (1994) as a way of understanding hierarchical neural processing. Suggestions by MacKay (1956); Pece (1992); Kawato, et al., (1993); Rao & Ballard (1997) can be seen in a similar light.

Nowlan (1991) introduced the mixtures of Gaussians architecture into neural networks. Mixture models are commonplace in statistics and are described by Titterington et al. (1985).

Factor analysis is described by Everitt (1984), and some of the differences and similarities between factor analysis and principal components analysis are brought out by Jolliffe (1986); Tipping & Bishop (1999); Roweis & Ghahramani (1999). Rubin & Thayer (1982) discuss the use of EM for factor analysis. Roweis (1998) discusses EM for principal components analysis.

Neal & Hinton (1998) describe F and its role in the EM algorithm (Baum, et al., 1970; Dempster et al., 1977). EM is closely related to mean field methods in physics, as discussed by Jordan et al. (1996); Saul & Jordan (2000). Hinton & Zemel (1994); Zemel (1994) used F for unsupervised learning in a backpropagation network called the autoencoder and related their results to minimum description length coding (Rissanen, 1989). Hinton et al. (1995); Dayan et al. (1995) use F in the Helmholtz machine and the associated wake-sleep algorithm.

Olshausen & Field (1996) suggest the sparse coding network based on Field's (1994) general analysis of sparse representations, and Olshausen (1996) develops some of the links to density estimation. Independent components analysis (ICA) was introduced as a problem by Herault & Jutten (1986). The version of ICA algorithm that we described is due to Bell & Sejnowski (1995); Roth & Baram (1996), using the natural gradient trick of Amari (1999), and the derivation we used is due to Mackay (1996). Pearlmutter & Parga (1996) and Olshausen (1996) also derive maximum

likelihood interpretations of ICA. Multi-resolution decompositions were introduced into computer vision by Witkin (1983); Burt & Adelson (1983), and wavelet analysis is reviewed in Daubechies (1992); Simoncelli et al. (1992); Mallat (1998).

Mathematical Appendix

The book assumes a familiarity with basic methods of linear algebra, differential equations, and probability theory, as covered in standard texts. This chapter describes the notation we use and briefly sketches highlights of various techniques. The references provide further information.

Linear Algebra

An operation O on a quantity z is called linear if, applied to any two instances z_1 and z_2 , $O(z_1 + z_2) = O(z_1) + O(z_2)$. In this section, we consider linear operations on vectors and functions. We define a vector \mathbf{v} as an array of N numbers (v_1, v_2, \dots, v_N) or equivalently v_a for $a = 1, 2, \dots, N$, which are called its components. These are sometimes listed in a single N -row column

$$\mathbf{v} = \begin{pmatrix} v_1 \\ v_2 \\ \vdots \\ v_N \end{pmatrix}. \quad (1)$$

When necessary, we write component a of \mathbf{v} as $[\mathbf{v}]_a = v_a$. We use $\mathbf{0}$ to denote the vector with all its components equal to zero. Spatial vectors, which are related to displacements in space, are a special case, and we denote them by \vec{v} with components v_x and v_y in two-dimensional space or v_x , v_y , and v_z in three-dimensional space.

The length or norm of \mathbf{v} , $|\mathbf{v}|$, when squared, can be written as a dot product

$$|\mathbf{v}|^2 = \mathbf{v} \cdot \mathbf{v} = \sum_{a=1}^N v_a^2 = v_1^2 + v_2^2 + \dots + v_N^2. \quad (2)$$

The dot product of two different N -component vectors, \mathbf{v} and \mathbf{u} is,

$$\mathbf{v} \cdot \mathbf{u} = \sum_{a=1}^N v_a u_a. \quad (3)$$

matrix \mathbf{W}

Matrix multiplication is a basic linear operation on vectors. An N_r by N_c matrix \mathbf{W} is an array of N_r rows and N_c columns

$$\mathbf{W} = \begin{pmatrix} W_{11} & W_{12} & \dots & W_{1N_c} \\ W_{21} & W_{22} & \dots & W_{2N_c} \\ \vdots & & & \\ W_{Nr1} & W_{Nr2} & \dots & W_{NrN_c} \end{pmatrix} \quad (4)$$

with elements W_{ab} for $a = 1, \dots, N_r$ and $b = 1, \dots, N_c$. In this text, multiplication of a vector by a matrix is written in the somewhat idiosyncratic notation $\mathbf{W} \cdot \mathbf{v}$. The dot implies multiplication and summation over a shared index, as it does for the dot product. If \mathbf{W} is an N_r by N_c matrix and \mathbf{v} is a N_c -component vector, $\mathbf{W} \cdot \mathbf{v}$ is an N_r -component vector with components

$$[\mathbf{W} \cdot \mathbf{v}]_a = \sum_{b=1}^{N_c} W_{ab} v_b. \quad (5)$$

In conventional matrix notation, the product of a matrix and a vector is written as $\mathbf{W}\mathbf{v}$, but we prefer to use the dot notation to avoid frequent occurrences of matrix transposes (see below). We similarly denote a matrix product as $\mathbf{W} \cdot \mathbf{M}$. Matrices can only be multiplied in this way if the number of columns of \mathbf{W} , N_c , is equal to the number of rows of \mathbf{M} . Then, $\mathbf{W} \cdot \mathbf{M}$ is a matrix with the same number of rows as \mathbf{W} and the same number of columns as \mathbf{M} , and with elements

$$[\mathbf{W} \cdot \mathbf{M}]_{ab} = \sum_{c=1}^{N_c} W_{ac} M_{cb}. \quad (6)$$

A vector, written as in equation 1, is equivalent to a one-column, N -row matrix, and the rules for various matrix operations can thus be applied to vectors as well.

square matrix identity matrix

Square matrices are those for which $N_r = N_c = N$. An important square matrix is the identity matrix \mathbf{I} with elements

$$[\mathbf{I}]_{ab} = \delta_{ab} \quad (7)$$

where the Kronecker delta is defined as

$$\delta_{ab} = \begin{cases} 1 & \text{if } a = b \\ 0 & \text{otherwise.} \end{cases} \quad (8)$$

diagonal matrix

Another important type of square matrix is the diagonal matrix, defined by

$$\mathbf{W} = \text{diag}(h_1, h_2, \dots, h_N) = \begin{pmatrix} h_1 & 0 & \dots & 0 \\ 0 & h_2 & \dots & 0 \\ \vdots & & & \\ 0 & 0 & \dots & h_N \end{pmatrix}, \quad (9)$$

which has components $W_{ab} = h_a \delta_{ab}$ for some set of h_a , $a = 1, 2, \dots, N$.

transpose

The transpose of an N_r by N_c matrix \mathbf{W} is an N_c by N_r matrix \mathbf{W}^T with elements $[\mathbf{W}^T]_{ab} = W_{ba}$. The transpose of a column vector is a row vector, $\mathbf{v}^T = (v_1 v_2 \dots v_N)$. This is distinguished by the absence of commas from (v_1, v_2, \dots, v_N) which, for us, is a listing of the components of a column vector. In the following table, we define a number of products involving vectors and matrices. In the definitions, we provide our notation and the corresponding expressions in terms of vector components and matrix elements. We also provide the conventional matrix notation for these quantities as well as the notation used by MATLAB, a computer software package commonly used to perform these operations numerically. For the MATLAB notation (which does not use bold or italic symbols), we denote two column vectors by \mathbf{u} and \mathbf{v} , assuming they are defined within MATLAB by instructions such as $\mathbf{v} = [\mathbf{v}(1) \ \mathbf{v}(2) \ \dots \ \mathbf{v}(N)]'$.

Quantity	Definition	Matrix	MATLAB
norm	$ \mathbf{v} ^2 = \mathbf{v} \cdot \mathbf{v} = \sum_a v_a^2$	$\mathbf{v}^T \mathbf{v}$	$\mathbf{v}' * \mathbf{v}$
dot product	$\mathbf{v} \cdot \mathbf{u} = \sum_a v_a u_a$	$\mathbf{v}^T \mathbf{u}$	$\mathbf{v}' * \mathbf{u}$
outer product	$[\mathbf{v}\mathbf{u}]_{ab} = v_a u_b$	$\mathbf{v}\mathbf{u}^T$	$\mathbf{v} * \mathbf{u}'$
matrix-vector product	$[\mathbf{W} \cdot \mathbf{v}]_a = \sum_b W_{ab} v_b$	$\mathbf{W}\mathbf{v}$	$\mathbf{W} * \mathbf{v}$
vector-matrix product	$[\mathbf{v} \cdot \mathbf{W}]_a = \sum_b v_b W_{ba}$	$\mathbf{v}^T \mathbf{W}$	$\mathbf{v}' * \mathbf{W}$
quadratic form	$\mathbf{v} \cdot \mathbf{W} \cdot \mathbf{u} = \sum_{ab} v_a W_{ab} u_b$	$\mathbf{v}^T \mathbf{W} \mathbf{u}$	$\mathbf{v}' * \mathbf{W} * \mathbf{u}$
matrix-matrix product	$[\mathbf{W} \cdot \mathbf{M}]_{ab} = \sum_c W_{ac} M_{cb}$	$\mathbf{W}\mathbf{M}$	$\mathbf{W} * \mathbf{M}$

Several important definitions for square matrices are:

Operation	Notation	Definition	MATLAB
transpose	\mathbf{W}^T	$\mathbf{W}_{ab}^T = W_{ba}$	\mathbf{W}'
inverse	\mathbf{W}^{-1}	$\mathbf{W} \cdot \mathbf{W}^{-1} = \mathbf{I}$	$\text{inv}(\mathbf{W})$
trace	$\text{tr}\mathbf{W}$	$\sum_a W_{aa}$	$\text{trace}(\mathbf{W})$
determinant	$\det \mathbf{W}$	see references	$\det(\mathbf{W})$

A square matrix only has an inverse if its determinant is nonzero. Square matrices with certain properties are given special names:

Property	Definition
symmetric	$\mathbf{W}^T = \mathbf{W}$ or $W_{ba} = W_{ab}$
orthogonal	$\mathbf{W}^T = \mathbf{W}^{-1}$ or $\mathbf{W}^T \cdot \mathbf{W} = \mathbf{I}$
positive-definite	$\mathbf{v} \cdot \mathbf{W} \cdot \mathbf{v} > 0$ for all $\mathbf{v} \neq \mathbf{0}$
Töplitz	$W_{ab} = f(a - b)$

where $f(a - b)$ is any function of the single variable $a - b$.

del operator ∇ For any real-valued function $E(\mathbf{v})$ of a vector \mathbf{v} , we can define the vector derivative (which is sometimes called del) of $E(\mathbf{v})$ as the vector $\nabla E(\mathbf{v})$ with components

$$[\nabla E(\mathbf{v})]_a = \frac{\partial E(\mathbf{v})}{\partial v_a}. \quad (10)$$

directional derivative The derivative of $E(\mathbf{v})$ in the direction \mathbf{u} is then

$$\lim_{\epsilon \rightarrow 0} \left(\frac{E(\mathbf{v} + \epsilon \mathbf{u}) - E(\mathbf{v})}{\epsilon} \right) = \mathbf{u} \cdot \nabla E(\mathbf{v}). \quad (11)$$

Eigenvectors and Eigenvalues

eigenvector An eigenvector of a square matrix \mathbf{W} is a non-zero vector \mathbf{e} that satisfies

$$\mathbf{W} \cdot \mathbf{e} = \lambda \mathbf{e} \quad (12)$$

eigenvalue for some number λ called the eigenvalue. Possible values of λ are determined by solving the polynomial equation

$$\det(\mathbf{W} - \lambda \mathbf{I}) = 0. \quad (13)$$

Typically, but not always, this has N solutions if \mathbf{W} is an N by N matrix, and these can be either real or complex. Complex eigenvalues come in complex-conjugate pairs if \mathbf{W} has real-valued elements. We use the index μ to label the different eigenvalues and eigenvectors, λ_μ and \mathbf{e}_μ . Note that μ identifies the eigenvector (and eigenvalue) to which we are referring; it does not signify a component of the eigenvector \mathbf{e}_μ .

degeneracy If \mathbf{e} is an eigenvector, $\alpha \mathbf{e}$ is also an eigenvector for any nonzero value of α . We can use this freedom to normalize eigenvectors so that $|\mathbf{e}| = 1$. If two eigenvectors, say \mathbf{e}_1 and \mathbf{e}_2 , have the same eigenvalues $\lambda_1 = \lambda_2$, they are termed degenerate. Then, $\alpha \mathbf{e}_1 + \beta \mathbf{e}_2$ is also an eigenvector with the same eigenvalue, for any α and β that are not both zero. Apart from such degeneracies, an N by N matrix can have at most N eigenvectors, although some matrices have fewer. If \mathbf{W} has N non-degenerate eigenvalues, the eigenvectors $\mathbf{e}_1, \dots, \mathbf{e}_N$ are linearly independent, meaning that $\sum_\mu c_\mu \mathbf{e}_\mu = \mathbf{0}$ only if the coefficients $c_\mu = 0$ for all μ . These eigenvectors can be used to represent any N component vector \mathbf{v} through the relation

$$\mathbf{v} = \sum_{\mu=1}^N c_\mu \mathbf{e}_\mu, \quad (14)$$

basis with a unique set of coefficients c_μ . They are thus said to form a basis.

symmetric matrix The eigenvalues and eigenvectors of symmetric matrices (for which $\mathbf{W}^T = \mathbf{W}$) have special properties, and for the remainder of this section, we con-

sider this case. The eigenvalues of a symmetric matrix are real, and the eigenvectors are real and orthogonal (or can be made orthogonal in the case of degeneracy). This means that, if they are normalized to unit length, the eigenvectors satisfy

$$\mathbf{e}_\mu \cdot \mathbf{e}_\nu = \delta_{\mu\nu}. \quad (15)$$

This can be derived by noting that, for a symmetric matrix \mathbf{W} , $\mathbf{e}_\mu \cdot \mathbf{W} = \mathbf{W} \cdot \mathbf{e}_\mu = \lambda_\mu \mathbf{e}_\mu$. Therefore, allowing the matrix to act in both directions we find $\mathbf{e}_\nu \cdot \mathbf{W} \cdot \mathbf{e}_\mu = \lambda_\mu \mathbf{e}_\nu \cdot \mathbf{e}_\mu = \lambda_\nu \mathbf{e}_\nu \cdot \mathbf{e}_\mu$. If $\lambda_\mu \neq \lambda_\nu$, this requires $\mathbf{e}_\nu \cdot \mathbf{e}_\mu = 0$. For orthogonal and normalized (orthonormal) eigenvectors, the coefficients in equation 14 take the values

$$c_\mu = \mathbf{v} \cdot \mathbf{e}_\mu. \quad (16)$$

Let $\mathbf{E} = (\mathbf{e}_1 \ \mathbf{e}_2 \ \dots \ \mathbf{e}_N)$ be an N by N matrix with columns formed from the orthonormal eigenvectors of a symmetric matrix. From equation 15, this satisfies $[\mathbf{E}^T \cdot \mathbf{E}]_{\mu\nu} = \mathbf{e}_\mu \cdot \mathbf{e}_\nu = \delta_{\mu\nu}$. Thus, $\mathbf{E}^T = \mathbf{E}^{-1}$, making \mathbf{E} an orthogonal matrix. \mathbf{E} generates a transformation from the original matrix \mathbf{W} to a diagonal form, which is called matrix diagonalization,

$$\mathbf{E}^{-1} \cdot \mathbf{W} \cdot \mathbf{E} = \mathbf{E}^T \cdot \text{diag}(\lambda_1 \mathbf{e}_1, \dots, \lambda_N \mathbf{e}_N) = \text{diag}(\lambda_1, \dots, \lambda_N). \quad (17)$$

Conversely,

$$\mathbf{W} = \mathbf{E} \cdot \text{diag}(\lambda_1, \dots, \lambda_N) \cdot \mathbf{E}^{-1}. \quad (18)$$

The transformation to and back from a diagonal form is extremely useful because computations with diagonal matrices are easy. Defining $\mathbf{L} = \text{diag}(\lambda_1, \dots, \lambda_N)$ we find, for example, that

$$\begin{aligned} \mathbf{W}^n &= (\mathbf{E} \cdot \mathbf{L} \cdot \mathbf{E}^{-1}) \cdot (\mathbf{E} \cdot \mathbf{L} \cdot \mathbf{E}^{-1}) \cdots (\mathbf{E} \cdot \mathbf{L} \cdot \mathbf{E}^{-1}) \\ &= \mathbf{E} \cdot \mathbf{L}^n \cdot \mathbf{E}^{-1} = \mathbf{E} \cdot \text{diag}(\lambda_1^n, \dots, \lambda_N^n) \cdot \mathbf{E}^{-1}. \end{aligned} \quad (19)$$

Indeed, for any function f that can be written as a power or expanded in a power series (including, for example, exponentials and logarithms),

$$f(\mathbf{W}) = \mathbf{E} \cdot \text{diag}(f(\lambda_1), \dots, f(\lambda_N)) \cdot \mathbf{E}^{-1}. \quad (20)$$

Functional Analogs

A function $v(t)$ can be treated as if it were a vector with a continuous label. *functions as vectors* In other words, the function value $v(t)$ parameterized by the continuously varying argument t takes the place of the component v_a labeled by the integer-valued index a . In applying this analogy, sums over a for vectors are replaced by integrals over t for functions, $\sum_a \rightarrow \int dt$. For example, the functional analog of the squared norm and dot product are

$$\int dt v^2(t) \quad \text{and} \quad \int dt v(t)u(t). \quad (21)$$

The analog of matrix multiplication for a function is the linear integral operator

$$\int dt' W(t, t') v(t') \quad (22)$$

*linear integral
operator*

with the function values $W(t, t')$ playing the role of the matrix elements W_{ab} . The analog of the identity matrix is the Dirac δ function $\delta(t - t')$ discussed at the end of this section. The analog of a diagonal matrix is a function of two variables that is proportional to a δ function, $W(t, t') = h(t)\delta(t - t')$, for any function h .

All of the vector and matrix operations and properties defined above have functional analogs. Of particular importance are the functional inverse (which is not equivalent to an inverse function) that satisfies

$$\int dt'' W^{-1}(t, t'') W(t'', t') = \delta(t - t'), \quad (23)$$

and the analog of the Töplitz matrix, which is a linear integral operator that is translationally invariant and thus can be written as

$$W(t, t') = K(t - t'). \quad (24)$$

The linear integral operator then takes the form of a linear filter,

$$\int dt' K(t - t') v(t') = \int d\tau K(\tau) v(t - \tau) \quad (25)$$

where we have made the replacement $t' \rightarrow t - \tau$.

The δ Function

Despite its name, the Dirac δ function is not a properly defined function, but rather the limit of a sequence of functions. In this limit, the δ function approaches zero everywhere except where its argument is zero, and there it grows without bound. The infinite height and infinitesimal width of this function are matched so that its integral is one. Thus,

$$\int dt \delta(t) = 1 \quad (26)$$

provided only that the limits of integration surround the point $t=0$ (otherwise the integral is zero). The integral of the product of a δ function with any continuous function f is

$$\int dt' \delta(t - t') f(t') = f(t) \quad (27)$$

for any value of t contained within the integration interval (if t is not within this interval, the integral is zero). These two identities normally

provide enough information to use the δ function in calculations despite its unwieldy definition.

The sequence of functions used to construct the δ function as a limit is not unique. In essence, any function that integrates to one and has a single peak that gets continually narrower and taller as the limit is taken can be used. For example, the δ function can be expressed as the limit of a square pulse

$$\delta(t) = \lim_{\Delta t \rightarrow 0} \begin{cases} 1/\Delta t & \text{if } -\Delta t/2 < t < \Delta t/2 \\ 0 & \text{otherwise} \end{cases} \quad (28)$$

or a Gaussian function

$$\delta(t) = \lim_{\Delta t \rightarrow 0} \frac{1}{\sqrt{2\pi}\Delta t} \exp\left[-\frac{1}{2}\left(\frac{t}{\Delta t}\right)^2\right]. \quad (29)$$

It is most often expressed as

$$\delta(t) = \frac{1}{2\pi} \int_{-\infty}^{\infty} d\omega \exp(i\omega t). \quad (30)$$

*δ function
definition*

This underlies the inverse Fourier transform, as discussed below.

Eigenfunctions

The functional analog of the eigenvector (equation 12) is the eigenfunction $e(t)$ that satisfies

$$\int dt' W(t, t') e(t') = \lambda e(t). \quad (31)$$

For translationally invariant integral operators, $W(t, t') = K(t - t')$, the eigenfunctions are complex exponentials,

$$\int dt' K(t - t') \exp(i\omega t') = \left(\int d\tau K(\tau) \exp(-i\omega\tau) \right) \exp(i\omega t), \quad (32)$$

as can be seen by making the change of variables $\tau = t - t'$. Here $i = \sqrt{-1}$, and the complex exponential is defined by the identity

$$\exp(i\omega t) = \cos(\omega t) + i\sin(\omega t). \quad (33)$$

*complex
exponential*

Comparing equations 31 and 32, we see that the eigenvalue for this eigenfunction is

$$\lambda(\omega) = \int d\tau K(\tau) \exp(-i\omega\tau). \quad (34)$$

In this case, the continuous label ω takes the place of the discrete label μ used to identify the different eigenvalues of a matrix.

A functional analog of expanding a vector using eigenvectors as a basis (equation 14) is the inverse Fourier transform, which expresses a function in an expansion using complex exponential eigenfunctions as a basis. The analog of equation 16 for determining the coefficient functions of this expansion is the Fourier transform.

Fourier Transforms

As outlined in the previous section, Fourier transforms provide a useful representation for functions when they are acted upon by translation invariant linear operators.

The Fourier transform of a function $f(t)$ is a complex function of a real argument ω given by

$$\tilde{f}(\omega) = \int_{-\infty}^{\infty} dt f(t) \exp(i\omega t). \quad (35)$$

The Fourier transform $\tilde{f}(\omega)$ provides a complete description of the original function $f(t)$ because it can be inverted through,

$$f(t) = \frac{1}{2\pi} \int_{-\infty}^{\infty} d\omega \tilde{f}(\omega) \exp(-i\omega t). \quad (36)$$

This provides an inverse because

$$\begin{aligned} & \frac{1}{2\pi} \int_{-\infty}^{\infty} d\omega \exp(-i\omega t) \int_{-\infty}^{\infty} dt' f(t') \exp(i\omega t') \\ &= \int_{-\infty}^{\infty} dt' f(t') \frac{1}{2\pi} \int_{-\infty}^{\infty} d\omega \exp(i\omega(t' - t)) = \int_{-\infty}^{\infty} dt' f(t') \delta(t' - t) = f(t) \end{aligned} \quad (37)$$

by the definition of the δ function in equation 30. The function $f(t)$ has to satisfy regularity conditions called the Dirichlet conditions for the inversion of the Fourier transform to be exact.

The convolution of two functions f and g is the integral

$$h(t) = \int_{-\infty}^{\infty} d\tau f(\tau) g(t - \tau). \quad (38)$$

This is sometimes denoted by $h = f * g$. Note that the operation of multiplying a function by a linear filter and integrating, as in equation 25, is a convolution. Fourier transforms are useful for dealing with convolutions because the Fourier transform of a convolution is the product of the Fourier transforms of the two functions being convolved,

$$\tilde{h}(\omega) = \tilde{f}(\omega) \tilde{g}(\omega). \quad (39)$$

To show this, we note that

$$\begin{aligned}\tilde{h}(\omega) &= \int_{-\infty}^{\infty} dt \exp(i\omega t) \int_{-\infty}^{\infty} d\tau f(\tau) g(t - \tau) \\ &= \int_{-\infty}^{\infty} d\tau f(\tau) \exp(i\omega\tau) \int_{-\infty}^{\infty} dt g(t - \tau) \exp(i\omega(t - \tau)) \\ &= \int_{-\infty}^{\infty} d\tau f(\tau) \exp(i\omega\tau) \int_{-\infty}^{\infty} dt' g(t') \exp(i\omega t') \quad \text{where } t' = t - \tau,\end{aligned}\tag{40}$$

which is equivalent to equation 39. A related result is Parseval's theorem,

$$\int_{-\infty}^{\infty} dt f(t)^2 = \frac{1}{2\pi} \int_{-\infty}^{\infty} d\omega |\tilde{f}(\omega)|^2.\tag{41}$$

If $f(t)$ is periodic, with period T (which means that $f(t + T) = f(t)$ for all t), it can be represented by a Fourier series rather than a Fourier integral. That is

$$f(t) = \sum_{k=-\infty}^{\infty} \tilde{f}_k \exp(-i2\pi kt/T)\tag{42}$$

where \tilde{f}_k is given by:

$$\tilde{f}_k = \frac{1}{T} \int_0^T dt f(t) \exp(i2\pi kt/T).\tag{43}$$

As in the case of Fourier transforms, regularity conditions have to hold for the series to converge and to be exactly invertible. The Fourier series has properties similar to Fourier transforms, including a convolution theorem and a version of Parseval's theorem. The real and imaginary parts of a Fourier series are often separated giving the alternative form

$$f(t) = \tilde{f}_0 + \sum_{k=1}^{\infty} \left(\tilde{f}_k^c \cos(2\pi kt/T) + \tilde{f}_k^s \sin(2\pi kt/T) \right)\tag{44}$$

with

$$\begin{aligned}\tilde{f}_0 &= \frac{1}{T} \int_0^T dt f(t), \quad \tilde{f}_k^c = \frac{2}{T} \int_0^T dt f(t) \cos(2\pi kt/T), \\ \tilde{f}_k^s &= \frac{2}{T} \int_0^T dt f(t) \sin(2\pi kt/T).\end{aligned}\tag{45}$$

When computed numerically, a Fourier transform is typically based on a certain number, N_t , of samples of the function, $f_n = f(n\delta)$ for $n = 0, 1, \dots, N_t - 1$. The discrete Fourier transform of these samples is then used as an approximation of the continuous Fourier transform. The discrete Fourier transform is defined as

$$\tilde{f}_m = \sum_{n=0}^{N_t-1} f_n \exp(i2\pi nm/N_t).\tag{46}$$

Note that $\tilde{f}_{N_t+m} = \tilde{f}_m$. An approximation of the continuous Fourier transform is provided by the relation $\tilde{f}(2\pi m/(N_t\delta)) \approx \delta\tilde{f}_m$. The inverse discrete Fourier transform is

$$f_n = \frac{1}{N_t} \sum_{m=0}^{N_t-1} \tilde{f}_m \exp(-i2\pi mn/N_t). \quad (47)$$

This equation implies a periodic continuation of f_n outside the range $0 \leq n < N_t$, so that $f_{n+N_t} = f_n$ for all n . Consult the references for an analysis of the properties of the discrete Fourier transform and the quality of its approximation to the continuous Fourier transform. Note in particular that there is a difference between the discrete-time Fourier transform, which is the Fourier transform of a signal that is inherently discrete i.e. is only defined at discrete points) and the discrete Fourier transform, given above, which is based on a finite number of samples of an underlying continuous function. If $f(t)$ is band-limited, meaning that $\tilde{f}(\omega) = 0$ for $|\omega| > \pi/\delta$, the sampling theorem states that $f(t)$ is completely determined by regular samples spaced at intervals $1/\delta$.

Fourier transforms of functions of more than one variable involve a direct extension of the equations given above to multi-dimensional integrals. For example,

$$\tilde{f}(\omega_x, \omega_y) = \int dx \int dy f(x, y) \exp(i(\omega_x x + \omega_y y)). \quad (48)$$

The properties of multi-dimensional transforms are similar to those of one-dimensional transforms.

Finding Extrema and Lagrange Multipliers

An operation frequently encountered in the text is minimizing a quadratic form. In terms of vectors, this typically amounts to finding the matrix \mathbf{W} that makes the product $\mathbf{W} \cdot \mathbf{v}$ closest to another vector \mathbf{u} when averaged over a number of presentations of \mathbf{v} and \mathbf{u} . The function to be minimized is the average squared error $\langle |\mathbf{u} - \mathbf{W} \cdot \mathbf{v}|^2 \rangle$, where the brackets denote averaging over all the different samples \mathbf{v} and \mathbf{u} . Taking the derivative of this expression with respect to \mathbf{W} gives the equation

$$\mathbf{W} \cdot \langle \mathbf{v} \mathbf{v} \rangle = \langle \mathbf{u} \mathbf{v} \rangle \quad \text{or} \quad \sum_{c=1}^N W_{ac} \langle v_c v_b \rangle = \langle u_a v_b \rangle. \quad (49)$$

Many variants of this equation, solved by a number of techniques, appear in the text.

Often, when a function $f(\mathbf{v})$ has to be minimized or maximized with respect to a vector \mathbf{v} there is an additional constraint on \mathbf{v} that requires another function $g(\mathbf{v})$ to be held constant. The standard way of dealing with

minimization of quadratic form

*Lagrange
multiplier*

this situation is to find the extrema of the function $f(\mathbf{v}) + \lambda g(\mathbf{v})$ where λ is a free parameter called a Lagrange multiplier. Once this is done, the value of λ is determined by requiring $g(\mathbf{v})$ to take the required constant value. This procedure can appear a bit mysterious when first encountered, so we provide a rather extended discussion.

The condition that characterizes an extreme value of the function $f(\mathbf{v})$ is that small changes $\Delta\mathbf{v}$ (with components Δv_a) in the vector \mathbf{v} should not change the value of the function, to first order in $\Delta\mathbf{v}$. This results in the condition

$$\sum_{a=1}^N f_a \Delta v_a = 0 \quad (50)$$

where we use the notation

$$f_a = [\nabla f]_a = \frac{\partial f}{\partial v_a} \quad (51)$$

to make the equations more compact. Without a constraint, equation 50 must be satisfied for all $\Delta\mathbf{v}$, which can only occur if each term in the sum vanishes separately. Thus, we find the usual condition for an extremum

$$f_a = \frac{\partial f}{\partial v_a} = 0 \quad (52)$$

for all a . However, with a constraint such as $g(\mathbf{v}) = \text{constant}$, equation 50 does not have to hold for all possible $\Delta\mathbf{v}$, only for those that satisfy the constraint. The condition on $\Delta\mathbf{v}$ imposed by the constraint is that it cannot change the value of g , to first order in $\Delta\mathbf{v}$. Therefore,

$$\sum_{a=1}^N g_a \Delta v_a = 0 \quad (53)$$

with the same notation for the derivative used for g as for f .

The most obvious way to deal with the constraint equation 53 is to solve for one of the components of $\Delta\mathbf{v}$, say Δv_c , writing

$$\Delta v_c = -\frac{1}{g_c} \sum_{a \neq c} g_a \Delta v_a. \quad (54)$$

Then, we substitute this expression into equation 50 to obtain

$$\sum_{a \neq c} f_a \Delta v_a - \frac{f_c}{g_c} \sum_{a \neq c} g_a \Delta v_a = 0. \quad (55)$$

Because we have eliminated the constraint, this equation must be satisfied for all values of the remaining components of $\Delta\mathbf{v}$, those with $a \neq c$, and thus we find

$$f_a - \frac{f_c}{g_c} g_a = 0 \quad (56)$$

for all $a \neq c$. The derivatives of f and g are functions of \mathbf{v} , so these equations can be solved to determine where the extremum point is located.

In the above derivation, we have singled out component c for special treatment. We have no way of knowing until we get to the end of the calculation whether the particular c we chose leads to a simple or a complex set of final equations. The clever idea of the Lagrange multiplier is to notice that the whole problem is symmetric with respect to the different components of $\Delta\mathbf{v}$. Choosing one c value, as we did above, breaks this symmetry and often complicates the algebra. To introduce the Lagrange multiplier we simply define it as

$$\lambda = -\frac{f_c}{g_c}. \quad (57)$$

With this notation, the final set of equations can be written as

$$f_a + \lambda g_a = 0. \quad (58)$$

Before we had to say that these equations only held for $a \neq c$ because c was treated differently. Now, however, notice that the above equation when a is set to c is algebraically equivalent to the definition of equation 57. Thus, we can say that equation 58 applies for all a , and this provides a symmetric formulation of the problem of finding an extremum that often results in simpler algebra.

The final realization is that equation 58 for all a is precisely what we would have derived if we had set out in the first place to find an extremum of the function $f(\mathbf{v}) + \lambda g(\mathbf{v})$ and forgot about the constraint entirely. Of course this lunch is not completely free. From equation 58, we derive a set of extremum points parameterized by the undetermined variable λ . To fix λ , we must substitute this family of solutions back into $g(\mathbf{v})$ and find the value of λ that satisfies the constraint that $g(\mathbf{v})$ equals the specified constant. This provides the solution to the constrained problem.

Differential Equations

The most general differential equation we consider takes the form

$$\frac{d\mathbf{v}}{dt} = \mathbf{f}(\mathbf{v}) \quad (59)$$

where $\mathbf{v}(t)$ is an N -component vector of time-dependent variables, and \mathbf{f} is a vector of functions of \mathbf{v} . Unless it is unstable, allowing the absolute value of one or more of the components of \mathbf{v} to grow without bound, this type of equation has three classes of solutions. For one class, called fixed points, $\mathbf{v}(t)$ approaches a time-independent vector \mathbf{v}_∞ ($\mathbf{v}(t) \rightarrow \mathbf{v}_\infty$) as $t \rightarrow \infty$. In a second class of solutions, called limit cycles, $\mathbf{v}(t)$ becomes

*fixed point
limit cycle*

chaos

periodic at large times and repeats itself indefinitely. For the third class of solutions, the chaotic ones, $\mathbf{v}(t)$ never repeats itself but the trajectory of the system lies in a limited subspace of the total space of allowed configurations called a strange attractor. Chaotic solutions are extremely sensitive to initial conditions.

We focus most of our analysis on fixed-point solutions. For \mathbf{v}_∞ to be a time-independent solution of equation 59, which is also called an equilibrium point, we must have $\mathbf{f}(\mathbf{v}_\infty) = 0$. General solutions of equation 59 when \mathbf{f} is nonlinear cannot be constructed, but we can use linear techniques to study the behavior of \mathbf{v} near a fixed point \mathbf{v}_∞ . If \mathbf{f} is linear, the techniques we use and solutions we obtain as approximations in the nonlinear case are exact. Near the fixed point \mathbf{v}_∞ , we write

$$\mathbf{v}(t) = \mathbf{v}_\infty + \boldsymbol{\epsilon}(t) \quad (60)$$

and consider the case when all the components of the vector $\boldsymbol{\epsilon}$ are small. Then, we can expand \mathbf{f} in a Taylor series,

$$\mathbf{f}(\mathbf{v}(t)) \approx \mathbf{f}(\mathbf{v}_\infty) + \mathbf{J} \cdot \boldsymbol{\epsilon}(t) = \mathbf{J} \cdot \boldsymbol{\epsilon}(t) \quad (61)$$

where \mathbf{J} is the called the Jacobian matrix and has elements

$$J_{ab} = \left. \frac{\partial f_a(\mathbf{v})}{\partial v_b} \right|_{\mathbf{v}=\mathbf{v}_\infty}. \quad (62)$$

In the second equality of equation 61, we have used the fact that $\mathbf{f}(\mathbf{v}_\infty) = 0$.

Using the approximation of equation 61, equation 59 becomes

$$\frac{d\boldsymbol{\epsilon}}{dt} = \mathbf{J} \cdot \boldsymbol{\epsilon}. \quad (63)$$

The temporal evolution of $\mathbf{v}(t)$ is best understood by expanding $\boldsymbol{\epsilon}$ in the basis provided by the eigenvectors of \mathbf{J} . Assuming that \mathbf{J} is real and has N linearly independent eigenvectors $\mathbf{e}_1, \dots, \mathbf{e}_N$ with different eigenvalues $\lambda_1, \dots, \lambda_N$, we write

$$\boldsymbol{\epsilon}(t) = \sum_{\mu=1}^N c_\mu(t) \mathbf{e}_\mu. \quad (64)$$

Substituting this into equation 63, we find that the coefficients must satisfy

$$\frac{dc_\mu}{dt} = \lambda_\mu c_\mu. \quad (65)$$

This produces the solution

$$\boldsymbol{\epsilon}(t) = \sum_{\mu=1}^N c_\mu(0) \exp(\lambda_\mu t) \mathbf{e}_\mu \quad (66)$$

*strange attractor**equilibrium point**Taylor series**Jacobian matrix*

where $\epsilon(0) = \sum_\mu c_\mu(0)\mathbf{e}_\mu$. The individual terms in the sum on the right side of equation 66 are called modes. This solution is exact for equation 63, but is only a valid approximation when applied to equation 59 if ϵ is small. Note that the different coefficients c_μ evolve over time independently of each other. This does not require the eigenvectors to be orthogonal. If the eigenvalues and eigenvectors are complex, $\mathbf{v}(t)$ will nonetheless remain real if $\mathbf{v}(0)$ is real, because the complex parts of the conjugate pairs cancel appropriately. Expression 66 is not the correct solution if some of the eigenvalues are equal. The reader should consult the references for the solution in this case.

modes

Equation 66 determines how the evolution of $\mathbf{v}(t)$ in the neighborhood of \mathbf{v}_∞ depends on the eigenvalues of \mathbf{J} . If we write $\lambda_\mu = \alpha_\mu + i\omega_\mu$,

$$\exp(\lambda_\mu t) = \exp(\alpha_\mu t) (\cos(\omega_\mu t) + i \sin(\omega_\mu t)). \quad (67)$$

This implies that modes with real eigenvalues ($\omega_\mu = 0$) evolve exponentially over time, and modes with complex eigenvalues ($\omega_\mu \neq 0$) oscillate with a frequency ω_μ . Recall that the eigenvalues are always real if \mathbf{J} is a symmetric matrix. Modes with negative real eigenvalues ($\alpha_\mu < 0$ and $\omega_\mu = 0$) decay exponentially to zero, while those with positive real eigenvalues ($\alpha_\mu > 0$ and $\omega_\mu = 0$) grow exponentially. Similarly, the oscillations for modes with complex eigenvalues are damped exponentially to zero if the real part of the eigenvalue is negative ($\alpha_\mu < 0$ and $\omega_\mu \neq 0$) and grow exponentially if the real part is positive ($\alpha_\mu > 0$ and $\omega_\mu \neq 0$).

Stability of the fixed point \mathbf{v}_∞ requires the real parts of all the eigenvalues to be negative ($\alpha_\mu < 0$ for all μ). In this case, the point \mathbf{v}_∞ is a stable fixed-point attractor of the system, meaning that $\mathbf{v}(t)$ will approach \mathbf{v}_∞ if it starts from any point in the neighborhood of \mathbf{v}_∞ . If any real part is positive ($\alpha_\mu > 0$ for any μ), the fixed point is unstable. Almost any $\mathbf{v}(t)$ initially in the neighborhood of \mathbf{v}_∞ will move away from that neighborhood. If f is linear, the exponential growth of $|\mathbf{v}(t) - \mathbf{v}_\infty|$ never stops in this case. For a nonlinear f , equation 66 only determines what happens in the neighborhood of \mathbf{v}_∞ , and the system may ultimately find a stable attractor away from \mathbf{v}_∞ , either a fixed point, a limit cycle, or a chaotic attractor. In all these cases, the mode for which the real part of λ_μ takes the largest value dominates the dynamics as $t \rightarrow \infty$. If this real part is equal to zero, the fixed point is called marginally stable.

attractor

unstable fixed point

marginal stability

As mentioned previously, the analysis presented above as an approximation for nonlinear differential equations near a fixed point is exact if the original equation is linear. In the text, we frequently encounter linear equations of the form

$$\tau \frac{dv}{dt} = v_\infty - v. \quad (68)$$

This can be solved by setting $z = v - v_\infty$, rewriting the equation as $dz/z =$

$-dt/\tau$ and integrating both sides

$$\tau \int_{z(0)}^{z(t)} dz' \frac{1}{z'} = \ln\left(\frac{z(t)}{z(0)}\right) = -\frac{t}{\tau}. \quad (69)$$

This gives $z(t) = z(0) \exp(-t/\tau)$ or

$$v(t) = v_\infty + (v(0) - v_\infty) \exp(-t/\tau). \quad (70)$$

In some cases, we consider discrete rather than continuous dynamics defined over discrete steps $n = 1, 2, \dots$ through a difference rather than a differential equation. Linearization about equilibrium points can be used to analyze nonlinear difference equations as well as differential equations, and this reveals similar classes of behavior. We illustrate difference equations by analyzing a linear case,

difference equation

$$\mathbf{v}(n+1) = \mathbf{v}(n) + \mathbf{W} \cdot \mathbf{v}(n). \quad (71)$$

The strategy for solving this equation is similar to that for solving differential equations. Assuming \mathbf{W} has a complete set of linearly independent eigenvectors $\mathbf{e}_1, \dots, \mathbf{e}_N$ with different eigenvalues $\lambda_1, \dots, \lambda_N$, the modes separate, and the general solution is

$$\mathbf{v}(n) = \sum_{\mu=1}^N c_\mu (1 + \lambda_\mu)^n \mathbf{e}_\mu \quad (72)$$

where $\mathbf{v}(0) = \sum_\mu c_\mu \mathbf{e}_\mu$. This has characteristics similar to equation 66. Writing $\lambda_\mu = \alpha_\mu + i\omega_\mu$, mode μ is oscillatory if $\omega_\mu \neq 0$. In the discrete case, stability of the system is controlled by the magnitude

$$|1 + \lambda_\mu|^2 = (1 + \alpha_\mu)^2 + (\omega_\mu)^2. \quad (73)$$

If this is greater than one for any value of μ , $|\mathbf{v}(n)| \rightarrow \infty$ as $n \rightarrow \infty$. If it is less than one for all μ , $\mathbf{v}(n) \rightarrow \mathbf{0}$ in this limit.

Electrical Circuits

Biophysical models of single cells involve equivalent circuits composed of resistors, capacitors, and voltage and current sources. We review here basic results for such circuits. Figures 1A & B show the standard symbols for resistors and capacitors, and define the relevant voltages and currents. A resistor (figure 1A) satisfies Ohm's law, which states that the voltage $V_R = V_1 - V_2$ across a resistance R carrying a current I_R is

Ohm's law

$$V_R = I_R R. \quad (74)$$

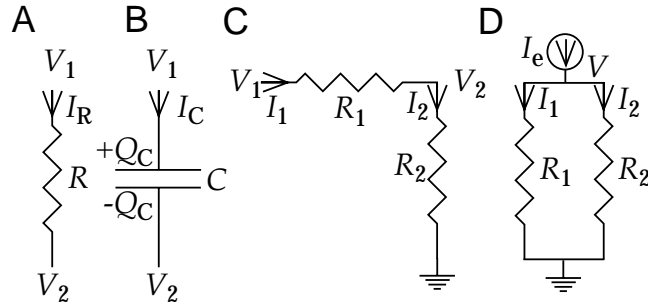


Figure 1: Electrical circuit elements and resistor circuits. A) Current I_R flows through a resistance R producing a voltage drop $V_1 - V_2 = V_R$. B) Charge $\pm Q_C$ is stored across a capacitance C leading to a voltage $V_C = V_1 - V_2$ and a current I_C . C) Series resistor circuit called a voltage divider. D) Parallel resistor circuit. I_e represents an external current source. The lined triangle symbol at the bottom of the circuits in C & D represents an electrical ground, which is defined to be at zero voltage.

Resistance is measured in ohms (Ω) defined as the resistance through which one ampere of current causes a voltage drop of one volt ($1 \text{ V} = 1 \text{ A} \times 1 \Omega$).

A capacitor (figure 1B) stores charge across an insulating medium, and the voltage across it $V_C = V_1 - V_2$ is related to the charge it stores Q_C by

$$CV_C = Q_C \quad (75)$$

where C is the capacitance. Electrical current cannot cross the insulating medium, but charges can be redistributed on each side of the capacitor, which leads to the flow of current. We can take a time derivative of both sides of equation 75 and use the fact that current is equal to the rate of change of charge, $I_C = dQ_C/dt$, to obtain the basic voltage-current relationship for a capacitor,

$$C \frac{dV_C}{dt} = I_C. \quad (76)$$

Capacitance is measured in units of farads (F) defined as the capacitance for which one ampere of current causes a voltage change of one volt per second ($1 \text{ F} \times 1 \text{ V/s} = 1 \text{ A}$).

The voltages at different points in a circuit and the currents flowing through various circuit elements can be computed using equations 74 and 76 and rules called Kirchoff's laws. These state that: 1) voltage differences around any closed loop in a circuit must sum to zero, and 2) the sum of all the currents entering any point in a circuit must be zero. Applying the second of these rules to the circuit in figure 1C, we find that $I_1 = I_2$. Ohm's law tells us that $V_1 - V_2 = I_1 R_1$ and $V_2 = I_2 R_2$. Solving these gives

V-I relation for capacitor

Kirchoff's laws

$V_1 = I_1(R_1 + R_2)$, which tells us that resistors arranged in series add, and $V_2 = V_1 R_2 / (R_1 + R_2)$, which is why this circuit is called a voltage divider.

In the circuit of figure 1D, we have added an external source passing the current I_e . For this circuit, Kirchoff's and Ohm's laws tell us that $I_e = I_1 + I_2 = V/R_1 + V/R_2$. This indicates how resistors add in parallel, $V = I_e R_1 R_2 / (R_1 + R_2)$.

Next, we consider the electrical circuit in figure 2A, in which a resistor and capacitor are connected together. Kirchoff's laws require that $I_C + I_R = 0$. Putting this together with equations 74 and 76, we find

$$C \frac{dV}{dt} = I_C = -I_R = -\frac{V}{R}. \quad (77)$$

Solving this, gives

$$V(t) = V(0) \exp(-t/RC) \quad (78)$$

showing the exponential decay (with time constant $\tau = RC$) of the initial voltage $V(0)$ as the charge on the capacitor leaks out through the resistor.

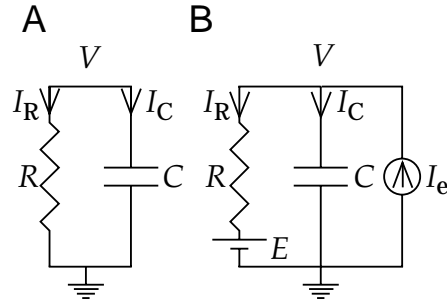


Figure 2: RC circuits. A) Current $I_C = -I_R$ flows in the resistor-capacitor circuit as the stored charge is released. B) Simple passive membrane model including a potential E and current source I_e . As in figure 1, the lined triangles represent a ground or point of zero voltage.

Figure 2B includes two extra components needed to build a simple model neuron, the voltage source E and the current source I_e . Using Kirchoff's laws, $I_e - I_C - I_R = 0$, and the equation for the voltage V is

$$C \frac{dV}{dt} = \frac{E - V}{R} + I_e. \quad (79)$$

If I_e is constant, the solution of this equation is

$$V(t) = V_\infty + (V(0) - V_\infty) \exp(-t/\tau) \quad (80)$$

where $V_\infty = E + RI_e$ and $\tau = RC$. This shows exponential relaxation from the initial potential $V(0)$ to the equilibrium potential V_∞ at a rate governed by the time constant τ of the circuit.

For the case $I_e = I \cos(\omega t)$, once an initial transient has decayed to zero, we find

$$V(t) = E + \frac{RI \cos(\omega t - \phi)}{\sqrt{1 + \omega^2 \tau^2}} \quad (81)$$

where $\tan(\phi) = \omega\tau$. Equation 81 shows that the cell membrane acts as a low pass filter, because the higher the frequency ω of the input current, the more the attenuation of the oscillations of the potential due to the factor $1/\sqrt{1 + \omega^2 \tau^2}$. The phase shift ϕ is an increasing function of frequency that approaches $\pi/2$ as $\omega \rightarrow \infty$.

Probability Theory

Probability distributions and densities are discussed extensively in the text. Here, we present a slightly more formal treatment. At the heart of probability theory lie two sets; a sample space, Ω and a measure. We begin by considering the simplest case in which the sample space is finite. In this case, each element ω of the full sample space Ω can be thought of as one of the possible outcomes of a random process, for example one results of rolling five dice. The measure assigns a number γ_ω to each outcome ω , and these must satisfy $0 \leq \gamma_\omega \leq 1$ and $\sum_\omega \gamma_\omega = 1$.

We are primarily interested in random variables (which are infamously neither random nor variable). A random variable is a mapping from a random outcome ω to a space such as the space of integers. An example is the number of ones that appear when five dice are rolled. Typically, a capital letter, such as S , is used for the random variable, and the corresponding lower case letter, s in this case, is used for a particular value it might take. The probability that S takes the value s is then written as $P[S = s]$. In the text, we typically shorten this to $P[s]$, but here we keep the full notation (except in the following table). $P[S = s]$ is determined by the measures of the events for which $S = s$ and takes the value

$$P[S = s] = \sum_{\substack{\omega \text{ with} \\ S(\omega)=s}} \gamma_\omega. \quad (82)$$

The notation $S(\omega)$ refers to the value of S generated by the random event labeled by ω , and the sum is over all events for which $S(\omega) = s$.

Some key statistics for discrete random variables include:

Quantity	Definition	Alias
mean	$\langle s \rangle = \sum_s P[s]s$	$\bar{s}, E[S]$
variance	$\text{var}(S) = \langle s^2 \rangle - \langle s \rangle^2 = \sum_s P[s]s^2 - \langle s \rangle^2$	$\sigma_s^2, V[S]$
covariance	$\langle s_1 s_2 \rangle - \langle s_1 \rangle \langle s_2 \rangle = \sum_{s_1 s_2} P[s_1, s_2]s_1 s_2 - \langle s_1 \rangle \langle s_2 \rangle$	$\text{cov}(S_1, S_2)$

where S_1 and S_2 are two random variables defined over the same sample space. This links the two random variables, in that

$$P[S_1=s_1, S_2=s_2] = \sum_{\substack{\omega \text{ with} \\ S_1(\omega)=s_1, \\ S_2(\omega)=s_2}} \gamma_\omega, \quad (83)$$

and provides a basis for them to be correlated. Means are additive,

$$\langle s_1 + s_2 \rangle = \langle s_1 \rangle + \langle s_2 \rangle, \quad (84)$$

but other quantities are typically not, for example

$$\text{var}(S_1 + S_2) = \text{var}(S_1) + \text{var}(S_2) + 2\text{cov}(S_1, S_2). \quad (85)$$

Two random variables are independent if $P[S_1 = s_1, S_2 = s_2] = P[S_1 = s_1]P[S_2 = s_2]$ for all s_1 and s_2 . If S_1 and S_2 are independent, $\text{cov}(S_1, S_2) = 0$, but the converse is not generally true.

Sample spaces can be infinite or uncountable. In the latter case, there are technical complications that are discussed in the references, but all the sums in the expressions for discrete sample spaces turn into integrals. Under suitable regularity conditions, a continuous random variable S , which is a mapping from a sample space to a continuous space such as the real numbers, has a probability density function $p[s]$ defined by

$$p[s] = \lim_{\Delta s \rightarrow 0} \left(\frac{P[s \leq S \leq s + \Delta s]}{\Delta s} \right). \quad (86)$$

Quantities such as the mean and variance of a continuous random variable are defined as for a discrete random variable but involve integrals over probability densities rather than sums over probabilities.

Some commonly used discrete and continuous distributions are:

Name	Range of s	Probability	Mean	Variance
Bernoulli	0 or 1	$p^s(1-p)^{1-s}$	p	$p(1-p)$
Poisson	positive integer	$\alpha^s \exp(-\alpha)/s!$	α	α
Exponential	$s > 0$	$\alpha \exp(-\alpha s)$	$1/\alpha$	$1/\alpha^2$
Gaussian	$-\infty < s < \infty$	$N[s; g, \Sigma]$	g	Σ
Cauchy	$-\infty < s < \infty$	$\frac{\beta}{\pi((s-\alpha)^2+\beta^2)}$	α	∞

where

$$N(s; g, \Sigma) = \frac{1}{\sqrt{2\pi\Sigma}} \exp\left(-\frac{(s-g)^2}{2\Sigma}\right). \quad (87)$$

Here, we use Σ to denote the variance of the Gaussian distribution, which is more often written as σ^2 . The Cauchy distribution has such heavy tails that the integral defining its variance does not converge.

The Gaussian distribution is particularly important because of the central limit theorem. Consider m continuous random variables $S_1, S_2, S_3, \dots, S_m$ that are independent and have identical distributions with finite mean g and variance σ^2 . Defining

$$z_m = \frac{1}{m} \sum_{k=1}^m S_k, \quad (88)$$

the central limit theorem states that, under rather general conditions,

$$\lim_{m \rightarrow \infty} P\left[\frac{\sqrt{m}(z_m - g)}{\sigma} \leq s\right] = \frac{1}{\sqrt{2\pi}} \int_{-\infty}^s dz \exp(-z^2/2) \quad (89)$$

for every s . This means that, for large m , z_m should be approximately Gaussian distributed with mean g and variance σ^2/m .

Annotated Bibliography

Most of the material in this chapter is covered in standard texts on mathematical methods such as Mathews & Walker (1971); Boas (1996). Discussion of relevant computational techniques, and code for implementing them, is available in Press et al. (1992). Linear algebra is covered by Strang (1976); linear and non-linear differential equations by Jordan & Smith (1977); probability theory by Feller (1968); and Fourier transforms and the analysis of linear systems and electrical circuits by Siebert (1986); Oppenheim & Willsky (1997). Mathematical approaches to biological problems are described in Edelstein-Keshet (1988); Murray (1993). Modern techniques of mathematical modeling are described by Gershenfeld (1999).

General references for the other bodies of techniques used in the book include, for statistics, Lindgren (1993) and Cox & Hinckley (1974); and, for information theory, Cover & Thomas (1991).

Exercises

Chapter 1

1. Generate spike sequences with a constant firing rate r_0 using a Poisson spike generator. Then, add a refractory period to the model by allowing the firing rate $r(t)$ to depend on time. Initially, $r(t) = r_0$. After every spike, set $r(t)$ to zero. Allow it to recover exponentially back to r_0 by setting $r(t + \Delta t) = r_0 + (r(t) - r_0) \exp(-\Delta t/\tau_{\text{ref}})$ after every simulation time step Δt in which no spike occurs. The constant τ_{ref} controls the refractory recovery rate. Initially, use $\tau_{\text{ref}} = 10$ ms. Compute the Fano factor and coefficient of variation, and plot the interspike interval histogram for spike trains generated without a refractory period and with a refractory period determined by τ_{ref} over the range from 1 to 20 ms.
2. Plot autocorrelation histograms of spike trains generated by a Poisson generator with A) a constant fire rate of 100 Hz, B) a constant firing rate of 100 Hz and a refractory period modeled as in exercise 1 with $\tau_{\text{ref}} = 10$ ms, and C) a variable firing rate $r(t) = 100(1 + \cos(2\pi t/25 \text{ ms}))$ Hz. Plot the histograms over a range from 0 to 100 ms.
3. Generate a Poisson spike train with a time-dependent firing rate $r(t) = 100(1 + \cos(2\pi t/300 \text{ ms}))$ Hz. Approximate the firing rate from this spike train by making the update $r_{\text{approx}} \rightarrow r_{\text{approx}} + 1/\tau_{\text{approx}}$ every time a spike occurs, and letting r_{approx} decay exponentially, $r_{\text{approx}} \rightarrow r_{\text{approx}} \exp(-\Delta t/\tau_{\text{approx}})$, if no spike occurs during a time step of size Δt . Make a plot the average squared error of the estimate, $\int dt (r(t) - r_{\text{approx}}(t))^2$ as a function of τ_{approx} and find the value of τ_{approx} that produces the most accurate estimate for this firing pattern.
4. Using the same spike trains as in exercise 3, construct estimates of the firing rate using square, Gaussian, and other types of window functions to see which gives the most accurate estimate.
5. For a constant rate Poisson process, every sequence of N spikes occurring during a given time interval is equally likely. This seems paradoxical because we certainly do not expect to see all N spikes appearing within the first 1% of the time interval. Yet this seems as likely as any other pattern. Resolve this paradox.
6. Build a white-noise stimulus. Plot its autocorrelation function and power spectrum, which should be flat. Discuss the range of relation of these results to those for an ideal white-noise stimulus given the value of Δt you used in constructing the stimulus.
7. Construct two spiking models using an estimate of the firing rate and a Poisson spike generator. In the first model, let the firing rate

be determined in terms of the stimulus s by $r_{\text{est}}(t) = [s]_+$. In the second model, the firing rate is determined instead by integrating the equation (see Appendix A of chapter 5 for a numerical integration method)

$$\tau_r \frac{dr_{\text{est}}(t)}{dt} = [s]_+ - r_{\text{est}}(t) \quad (1)$$

with $\tau_r = 10$ ms. In both cases, use a Poisson generator to produce spikes at the rate $r_{\text{est}}(t)$. Compare the responses of the two models to a variety of time-dependent stimuli including approximate white-noise, and study the responses to both slowly and rapidly varying stimuli.

8. Use the two models constructed in exercise 7, driven with an approximate white-noise stimulus, to generate spikes, and compute the spike-triggered average stimulus for each model. Show how the spike-triggered average depends on τ_r in the second model by considering different values of τ_r .

Chapter 2

1. Build a model neuron (based on the electrosensory lateral-line lobe neuron discussed in chapter 1) using a Poisson generator firing at a rate predicted by equation ?? with $r_0 = 50$ Hz and

$$D(\tau) = \cos\left(\frac{2\pi(\tau - 20 \text{ ms})}{140 \text{ ms}}\right) \exp\left(-\frac{\tau}{60 \text{ ms}}\right) \text{ Hz.}$$

Use a Gaussian white noise stimulus constructed using a time interval $\Delta t = 10$ ms with $\sigma_s^2 = 10$. Compute the firing rate and spike train for a 10 s period. From these results, compute the spike-triggered average stimulus $C(\tau)$ and the firing rate-stimulus correlation function $Q_{rs}(\tau)$ and compare them with the linear kernel given above. Verify that the relations in equation ?? hold. Repeat this exercise with a static nonlinearity so that the firing rate is given by

$$r(t) = 10 \left| r_0 + \int_0^\infty d\tau D(\tau) s(t - \tau) \right|^{1/2} \text{ Hz}$$

rather than by equation ?? . Show that $C(\tau)$ and $Q_{rs}(-\tau)$ are still proportional to $D(\tau)$ in this case, though with a different proportionality constant.

2. For a Gaussian random variable x with zero mean and standard deviation σ , prove that

$$\langle x F(\alpha x) \rangle = \alpha \sigma^2 \langle F'(\alpha x) \rangle$$

where α is a constant, F is any function, F' is its derivative,

$$\langle xF(\alpha x) \rangle = \int dx \frac{1}{\sqrt{2\pi}\sigma} \exp\left(-\frac{x^2}{2\sigma^2}\right) xF(\alpha x),$$

and similarly for $\langle F'(\alpha x) \rangle$. By extending this basic result first to multivariate functions and then to the functionals, the identity ?? can be derived.

3. Using the inverses of equations ?? and ??

$$\epsilon = \epsilon_0 (\exp(X/\lambda) - 1) \quad \text{and} \quad a = -\frac{180^\circ(\epsilon_0 + \epsilon)Y}{\lambda\epsilon\pi},$$

map from cortical coordinates back to visual coordinates and determine what various patterns of activity in the primary visual cortex would 'look like'. Consider straight lines and bands of constant activity extending across the cortex at various angles. Ermentrout and Cowan (1979) used these results as a basis of a mathematical theory of visual hallucinations.

4. Compute the integrals in equations ?? and ?? for the case $\sigma_x = \sigma_y = \sigma$ to obtain the results

$$\begin{aligned} L_s &= \frac{A}{2} \exp\left(-\frac{\sigma^2(k^2 + K^2)}{2}\right) (\cos(\phi - \Phi) \exp(\sigma^2 k K \cos(\Theta)) \\ &\quad + \cos(\phi + \Phi) \exp(-\sigma^2 k K \cos(\Theta))) . \end{aligned}$$

and

$$L_t(t) = \frac{\alpha^6 |\omega| \sqrt{\omega^2 + 4\alpha^2}}{(\omega^2 + \alpha^2)^4} \cos(\omega t - \delta).$$

with

$$\delta = \arctan\left(\frac{\omega}{\alpha}\right) + 8 \arctan\left(\frac{2\alpha}{\omega}\right) - \pi.$$

and verify the selectivity curves in figures ?? and ???. In addition, plot δ as a function of ω . The integrals can be also be done numerically to obtain these curves directly.

5. Compute the response of a model simple cell with a separable space-time receptive field to a moving grating

$$s(x, y, t) = \cos(Kx - \omega t) .$$

For D_s use equation ?? with $\sigma_x = \sigma_y = 1^\circ$, $\phi = 0$, and $1/k = 0.5^\circ$. For D_t use equation ?? with $\alpha = 1/(15 \text{ ms})$. Compute the linear estimate of the response given by equation ?? and assume that the actual response is proportional to a rectified version of this linear response estimate. Plot the response as a function of time for $1/K = 1/k = 0.5^\circ$ and $\omega = 8\pi/\text{s}$. Plot the response amplitude as a function of ω for $1/K = 1/k = 0.5^\circ$ and as a function of K for $\omega = 8\pi/\text{s}$.

6. Construct a model simple cell with the nonseparable space-time receptive field described in the caption of figure ??B. Compute its response to the moving grating of exercise 4. Plot the amplitude of the response as a function of the velocity of the grating, ω/K , using $\omega = 8\pi/\text{s}$ and varying K to obtain a range of both positive and negative velocity values (use negative K values for this).
7. Compute the response of a model complex cell to the moving grating of exercise 5. The complex cell should be modeled by squaring the linear response estimate of the simple cell used in exercise 5, and adding this to the square of the response of a second simple cell with identical properties except that its spatial phase preference is $\phi = -\pi/2$ instead of $\phi = 0$. Plot the response as a function of time for $1/K = 1/k = 0.5^\circ$ and $\omega = 8\pi/\text{s}$. Plot the response amplitude as a function of ω for $1/K = 1/k = 0.5^\circ$ and as a function of K for $\omega = 8\pi/\text{s}$.
8. Construct a model complex cell that is disparity tuned but insensitive to the absolute position of a grating. The complex cell is constructed by summing the squares of the responses of two simple cells, but disparity effects are now included. For this exercise, we ignore temporal factors and only consider the spatial dependence of the response. Each simple cell response is composed of two terms that correspond to inputs coming from the left and right eyes. Because of disparity, the spatial phases of the image of a grating in the two eyes, Φ_L and Φ_R , may be different. We write the spatial part of the linear response estimate for a grating with the preferred spatial frequency ($k = K$) and orientation ($\Theta = \theta = 0$) as

$$L_1 = \frac{A}{2} (\cos(\Phi_L) + \cos(\Phi_R))$$

assuming that $\phi = 0$ (this equation is a generalization of ??). Let the complex cell response be proportional to $L_1^2 + L_2^2$ where L_2 is similar to L_1 but with the cosine functions replaced by sine functions. Show that the response of this neuron is tuned to the disparity, $\Phi_L - \Phi_R$, and is independent of the absolute spatial phase of the grating, $\Phi_L + \Phi_R$. Plot the response tuning curve as a function of disparity. (See Ohzawa *et al.*, 1991).

9. Determine the selectivity of the LGN receptive field of equation ?? to spatial frequency and of the temporal response function for LGN neurons, equation ??, to temporal frequency by computing their integrals when multiplied by cosine functions of space or time respectively. Use $\sigma_c = 0.3^\circ$, $\sigma_s = 1.5^\circ$, $B = 5$, $1/\alpha = 16 \text{ ms}$, and $1/\beta = 64 \text{ ms}$. Plot the resulting spatial and temporal frequency tuning curves.
10. Construct the Hubel-Wiesel simple and complex cell models of figure ???. Use difference-of-Gaussian and Gabor functions to model the LGN and simple cell response. Plot the spatial receptive field of the

simple cell constructed in this way. Compare the result of summing appropriately placed LGN center-surround receptive fields (figure ??A) with the results of the Gabor filter model of the simple cell that uses the spatial kernel of equation ?? . Compare the responses of a complex cell constructed by linearly summing the outputs of simple cells (figure ??B) with different spatial phase preferences with the complex cell model obtained by squaring and summing two simple cell responses with spatial phases 90° apart as in equation ??.

Chapter 3

1. Suppose that the probabilities that a neuron responds with a firing rate between r and $r + \Delta r$ to two stimuli labeled plus and minus are $p[r|\pm]\Delta r$ where

$$p[r|\pm] = \frac{1}{\sqrt{2\pi}\sigma_r} \exp\left(-\frac{1}{2}\left(\frac{r - \langle r \rangle_{\pm}}{\sigma_r}\right)^2\right).$$

Assume that the two mean rate parameters $\langle r \rangle_+$ and $\langle r \rangle_-$ and the single variance σ_r^2 are chosen so that these distributions produce negative rates rarely enough that we can ignore this problem. Show that

$$\alpha(z) = \frac{1}{2} \operatorname{erfc}\left(\frac{z - \langle r \rangle_-}{\sqrt{2}\sigma_r}\right) \quad \text{and} \quad \beta(z) = \frac{1}{2} \operatorname{erfc}\left(\frac{z - \langle r \rangle_+}{\sqrt{2}\sigma_r}\right)$$

and that the probability of a correct answer in a two-alternative forced choice task is given by equation ?? . Derive the result of equation ?? . Plot ROC curves for different values of the discriminability

$$d' = \frac{\langle r \rangle_+ - \langle r \rangle_-}{\sigma_r}.$$

By simulation, determine the fraction of correct discriminations that can be made in a two-alternative forced choice task involving discriminating between plus-then-minus and minus-then-plus presentations of two stimuli. Show that the fractions of correct answer for different values of d' are equal to the areas under the corresponding ROC curves.

2. Model the responses of the cercal system of the cricket by using the tuning curves of equation ?? to determine mean response rates and generating spikes with a Poisson generator. Simulate a large number of responses for a variety of wind directions randomly, use the vector method to decode them on the basis of spike counts over a predefined trial period, and compare the decoded direction with the actual direction used to generate the responses to determine the decoding accuracy. Plot the root-mean-square decoding error as a function of wind direction for several different trial durations. The results may not match those of figure ?? because a different model of variability was used in that analysis.

3. Show that if an infinite number of unit vectors \vec{c}_a is chosen from a probability distribution that is independent of direction, $\sum(\vec{v} \cdot \vec{c}_a)\vec{c}_a \propto \vec{v}$ for any vector \vec{v} . How does the sum approach this limit for a finite number of terms?
4. Show that the Bayesian estimator that minimizes the expected average value of the loss function $L(s, s_{\text{bayes}}) = (s - s_{\text{bayes}})^2$ is the mean given by equation ?? and that the median corresponds to minimizing the expected loss function $L(s, s_{\text{bayes}}) = |s - s_{\text{bayes}}|$.
5. Simulate the response of a set of M1 neurons to a variety of arm movement directions using the tuning curves of equation ?? with randomly chosen preferred directions, and a Poisson spike generator. Choose the arm movement directions and preferred directions to lie in a plane so that they are characterized by a single angle. Study how the accuracy of the vector decoding method depends on the number of neurons used. Compare these results with those obtained using the ML method by solving equation ?? numerically.
6. Show that the formulas for the Fisher information in equation ?? and also be written as

$$I_F(s) = \left\langle \left(\frac{\partial \ln p[\mathbf{r}|s]}{\partial s} \right)^2 \right\rangle = \int d\mathbf{r} p[\mathbf{r}|s] \left(\frac{\partial \ln p[\mathbf{r}|s]}{\partial s} \right)^2$$

or

$$I_F(s) = \int d\mathbf{r} \frac{1}{p[\mathbf{r}|s]} \left(\frac{\partial p[\mathbf{r}|s]}{\partial s} \right)^2.$$

Use the fact that $\int d\mathbf{r} p[\mathbf{r}|s] = 1$.

7. The discriminability for the variable Z defined in equation ?? is the difference between the average Z values for the two stimuli $s + \Delta s$ and s divided by the standard deviation of Z . The average of the difference in Z values is

$$\langle \Delta Z \rangle = \int d\mathbf{r} \frac{\partial \ln p[\mathbf{r}|s]}{\partial s} (p[\mathbf{r}|s + \Delta s] - p[\mathbf{r}|s]).$$

Show that for small Δs , $\langle \Delta Z \rangle = I_F(s)\Delta s$. Also prove that the average value of Z ,

$$\langle Z \rangle = \int d\mathbf{r} p[\mathbf{r}|s] \frac{\partial \ln p[\mathbf{r}|s]}{\partial s}$$

is zero and that the variance of Z is $I_F(s)$. Computing the ratio, we find from these results that $d' = \Delta s \sqrt{I_F(s)}$ which matches the discriminability ?? of the ML estimator.

-
8. Extend equation ?? to the case of neurons encoding a D -dimensional vector stimulus \vec{s} with tuning curves given by

$$f_a(\vec{s}) = r_{\max} \exp\left(-\frac{|\vec{s} - \vec{s}_a|^2}{2\sigma_r^2}\right)$$

and perform the sum by approximating it as an integral over uniformly and densely distributed values of \vec{s}_a to derive the result in equation ??.

9. Derive equation ?? by minimizing the expression ?? . Use the methods of Appendix A in chapter 2.
10. Use the electric fish model from problem 1 of chapter 2 to generate a spike train response to a stimulus $s(t)$ of your choosing. Decode the spike train and reconstruct the stimulus using an optimal linear filter. Compare the optimal decoding filter with the optimal kernel for rate prediction, $D(\tau)$. Determine the average squared error of your reconstruction of the stimulus. Examine the effect that various static nonlinearities in the model for the firing rate that generates the spikes have on the accuracy of the decoding.

Chapter 4

1. Show that the distribution that maximizes the entropy when the firing rate is constrained to lie in the range $0 \leq r \leq r_{\max}$ is given by equation ?? and its entropy for a fixed resolution Δr is given by equation ?? . Use a Lagrange multiplier (chapter 12) to constrain the integral of $p[r]$ to one.
2. Show that the distribution that maximizes the entropy when the mean of the firing rate is held fixed is an exponential, and compute its entropy for a fixed resolution Δr . Assume that the firing rate can fall anywhere in the range from zero to infinity. Use Lagrange multipliers (chapter 12) to constrain the integral of $p[r]$ to one and the integral of $p[r]r$ to the fixed average firing rate.
3. Show that the distribution that maximizes the entropy when the mean and variance of the firing rate are held fixed is a Gaussian, and compute its entropy for a fixed resolution Δr . To simplify the mathematics, allow the firing rate to take any value between minus and plus infinity. Use Lagrange multipliers (chapter 12) to constrain the integral of $p[r]$ to one, the integral of $p[r]r$ to the fixed average firing rate, and the integral of $p[r](r - \langle r \rangle)^2$ to the fixed variance.
4. Using Fourier transforms solve equation ?? to obtain the result of equation ?? .

5. Suppose the filter $L_s(\vec{a})$ has a correlation function that satisfies equation ?? . We write a new filter in terms of this old one by

$$L'_s(\vec{a}) = \int d\vec{c} U(\vec{a}, \vec{c}) L_s(\vec{c}). \quad (2)$$

Show that if $U(\vec{a}, \vec{c})$ satisfies the condition of an orthogonal transformation,

$$\int d\vec{c} U(\vec{a}, \vec{c}) U(\vec{b}, \vec{c}) = \delta(\vec{a} - \vec{b}), \quad (3)$$

the correlation function for this new filter also satisfies equation ??.

6. Construct an integrate-and-fire neuron model, and drive it with an injected current consisting of the sum of two or more sine waves with incommensurate frequencies. Compute the rate of information about the injected current contained in the spike train produced by this model neuron the method discussed in the text.

Chapter 5

1. Write down the analytic solution of equation ?? when $I_e(t)$ is an arbitrary function of time. The solution will involve integrals that cannot be performed unless $I_e(t)$ is specified.
2. Construct the model of two, coupled integrate-and-fire model neurons of figure ?? . Show how the pattern of firing for the two neurons depends on the strength, type (excitatory or inhibitory), and time constant of the reciprocal synaptic connection (see Van Vreeswijk *et al*, 1994).
3. Plot the firing frequency as a function of constant electrode current for the Hodgkin-Huxley model. Show that the firing rate jumps discontinuously from zero to a finite value when the current passes through the minimum value required to produce sustained firing.
4. Demonstrate postinhibitory rebound in the Hodgkin-Huxley model.
5. The Nernst equation was derived in this chapter under the assumption that the membrane potential was negative and the ion being considered was positively charged. Rederive the Nernst equation, ?? , for a negatively charged ion and for the case when E is positive to verify that it applies in all these cases.
6. Compute the value of the release probability P_{rel} at the time of each presynaptic spike for a regular, periodic, constant-frequency presynaptic spike train as a function of the presynaptic firing rate. Do this for both the depression and facilitation models discussed in the text.

7. Verify that the state probabilities listed after equation ?? are actually a solution of these equations if n satisfies equation ?? . Show that an arbitrary set of initial values for these probabilities, will ultimately settle into this solution.
8. Construct and simulate the K^+ channel model of figure ?? . Plot the mean squared deviation between the current produced by N such model channels and the Hodgkin-Huxley current as a function of N , matching the amplitude of the Hodgkin-Huxley model so that the mean currents are the same.
9. Construct and simulate the Na^+ channel model of figure ?? . Compare the current through 100 such channels with the current predicted by the Hodgkin-Huxley model at very short times after a step-like depolarization of the membrane potential. What are the differences and why do they occur?

Chapter 6

Chapter 7

Chapter 8

Chapter 9

Chapter 10

Chapter 11

Chapter 12